

Structural Engineering Report No. ST-03-1

**DAMAGE ASSESSMENT OF CONCRETE-FILLED
STEEL TUBE MEMBERS AND FRAMES
FOR PERFORMANCE-BASED DESIGN**

Cenk Tort and Jerome F. Hajjar

April 2003

**Department of Civil Engineering
Institute of Technology
University of Minnesota
Minneapolis, Minnesota 55455**

Abstract

Damage evolution of rectangular concrete-filled steel tube (RCFT) members, connections, and frames as documented in experimental tests was investigated in this research. Based on the experimental data, appropriate limit states for RCFTs were defined at different levels of loading. For each limit state, the performance of the specimens was judged with the use of damage indices. The report also documents how to use these damage measures to assess capacity within the context of a reliability-based performance-based design methodology.

A database study was first conducted to document worldwide experimental RCFT research. RCFT members, including columns, beam-columns, panel-zones, pinned and moment-resisting connections, and frames, were covered in the database for both monotonic and cyclic loading conditions. Detailed information about the material and geometric properties of the specimens were recorded in the database. In addition, the peak force and deformation capacities of the specimens were stored. For each RCFT member type, the specific damage levels observed during the tests were also identified. The occurrence time of the damage levels during the tests were entered into the database in terms of appropriate force and deformation quantities.

Two types of damage indices were defined and used to assess damage, including a deformation-based damage index and an energy-based damage index. These damage indices were applied to the RCFT members, connections, and frames stored in the database. The damage index values attained at the specific damage levels were correlated to the geometric and material properties of the RCFT members and equations were derived to estimate damage index values. These damage index values thus provided quantified data to determine the governing damage levels for the RCFT members at different levels of loading. A parametric study was then conducted for the equations derived to explore the relative magnitude of the damage indices for the different limit states. Based on the results from the parametric study, each damage level identified for the RCFT members was mapped onto appropriate performance objectives, including immediate occupancy, life safety, near collapse, and collapse prevention, to identify how this information may be used in the context of a performance-based design methodology.

Acknowledgments

The authors would like to thank Dr. Robert T. Leon of the Georgia Institute of Technology, Dr. Amit H. Varma of Michigan State University, and Dr. Shosuke Morino and Dr. Jun Kawaguchi of Mie University in Japan for providing details of their experimental tests for use in this research.

This research was funded by the National Science Foundation (Grant No. CMS-0084848) under Dr. Vijaya Gopu and by the University of Minnesota. The authors would like to thank Angela Kingsley for her assistance with the preparation of this report. Any opinions, findings, and conclusions or recommendations expressed in this material are those of the authors and do not necessarily reflect the views of the National Science Foundation.

Table of Contents

| | |
|---|-----|
| Abstract | ii |
| Acknowledgements | iii |
| Table of Contents | iv |
| 1 Introduction | 1 |
| 1.1 Performance-Based Seismic Guidelines for Building Structures in the U.S. | 4 |
| 1.2 Past Research in Performance-Based Design of Composite Steel/Concrete Structures | 7 |
| 1.3 Scope and Objective of the Research | 8 |
| 1.4 Organization of the Report | 9 |
| 2 RCFT Experimental Database | 10 |
| 2.1 Prior Research on Documentation of RCFT Tests | 11 |
| 2.2 Database Description | 12 |
| 2.2.1 RCFT Column Database | 13 |
| 2.2.1.1 Monotonically-Loaded RCFT Column Database | 13 |
| 2.2.1.2 Cyclically-Loaded RCFT Column Database | 21 |
| 2.2.2 RCFT Beam-Column Database | 24 |
| 2.2.2.1 Monotonically-Loaded RCFT Beam-Column Database | 24 |
| 2.2.2.2 Cyclically-Loaded RCFT Beam-Column Database..... | 32 |
| 2.2.3 RCFT Panel Zone Database..... | 36 |
| 2.2.3.1 Monotonically-Loaded RCFT Panel Zone Database..... | 36 |
| 2.2.4 RCFT Pinned Connection Database | 38 |
| 2.2.4.1 Monotonically-Loaded RCFT Pinned Connection Database | 38 |

| | |
|--|-----------|
| 2.2.5 RCFT Moment Connection Database | 42 |
| 2.2.5.1 Monotonically-Loaded RCFT Moment Connection Database | 42 |
| 2.2.5.2 Cyclically-Loaded RCFT Moment Connection Database | 45 |
| 2.2.6 RCFT Frame Database | 52 |
| 2.2.6.1 Monotonically-Loaded RCFT Frame Database | 52 |
| 2.2.6.2 Cyclically-Loaded RCFT Frame Database | 55 |
| 3 Damage Assessment of RCFT Members | 96 |
| 3.1 Damage Levels for RCFT members | 96 |
| 3.1.1 Structural Damage Functions for RCFT Beam-Columns and Connections | 97 |
| 3.1.1.1 Non-Cumulative Local Structural Damage Functions for RCFT Beam-Columns and Connections..... | 98 |
| 3.1.1.2 Cumulative Local Structural Damage Functions for RCFT Beam-Columns and Connections | 100 |
| 3.2 Monotonically Loaded RCFT Columns | 106 |
| 3.3 Monotonically Loaded RCFT Beam-Columns | 116 |
| 3.4 Cyclically Loaded RCFT Beam-Columns | 136 |
| 3.5 Monotonically Loaded RCFT Panel Zones | 148 |
| 3.6 Monotonically Loaded Steel Girder-to-RCFT Column Pinned Connections | 154 |
| 3.6.1 Beam Columns | 155 |
| 3.6.2 Steel Girders | 158 |
| 3.6.3 Connection Components | 158 |
| 3.7 Monotonically Loaded Steel Girder-to-RCFT Column Moment Connections | 158 |
| 3.7.1 Beam-Columns | 159 |

| | |
|--|-----|
| 3.7.2 Panel Zone | 160 |
| 3.7.3 Steel Girder | 161 |
| 3.7.4 Connection Components | 162 |
| 3.8 Cyclically Loaded Steel Girder-to-RCFT Column Moment Connections | 162 |
| 3.8.1 Beam-Columns | 165 |
| 3.8.2 Panel Zone | 168 |
| 3.8.3 Steel Girders | 169 |
| 3.8.4 Connection Components | 171 |
| 3.9 Monotonically Loaded RCFT Frames | 171 |
| 3.10 Cyclically Loaded RCFT Frames | 176 |
| 3.11 Ductility of RCFT Members | 181 |
| 3.11.1 Monotonically-Loaded Columns | 181 |
| 3.11.2 Monotonically-Loaded Beam-Columns | 183 |
| 3.11.3 Cyclically Loaded Beam-Columns | 185 |
| 3.11.4 Monotonically Loaded Panel Zones | 186 |
| 3.11.5 Monotonically Loaded Pinned Connections | 186 |
| 3.11.6 Monotonically Loaded Moment Connections | 187 |
| 3.11.7 Cyclically Loaded Moment Connections | 187 |
| 3.11.8 Monotonically Loaded Frame Tests | 188 |
| 3.11.9 Cyclically Loaded Frame Tests | 189 |
| 3.12 Comparison of Damage Levels for RCFT Members | 190 |
| 3.12.1 Monotonically-Loaded Columns | 191 |
| 3.12.2 Monotonically-Loaded Beam-Columns | 192 |

| | |
|--|------------|
| 3.12.3 Cyclically Loaded Beam-Columns | 195 |
| 3.12.4 Monotonically Loaded Panel Zones | 196 |
| 3.12.5 Monotonically Loaded Pinned Connections | 197 |
| 3.12.6 Monotonically Loaded Moment Connections | 198 |
| 3.12.7 Cyclically Loaded Moment Connections | 198 |
| 3.12.8 Monotonically Loaded Frame Tests | 199 |
| 3.12.9 Cyclically Loaded Frame Tests | 200 |
| 4 Conclusions | 297 |
| Appendix A | 311 |
| Appendix B | 313 |
| Appendix C | 331 |

Chapter 1

Introduction

The substantial economic losses due to damages after earthquakes continually motivate researchers and practitioners to improve the national seismic codes. In the seismic design provisions used over the last several decades (e.g., BSSC, 2001; ACI, 2002; AISC, 2002), the primary objective of the provisions was to provide life safety in the case of a major earthquake (Wen, 1995). However, business interruption and repair cost of the building are among the primary needs of the building owners that should be considered by engineers during the design process. Reliability-based performance-based engineering provides a methodology for enhancing the seismic design provisions through incorporation of multiple performance objectives in the seismic design of structures (e.g., Bertero, 1997; Krawinkler, 1998; Hamburger, 1998; Wen, 2001).

Performance-based design approaches are based upon documentation of two key quantities for structural components and systems: capacity and demand. Capacity represents the ability of a structural component or system to resist externally applied loads, while demand represents the effects of the externally applied loads on the structural component or system. The general objective within any reliability-based performance-based design methodology is to ensure for each structural component and system that capacity is greater than demand within a prescribed level of confidence. This check between capacity and demand is performed at specific performance objectives, with different capacity levels being appropriate for checking within the different

performance objectives, and with the demand levels being calculated based upon hazard levels are associated with each specific performance objective. In addition, within this design framework, the capacity and demand should also be adjusted for the uncertainties and randomness embedded in their calculation process. As part of this adjustment, it is often possible for an engineer to target a specific confidence level within the design of each structural component and system, with higher levels of confidence often being possible to attain, e.g., by increasing the demand or with the use of more accurate computational models for performance evaluation.

In a reliability-based performance-based design methodology, the design starts by choosing a performance objective. As described in Bertero (1997), a performance objective is a statement describing the desired performance level for the building for each earthquake design level. Therefore, a performance objective includes a hazard level (which leads directly to loading characteristics) and a performance level (i.e., a damaged state, such as immediate occupancy, or collapse prevention) for the building. Thus, a matrix of performance objectives can be established, such as targeting having immediate occupancy for ground motion having a 50% chance of recurrence within 50 years, or collapse prevention for a ground motion having a 2% chance of recurrence within 50 years, etc. The design of structural components is made according to each of the appropriate performance objectives.

Each performance level includes appropriate limit states of the structural components, e.g. steel yielding, local buckling, etc. Therefore, identification of the limit states and mapping of the limit states to the specific performance levels is an essential step in establishing this design methodology, and is a focus of this research. The limit states of the structural components are represented by appropriate quantifiable design parameters, and the capacity, whether it is deformation-based, force-based, or energy-based, becomes the limiting value of the design parameters at these distinct limit states. The demand parameters must correspond to the capacity parameters, and are calculated for each performance objective by analyzing the building under the seismic loading scheme (i.e., hazard level) described in the performance objective. Once both the demand and capacity are both obtained for a specific limit state for a specific structural component, they are both adjusted for uncertainties and randomness, and the structural

component is checked to satisfy the desired performance objective with a desired level of confidence.

This research is the first stage of a study for developing reliability-based performance-based design guidelines for rectangular concrete-filled tube (RCFT) structures. In recent years, RCFT members have become increasingly popular in high-rise buildings due to their excellent seismic behavior and economic advantages. Therefore, in the last several decades, a wide range of experimental, computational, and analytical research studies have been completed on RCFT members and connections to better understand their behavior and develop more efficient design techniques (Gourley et al., 2001; Morino, 2000; Hajjar, 2002). In addition, recent research in Japan has established basic performance-based design provisions for CFTs (Morino, 2000). However, U.S. non-seismic and seismic design provisions for CFTs remain limited (AISC, 1999; BSSC, 2001; AISC, 2002; ACI 2002).

The research reported herein is part of a larger project to establish reliability-based, performance-based design provisions for rectangular concrete-filled steel tubes and RCFT connections. The focus of this research relates primarily to identifying specific issues related to the composite interaction of these structural components that require special attention in developing a performance-based design strategy. In this report, the first step in this research is documented, including assessing the accumulation of damage in RCFT members and connections based upon investigation of the worldwide experimental literature. Through documentation of RCFT capacity at all load levels, performance-based design provisions may be established once linked with a corresponding assessment of demand in RCFT components in future research.

In this chapter, a brief literature review will be given, discussing performance-based seismic design provisions within the U.S., as well as identifying relevant recent research in performance-based design, with a particular focus on the design of composite members. In addition, the objectives and scope current research will be presented. A layout of the remaining chapters will also be given.

1.1 Performance-Based Seismic Guidelines for Building Structures in the U.S.

Following the Northridge, California earthquake in 1994, the importance of performance based-design became more evident in structural engineering practice. During this earthquake, many steel moment frame structures experienced brittle fractures in their built-in connections. Although these fractures did not cause any total collapses of steel buildings (one steel sign structure collapsed), the repair costs were so high that some buildings were demolished and rebuilt rather than repairing. This caused significant economical costs to the building owners and insurance companies. Subsequently, a substantial amount of computational and experimental research has been conducted to contribute to the development of performance-based design guidelines. This research mainly focused either on steel or reinforced concrete structures, although research in other materials has been progressing as well. As a result of this past research, key performance-based design guidelines that have been produced to date, including VISION 2000 (1995), FEMA (1997), FEMA (2000b), ATC (1996), and FEMA (2000a).

One of the first attempts for documenting performance-based design guidelines for seismic design of structures is the recommendations in VISION 2000 (1995), which was initiated before the Northridge Earthquake (1994) and was finalized in 1995. This document provides a general methodology for performance-based design of concrete, masonry, and steel structures, and forms the basis for the following guideline documents that were issued in subsequent years. In VISION 2000 (1995), five types of performance levels were defined, including fully operational, operational, life safe, near collapse, and collapse. The same performance levels are used for both structural and nonstructural components. The performance level definitions included qualitative terms of damages of the components and also quantitative interstory drift limitations at the system level. Several design and analysis approaches were proposed and their applicability for different structures and performance objectives were discussed. Regarding the seismic capacity assessment of the buildings, in VISION 2000 (1995), no specific acceptance rule is provided at the component or system levels.

FEMA (1997) and FEMA (2000b) contain the guidelines for seismic rehabilitation of all types of building structures. Although FEMA (1997) precedes

FEMA (2000b), the given performance based-design methodologies are similar. The provisions in these two documents discuss the seismic resistance of both the overall structural system and its components. The building performance levels are defined as a combination of individual structural and non-structural performance levels. The structural performance levels include immediate occupancy, life safety, and collapse prevention. With respect to assessment of seismic capacity, the damage states of the building and its components corresponding to the structural performance levels are provided both quantitatively and qualitatively. The components of the building are defined as either force-controlled or deformation-controlled. The capacities of the components are provided in the form of normalized load-deflection curves. Regarding the assessment of seismic demand, FEMA (1997) and FEMA(2000b) allow the use of linear (linear elastic static, and linear elastic dynamic) and nonlinear analysis (first-order or second-order inelastic static, and first-order or second-order inelastic dynamic) procedures to evaluate the demand imposed on the structure. It is recommended that parameters like interstory drift ratios, strength demands, and ductility demands of the individual members might be used for performance evaluation. The acceptance checks for the performance levels are only made at the member level. FEMA (1997) and FEMA (2000b) notes the uncertainty in these performance checks. However, no methodology to calculate the confidence level in performance evaluation is given.

ATC (1996) provides guidelines for seismic retrofit of concrete structures. Similar to FEMA (1997), the structural and non-structural performance levels are defined independently. The structural performance levels include immediate occupancy, life safety, and structural stability. With regard to seismic capacity, the capacity at the system level is assessed through consideration of gravity loads, lateral loads, and lateral deformations. For the latter two capacities, numerical values were provided. At the component level, the members are classified as deformation-controlled members or force-controlled members. The deformation-controlled members are allowed to undergo inelastic displacements provided that they have adequate expected strength. Force-controlled members typically exhibit brittle responses. For both types of the members, the seismic capacity is assessed through deformation limits in ATC (1996), which were obtained either experimentally or analytically. The seismic hazard is represented through

three different earthquake levels defined as the serviceability earthquake, the design earthquake and the maximum earthquake. They have return periods of 75, 500, and 2500 years, respectively. Both linear and nonlinear analysis methods are introduced in ATC (1996) to evaluate the seismic demand. The elastic analysis methods include the equivalent lateral load method, elastic dynamic analysis, and demand/capacity ratio procedures. Among the nonlinear analysis methods, ATC (1996) gives a special attention to capacity spectrum method and also allows the use of nonlinear time history analysis. The acceptance checks for the performance objectives are made both at the component level and at the system level, and no confidence level of the performance assessments is given.

FEMA (2000a) provides design recommendations for new steel moment-frames. This document is based on the provisions in FEMA (2000a) and AISC Seismic Specification (AISC, 1997). It presents new connection details that were developed after Northridge earthquake and provides the design methods for these connections. In addition, FEMA (2000a) establishes reliability-based performance evaluation techniques for the designed frames. The given techniques are applicable to regular welded steel moment frames. The performance objectives are defined only for structural components. Non-structural components were not included in performance evaluation. Two types of performance levels were defined, including immediate occupancy and collapse prevention. The performance evaluation of the building was made both at the system level and at the member level. The recommended parameters were interstory drift and axial forces on individual columns. The acceptance criteria were reliability-based and the uncertainties in the capacity and demand were taken into account by resistance factors (ϕ) and demand variability factors (γ), respectively. The ratio between the factored demand and factored capacity was defined as the confidence level for the given design. With regard to the assessment of demand, FEMA (2000a) allows the use of linear static and linear dynamic analysis. Among the nonlinear methods, either nonlinear static or nonlinear dynamic analysis procedures can be used.

The documents presented above focused on either steel or reinforced concrete structure, and no reliability-based performance-based design guidelines were provided for the composite structures. In all the documents, acceptance criteria at the component level

are given in terms of interstory drift limits. Also, the variability of the acceptance criteria with respect to the material and geometric properties of the members was not investigated in detail.

1.2 Past Research in Performance-Based Design of Composite Steel/Concrete Structures

Mehanny and Deierlein (2000, 2001) conducted an analytical study to assess the performance of composite frames made up of reinforced concrete columns and steel girders. One of the objectives of the research study was to help develop future performance-based guidelines for composite frames. The performance of the frames was investigated both at the component level and the system level. Two new damage indices were derived for concrete columns, steel and composite girders, and composite connections. These damage indices were used to quantify the local damage observed during the tests. Based on the damage index values, the local damage observed during the tests were mapped into performance levels. Mehanny and Deierlein (2000, 2001) also proposed a new method to assess the system response based on the amount of damage accumulated in the members. This requires the use of nonlinear time history analysis and static nonlinear analysis, simultaneously. First, nonlinear transient dynamic analysis is performed for a single earthquake record. Subsequently, according to the damage accumulation of the members, the structural stiffness properties of the frames are updated and a nonlinear static analysis is conducted. This process is repeated for multiple earthquake records. The performance of the frame is decided based on the ratio of the vertical gravity load capacity to the unfactored gravity loads. The research study by Mehanny and Deierlein (2000, 2001) is important, as their main focus is composite frames, and they used damage index values to quantify damage instead of only drift limits, which do not take into account energy absorption and cyclic load history effect into account.

1.3 Objectives and Scope of the Research

The objectives of this research are as follows.

1. The experimentally-observed limit states (damage types) of rectangular concrete-filled steel columns, beam-columns, connections, and frames are established for use of RCFTs in composite frames. Comprehensive definition of the limit states and assessing their effect to the response of RCFT members is one of the initial steps in developing performance-based design provisions. This objective is accomplished through careful examination of the experimental test results of RCFT members and connections from around the world. The experimental studies also provide information to assess the uncertainties in determination of the member capacities. Therefore, as part of achieving this objective, the first task in this research study was to prepare a database documenting the results of the tests conducted on RCFT members including columns, beam-columns, panel-zones, connections and frames. Both monotonic tests and cyclic tests were investigated. The database consisted of nominal and measured values of the material and geometric properties of the specimens. The force and displacement capacities and failure modes of the specimens were recorded. In addition, the common damage levels or limit states observed during the experiments were noted and their point of occurrence in terms of force, displacement, and cycle number were stored.
2. The second objective of this research is to quantify the damage evolution of the RCFT members. For this purpose, damage functions applicable to any type RCFT member or connection were developed. Based on the information taken from the database, the damage functions were evaluated at specific damage levels throughout the loading history of the specimens. Based on the values of the damage functions, the effect of the damage levels of the member response was judged and every damage level was correlated to a performance level.

The scope of this research is limited to composite frames consisting of steel girders framing into rectangular concrete-filled steel tube beam-columns with either pin

or fully-restrained (moment) connections. For the various limit states and damage indices investigated, the specific scope of material and geometric parameters available in the experimental literature is documented in detail, and the scope of this research is necessarily constrained to be within the scope of parametric values identified throughout this thesis.

1.4 Organization of the Report

This report consists of two primary parts. The first part of the report presents the development of the database compiled for RCFT members. The second part of the report documents the damage evaluation for RCFT members and connections.

In Chapter 2, a brief literature review for database studies of CFT members is given. This is followed by a detailed description of each database developed in this research. The quantities stored in the database and the variations and trends observed in the experimental data were discussed.

In Chapter 3, a literature review on damage functions was given. The damage functions used in this research are described and the damage evolution of the specimens are investigated by using the selected damage functions. The correlation of the values of the damage functions with the experimental results at specific damage levels is also studied, and equations are proposed to estimate these values. The ductility of the RCFT members were assessed and equations were derived estimate ductility. Finally, a parametric study is presented that was conducted to compare the effect of different damage levels on the response of RCFT members and connections.

Chapter 4 gives a brief summary and the conclusions drawn from interpretation of the results of the research study, including summarizing the performance levels that are most appropriate for each of the limit states identified for RCFTs in this research. Recommendations for future research are also discussed.

Chapter 2

RCFT Experimental Database

The objective of performance-based design is to develop design techniques to produce structures with predictable damage. To facilitate development of these procedures, multiple damage states of the structure and its structural components must be identified and the behavior of the components from the undamaged state to failure must be characterized as being within distinct damage levels. This is only possible if the limit states at the component level and at the global structural level are well defined.

The current structural design specifications (AISC, 1999; BSSC, 2001; ACI, 2002; AISC, 2002) for composite members, and for concrete-filled steel tubes in particular, are based on transformation of the composite members into equivalent steel or reinforced concrete members, and only the ultimate strength limit states are considered. These existing procedures do not reflect the full range of response of the composite members, and the reliability provided by AISC, 1999 does not yield the target reliability level for CFTs (Lundberg and Galambos, 1996). Therefore, there is a need to develop new techniques for capacity assessment of composite systems for multiple limit states, specifically for CFT members. This can be achieved through a careful examination of the experimental research on CFT members.

In this study, a database of experimental results from around the world covering rectangular CFT columns, beam-columns, connections, panel zones, and frames was prepared. Only CFTs having cold-formed or hot-rolled steel tubes were considered. For each test series, material properties, load capacities, deformation capacities, and damage levels were recorded in detail. The total number of specimens included for each type of

CFT member may be seen in Figure 2.1. The test results were documented separately for monotonically loaded and cyclically loaded tests. This chapter highlights the details of this database.

2.1 Prior Research on Documentation of RCFT Tests

Lundberg and Galambos (1996) constructed a database documenting worldwide test results of composite columns and beam-columns including steel reinforced concrete encased-shapes (SRC) and CFTs. This database, which covered only monotonically loaded specimens, consisted of material properties of the specimens as well as their experimental peak strengths. A Monte-Carlo analysis of the calculated strength of composite columns and beam-columns was performed and the reliability of the 1993 AISC-LRFD design procedures for composite columns and beam-columns was investigated. It was determined that the reliability indices provided for CFT columns and beam-columns were below the target reliability indices. Therefore, Lundberg and Galambos (1996) recommended that the design methods for CFT sections in the 1993 AISC-LRFD provisions required modifications.

Aho and Leon (1997) also compiled a database for SRCs and CFTs. The database included material properties, loading method, and experimental peak strengths of composite column and beam-column specimens. Only monotonically loaded tests were considered. They obtained even lower reliability levels CFT than Galambos and Lundberg (1996) did, with the average reliability index being on the order of 2.35 for the 1993 AISC LRFD provisions (versus a target reliability index being on the order of 2.7). Using the data obtained from the experiments, several alternative design schemes were proposed to replace the design guidelines in the 1993 AISC-LRFD Specifications for composite members.

Kawaguchi et al. (1998) developed a database for CFT beam-columns from the Japanese literature. Both monotonically loaded and cyclically loaded tests were covered. Size, material properties, experimental stiffness, load capacities and deformation capacities of the specimens were all recorded. In contrast to the previous database studies, Kawaguchi et al. (1998) also recorded the deformation levels or load levels of the

specimens at specific instances, such as when the strength of the member decreased to 95% of its peak value, or when the rotation angle of a CFT beam-column reached to 1/100. Using the test results, analytical models were proposed to calculate the flexural strength and rotation capacity of CFT beam-columns.

Gourley et al. (2001) compiled a comprehensive database covering CFT columns, beam-columns, connections, and frames. Both monotonically loaded and cyclically loaded tests of circular and rectangular CFTs were considered. The database was divided into six main parts for column tests, beam-column tests, frame tests, torsion tests, connection tests, and bond tests. While experimental research was primarily reported, several research contributions focusing on computational and analytical research on CFTs were also summarized. A summary of the reported research was given, and material properties, geometric properties, and test results (where available) were provided in separate tables prepared for each of the six test types. Gourley et al. (2001) also constructed tables of significant reported experimental research on CFT columns and beam-columns that make it possible to scan the available tests according to key parameters, including f'_c , f_y , D/t and L/D .

Nishiyama et al. (2002) developed a database by gathering the CFT research from Japan conducted as part of the U.S.-Japan Cooperative Research Program on Composite and Hybrid Structures. Both analytical and experimental studies of monotonically loaded and cyclically loaded CFTs were summarized, and the test results were provided. The CFT research of circular and rectangular sections was presented separately for centrally-loaded stub-columns, eccentrically-loaded stub columns, beam-columns and subassemblages. Design formulas developed from the experimental results were given to calculate the strengths and deformation capacities of the CFT members. Finally, the properties of CFT systems e.g., stiffness, period of vibration, cost, and related properties, were reported based upon trial design studies using the given design formulas.

2.2. Database Description

In the current research, six main databases were constructed for rectangular concrete-filled steel tubes (RCFT), including columns, beam-columns, panel zones,

pinned connections, moment connections and frames. Each of the six databases was divided into separate subdivisions for monotonically loaded and cyclically loaded tests if well documented tests were available in the literature. The content of each database entry is described within four different sections in the database, including the test description, material properties, geometric properties, and test results.

2.2.1 RCFT Column Database

A total of 109 monotonically loaded and 3 cyclically loaded RCFT column specimens (i.e., specimens having predominantly axial compression applied) were included in the database. The column database includes tests from the literature ranging between 1976 and 2002, and from the United States, Canada, Europe, Japan, and Australia.

2.2.1.1 Monotonically Loaded RCFT Column Database

The first section of each database includes a description of the tests. The available information about the method of testing and boundary conditions was provided. The usual method of testing RCFT columns was axial compression force applied on both steel and concrete simultaneously through thick end plates welded to the steel tube. The application of load on both the steel and concrete together is a requirement for composite action along the full length of the specimen, and this was ensured by grouting or capping the ends of the columns in many of the experiments (e.g., Bridge, 1976; Lu and Kennedy, 1992; Lu and Kennedy, 1994). The tests were conducted using either load control (e.g., Schneider, 1998) or deformation control (e.g., Bergmann, 1994).

The measured material properties reported in the monotonically loaded RCFT column database include yield strength of the steel tube (f_y), ultimate strength of the steel tube (f_u), modulus of elasticity of the steel tube (E_s), modulus of elasticity of the steel tube at strain hardening (E_{sh}), residual stress in the steel tube (f_r), cylinder compressive strength of the concrete (f'_c), cube compressive strength of the concrete (f'_{cub}), compressive strength of the cored concrete (f'_{ccor}), modulus of the concrete (E_c), and

modulus of the cored concrete (E_{ccor}). In addition to the measured material properties, the nominal values for yield strength of the steel tube (f_{yo}), modulus of elasticity of the steel tube (E_{so}), and cylinder compressive strength of the concrete (f'_{co}) were also recorded in the database.

The measured yield strength of the steel tubes for the monotonically loaded RCFT column tests ranged between 194.2 and 835.0 MPa (28.2 – 121.1 ksi). The histogram of the yield strength of steel can be seen in Figure 2.2. The frequency distribution of the yield strength shows that the behavior of the specimens with low strength [less than 450 MPa (65 ksi)] and high strength [greater than 600 MPa (87 ksi)] steel tubes were investigated more comprehensively than the specimens with moderate strength steel tubes [450 – 600 MPa (65 – 87 ksi)]. As a common practice in monotonically loaded RCFT column tests, the material properties of the steel tubes were measured from coupon specimens taken from various positions along the perimeter and then the results were averaged (Lu and Kennedy, 1992; Lu and Kennedy, 1994; Varma, 2000; Varma et al., 2001). However, the yield strength of the steel tube exhibits a variation depending on the position of the coupons around the perimeter. Bridge (1976), Clarke and Hancock (1991), and Sully and Hancock (1996) found that the mean ratio of corner region yield strength to flat region yield strength was 1.12, 1.29, and 1.34, respectively. The larger strength of the corner regions is usually attributed to the intensive cold-forming process at those regions. The measured and nominal yield strengths of the steel tubes also exhibit a variation due to testing method and cold-forming process. Figure 2.3 shows the comparison of measured and nominal yield strengths of steel tubes for the RCFT column tests as well as, for comparison, the other tests in the database, if the reported data was available¹. This figure shows that in approximately all of the RCFT column tests, the measured yield strength was greater than the nominal yield strength and the mean f_y/f_{yo} ratio was found to be 1.145, with a standard deviation of 0.111. The mean f_y/f_{yo} ratio of all of the tests with available data was 1.218, while the standard deviation was 0.211. This indicates that with respect to the variation of measured versus nominal yield strength

¹ Where appropriate throughout this report, plots of data of the type of tests being discussed are shown with black data points; where data for other types of tests are available, they are shown in gray for comparison.

of the steel tubes, the trend of the monotonically loaded RCFT column tests is not significantly different from RCFT tests as a whole.

The nominal modulus of elasticity of the steel tubes was reported by Cederwall et al. (1990), Grauers (1993), Nakahara et al. (1998). When the measured and nominal values for the modulus of elasticity of steel for the RCFT columns are compared in Figure 2.4, it can be seen that the measured modulus of elasticity and its nominal value are approximately equal to each other, with a mean E_s/E_{so} ratio of 1.005 and a standard deviation of 0.009. For all of the tests in the database where the data was available, the mean value and standard deviation of E_s/E_{so} are 1.006 and 0.017, respectively, which are similar results to the RCFT column tests. These results show that the measured and nominal modulus of elasticity of the steel tubes may be considered equal. In contrast to the results presented for the steel tube yield strength, the modulus of elasticity of the steel tube exhibits insignificant variation around the perimeter of the tube. In their monotonically loaded column tests, Lu and Kennedy (1992), Lu and Kennedy (1994) found the mean ratio of modulus of elasticity of the corner regions to the flats regions as 0.985. This ratio was found as 1.000 by Clarke and Hancock (1991) and 0.938 by Sully and Hancock (1996).

When the coupon specimens are loaded beyond the yield point, strain hardening takes place, and the stress continues to increase with a modulus value initially equal to the strain hardening modulus. The strain hardening modulus values obtained from coupon tests were included in the database. The mean value of E_{sh}/E_s using the available data from Tomii and Sakino (1977), Varma (2000), and Varma et al. (2001) was found as 0.01, and the corresponding standard deviation was 0.003. The mean value of E_{sh}/E_s for all of the RCFT tests with the available data was 0.0086, with a standard deviation was 0.002, which is similar to the results from the RCFT column tests. The variation of E_{sh}/E_s with respect to f_y can be seen in Figure 2.5. The monotonically loaded RCFT column tests show the same trend as the other tests, indicating that E_{sh}/E_s decreases as f_y increases.

Another parameter added from the coupon tests into the database is the steel tube ultimate strength. As shown in Figure 2.6, the ratio of the measured ultimate strength to the measured yield strength of the steel tube decreases as the yield strength of the steel

tube increases. This trend is the same for both the monotonically loaded RCFT column tests and for the other RCFT tests in the database. The mean value and standard deviation of f_u/f_y for the RCFT column tests was found to be 1.278 and 0.201, respectively. These two parameters are equal to 1.304 and 0.193 for all RCFT tests having the available data. No residual stress measurements in the steel tubes were made for the specimens in the column database. Therefore, in the database, it was only noted if the specimens were annealed and free from residual stresses.

The histogram of the concrete compressive strength can be seen in Figure 2.7. The maximum cylinder compressive strength of the concrete in the RCFT column database is 119 MPa (17.26 ksi), while the minimum value is 19.8 MPa (2.87 ksi). This histogram shows that the RCFT column tests were mainly performed on columns having either low strength [$f'_c < 45$ MPa (6.5 ksi)] or high strength concrete [$f'_c > 75$ MPa (10.9 ksi)]. The number of specimens having medium strength concrete [45 MPa (6.5 ksi) $< f'_c < 75$ MPa (10.9 ksi)] is relatively less. Note that curing details for the cylinders were often not reported and are not considered in this figure or in other similar concrete strength data reported throughout this chapter. Similar to the yield strength of steel, the measured and nominal compressive strength of the concrete show some variation. The comparison of measured and nominal compressive strength of the concrete can be seen in Figure 2.8. This figure shows that in 60% of the RCFT column tests, the measured compressive strengths are larger than the nominal values. The mean value of the f'/f'_{co} was found to be 1.15 with a standard deviation of 0.21. For all of the tests in database having the available data, the measured strength of the concrete was also larger than its nominal value, with mean and standard deviation values of the f'/f'_{co} ratio equal to 1.089 and 0.19, respectively. The difference between the measured and nominal concrete compressive strengths might be attributed to variations in the concrete mix from the target properties, as well as curing and aging of the concrete cylinders after they are poured. Figure 2.9 demonstrates the variation of f'/f'_{co} with respect to the f'_c and for both column tests and the other tests in the database. The ratio f'/f'_{co} approaches 1.0 as the compressive strength of concrete increases. High strength concrete often requires more careful work to prepare and therefore it is more probable to attain the target strength. It is also possible to determine the compressive strength of concrete by testing

cube concrete specimens rather than cylindrical ones. However, cube compressive strengths of concrete typically give a higher strength value than cylindrical specimens. Bergmann (1994) reported the cube compressive strength of concrete, and a conversion factor of 0.8 was used to convert cube concrete compressive strength to cylinder concrete compressive strength. From the tests of Cederwall et al. (1990), Grauers (1993), the mean value of the f'_c/f'_{cu} is 0.77 with a standard deviation of 0.08, indicating that the ratio of 0.8 given by Bergmann (1994) is a reasonable factor.

In addition to compressive strength, the modulus of concrete is also recorded in the column database. The value of E_c is mainly affected by the concrete compressive strength. The variation of E_c with respect to f'_c and f'_{cu} is examined in Figure 2.10 for both the RCFT column tests and for the other tests available in the database. The value of E_c increases when the compressive strength of the concrete increases.

The most realistic concrete properties can be found using cylinder cores extracted from untested RCFT specimens. Varma (2000) and Varma et al. (2001) used cored concrete cylinders to determine concrete strength and concrete modulus. It was found that the f'_{ccor} and E_{ccor} matched with the results from the standard cylinder tests.

In order to define the geometric properties of the specimens, depth, width, thickness, and length of the columns were recorded in the database. Because the cold-forming process is effective in modifying the cross-sectional dimensions of the steel tubes, both measured and nominal values of the aforementioned parameters were stored in the database where available. The measured depths of the steel tubes are compared with the nominal values in Figure 2.11. The mean value of the D/D_o ratio was found to be 1.001 with a standard deviation of 0.006, which indicates that the measured and nominal values of the depth of the specimens are almost equal to each other. For all of the tests in the RCFT database, the respective values of the mean and standard deviation of D/D_o becomes 1.003 and 0.005. It can be seen in Figure 2.11 that there is slight increase in D/D_o for large values of D . When measured and nominal thicknesses of the steel tubes are compared in Figure 2.12, it is found that for the RCFT column specimens, measured thickness is slightly greater than the nominal thickness with a mean t/t_o ratio of 1.019 and a standard deviation of 0.06. However, for all of the tests in the database, the nominal thicknesses of the specimens are less than the measured thicknesses. In this

case, the mean value and the standard deviation of t/t_o are 0.991 and 0.059, respectively. The slight differences between the measured and nominal thickness of the specimens might be attributed to the pressing and bending action during cold forming process, or to standard manufacturing tolerances.

The D/t ratio of the specimens in the monotonically loaded RCFT column database ranges between 15.0 and 74.0. The histogram given in Figure 2.13 indicates that fewer specimens were tested with large D/t ratios ($D/t > 50$) compared to specimens having medium ($30 < D/t < 50$) and low ($D/t < 30$) D/t values. In many of the monotonically loaded RCFT column tests (e.g., Lu and Kennedy, 1992; Lu and Kennedy, 1994; Varma, 2000; Varma et al., 2001), the researchers reported the measured and nominal values of D/t separately. If these two values are compared, the mean ratio of $(D/t)/(D/t)_o$ was found to be 1.138, with a standard deviation of 0.144. Figure 2.14 indicates that both for the monotonically loaded RCFT column tests and the other tests in the database with the available data, the measured D/t ratio is greater than its nominal value. The slenderness of RCFT columns is defined as the length over depth ratio. Figure 2.15 shows the histogram for the L/D ratio of the specimens in the monotonically loaded RCFT column database. Unfortunately, there are not many experimental studies investigating slender RCFT columns. The minimum and maximum L/D ratios in the RCFT column database are 2.0 and 30.0, respectively.

The main experimental results presented in the reports are the axial load strengths and axial load versus axial deformation plots. Among the axial load strengths of the specimens stored in the database, except for Liu and Goel (1987), all the values were taken from tables given in the reports. For the tests by Liu and Goel (1987), the peak axial load was obtained from the axial load versus axial deformation plots by scaling. The second experimental result recorded in the database is the axial strain value of the composite section at the time of peak axial load. This parameter is important to assess the axial deformation capacity of the section. It can also be used for normalization while defining the occurrence time of damage levels, as will be described later. In none of the tests was this parameter reported numerically. Therefore, they were obtained from axial load versus axial displacement or axial load versus axial strain plots by scaling the strain values corresponding to the peak loads. However, the specimens do not always have a

definitive peak point. In these cases, a tangent line was drawn on the axial load versus axial deformation plot at the level of the peak axial load, and the first point where the tangent line intersects the axial load versus axial deformation plot was assumed to be the peak point, as shown in Figure 2.16. The variation of strain at peak axial load (ε_o) with

respect to the parameter $\frac{D}{t} \cdot \sqrt{\frac{f_y}{E}} \cdot \frac{f'_c}{f_y} \cdot \frac{1}{L/D}$ can be seen in Figure 2.17. The ε_o value is

mainly dependent on the variation in the D/t ratio. It achieves higher values when D/t decreases. The trend of ε_o with respect to the f'_c/f_y ratio indicates that if a higher strength steel tube is used, an increase in the value of ε_o takes place. The compressive strength of concrete is another factor governing the value of ε_o . For low strength concrete where the behavior is dominated by the steel tube, any increase in concrete strength also causes an increase in ε_o . In contrast, for high strength concrete, due to its larger stiffness, the concrete starts to carry more load and its contribution to the behavior increases. However, the brittle nature of high strength concrete affects the member behavior and ε_o cannot attain large values. If the length of the member increases, stability becomes critical, which also prevents large axial strains to be achieved. Therefore, as the L/D ratio gets larger, the value of ε_o becomes smaller.

As will be explained in more detail in Chapter 3, the specific damage levels or limit states observed in the RCFT column tests are steel yielding in compression, local buckling of the steel tube, concrete crushing, and fracture of steel tube. The load levels and axial strain levels corresponding to these events during testing were added into the database. These specific points for the damage levels were either taken from the tabulated values in the reports if they were available or by scaling from the axial load versus axial deformation plots.

In none of the column tests in the database was the lateral stress distribution of the steel tube throughout the test provided. Therefore, for the assessment of damage levels within the RCFT column database, lateral stresses in the steel tubes were neglected and the steel tube was assumed to be in a uniaxial stress state. Thus, the axial load level at the initiation of steel yielding, P_y , was calculated by multiplying the yield strain of concrete by the axial rigidity of the composite section, as follows:

$$P_y = \varepsilon_y \times (E_s \times A_s + E_c \times A_c) \quad (2.1)$$

In previous studies by Bridge (1976) and Inai and Sakino (1996), no confinement was observed from the rectangular steel tube on the concrete core until the concrete begins to crush. As this often is close to the attainment of the peak load in RCFT columns, no significant enhancement in the peak strength of an RCFT is expected due to lateral pressure from the steel tube (Gourley et al., 2001). Confinement is only effective in the post-peak response, as it often improves the ductility of the RCFT member. This indicates that the level of lateral stress in the steel tube is often insignificant before the peak load and that the yield condition of steel tube based on a uniaxial stress state is a reasonable assumption. Therefore, the method presented above for determining steel yielding was used only in the pre-peak region of the axial load versus axial deformation plots of the available tests. In the post-peak region, steel yielding points were scaled from the axial load versus axial deformation plots.

The second damage level recorded in the database was the local buckling of the steel tube walls. The instant of local buckling in the experiments was usually determined by observation of the experiment. It is also possible to detect local buckling more accurately using the longitudinal strain distributions over the steel tube wall. When steel tube buckles, the compressive axial strain undergoes a reduction at the locally buckled region and then increases as soon as concrete crushes and fills the locally buckled region (Matsui, 1986; Liu and Goel, 1987). This method requires the estimation of the local buckling region and putting strain gauges at those locations. However, this type of data was not available for any of the tests included in the RCFT database. Therefore, if the local buckling points are indicated on the axial load versus axial deformation plots, these points were scaled from the plots.

Because confinement action in rectangular RCFTs subjected to axial compression starts as the concrete begins to crush, until the initiation of concrete crushing, little interaction between the steel and concrete exists when subjected to pure axial compression, and the steel and concrete share the applied load independently of each

other (Gourley et al., 2001). Therefore, the concrete inside the rectangular steel tube is often treated approximately as plain concrete until the initiation of crushing (Inai and Sakino, 1996; Hajjar et al., 1998). As in the case of steel yielding in compression, few of the tests in the monotonically loaded RCFT column database provided any load or deformation level for the occurrence concrete crushing. Only in the reports by Varma (2000) and Varma et al. (2001) were concrete crushing points indicated on the axial load versus axial deformation plots, along with the other damage levels. If the concrete crushing points were indicated on the axial load versus axial deformation plots, the corresponding load and deformation levels were scaled from the plots and both values were stored in the database. However, in most of the tests, the concrete crushing was detected by comparing the crushing strain of plain concrete with the axial strain of the composite RCFT cross section. The concrete was assumed to be in a uniaxial stress state and it was assumed to crush when the axial strain of the composite RCFT cross section exceeded the crushing strain of the concrete.

The fourth damage level recorded in the database for the RCFT columns was the fracture of the steel tube wall. This damage level was only reported in the tests performed by Varma (2000) and Varma et al. (2001). The fracture occurred at the seam weld location in the post-peak region of load-deformation response. Varma (2000) and Varma et al. (2001) indicated the occurrence of the steel tube fracture on the axial load versus axial deformation plots. The corresponding force level and deformation level were scaled and stored into the database.

The final damage level recorded in the database is the axial load level at the point of flexural buckling, which occurs for columns with high L/D ratios.

2.2.1.2 Cyclically Loaded RCFT Column Database

Similar to the monotonically loaded column tests, the first section of the cyclically loaded column database includes the description of the tests. Available information about the loading scheme, boundary conditions, and test setup were provided. Cyclic axial load tests are usually performed to investigate the behavior of CFT columns used as slender bracing members or truss elements (e.g., Liu and Goel,

1987; Matsui and Kawano, 1988; Kawano and Matsui, 1988; Kawano and Matsui, 1996). The CFT columns are tested under displacement-controlled loading scheme, and pinned-end conditions are sometimes provided through the use of gusset plates attached at the ends (Liu and Goel, 1987). The only cyclically loaded column tests for rectangular RCFTs were carried out by Liu and Goel (1987). Therefore, the cyclically loaded column database includes only this set of tests.

In the second part of the cyclically loaded column database, the geometric and material properties of the specimens were stored. The same parameters as in the monotonically loaded database were included. The measured and nominal values were entered separately.

In the cyclically loaded column tests, only A500 Grade B type steel was used to manufacture the specimens. The measured yield stress ranged from 372.3 MPa (54 ksi) to 413.7 MPa (60 ksi). Liu and Goel (1987) also noted the variation of the yield stress around the perimeter of the steel tube. The mean ratio of yield strength of the corners to the yield strength of the flats was found as 1.19. The fracture elongation of the coupon specimens also showed variation for the corners and flats. It was found that the fracture strain of the flats is approximately 43% larger than that of the corners. This shows that the increase in yield strength caused a reduction in ductility at the corners. The coupon specimens did not exhibit a definite strain-hardening region. There was a smooth transition region between the pre-peak and post-peak response. Due to the cold forming process, the proportional limit decreased, and a proportional limit that was 50% of the yield strength of the steel tube was recommended. The level of this proportional limit was also consistent with the results by Furlong (1968) and Clarke and Hancock (1991), which reported proportional limits of 50% and 54.5% of the yield stress, respectively. The ultimate strength of the steel tubes was 1.15 times greater than the yield stress. The variation of the ultimate strength around the steel tube was similar to that reported for the yield strength. When the ultimate strength of the steel tube in the corners and in the flats were compared, it was found that the mean ratio of ultimate strength of the corners to the flats was 1.19.

The compressive strength of the concrete ranged from 31.4 MPa (4.6 ksi) to 46.7 MPa (6.8 ksi). The mean ratio of the measured concrete strength to the nominal concrete

strength was 1.13 with a standard deviation 0.006 for the cyclically loaded column specimens. The mean ratio and standard deviation for the whole database was 1.089 and 0.189 showing that cyclically loaded columns have similar mean value for the ratio of measured to nominal concrete strength with the whole database.

A constant D/t ratio of 30 was selected for the specimens. As the RCFT columns under cyclic loading are used as bracing members, it is not efficient to use large D/t ratios. In their cyclically loaded column tests of circular CFTs, Kawano and Matsui (1988) also used steel tubes having D/t ratios close to 30.

The L/D of the specimens in the cyclically loaded column tests were larger than many of the other specimens in the database, which is a typical characteristic of CFT bracing members. The L/D ratio of the specimens ranged between 22.7 and 34.3.

The first experimental result recorded in the cyclically loaded column database is the peak axial load level. As the loading is applied in two directions, both the peak compressive force and tension force were stored, separately. For the specimens tested by Liu and Goel (1987), the cyclic load deflection plots were provided in normalized form and the value of the parameter used for normalization was not provided. Therefore, the peak axial loads were scaled from the hysteresis loops and recorded in normalized form. The axial strains at peak axial loads and the ultimate axial strain values for both tension and compression were also scaled from the hysteresis loops and stored in the database. The normalized axial displacement values from the load deflection curves were multiplied by the given yield displacements and the resulting axial displacement values were divided by the specimen length to get the axial strain.

The behavior of the slender RCFT columns is usually governed by the steel, and composite interaction between steel and concrete is not significant (Shakir-Khalil and Zeghiche, 1991; Gourley and Hajjar, 1994; Hajjar and Gourley, 1996). Based on this fact, five different types of damage levels were defined for the cyclically loaded column tests. These damage levels include steel yielding, initiation of flexural buckling, local buckling, concrete crushing, and steel tube fracture. It is less likely that for slender members initial cracking of the concrete can affect the behavior noticeably. Therefore, this event was excluded from the damage levels.

In the case of cyclic loading, the column is subjected to subsequent compressive loads. Once the compressive load is relieved and tension load is started to be applied, the column can recover some of its compressive deformation. This causes the column to undergo flexural buckling several times until it fails. However, after initial flexural buckling occurs, the resistance of the column in compression decreases significantly. Therefore, the initiation point of the first instance of flexural buckling was recorded in the database and this event was defined as a damage parameter which is specific to this type of tests. This damage level corresponds to the attainment of peak load for slender monotonic columns. Liu and Goel (1987) indicated the occurrence of the aforementioned damage levels on the load-deflection plots. The load and deformation levels corresponding to these events were scaled from the load-deflection plots and stored in the database.

2.2.2 RCFT Beam-Column Database

The beam-column database includes specimens tested under axial load and combined bending moment. A total of 261 specimens were selected from the literature between 1976 and 2001. The collected data represents worldwide practice in RCFT beam-columns and covers the experimental research programs conducted in the United States, Canada, Europe, Japan and Australia.

2.2.2.1 Monotonically Loaded RCFT Beam-Column Database

In monotonically loaded beam-column database, RCFT members tested under combined axial load and bending moment and RCFT members tested under pure bending were included. Similar to the previous databases, the first part of the database presents information about the type of loading, test setup and boundary conditions. In the monotonically loaded beam-column tests, bending moment was applied either by an eccentrically applied axial load or by means of other mechanisms independent of the axial load, e.g., a lateral load or applied end moments. Based on the manner of introducing the bending moment, the testing methods were divided into four groups,

which were designated as MI, MII, MIII and MIV, where M stands for monotonic loading. The schematic view of the test setups can be seen in Figure 2.18. Method MI represents the eccentrically loaded members (e.g., Bridge, 1976; Cederwall et al., 1990; Grauers, 1993). In method MII, a lateral load is applied at the ends combined with axial load (e.g., Tomii and Sakino, 1979b; Sakino and Ishibashi, 1985). Method MIII has axial load at the ends combined with bending moment applied through a loading girder or a couple generated at the end region of the member causing members to undergo single curvature (e.g., Tomii and Sakino; 1979a, Nakahara and Sakino, 1998; Varma , 2000; Varma et al., 2002a). Method MIV is the standard four point bending type loading which is mainly used for pure bending tests (e.g., Lu and Kennedy, 1992; Lu and Kennedy, 1994). As can be seen in Figure 2.19 from the histogram of the loading methods for the monotonically loaded beam-column tests, eccentrically loaded specimens were more commonly investigated than the other testing procedures.

The second part of this database includes the measured and nominal material properties of the specimens. The same types of parameters as in the case of monotonically loaded column database were recorded.

The measured yield strengths of the steel tubes range from 194.2 MPa (28.2 ksi) to 834.8 MPa (121.1 ksi). The histogram given in Figure 2.20 shows that beam-columns with low strength steel tubes were more comprehensively investigated than medium strength and high strength steel tubes. The material properties of the steel tubes are highly dependent on the residual stress distribution around the perimeter. There are two possible ways to study the effect of residual stresses. Either coupon specimens are taken from different positions around the steel tube or short bare steel tubes are tested under compression. The comparison of the yield strengths obtained from the coupons around the perimeter has already been made in section 2.2.1.1 for monotonically loaded column specimens and it was found that yield strength of the corners were larger than the flats. In the beam-column tests, stub columns were frequently used to determine the yield strength of the steel tubes (Shakir-Khalil and Zeghiche, 1989; Shakir-Khalil and Mouli, 1990; Shakir-Khalil, 1994; Chung et al., 2001) and these values were also stored in the monotonically loaded beam-column database. It is also possible to see the comparison of the yield strength from the coupon tests with the yield strength from the stub columns in

Figure 2.21. The mean value of the ratio of yield strength from the coupon tests to the yield strength from stub column tests was found as 1.009 with a standard deviation of 0.065. In the tests by Shakir-Khalil and Mouli (1990) and Shakir-Khalil (1994) on 100 mm stubs, for the majority of the specimens the yield strength from stub columns were larger than coupon tests. In the tests by Chung et al. (2001), 375 mm stub columns were used and due to local instability of the steel tubes, the resulting yield stresses were lower than the coupons. Therefore, it can be concluded that stub columns tend to have higher yield strength values than coupon tests. Figure 2.22 shows the comparison of nominal yield stress and measured yield stress values of monotonically loaded beam-column tests and the other tests in the database with available data. The monotonically loaded beam-column tests have a mean value of 1.146 and standard deviation of 0.166 for f_y/f_{yo} ratio. These values are close to the mean and standard deviations for all of the tests in the database, which were found as 1.218 and 0.211, respectively.

The comparison of nominal modulus of elasticity and measured modulus of elasticity for the monotonically loaded beam-column tests and the other tests in the database with available data can be seen in Figure 2.23. The mean ratio of the E_s/E_{so} for the monotonically loaded beam-column tests was found to be 1.009 with a standard deviation of 0.01. This shows that for these tests the variation between the elastic modulus and nominal modulus is very small and they can be assumed to be equal to each other. In addition, the values of mean and standard deviation found for the monotonically loaded beam-columns are close to the results obtained for all of the tests in the database, which has a mean value of 1.006 and a standard deviation of 0.017.

For the monotonically loaded beam-column tests, the ultimate strength of the steel tubes was also recorded in the database. Figure 2.24 shows the variation of ultimate strength of the steel tube with respect to the yield strength for the monotonically loaded beam-column tests and for the other tests in the database with available data. There is a clear trend for both sets of data that the ratio of ultimate strength of steel tube to the yield strength approaches to 1.0 as the yield strength of the steel tube increases. No residual stress measurements in the steel tubes were made for the specimens in the beam-column database. Therefore, in the database, it was only noted if the specimens were annealed and free from residual stresses.

The histogram of the measured compressive strength of concrete for the monotonically loaded beam-column database can be seen in Figure 2.25. The compressive strength of concrete ranges between 19.8 MPa (2.9 ksi) to 119 MPa (17.3 ksi). The histogram in Figure 2.25 also indicates that the number of specimens with medium strength of concrete is relatively low compared to the specimens with low strength or high strength concrete. The comparison of nominal strength of concrete and measured compressive strength of concrete is shown in Figure 2.26 for both the monotonically loaded beam-column tests and the other tests in the database with available data. This figure indicates that for both sets of data the measured values of concrete compressive strength were larger than the nominal values. The mean ratio of measured compressive strength of concrete to the nominal compressive strength of concrete for monotonically loaded beam-column specimens was found as 1.094 with a standard deviation of 0.205. Similar results were obtained for all of the tests in the database with a mean value of 1.089 and a standard deviation of 0.189. Figure 2.27 shows the variation of the ratio of measured compressive strength of concrete to the nominal compressive strength of concrete with respect to the nominal strength concrete. This figure demonstrates that both for the monotonically loaded beam-column specimens and the other tests in the database a decrease in the ratio of f'_c/f'_{co} is evident as the nominal compressive strength of concrete increases. Among the monotonically loaded beam-column tests, Shakir-Khalil and Mouli (1990), Cederwall et al. (1990), Grauers (1993) and Shakir-Khalil (1994) reported the cubic compressive strength of concrete. From these test results, the mean ratio of cubic compressive strength of concrete to the cylinder compressive strength of concrete was found as 0.792 with a standard deviation of 0.114. This result also supports the 0.8 factor recommended by Bergmann (1994) to convert cylinder compressive strength of concrete to its cube strength.

The variation of E_c with respect to f'_c and f'_{cub} is examined in Figure 2.28 for both the monotonically loaded beam-column tests and the other tests available in the database. It was found that for both sets of the data, the value of E_c increases when the compressive strength of the concrete increases.

In the geometric properties section of the monotonically loaded beam-column database, measured and nominal values of depth, thickness, and length of the specimens

were stored. In addition, D/t and L/D ratio of the specimens, which are the two key geometric parameters affecting the behavior of the RCFT members, were recorded. For the D/t ratio, in the majority of the tests both nominal and measured values were reported. As the D/t ratio defines the cumulative variation of the measured depth and measured thickness of the steel tubes with respect to their nominal values, the nominal and measured values of the D/t ratio were stored in the database separately. Figure 2.29 demonstrates the comparison of the measured depth and nominal depth of the specimens for both the monotonically loaded beam-column database and for the overall database. No specific trend for D/D_o was observed for the monotonically loaded beam-column specimens, while for the overall database there is an increase in D/D_o as the value D gets larger. In the monotonically loaded beam-column database, the nominal depth of the specimens was only reported by Bridge (1976). The mean value of D/D_o for these specimens was found to be 1.02 with a standard deviation of 0.003. The mean and standard deviation of D/D_o for the whole database were 1.003 and 0.005, respectively. The comparison of measured and nominal thickness of the steel tubes for the monotonically loaded beam-column tests and for the other specimens in the database with the available data is shown in Figure 2.30. Among the monotonically loaded beam-column specimens, for approximately 54% of the specimens, the value of t/t_o was less than 1.0. For the same specimens, the mean value of t/t_o was found as 0.994 with a standard deviation of 0.065. A similar trend was also observed in the case of the overall database, for which the mean value of t/t_o ratio was found as 0.991 with a standard deviation of 0.059. The D/t ratio of the specimens in the monotonically loaded beam-column database ranged from 12.8 to 74.0. The histogram of the beam-column specimens for D/t ratio is shown in Figure 2.31. This histogram shows that specimens with a small D/t ratio were tested more comprehensively, while fewer specimens were tested with D/t ratios above 70. The comparison between the nominal and measured D/t ratios is demonstrated in Figure 2.32 for the monotonically loaded beam-column specimens and for the other specimens in the database with available data. In the majority of the monotonically loaded beam-column tests, the measured D/t ratio was greater than the nominal value. The same trend was also observed for the overall database.

The histogram of the monotonically loaded beam-column specimens for the L/D ratio is shown in Figure 2.33. This figure shows that the number of slender specimens ($L/D > 15$) in the beam-column database is less than the short specimens ($L/D < 15$). However, compared to the monotonically loaded column database, there are more slender members in the monotonically loaded beam-column database.

The last geometric property stored in the beam-column database is the amount of eccentricity provided for the specimens tested by the loading method MI. About 10% of the specimens tested by loading method MI were subjected to biaxial bending. Therefore, eccentricities with respect to major axis and minor axis were stored separately. If the amount of eccentricity is normalized with respect to the depth of the specimens, it was found that the maximum e/D ratio was on the order of $1.4D$.

In the experimental results section of the monotonically loaded beam-column database load capacities, deformation capacities and specific damage levels in terms of load and deformation values were stored. The specimens were tested under axial load and bending moment. Therefore, the peak values of both of these parameters were stored in the database if they were made available. These values were either taken from the tables given in the reports or they were scaled from the load-deflection curves. Different types of deformation measures were provided in the tests including mid-height curvatures, end rotations, and lateral displacements at mid-height. For each specimen, the deformation level at the peak load and at the end of the test were recorded. In the majority of the tests, these values were scaled from the load deflection plots. The peak points on the load deflection plots were defined using the same method adopted in the case of monotonically loaded column database. The initial flexural stiffness of the specimens was also recorded in this part of the database, and all of these values were taken from the tables given in the reports. Finally, the failure location of the specimens was noted if it was described in the report. Figure 2.34 demonstrates the trend of end

rotation at the peak axial load with respect to the parameter $\frac{D}{t} \cdot \sqrt{\frac{f_y}{E}} \cdot \left(\frac{f'_c}{f_y}\right)^{-1} \cdot \frac{L}{D}$ for the

specimens tested by loading scheme MI. For these specimens, the end rotation was calculated as the ratio of mid-height displacement over half-column length. Figure 2.34

indicates that when the parameters $\frac{D}{t} \cdot \sqrt{\frac{f_y}{E}}$ and L/D get larger, an increase in the end rotation at the peak axial load is evident due to reduced stiffness of the member. If the parameter $\frac{f'_c}{f_y}$ increases, the brittle nature of the concrete governs the behavior of the member and the end rotation at the peak axial load reduces.

Six different types of local damage levels were defined for the beam-column members. The damage levels consist of initial concrete cracking, steel yielding in compression, concrete crushing, steel yielding in tension, local buckling in column compression flange and local buckling of column web. Both the load levels and deformation levels at these specific events were stored in the database if they were made available. These points were either taken from the tabulated values in the reports, by scaling from the load-deformation plots, or through analytical calculations based upon related experimental results.

The first local damage level for the beam-column specimens was initial concrete cracking. The concrete cracking points were determined by assuming that it took place when the strains in the tension flange of the beam-columns become tensile. This method was only used if the strain distribution on the tension flange of the steel tube was available in the reports (Shakir-Khalil and Zeghiche, 1989; Shakir-Khalil and Mouli, 1990 and Shakir-Khalil, 1994). As the tensile strength of concrete is as low as 10% of its compressive strength, it is most probable that concrete cracking will take place soon after tensile stresses starts act on concrete. Due to the small thickness of the steel tubes, it is reasonable to presume that tensile stresses in the concrete will be generated when the stresses in the steel tube become tensile due to combined axial compression and flexure. If the initial concrete cracking points were indicated on the load deflection curves, the load and deformation levels were scaled from these plots (Varma, 2000; Varma et al., 2002a).

For detecting the steel yielding points in tension and in compression, the strain distribution on the steel tube at mid-height of the specimens was used. It was assumed that the steel tube at the mid-span has an approximately uniaxial stress state for each of the loading types defined previously. Therefore, yielding was assumed to occur when the

strain of the steel tube reached the measured yield strain value obtained from the coupon specimens. This method was only used for the specimens of Shakir-Khalil and Zeghiche (1989), Shakir-Khalil and Mouli (1990), Lu and Kennedy (1992), Lu and Kennedy (1994), and Shakir-Khalil (1994). In all of these tests, no local buckling was observed and the confinement effect was low due to the large L/D ratio. On the other hand, for the majority of the beam-column tests, the researchers indicated the steel yielding points on the load-deflection curves. For these cases, the load and deformation levels were scaled from the load-deflection plots (e.g., Bridge, 1976; Cederwall et al. (1990); Grauers, 1993).

Concrete crushing was also detected using different methods depending on the data presented in the reports. Lu and Kennedy (1992), Lu and Kennedy (1994) provided the strain distribution of concrete along the depth of the steel tubes. Concrete crushing was assumed to take place when the compressive strain of the concrete at the extreme fiber reaches the crushing strain. For the specimens having a high strength of concrete or a high D/t ratio, the concrete crushing usually occurred near the peak load. For these specimens, if the load-deflection plots had a distinct peak point and concrete crushing at the peak point was reported in the paper, the load and deformation levels at the peak points were scaled and assumed to be the occurrence of concrete crushing (e.g., Nakahara and Sakino, 1998). Otherwise, whenever the concrete crushing points were indicated on the load-deflection plots, the corresponding load and deformation levels were scaled (Varma, 2000; Varma et al., 2002a). However, such values were not reported for CFTs having low D/t ratios or low strength concrete, as these ductile specimens have gradual and significant concrete crushing that is difficult to detect experimentally.

The bending moment acting on the steel tubes causes a strain gradient along the depth of the specimens. This strain gradient makes the flanges of the steel tubes more susceptible to local buckling than the webs. Consequently, different from the monotonically loaded column tests, the local buckling of the steel tube was defined as two distinct damage levels for the web and flange, separately. In all of the tests that experienced local buckling in the steel tube flange, web, or both, the occurrence of these events was shown on the load-deflection plots (Tomii and Sakino, 1979a; Sakino and Ishibashi, 1985; Varma, 2000; Varma et al., 2002). Therefore, the corresponding load

and deformation levels were scaled from the load-deflection plots and recorded in the database.

The last damage parameter recorded in the monotonically loaded beam-column database was the fracture of the steel tube. This event usually defined the end of the tests and it was indicated on the load-deflection plots. In the beam-column database, this damage level was only reported by Fujimoto et al. (1995), Varma et al. (2000), and Varma et al. (2002a). The corresponding load and deformation levels were scaled from the given load-deflection plots and recorded in the database.

2.2.2.2 Cyclically Loaded RCFT Beam-Column Database

The cyclically loaded beam-column database includes the specimens tested under cyclic bending moment and constant or variable axial load. The first part of the database describes the loading condition, test set-up, and boundary conditions. For the cyclically loaded beam-column specimens, two types of testing methods were used, which were designated as CI and CII, where C stands for cyclic loading. The type CI loading has a cyclic lateral load and a constant or variable axial load applied at the ends. These specimens are subjected to double curvature bending with built-in supports at both ends. In the case of type CII loading, cantilevered specimens were subjected to single curvature bending with a cyclic lateral load and a constant or variable axial load applied at the free end. The schematic view and the histogram for the test methods can be seen in Figure 2.35 and Figure 2.36, respectively. Figure 2.36 shows that type CII loading was more commonly used for the cyclically loaded beam-column specimens.

In the second part of the cyclically loaded beam-column database, nominal and measured material properties of the specimens were recorded. The same parameters as in the case of the monotonically loaded column database were included. The nominal and measured properties were reported separately.

The measured yield strength of the steel tubes were ranging from 259 MPa (37.57 ksi) to 825 MPa (119.67 ksi). In Figure 2.37, the histogram of yield strength of steel for the cyclically loaded beam-column database shows that specimens with low strength steel were more comprehensively investigated than the specimens with medium or high

strength steel. The comparison of measured and nominal yield strength of the steel can be seen in Figure 2.38 for both the cyclically loaded beam-column specimens and the other specimens in the database with available data. The mean value of f_y/f_{yo} for the cyclically loaded beam-column specimens was found as 1.414 with a standard deviation of 0.243. However, for the overall database, the mean value of f_y/f_{yo} was 1.213, which is lower than the mean value for the cyclically loaded beam-columns. This is because the cyclically loaded beam-columns were mainly tested by Japanese researchers, and the variation between measured and nominal yield strength of steel appears to be larger in Japanese practice. The ultimate strength of the cyclically loaded beam-columns also exhibits a definite trend, such that with an increase in yield strength, the value of the ultimate strength approaches that of the yield strength of the steel tube, as can be seen in Figure 2.39. For the cyclically loaded beam-column specimens, the mean ratio of f_u/f_y was found as 1.200 with a standard deviation of 0.125. These statistical parameters are also close to the ones calculated for the overall database, which has a mean f_u/f_y ratio of 1.304 and standard deviation of 0.193. None of the specimens in the cyclically loaded beam-column database was reported to be annealed and no residual stress measurement was given in the reports.

In this database, the compressive strength of the concrete ranges between 17.60 MPa (2.55 ksi) and 110.00 MPa (15.96 ksi). Figure 2.40 shows the histogram of the compressive strength of concrete for the cyclically loaded beam-column specimens. This figure indicates that very few specimens with medium strength concrete were tested compared to the specimens having low strength or high strength concrete. The variation between the measured and nominal values of the compressive strength of concrete for the cyclically loaded beam-columns and the other specimens in the database with the available data is demonstrated in Figure 2.41. For the majority of the specimens, the measured concrete strength was larger than its nominal value and the mean value of f'_c/f'_{co} for the cyclically loaded beam-columns was found to be 1.023 with a standard deviation of 0.0378. This is similar to the trend of the f'_c/f'_{co} ratio for the overall database, which has a mean value of 1.064 and standard deviation of 0.201. The variation of the f'_c/f'_{co} ratio with respect to the compressive strength of concrete is examined in Figure 2.42. No clear trend was obtained for the cyclically loaded beam-

column specimens, whereas in the case of the overall database, f'_c / f'_{co} was decreasing with an increase in concrete strength. For the specimens in the cyclically loaded beam-column database, limited or no data was provided for the cube compressive strength and modulus of elasticity of concrete. Therefore, it was not possible to draw any conclusion about their trends.

In the geometric properties section of the cyclically loaded beam-column database, nominal and measured values of depth, thickness, and length of the specimens were recorded. In addition, major parameters including D/t and L/D ratios were also stored. For the D/t ratio, both the nominal and measured values were entered into the database. The nominal depth (in addition to the measured depth) of the cyclically loaded beam-column specimens was only provided by Kawaguchi (2000), Kawaguchi and Morino (2001). Figure 2.43 shows the variation between the nominal depth and measured depth of the cyclically loaded beam-column specimens, as well as the other specimens in the overall database with available data. Similar to the results obtained for the overall database, the measured and nominal depth of the specimens in the cyclically loaded beam-column database were approximately equal to each other, with a mean value of 1.000 and a standard deviation of 0.002 for the D/D_o ratio. The comparison of the nominal and measured thickness of the cyclically loaded beam-columns and the other specimens in the overall database are shown in Figure 2.44. In approximately 80% percent of the cyclically loaded beam-column tests, the measured thickness of the specimens were less than the nominal values, and the mean value of the t/t_o was found to be 0.968 with a standard deviation of 0.0527. These parameters are also close to the mean and the standard deviation values obtained for the overall database, which were found as 0.993 and 0.0597, respectively. The histogram of D/t ratio for the cyclically loaded beam-column specimens is shown in Figure 2.45. The D/t ratio of the specimens ranged from 18 to 52; very few specimens were tested for large D/t ratios. The nominal and measured D/t ratios of the cyclically loaded beam-column specimens and the other specimens in the database with available data are shown in Figure 2.46. In both sets of the data, the measured D/t ratio of the specimens was larger than their nominal D/t ratio. The mean $(D/t)/(D/t)_o$ ratio for the cyclically loaded beam-columns was 1.009 and the corresponding standard deviation was 0.041.

The L/D ratio of the specimens ranged between 3 and 10.5. The histogram for L/D ratio of the cyclically loaded beam-column specimens is shown in Figure 2.47. This figure indicates that no specimen was tested having an L/D ratio greater than 15.

The experimental results recorded in the cyclically loaded beam-column database include load capacities, deformation capacities, and damage levels of the specimens. In the majority of the tests, the load capacity of the specimens were given in terms of axial load, lateral load (where applicable), and bending moment. The peak values of all these load parameters were stored in the database. These values were either taken from the tables or they were determined by scaling from the load-deflection curves. As the loads were applied in two directions, the peak value in each direction was added to the database. Two types of deformation capacities were stored. The first one is the deformation level at the peak lateral load or bending moment and the second one is the ultimate deformation level. The deformation levels were also recorded separately for both directions of loading. Different deformation measures were presented depending on the type loading and in the majority of the tests either lateral displacements (Δ) or chord rotations (R) were given. Figure 2.48 shows the variation of R_o with respect to the

$$\text{parameter } \frac{D}{t} \cdot \sqrt{\frac{f_y}{E}} \cdot \frac{f'_c}{f_y} \cdot \frac{1}{L/D}.$$

For the specimens where lateral displacements were reported, the value of R_o was calculated by dividing the lateral displacement at the peak lateral load by the length of the member (all such specimens were cantilevers). It is observed in Figure 2.48 that the R_o

values get smaller when the parameter $\frac{D}{t} \cdot \sqrt{\frac{f_y}{E_s}} \cdot \frac{f'_c}{f_y} \cdot \frac{1}{L/D}$ increases.

A total of eight different damage levels were defined for the cyclically loaded beam-column specimens. These damage levels consist of initial concrete cracking, steel yielding in compression, steel yielding in tension, concrete crushing, local buckling in the compression flange, local buckling in the web, and fracture of steel tube. The load and deformation values at the occurrence of each damage level were recorded. This was done for both directions of loading, and the corresponding cycle numbers at which the damage occurred were also stored in the database if they were reported. In most of the cases, the researchers indicated the occurrence of the damage levels on the load-deflection curves

and the corresponding load and deformation values were simply scaled. Otherwise, the damage levels were extracted from experimental load-deflection curves by analytical methods as will be described in Chapter 3. The cycle numbers at which the local damage took place were either reported in the papers or they were determined by counting the peak points of the loading cycles if the load-deflection curves were clearly drawn.

2.2.3 RCFT Panel Zone Database

The RCFT panel zone database embraces panel zone tests conducted by testing short RCFT members under shear force combined with or without axial loading. A total of nine specimens were selected. The specimens were taken from the research studies carried out in Japan and in the United States within the period 1991 to 1995.

2.2.3.1 Monotonically Loaded RCFT Panel Zone Database

The behavior of panel zone is important, especially, in high rise frames. Under lateral loading, the contribution of the panel zone to the interstory drift becomes significant. In addition, the deformation of the panel zone contributes to the energy dissipation capacity of the overall structural system. RCFT frame structures have the advantage that both concrete and steel resist the shear forces coming to the panel zone through the girder flanges. However, the contribution of the concrete to the panel zone behavior is not completely understood and it is a subject of ongoing research. Therefore, the tests isolating the behavior of the panel zone are very valuable and these tests were documented in a separate database.

The panel zone database was introduced in four sections, including the test description, material properties, geometric properties, and experimental results. Similar to the other databases, the test description section gives general information of the test setup, loading method, and boundary conditions. The material properties and geometric properties sections contain the same type of information for the steel tube and concrete as in the case of the RCFT column and beam-column databases. One of the main parameters examined in the panel zone tests was the existence of the interior diaphragm

plate. Therefore, in the geometric properties section, it was also noted if the diaphragm plates are placed inside the steel tube and the thickness of the diaphragm plates was given if it was made available in the reports. The L/D ratio was not recorded, as the slenderness of the specimens is not an issue for the panel zone tests. However, the aspect ratio of the panel zone (d_g/D) was stored in the database.

The panel zone specimens are usually tested using simpler test setups than the connection subassemblies. The loading condition in the panel zone region is generated by applying shear couples through application of a transverse concentrated load at the mid-height of a simply-supported RCFT column. It is also common to apply an axial load combined with the shear couples to simulate the loads acting from the upper stories on to the RCFT columns.

The yield strengths of the steel tubes were ranging from 333.5 MPa (48.38 ksi) to 412 MPa (59.76 ksi). For the majority of the specimens, a low compressive strength of concrete ranging from 23.3 MPa (3.38 ksi) to 39.0 MPa (5.66 ksi) was utilized. The D/t ratio of the specimens also did not have a wide range of values, with minimum and maximum values of 27 and 48, respectively.

In the experimental results section of the database load capacities, deformation capacities, and damage levels of the specimens were recorded. The load capacities were defined by the peak axial load and peak shear force applied to the panel zone. Two types of deformation levels were stored, including the shear deformation at the peak shear load and the ultimate shear deformation. These values were either taken from the tables or scaled from the load-deformation plots. In addition, the initial stiffness of the specimens was recorded in this section if it was made available in the reports.

The damage levels defined for the monotonic panel zone specimens were shear cracking of concrete, yielding of steel tube, local buckling of the steel tube, and concrete crushing. The load and deformation levels corresponding to the aforementioned damage levels were either calculated analytically or they were scaled from the load–deformation plots.

2.2.4 RCFT Pinned Connection Database

The tests performed on shear connections between RCFT columns and steel girders are presented in this database. Only the connection tests with insignificant transfer of bending moment were considered. A total of 38 specimens were selected from experimental studies carried out in Canada and Europe within the period from 1987 to 1999. No cyclic RCFT pinned connection tests were included in the database.

2.2.4.1 Monotonically Loaded RCFT Pinned Connection Database

One of the advantages of the CFT members is that they can be used in both unbraced and braced frame construction. In the recent years, braced frames with CFT columns have started to become popular on the west coast of the United States (Gunderson, 2002). However, braced frame construction requires the use of shear connections at the beam-column joints. This type of connection may be subjected to excessive slip, and shear studs may be needed to ensure the composite action, which makes the connections more costly. Therefore, monotonically loaded pinned connection tests are critical to understand the response of braced frames. In this database, only the connections having no shear connectors are presented.

The pinned connections can be divided into two groups as PCI and PCII according to their loading type. As shown in Figure 2.49, PCI specimens have the RCFT columns loaded on both sides of the CFT. Axial load on the column is applied simultaneously with the shear loads acting at the tips of the girders. There exist two types of PCI specimens, which are identified as PCIa and PCIb. PCIa specimens have equal eccentricities on both sides, while PCIb specimens were subjected to unequal eccentricities. On the other hand, PCII specimens have RCFT columns connected to a steel girder only on one side. Therefore, PCII specimens are loaded unsymmetrically. PCII specimens can be further categorized into two subgroups. In the first subgroup (PCIIa), the axial load acting on the column and the shear load at the girder tip increase proportionally. For the second group (PCIIb), the axial load is kept constant while the shear load is increased. Figure 2.50, shows the histogram of the pinned connections with

respect to their loading scheme. PCI type specimens were investigated more commonly than PCII type specimens.

The monotonically loaded pinned connection database was divided into 5 main sections, which were designated as test description, connection properties, girder properties, RCFT column properties and experimental results. The test description section provides information about the test setup, loading scheme, and boundary conditions of the specimens. The connection properties section was separated into two subsections for connection description and main connection component properties. In the former sub-section, the connection and its detailing are described. Then, in the latter sub-section, the material and geometric properties of the main connection components are presented. A main connection component is defined as an element of the connection that is primarily responsible for the load transfer. For the material properties of the main connection components, the measured yield strength (f_{yme}), measured ultimate strength (f_{ume}) and measured modulus of elasticity (E_{sme}) were recorded (distinction between nominal and measured material properties were rarely made in the pinned connection tests). The geometric properties consist of the section type, length (L_{me}), depth (D_{me}), width (B_{me}), and thickness (t_{me}). No distinction was made between the measured and nominal values of the geometric properties. However, if both of them were provided in the reports, the priority was given to the measured values. In addition, the bolt types and bolt diameters (ϕ_{bolt}) used to attach the main connection components to the girder and to the steel tube are provided in this subsection. In the girder properties main section, the material and geometric properties of the steel girders are given. The material properties reported in this section are measured yield strength (f_{yg}), measured ultimate strength (f_{ug}) and measured modulus of elasticity (E_{sg}) of the steel girders. The section type, measured depth (d_g), measured width (b_g), measured flange thickness (t_f) and measured web thickness (t_w) of the girders are presented as their geometric properties. In addition, the eccentricities of the shear loads acting through the steel girders are also given in this section. The RCFT column properties are the same as in the case of column and beam-column databases.

The pinned connection subassemblages are tested under constant axial load applied to the column and monotonic shear load acting at the ends of the girders.

Although the shear connections exhibit some moment resistance, it is not significant and practically they can be treated as pinned connections. The boundary conditions of the columns are critical for the load transfer between the steel tube and the concrete core. The majority of the specimens in the database have uncapped ends.

Three types of main connection components were used for the specimens in the database, including structural tees, single plates, and end-plates. The histogram given in Figure 2.51 shows that the majority of the specimens have structural tees as their main connection components, where the flange of the tees were attached to the columns and the tee stems were attached to the girders web. The single plates were welded to the steel tube and bolted or welded to the girder web. The end-plates were attached to the columns by the blind bolting technique as will be described in section 2.2.5.1.

The yield strengths of the steel tubes were ranging between 300 MPa (43.5 ksi) and 450 MPa (65.3 ksi). This indicates that pinned connections to RCFT columns with high strength steel tubes were not investigated adequately. For the pinned connection specimens, the measured and nominal yield strength of the specimens also exhibited a variation as shown in Figure 2.52. The mean value of f_y/f_{y0} was found as 1.136 with a standard deviation of 0.10. These values are slightly less than 1.213 and 0.21 which were the mean and standard deviation values of f_y/f_{y0} calculated using the data of the overall RCFT column and beam-column database. This is because the tests conducted in Japan which have high f_y/f_{y0} ratio caused the mean value and standard deviation of f_y/f_{y0} to increase for the tests in the overall database. However, there are no tests from Japan in the monotonically loaded pinned connection database. The variation of f_u/f_y with respect to f_y is shown in Figure 2.53 for both the monotonically loaded pinned connection tests and the other tests in the overall database. For both sets of data, f_u/f_y exhibits a decreasing trend when the yield strength of the steel tube gets larger. In the majority of the monotonically loaded pinned connection tests, the nominal and measured values of modulus of elasticity of steel tube were given. Figure 2.54 shows the comparison of these two values for both the monotonically loaded pinned connection database and the overall database, simultaneously. The trend for both sets of data was that the variation of nominal and measured values of modulus of elasticity is not significant, with the mean E_s/E_{s0} values of 1.002 and 1.006, respectively.

In the pinned connection tests, the compressive strength of the concrete did not span a wide range of values. The maximum and minimum values of cylinder compressive strength of concrete was 17.4 MPa (2.52 ksi) and 41.7 MPa (6.05 ksi), respectively. Shakir-Khalil and Al-Rawdan (1995), Shakir-Khalil and Mahmoud (1995) provided both cube compressive strength of concrete and cylinder compressive strength of concrete for his specimens. Using the data by Shakir-Khalil and Al-Rawdan (1995), Shakir-Khalil and Mahmoud (1995), the average value of f'_c/f'_{cub} was found as 0.83 with a standard deviation of 0.094. As can be seen in Figure 2.55, for the monotonically loaded pinned connection specimens, the elastic modulus of concrete does not exhibit a definite trend with respect to compressive strength of concrete, while for the other tests in the database the elastic modulus of concrete increases when concrete strength achieves higher values.

Among the geometric properties of the monotonically loaded pinned connection specimens, the D/t ratio ranges from 20.8 to 37.1. This is a limited range for D/t ratios and signals the need for pinned connections tests for RCFT columns with larger D/t values. On the other hand, a wide range of L/D ratios were covered, ranging from 7.5 to 29, as can be seen in Figure 2.56. In most of the tests, the lengths of the columns were selected to represent a story height in a typical building. This makes the pinned connection tests more realistic.

The experimental results of the pinned connections stored in the database includes the load capacities and deformation capacities of the specimens. The load capacities of the specimens were defined by recording the peak axial load on the column and the peak moment applied through the girders. The deformation capacities were ultimate rotation at the end of the test and the rotation at the peak moment.

A total number of eleven damage levels were defined for the monotonically loaded pinned connections. These damage levels include initial concrete cracking, yielding of column flange, local buckling of column flange, concrete crushing, yielding of a main connection component, yielding of the girder web, local buckling of the main connection component, weld fracture, bolt failure, fracture of main connection component element, and fracture of the steel tube. The deformation levels and axial load levels corresponding to these damage levels were scaled from the load-deflection plots.

Otherwise, they were calculated by some analytical methods as will be described in Chapter 3.

2.2.5 RCFT Moment Connection Database

The moment connection database consists of the tests having RCFT columns framed by steel girders. In addition, RCFT frame tests designed for having weak connections were also covered within this database. A total number of 39 specimens were selected from the literature between 1987 and 2001. The collected data were taken from tests conducted in the United States, Japan, and Europe.

2.2.5.1 Monotonically Loaded RCFT Moment Connection Database

This database contains monotonically loaded connection tests where steel girders frame into RCFT columns. Monotonically loaded connection tests provide valuable information about the moment and rotation capacity of the connections. Therefore, this type of test is presented in a separate database, although the number of tests is small given the wide range of connection topologies that may be used for moment connections.

The monotonically loaded moment connections database consist of 5 main parts, which were defined as test description, connection properties, girder properties, RCFT beam-column and panel zone properties, and experimental results. Excluding the test description section, each of the other sections was divided into subsections depending on the type of data that was presented.

The first main section of the monotonically loaded moment connection database provides information about the test setup, boundary conditions, and loading method. A typical moment connection specimen is tested under constant axial load applied to the pin-ended beam-column and a shear force acting at the end of the girder that frames into the beam-column (all monotonically loaded moment connections represented exterior beam-to-column connections, with one girder framing into the beam-column).

The connection properties section was divided into three subsections. The first subsection presents the general description of the tested connection type. It is indicated

whether the connection is considered to be fully-restrained or partially restrained. The type of detail used to attach the girder to the column is then introduced. The following subsection provides the material and geometric properties of the main connection components. The type of material and geometric properties of the main connection components are the same as in the case of the monotonically loaded pinned connections database. In the next subsection, information about the auxiliary connection components is presented. Auxiliary connection components are defined as the components of the connection that are not primarily responsible for load transfer, e.g., cover plates, washer plates, etc. Both the material and geometric properties of the auxiliary components were stored. The material properties include the measured yield strength (f_{yae}) and measured ultimate strength (f_{uae}). For the geometric properties, the measured or nominal values of length, height, width, and thickness were recorded. The auxiliary component subsection also contains information about the shear-tabs and shear studs. The section type, bolt type, and bolt diameter (ϕ_{bolt}) of the shear tabs are given. The shear studs are described using their geometric properties, including the length and diameter.

The next main section of the monotonic connection tests contains the information for the girders framing to the RCFT columns. The material properties were recorded for the flange and the webs separately if they were available in the reports. Both the nominal (f_{yf}, f_{yw}) and measured yield strength (f_{yf}, f_{yw}) values were recorded. However, for the ultimate strength (f_{uf}, f_{uw}) and modulus of elasticity (E_{sf}, E_{sw}), only measured values were included. To define the geometric properties, the section type, measured length (L_g), measured depth (d_g) and measured thickness of the girders were stored. The thickness was entered to the database for the webs (t_w) and flanges (t_f), separately. The material and geometric properties of the column and panel zone is presented in the next main section of the monotonically loaded moment connection database. The material properties and geometric properties of the steel tube were stored for column and panel zone, separately. The material properties of the steel tube recorded in this section include measured yield strength (f_y, f_{py}), measured ultimate strength (f_u, f_{pu}), measured modulus of elasticity (E_s, E_{ps}), and measured strain hardening modulus (E_{sh}, E_{psh}) for the column and panel zone. In addition, the nominal values of yield strength (f_{yo}, f_{pyo}) and modulus of elasticity (E_{so}, E_{pso}) of the steel tube were stored. The residual stress in the steel tube was

also noted if it was made available in the reports. The recorded concrete material properties are exactly the same as in the case of column and beam-column databases. The geometric dimensions of the column and panel zone stored in the database include the measured and nominal values of depth (D, D_o), width (B, B_o), length (L, L_o) and thickness (t, t_o) of the steel tube. The measured and nominal thickness of the steel tube were given for the panel zone (t_p, t_{po}) separately. However, if it was not provided in the report, the thickness of the column and the panel zone were assumed to be the same. The measured and nominal values of the depth over thickness ratio were stored for both the column [$D/t, (D/t)_o$] and the panel zone [$(D/t)_p, (D/t)_{po}$]. Finally, the measured and nominal values of the length of the column (L, L_o) and the L/D ratio were also entered into the database.

In the monotonically loaded moment connection database, the available tests consist only of partially-restrained connections having blind-bolted details. The blind bolted connections are prepared through use of the flow-drilling technique. As shown in Figure 2.57, flow drilling involves drilling the steel tube thermally by means of a tungsten carbide without removing any material. At the end, the hole is threaded and a standard bolt can be inserted. The type of main connection component used in the blind-bolted connection tests was the end-plate placed between the girder and the steel tube. No auxiliary connection component or shear tab was utilized. The steel girder attached to the column had a yield strength of 275 MPa (39.89 ksi). The RCFT columns in this database were continuous and therefore the panel zone and the column were assumed to have the same material and geometric properties. The measured yield strength of the steel tubes varied from 275 MPa (39.89 ksi) to 355 MPa (51.49 ksi). The cylinder compressive strength of concrete was 40 MPa (5.80 ksi). The compressive cube strength was also provided and the ratio of cylinder strength to cube concrete strength was found to be 0.79. A constant D/t ratio of 20 and a constant L/D ratio of 7.5 was adopted was adopted in the tests.

The load capacities recorded in the monotonically loaded moment connection database included the peak axial loads and peak moments. All of these parameters were taken from the tables given in the reports. In addition, to define the deformation capacity of the connections, the ultimate rotations and the rotations at the peak moments were

stored. The former deformation measures of the specimens were scaled from the load-deformation plots. However, the latter ones were taken from the tables given in reports. The initial stiffness of the connections was also entered to the database if it was made available.

A total of 18 damage levels were defined for the connections. It is possible to divide the damage levels into 4 groups representing each part of the RCFT subassembly. Different damage levels were reported for the panel zone, column, main connection components, and girders. The damage levels for the panel zone includes initial concrete cracking, panel zone yielding, panel zone buckling, and concrete crushing. Concrete cracking, yielding of the column flange in compression, yielding of the column flange in tension, concrete crushing, local buckling of column flange, local buckling of the column web, and fracture of the steel tube characterize the damage levels of the columns. The types of damage levels for the main connection components cover yielding of the main connection component, local buckling of the main connection component, fracture of the main connection component, weld fracture, and bolt failure. Finally, the damage levels of the girders include yielding of the girder flange, local buckling of the girder flange, fracture of the girder flange and initiation of plastic hinging. The load and deformation values at the time of occurrence of the damage levels presented above were recorded in the database if they were available in the reports either in tabulated form or on the load-deflection plots. Analytical methods were also utilized to detect some of the damage levels as will be described in Chapter 3.

2.2.5.2 Cyclically Loaded RCFT Moment Connection Database

CFT members in lateral-resistance systems are used to resist lateral loads from earthquake or wind. Cyclically loaded connection tests are important to understand the mechanism of load transfer at the joint regions. Different connection details are used around the world depending on the common construction practices in that region of the world. However, the design of the most efficient and affordable connection detail for RCFT joints is still a subject of ongoing worldwide research. This database contains cyclically loaded connection tests where steel girders frame into RCFT columns.

Although no restriction about the type of detail was made in the database, the split-tee connections are particularly of interest as these connections have been shown to be appropriate for the U.S. construction practice (Koester et al., 2000; Koester, 2000; Peng et al., 2000; Peng, 2001).

The organization of the cyclically loaded moment connection database is exactly the same as the monotonically loaded moment connection database presented in the previous section. A total of five main parts were generated, which included test description, connection properties, girder properties, RCFT column and panel zone properties, and experimental results.

The cyclically loaded moment connections are usually tested under constant axial load and cyclically applied shear forces. The constant axial load acts at the top of the RCFT column while shear force may be applied in two different ways. The cyclic shear force is either generated at the ends of the girders or it is applied at the top of the column. The ends of the columns and girders in a cyclically loaded connection test represent the inflection points of columns and girders in a frame. Therefore, all of the supports are free to rotate in the plane of the joint.

The types of connection details existing in the cyclically loaded moment connections database are listed below:

- Through Diaphragm
- External Diaphragm
- Vertical Stiffener
- Interior Diaphragm
- Extended Tee
- Split Tee
- Post-Tensioned Strands
- Seat Angle
- End Plate

Through diaphragm connections are constructed by extending the girder flange through the RCFT column. Usually, an opening on the diaphragm plate is left for concrete pouring (e.g., Kanatani et al., 1987; Kawaguchi et al., 1997; Kawaguchi, 2000). In the case of external diaphragm connections, the girder flanges flares to the RCFT column

around its perimeter at a certain degree of angle (e.g., Kawano et al., 2000). The external diaphragms may limit the placement of the external walls of the buildings if the dimensions of the diaphragm plates are large. To overcome this problem, vertical diaphragm connection details were designed by replacing the external diaphragm at one side of the RCFT column with a vertical stiffener (e.g., Kawano et al., 2000). Interior diaphragms are similar to the through diaphragm plates. However, the diaphragm plate is welded to the inside of the steel tube and then the girders are welded outside the steel tube rather than extending the girder flanges through the RCFT column (e.g., Vermaas, 1995; Ricles et al., 1995).

The extended tee connections are made up of external tee stiffeners connecting the girder flanges to the RCFT column corners (e.g., Vermaas, 1995; Ricles et al., 1995). The stiffeners are welded to the corners of the CFT columns and flanges of the girders. In split tee connections, the stem of the structural tees are connected to the girder flanges through bolting or welding. The structural tee flanges are then attached to the RCFT column by tension bolts through the depth of the column.

The connections with post-tensioned struts are considered to be partially-restrained connections. The girder flanges are attached to the columns using seat angles. In addition, post-tensioned struts pass through the column; the struts are then anchored outside the connection (e.g., Peng et al., 2000; Peng, 2001). Seat angle connections are also considered to be partially-restrained. The girder is attached to the RCFT column using seat angles on both flanges (e.g., Peng et al., 2000; Peng, 2001). In the case of connections with the end plate detail, the steel girder is attached to the RCFT column with a welded end plate (e.g., Kanatani, 1987). The histogram for the connection details in Figure 2.58 shows that the split tee connections were investigated more than the others within this database.

The connection details are usually named according to the type of main connection component of the connection. As the designation of the connection details presented above imply, the main connection components in the cyclically loaded moment connection database include diaphragm plates, extended tees, structural tees, post-tensioned strands, and seat angles. The yield strengths of these components were ranging from 206 MPa (29.88 ksi) to 408 MPa (59.18 ksi). For 80% percent of the connections in

the database, the yield strengths of the main connection components were less than the yield strength of the steel tubes. If the yield strengths of the main connection components and steel girders are compared, for 56% percent of the connections in the database, the girders has a lower yield strength than the main connection components. The dimensions of these components with respect to the depth of the column is important in design and might have influence in the force transfer at the connection region. The ratio of the width of the structural tee to the depth of the RCFT columns ranged from 56% to 93%. The same ratio was equal to 62% for the seat angle connections. In the case of external or vertical stiffener type connections, the width of the diaphragm plate around the RCFT column was approximately 6% to 9% of the depth of the RCFT column. Another geometric dimension that also deserves attention for the main connection components is the thickness. The comparison of the steel tube thickness with the thickness of the main connection components is shown in Figure 2.59. In all of the cases, the ratio of the thickness of the main connection components to the steel tube thickness was larger than 1.0, and for the through diaphragm type connections it reached up to 4.3. The auxiliary components in the connections are mainly used for reinforcing the girder flange or steel tube. The common types of auxiliary components include washer plates, girder stiffeners, bearing plates, and cover plates. The yield strength of these components ranged from 263 MPa (38.15 ksi) to 346 MPa (50.19 ksi). The dimensions and thicknesses vary depending on the topology of the component. The ratio of the thickness of the auxiliary components to the steel tube thickness ranges from 0.4 to 1.9. The largest thickness for the auxiliary components in the database is used for the components reinforcing the steel girders.

The material and geometric properties of the girders can govern the failure sequence in a connection. Therefore, the material and geometric properties of the girders were included in the database as a separate section. The yield strength of the girders ranged from 229.6 MPa (33.30 ksi) to 379.2 MPa (55.00 ksi). When these values are compared to the yield strength of the steel tubes, in the majority of tests, the steel tubes had larger yield strengths. Figure 2.60 demonstrates the depth of the steel girders with the depth of the steel tubes to which they were attached. For every cyclically loaded connection test with available data, the depth of the steel girders is always larger than the

depth of the steel tubes. The thickness of the steel tubes and that of the steel girder flanges are compared in Figure 2.61. Similar to the trend obtained for the depth, the steel girders always had a larger thickness than the steel tubes. The larger geometric dimensions of the girders compared to the columns is typical of moment frames and is attributed partially to the fact that moment connections are commonly used in unbraced frames where the steel girder has a significant contribution to the interstory drift.

The type of geometric and material properties recorded for the RCFT columns are similar to the previous databases. The yield strengths of the steel tubes ranged from 350 MPa (50.77 ksi) to 420 MPa (60.92 ksi) indicating that the variation of the yield strength of the steel tube was not comprehensively investigated in the cyclically loaded connection tests. The yield strength and ultimate strength of the steel tubes are compared in Figure 2.62. On the same figure, the same parameters of the other tests in the overall database are also shown. For the cyclically loaded connection tests, the mean ratio of f_u/f_y was found as 1.218 and the standard deviation was 0.112. However, due to the limited range of yield strength, no specific trend of f_u/f_y with respect to f_y was observed for this group of specimens. In the tests conducted by Kawaguchi et al. (1997), Kawaguchi (2000), the panel zones of the specimens were constructed with a different type of section to ensure the failure to occur at the connection. For these specimens, the yield strength of the panel zones was approximately 85% of the yield strength of the steel tubes.

In the cyclically loaded moment connection database, the compressive strength of concrete ranged between 18.5 MPa (2.68 ksi) and 79.6 MPa (11.55 ksi). The histogram in Figure 2.63 for concrete strength shows that very few specimens were tested having high strength concrete, while specimens with medium and low strength concrete were investigated more commonly. In his connection tests, Peng et al. (2000), Peng (2001) provided the compressive concrete strengths obtained from the cored cylinders. When these values were compared with the concrete strengths from standard cylinder tests, the mean ratio of the f'_c/f'_{ccor} was found to be 0.86 with a standard deviation of 0.021. However, in the column and beam-column databases, Varma (2000) and Varma et al. (2001) obtained very close concrete strengths for both standard cylinders and cored cylinders. In both sets of tests, the concrete cylinders were subjected to wet curing. The cylinder tests performed by Peng et al. (2000), Peng (2001) showed up to 30% difference

in strength within the time period between 28 days and the time of testing. However, Varma (2000) and Varma et al. (2001) reported that the curing did not have any significant effect on the concrete strength. Therefore, it can be concluded that the difference between the values of f'_c and f'_{ccor} and also the effect of concrete curing might depend on the strength of concrete, because Varma (2000) and Varma et al. (2001) used 110 MPa (15.96 ksi) concrete and the maximum 28-day concrete strength was 40 MPa (5.80 ksi) in the majority of the specimens by Peng et al. (2000), Peng (2001), although other factors may contribute to this difference as well. Figure 2.64 shows the variation of E_c with respect to f'_c for the cyclically loaded connection tests and also for the other tests in the overall database. Both sets of data show the same trend that E_c increases with f'_c .

The geometric dimensions of the RCFT columns were defined by the depth, width, and thickness of the specimens. In addition, the dimensionless parameters like D/t and L/D were also recorded. In some of the tests, the geometric dimensions of the panel zones were made smaller than the columns to weaken the connection (Kawaguchi et al., 1996). Therefore, different from the databases presented in the previous sections, the thickness (t_p, t_{po}) and depth over thickness ratio of the panel zones ($D/t_p, (D/t_p)_o$) were included in the database separately including their nominal and measured values. The variation D/D_o with respect to D is shown in Figure 2.65 for both the cyclically loaded connection tests and the other tests with available data. According to the former sets of data, D/D_o values start to decrease when the depth of the specimens gets larger. However, this trend is opposite to the one observed for the other sets of data. For the cyclically loaded connection specimens, the mean value of D/D_o was found as 1.003 with a standard deviation of 0.003. These values were close to the ones obtained for the overall database, which were 1.003 and 0.005, respectively.

The comparison of nominal and measured values of the tube thickness for the cyclically loaded moment connections and the other specimens in the overall database is examined in Figure 2.66. This figure shows that for the specimens in the cyclically loaded moment connection database, the measured thickness is less than its nominal value, and the mean value of t/t_o was found to be 0.967 with a standard deviation of 0.011. These two parameters are close to the values obtained for the overall database, which were calculated as 0.993 and 0.0597, respectively.

The histogram of the cyclically loaded moment connection database for the D/t ratio is shown in Figure 2.67. The majority of the specimens have D/t ratios less than 50 with a maximum D/t ratio of 42 indicating that connections to thin-walled members were not investigated comprehensively. For all the cyclically loaded moment connection specimens, the measured D/t ratio is larger than the $(D/t)_o$ as shown in Figure 2.68. The same trend can be observed for overall database. The cyclically loaded moment connection database mainly consists of short members having L/D ratios less than 15 as can be seen in Figure 2.69.

In the experimental results section of the cyclically loaded moment connections database, load capacities, deformation capacities, and damage levels were recorded. During the tests, it was common to apply a constant axial load on to the column to simulate the vertical force acting from the upper stories in a real building. Therefore, the axial load level of the column is the first quantity entered into this section. The effect of lateral loading is quantified in various ways depending on the data and load-deformation plots presented in the reports. The force quantities stored in the database defining the effect of lateral loading include the peak values of lateral load applied to the end of the column or to the ends of the girders, moment at the face of the column, and panel-zone shear. As the loading is applied in two directions, the peak values of the force quantities were recorded for both directions. For this purpose, either tabulated values of the peak loads were directly taken from the reports or they were scaled from the load–deformation plots. The deformation capacity of the specimens was defined using three different deformation measures. These measures differ from test to test depending on the reported data. The main deformation measures defined in the cyclic connection tests are interstory drift ratio, interstory drift, and girder rotation. The values of these parameters at the peak load level and also their ultimate values at the end of the tests were stored. Either the tabulated values of the deformation measures were taken from the reports or they were scaled from the load deformation plots. All the deformation capacities were recorded for both directions of the loading. In addition to the load and deformation capacity of the specimens, the initial stiffnesses were also recorded in the database if they were made available in the reports.

The damage levels defined for the cyclic connections are exactly the same as the damage levels defined for their monotonic counterparts. The load and deformation levels at the occurrence of the damage levels were stored separately for both directions of loading. In the majority of the tests, the damage levels were scaled from the load deformation curves using the points indicated on the load-deformation plots. However, sometimes analytical methods were also utilized to detect the damage levels on the load deflection plots. If sudden changes on the load deformation plots were reported to correspond to a specific damage level, these points were also traced on the given plots and then the corresponding load and deformation levels were scaled.

2.2.6 RCFT Frame Database

The CFT frames database includes the tests conducted on portal frames made up of two RCFT columns with a steel girder framing between them using fully-restrained connections. A total number of 12 specimens were added to the database. All the specimens were tested in Japan within the period 1986 and 1997.

2.2.6.1 Monotonically Loaded RCFT Frame Database

As stated in the previous sections, RCFT members are commonly used in the perimeter frames of the buildings where steel girders frame into RCFT beam-columns. Therefore, the best way to investigate the interaction between the steel girder and RCFT column is by testing single story or if possible multistory frames consisting of steel girders and RCFT beam-columns. The individual member tests and subassemblage tests are idealized cases and the support conditions, as well as, the loads acting on the RCFT beam-columns do not simulate the conditions in a real frame. Among the type of tests in the overall RCFT database of this study, portal frame tests show the most realistic RCFT member behavior. However, the number of tests on RCFT frames is limited due to the cost of this type of tests. The monotonic part of the RCFT frame database includes the tests conducted by Matsui (1986). The main purpose of this database is to investigate the

RCFT beam-column and steel girder interaction. Therefore, the specimens that failed in the connection region were excluded from the database.

The RCFT monotonically loaded frame database was divided into five main sections including test description, connection properties, girder properties, RCFT beam-column properties and experimental results. The test description section presents information about the test setup, loading procedure, and boundary conditions. The next main section defines the connection properties and provides information about the material and geometric properties of panel zones and main connection components. The material properties given in this section embraces the yield strength of the panel zone steel (f_{yp}), the ultimate strength of panel zone steel (f_{up}), the yield strength of main connection components (f_{yme}), and the ultimate strength of the main connection components (f_{ume}). No distinction about the nominal and measured values has been made. However, the priority was given to the measured values. The geometric properties given in this section were the depth of the panel zone tube (D_p), width of the panel zone tube (b_p), thickness of the panel zone tube (t_p), section type of the main connection components, length of the main connection components (L_{me}), width of main connection components (B_{me}) and thickness of the main connection components (t_{me}). Measured or nominal values were stored depending upon what was provided in the report, with the priority being given to the measured values. The following section in the database describes the material and geometric properties of the girders spanning between the RCFT beam-columns. The material properties cover the measured yield strength (f_{yg}), measured ultimate strength (f_{ug}), and measured modulus of elasticity of the steel girder (E_{sg}). The geometric properties of the steel girders were described by section type of the girder, measured length of the girder (L_g), measured depth of the girder (d_g), measured width of the girder (b_g), measured thickness of the girder web (t_w) and measured thickness of the girder flange (t_f). The geometric and material properties used to describe the RCFT members were exactly the same as in the case of the RCFT column or RCFT beam-column databases.

The tests in the monotonically loaded RCFT frame database were conducted under a constant axial load applied to the beam-columns and a monotonic lateral load applied to the top of the windward RCFT beam-column. All the specimens were portal

frames with fixed-ended beam-columns. Although the tests were conducted under monotonically-applied load, Matsui (1986) also tested each of the specimens under one cycle of reversed lateral loading.

The connection detail used for the specimens was either a through diaphragm or external diaphragm. For both connection types, the main connection detail was a diaphragm plate. The external diaphragm flared to the RCFT beam-column at an angle of 45° and the width of the external diaphragm plate around the RCFT beam-column was 5% of the depth the RCFT beam-column.

All the steel girders were H-shaped members according to the Japanese standards, with equal thicknesses of web and flange. The yield strengths of the girders ranged from 266.8 MPa (38.70 ksi) to 357.1 MPa (51.80 ksi). Both the depth and thickness of the girders were larger than the depth and thickness of the RCFT beam-columns.

The steel tubes of the RCFT beam-columns were manufactured from STKR 41 type steel with a nominal yield strength of 245 MPa (35.54 ksi). The measured yield strength of the steel tubes was 288 MPa (41.78 ksi). Therefore, the f_y/f_{yo} ratio was equal to 1.23 for all the specimens. A nominal concrete cylinder compressive strength of 29.4 MPa (4.26 ksi) was selected and the mean value of f'_c/f'_{co} was equal to 1.24. The nominal D/t ratios of the specimens were 47 and 68. The L/D ratio was 6.7 for all the specimens.

In the experimental results section of the database, the load capacities and the deformation capacities of the specimens were recorded. The constant axial load level, peak moment, and peak horizontal load acting on the RCFT beam-columns were also recorded. The deformation capacities were defined by the horizontal displacement of the frame at the peak horizontal load, as well as the horizontal displacement at the end of the test. In addition, the failure locations of the specimens were recorded if they were made available. The deformation and load capacities were either taken from the tables given in the reports or scaled from the load-deflection plots.

The RCFT beam-columns of the frames were categorized as windward and leeward depending on the direction of loading. Matsui (1986) reported the damage levels for the top region and bottom regions of the RCFT beam-columns separately. Therefore, both the windward and leeward beam-columns were investigated in two groups for the

top and bottom of the RCFT beam-columns. A total of seven damage levels were defined for the beam-columns of the monotonically loaded frame database. These damage levels included initial concrete cracking, steel yielding in compression, yielding of the steel tube in tension, concrete crushing, local buckling of steel tube compression flange, local buckling of the steel tube web, and fracture of steel tube. The load and deformation levels corresponding to these damage levels were either scaled from the load–deformation plots or they were calculated by analytical methods.

2.2.6.2 Cyclically Loaded RCFT Frame Database

Cyclic frame tests are useful to investigate the interaction between the girders and RCFT beam-columns subjected to seismic loading. This database contains RCFT portal frame specimens tested under cyclically applied lateral loading. Due to limited number of RCFT frame experiments reported in detail in the literature, only the tests conducted by Kawaguchi et al. (1997), Kawaguchi (2000) were included. As with the monotonically loaded frame database, the specimens that failed in the connection region were excluded from the database.

The organization of the cyclically loaded frames database was the same as its monotonic counterpart. The data given in the reports were grouped into five sections, including the test description, connection properties, girder properties, RCFT beam-column properties, and experimental results. The type of information in each section has already been discussed in the prior section.

All the specimens were portal frames with RCFT beam-columns built into large plate girders at the base to simulate fixed support conditions. The top of the frame was restrained from sidesway motion. A constant axial load was applied to the RCFT beam-columns, followed by application of a cyclic horizontal loading to the plate girder at the base, which in turn was supported on roller supports. In the database, the RCFT beam-column under which the lateral loading had been generated was designated as the windward beam-column, while the other beam-column was designated as the leeward beam-column. The loading proceeded with a displacement-controlled protocol and the

sidesway displacements were measured with respect to the top of the leeward beam-column.

For all the specimens, the through diaphragm connection detail was used. The main connection component was the diaphragm plate, with a 70 or 85 mm opening at the middle to aid in the concrete pouring. The diaphragm plates did not flare to the RCFT beam-column, and the thickness of the plate around the RCFT beam-column was approximately 25% of the depth of the steel tube. For the majority of these specimens, the panel zone and the beam-column had the same yield strength and thickness.

In the cyclic frames, the girders were designed to remain elastic in order to examine the damage of the RCFT beam-columns. H-shaped steel girders made from SS400 grade steel according to the Japanese Standards were used.

The yield strengths of the steel tubes were ranging from 251.04 MPa (36.41 ksi) to 403.32 MPa (58.50 ksi). The steel grades used for the RCFT beam-columns were SS 400 and STKR 400, which, while unreported in Kawaguchi et al. (1997), Kawaguchi (2000), are known to have 245 MPa nominal yield strength from other available resources. The comparison of nominal and measured values of yield strength of the steel tubes is shown in Figure 2.70 for both the cyclic frame tests and the overall database. Using these data, the mean value of f_y/f_{yo} for the cyclic frame tests was found to be 1.324 with a standard deviation of 0.265. These values are larger than the ones found for the specimens in the overall database, which, as discussed earlier, may be due to the larger variation of the measured and nominal yield strength values typical of Japanese specimens. The variation of the f_u/f_y ratio with respect to f_y is shown in Figure 2.71 for the cyclically loaded frame tests and for the other tests in the overall database. For both sets of the data, there is a decrease in f_u/f_y ratio when the yield strength of the steel tube increases. The concrete cylinder compressive strengths of the specimens ranged from 13.7 MPa (1.99 ksi) to 24.4 MPa (3.54 ksi), showing that in the cyclically loaded frame tests the effect of concrete strength was not investigated adequately.

Among the geometric properties of the RCFT beam-columns, the variation of the nominal and measured depth of the steel tubes is shown in Figure 2.72. The mean value of D/D_o was found as 1.004 with a standard deviation of 0.003. No specific trend of D/D_o with respect to D was observed for the cyclically loaded frame specimens, while

there was a clear trend for the other specimens in the overall database that the D/D_o ratio was increasing for large values of D . The nominal and measured thicknesses of the steel tubes are compared in Figure 2.73. For the majority of the cyclically loaded frame specimens, the measured thickness is larger than its nominal value. The average value of t/t_o was calculated as 1.04 with a standard deviation of 0.076. The D/t ratio of the cyclically loaded frame specimens ranged from 21.6 to 57.4. This range of D/t ratio indicates the lack of specimens with high D/t ratios. The comparison of the nominal and measured D/t ratio is shown in Figure 2.74 for both the cyclically loaded frame specimens and the other specimens in the overall database. For both sets of data the measured value of D/t is greater than its nominal value in the majority of the tests. For the cyclic frame tests, the mean value of $(D/t)/(D/t)_o$ was found as 1.046 with a standard deviation of 0.025. Similar values were found for the overall database with 1.037 and 0.066 as the mean value and standard deviation of $(D/t)/(D/t)_o$, respectively. In the cyclically loaded frame tests, all the beam-columns were relatively short members, and the L/D ratios less than 15.

In the experimental results section, the load and deformation capacities of the specimens were stored for both directions for loading. The load capacity of the specimens presented by providing the peak axial load, peak moment and peak horizontal load levels. Interstory drift ratio was utilized as the deformation measure to define the deformation capacities of the specimens. For each specimen the interstory drift ratio at the peak horizontal load and the ultimate interstory drift ratio at the end of the test was recorded. In this section of the database, the failure location of the specimens was also given if it was made available in the reported. The load and deformation capacity of the specimens were either taken from the tables given in the reports or scaled from the load deflection plots. In addition, analytical methods were also utilized to calculate the damage levels.

Similar to the monotonically loaded frames database, each frame specimen was examined in two parts for the leeward and windward beam-column. In addition, the damage levels for the top and bottom parts of each beam-column were recorded separately. The same types of damage levels were defined as in the case of the monotonically loaded frames database. However, the deformation and load levels at the

occurrence of the damage levels were recorded for both directions of loading. This was achieved by scaling the deformation and load levels corresponding to the damage levels from the load deflection plots.

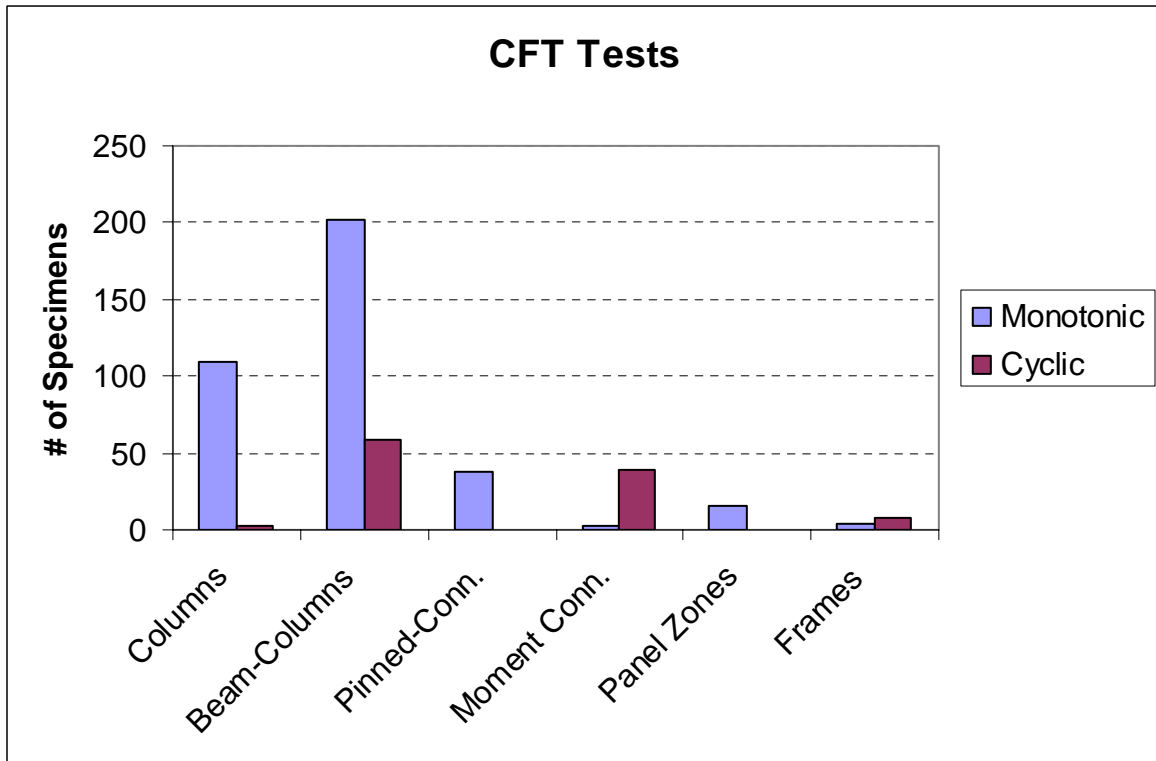


Figure 2.1: Number of CFT Experiments in the Complete RCFT Database

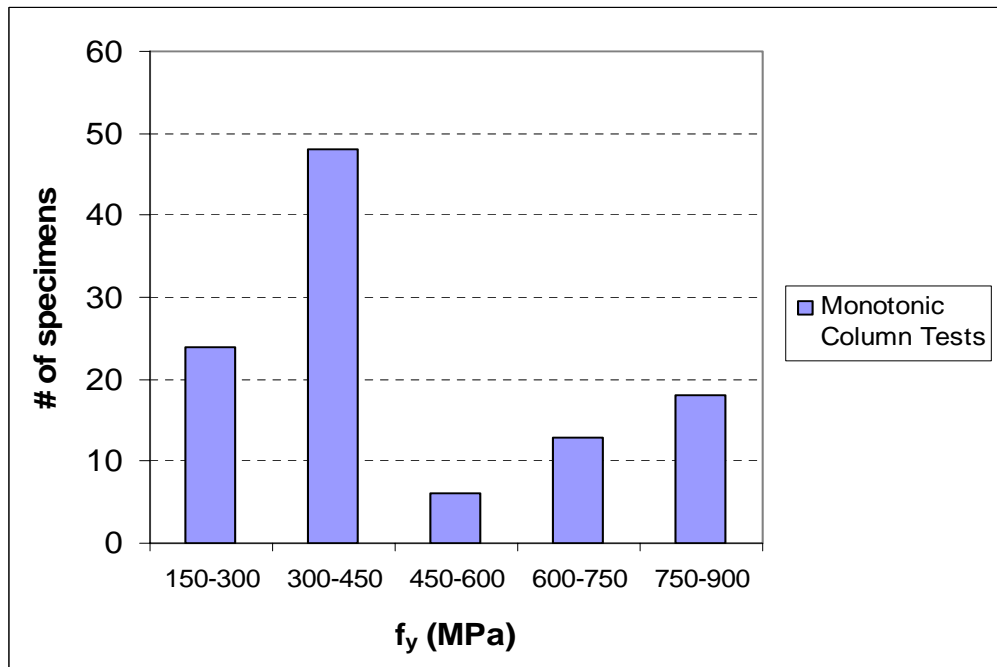


Figure 2.2: Measured Yield Strength of the Steel Tubes: Monotonically-Loaded RCFT Column Tests

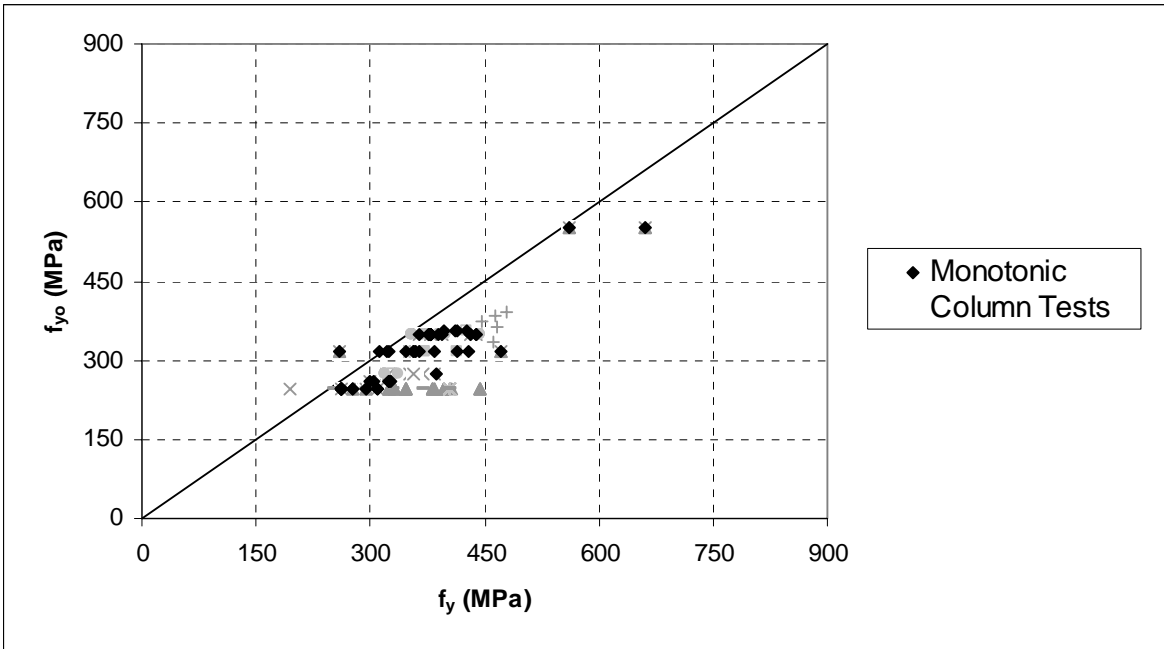


Figure 2.3: Comparison of Measured and Nominal Yield Strength of the Steel Tubes: Monotonically-Loaded RCFT Column Tests

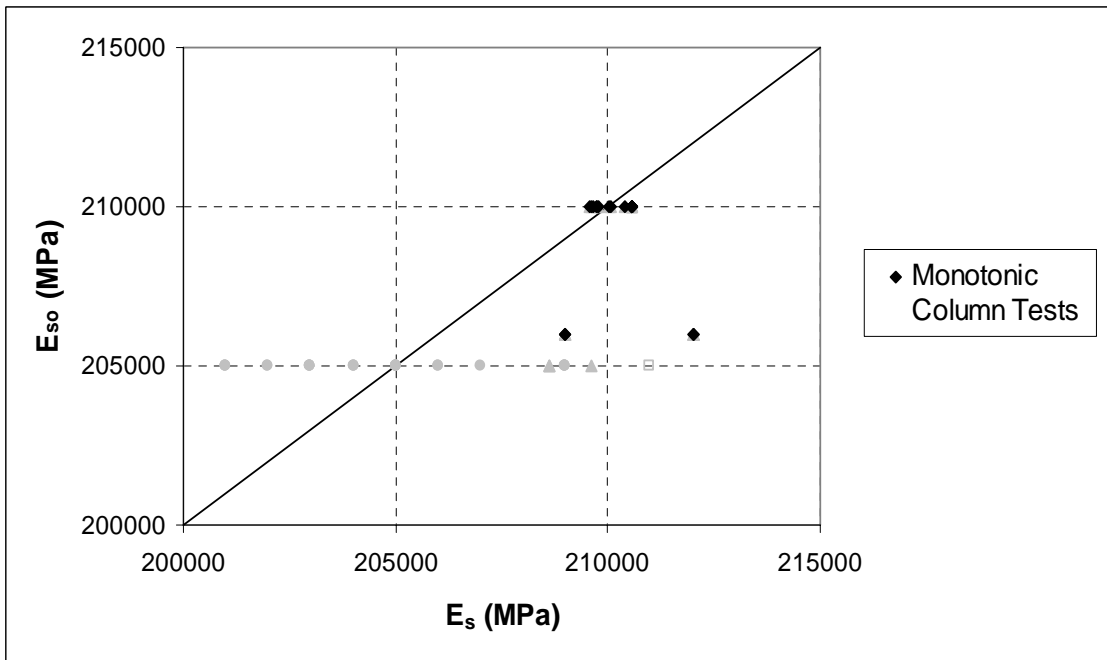


Figure 2.4: Comparison of Measured and Nominal Modulus of Elasticity of the Steel Tubes: Monotonically-Loaded RCFT Column Tests

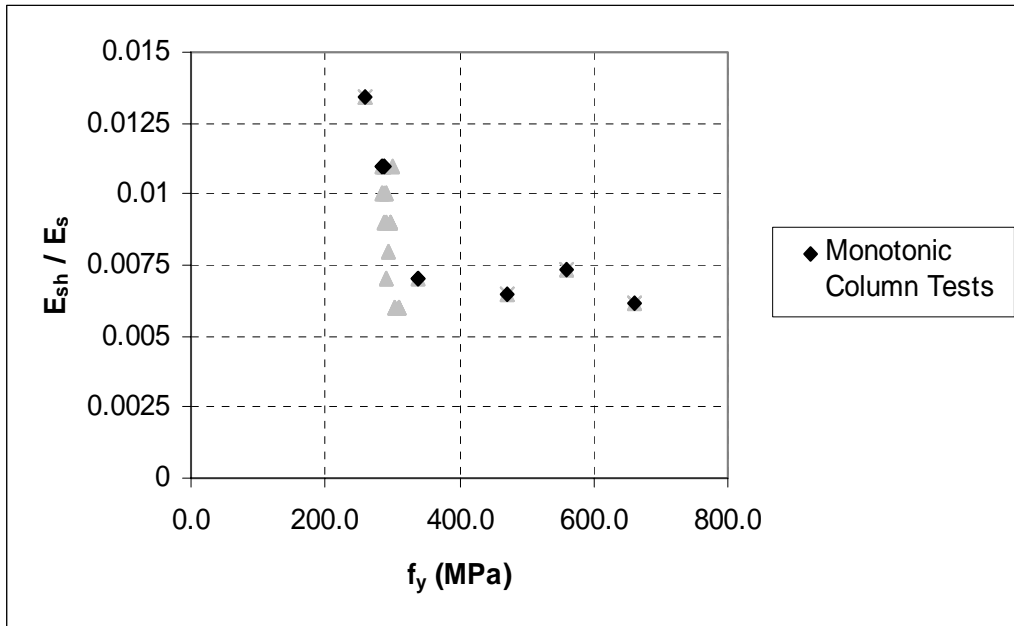


Figure 2.5: Comparison of E_{sh}/E_s versus Measured Yield Strength of the Steel Tubes: Monotonically-Loaded RCFT Column Tests

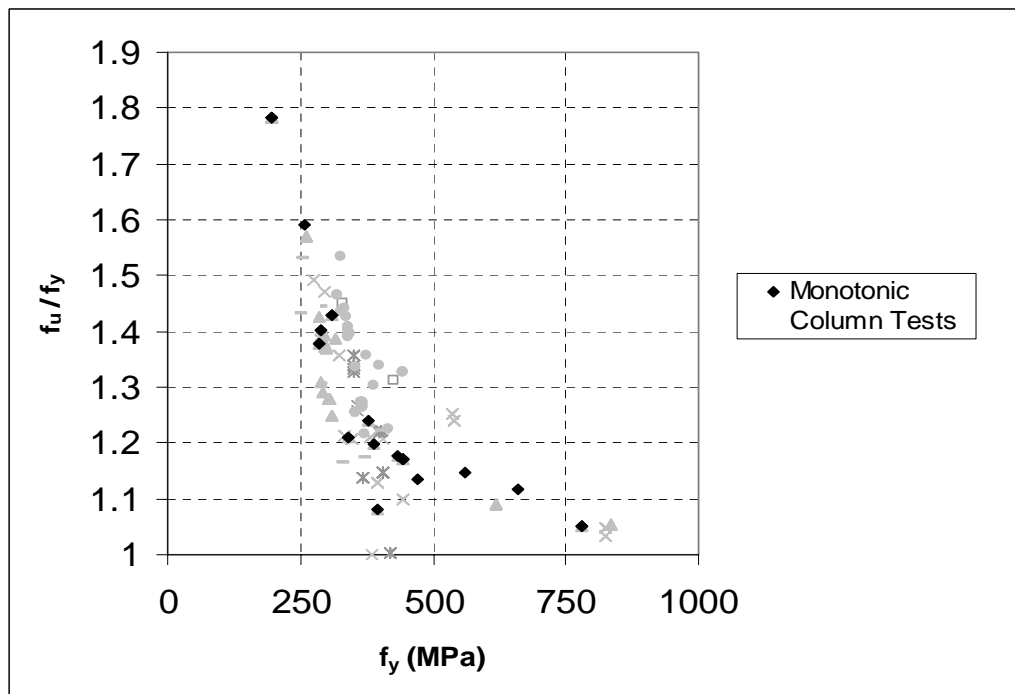


Figure 2.6: Comparison of f_u/f_y versus Measured Yield Strength of the Steel Tubes: Monotonically-Loaded RCFT Column Tests

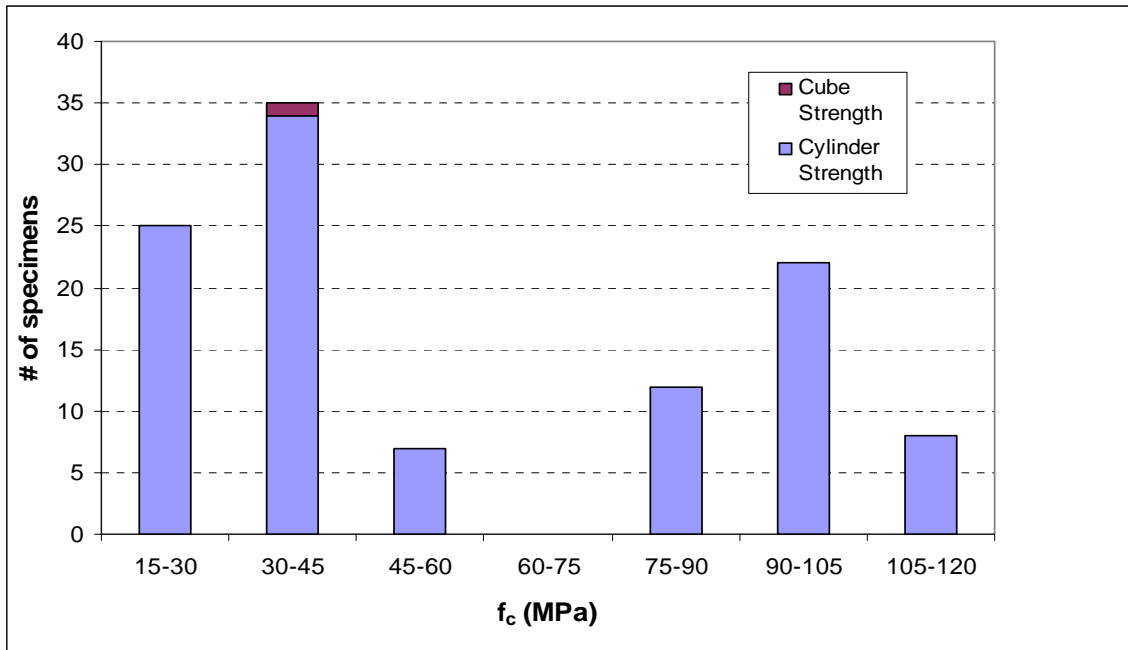


Figure 2.7: Compressive Strength of the Concrete: Monotonically-Loaded RCFT Column Tests

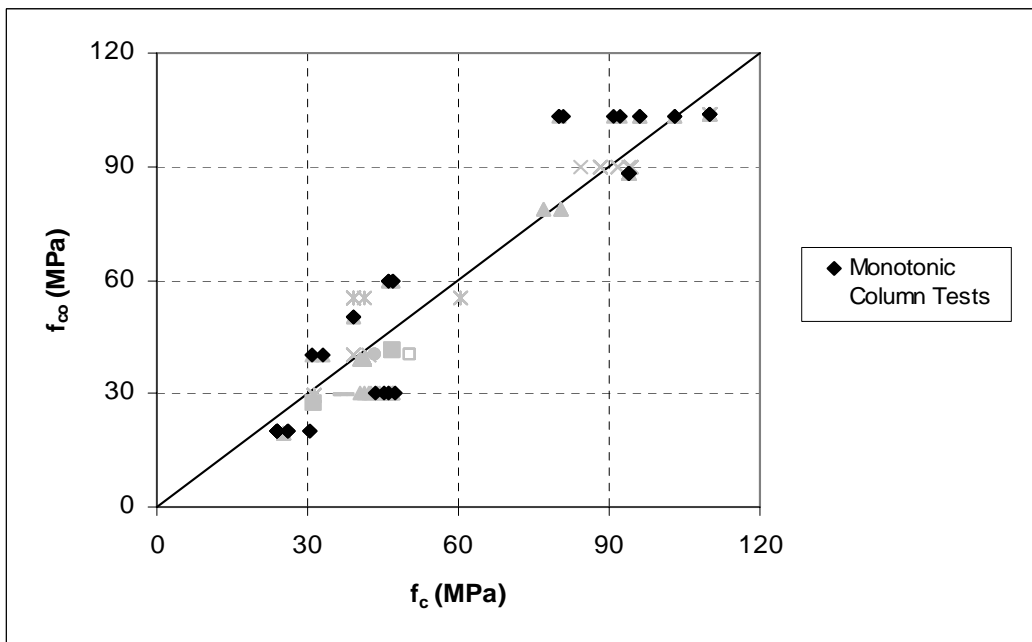


Figure 2.8: Comparison of Measured and Nominal Compressive Strength of the Concrete: Monotonically-Loaded RCFT Column Tests of the Concrete

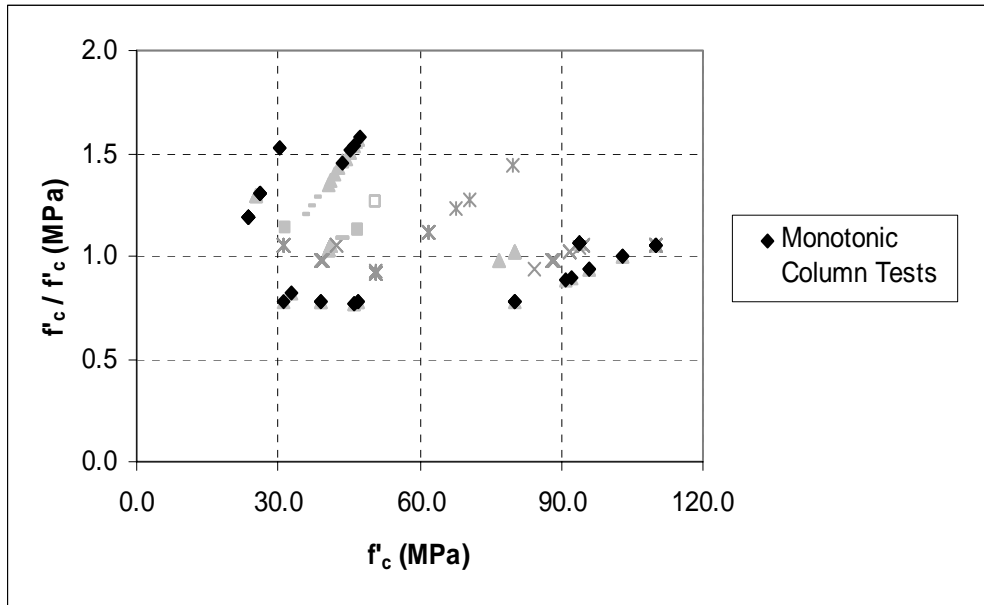


Figure 2.9: Comparison of f'_c / f'_{co} versus Measured Compressive Strength of the Concrete: Monotonically-Loaded RCFT Column Tests

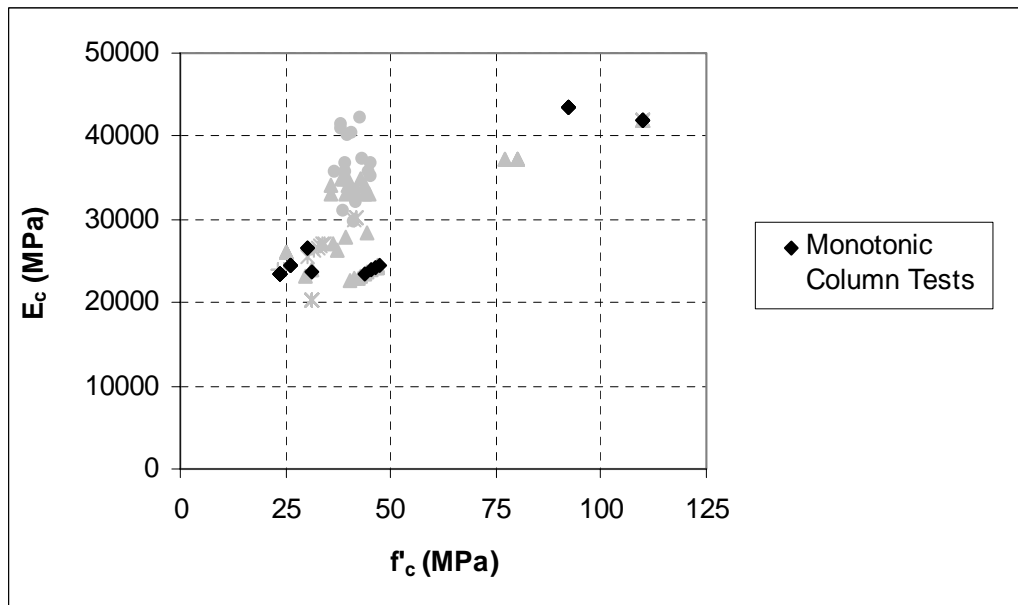


Figure 2.10: Comparison of E_c versus Measured Compressive Strength of the Concrete: Monotonically-Loaded RCFT Column Tests

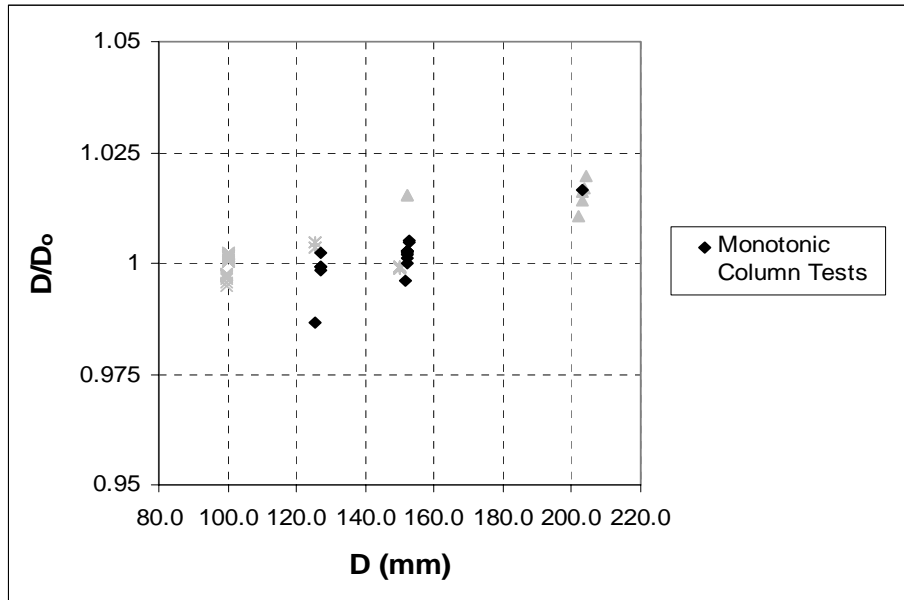


Figure 2.11: Comparison of D/D_o versus Measured Depth of the Steel Tubes: Monotonically-Loaded RCFT Column Tests

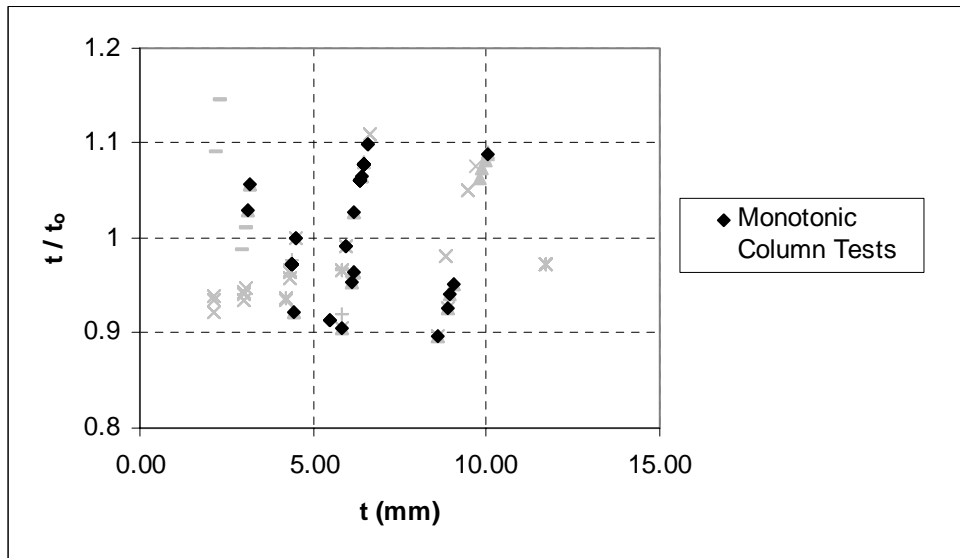


Figure 2.12: Comparison of t/t_o versus Measured Thickness of the Steel Tubes: Monotonically-Loaded RCFT Column Tests

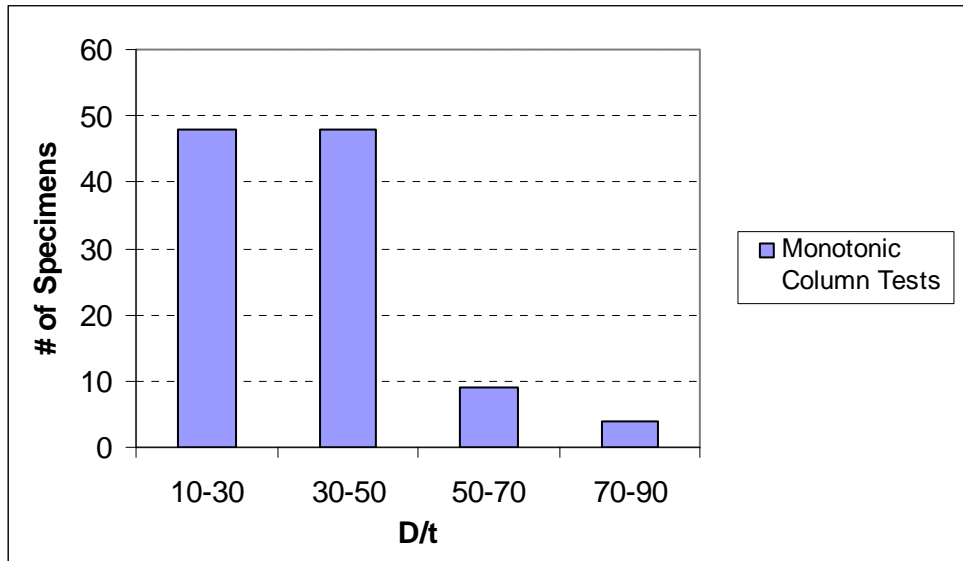


Figure 2.13: D/t Ratio: Monotonically-Loaded RCFT Column Tests

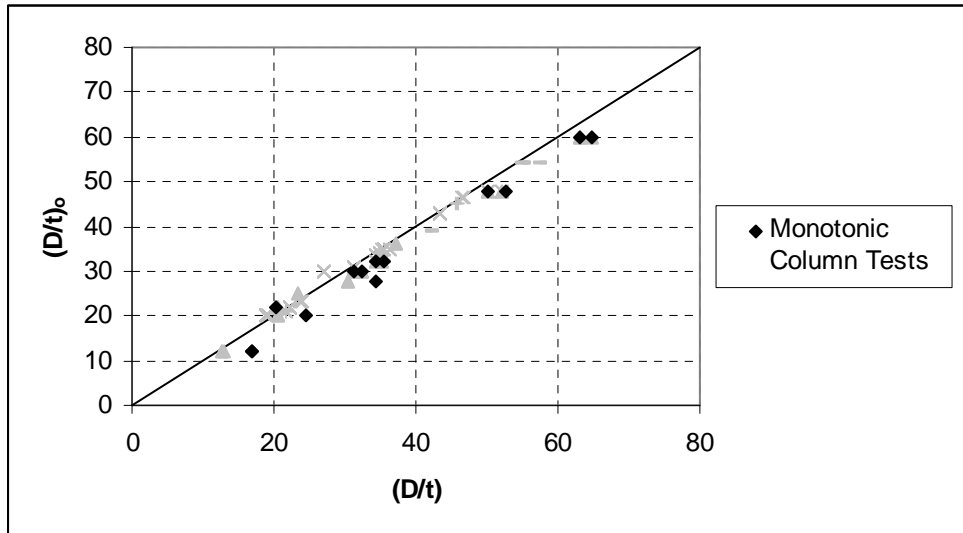


Figure 2.14: Comparison of Measured and Nominal D/t Ratios of the Steel Tubes: Monotonically-Loaded RCFT Column Tests

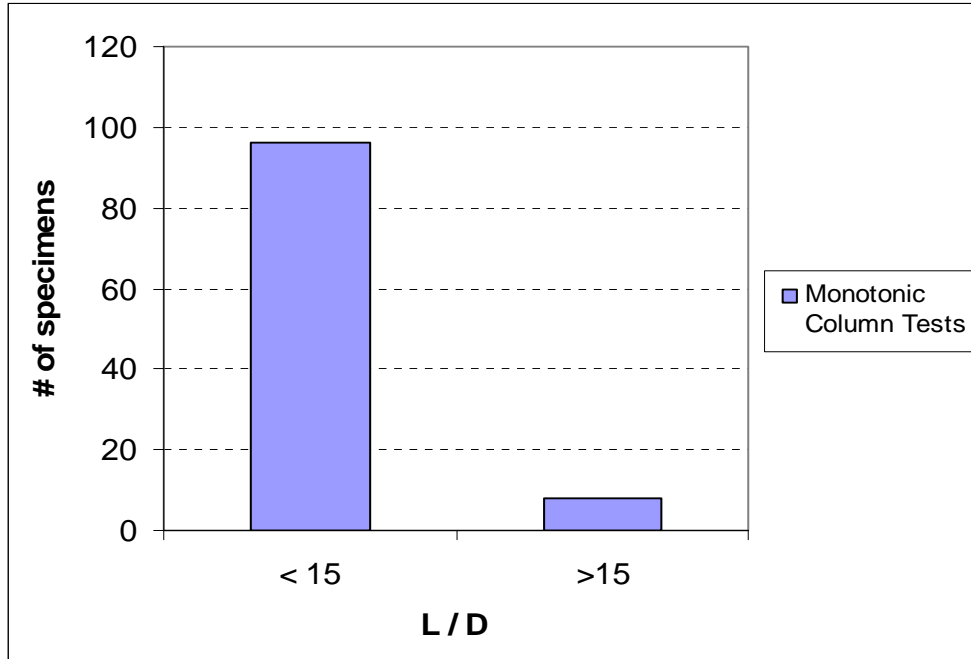


Figure 2.15: *L/D* Ratio: Monotonically-Loaded RCFT Column Tests

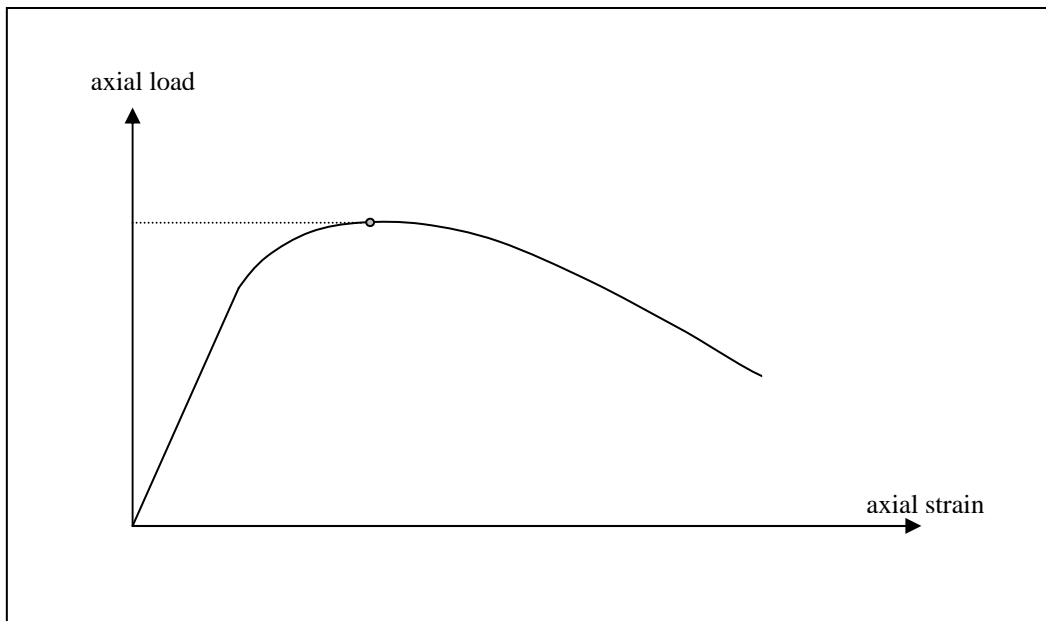


Figure 2.16: Determination of the Peak Point in Axial Displacement versus Axial Force Plots

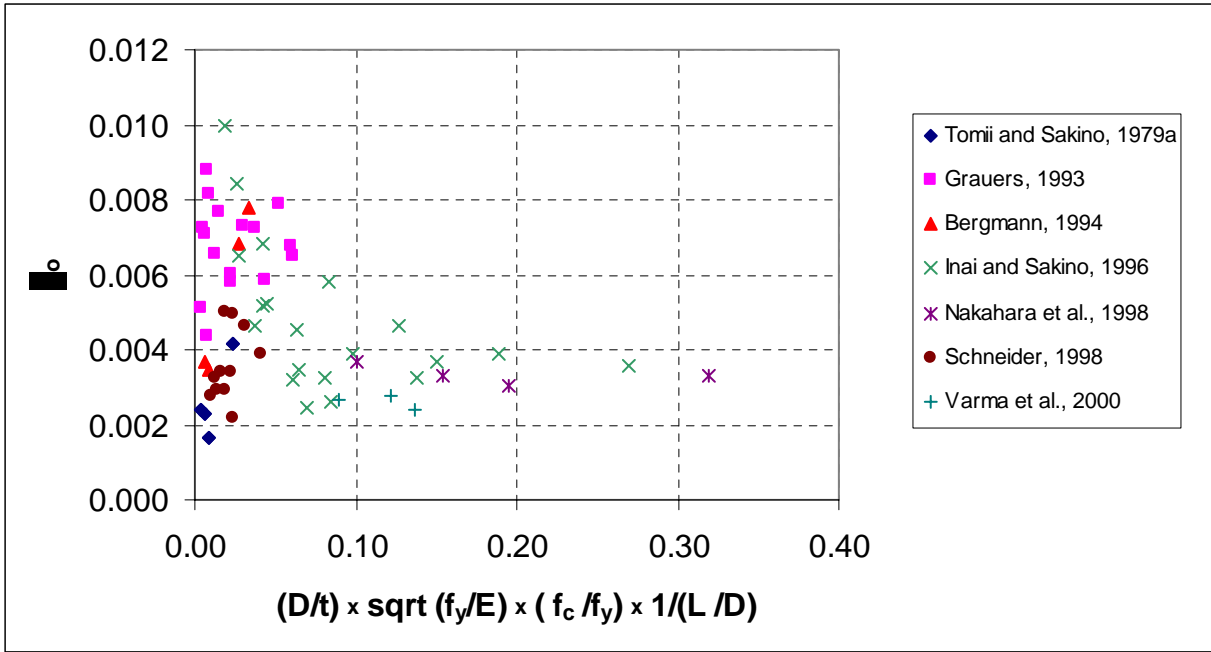


Figure 2.17: Comparison of ϵ_0 versus $\frac{D}{t} \cdot \sqrt{\frac{f_y}{E_s}} \cdot \frac{f'_c}{f_y} \cdot \frac{1}{L/D}$: Monotonically-Loaded RCFT Column Tests

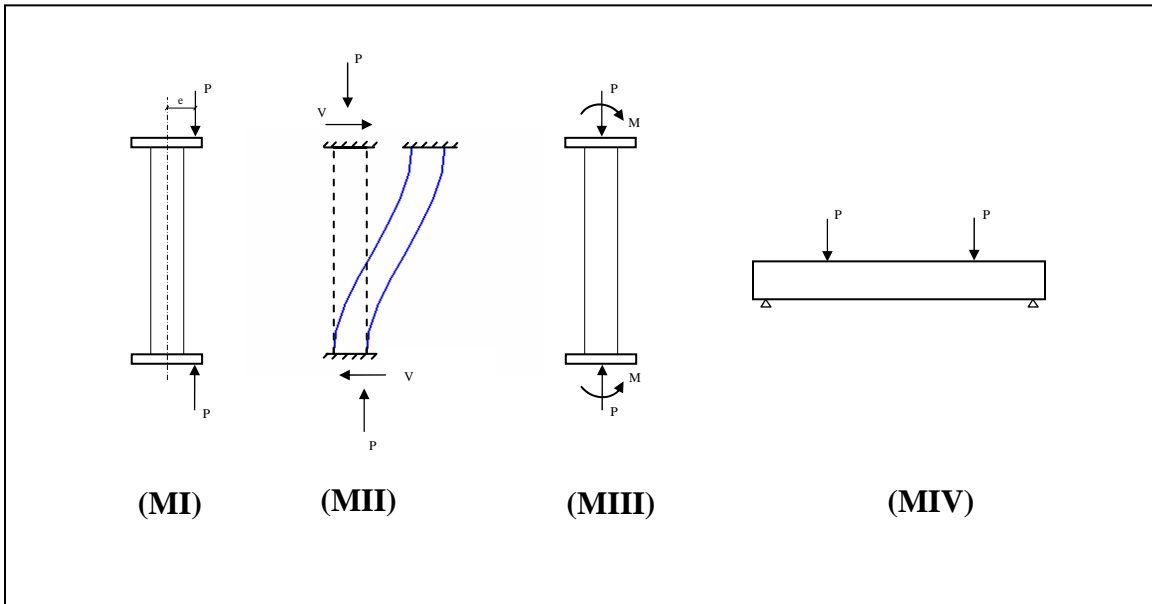


Figure 2.18: Loading Schemes: Monotonically-Loaded RCFT Beam-Column Tests

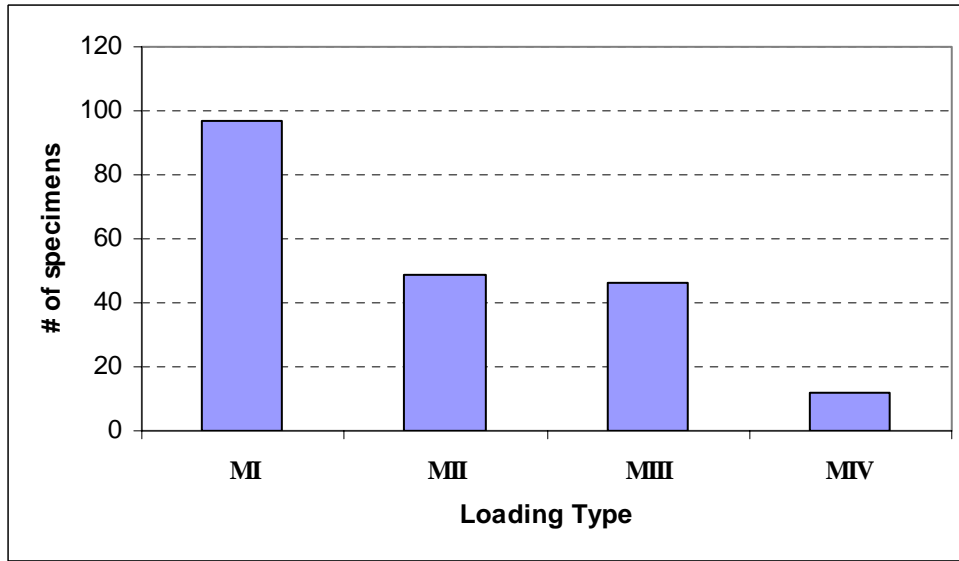


Figure 2.19: Loading Schemes: Monotonically-Loaded RCFT Beam-Column Tests

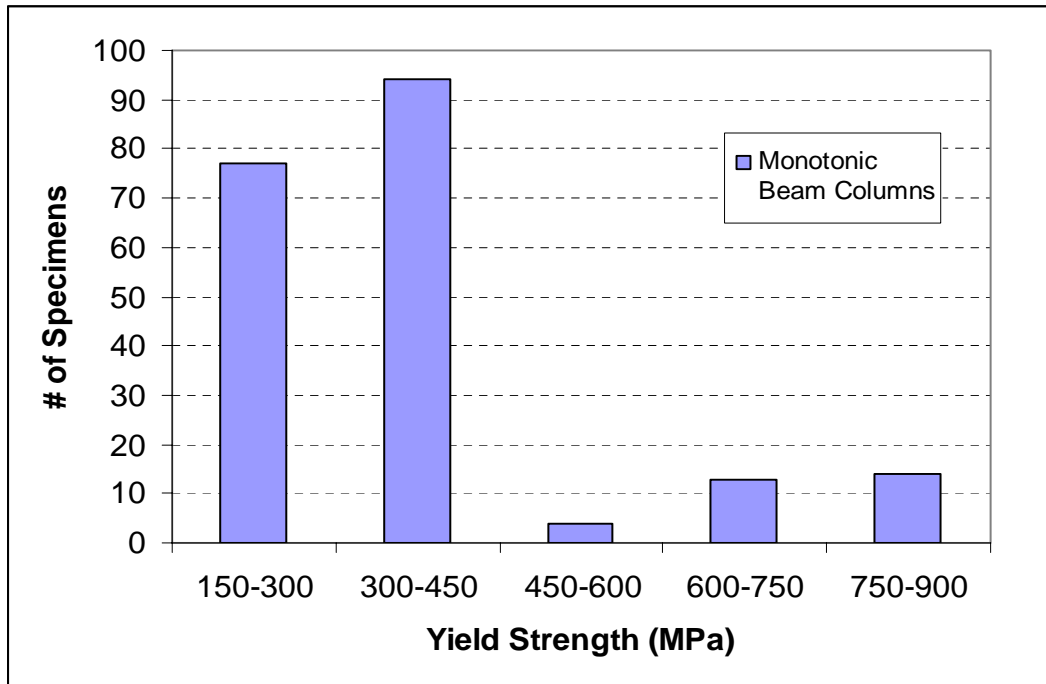


Figure 2.20: Measured Yield Strength of the Steel Tubes: Monotonically-Loaded RCFT Beam-Column Tests

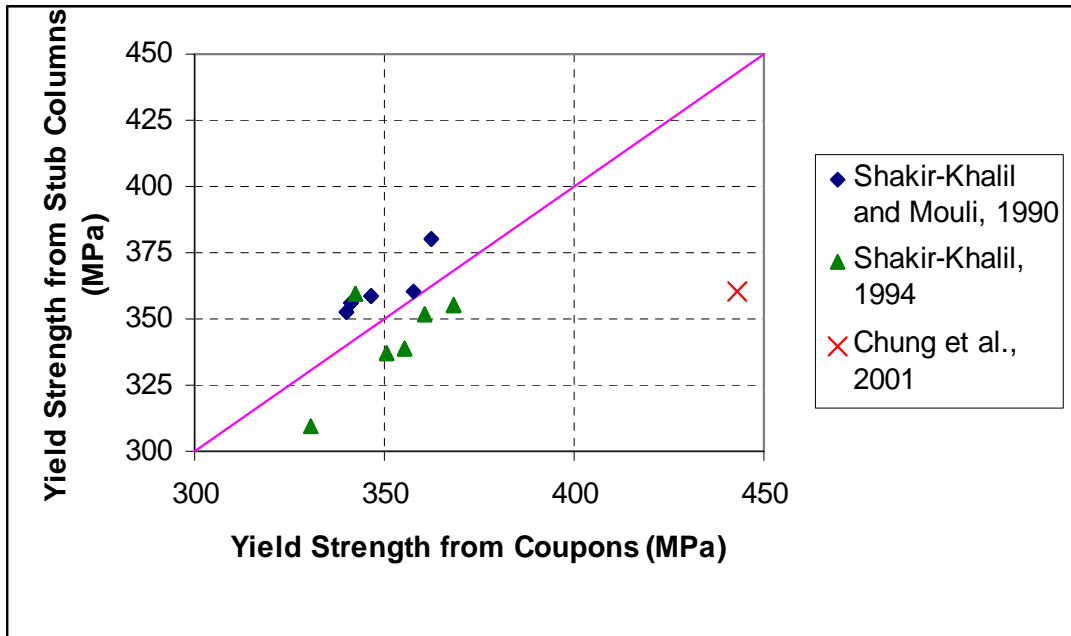


Figure 2.21: Comparison of Measured Yield Strength from Coupon Tests and Stub Column Tests: Monotonically-Loaded RCFT Beam-Column Tests

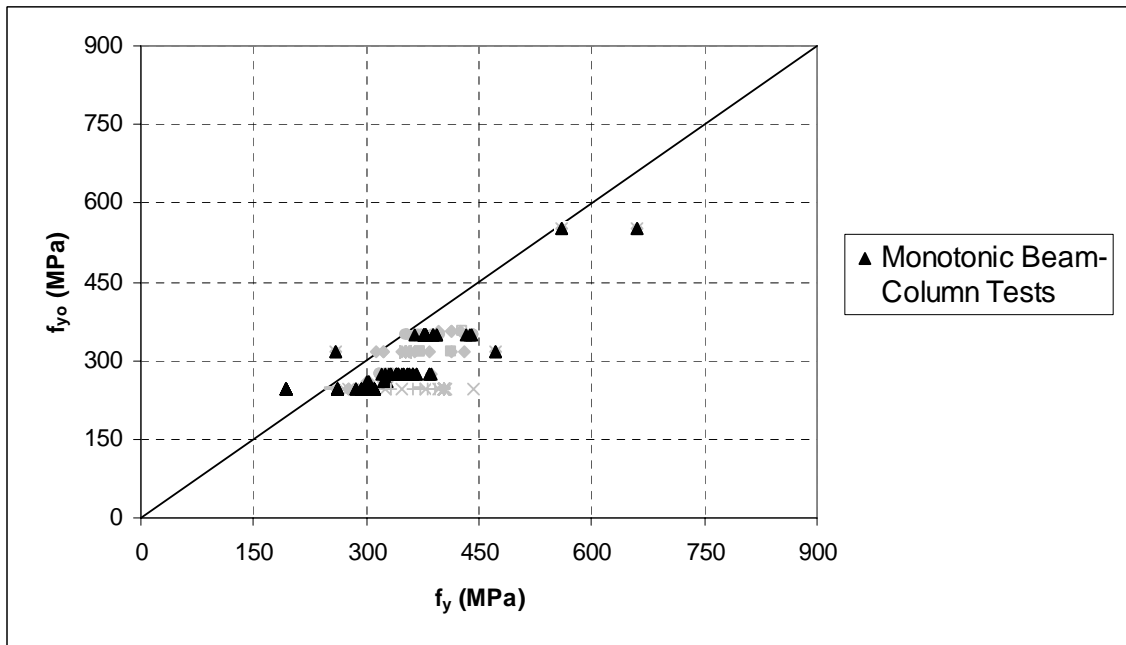


Figure 2.22: Comparison of Measured and Nominal Yield Strength of the Steel Tubes: Monotonically-Loaded RCFT Beam-Column Tests

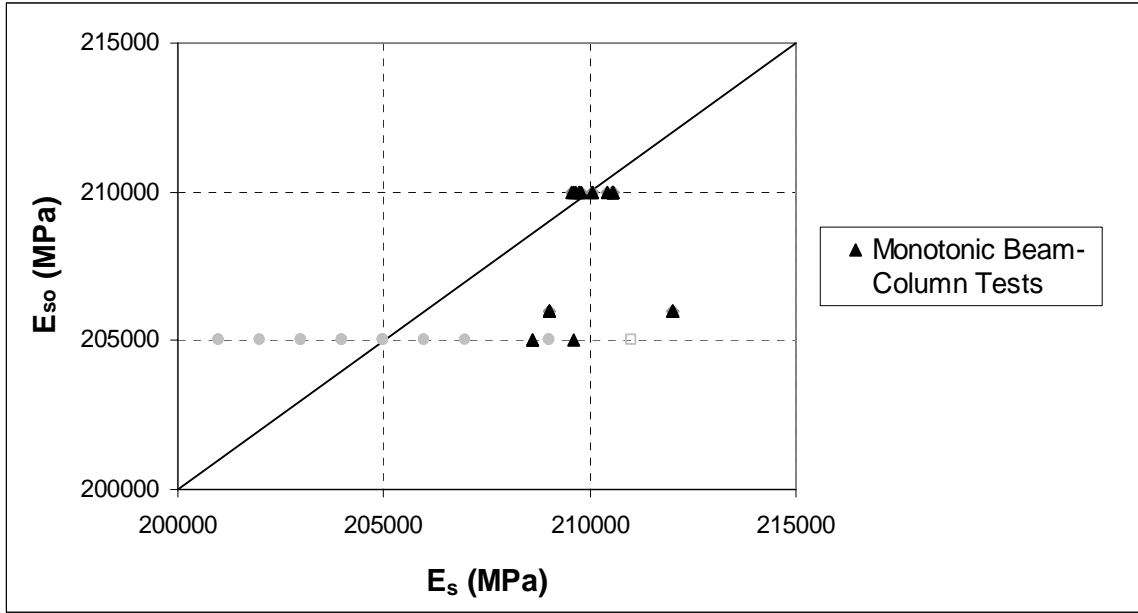


Figure 2.23: Comparison of Measured and Nominal Modulus of Elasticity of the Steel Tubes: Monotonically-Loaded RCFT Beam-Column Tests

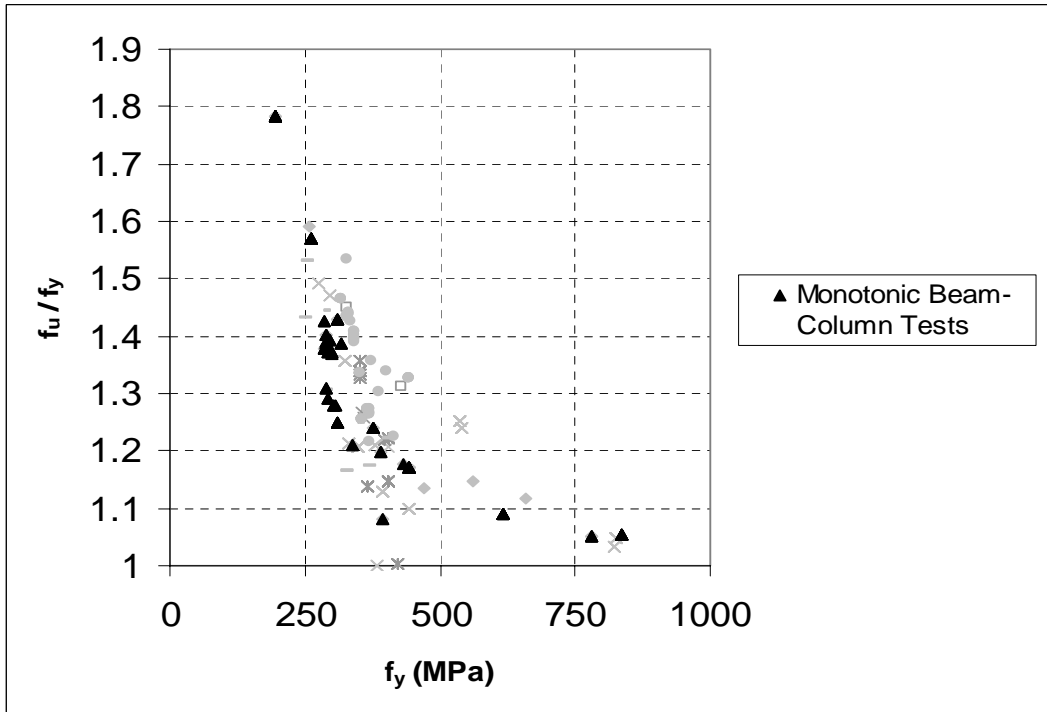


Figure 2.24: Comparison of f_u/f_y versus Measured Yield Strength: Monotonically-Loaded RCFT Beam-Column Tests

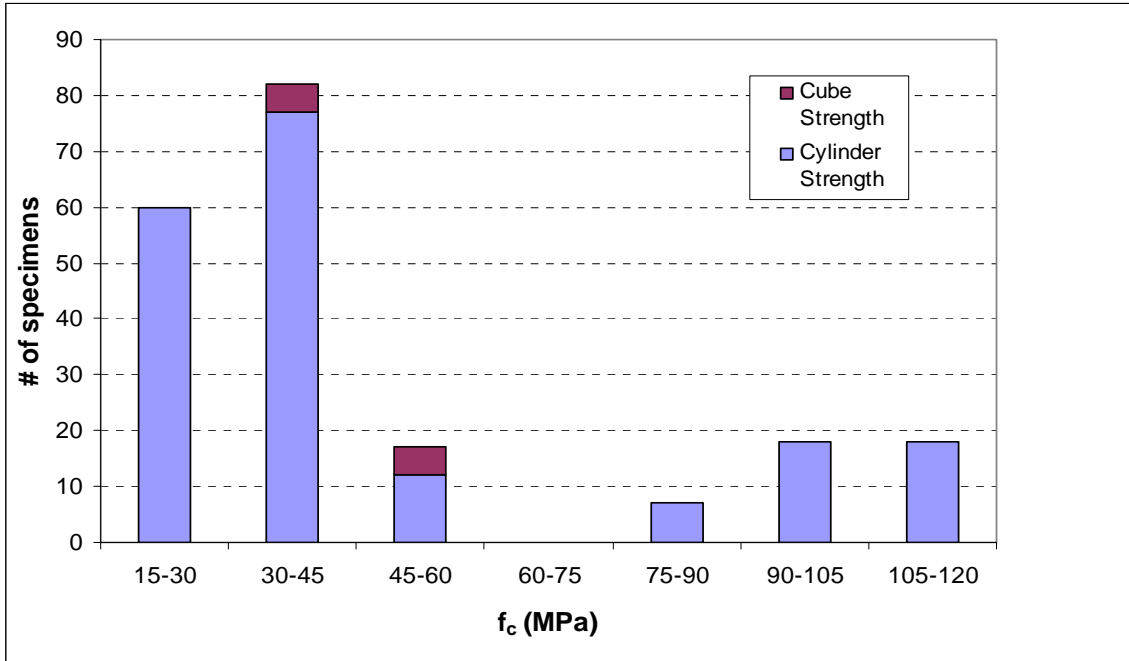


Figure 2.25: Compressive Strength of the Concrete: Monotonically-Loaded RCFT Beam-Column Tests

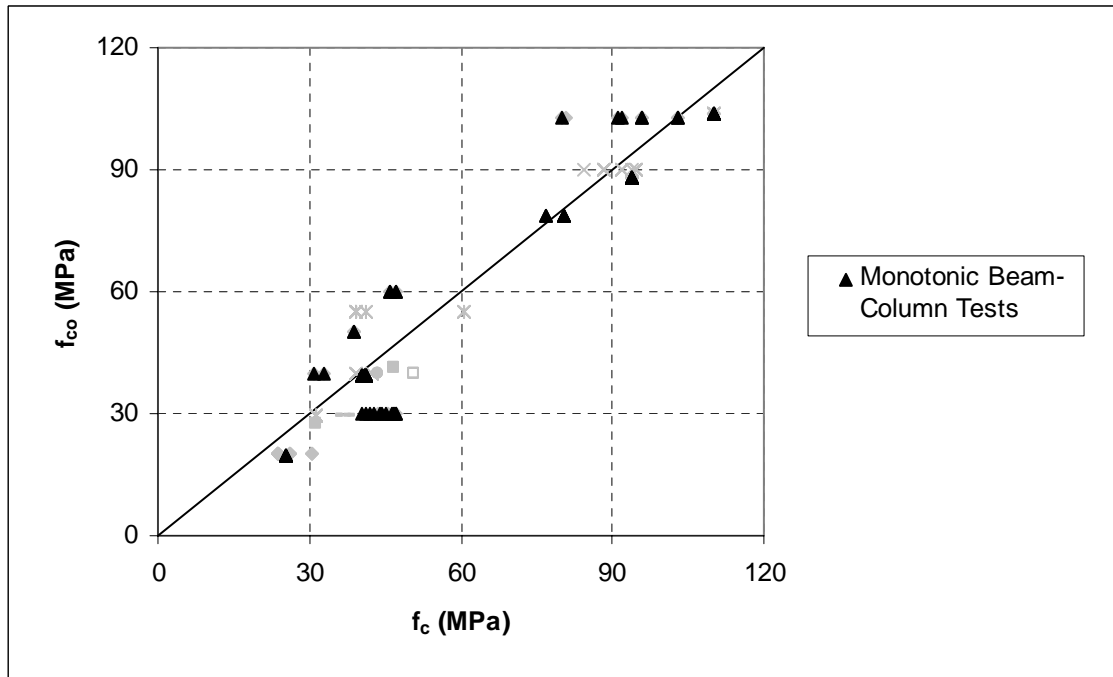


Figure 2.26: Comparison of Measured and Nominal Compressive Strength of the Concrete: Monotonically-Loaded RCFT Beam-Column Tests

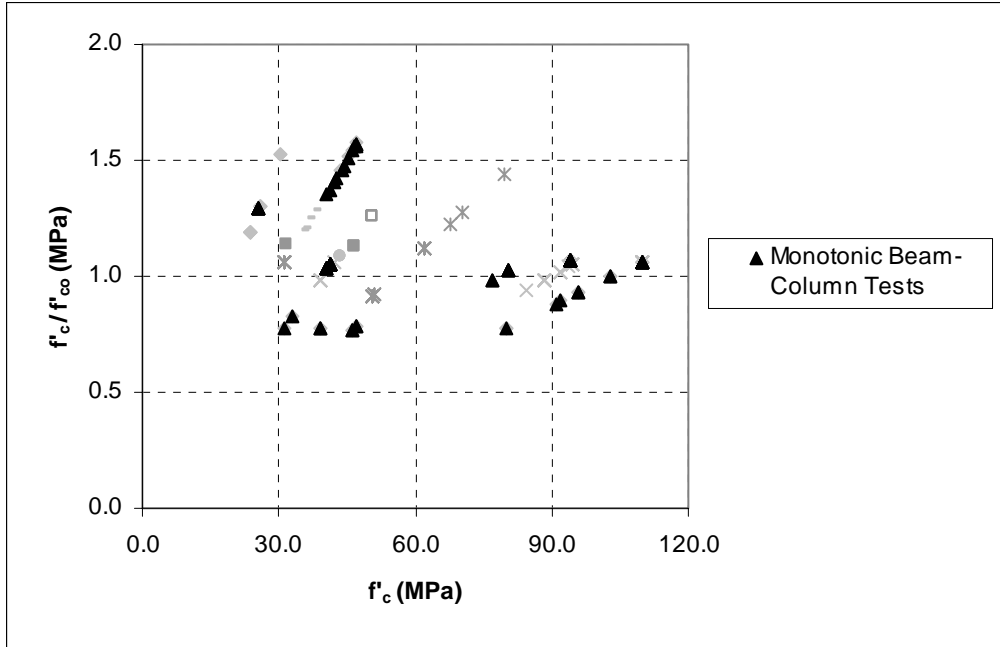


Figure 2.27: Comparison of f'_c/f'_{co} versus Measured Compressive Strength of the Concrete: Monotonically-Loaded RCFT Beam-Column Tests

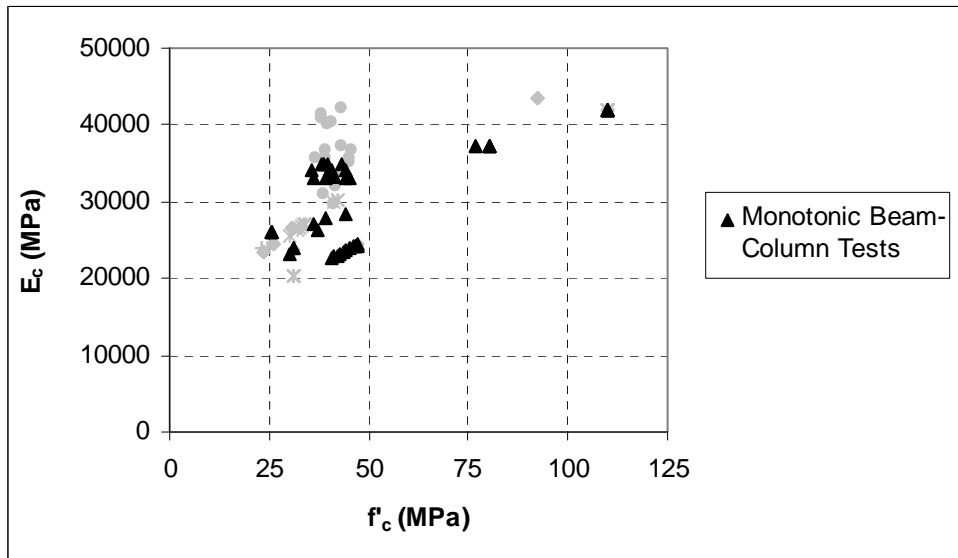


Figure 2.28: Comparison of E_c versus Measured Compressive Strength of the Concrete: Monotonically-Loaded RCFT Beam-Column Tests

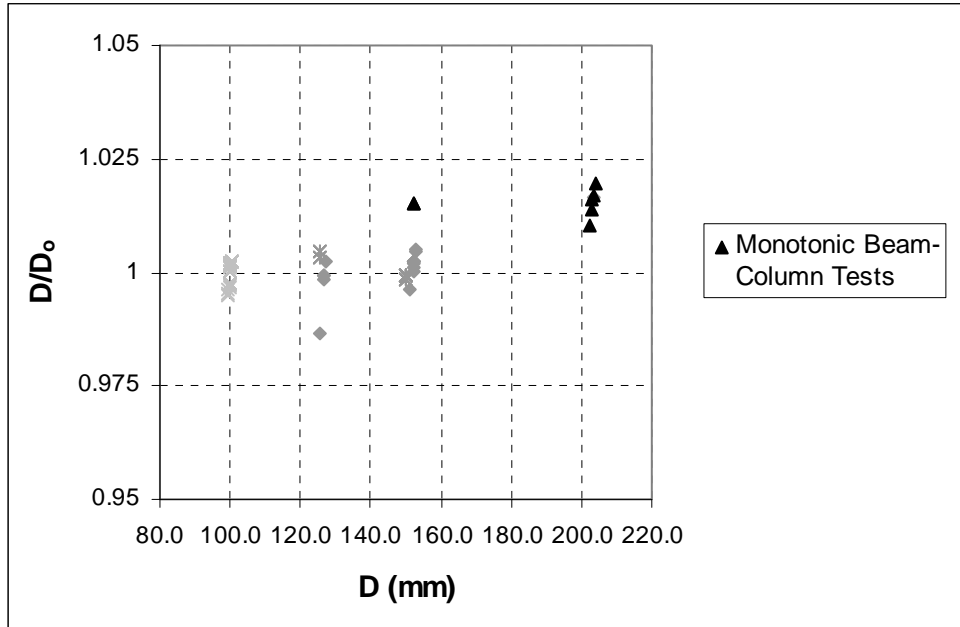


Figure 2.29: Comparison of D/D_0 versus Measured Depth of the Steel Tubes: Monotonically-Loaded RCFT Beam-Column Tests

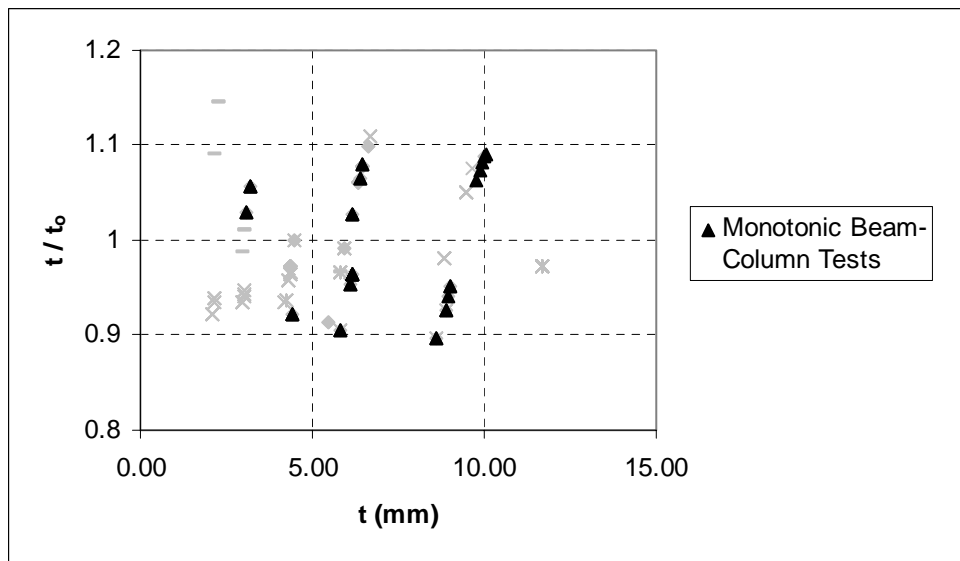


Figure 2.30: Comparison of t/t_0 versus Measured Thickness of the Steel Tubes: Monotonically-Loaded RCFT Beam-Column Tests

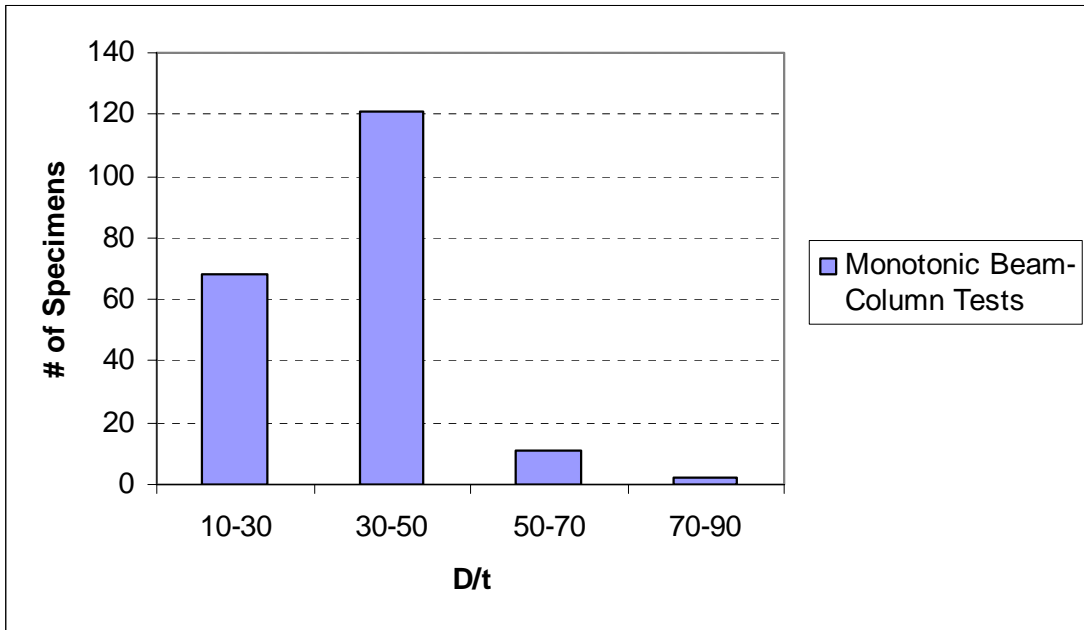


Figure 2.31: D/t Ratio: Monotonically-Loaded RCFT Beam-Column Tests

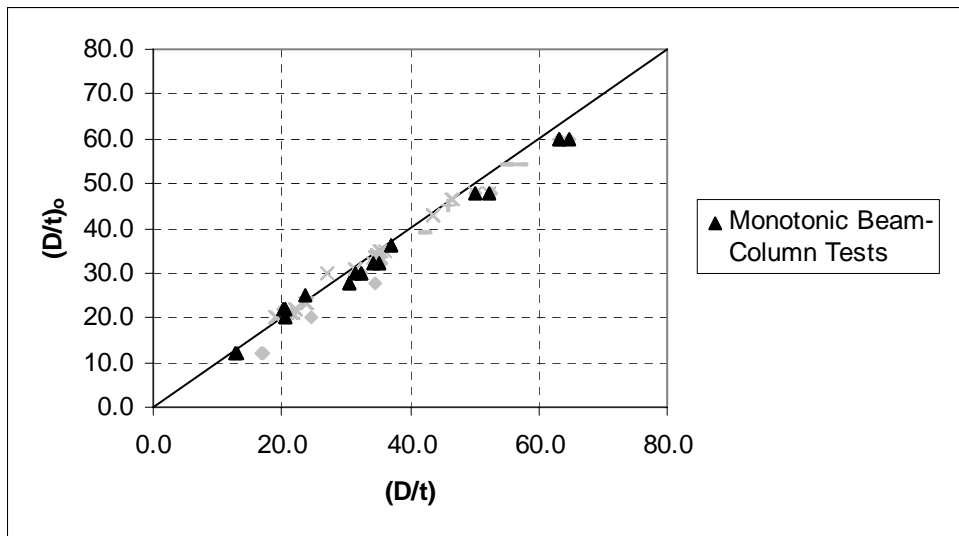


Figure 2.32: Comparison of Measured and Nominal D/t Ratio: Monotonically-Loaded RCFT Beam-Columns Tests

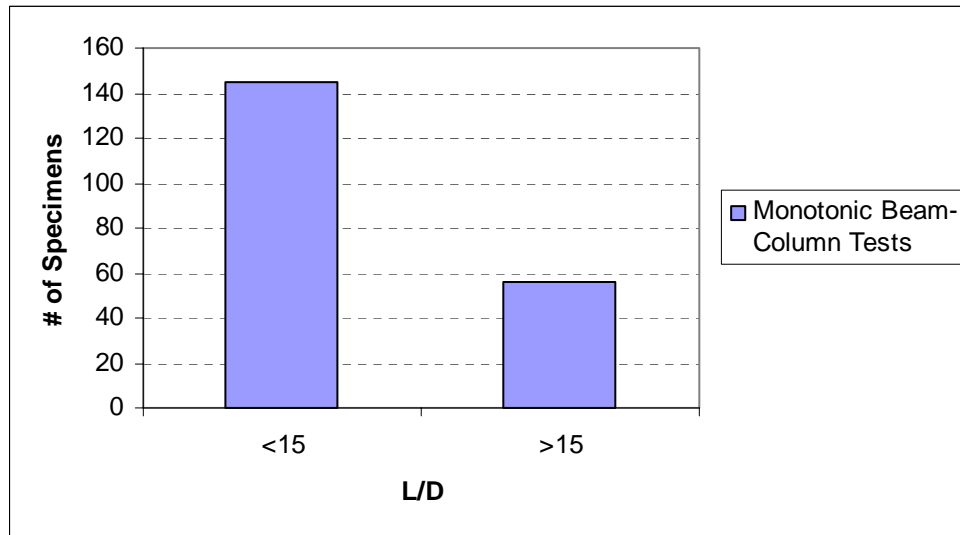


Figure 2.33: L/D Ratio: Monotonically-Loaded RCFT Beam-Column Tests

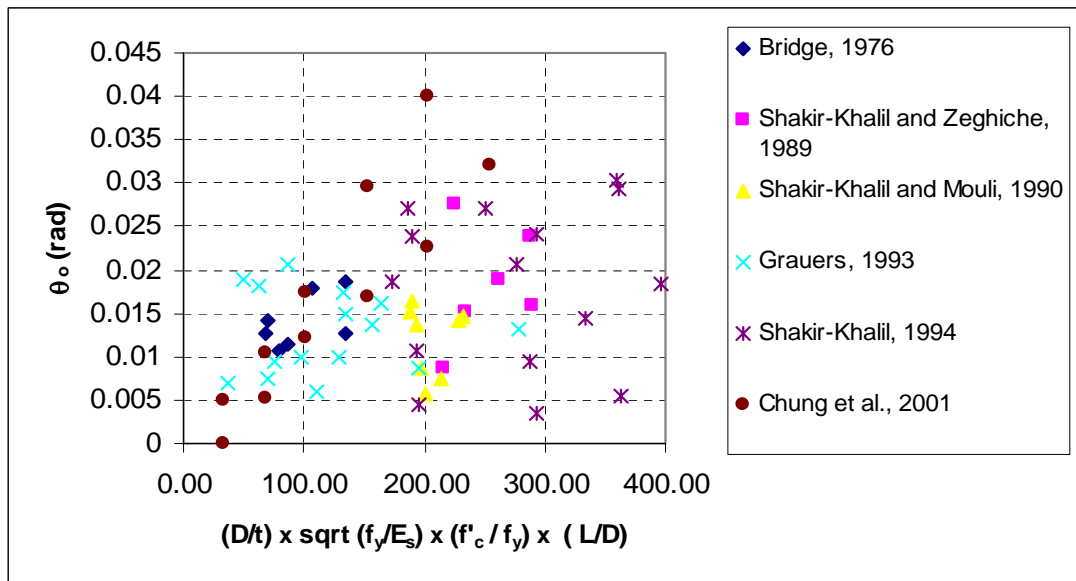


Figure 2.34: Comparison of θ_o versus $\frac{D}{t} \cdot \sqrt{\frac{f_y}{E_s}} \cdot \left(\frac{f'_c}{f_y}\right)^{-1} \cdot \frac{L}{D}$: Monotonically-Loaded RCFT Beam-Column Tests

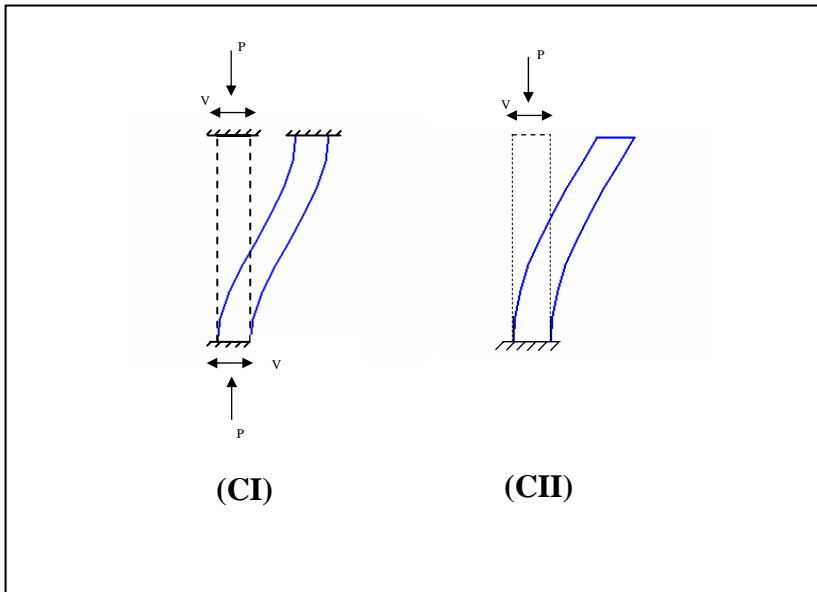


Figure 2.35: Loading Schemes: Cyclically-Loaded RCFT Beam-Column Tests

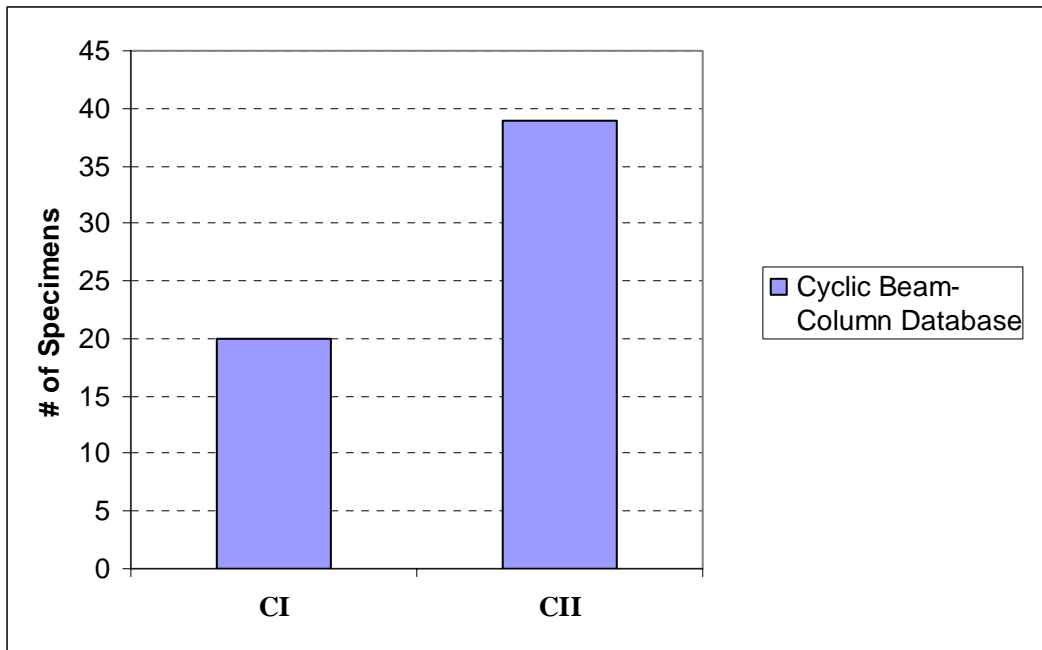


Figure 2.36: Loading Schemes: Cyclically-Loaded RCFT Beam-Column Tests

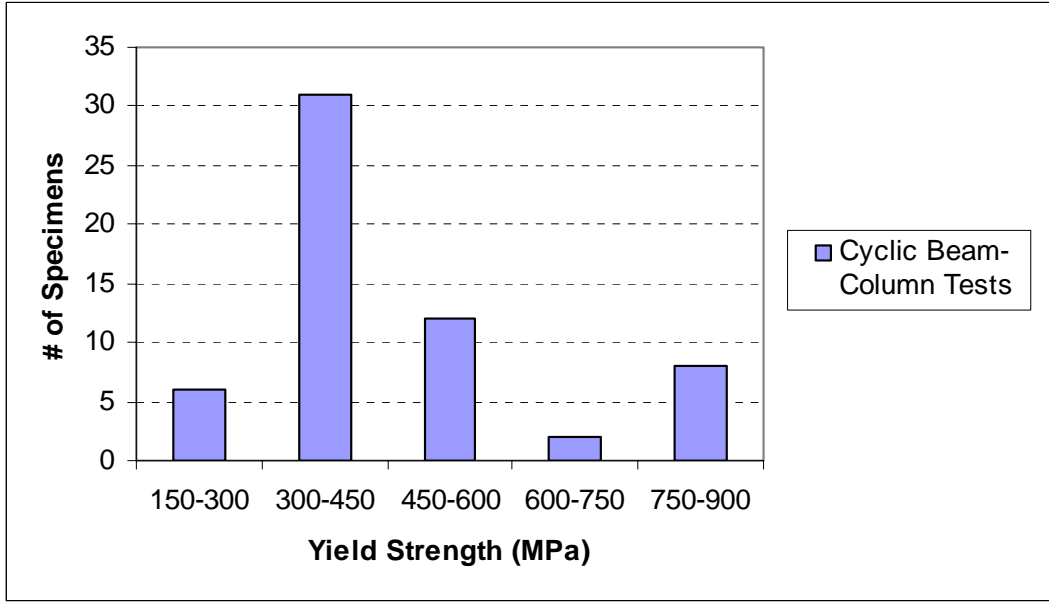


Figure 2.37: Measured Yield Strength of the Steel Tubes: Cyclically-Loaded RCFT Beam-Column Tests

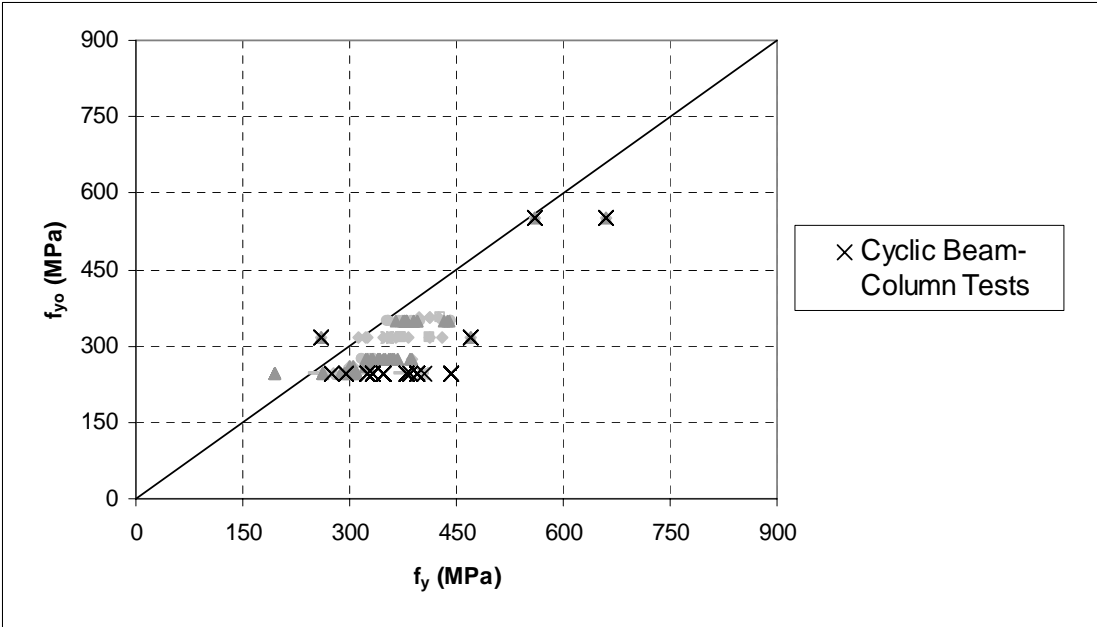


Figure 2.38: Comparison of Measured and Nominal Yield Strength of the Steel Tubes: Cyclically-Loaded RCFT Beam-Column Tests

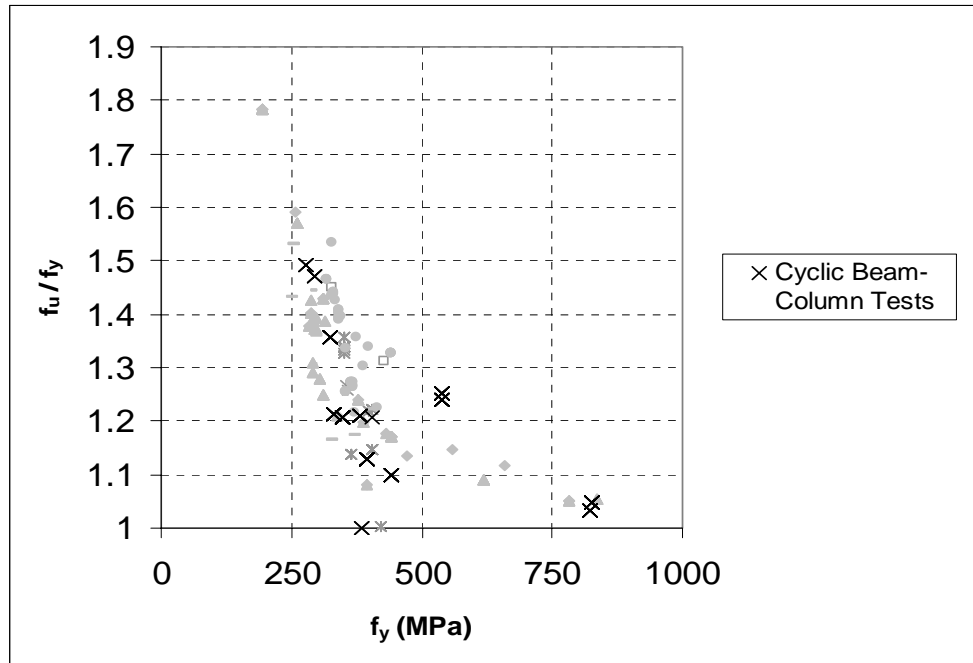


Figure 2.39: Comparison of f_u/f_y versus Measured Yield Strength of the Steel Tubes: Cyclically-Loaded RCFT Beam-Column Tests

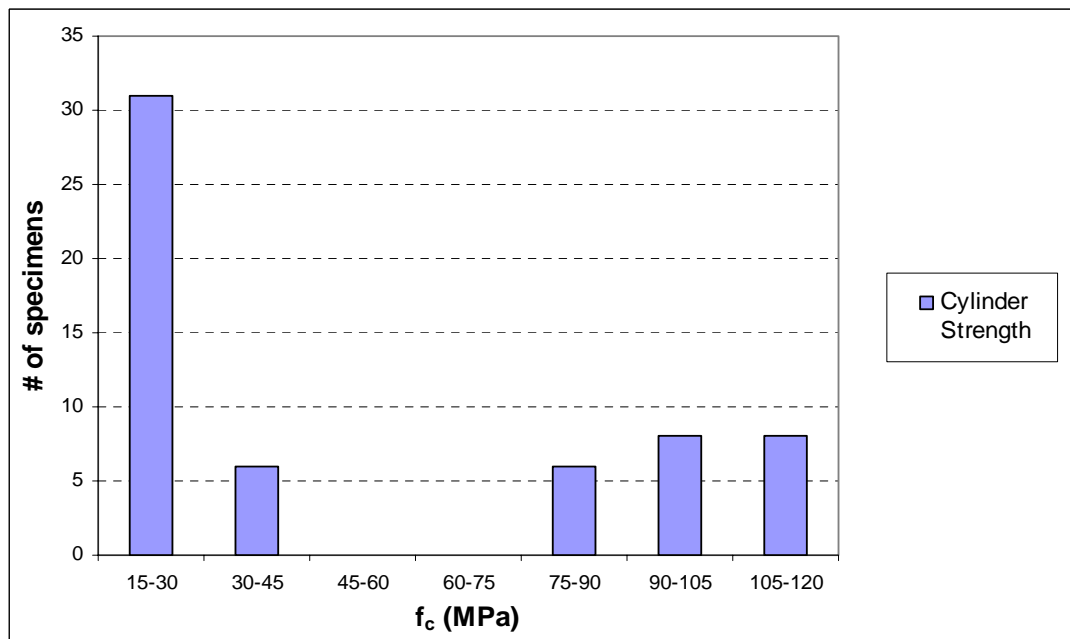


Figure 2.40: Compressive Strength of the Concrete: Cyclically-Loaded RCFT Beam-Column Tests

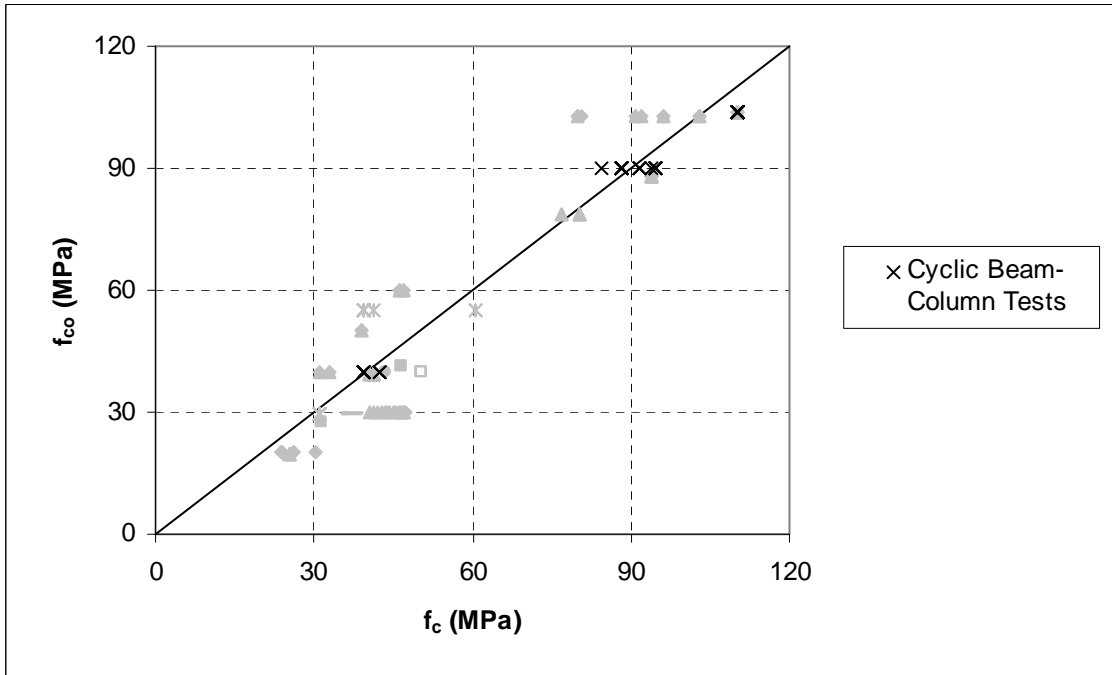


Figure 2.41: Comparison of Measured and Nominal Compressive Strength of the Concrete: Cyclically-Loaded RCFT Beam-Column Tests

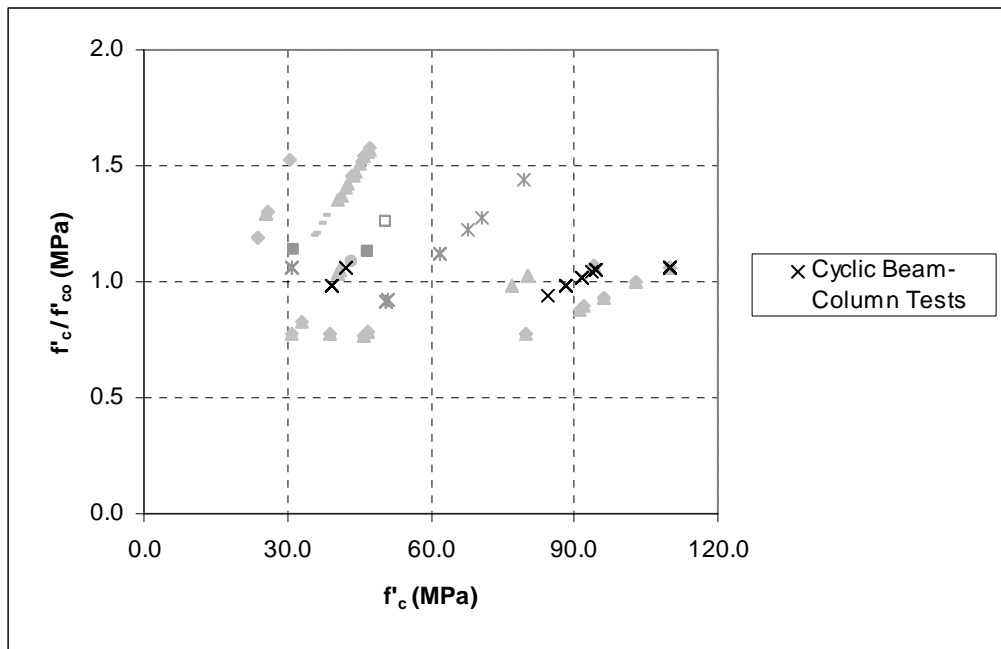


Figure 2.42: Comparison of f'_c/f'_{co} versus Measured Compressive Strength of the Concrete

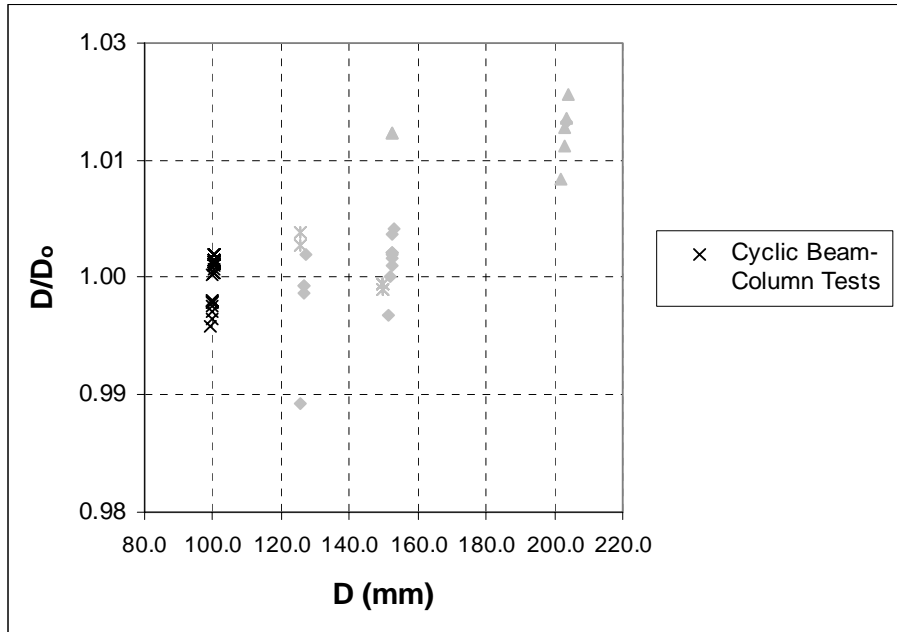


Figure 2.43: Comparison of D/D_0 versus Measured Depth of the Steel Tubes: Cyclically-Loaded RCFT Beam-Column Tests

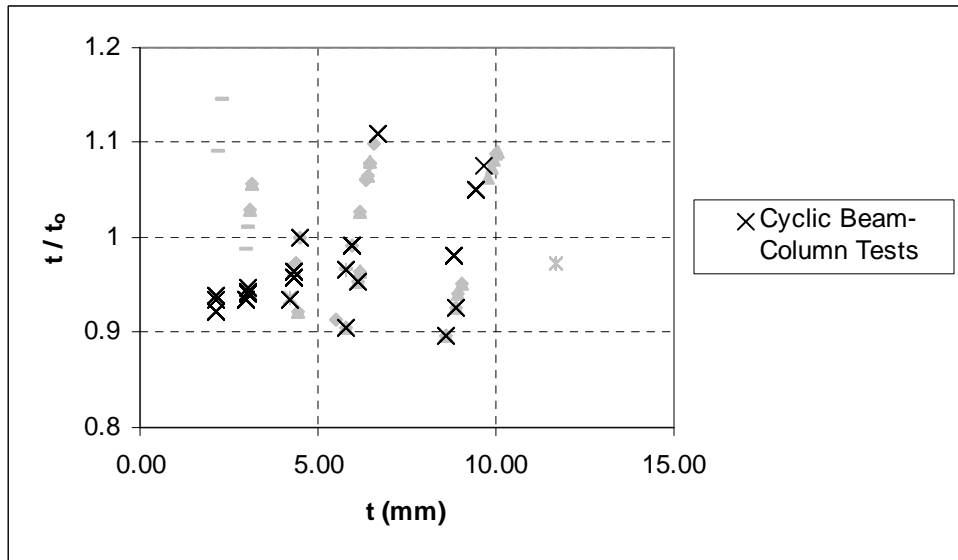


Figure 2.44: Comparison of t/t_0 versus Measured Thickness of the Steel Tubes: Cyclically-Loaded RCFT Beam-Column Tests

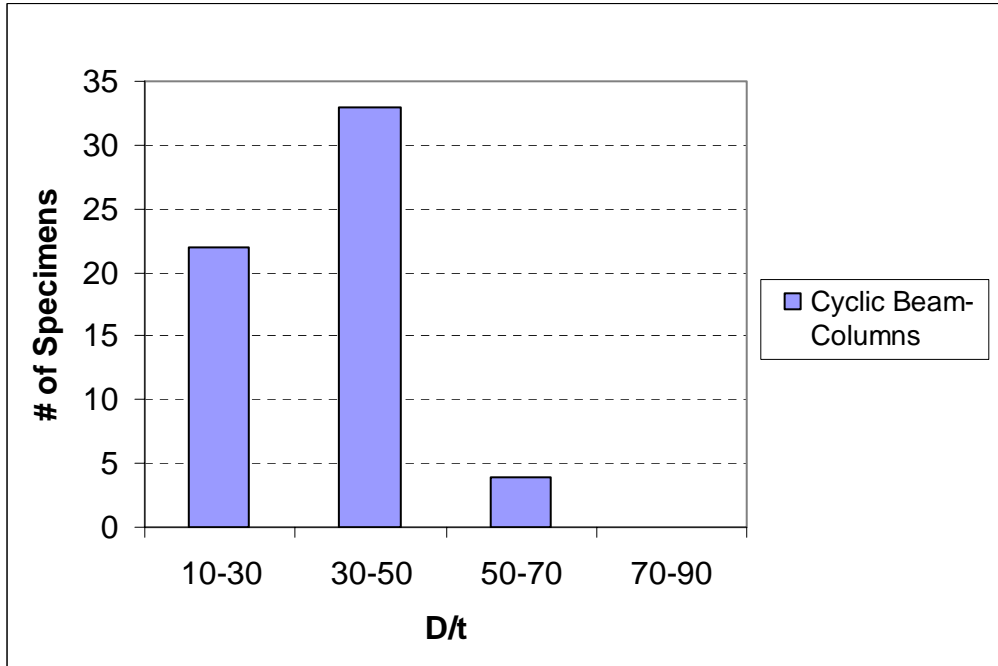


Figure 2.45: D/t Ratio : Cyclically-Loaded RCFT Beam-Column Tests

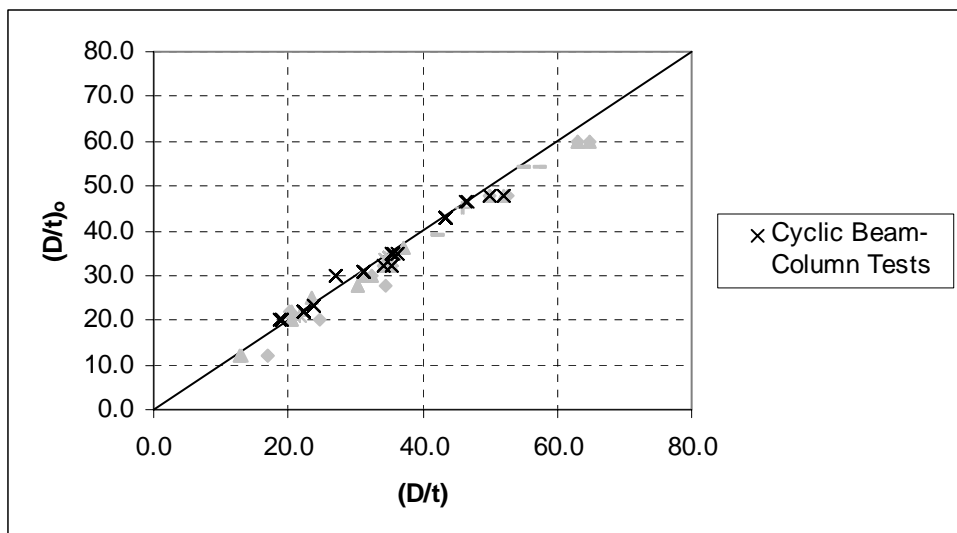


Figure 2.46: Comparison of Measured and Nominal D/t Ratio: Cyclically-Loaded RCFT Beam-Column Tests

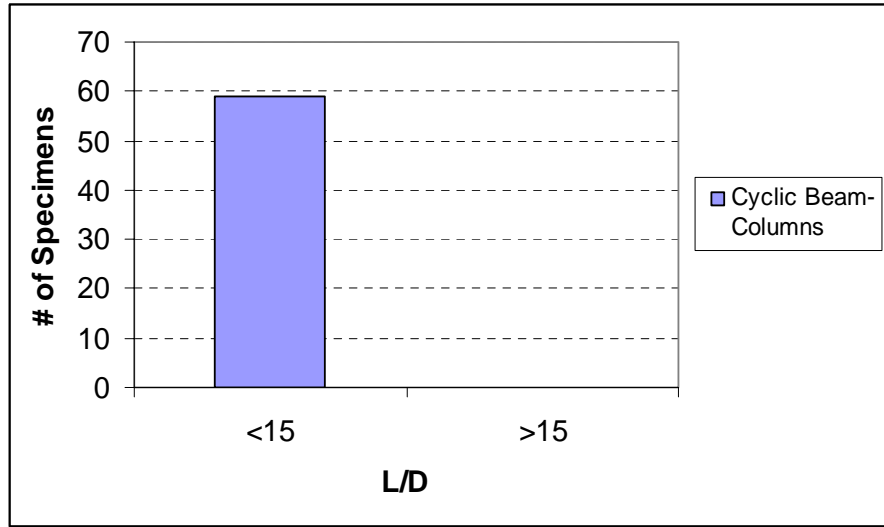


Figure 2.47: L/D Ratio: Cyclically-Loaded RCFT Beam-Column Tests

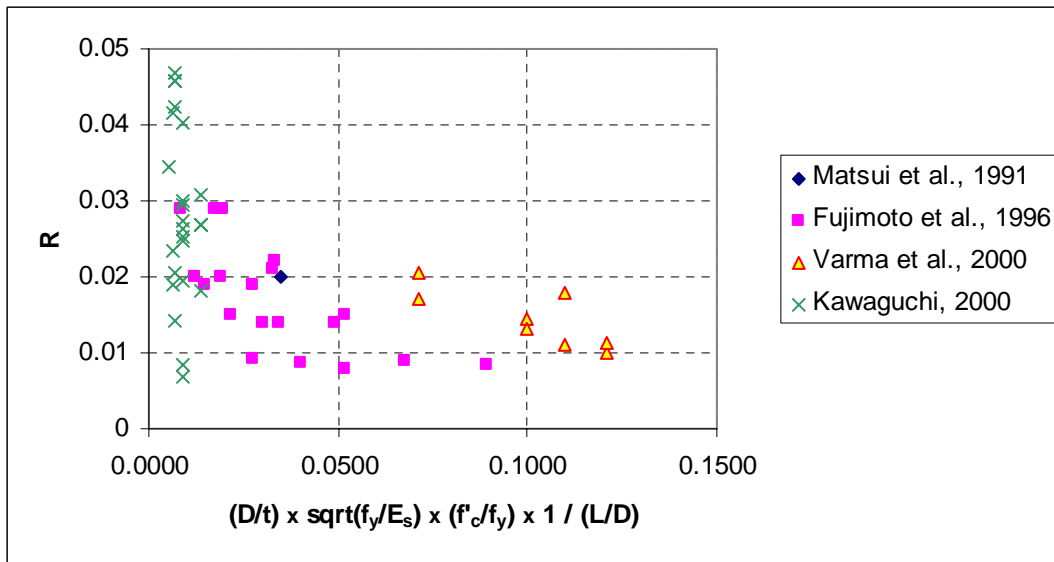


Figure 2.48: Comparison of R versus $\frac{D}{t} \cdot \sqrt{\frac{f_y}{E_s}} \cdot \frac{f'_c}{f_y} \cdot \frac{1}{L/D}$: Cyclically-Loaded RCFT Beam-Column Tests

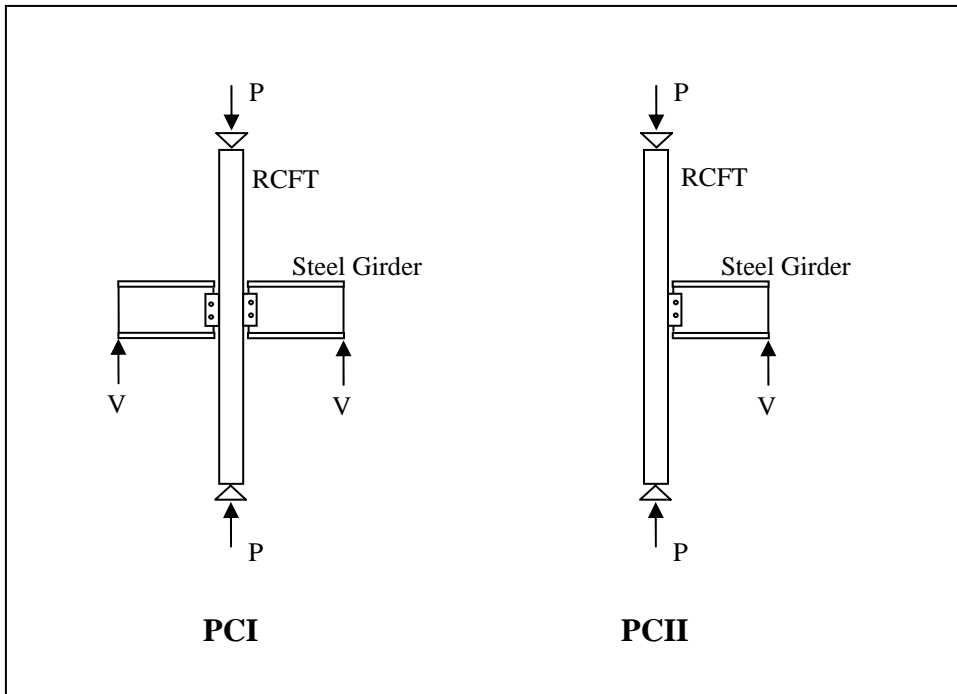


Figure 2.49: Loading Schemes: Monotonically-Loaded RCFT Pinned-Connection Tests

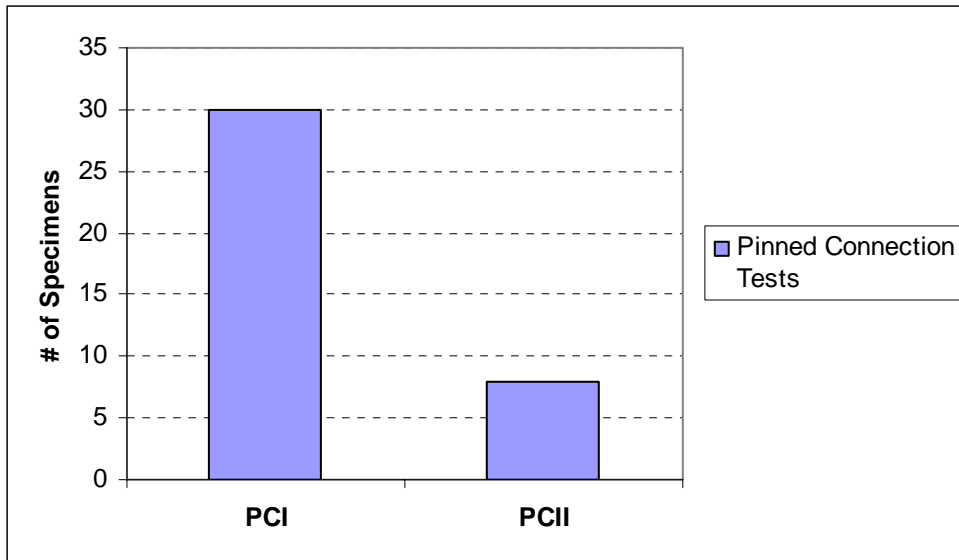


Figure 2.50: Loading Schemes: Monotonically-Loaded RCFT Pinned-Connection Tests

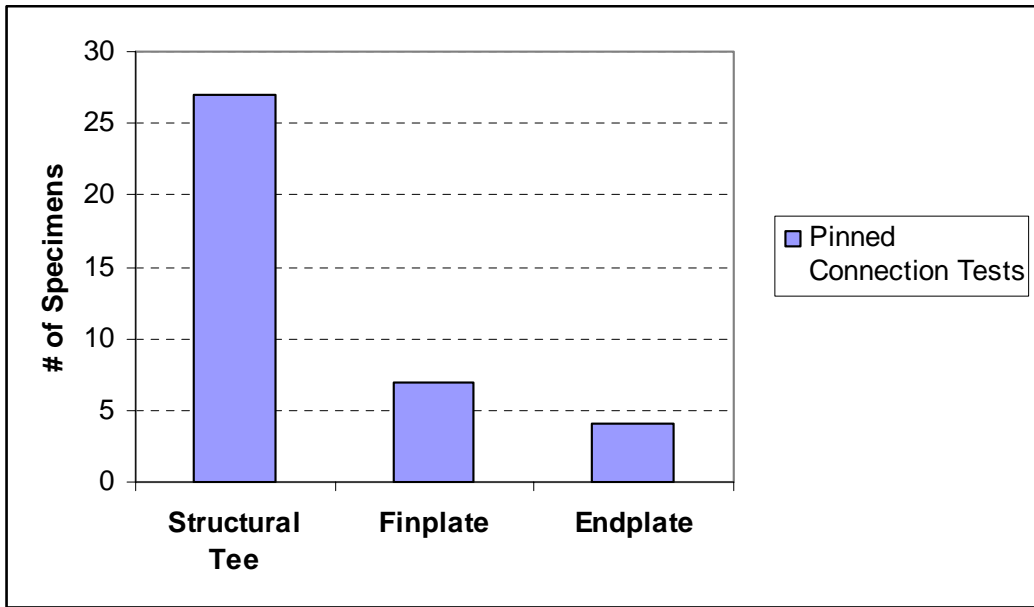


Figure 2.51: Main Connection Elements: Monotonically-Loaded RCFT Pinned-Connection Tests

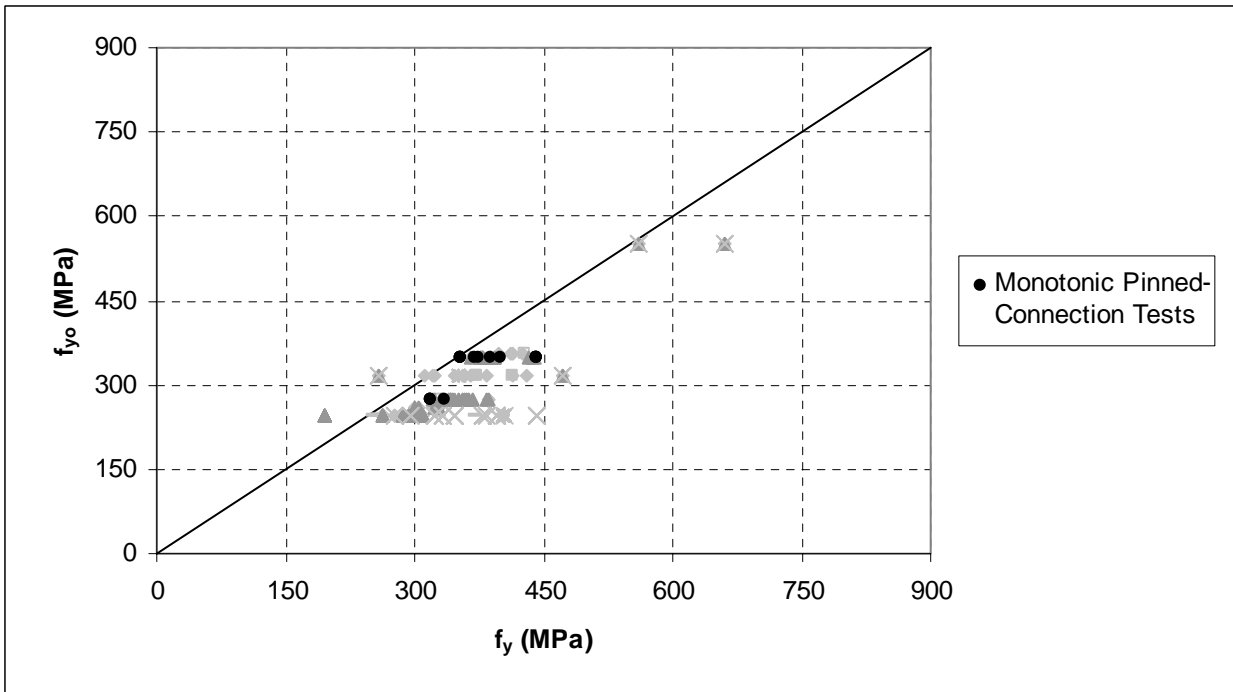


Figure 2.52: Comparison of Measured and Nominal Yield Strength of the Steel Tubes: Monotonically-Loaded RCFT Pinned-Connection Tests

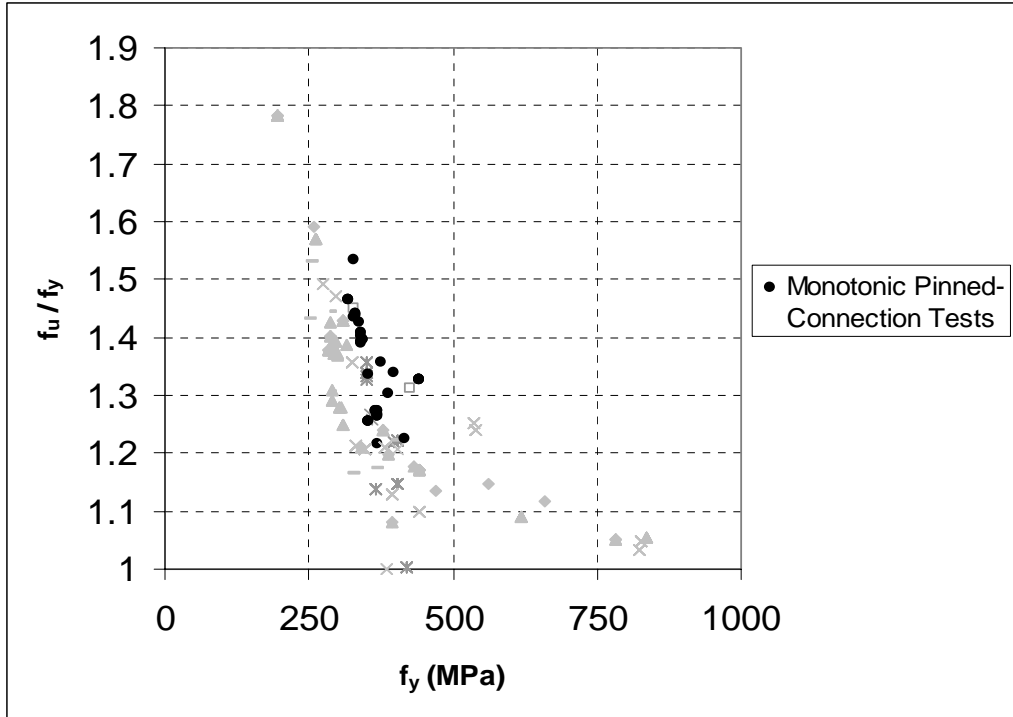


Figure 2.53: Comparison of f_u/f_y versus Measured Yield Strength of the Steel Tubes: Monotonically-Loaded RCFT Pinned-Connection Tests

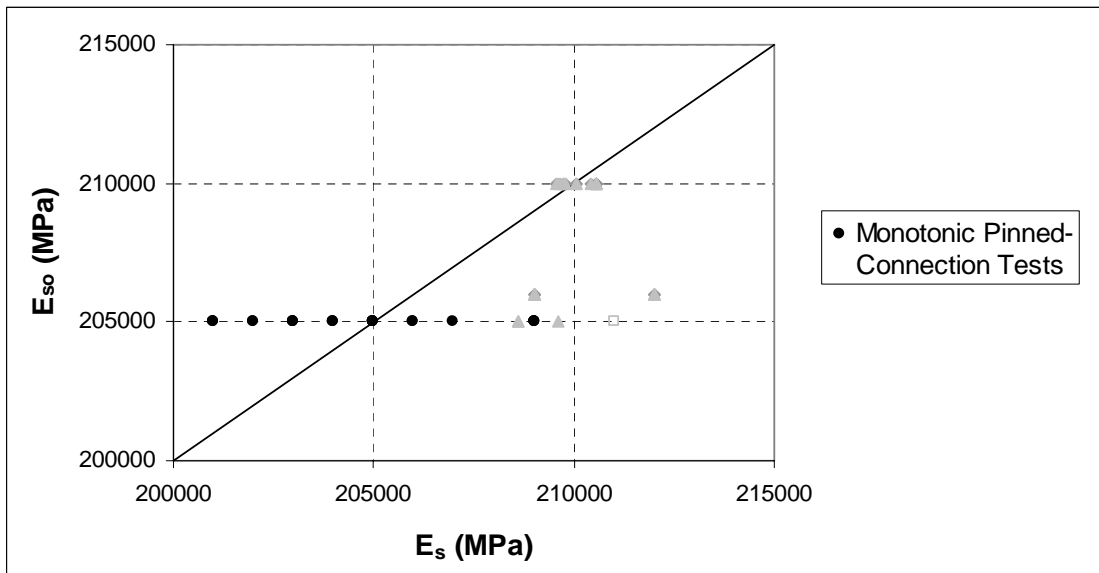


Figure 2.54: Comparison of Measured and Nominal Modulus of Elasticity of the Steel Tubes: Monotonically-Loaded RCFT Pinned-Connection Tests

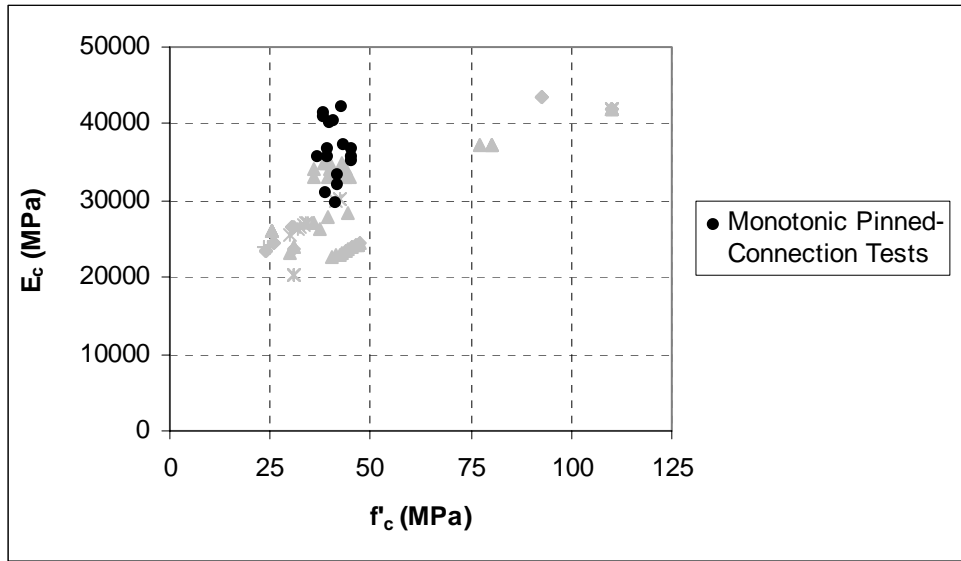


Figure 2.55: Comparison of E_c versus Measured Compressive Strength of the Concrete: Monotonically-Loaded RCFT Pinned-Connection Tests

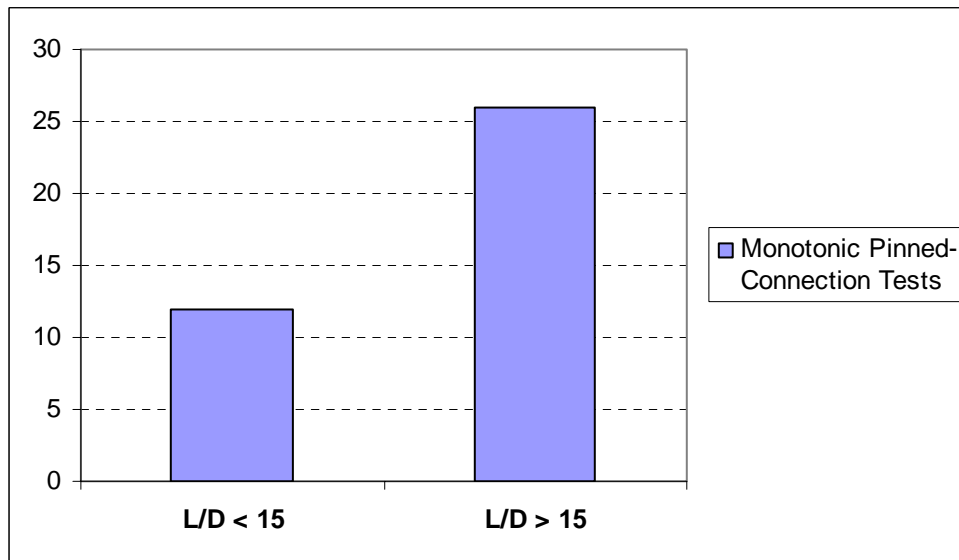


Figure 2.56: L/D Ratio: Monotonically-Loaded RCFT Pinned-Connection Tests

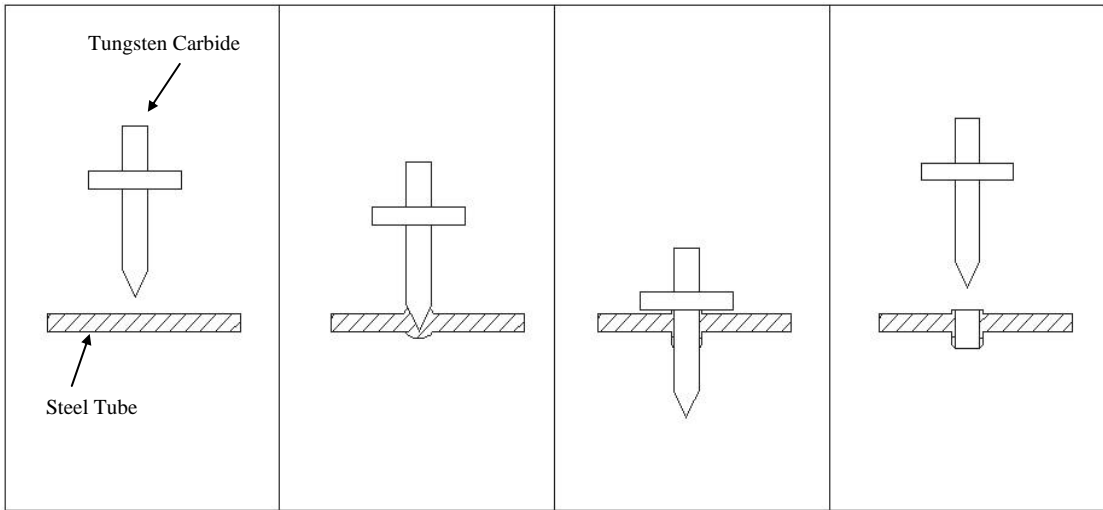


Figure 2.57: Flow-drilling Stages: Blind-Bolted RCFT Moment Connections

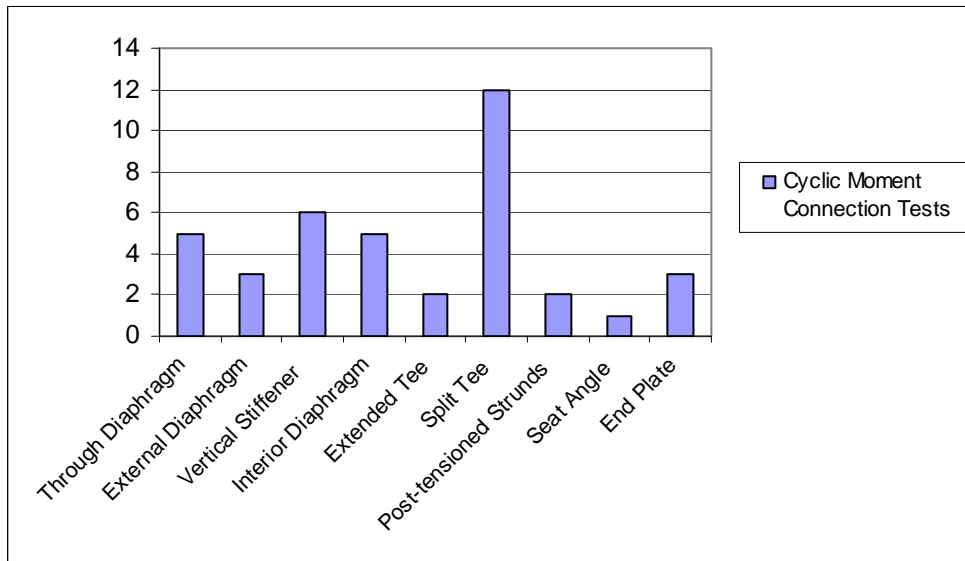


Figure 2.58: Connection Details: Cyclically-Loaded RCFT Moment Connection Tests

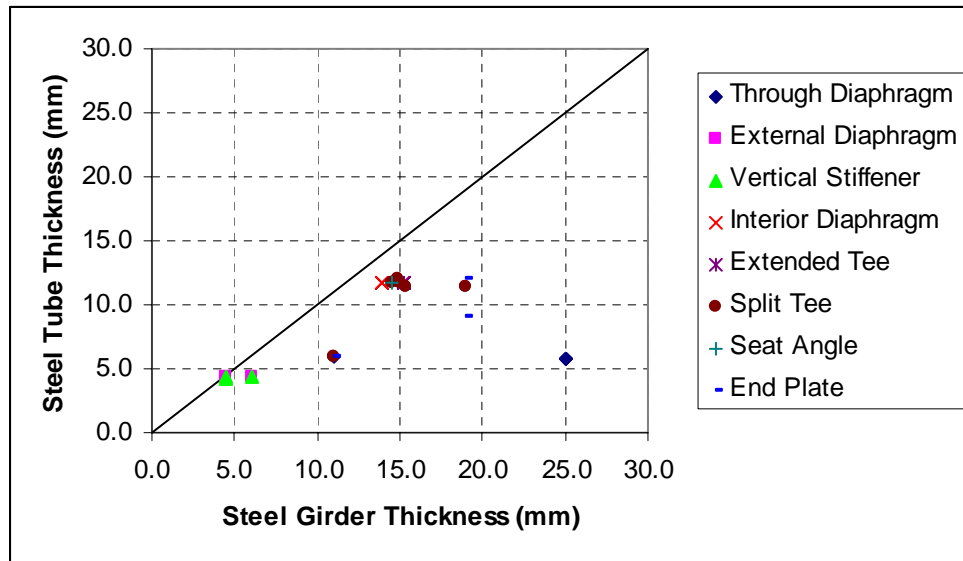


Figure 2.61: Comparison of Girder Flange Thickness and Steel Tube Thickness: Cyclically-Loaded RCFT Moment Connection Tests

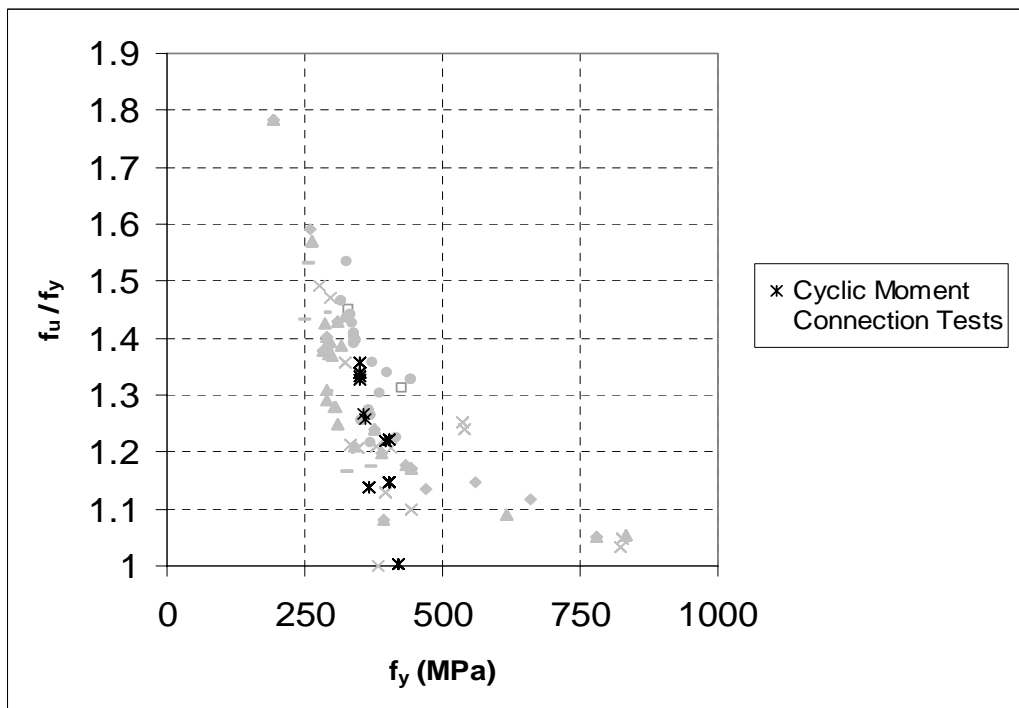


Figure 2.62: Comparison of f_u/f_y versus Measured Yield Strength of the Steel Tubes: Cyclically-Loaded RCFT Moment Connection Tests

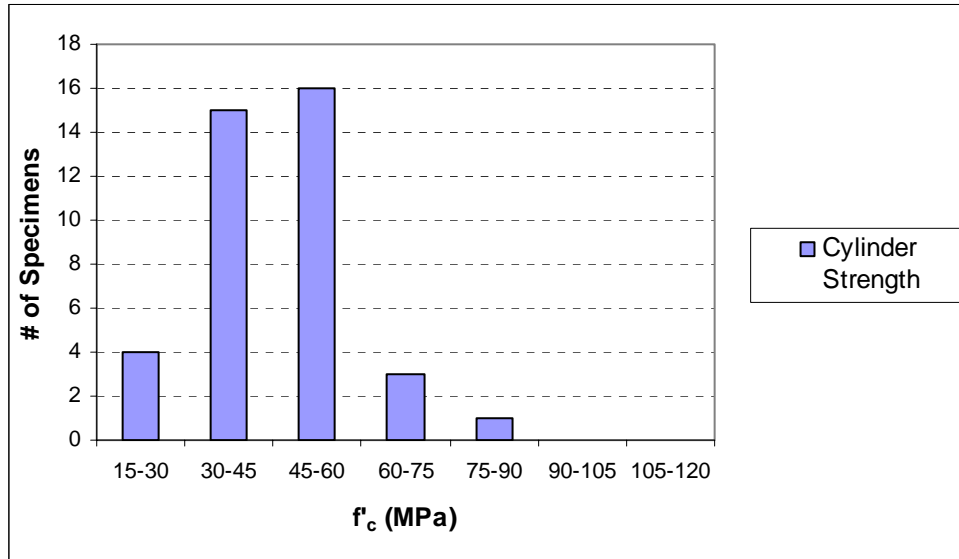


Figure 2.63: Compressive Strength of the Concrete: Cyclically-Loaded RCFT Moment Connection Tests

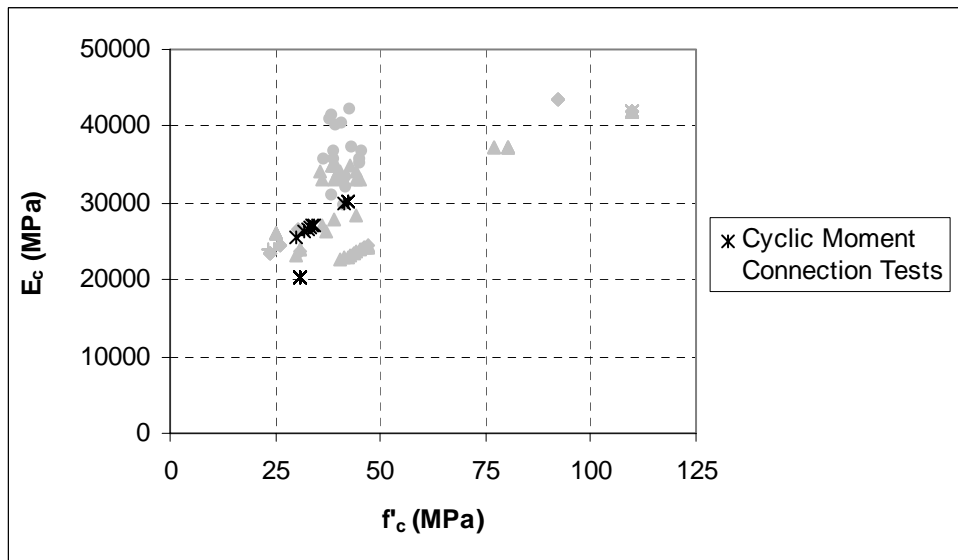


Figure 2.64: Comparison of E_c versus Measured Compressive Strength of the Concrete: Cyclically-Loaded RCFT Moment-Connection Tests

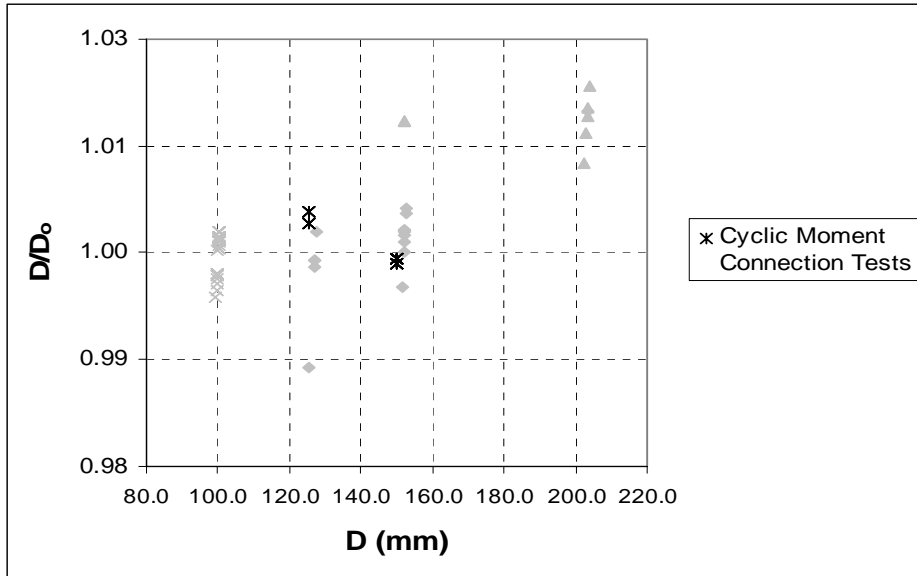


Figure 2.65: Comparison of D/D_o versus Measured Depth of the Steel Tubes: Cyclically-Loaded RCFT Monotonic Connection Tests

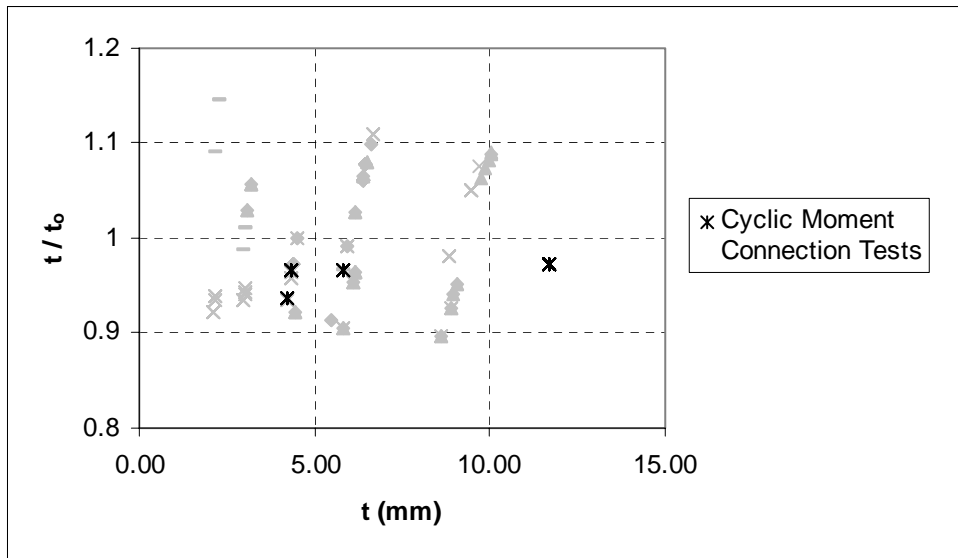


Figure 2.66: Comparison of t/t_o versus Measured Thickness of the Steel Tubes: Cyclically-Loaded RCFT Moment Connection Tests

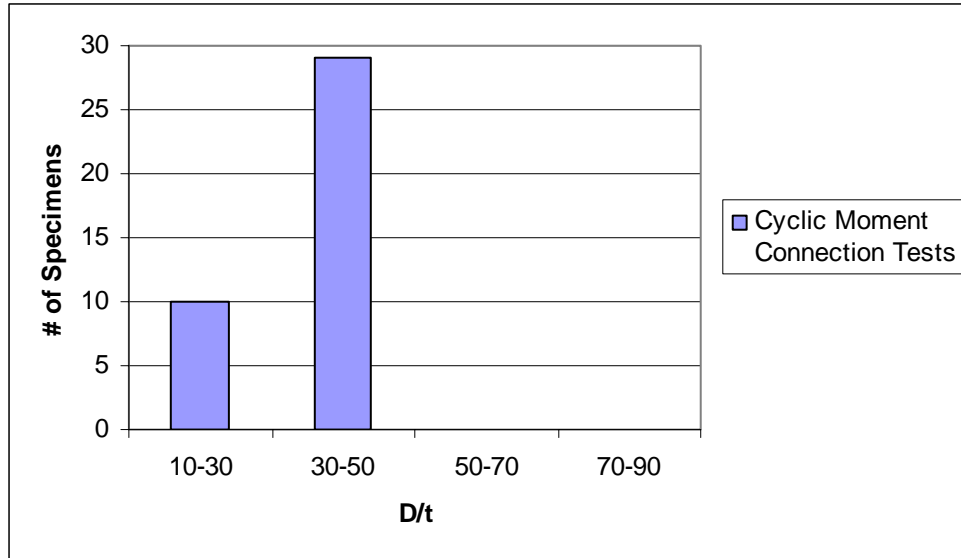


Figure 2.67: D/t Ratio: Cyclically-Loaded RCFT Moment Connection Tests

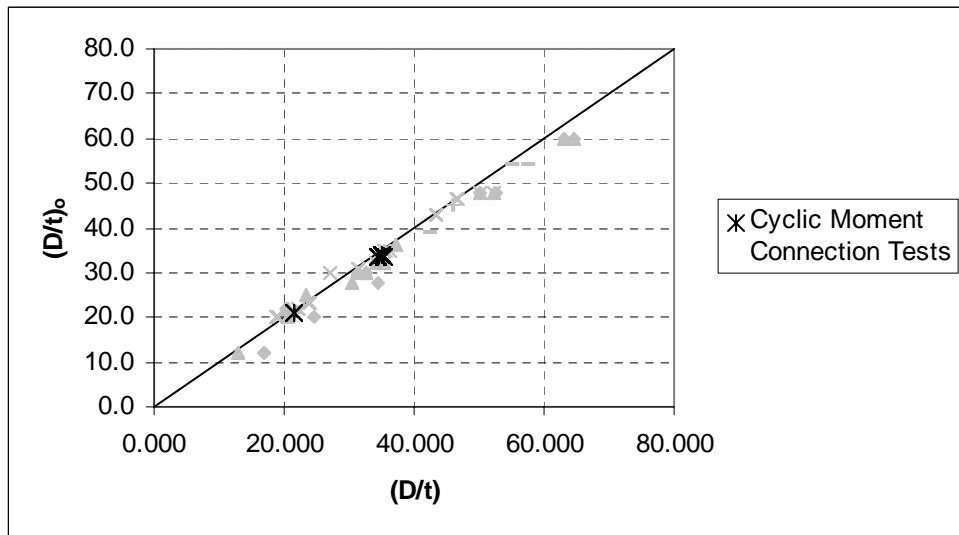


Figure 2.68: Comparison of Measured and Nominal D/t Ratio: Cyclically-Loaded RCFT Moment Connection Tests

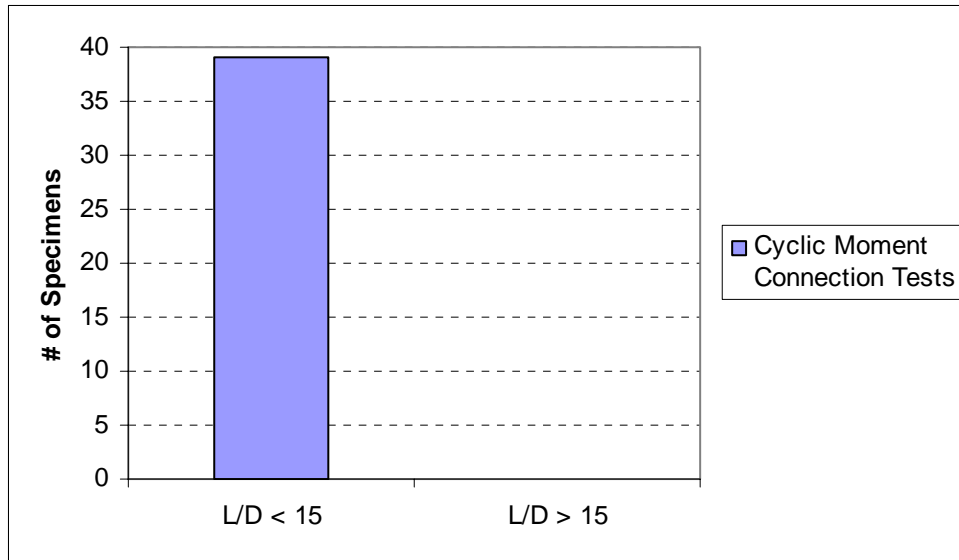


Figure 2.69: *L/D* Ratio: Monotically-Loaded RCFT Moment Connection Tests

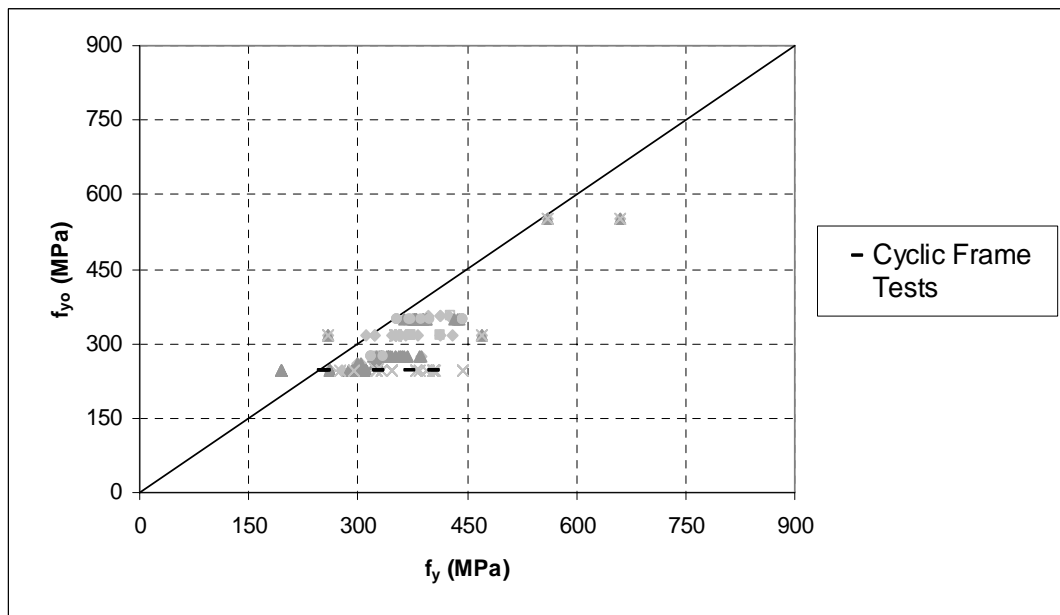


Figure 2.70: Comparison of Measured and Nominal Yield Strength of the Steel Tubes: Cyclically-Loaded RCFT Frame Tests

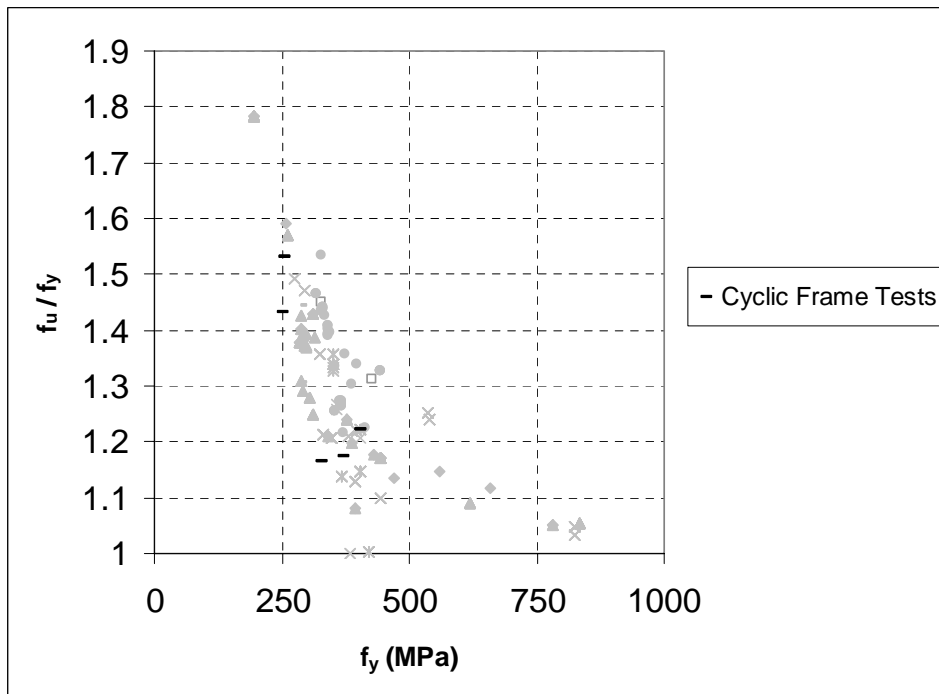


Figure 2.71: Comparison of f_u/f_y versus Measured Yield Strength of the Steel Tubes: Cyclically-Loaded RCFT Frame Tests

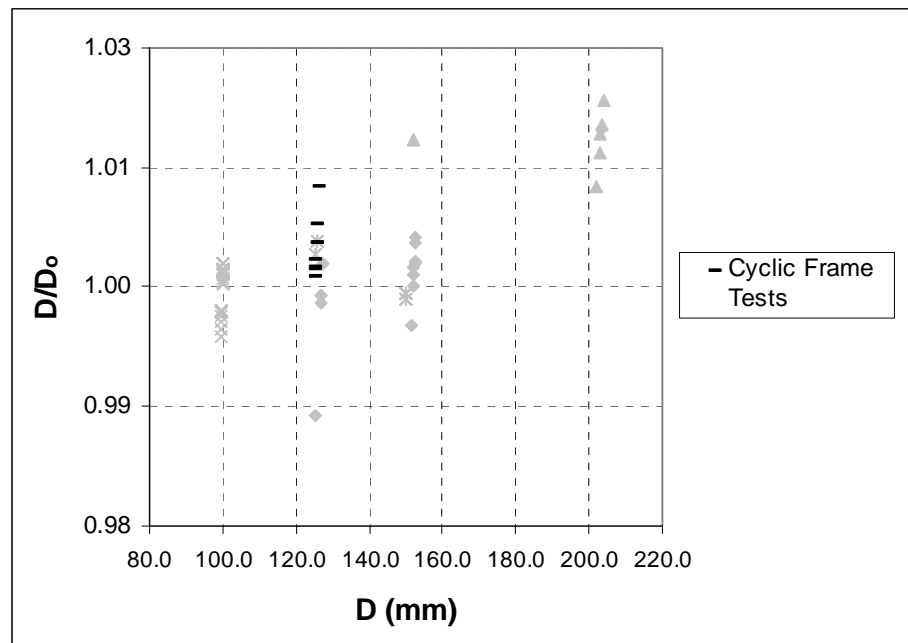


Figure 2.72: Comparison of D/D_0 versus Measured Depth of the Steel Tubes: Cyclically-Loaded RCFT Frame Tests

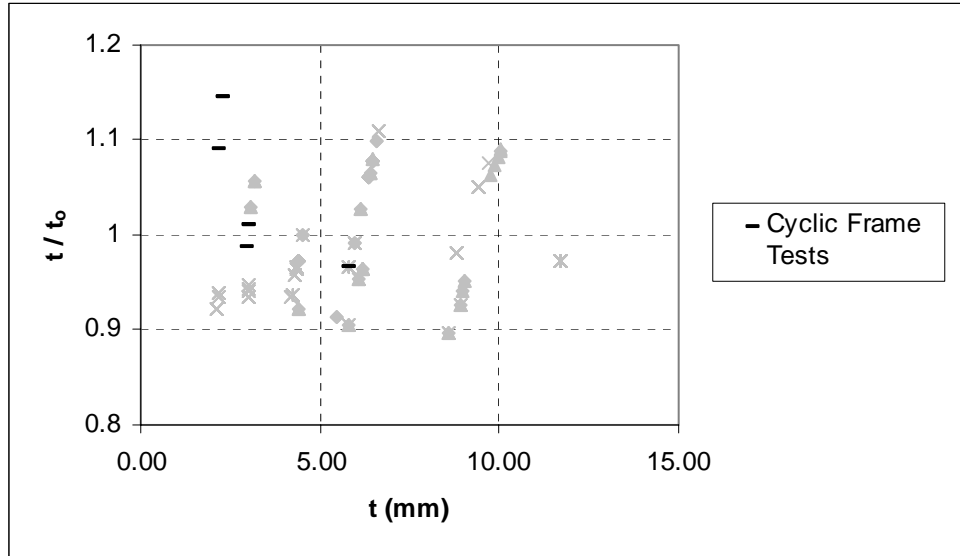


Figure 2.73: Comparison of t/t_0 versus Measured Thickness of the Steel Tubes: Cyclically-Loaded RCFT Frame Tests

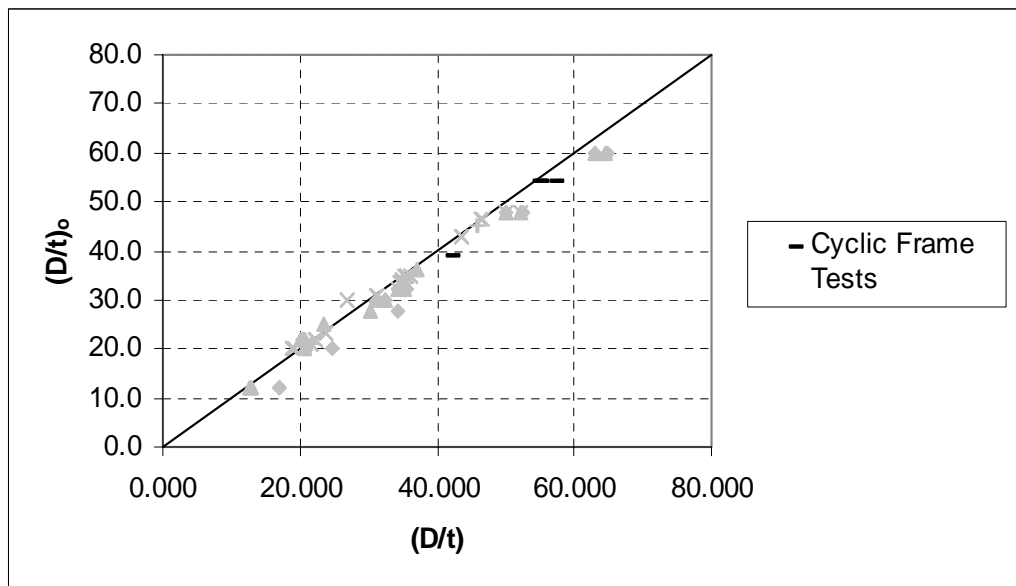


Figure 2.74: Comparison of Measured and Nominal D/t Ratio: Cyclically-Loaded RCFT Frame Tests

Chapter 3

Damage Assessment of RCFT Members

In this chapter, damage levels and their effect on the RCFT members at all levels of both monotonic and cyclic loading will be documented in detail. This information can provide the foundation for establishing predictions of capacity for use in developing performance-based design provisions for RCFT members, connections, and frames.

3.1 Damage Levels for RCFT members

Performance-based design of RCFTs requires consistent definition of the limit states of composite RCFT members and frames. In order to achieve this, the answers to the following questions must be assessed using the available experimental data from the literature:

1. Which damage levels are most significant at each level of performance in the RCFT member, connection, or frame?
2. What is the best method for quantifying the damage sustained by the RCFT members, connections, or frames?
3. How do local damage levels observed during the experiments affect the global behavior of the composite RCFT frame?

In this study, past experimental results, as discussed in Chapter 2, are synthesized to document the damage levels for RCFT beam-columns, connections, and frames. This

information may be used directly to help establish measures of capacity of RCFT members at all levels of loading, for use in developing performance-based design provisions for RCFT beam-columns, connections, and frames.

3.1.1 Structural Damage Functions for RCFT Beam-Columns and Connections

The damage in the structural members may be quantified through the use of structural damage functions, which are mathematical expressions operating on variables (e.g., stiffness, strength, deformation, force, energy) representing the state of the member under loading. A damage index is the value of a damage function at a specific instant in the loading history. In the current literature, structural damage functions are mainly used for (Williams and Sexsmith, 1995; Kappos, 1997):

- Post-earthquake assessment of structures following an earthquake
- Disaster planning
- Seismic performance prediction of structures

Structural damage indices can be related to the loss of load or reduction in deformation capacity of the members or buildings. Economical damage indices can also represent the damage in terms of repair and replacement cost of the structures. The damage is usually expressed in terms of normalized dimensionless values. A common property of all the structural damage indices is that they often are defined so as to achieve a value of unity at the failure state of the structural component or system.

Damage functions may be broadly categorized as local and global. Local damage functions typically refer to a single member or connection, while the global damage functions quantify the damage of a whole structural subassembly of system. In this study, a primary focus will be documentation of local damage indices.

Another common type of classification of the damage functions is whether the damage function takes into account the effect of repeated loading or it is independent of the nature of the loading sequence. The cumulative damage functions integrate the effect

of loading cycles up to the current state of the member. However, non-cumulative damage functions depend on parameters without taking into account the effect of loading.

More extensive classifications of damage indices exist in the literature. Williams and Sexsmith (1995) and Kappos (1997) provide comprehensive discussions on classification of the damage indices.

When members are subjected to cyclic loading, they exhibit degradation both in strength and stiffness. The amount of degradation is dependent on a number of parameters, such as the amount that a critical force or deformation level is exceeded, and the number of cycles to which the component is subjected. Consequently, non-cumulative damage functions are unconservative in that they do not account for cumulative strength or stiffness degradation (including low-cycle fatigue) due to cyclic excitation. However, they are simpler to implement and provide preliminary estimations for the damage states of members subjected to cyclic loading.

3.1.1.1 Non-Cumulative Local Structural Damage Functions for RCFT Beam-Columns and Connections

Banon et al. (1981) proposed rotation ductility (μ_θ) and curvature ductility (μ_ϕ) as damage functions for reinforced concrete (RC) frame members subjected to flexure. These damage functions are calculated by taking the ratio of maximum rotation (θ_{max}) and maximum curvature (ϕ_{max}) to their yield values (θ_y and ϕ_y , respectively). Rotation ductility and curvature ductility are successful to examine the permanent deformations sustained by flexural members, including beam-columns. However, strength degradation cannot be captured. Therefore, Banon et al. (1981) recommended an alternative damage function called the Flexural Damage Ratio (*FDR*). It was derived by modifying the damage ratio originally derived by Lybas and Sozen (1977). *FDR* is calculated by taking the ratio of the cracked flexural stiffness of an RC member (K_f) to its reduced secant stiffness at the end of the test (K_r). The cracked flexural stiffness of the RC member was taken as $K_f = 24EI / L^3$, where EI is the flexural rigidity and L is the member length. The formulas for rotation ductility, curvature ductility, and *FDR* are given below:

$$\mu_{\theta} = \frac{\theta_{\max}}{\theta_y} \quad \mu_{\phi} = \frac{\phi_{\max}}{\phi_y} \quad FDR = \frac{K_f}{K_r} \quad (3.1)$$

A non-cumulative damage function based on the reduction of the flexural stiffness was also introduced by Roufaiel and Meyer (1987) for RC members. The amount of damage at a point during the test is calculated by taking the ratio of the reduction in secant stiffness between the yield point and the current loading point to the reduction in secant stiffness between the yield point and the end point of the test. The damage indices are calculated for the positive and negative directions of loading separately, and the larger value is taken as the modified flexural damage ratio (*MDFR*). The general formula for the proposed damage function is given below:

$$MDFR = \frac{\frac{\phi_x}{M_x} - \frac{\phi_y}{M_y}}{\frac{\phi_m}{M_m} - \frac{\phi_y}{M_y}} \quad (3.2)$$

where:

ϕ_x = curvature at the current point of loading

ϕ_y = yield curvature

ϕ_m = curvature at the end of the test

M_x = moment at the current point of loading

M_y = yield moment

M_m = moment at the end of loading

The graphical illustration of the calculation of *MDFR* is shown in Figure 3.1. *MDFR* is equal to zero in the case of no damage and it becomes equal to unity when the specimen fails. Both strength degradation and plastic deformation sustained by the member can be captured through this parameter.

Fajfar (1992) introduced a more general non-cumulative damage function based on the assumption that failure is due to the plastic deformation that structural members undergo. It is calculated by taking the ratio of current plastic deformation of the structural member to its total plastic deformation. The plastic deformation may be defined appropriately for a given member, i.e., it may be axial, flexural, torsional, etc. The damage index (*DM*) is equal to zero, indicating no damage, if the current

deformation (D) is less than or equal to the yield deformation (D_y). DM becomes equal to unity when the current deformation attains the ultimate deformation level (D_u). This damage index has the disadvantage that strength degradation of the member is not accounted for. The formula to calculate DM is given below:

$$DM = \frac{D - D_y}{D_u - D_y} \quad (3.3)$$

3.1.1.2 Cumulative Local Structural Damage Functions for RCFT Beam-Columns and Connections

Cyclic load reversals for both steel and concrete cause structural members to experience more damage than they do under monotonic loading at comparable levels of loading or deformation. This effect is taken into account by adopting cumulative damage indices for the structural members. The cumulative damage indices can be deformation-based (e.g., a low-cycle fatigue formulation), energy-based, or they can have a combination of both deformation and energy-based terms.

A deformation-based cumulative damage index was derived analytically by Banon et al. (1981) for RC frames. This index was designated as the normalized cumulative rotation (NCR). A finite element method denoted as a single component model was developed to simulate the cyclic behavior of RC frames. In this method, RC members were modeled by beam elements with inelastic rotational springs at the two ends. Once the computational model was verified to reproduce the cyclic load-deflection response of experiments of RC members, the NCR was calculated as the sum of the plastic rotations of the inelastic springs ($\sum |\theta_p|$) normalized by the yield rotation (θ_y). The formula for NCR is given below:

$$NCR = \frac{\sum |\theta_p|}{\theta_y} \quad (3.4)$$

The NCR was evaluated for more than 30 tests on RC beam-columns and subassemblages. However, the value of NCR at failure showed considerable scatter.

Park and Ang (1985) proposed a damage model for RC beam-columns in terms of the maximum deformation and the absorbed hysteretic energy of the members. The

given damage index, which is written generically and may be applied to any appropriate load-deformation relationship, is a linear combination of these two quantities as follows:

$$D = \frac{\delta_M}{\delta_u} + \frac{\beta}{Q_y \cdot \delta_u} \int dE \quad (3.5)$$

where:

δ_M = maximum deformation under cyclic loading

δ_u = maximum deformation under monotonic loading

Q_y = calculated yield strength

dE = incremental absorbed hysteretic energy

β = non-negative parameter

The effect of cyclic loading is taken into account by the second term of the damage function through the β parameter. Park and Ang (1985) assumed that this effect was constant at each deformation level. The parameters δ_u , Q_y , and β were all determined empirically. The β parameter was calibrated for the damage index to be equal to unity at failure. For this purpose, the load-deformation responses of over 250 specimens were traced and the value of β was calculated at failure such that D equaled unity. Then, a curve fit was made to the obtained data for β in terms of some key variables of RC members e.g., shear span depth ratio, reinforcement ratio, and axial stress. When the proposed equation for the damage index was applied to experiments, a large scatter was obtained. Therefore, a log-normal distribution was determined to be appropriate for use of this damage index.

McCabe and Hall (1989) developed two new damage indices. The first damage index was derived from the concept of equivalent hysteretic cycles. The number of cycles until failure was considered to be a measure of the damage. As each cycle that structural members underwent is not the same, an equivalent hysteretic cycle concept was introduced. The total dissipated hysteretic energy was divided by the amount of energy in a standard hysteretic cycle, which yielded the number of equivalent hysteretic cycles as a damage measure. The amount of energy in a standard hysteresis cycle was calculated by multiplying the yield resistance by an appropriate displacement measure. This method of damage assessment is successful in representing the effect of hysteretic loading and the random nature of the hysteretic cycles. The second damage index was adopted from low-

cycle fatigue theory of the metals. It was assumed that earthquake damage within a structure has similar characteristics to the low-cycle fatigue damage in metals. The ductility was defined in two parts, including elastic ductility and plastic ductility. Plastic ductility was then further subdivided into monotonic plastic ductility (μ_p) and hysteretic plastic ductility (μ^*). Similar to the analogy of other low-cycle fatigue damage models in the literature, the hysteretic plastic ductility for steel structures was given as follows:

$$\mu^* = \mu_p \cdot (2.N_f)^{-0.6} \quad (3.6)$$

where:

N_f - number of load reversals to failure

Assuming all the deformation amplitudes to be of equal size for a fully damaged condition after $2N_f$ load reversals, the total hysteretic energy (H_t) can be calculated as follows:

$$H_t = (\mu^h \cdot U_y) \cdot R_y \cdot (2.N_f) \quad (3.7)$$

where:

U_y - yield displacement

R_y - yield resistance

Finally, the damage index (DI) was derived to represent the ratio of the actual hysteretic energy dissipated to the hysteretic energy corresponding to complete damage as given above. A second-degree relation was derived between the energy terms. The formula for the DI is given below:

$$DI = \left(\frac{H_p + H_n}{H_t}\right)^2 + \left(\frac{H_p - H_n}{H_t}\right)^2 \quad (3.8)$$

where:

H_p - positive resistance hysteretic energy

H_n - negative resistance hysteretic energy

If the DI obtains values larger than 1.0, this indicates that the structure is completely damaged. The damage model presented above was applied to experiments of steel cantilever columns from the literature and good correlation with experimental results was obtained.

Kanno (1993) tested joint specimens between RC columns and steel girders. The seismic performance of the joints was evaluated through damage indices. Various damage indices were applied to the tested specimens and it was found that the evolution of the damage during the tests was best simulated when deformation-based and energy-based indices were combined. Therefore, Kanno (1993) proposed a new damage index by combining an energy-based index and a deformation-based index nonlinearly as follows:

$$D = \sqrt{(A(\max(\mu_i) - 1)^\alpha)^2 + (B(\sum \beta_i)^\gamma)^2} \quad (3.9)$$

where:

μ_i - ductility ratio at the i^{th} cycle

β_i - energy dissipation ratio at the i^{th} cycle

A, B, α and γ are experimental constants of 1, 1.35, 1.5, 0.45, respectively

The new damage index gave consistent values both for the failure points and the local damage points. Based on the results from the new damage index, Kanno (1993) developed seismic design provisions for the joints in composite frames with RC columns and steel girders.

An energy-based and a deformation-based damage indices were proposed by Mehanny and Deierlein (2000, 2001) for columns, girders, joints and sub-assemblages in composite frames made up of RC columns and steel girders. The energy-based index was adopted from Kradzig et al. (1985). The deformation cycles applied to the specimens were categorized as primary half cycles and follower half cycles. The damage index was equal to the total energy dissipation in the primary and follower half cycles normalized by the summation of the energy dissipation under monotonic loading and the energy dissipation in the follower half cycles. Primary half cycles correspond to those cycles that achieve a new peak deformation level in the loading history. Subsequent cycles having amplitudes less than or equal to the primary half cycles were categorized as follower half cycles. Once the deformation level in a follower half cycle is exceeded in the next step, a new primary half cycle is defined. The proposed energy-based index (D_E) is calculated for the positive (D_E^+) and negative half cycles (D_E^-) separately, and then the

two resulting indices are combined in a nonlinear manner. The formulations for the energy-based damage index are given below:

$$D^+_{E} = \frac{(\sum_{i=1}^{n^+} E^+_{PHC,i})^\alpha + (\sum_{i=1}^{n^+} E^+_{FHC,i})^\beta}{(E^+_f)^\alpha + (\sum_{i=1}^{n^+} E^+_{FHC,i})^\beta} \quad \text{(positive half cycles)} \quad (3.10)$$

$$D^-_{E} = \frac{(\sum_{i=1}^{n^-} E^-_{PHC,i})^\alpha + (\sum_{i=1}^{n^-} E^-_{FHC,i})^\beta}{(E^-_f)^\alpha + (\sum_{i=1}^{n^-} E^-_{FHC,i})^\beta} \quad \text{(negative half cycles)} \quad (3.11)$$

$$D_E = \sqrt{(D^+_{E})^\gamma + (D^-_{E})^\gamma} \quad (3.12)$$

where:

$E^+_{PHC,i}$ - energy dissipation during positive primary half cycles

$E^-_{PHC,i}$ - energy dissipation during negative primary half cycles

E^+_f - energy dissipation in monotonic loading for positive direction

E^-_f - energy dissipation in monotonic loading for negative direction

α, β, γ - calibration parameters

A value of D_E greater than or equal to 1.0 represents failure. The energy dissipation in the follower half cycles exists both in the numerator and in the denominator. Therefore, the amount damage is mainly dependent upon the primary half cycles. Calculating the energy dissipation in both directions makes the damage calculation for unsymmetrical sections more accurate. The idea of categorizing the loading cycles as primary and follower allows the damage index to account for damage due the effect of loading sequence.

The second damage index by Mehanny and Deierlein (2000, 2001) is based on the accumulation of plastic deformation with the idea that failure is caused primarily due to inelastic deformations. The damage index is calculated by normalizing the total plastic rotations at the primary and follower half cycles with respect to the monotonic plastic rotation at failure. Similar to the energy-based damage index the cumulative rotation of

the follower half cycles also exists in both the numerator and denominator, and the damage index is calculated for both directions of loading. The formulation for the deformation-based damage index (D_θ) is given below:

$$D^+_\theta = \frac{(\theta^+_{p \mid currentPHC})^\alpha + \left(\sum_{i=1}^{n^+} \theta^+_{p \mid FHC,i}\right)^\beta}{((\theta_f - \theta_y)^+)^{\alpha} + \left(\sum_{i=1}^{n^+} \theta^+_{p \mid FHC,i}\right)^\beta} \quad (\text{positive half cycles}) \quad (3.13)$$

$$D^-_\theta = \frac{(\theta^-_{p \mid currentPHC})^\alpha + \left(\sum_{i=1}^{n^-} \theta^-_{p \mid FHC,i}\right)^\beta}{((\theta_f - \theta_y)^-)^{\alpha} + \left(\sum_{i=1}^{n^-} \theta^-_{p \mid FHC,i}\right)^\beta} \quad (\text{negative half cycles}) \quad (3.14)$$

$$D_\theta = \sqrt[\gamma]{(D^+_\theta)^\gamma + (D^-_\theta)^\gamma} \quad (3.15)$$

where:

$\theta^+_{p \mid currentPHC}$ - current maximum positive plastic rotation corresponding to the latest primary half cycle

$\theta^+_{p \mid FHC,i}$ - maximum plastic rotation corresponding to the i^{th} follower half cycle

$(\theta_f - \theta_y)^+$ - plastic rotation capacity under monotonic loading for positive direction

$(\theta_f - \theta_y)^-$ - plastic rotation capacity under monotonic loading for negative direction

α, β, γ - calibration parameters

A value of D_θ greater than or equal to 1.0 represents failure.

This past research forms the foundation for the damage functions developed in the current work. Deformation-based and energy-based damage functions were developed to quantify the damage evolution of RCFT members. The displacement-based functions are non-cumulative and are applied to tests of RCFT members subjected to monotonic loading. The energy-based functions are appropriate for both monotonic and cyclic loading, and account approximately for the cyclic load history effect. In the following sections, these damage functions will be described in detail for RCFT columns, beam-columns, connections, and frames.

3.2 Monotonically Loaded RCFT Columns

The damage levels of the monotonically loaded RCFT columns were defined in this work as steel yielding, local buckling, and concrete crushing.

Yielding of Steel Tube

Due to its higher strength and stiffness than concrete, the steel tube often dominates the behavior of RCFT columns. Therefore, once the steel tube yields, it is expected that there will be a reduction in the overall stiffness of the composite section. This reduction is more evident for RCFTs having a large D/t ratio and low strength concrete. Shortly after steel yielding occurs, more axial force will be transferred to concrete, and crushing takes place. After this point, the capacity of the composite section starts to degrade significantly (Gourley et al. 2001).

The desired ductile response of the columns is achieved if steel yielding takes place before concrete crushing. For D/t ratios within the typical range of use in RCFTs (e.g., covering D/t ratios less than 50), this is the usual sequence, so long as the yield strength of the steel is not greater than 345 MPa (Furlong, 1967). However, even in stub column tests with 550 MPa steel tubes and D/t ratio of 32, Varma (2000) and Varma et al. (2001) also found that steel yielding took place after concrete crushing. If the slenderness of an RCFT column, L/D , increases, it is possible that the column is going to buckle elastically or at the onset of steel yielding. The column tests conducted by Bridge (1976), Shakir-Khalil and Zeghiche (1989), and Wang (1999) failed by inelastic buckling approximately at the time that steel yielding initiated.

The available damage functions in the literature are mostly calibrated with respect to the ultimate strength limit state. However, in order to define the complete performance of a structural member, the damage functions should also be calibrated for the intermediate limit states. The monotonic axial load-deflection response of a typical RCFT column member can be investigated in two parts, including a pre-peak region and a post-peak region, with reference to the peak axial load value achieved by the RCFT

column specimen. The two most significant events throughout the deformation history of the member constitute reaching its peak axial load level and then failing at the ultimate deformation level. For the column tests, the ultimate deformation level was defined as the point in the post-peak response where the stiffness of the specimen ceases to be non-zero. Therefore, it is appropriate to normalize the pre-peak and post-peak damage levels with respect to the peak axial load level and ultimate deformation level, respectively. As the steel yielding damage level is expected to occur in the pre-peak region, a non-cumulative damage function ($D_y^{RCFT-Col-m} = d_y / d_o$) was defined as a function of the deformation at the point of steel yielding (d_y), determined as reported in Section 2.2.1.1, and the deformation at the peak axial load level (d_o). For the specimens in the monotonic column database with available data, Figure 3.2 and Figure 3.3 illustrate the correlation of d_y/d_o with respect to the parameter P_s/P_o for the specimens with the L/D ratios of 2 to 4 and 15 to 23, where:

$$P_s - \text{nominal axial load capacity of steel tube, } P_s = A_s \times f_y$$

$$P_o - \text{nominal axial load capacity of composite section, } P_o = A_s \times f_s + A_c \times f'_c$$

The trend obtained in Figure 3.2 and Figure 3.3 indicates that d_y/d_o increases as P_s/P_o increases. This is due to the fact that as the steel tube becomes more dominant compared to the concrete, the effect of steel yielding is more significant and therefore the damage level is larger. If the L/D value increases, an increase in d_y/d_o is also evident. This is because for the slender members, steel yielding generally takes place at the peak axial load level.

Linear curve fits were made to the data obtained in Figures 3.2 and Figure 3.3, separately to define d_y/d_o as a function of P_s/P_o . These two linear equations given in Equation 3.16 and Equation 3.17 represent the formulations of $D_y^{RCFT-Col-m}$ applicable to L/D ratios ranging from 2 to 4 and 15 to 23, respectively. The equations were derived from the data in the monotonic column database for steel tube yielding. All the available data were investigated and outlier points were eliminated if the data points have a residual (i.e., predicted value minus measured values) to predicted ratio of greater than 1.0.

$$D_y^{RCFT_Col_m} = \frac{d_y}{d_o} = 0.61 \frac{P_s}{P_o} + 0.044 \quad \text{for } 2 \leq L/D \leq 4 \quad (3.16)$$

$$D_y^{RCFT_Col_m} = \frac{d_y}{d_o} = 1.76 \frac{P_s}{P_o} - 0.26 \quad \text{for } 15 \leq L/D \leq 23 \quad (3.17)$$

A lower bound value of 0.10 and an upper bound value of 1.0 were obtained for $D_y^{RCFT_Col_m}$ based upon observation of the data in Figures 3.2 and 3.3.

Figure 3.4 illustrates the comparison of the experimental d_y/d_o values with the ones calculated from Equation 3.16 and Equation 3.17. Despite the scatter in the data, Equation 3.16 and Equation 3.17 seem to be a fairly accurate representation of the d_y/d_o values.

The damage measure d_y/d_o is useful to evaluate the effect of steel yielding in the pre-peak region. However, it is common to calibrate damage functions to a value of 1.0 at failure. Therefore, the intermediate damage levels should be evaluated with a similar scale. This can be achieved by defining a new energy-based damage function

($E_y^{RCFT_Col_m} = E_y / E_{total}$) as the ratio of energy absorption until steel yielding (E_y) divided by the total energy under the axial load-deformation curve of the specimens (E_{total}). The E_y and E_{total} values were calculated for the specimens with available data in the monotonic column database. This damage index is equal to 1.0 at failure and it is equal to zero when the structural member has no load acting on it. While calculating the E_{total} values of the specimens, it was required to define the ultimate deformation levels of the specimens. These points were clear for the specimens with a sudden failure pattern. However, if the specimens failed gradually, the failure was assumed to take place when the stiffness of the members approaches zero after having significant post-peak response with a descending branch of the axial load-deformation curve. The histogram of E_y / E_{total} in Figure 3.5 indicates that the majority of the specimens underwent steel yielding when the damage index is less than 0.1. Equation 3.18 was derived by correlating E_y/E_{total} to the parameters L/D and P_s/P_o . While deriving Equation 3.18, outlier data points were eliminated if the residual to predicted ratio was greater than 1.0.

$$E_y^{RCFT-Col-m} = \frac{E_y}{E_{total}} = 0.20 \frac{P_s}{P_o} + 0.021 \frac{L}{D} - 0.17 \quad (3.18)$$

In Equation 3.18, it is seen that the energy-based damage index attains larger values once the contribution of the steel tube to the response of the RCFT column increases. This type of trend can be seen for large values of P_s/P_o . In addition, slender specimens having large L/D ratios were also found to have larger damage index values at steel tube yielding. This was evident from the experimental results on slender RCFT columns where steel yielding was commonly delayed until flexural buckling took place, causing E_y/E_{total} to increase. Figure 3.6 illustrates the comparison of the experimental and computational values of E_y/E_{total} , for which good correlation was attained for the majority of the specimens.

Due to the ductile nature of steel, any yielding occurring in the steel tube typically does not cause a sudden reduction in strength. In general, the effect of steel yielding is reflected in the member behavior as a reduction in axial stiffness. For the RCFT columns with low f'_c/f_y ratio or low D/t ratio, steel yielding is followed by a nonlinear region of the axial load-deformation curve with a shallow or zero slope. Therefore, a major portion of the axial stiffness is reduced (Cederwall et al., 1990; Grauers, 1993; Schneider, 1998). This type of member behavior is referred to as Type I and is illustrated in Figure 3.7 (Grauers, 1993). In the case of RCFT columns where the contribution of concrete to the member behavior is dominant, the axial load-deformation curves usually have a distinct peak axial load level followed by a sudden reduction in strength. This type of axial load-deformation curve is designated as Type II (Cederwall et al., 1990; Grauers, 1993) in Figure 3.7. The columns having the characteristics of Type II axial load-deformation curves also experience a reduction in axial stiffness, prior to achieving the peak axial load level, as steel yielding progresses. The amount of the reduction in stiffness depends on the values of the f'_c/f_y and D/t ratios. Figure 3.8 illustrates the reduction in the initial axial stiffness after steel yielding, which is calculated for the specimens in the database with a Type II axial load-deformation curve. To construct Figure 3.8, the slope of the line between the origin and point of steel yielding was calculated. Then, the slope from steel yielding point either to the next damage level or to the peak axial load level was

determined. The difference between these two slopes approximates the reduction in stiffness due to steel yielding prior to achieving the peak axial load level. According to Figure 3.8, the reduction in axial stiffness can be above 80% of the initial stiffness.

The results from the experiments stored in the database shows that for the columns having either Type I and Type II axial load-deformation curves, steel yielding causes a potentially significant reduction in stiffness. The reduced stiffness at the member level might affect the overall performance of the structure.

Concrete Crushing

One of the main factors making composite columns superior to other type of materials is the introduction of concrete and utilizing its compressive capacity effectively. In rectangular RCFT columns, the contribution of concrete to the axial load capacity typically ranges from 20% to 70% for common D/t ratios and material strengths. Therefore, crushing of concrete should have a significant impact on the load deformation behavior of the RCFT columns by decreasing both the axial stiffness and strength.

Unreinforced concrete itself often exhibits a brittle type of behavior in compression. For the specimens with low f'_c/f_y and low D/t ratios where the behavior is dominated by the steel tube, the effect of concrete crushing can only be noticeable after steel yielding (Furlong, 1967; Lu and Kennedy, 1992, 1994; Schneider, 1998). However, in the case of low f'_c/f_y and high D/t ratios, the brittle behavior of concrete becomes noticeable and concrete crushing causes a significant strength drop after the peak load (Cederwall et al., 1990; Grauers, 1993; Inai and Sakino, 1996; Nakahara and Sakino, 1998).

The desired response of RCFT columns is obtained if it is ensured that concrete crushing takes place after significant steel yielding. However, for specimens with large D/t ratios, local buckling often occurs prior to steel yielding, with concrete crushing usually following local buckling. In particular, once the steel tube buckles in the outward direction, a significant portion of the axial load is transferred to the concrete core and the concrete starts crushing (Inai and Sakino, 1996; Lu and Kennedy, 1992, 1994). After crushing, if concrete successfully flows to the locally buckled region of the steel tube,

improvement in the concrete strength can be observed due to confinement. This might cause an increase in the axial load capacity of the section. Liu and Goel (1987) observed this type of response in their stub column tests. This type of behavior is usually expected for low strength concrete, as the expansion after crushing is larger as compared to the high strength concrete.

For slender members, concrete crushing is rarely observed. For such members, the flexural buckling instability of the member is critical and the load-deflection behavior mainly depends on elastic rigidity of the composite section. In the slender column tests by Bridge (1976), Shakir-Khalil and Zeghiche (1989), Shakir-Khalil and Mouli (1990), Wang (1999) and Chung et al. (2001), no concrete crushing was reported at the ultimate limit state.

The damage sustained by the RCFT columns prior to concrete crushing is proposed to be calculated by two types of damage functions. Similar to steel yielding, the first damage function ($D_c^{RCFT-Col-m} = d_c / d_o$) is deformation-based and it is defined with respect to the peak point of the load-deflection curve. It is calculated by normalizing the deformation level at the point of concrete crushing (d_c), determined as reported in Section 2.2.1.1, with respect to the deformation level at the peak axial load level (d_o). The experimental results indicate that the deformation level of concrete crushing is affected by both material and geometric properties of the specimens. The material strengths (f'_c, f_y) and cross-sectional dimensions (D/t) can be represented in terms of a dimensionless variable as P_c/P_o . The slenderness ratio of the RCFT columns is taken into account by the L/D ratio. The parameters P_c/P_o and L/D ratios cover all the significant geometric and material properties of the RCFT columns and they can be taken as the two dimensionless parameters influencing the occurrence of concrete crushing. Figure 3.9 exhibits the variation of d_c/d_o with respect to P_c/P_o . For the specimens with L/D ratios less than 5, d_c/d_o values increase when P_c/P_o gets larger. If the L/D ratio is larger than 15, d_c/d_o values become equal to unity and they are not affected by the value of P_c/P_o . This is because slender columns are susceptible to overall flexural buckling at relatively low axial strain levels. Even if the strain levels attained by the slender members are high enough to initiate concrete crushing, it is likely that the columns will

buckle immediately after crushing, as their stiffness is reduced significantly when concrete crushing proceeds. Alternately, as soon as flexural buckling initiates, so too would concrete crushing due to the large deformations of the member. This means that for slender members, d_c/d_o is expected to be equal approximately to 1.0.

To better understand how slender a RCFT beam-column needs to be before it has essentially no concrete crushing prior to failure, Figure 3.10 illustrates the histogram of the ratio of $(P_c/P_o) / (L/D)$ for the specimens in the monotonic column database with $L/D \geq 15$. Among the specimens that did not experience any concrete crushing, the upper bound of $(P_c/P_o) / (L/D)$ ratio is 0.021 and this upper bound value, rounded down to 0.020, is reasonable to use as the limiting parameter for determining when concrete crushing may occur in relatively slender RCFT columns.

In the case of short RCFT columns, a multivariate linear curve fitting was performed with P_c/P_o as the independent variables to detect concrete crushing using the data presented in Figure 3.9. The resulting equation is given below as Equation 3.19. Equation 3.19 was derived using the specimens in the monotonic column database having L/D ratios less than or equal to 5.0. The specimens with no data on concrete crushing were excluded.

$$D_c^{RCFT_Col_m} = \frac{d_c}{d_o} = 1.03 \frac{P_c}{P_o} + 0.20 \quad (3.19)$$

The lower bound value of 0.24 and an upper bound value of 1.23 on d_c/d_o were obtained based upon observation of the data in Figure 3.9. In Figure 3.11, d_c/d_o values from Equation 3.19 are compared with the experimental values. Equation 3.19 is fairly successful in estimating the d_c/d_o values, with an R^2 equal to 0.51.

In summary, $D_c^{RCFT_Col_m}$ can be calculated for monotonic RCFT columns as given in Equation 3.20.

$$\left. \begin{aligned}
D_c^{RCFT-Col-m} = \frac{d_c}{d_o} = 1.03 \frac{P_c}{P_o} + 0.20 & \left. \vphantom{\frac{d_c}{d_o}} \right\} L/D \leq 5 \\
D_c^{RCFT-Col-m} = \frac{d_c}{d_o} = 1; \frac{P_c/P_o}{L/D} \geq 0.020 & \\
\text{No crushing prior to peak; } \frac{P_c/P_o}{L/D} \leq 0.020 & \left. \vphantom{\frac{P_c/P_o}{L/D}} \right\} L/D \geq 15
\end{aligned} \right\} \quad (3.20)$$

The second damage function ($E_c^{RCFT-Col-m} = E_c / E_{total}$) for concrete crushing is energy-based and it is defined as the energy absorption until concrete crushing (E_c), determined by calculating the area underneath the load-deflection curves of the specimens in the monotonic column database with available data, normalized by the total energy absorption until failure (E_{total}), determined in the same way as discussed in the previous sub-section for steel yielding.

Figure 3.12 illustrates the variation of E_c/E_{total} with respect to P_c/P_o for the specimens in the monotonic column database with available data. For all ranges of L/D ratios, there is a clear trend that E_c/E_{total} increases when P_c/P_o gets larger. A multi-variate linear regression was made to the data given in Figure 3.12 in terms of the variables P_c/P_o and L/D . This gave Equation 3.21 to calculate $E_c^{RCFT-Col-m}$. Equation 3.21 was derived using the data presented in Figure 3.12. However, the outlier data was excluded if the ratio of residual over predicted value is greater than 1.0. In order to avoid any negative value to be obtained from Equation 3.21, P_c/P_o should be taken as greater or equal to 0.34.

$$E_c^{RCFT-Col-m} = \frac{E_c}{E_{total}} = 0.28 \frac{P_c}{P_o} + 0.022 \frac{L}{D} - 0.14 \quad (3.21)$$

The comparison of the experimental values of E_c/E_{total} with the calculated values from Equation 3.21 is shown in Figure 3.13. Equation 3.21 estimated the E_c/E_{total} values in a fairly accurate manner, with an R^2 of 0.73.

Local Buckling of Steel Tube

The introduction of high strength concrete allows more slender steel tubes to be used in RCFT columns. However, thin-walled members are prone to local buckling, and local buckling can have detrimental effects both on the strength and ductility of RCFTs columns.

As discussed earlier, in RCFT columns, local buckling takes place in the outward direction. This is a higher mode of buckling and causes an increase in buckling strength compared to hollow structural steel sections. In addition, concrete increases the half wavelength of local buckling, which makes the steel tube less prone to steel fracture (Wright, 1993). Local buckling mainly depends on the D/t ratio of the specimens. For low D/t ratios, it usually takes place at the post-peak region of the load-deflection curve of the columns. This type of response is ductile and it is ensured in the current design codes by limiting the D/t value. However, for RCFT columns with large D/t values, local buckling might take place elastically. This causes the majority of the load to be transferred to the concrete core, and the concrete core typically crushes soon after elastic local buckling. Therefore, specimens that experience elastic local buckling cannot reach their nominal capacities, and they fail suddenly, as their response near the ultimate load is governed by the concrete.

For RCFT columns with large L/D ratios, the overall stability of the members is more critical than their local stability. The columns undergo overall buckling before adequate axial strains are formed to initiate local buckling. Therefore, local buckling generally either takes place approximately at the ultimate load or in the post-peak range. In the slender RCFT column tests by Bridge (1976), Shakir-Khalil and Zeghiche (1989), Shakir-Khalil and Mouli (1990), and Wang (1999), no local buckling was reported. However, the slender columns tested by Chung et al. (2001) underwent local buckling mostly at the post-peak range.

The damage level attained by the RCFT columns until the point of local buckling may be represented using the damage function ($D_{lb}^{RCFT-Col-m} = d_{lb} / d_o$), which is obtained by normalizing the deformation at the point of local buckling (d_{lb}), determined as reported in Section 2.2.1.1, to the deformation at the peak axial load level (d_o).

The dimensionless parameters affecting local buckling strain level were selected as D/t and f_y/E_s of the steel tube. The strength of concrete is assumed here to have negligible effect on the local buckling strain.

Figure 3.14 shows the comparison of d_{lb}/d_o with respect to the combined parameter $\frac{D}{t} \sqrt{\frac{f_y}{E_s}}$ for the column specimens in the monotonic column database with available data. $\frac{D}{t} \sqrt{\frac{f_y}{E_s}}$ is proportional to the limiting parameter in AISC (1999) to prevent local buckling. A clear trend in Figure 3.14 can be seen that as the D/t ratio and f_y of the steel tube increases, d_{lb}/d_o decreases. A nonlinear curve fit was made to the data in Figure 3.14 for estimating local buckling strain level of the column specimens as follows given in Equation 3.22.

$$D_{lb}^{RCFT-Col-m} = \frac{d_{lb}}{d_o} = 2.68 \times \left(\frac{D}{t} \sqrt{\frac{f_y}{E_s}} \right)^{-1.02} \quad (3.22)$$

Equation 3.22 was calibrated for the specimens with $L/D < 15$ and it has an R^2 value of 0.55. The computational values of d_{lb}/d_o are compared with the experimental results in Figure 3.15. For the slender specimens with $L/D \geq 15$, local buckling in the pre-peak range is not likely to take place. This limit seemed to be reasonable according to the experimental results by Bridge (1976), Shakir-Khalil and Zeghiche (1989), Shakir-Khalil and Mouli (1990), Wang (1999), and Chung (2001).

Energy absorption until the time of local buckling may also be used as a damage parameter for the RCFT columns. The value of the damage function ($E_{lb}^{RCFT-Col-m} = E_{lb}/E_{total}$) adopted here uses the ratio of the energy absorption at the point of local buckling (E_{lb}), determined by calculating the area underneath the load-deflection curves of the specimens in the monotonic column database with available data, normalized by the total energy absorption until failure (E_{total}), determined as discussed in the previous subsections for steel yielding and concrete crushing.

Figure 3.16 shows the variation of E_{lb} / E_{total} for the specimens in the monotonic column database with respect to the parameter $\frac{D}{t} \sqrt{\frac{f_y}{E_s}}$. According to the trend in Figure 3.16, a decrease in E_{lb} / E_{total} can be seen when there is an increase in $\frac{D}{t} \sqrt{\frac{f_y}{E_s}}$. A nonlinear curve fit was made to the data in Figure 3.16 to estimate $E_{lb}^{RCFT_Col_m}$ as a function of $\frac{D}{t} \sqrt{\frac{f_y}{E_s}}$. The resulting Equation 3.23 is given below; it has an R^2 value of 0.41.

$$E_{lb}^{RCFT_Col_m} = \frac{E_{lb}}{E_{total}} = 0.50 \left(\frac{D}{t} \sqrt{\frac{f_y}{E_s}} \right)^{-1.04} \quad (3.23)$$

The computational values of E_{lb} / E_{total} are compared with the experimental results in Figure 3.17 and a fairly good correlation was obtained.

The summaries of the equations for the displacement-based and energy-based damage functions of the monotonic column tests are given in Table 3.1 and Table 3.2, respectively. These tables, and similar tables given throughout this chapter for RCFT beam-columns, connections, and frames, document all damage indices derived in this work, along with any upper and lower bounds of the independent parameters on these indices. Statistical information of the calculated versus experimental damage indices are also documented, along with the sources of the experimental data.

3.3 Monotonically Loaded RCFT Beam-Columns

RCFT beam-columns were investigated in three groups depending on the loading scheme of the specimens. The loading schemes MI, MII, MIII, and MIV were already defined in section 2.2.2.1 as follows:

- MI – Eccentrically applied axial load
- MII – Lateral load combined with nonproportional axial load
- MIII – Uniform bending moment combined with nonproportional axial load
- MIV – Uniform bending with no axial load

In this section, the specimens with loading types MIII and MIV were studied together, as loading type MIV is similar to loading type MIII with no axial load. This resulted in three groups of specimens, identified as MI, MII and MIII.

The damage levels of RCFT beam-columns examined in this section cover tension cracking of concrete, compression yielding of steel tube, tension yielding of steel tube, concrete crushing, local buckling of steel tube flange, and local buckling of steel tube web.

Tension Cracking of Concrete

For the beam-column specimens, both tensile and compressive characteristics of concrete become critical. When RCFT members are subjected to bending moment, tensile stresses develop along the section depth and the concrete starts to crack at the early stages of the loading. As the neutral axis depth continues to shift, more concrete goes into tension and further cracking takes place. The cracking of the concrete results in a reduction in the stiffness of the specimens and, if the axial load levels are low, the concrete becomes less effective in the post-peak behavior of the specimens. Specimens with loading types MI and MIII were available.

In the monotonic beam-column tests, concrete cracking was assumed to occur when tensile stresses start to develop at the tensile flange of the steel tubes. The damage index ($D_{cr}^{RCFT-Bc-m} = d_{cr} / d_o$) when tension cracking of the concrete occurred was defined as the ratio of the current deformation (d_{cr}) to the deformation at the peak load (d_o).

For the specimens tested by loading type MI and having reported data on concrete cracking, d_{cr} / d_o was estimated with a curve fit to the available data in terms of the following parameters: eccentricity over depth (e/D) and nominal strength of concrete core over nominal strength of composite section (P_c/P_o). This process resulted Equation 3.24 with an R^2 value of 0.90.

$$D_{cr}^{RCFT-Bc-m} = \frac{d_{cr}}{d_o} = -1.02 \frac{e}{D} - 3.74 \frac{P_c}{P_o} + 1.76 \quad (3.24)$$

According to Equation 3.24 when the e/D ratio increases, a reduction in the d_{cr}/d_o ratio takes place. This is because bending moment is proportional to the amount of eccentricity, and a larger bending moment causes concrete cracking to occur earlier. If the value of P_c/P_o ratio gets larger, the contribution of the concrete to the behavior increases. As the concrete core has a lower modulus than the steel tube, the overall stiffness of the section decreases and concrete cracking occurs earlier. The comparison of computational and experimental values of d_{cr}/d_o can be seen in Figure 3.18. This figure shows that for one specimen, Equation 3.24 gives a negative value. From the ranges of material and geometric properties used to derive Equation 3.24, it was concluded that Equation 3.24 is limited to beam-columns with P_c/P_o values less than 0.33 to avoid negative values of d_{cr}/d_o .

The energy-based damage function at concrete cracking ($E_{cr}^{RCFT-Bc-m} = E_{cr}/E_{total}$) was also evaluated for the MI type specimens. The damage indices were calculated as the ratio of energy absorption until concrete cracking (E_{cr}) to the total energy absorption (E_{total}). The damage index values were correlated to the structural parameters e/D and P_c/P_o and Equation 3.25 was derived with an R^2 value of 0.82.

$$E_{cr}^{RCFT-Bc-m} = \frac{E_{cr}}{E_{total}} = -1.40 \frac{P_c}{P_o} - 0.33 \frac{e}{D} + 0.64 \quad (3.25)$$

Similar to the deformation-based damage index at concrete cracking, Equation 3.25 shows that E_{cr}/E_{total} values decrease when the specimens have thin-walled tubes or when the e/D ratio gets larger. The comparison of Equation 3.25 with the experimental results can be seen in Figure 3.19.

In the case of the specimens with the loading scheme MIII, the d_{cr}/d_o ratio was correlated to the ratio of applied axial load (P) to the nominal strength of composite section (P_o) and the ratio of P_c/P_o . The d_{cr}/d_o ratio was estimated by performing a multivariate linear regression for the variables P/P_o and P_c/P_o . The resulting equation

derived for the d_{cr} / d_o ratio was Equation 3.26 with an R^2 of 0.95 and its formulation is given below:

$$D_{cr}^{RCFT-Bc-m} = \frac{d_{cr}}{d_o} = 0.42 \frac{P_c}{P_o} + 1.13 \frac{P}{P_o} - 0.38 \quad (3.26)$$

From Equation 3.26, it is clear that d_{cr} / d_o increases when P_c / P_o gets larger. It is possible to enhance the nominal strength of the concrete core either by increasing f'_c or the D/t ratio. When f'_c increases, the tensile strength of concrete also improves, and this might cause a delay in concrete cracking. However, this should be insignificant, as the tensile strength of concrete does not vary substantially. On the other hand, if the D/t ratio of the members increases, concrete becomes dominant and the peak deformation of the composite section decreases. Therefore, d_{cr} / d_o achieves larger values when P_c / P_o increases. The trend in Equation 3.26 also shows that the axial load reduces the amount of concrete section subjected to tension and delays concrete cracking. Therefore, d_{cr} / d_o increases for high values of axial load. The comparison of Equation 3.26 with the experimental results in Figure 3.20 shows that Equation 3.26 is successful in predicting d_{cr} / d_o for the specimens tested with loading scheme MIII.

For the MIII type beam-column specimens, the energy-based damage index at concrete cracking ($E_{cr}^{RCFT-Bc-m} = E_{cr} / E_{total}$) was also investigated. Equation 3.27 was developed to estimate E_{cr} / E_{total} and the R^2 was found to be 0.44.

$$E_{cr}^{RCFT-Bc-m} = \frac{E_{cr}}{E_{total}} = -0.16 \frac{P_c}{P_o} + 0.11 \frac{P}{P_o} + 0.11 \quad (3.27)$$

As can be seen from Equation 3.27, E_{cr} / E_{total} exhibits a similar trend as d_{cr} / d_o with respect to the parameter P / P_o . However, E_{cr} / E_{total} was found to decrease for large values of P_c / P_o . The computational values of E_{cr} / E_{total} from Equation 3.27 are compared with experimental results in Figure 3.21, where fairly good correlation can be seen.

Yielding of Compression Flange of Steel Tube

In the beam-column tests, compression flanges of the members are subjected to compressive strains due to the axial load and bending moment, simultaneously. Therefore, compression flanges of the steel tubes are more susceptible to yielding than the tension flanges. In the majority of the beam-column tests, steel compression flange yielding occurs in the pre-peak-region and it is the second damage level observed after tension cracking of the concrete core. Similar to the column tests, a reduction in stiffness of the specimens is probable after yielding. When the specimens are tested under bending moment and constant axial load, the contribution of concrete core to the overall behavior reduces and the steel tube becomes more dominant. Therefore, yielding of the steel tube might have a greater impact on the behavior of the specimens than it has in the case of column tests.

The available data for steel compression flange yielding from the beam-column database were investigated for the specimens with loading schemes MI, MII, and MIII, separately. Either deformation-based ($D_{cy}^{RCFT-Bc-m}$) or energy-based damage functions ($E_{cy}^{RCFT-Bc-m}$) were employed to quantify the occurrence of steel compression flange yielding.

For the specimens tested by loading scheme MI, the amount of eccentricity is one of the key parameters affecting the beam-column behavior. Therefore, the eccentricity over depth ratio (e/D) is included in the list of the parameters used to estimate the damage function for steel compression flange yielding. The damage at compression steel yielding was quantified using both deformation-based and energy-based damage functions. The deformation-based damage function ($D_{cy}^{RCFT-Bc-m} = d_{cy} / d_o$) was defined as the ratio of deformation at compression yielding (d_{cy}) to the deformation at the peak load (d_o). The most common deformation measure used for the MI type beam-columns was mid-height deflection. Equations 3.28 and 3.29 were derived to estimate the values of d_{cy}/d_o by investigating the available specimens in the database in two groups depending on the value of the parameter e/D . The R^2 for Equation 3.28 and 3.29 were found to be 0.41 and 0.84, respectively.

$$D_{cy}^{RCFT-Bc-m} = \frac{d_{cy}}{d_o} = 0.035 \frac{L}{D} + 0.021 \frac{D}{t} - 0.31 \quad (e/D < 0.20) \quad (3.28)$$

$$D_{cy}^{RCFT-Bc-m} = \frac{d_{cy}}{d_o} = 0.026 \frac{L}{D} + 0.045 \frac{D}{t} - 1.03 \quad (e/D \geq 0.20) \quad (3.29)$$

Equations 3.28 and 3.29 illustrate that an increase in D/t causes d_{cy}/d_o to take larger values. This might be attributed to the fact that as the specimens become thin-walled the majority of the load is transferred to the concrete core and steel yielding is delayed. The specimens tested by loading schemes MI are all slender members with L/D ratios greater than 10. These types of members usually fail by overall buckling at the onset of steel yielding in compression. Therefore, as the L/D ratios get larger, d_{cy}/d_o increases. The computational d_{cy}/d_o values from Equation 3.28 and 3.29 are compared with the experimental results in Figure 3.22 and good correlation was achieved for the majority of the specimens.

An energy-based damage function of the MI type beam-columns at compression steel yielding ($E_{cy}^{RCFT-Bc-m} = E_{cy} / E_{total}$) was defined as the ratio of energy absorption at the point of steel yielding to the total energy absorption at failure. Equation 3.30 was formulated with an R^2 of 0.81 to calculate E_{cy} / E_{total} .

$$E_{cy}^{RCFT-Bc-m} = 0.49 \frac{e}{D} + 0.0092 \frac{D}{t} + 0.016 \frac{L}{D} - 0.49 \quad (3.30)$$

For the majority of the specimens, it was found that the specimens having a larger eccentricity have steel yielding earlier in the load history. However, increasing the eccentricity also caused the energy absorption of the specimens to decrease. Therefore, for larger values of e/D , E_{cy} / E_{total} exhibited an increasing trend. Similar to the deformation-based damage index given in Equations 3.28 and 3.29, E_{cy} / E_{total} was found to increase when D/t or L/D gets larger since steel yielding is delayed. The comparison of Equation 3.30 with the experimental results is shown in Figure 3.23 and good agreement was achieved.

Two independent dimensionless parameters, P/P_o and P_s/P_o were selected as having a significant effect on steel compression flange yielding for the beam-columns tested with the loading scheme MII. Steel compression flange yielding points for the

specimens tested by loading scheme MII were only provided by Sakino and Ishibashi (1985). For the available data in the monotonic beam-column database, a multivariate linear regression was made using the variables P/P_o , P_s/P_o presented above. Equation 3.31 was obtained to estimate the deformation-based damage function of the beam-columns tested by loading scheme MII, with an R^2 of 0.86. Equation 3.31 does not include the parameter L/D ratio, as it was kept constant for the specimens tested by Sakino and Ishibashi (1985).

$$D_{cy}^{RCFT-Bc-m} = \frac{d_{cy}}{d_o} = -1.60 \frac{P}{P_o} - 2.47 \frac{P_s}{P_o} + 2.64 \quad (3.31)$$

Equation 3.31 indicates that d_{cy}/d_o decreases when P gets larger. This is an expected trend, as larger compressive forces cause early steel yielding. If the P_s of the beam-columns increases, the specimens have more reserve strength after steel compression flange yielding to undergo larger peak displacements. This causes d_{cy}/d_o to become smaller. Equation 3.31 and the experimental results show good correlation, as shown in Figure 3.24.

The energy-based damage index at yielding of compression flange (E_{cy} / E_{total}) was correlated to the parameters P/P_o and $\frac{D}{t} \sqrt{\frac{f_y}{E_s}}$. Equation 3.32 was formulated to estimate E_{cy} / E_{total} and the R^2 of Equation 3.32 was determined as 0.68.

$$E_{cy}^{RCFT-Bc-m} / E_{total} = \frac{E_{cy}}{E_{total}} = 0.068 \frac{D}{t} \sqrt{\frac{f_y}{E_s}} - 0.073 \frac{P}{P_o} - 0.014 \quad (3.32)$$

The trend in Equation 3.32 indicates that the specimens having large $\frac{D}{t} \sqrt{\frac{f_y}{E_s}}$ values have steel tube yielding delayed. On the other hand, it is expected that if high axial load is applied to the specimens, steel yielding in compression will take place earlier, causing small values of E_{cy} / E_{total} to be attained. Comparison of Equation 3.32 with the experimental results is shown in Figure 3.25, exhibiting close agreement.

For the specimens tested by loading scheme MIII, the damage level at steel compression yielding was evaluated by using the deformation-based damage function.

The parameters P/P_o , P_s/P_o , and L/D were correlated to d_{cy}/d_o by multivariate linear regression and Equation 3.33 given below was derived with an R^2 value of 0.60.

$$D_{cy}^{RCFT-Bc-m} = \frac{d_{cy}}{d_o} = -1.16 \frac{P}{P_o} - 0.97 \frac{P_s}{P_o} - 0.19 \frac{L}{D} + 1.95 \quad (3.33)$$

Similar to the specimens tested by loading scheme MI, Equation 3.33 shows that d_{cy}/d_o decreases when there is an increase in P/P_o or P_s/P_o . The effect of L/D on the beam-columns is reflected through second-order moments. For high L/D ratios, the bending moment applied to the beam-columns increases, which causes more compressive stresses to develop. Therefore, the trend in Equation 3.33 shows that d_{cy}/d_o gets smaller for higher L/D ratios. If the predicted values of d_{cy}/d_o from Equation 3.33 are compared with the experimental results, for the majority of the specimens good correlation was achieved. However, as it can be seen in Figure 3.26, for P_s/P_o values greater than 0.74, Equation 3.33 produces a negative value of d_{cy}/d_o . Therefore, it is recommended to use Equation 3.33, for P_s/P_o values less than 0.74.

In Equation 3.34, the correlation of E_{cy}/E_{total} with respect to the parameters P/P_o , P_s/P_o , and L/D is given. The R^2 for Equation 3.34 was determined as 0.38. While deriving Equation 3.34, one of the specimens was treated as an outlier point as it had a very high value of residual to predicted ratio.

$$E_{cy}^{RCFT-Bc-m} = \frac{E_{cy}}{E_{total}} = 0.0038 \frac{L}{D} - 0.056 \frac{P_s}{P_o} - 0.046 \frac{P}{P_o} + 0.064 \quad (3.34)$$

It was found that E_{cy}/E_{total} exhibits a decreasing trend for large values of P/P_o and P_s/P_o . This trend was also observed for the deformation-based damage index given in Equation 3.33. However, E_{cy}/E_{total} was found to attain high values for slender specimens having large L/D ratios. This is due to the fact that as the L/D ratio of the specimens increases E_{total} decreases at a larger rate than E_{cy} causing E_{cy}/E_{total} to increase. In Figure 3.27, Equation 3.34 was compared with the experimental results. Despite the relatively low value of R^2 , for the majority of the specimens a good correlation can be seen.

Yielding of Tension Flange of Steel Tube

When RCFT members are subjected to bending moments, the tension flange of the steel tubes starts to yield after the tensile stresses due to flexure exceed the compressive stresses caused by the axial load and progress to the yield stress. Axial load delays the occurrence steel tension flange yielding, and it is usually preceded by steel compression flange yielding. After the steel tube yields at both flanges, the stiffness of the composite section reduces significantly. Therefore, steel tension flange yielding of the beam-columns signals that beam-column members are close to their ultimate capacity.

Steel tension flange yielding damage level was studied for specimens with loading schemes MI, MII, and MIII, separately. For each set of data, tension flange yielding was quantified using the deformation-based damage index or energy-based damage index given in Equations 3.35 and 3.36, respectively.

$$D_{yt}^{RCFT-Bc-m} = \frac{d_{yt}}{d_o} \quad (3.35)$$

$$E_{yt}^{RCFT-Bc-m} = \frac{E_{yt}}{E_{total}} \quad (3.36)$$

where:

d_{yt} – deformation level at tension flange yielding

E_{yt} – energy absorption until tension flange yielding

For the specimens tested with the loading scheme MI, both the deformation-based and the energy-based damage functions were used to quantify the amount of damage at steel tension flange yielding. The structural parameters e/D , P_s/P_o , and L/D were correlated to the damage indices and equations were derived to estimate d_{yt}/d_o and E_{yt}/E_{total} .

Equations 3.37 and 3.38 were derived to estimate d_{yt}/d_o . The specimens were investigated in two groups depending on the L/D ratio. The R^2 of Equations 3.37 and 3.38 was found to be 0.68 and 0.57, respectively.

$$D_{yt}^{RCFT-Bc-m} = \frac{d_{yt}}{d_o} = 8.63 \frac{P_s}{P_o} - 1.88 \frac{e}{D} - 0.90 \quad (L/D \leq 15) \quad (3.37)$$

$$D_{yt}^{RCFT-Bc-m} = \frac{d_{yt}}{d_o} = 3.04 \frac{P_s}{P_o} - 4.76 \frac{e}{D} + 0.99 \quad (L/D > 15) \quad (3.38)$$

It was found that increasing P_s / P_o delays tension flange yielding and causes the specimens to take larger d_{yt} / d_o values. On the other hand, the specimens having large e / D or L / D values experience tension flange yielding earlier and have smaller d_{yt} / d_o values. Equations 3.37 and 3.38 were compared with the experimental results in Figure 3.28 and good correlation was achieved for the majority of the specimens.

The energy-based damage index at tension flange yielding was presented in Equation 3.39. E_{yt} / E_{total} was correlated to the parameters e / D , P_s / P_o , and L / D . The R^2 for Equation 3.39 was found to be 0.70.

$$E_{yt}^{RCFT-Bc-m} = \frac{E_{yt}}{E_{total}} = 0.16 \frac{e}{D} + 0.47 \frac{P_s}{P_o} + 0.011 \frac{L}{D} - 0.18 \quad (3.39)$$

The tensile stresses acting on the flange of the steel increase when the amount of eccentricity gets higher. This causes early steel yielding at the tension flange of the steel tube. However, increasing the eccentricity also causes a decrease in E_{total} . Equation 3.39 shows that the rate of reduction in E_{total} is large, and if e / D values get larger, this causes an increase in E_{yt} / E_{total} . Increasing the nominal resistance of the steel tube improves the energy absorption capacity and also delays the occurrence of steel tension flange yielding. For the specimens used to derive Equation 3.39, the rate of increase in E_{yt} is greater than the rate of increase in E_{total} . Therefore, the trend in Equation 3.39 indicates that E_{yt} / E_{total} increases when nominal strength of steel tube gets larger. For slender specimens, steel yielding in the tension flange of the steel tube occurs close to the ultimate load. As can be seen from Equation 3.39, this causes E_{yt} / E_{total} to have a larger value when L / D of the specimens increases. Figure 3.29 exhibits the comparison of predicted values from Equation 3.39 with the experimental results. Good correlation exists between the computational and experimental data.

The second set of data studied for tensile flange yielding was taken from the tests conducted using the loading scheme MII. The parameters P/P_o and P_s/P_o were correlated to d_{yt}/d_o using multivariate linear regression and Equation 3.40 was obtained with an R^2 value of 0.70.

$$D_{yt}^{RCFT-Bc-m} = \frac{d_{yt}}{d_o} = 1.47 \frac{P}{P_o} - 5.28 \frac{P_s}{P_o} + 3.85 \quad (3.40)$$

Equation 3.40 illustrates that as the axial load level on the beam-columns increases the occurrence of tension flange yielding is delayed and d_{yt}/d_o gets larger. If the nominal strength of the steel tube is improved both d_{yt} and d_o of the member increase. However, for the majority of the specimens the rate of increase in d_o is greater than that of d_{yt} . Therefore, in Equation 3.40, d_{yt}/d_o decreases when P_s/P_o gets larger. All the data that Equation 3.40 was derived was taken from the specimens with L/D ratios equal to either 3.0 or 2.5. Consequently, L/D ratio was not taken as a parameter to estimate d_{yt}/d_o for the specimens tested by the loading scheme MII. The experimental and computational results for d_{yt}/d_o were compared in Figure 3.30 and a reasonable correlation was attained.

Yielding of the tension flange of the steel tube for MII type specimens was also investigated using the energy-based damage function (E_{yt}/E_{total}). The parameters P/P_o and P_s/P_o were considered to affect yielding of tension flange. Equation 3.41 was derived to estimate E_{yt}/E_{total} and R^2 was found to be 0.60.

$$E_{yt}^{RCFT-Bc-m} = \frac{E_{yt}}{E_{total}} = 0.62 \frac{P}{P_o} - 0.16 \frac{P_s}{P_o} + 0.039 \quad (3.41)$$

Similar to the deformation-based damage index given in Equation 3.40, E_{yt}/E_{total} exhibited a decreasing trend for large values of P_s/P_o while an increasing trend was evident when the axial load level acting on the specimens increases. In Figure 3.31, it can be seen that Equation 3.41 and experimental results exhibit a close agreement for the majority of the specimens.

For the specimens tested by the loading scheme MIII, d_{yt}/d_o was correlated to the variables P/P_o , P_s/P_o , and L/D by multivariate linear regression and the Equation 3.42 was obtained with an R^2 of 0.60.

$$D_{yt}^{RCFT-Bc-m} = \frac{d_{yt}}{d_o} = 1.52 \frac{P}{P_o} - 0.21 \frac{P_s}{P_o} - 0.034 \frac{L}{D} + 0.59 \quad (3.42)$$

When the beam-columns are subjected larger compressive forces, yielding of the tension flange is delayed. Therefore, in Equation 3.42, d_{yt}/d_o increases when P/P_o gets larger. Equation 3.42 was derived from the test data of RCFT beam-columns where the majority of the specimens have either low D/t ratio or low f'_c . As the behavior of these specimens is controlled by the steel tube, an increase in P_s/P_o makes the section more ductile and increases the peak displacement. On the other hand, an increase in P_s/P_o also delays the steel tension flange yielding. However, for the majority of the specimens the rate of increase in peak displacement is larger than that of the displacement at tension flange yielding. Therefore, Equation 3.42 shows that d_{yt}/d_o reduces when P_s/P_o gets larger. Slender specimens with high L/D ratios are susceptible to second order moments, which increases the tensile stresses acting on the steel tube sections. This causes early yielding in tension flange and Equation 3.42 shows that d_{yt}/d_o is lower for high L/D ratios. As can be seen from Figure 3.32, the experimental results were predicted using Equation 3.42 in a fairly accurate manner.

The formulation derived to estimate the damage index at tension yielding of the steel tube is given in Equation 3.43. E_{yt}/E_{total} was correlated to parameters P_s/P_o , P/P_o , and L/D and the R^2 was determined as 0.57.

$$E_{yt}^{RCFT-Bc-m} = \frac{E_{yt}}{E_{total}} = 0.024 \frac{P_s}{P_o} + 1.07 \frac{P}{P_o} + 0.045 \frac{L}{D} - 0.26 \quad (3.43)$$

Equation 3.43 shows that E_{yt}/E_{total} exhibits a similar trend to d_{yt}/d_o with respect to the parameter P/P_o . However, different from d_{yt}/d_o , E_{yt}/E_{total} increases for large values of P_s/P_o and L/D . For the specimens having thick-walled or high strength steel tubes, with large values of P_s/P_o , steel tube yielding is delayed causing E_{yt}/E_{total} to increase.

On the other hand, for slender specimens having large L/D ratios, both E_{yt} and E_{total} decrease where the rate of reduction in E_{total} is greater than E_{yt} . Therefore, in Equation 3.43, E_{yt} / E_{total} increases for large values of L/D . In Figure 3.33, Equation 3.43 was compared with the experimental results and good correlation was attained for the majority of the specimens.

Concrete Crushing

In the RCFT beam-column tests, the contribution of concrete to the capacity of the composite section is typically not as significant as in the case of the RCFT column tests. Bridge (1976) found that concrete core provides only 7.5 % of the capacity of the composite section under pure bending. Therefore, the plastic moment of the steel tube is close to the moment capacity of the composite section under pure bending (Lu and Kennedy, 1992, 1994). However, the use of thin-walled tubes with high strength concrete for RCFTs makes the cross section have an ultimate moment capacity larger than the plastic moment capacity of the steel tube (O'Shea and Bridge, 1997). In addition, when axial load is introduced combined with bending moment, the neutral axis depth of the cross section increases and more concrete is involved in resisting the applied loading. This causes concrete crushing to affect the beam-column behavior more severely.

The available tests where concrete crushing was reported are all tested by the loading scheme MIII. The damage level at the time of concrete crushing was represented using both the deformation-based damage index ($D_c^{RCFT-Bc-m} = d_c / d_o$) and the energy-based damage index ($E_c^{RCFT-Bc-m} = E_c / E_{total}$).

The deformation damage index of the specimens did not show significant variation for the majority of the specimens. The average value of d_c / d_o was determined as 0.88 with a standard deviation of 0.18. The histogram of d_c / d_o for the MIII type beam-columns can be seen in Figure 3.34 where it was found that for the majority of the

specimens concrete crushing was found to take place at the same time when the peak load was attained (d_c / d_o).

To investigate the energy-based damage index at concrete crushing, a multivariate regression analysis was performed for the parameters P/P_o , P_c/P_o , and L/D . Equation 3.44 was derived to estimate E_c / E_{total} , with an R^2 value of 0.76.

$$E_c^{RCFT-Bc-m} = -0.25 \frac{P}{P_o} - 1.11 \frac{P_c}{P_o} - 0.034 \frac{L}{D} + 1.22 \quad (3.44)$$

Axial force acting on the composite section causes the neutral axis depth to shift downward. Once the neutral axis depth shifts downward, the compressive strains of the concrete fibers get larger and therefore concrete crushing takes place earlier. Therefore, as can be seen in Equation 3.44, E_c / E_{total} decreases when P/P_o gets larger. Equation 3.44 illustrates that if the nominal strength of the concrete core improves, E_c / E_{total} decreases. This is because high strength concrete causes the energy absorption in the post-peak region to be significantly larger than the pre-peak response. The effect of the second-order moments can also be seen in Equation 3.44. For members with high L/D ratios, the moment acting on the RCFT beam-column increases due to geometric nonlinearity, which results early crushing of concrete. Thus, in Equation 3.44, E_c / E_{total} gets smaller for large L/D ratios. The computational results from Equation 3.44 were compared with the experimental data in Figure 3.35 and good agreement was obtained.

Local Buckling of Steel Tube Flange

Local buckling of the steel tube is primarily observed at the compression flange of the RCFT beam-columns. It always takes place in the outward direction due to the restraint provided by the concrete core. The steel tube forms a bulb at a length approximately equal to the depth the steel tube (Liu and Goel, 1987). This mode of buckling is advantageous for two reasons. First, the dimension of the steel section does not reduce and second, as the local buckling does not took place as a narrow kink, the steel tube becomes less susceptible to fracture. The majority of the load carried by the

steel tube is transferred to the concrete after local buckling. Following concrete crushing, the locally buckled region is filled with concrete and this might result in an improvement in the post-peak behavior of the specimens (Fujimoto et al., 1995).

The damage level when local buckling of the compression flange occurs was represented by the deformation-based damage index ($D_{lbf}^{RCFT-Bc-m}$) and the energy-based damage index ($E_{lbf}^{RCFT-Bc-m}$) given in Equations 3.45 and 3.46 below:

$$D_{lbf}^{RCFT-Bc-m} = \frac{d_{lbf}}{d_o} \quad (3.45)$$

$$E_{lbf}^{RCFT-Bc-m} = \frac{E_{lbf}}{E_{total}} \quad (3.46)$$

where:

d_{lbf} – deformation at local buckling of compression flange

E_{lbf} – energy absorption until buckling of compression flange

Among the tests existing in the monotonic beam-column database with the loading scheme MI, local buckling points were reported only by Chung et al. (2001). Using the available data, Equation 3.47 was developed to predict d_{lbf}/d_o . All the specimens had a constant P_s/P_o ratio of 0.3. Therefore, d_{lbf}/d_o was correlated to e/D and L/D . The resulting equation given below had an R^2 value of 0.53.

$$D_{lbf}^{RCFT-Bc-m} = \frac{d_{lbf}}{d_o} = -0.42 \frac{e}{D} - 0.047 \frac{L}{D} + 2.51 \quad (3.47)$$

As can be seen in Equation 3.47, when the eccentricity of the beam-columns increases, the compressive stresses at the flange also increase and local buckling takes place earlier. In addition, slender members are subjected to larger moments due to geometric nonlinearity. This also increases the compressive stresses at the steel tube flange and causes early local buckling. Therefore, in Equation 3.47, d_{lbf}/d_o decreases for large values of e/D and L/D . Equation 3.47 shows good correlation with experimental results as can be seen in Figure 3.36.

Energy-based damage function ($E_{lbf}^{RCFT-Bc-m}$) was also evaluated for MI type beam-columns at local buckling of compression flange. Equations 3.48 and 3.49 were

derived to estimate E_{lbf} / E_{total} values. The R^2 of Equations 3.48 and 3.49 was found to be 0.99 and 0.76, respectively.

$$E_{lbf}^{RCFT-Bc-m} = \frac{E_{lbf}}{E_{total}} = 0.031 \frac{L}{D} - 0.027 \quad (e/D = 0.16) \quad (3.48)$$

$$E_{lbf}^{RCFT-Bc-m} = \frac{E_{lbf}}{E_{total}} = 0.039 \frac{L}{D} + 0.041 \quad (e/D = 0.50) \quad (3.49)$$

In both Equation 3.48 and 3.49, it was found that as the L/D ratio of the specimens increases, E_{lbf} / E_{total} also increases for the same specimens. The deformation-based damage index given Equation 3.47 previously showed that slender specimens experience steel yielding earlier. Therefore, the trend in Equation 3.48 and 3.49 might be attributed to the fact that as the L/D ratio of the specimen increases, a reduction in E_{total} takes place. In addition, Equation 3.48 and 3.49 show that specimens with large e/D ratios usually have a larger E_{lbf} / E_{total} values. This fact might also be attributed to reduction in E_{total} for large values of e/D . Figure 3.37 shows the comparison of Equation 3.48 and 3.49 with the experimental results and good correlation between the computational and experimental results can be noticed.

For the specimens tested by the loading scheme MII, the damage indices at local buckling of the compression flange were correlated to the parameters P/P_o , P_s/P_o and L/D . To estimate the deformation-based damage index (d_{lbf} / d_o), Equation 3.50 was derived with an R^2 of 0.42. While deriving Equation 3.50, outlier points were eliminated if the residual over predicted ratio is larger than 1.0.

$$D_{lbf}^{RCFT-Bc-m} = \frac{d_{lbf}}{d_o} = -3.68 \frac{P_s}{P_o} - 3.11 \frac{P}{P_o} + 3.98 \quad (3.50)$$

The trend of the data to estimate Equation 3.50 showed that increasing P/P_o causes local buckling to take place earlier and d_{lbf} / d_o gets smaller. On the other hand, increasing P_s/P_o delays local buckling to take place. However, for large values of P_s/P_o , d_o also increases. As the rate of increase of d_o is larger than that of d_{lbf} , d_{lbf} / d_o exhibits a decreasing trend for large values of P_s/P_o . The comparison of Equation 3.50 with the experimental results can be seen in Figure 3.38.

Equation 3.51 was derived for MII type beam-column specimens to estimate the energy-based damage index at local buckling of the compression flange (E_{lbf} / E_{total}). In Equation 3.51, E_{lbf} / E_{total} was correlated to the parameters P / P_o and P_s / P_o and the R^2 was found as 0.41.

$$\frac{E_{lbf}^{RCFT-Bc-m}}{E_{total}} = \frac{E_{lbf}}{E_{total}} = -0.41 \frac{P}{P_o} - 0.32 \frac{P_s}{P_o} + 0.46 \quad (3.51)$$

Similar to the deformation-based damage index in Equation 3.50, E_{lbf} / E_{total} was found to decrease for large values of P / P_o and P_s / P_o . Equation 3.51 was compared with the experimental results in Figure 3.39.

For the specimens tested by the loading scheme MIII, the ductility-based damage-index was correlated to the variables P / P_o , P_s / P_o and L / D using multivariate linear regression and Equation 3.52 was derived, with an R^2 value of 0.69. While deriving Equation 3.52, outlier points were eliminated if the residual over predicted ratio is greater than 1.

$$D_{lbf}^{RCFT-Bc-m} = \frac{d_{lbf}}{d_o} = -15.64 \frac{P}{P_o} - 5.57 \frac{P_s}{P_o} - 3.47 \frac{L}{D} + 23.01 \quad (3.52)$$

Equation 3.52 indicates that high axial load causes earlier local buckling and d_{lbf} / d_o decreases when P / P_o gets larger. High axial loads cause larger compressive stresses to develop at the steel tube flange and this increases the possibility of local buckling to take place. The nominal strength and peak displacement of the RCFT beam-columns improve by either increasing f_y or decreasing D / t ratio of the steel tube. The resistance to local buckling also improves when D / t ratio of the steel tube gets smaller. However, for the majority of the specimens for which Equation 3.52 was derived, the rate of increase in peak displacement was larger than the rate of increase in d_{lbf} . Therefore, in Equation 3.52, there is a decrease in d_{lbf} / d_o as P_s / P_o takes larger values. For slender members, the additional moments due to second-order effects increases the compressive stresses acting on the steel tube, which causes earlier local buckling. The trend in Equation 3.52 exhibits a reduction in d_{lbf} / d_o when L / D increases. Equation 3.52 also exhibits good correlation with the experiments as can be seen in Figure 3.40. However, it

should be noted that Equation 3.52 results in negative values for high P/P_o ratios. Therefore, it is recommended that Equation 3.52 be used for P/P_o ratios less than 0.60.

For the MIII type beam-column specimens, the energy-based damage index at local buckling (E_{lbf} / E_{total}) was investigated in Equation 3.53 where E_{lbf} / E_{total} was correlated to the parameters P/P_o , $\frac{D}{t} \sqrt{\frac{f_y}{E_s}}$ and L/D . While deriving Equation 3.53, some of the specimens were treated as outliers if the residual to predicted ratio was greater than 1.0. The R^2 of Equation 3.53 was determined as 0.55.

$$E_{total}^{RCFT-Bc-m} = \frac{E_{lbf}}{E_{total}} = 0.015 \frac{L}{D} - 0.25 \frac{D}{t} \sqrt{\frac{f_y}{E_s}} - 0.75 \frac{P}{P_o} + 0.97 \quad (3.53)$$

It was found that any increase in the parameters P/P_o and $\frac{D}{t} \sqrt{\frac{f_y}{E_s}}$ causes a reduction in the value of E_{lbf} / E_{total} . A similar trend can also be observed for d_{lbf} / d_o given in Equation 3.52. Equation 3.53 also shows that specimens with large L/D values attain larger values of E_{lbf} / E_{total} when local buckling takes place. Equation 3.53 was compared with the experimental results in Figure 3.41 and for the majority of the specimens a satisfactory correlation was attained.

Local Buckling of Steel Tube Web

In the post-peak range of the RCFT beam-columns, it is common for the steel tube web to locally buckle. After the flange of the steel tube buckled and concrete core crushed, the majority of the axial load and bending moment is transferred to the steel tube web and local buckling of the web takes place. This damage level usually takes place at high strains and signifies that the member is close to its ultimate state. Similar to flange of the steel tubes, steel tube webs with high D/t ratios are expected to be more susceptible to local buckling. The data for local buckling of the steel tube web was only available for the specimens tested by MII and MIII type of loadings. No local buckling was reported for the specimens tested under MI type of loading.

The deformation-based ($D_{lbw}^{RCFT-Bc-m}$) and energy-based ($E_{lbw}^{RCFT-Bc-m}$) damage indices used to quantify the damage at local buckling of the steel tube web are given below:

$$D_{lbw}^{RCFT-Bc-m} = \frac{d_{lbw}}{d_o} \quad (3.54)$$

$$E_{lbw}^{RCFT-Bc-m} = \frac{E_{lbw}}{E_{total}} \quad (3.55)$$

where:

d_{lbw} – deformation at local buckling of steel tube web

E_{lbw} – energy absorption until local buckling of steel tube web

Analyzing the available data in the database, the deformation-based damage index at local buckling of the steel tube web was correlated to the parameters P/P_o and P_s/P_o for MII type beam-columns. The formulation developed to estimate d_{lbw}/d_o is given in Equation 3.56 and the R^2 of Equation 3.56 was determined as 0.62.

$$D_{lbw}^{RCFT-Bc-m} = \frac{d_{lbw}}{d_o} = -4.81 \frac{P}{P_o} - 10.49 \frac{P_s}{P_o} + 10.81 \quad (3.56)$$

According to Equation 3.56, it can be concluded that local buckling of the web takes place earlier for high axial load ratios. However, the trend of d_{lbw}/d_o with respect to the parameter P_s/P_o was found to be unusual since it is often expected that local buckling is delayed for large values of P_s/P_o rather than it takes place earlier. This unexpected trend might be attributed to the interaction between steel tube and concrete core as a result of the composite nature of RCFTs. Equation 3.56 was compared with the experimental results in Figure 3.42 where good correlation was achieved.

The damage level at local buckling of the steel tube web for MII type specimens was also investigated using energy-based damage function. For this purpose, the available specimens in the database were examined in two groups with respect to the level axial load acting on the specimens. Equations 3.57 and 3.58 were derived to estimate the energy based damage index (E_{lbw}/E_{total}). The R^2 values for Equation 3.57 and 3.58 were determined as 0.59 and 0.90 respectively. While formulating Equation 3.57, outlier points were excluded if the residual to predicted ratio is greater than 1.0.

$$E_{lbw}^{RCFT-Bc-m} = \frac{E_{lbw}}{E_{total}} = -0.75 \frac{P_s}{P_o} + 0.84 \quad (P/P_o < 0.40) \quad (3.57)$$

$$E_{lbw}^{RCFT-Bc-m} = \frac{E_{lbw}}{E_{total}} = 1.03 \frac{P_s}{P_o} - 0.34 \quad (P/P_o \geq 0.40) \quad (3.58)$$

For the specimens having small axial load ratios ($P/P_o < 0.40$), E_{lbw}/E_{total} exhibited a similar trend to the deformation-based damage index given Equation 3.56 and it was found that E_{lbw}/E_{total} decreases when P_s/P_o gets larger. However, as the axial load ratio increases, it was found that local buckling of the steel tube web is delayed if P_s/P_o increases. The comparison of Equations 3.57 and 3.58 with the experimental results is presented in Figure 3.43 and a good correlation can be seen.

The damage level at local buckling of the steel tube web was also studied for MIII type beam-column specimens. In Equation 3.59 and 3.60, the correlation of d_{lbw}/d_o with respect to the parameters $\frac{D}{t} \sqrt{\frac{f_y}{E_s}}$ and P/P_o was studied.

$$D_{lbw}^{RCFT-Bc-m} = \frac{d_{lbw}}{d_o} = 0.63 \frac{D}{t} \sqrt{\frac{f_y}{E_s}} + 0.33 \quad (P/P_o < 0.40) \quad (3.59)$$

$$D_{lbw}^{RCFT-Bc-m} = \frac{d_{lbw}}{d_o} = 1.88 \quad (P/P_o \geq 0.40) \quad (3.60)$$

For the specimens in the database, it was found that if the tests are performed under high axial load level, the value of d_{lbw}/d_o did not show significant variation. On the other hand, if the axial load level is low, d_{lbw}/d_o exhibited an increasing trend as $\frac{D}{t} \sqrt{\frac{f_y}{E_s}}$ gets larger. The R^2 of Equation 3.59 was determined as 0.46 while no R^2 was calculated for Equation 3.44 since d_{lbw}/d_o was assumed to remain constant. However, the mean and standard deviation of d_{lbw}/d_o for the specimens with high axial load was calculated as 1.88 and 0.20, respectively. Equation 3.59 and 3.60 were compared with the experimental results in Figure 3.44 and a good correlation was achieved.

The damage level at local buckling of the steel tube was also quantified using the energy-based damage function for MIII type beam-column specimens. Similar to the

deformation-based damage indices in Equations 3.59 and 3.60, two parameters including $\frac{D}{t} \sqrt{\frac{f_y}{E_s}}$ and P/P_o were considered to affect E_{lbw}/E_{total} and Equation 3.61 was derived to calculate E_{lbw}/E_{total} . The R^2 of Equation 3.61 was calculated as 0.38.

$$E_{lbw}^{RCFT-Bc-m} / E_{total} = \frac{E_{lbw}}{E_{total}} = 0.25 \frac{D}{t} \sqrt{\frac{f_y}{E_s}} + 1.42 \frac{P}{P_o} - 0.38 \quad (3.61)$$

E_{lbw}/E_{total} was found to have an increasing trend if $\frac{D}{t} \sqrt{\frac{f_y}{E_s}}$ or P/P_o gets larger. The comparison of Equation 3.61 with the experimental results is shown in Figure 3.45. Despite the low R^2 attained by Equation 3.61, computational and experimental results exhibited a good agreement.

The summaries of the equations for the displacement-based and energy-based damage functions of the monotonic beam-column tests are given in Table 3.3 and Table 3.4, respectively, including appropriate statistical information and bounds on the independent variables for all the equations based upon the range of values available from the experimental research.

3.4 Cyclically Loaded RCFT Beam-Columns

Cyclically loaded beam-columns in the database can be categorized into two groups depending on the type of loading. In the first group, the specimens are subjected to double curvature bending under constant axial load and cyclic lateral load. In the second group, cantilever specimens are tested in single curvature under constant axial load and cyclically applied lateral loading. However, the former group of specimens can be idealized as two cantilever beam-columns under single curvature bending. This idealization eliminates the need to investigate the type of loading as a parameter while studying the damage levels.

The damage levels observed in the cyclic beam-column tests are the same as their monotonic counterparts. The damage observed during both directions of the loading was examined.

In the cyclic beam-column tests available in the database, the authors provided limited amount of damage levels in their reports. Therefore, an alternative method was needed to extract more damage points from the experimental hysteresis curves of the specimens. The concrete cracking, steel compression flange yielding, and steel tension flange yielding damage levels were computed with the help of a moment-curvature analysis program developed for rectangular RCFT cross sections (see Appendix A). The purpose of investigating the moment-curvature response of the RCFT members was to calculate the moment levels at concrete cracking, steel compression flange yielding, and steel tension flange yielding. First, the cross-section analysis program was executed for several MIII type monotonic beam-column tests from the literature, including tests by Tomii and Sakino (1979a), Varma (2000) and Varma et al. (2002a, 2002b). For the tests by Tomii and Sakino (1979a), the constitutive material models of steel and concrete developed by Gourley and Hajjar (1994) and Hajjar and Gourley (1996) were used, while the specimens by Varma (2000) and Varma et al. (2002a, 2002b) were analyzed by employing the constitutive models provided by Varma (2000) and Varma et al. (2002b). The range of parameters for these specimens included D/t ranging from 24 to 48 and P/P_o ranging from 0 to 0.57. With respect to the material parameters, f_y ranged from 284.5 to 552 MPa and f'_c ranged from 19.8 to 110 MPa. Figures 3.46 to Figure 3.51 show the comparison of experimental and analytical moment-curvature graphs of typical specimens from the tests by the aforementioned researchers. For both sets of tests, it can be seen that the cross-section analysis program reproduced the experimental response of the majority of specimens accurately. However, it is evident in Figure 3.48 and Figure 3.51 that the degree of accuracy in the post-peak region is not satisfactory when both the D/t and P/P_o ratios of the specimens are large. On the other hand, the pre-peak response of all the specimens was estimated accurately. In the monotonic beam-column database, it was found that the three damage levels of concrete cracking, steel compression flange yielding, and steel tension flange yielding take place either before or very near the occurrence of peak load. Therefore, the cross-section analysis program can be used to estimate accurately the moment levels of concrete cracking, steel compression flange yielding, and steel tension flange yielding. Varma (2000) and Varma et al. (2002a, 2002b) also provided steel compression flange yielding and steel tension flange yielding

points of the specimens obtained from strain gage data. The same specimens were analyzed by the cross-section analysis program and the moment levels at steel compression yielding and steel tension yielding were compared in Figure 3.52 and Figure 3.53, respectively. In these figures, computational and experimental steel yielding points showed good correlation.

The well-developed damage functions in the literature (e.g., Park and Ang, 1985; Mehanny and Deierlein, 2000, 2001), as discussed in Section 3.1.1.2, involve the integration of the experimental hysteresis curves. In order to apply these types of damage functions for the RCFT beam-columns, either points in an experimental hysteresis curve are required at a refined level of detail, or an analysis program simulating the cyclic pre-peak and post-peak response of the tested specimens is needed. However, both of these options are not available at the current stage of this research. Therefore, a new and simpler damage function is proposed to calculate the damage levels of the RCFT members at the occurrence of concrete cracking, steel tube yielding, and steel tube local buckling. The proposed damage function given in Equation 3.38 is based on the damage function first developed by Kradzig et al. (1985) and later modified by Mehanny and Deierlein (2000, 2001).

$$E^{RCFT_Bc_c} = \frac{E_{cb}}{E_m} \quad (3.62)$$

where:

E_{cb} = area under the cyclic back-bone curve until the specified damage level

E_m = area under the complete cyclic back-bone curve

The graphical representations of E_{cb} and E_m are shown in Figure 3.54 and Figure 3.55, respectively. It was assumed that the damage is mainly caused by primary half cycles in the loading history and the secondary half cycles are assumed to be negligible. This is a reasonable assumption, as the proposed damage function was only used to quantify the damage levels that are relatively independent of cyclic load history (e.g., concrete cracking, steel tube yielding, and steel tube local buckling). These damage levels often occur either before or very near the occurrence of peak, where the damage due to cyclic load reversals is not significant. For small D/t ratios, steel tube local buckling might also take place at the post-peak region. In that case, the damage function given in Equation

3.63 may not be appropriate. However, for the specimens in the cyclic beam-column database, local buckling always took place either before or very near the occurrence of peak.

The cyclic back-bone curves of the specimens were scaled from the experimental hysteresis curves as shown in Figure 3.54. The monotonic moment (M) vs. chord rotation (R) curve for RCFT beam-columns consisted of three regions including elastic, elasto-plastic and softening. In the elastic region of the M - R curve, both concrete and steel were assumed to be free of permanent strains and the reduction in stiffness for concrete cracking was neglected. The initial stiffness was adopted from the hysteresis model developed by Fujinaga et al. (2000) for rectangular RCFT beam-columns. In the given model, the initial stiffness of the RCFT beam-columns was assumed to have two parts, including bending stiffness (K_b) and shear stiffness (K_s) presented in Equations 3.63 and 3.64, respectively.

$$K_b = \frac{P.k}{\tan(kL_s) - kL_s} \quad (3.63)$$

$$K_s = \frac{G_s \cdot \kappa_s \cdot A_s + G_c \cdot \kappa_c \cdot A_c}{L_s} \quad (3.64)$$

where:

P – axial load

L_s – shear span

$k^2 = P / (E_s \cdot I_s + E_c \cdot I_c)$

G_s, G_c – shear modulus of steel and concrete, respectively

κ_s, κ_c – shape coefficient of steel tube and concrete, respectively (0.436, 0.843)

The bending stiffness is a function of the axial force (taken as positive in compression for these formulas) to account approximately for the effects of geometric nonlinearity on the cyclic back-bone curve. The bending stiffness and shear stiffness were combined to obtain the total lateral stiffness (K_H) of the RCFT beam-columns in Equation 3.65 as follows:

$$K_H = 0.85 \cdot \left(\frac{1}{K_b} + \frac{1}{K_s} \right)^{-1} \quad (3.65)$$

The initial stiffness of the moment-chord rotation curve of Figure 3.55 (K_M) is defined as the amount of required moment for a unit chord rotation. Therefore, K_H was converted into K_M using Equations 3.66 and 3.67 as given below:

$$M = H \times L + P \times \Delta \quad (3.66)$$

$$K_M = K_H \times L^2 + P \times L \quad (3.67)$$

where:

M – moment

H – horizontal load

Δ - lateral deflection

Fujinaga et al. (2000) assumed that the elastic region of the M - R curve for RCFT beam-columns ends at one third of the peak moment. The same elastic limit proposed by Fujinaga et al. (2000) was also used in this study.

The elasto-plastic region of the monotonic M - R curve was taken as linear between the peak point and the end point of the elastic region. The next point on the M - R curve to be identified is the peak point. The peak moment values are also obtained using the cross-section analysis program that was utilized for assessing the local damage of monotonic RCFT beam-columns. For the chord rotation at the peak load level (R_o), Equation 3.68 proposed by Kawaguchi et al. (1998) has been utilized. Equation 3.68 was derived from regression analysis of experimental results of monotonic beam-column tests:

$$R_o = 5.61 - 7.30 \cdot \left(\frac{P}{P_o}\right) + (-0.10 + 0.16 \cdot \left(\frac{P}{P_o}\right)) \cdot \frac{D}{t} \quad (3.68)$$

The post-peak region of the moment rotation curve followed a linear part until the peak point. The failure point of the M - R curve was identified by the ultimate moment and ultimate chord rotation. The ultimate moment (M_u) was calculated from the experimental data in the monotonic beam-column database by performing a multi-linear regression analysis. Figure 3.56 indicates that M_u / M_o is mainly affected P/P_o and it takes smaller values with an increase in P/P_o . In addition, a decrease in M_u / M_o is also evident for large D/t ratios. Equation 3.69 was developed to calculate M_u with an R^2 of 0.75.

$$M_u = M_o \cdot (-0.008 \cdot \frac{D}{t} - \frac{P}{P_o} + 1.5) \quad (3.69)$$

In the monotonic RCFT beam-column tests, typically, the specimens exhibit large ductility levels if the axial load acting on the members is not significantly high. However, once the member is subjected to excessive deflection, it can still be considered as failed even though there is not significant strength degradation. To locate the failure point of the monotonic beam-column tests, an ultimate rotation (R_u) value should be calculated. Based on the tests conducted by Tomii and Sakino (1979b) and Sakino and Ishibashi (1985), a constant R_u value of 6% was selected. Note that these monotonic tests are being assumed here to provide appropriate values for the cyclic back-bone curve. This assumption was also verified by Varma (2000) and Varma et al. (2002b) in the monotonic and cyclic tests of equivalent beam-column specimens. After obtaining the experimental back-bone curves and computational M - R curve of the specimens, the damage function given in Equation 3.62 was applied to the available cyclic beam-columns specimens in the database. Analytical expressions were then investigated to relate the damage index values at specific local damage levels to RCFT properties.

In the cyclic beam-column tests stored in the database, the experimental load-deflection data of the specimens was given in two different forms, including M vs. R or horizontal load (H) vs. lateral deflection (Δ). In order to apply the damage function in Equation 3.62, the H vs. Δ graphs should be converted into M vs. R type curves. As also recommended by Fujinaga et al. (2000) and Kawaguchi (2000), the following conversions were used for H to M and Δ to R in the Equation 3.70 and Equation 3.71 as follows:

$$M = H \times L + P \times \Delta \quad (3.70)$$

$$R = \Delta / L \quad (3.71)$$

Concrete Cracking

Concrete cracking is the first damage level to be observed in the cyclic beam-column tests. As tensile strains start to develop at the outermost fibers of the concrete core, concrete cracking initiates. Cracking in the concrete section might cause an initial small degradation in the stiffness of the member.

As mentioned previously, the concrete cracking moment level was first determined using the cross-sectional analysis program developed for rectangular RCFT sections. As the thickness of the steel tube is small compared to the depth of the concrete core, cracking in the concrete was assumed to occur when the strain at the outermost steel fiber reaches the cracking strain of concrete. Once this moment was computed, the point corresponding to that moment on the actual experimental back-bone curve for a given specimen was identified from the available experimental data. The numerator value E_{cr} was then computed from that experimental back-bone curve. The formulas above were then used to compute E_m for the specimen, and the damage index at concrete cracking ($E_{cr}^{RCFT-Bc-c} = E_{cr} / E_m$) was computed. The concrete was assumed to behave linearly until its rupture strength and the concrete modulus in tension was taken as equal to that in compression. The rupture strength of concrete was calculated by the Equation 3.72 proposed by Carreria and Chu (1986a).

$$f_r = 0.5 \cdot \sqrt{f'_c} \quad (3.72)$$

Therefore, the rupture strain of concrete (ε_r) was determined by dividing f_r with the elastic modulus of concrete as given in Equation 3.73.

$$\varepsilon_r = \frac{f_r}{E_c} \quad (3.73)$$

The available data for tension cracking of concrete indicates that the ratio of E_{cr} / E_m increases when P_c/P_o ratios get larger. This might be attributed to the fact that concrete dominates the response of the specimens in the case of large P_c/P_o ratios. High axial loads cause more compressive strains on concrete and delay concrete cracking. Using the available data in the database, Equation 3.74 was developed to estimate

E_{cr} / E_m by linear multivariate regression. The R^2 for Equation 3.74 was calculated as 0.53.

$$E_{cr}^{RCFT-Bc-c} (\%) = \frac{E_{cr}}{E_m} (\%) = 3.21 \frac{P}{P_o} + 0.30 \frac{P_c}{P_o} - 0.52 \quad (3.74)$$

Figure 3.57 exhibits the comparison of computational and experimental values of E_{cr} / E_m . For low values of P/P_o , Equation 3.74 produces negative values, which does not have any physical significance. Therefore, for P/P_o values smaller than 0.1, it is not recommended to use Equation 3.74 to estimate E_{cr} / E_m .

Yielding of Compression Flange of Steel Tube

The steel tube flanges of the cyclic beam-column specimens are subjected to compression strains due to axial load and bending moment, simultaneously. Therefore, steel compression flange yielding is expected to occur after concrete cracking. Following steel compression flange yielding, a reduction in stiffness of the columns takes place.

Compression steel yielding points for the cyclic beam-column specimens were determined using two methods. For the first method, points were directly scaled from the experimental curves if they were made available. For the second method, the cross-sectional analysis program was used to determine the moment level for compression steel yielding and then the chord rotation corresponding to the calculated yield moment was scaled from the experimental curves. E_{yc} was then calculated directly using the results from either approach. Steel yielding at the compression flange of the specimens was assumed to occur when the strain at the most extreme steel fiber reaches its yield strain.

The energy-based damage index ($E_{cy}^{RCFT-Bc-c} = E_{cy} / E_m$) values gathered from the experimental data exhibit a decrease when the axial load acting on the specimens increases. This is an expected trend as the compressive strains on the steel tube get larger for high axial loads. On the other hand, an increase in E_{cy} / E_m is also evident in the gathered data if the ratio of P_s/P_o gets larger. An increase in P_s/P_o augments both the strength and stiffness of the specimens. This causes a delay in compression steel yielding and E_{cy} / E_m increases. In Figure 3.58, the variation of E_{cy} / E_m with respect to P_s/P_o for

different values of P/P_o can be seen. Using the data presented in Figure 3.58, Equation 3.75 was derived to estimate E_{cy} / E_m by performing multi-linear regression analysis.

The R^2 for Equation 3.75 was found as 0.56.

$$E_{cy}^{RCFT-Bc-c} = \frac{E_{cy}}{E_m} = -0.15 \frac{P}{P_o} + 0.11 \frac{P_s}{P_o} + 0.038 \quad (3.75)$$

Figure 3.59 shows that Equation 3.75 shows good correlation with experimental E_{cy} / E_m values.

Yielding of Tension Flange of Steel Tube

Tension yielding at the flange of the steel tubes was defined as the third damage level for the cyclic beam-columns. Steel tension flange yielding occurs after steel compression flange yielding as long as the yield stress in tension and in compression do not differ from each other significantly. It is also common that steel yielding takes place close to the peak point.

Similar to steel compression flange yielding, the occurrence steel tension flange yielding was determined either directly from the experiments or it was calculated with the cross-sectional analysis program.

The data from the experiments show that E_{yt} / E_m is mainly correlated to the parameter P_s / P_o . According to the data points, E_{yt} / E_m gets larger as P_s / P_o ratios increase. This might be attributed to the fact that for large P_s / P_o ratios, the specimens have tension flange yielding delayed. The other parameter that is expected to affect steel yielding was P/P_o and two different equations were proposed depending on the axial load acting on the specimens. Equations 3.76 and 3.77 were developed to estimate E_{yt} / E_m . The R^2 for Equations 3.76 and 3.77 was found as 0.66 and 0.56, respectively. While deriving the equations, outlier points were eliminated when the ratio of the residual to the predicted ratio was greater than 1.0.

$$E_{yt}^{RCFT-Bc-c} = \frac{E_{yt}}{E_m} = 0.56 \frac{P_s}{P_o} - 0.059 \quad (P / P_o \leq 0.20) \quad (3.76)$$

$$E_{yt}^{RCFT-Bc-c} = \frac{E_{yt}}{E_m} = 0.24 \frac{P_s}{P_o} - 0.024 \quad (P/P_o > 0.20) \quad (3.77)$$

The comparison of experimental and computational values of E_{yt}/E_m can be seen in Figure 3.60. Figure 3.60 shows that Equation 3.76 and 3.77 achieve a fairly good accuracy in predicting E_{yt}/E_m .

Concrete Crushing

Initiation of concrete crushing causes strength degradation in the RCFT beam-columns. Concrete crushing is usually affected by the cyclic loading protocol of the specimens. Therefore, concrete accumulates damage throughout the loading history.

To quantify the amount of damage at the time of concrete crushing, the cyclic load effects should be taken into account. However, this requires either test data or a calibrated analysis model, both of which are not available at the current stage of the research. Therefore, the energy-based damage index (E) proposed by Kradzig et al. (1989) given in Equation 3.78 was applied only to a representative specimen from Varma (2000) and Varma et al. (2002a, 2002b).

$$E = \frac{\sum_i E_{s_i} + \sum_i E_i}{E_u + \sum_i E_i} \quad (3.78)$$

where:

E_{s_i} - energy dissipation during primary half cycles

E_i - energy dissipation during secondary half cycles

E_u - energy dissipation in monotonic loading

The data required to calculate E was scaled from the experimental report by Varma (2000) and Varma et al. (2002a, 2002b) and E was calculated for both directions of loading. Figure 3.61 shows the evolution of damage for the specimen CBC-32-46-20 by Varma (2000) and Varma et al. (2002a, 2002b). The value of E at the time of concrete crushing was found to be 0.29 and 0.34 for the positive and negative directions of loading, respectively. At the end of test the value of E was close to 1.0, indicating failure.

Local Buckling of Steel Tube Flange

As the compressive strains at the flange of the beam-columns increase, local buckling might take place either in the pre-peak or post-peak region of the load-deflections curves. If the D/t ratio of the steel tube is large enough, local buckling causes a reduction in both strength and stiffness of the RCFT beam-columns. For the specimens in the cyclic beam-column database, local buckling either took place at the same time or before reaching the peak load.

The correlation of the energy based-damage index at local buckling given in Equation 3.79 with respect to the variables $\frac{D}{t} \times \sqrt{\frac{f_y}{E}}$ and P/P_o was investigated in Figure 3.62.

$$E_{lbf}^{RCFT-Bc-c} = E_{lbf} / E_m \quad (3.79)$$

where:

E_{lbf} — energy absorption until local buckling of the steel tube flange

The trend in the data indicates that as the $\frac{D}{t} \times \sqrt{\frac{f_y}{E}}$ values get larger, the specimens

experience local buckling earlier. This is because the steel tubes with large $\frac{D}{t} \times \sqrt{\frac{f_y}{E}}$ ratios are more susceptible to local buckling. The second parameter that is effective in local buckling of the steel tubes was taken as the axial load ratio (Kawaguchi, 2000; Kawaguchi and Morino, 2001). Although the data in Figure 3.62 is poorly correlated to P/P_o , it is still possible to see a trend that as P/P_o increases, as E_{lbf} / E_m gets smaller.

Equations 3.80 and 3.81 were developed to estimate E_{lbf} / E_m with R^2 values of 0.38 and 0.54, respectively. The comparison of computational and experimental values of E_{lbf} / E_m can be seen in Figure 3.63.

$$E_{lbf}^{RCFT-Bc-c} = \frac{E_{lbf}}{E_m} = -0.067 \frac{D}{t} \sqrt{\frac{f_y}{E_s}} + 0.32 \quad (\text{for } P/P_o \leq 0.20) \quad (3.80)$$

$$E_{lbf}^{RCFT-Bc-c} = \frac{E_{lbf}}{E_m} = -0.20 \frac{D}{t} \sqrt{\frac{f_y}{E_s}} + 0.49 \quad (\text{for } P/P_o > 0.20) \quad (3.81)$$

Local Buckling of Steel Tube Web

The last damage level investigated for the cyclic beam-columns is local web buckling. For the data collected in the cyclic beam-column database, this damage level was quantified using the energy-based damage index given in Equation 3.82.

$$E_{lbw}^{RCFT-Bc-c} = \frac{E_{lbw}}{E_{total}} \quad (3.82)$$

where:

E_{lbw} — energy absorption until local buckling of the steel tube web

E_{lbw} / E_{total} was correlated to the parameter $\frac{D}{t} \times \sqrt{\frac{f_y}{E}}$ only since the axial load

level for the majority of the specimens remained constant. Equation 3.83 was developed to calculate E_{lbw} / E_{total} and the R^2 for Equation 3.83 was determined as 0.41.

$$\frac{E_{lbw}}{E_m} = -0.24 \frac{D}{t} \sqrt{\frac{F_y}{E_s}} + 1.01 \quad (3.83)$$

As can be seen from Equation 3.83, E_{lbw} / E_{total} was found to get smaller for the specimens with thin-walled or high strength steel tubes. The comparison of Equation 3.83 with the experimental results is presented in Figure 3.64 and good agreement can be seen.

The summaries of the equations for the energy-based damage functions of the monotonic beam-column tests are given in Table 3.5, including appropriate statistical information and bounds on the independent variables for all the equations based upon the range of values available from the experimental research.

3.5 Monotonically Loaded RCFT Panel Zones

The damage levels of the concrete and steel portions of the RCFT panel zones were investigated separately. The shear load vs. shear deformation graphs of the specimens were examined to capture the damage levels. This was achieved using both pure empirical data or semi-empirical methods supplemented with analysis. Both deformation-based damage indices and energy based-damage indices were employed to quantify the damage. It was determined that the specimens would be deemed as having failed when they achieved a displacement ductility ratio of 6.0.

In order to facilitate the development of the panel zone damage indices, models relating shear load to shear deformation were required so as to relate experimental shear load-shear deformation results to other quantities needed for the damage indices. Kawaguchi (2000) provided shear load vs. shear deformation relationships for the concrete core and steel tube portions of CFT panel zones. The shear force-deformation relation for the steel panel can be seen in Figure 3.65. The steel tube was assumed to follow a linearly elastic region with a slope equal to its shear modulus (G_s), followed by a perfectly plastic region. The shear modulus (G_s) and yielding shear force (V_y) were calculated as given in Equations 3.84 and 3.85:

$$G_s = \frac{E_s}{2(1+\nu)} \quad (3.84)$$

$$V_y = \frac{A_s}{2} \cdot \frac{f_y}{\sqrt{3}} \quad (3.85)$$

where:

ν - Poisson's ratio of steel (0.3)

A_s - Area of steel tube

The shear force-deformation relation for the concrete panel proposed by Kawaguchi (2000) is shown in Figure 3.66. It was assumed that concrete exhibits a tri-linear load deformation behavior. The shear force is assumed to increase linearly until cracking occurs, with a slope equal to shear modulus of concrete (G_c), which can be taken as 40% of its elastic modulus (Ersoy, 1997). After cracking, the stiffness of the concrete panel decreases and again follows a linear path until the maximum shear force (V_{cc}) is achieved. The behavior of the concrete panel is then assumed to become perfectly plastic. The

shear force at concrete cracking (V_{cr}) is calculated as given in Equation 3.86 (Kawaguchi, 2000; Kamba et al., 1991).

$$V_{cr} = A_c \times \tau_{cr}$$

$$\tau_{cr} = 0.0981 \times \min \left[3.0 \left(5.0 + \frac{f'_c}{9.81} \right), \frac{10}{9.81} f'_c \right] \quad (3.86)$$

where:

τ_{cr} – cracking stress of concrete (MPa)

A_c – area of concrete core

As recommended by Ricles et al. (1995) and Koester (2000), V_{cc} can be calculated from ACI (2002) as given in Equation 3.87 by assuming that concrete core is adequately confined.

$$V_{cc} = 20 \times \sqrt{f'_c} \times A_c \quad (3.87)$$

The last parameter required to define the load deflection behavior of concrete is the shearing strain (γ_{cc}) when V_{cc} is achieved. The formula for γ_{cc} was adopted from Kawaguchi (2000) as given in Equation 3.88:

$$\gamma_{cc} = \frac{\varepsilon_{cc}}{\sin(\theta) \cos(\theta)} \quad (3.88)$$

where:

ε_{cc} – crushing strain of concrete (0.002)

θ - angle between the width and diagonal of the panel zone region

Concrete Cracking

Concrete cracking in the panel zone of the specimens occurred at the early stages of the tests. The concrete cracking points were extracted from the experimental data by superimposing the assumed load-deflection behavior of the steel tube and concrete core in Figures 3.65 and 3.66, respectively.

First, the concrete cracking shear force was calculated using Equation 3.86. Then, V_{cr} was divided by G_c to calculate the shearing strain corresponding to concrete cracking (γ_{cr}). The shearing strain in the steel tube at concrete cracking was also assumed to be equal to γ_{cr} , and based on the load-deflection behavior given in Figure 3.65, the shear

force in the steel tube was calculated. Finally, the sum of the shear force in the steel tube and concrete core at γ_{cr} gave the shear force of the composite section at the initiation of concrete cracking.

The damage level at concrete cracking was quantified by using the deformation-based damage index ($D_{cr}^{RCFT-Pz-m} = d_{cr} / d_o$) which is defined as the ratio of the deformation at concrete cracking (d_{cr}) to the deformation at the peak load (d_o). The parameters L_p / D and P_c / P_o were correlated to d_{cr} / d_o and Equation 3.89 was formulated to calculate d_{cr} / d_o . The R^2 of Equation 3.89 was determined as 0.74.

$$D_{cr}^{RCFT-Pz-m} = \frac{d_{cr}}{d_o} = 0.050 \frac{P_c}{P_o} + 0.062 \frac{L_p}{D} - 0.031 \quad (3.89)$$

where:

L_p – length of panel zone

Equation 3.89 shows that d_{cr} / d_o increases when P_c / P_o gets larger. This can be attributed to the fact that any increase in P_c / P_o ratio improves the resistance of concrete core to cracking. The available specimens with large L_p / D ratio had more energy absorption due to their low stiffness and they underwent more deformation before cracking occurred. This type of response causes an increase in d_{cr} . As shown in Figure 3.67, Equation 3.89 achieves good correlation with the experiments.

The energy-based damage ($E_{cr}^{RCFT-Pz-m} = E_{cr} / E_{total}$) index was calculated as the ratio of energy absorption until concrete cracking (E_{cr}) to the total energy absorption (E_{total}) (i.e., when a displacement ductility of 6.0 was achieved). The two parameters affecting the occurrence of concrete cracking were taken as L_p / D and P_c / P_o . A multi-linear regression analysis was performed and Equation 3.90 was derived to estimate E_{cr} / E_{total} . The R^2 for Equation 3.90 was found as 0.87.

$$E_{cr}^{RCFT-Pz-m} = \frac{E_{cr}}{E_{total}} = 0.0025 \frac{L_p}{D} + 0.0034 \frac{P_c}{P_o} - 0.0037 \quad (3.90)$$

Similar to the deformation-based damage index in Equation 3.89, Equation 3.90 shows that E_{cr} / E_{total} increases when P_c / P_o or E_{cr} / E_{total} gets larger. Equation 3.90 achieves good correlation with the experiments as can be seen from Figure 3.68.

Steel Yielding

Similar to concrete cracking, the steel yielding points in the experimental tests were found by superimposing the load-deflection behavior of the steel tube and concrete core given in Figures 3.65 and 3.66, respectively.

The shearing force acting on the steel tube at steel yielding was calculated from Equation 3.85. The shear force carried by the concrete core at steel yielding was then determined based on the shear deformation compatibility of the steel tube and concrete core. First, the shear deformation of the steel tube at yielding (γ_y) was determined by dividing V_y by G_s . Then, the shear force carried by the concrete core at γ_y was calculated from the shear force-deformation relationship of the concrete core given in Figure 3.66. When the shear forces carried by the steel tube and concrete core were summed, the shear force acting on the composite section at steel tube yielding was obtained. Finally, the steel yielding points were scaled from the experimental curves based on the calculated values of V_y .

In Equation 3.91, the deformation-based damage index at steel yielding ($D_y^{RCFT-Bc-m} = d_y / d_o$) was given as a function of P_s / P_o and L_p / D . d_y / d_o was predicted with an R^2 of 0.67 in Equation 3.91.

$$D_y^{RCFT-Bc-m} = \frac{d_y}{d_o} = 0.18 \frac{P_s}{P_o} + 0.37 \frac{L_p}{D} - 0.27 \quad (3.91)$$

It was found that increasing P_s / P_o or L_p / D delays steel yielding and causes d_y / d_o to attain large values. As shown in Figure 3.69, Equation 3.91 matches with experimental results satisfactorily.

The energy-based damage function at steel yielding ($E_y^{RCFT-Pz-m} = E_y / E_{total}$) was also evaluated for the panel-zone specimens available in the database. E_y / E_{total} was

correlated to the parameters P_s / P_o and L_p / D in Equation 3.92. The R^2 of Equation 3.92 was determined as 0.77.

$$E_y^{RCFT-Pz-m} / E_{total} = \frac{E_y}{E_{total}} = 0.020 \frac{P_c}{P_o} + 0.053 \frac{L_p}{D} - 0.058 \quad (3.92)$$

The trend of E_y / E_{total} was similar to d_y / d_o given in Equation 3.91. It was found that E_y / E_{total} increases for large values of P_s / P_o and L_p / D . The comparison of Equation 3.92 with the experimental results is shown in Figure 3.70 and good correlation is attained.

Concrete Crushing

While tracking concrete crushing points on the experimental-deflection curves, it was assumed that concrete crushing occurs when the level of shear force carried by the concrete core reaches V_{cc} . V_{cc} is determined using Equation 3.87. The shearing strain level at concrete crushing (γ_{cc}) is then calculated from the load-deflection relationship given in Figure 3.66. Assuming shear strain compatibility between the steel tube and concrete core, the shearing force acting on the steel tube at concrete crushing was calculated from shear load-deflection relationship for the steel tube given in Figure 3.65. The total shear force acting on the composite section was determined by adding the shear forces acting on the steel and concrete components. After that, concrete crushing points were scaled from the experimental plots.

The damage level at concrete crushing was evaluated using the deformation-based damage index ($D_c^{RCFT-Pz-m} = d_c / d_o$) and the formulation in Equation 3.93 was derived as a function of P_c / P_o and L_p / D to estimate d_c / d_o . The R^2 of Equation 3.93 was calculated as 0.41. While deriving Equation 3.93, outlier points were discarded if the residual to predicted ratio is greater than 1.0.

$$D_c^{RCFT-Pz-m} = \frac{d_c}{d_o} = 0.28 \frac{L_p}{D} - 0.48 \frac{P_c}{P_o} + 0.38 \quad (3.93)$$

The trend in Equation 3.93 shows that the panel zone specimens having a larger L_p / D ratio has concrete crushing delayed and for these specimens d_c / d_o values are larger. On the other hand, d_c / d_o values are found be smaller when P_c / P_o gets larger. Equation 3.93 is compared the experimental results in Figure 3.71 and a good correlation can be seen for the majority of the specimens.

Similar to steel yielding, the energy-based damage index ($E_c^{RCFT-Pz-m} = E_c / E_{total}$) was correlated to the variables P_c / P_o and L_p / D . The trend in the available data shows that E_c / E_{total} gets larger values if L_p / D ratio increases. On the other hand, a reduction in E_c / E_{total} was evident when P_c / P_o ratio gets larger. Equation 3.94 was developed to estimate E_c / E_{total} and the R^2 of Equation 3.94 was found to be 0.53. While deriving Equation 3.94, outlier points were discarded if the residual over predicted ratio is greater than 1.0. Equation 3.94 is compared with the experimental results in Figure 3.72 and a fairly good correlation is achieved.

$$E_c^{RCFT-Pz-m} = \frac{E_c}{E_{total}} = 0.060 \frac{L_p}{D} - 0.14 \frac{P_c}{P_o} + 0.041 \quad (3.94)$$

Local Buckling

In the monotonic panel zone database, local buckling points were reported in a limited number of specimens. Both deformation-based ($D_{lb}^{RCFT-Pz-m} = d_{lb} / d_o$) and energy-based damage indices ($E_{lb}^{RCFT-Pz-m} = E_{lb} / E_{total}$) were investigated.

The available data in the database showed that both d_{lb} / d_o and E_{lb} / E_{total} remained almost constant. The average value of d_{lb} / d_o was found as 0.25 with a standard deviation of 0.01. The average value and standard deviation of E_{lb} / E_{total} were 0.011 and 0.001, respectively. Local buckling was observed for the specimens with D/t ratios above 30. The damage indices attained lower values for local buckling as compared to the corresponding values for RCFT beam-columns. Therefore, it may be concluded that the steel tube is more susceptible to local buckling under high shear.

The summaries of the equations for the and deformation-based and energy-based damage functions of the monotonically loaded panel zone tests are given in Tables 3.6 and 3.7, including appropriate statistical information and bounds on the independent variables for all the equations based upon the range of values available from the experimental research.

3.6 Monotonically Loaded Steel Girder-to-RCFT Column Pinned Connections

In this section, the damage assessment of monotonically loaded pinned connections is reported. The specimens with loading schemes PC1b, PCIIa and PCIIb were investigated. There was insufficient experimental data in the database to study specimens loaded by loading scheme PC1a.

The pinned connection specimens were assumed to consist of three main parts including RCFT beam-columns, steel girders, and connection components. The damage levels at each of the aforementioned components were studied by relating this damage directly to the overall load-deformation response of the connection. The occurrence of the damage levels were tracked using either pure experimental data or by using analytical methods.

For the specimens with loading schemes PC1b and PCIIa, the end of the tests was decided as the point at which flexural buckling of the RCFT beam-columns occurred. However, PCIIb type specimens exhibited a hardening type of behavior and the failure point of the specimens was taken as the point at which a displacement ductility of 6 was attained.

The RCFT cross-sectional analysis program initially developed for constant axial loads (see Appendix A) was modified to analyze RCFT cross-sections having variable axial loads. For this purpose, for each damage level, the corresponding strain of the outermost steel fiber of the RCFT cross section held fixed during the analysis. The axial load was then increased incrementally until the failure load of the specimen given the reports is reached. At each increment of axial load, the cross-sectional moment was calculated and compared to the applied moment from the girders. As the axial load on the column and steel girder are proportional, the moment acting through the girder can be calculated by multiplying a fraction of the axial load with the given eccentricity. The

analysis stops when the RCFT cross-sectional moment and the applied moment are equal within a tolerance for equilibrium. The final cross-sectional moment value from the analysis gives the moment level at the occurrence of the desired damage level. This value is used in the experimental load-deformation plots and the occurrence of the desired damage level is detected. This method is only applied to the specimens with PCIb and PCIIa type loading, where the axial load and shear force are proportionally applied. On the other hand, for the specimens having PCIIb type loading, the cross-section analysis was used as it is originally developed in Appendix A. First, the moment level for the local damage condition was calculated for a constant amount of axial load, and then the points corresponding to the damage level were scaled from experimental plots. For the specimens in the monotonically loaded pinned connections database, the material strength ranges were within the limits of the constitutive models given by Gourley and Hajjar (1994) and Hajjar and Gourley (1996). Therefore, in all of the cross-section analysis performed in this section, the steel and concrete material models by Gourley and Hajjar (1994) and Hajjar and Gourley (1996) were used.

3.6.1 Beam-Columns

The beam-columns of the pinned connection specimens are subjected high axial loads and also a certain amount of bending moment, simultaneously. Therefore, damage levels specific to columns and beam-column can be observed. For the available specimens in the database, two damage levels were investigated, including concrete cracking and steel yielding in compression.

No concrete crushing was reported for specimens with loading scheme PCIb and PCIIa in the database. This result is consistent with the monotonic column tests where no crushing is observed for high L/D ratios. Using the modified version of the cross-section analysis program, discussed in Appendix A, the concrete crushing moment levels were calculated. As no crushing was reported in the pre-peak region, the moment level from the analysis program was decided to occur in the post-peak region where no experimental data was given. Local crushing due to bolt rotation was noted for the specimens with loading scheme PCIIb. However, no information was given about the load or

deformation level of concrete crushing, and it could not be calculated by analytical means.

Local buckling of the steel tube was not reported with sufficient detail for any of the specimens. At this stage of the research, it was not possible to estimate the occurrence of local buckling by analytical means. Therefore, this damage level also could not be investigated.

Concrete Cracking

Despite the fact that the moment level carried by the pinned-connections is not significant, concrete cracking is still possible if the specimens are tested under low axial load. Therefore, concrete cracking is presented as a damage level for the pinned-connections.

Type PCIb and PCIIa specimens were all subjected to high axial load levels. The results from the modified version of the cross-section analysis program described in Appendix A indicated that concrete cracking took place in the post-peak response. However, the tests were stopped when flexural buckling of the RCFT beam-column took place, and the post-peak data of the tests was not available. Therefore, the damage level at concrete cracking could not be quantified for the specimens with loading schemes PCIb and PCIIa.

The specimens tested with the loading scheme PCIIb experienced concrete cracking in the early stages of the loading. The damage evaluation was performed by both employing deformation-based ($D_{cr}^{RCFT-Pc-m} = d_{cr} / d_o$) and energy-based ($E_{cr}^{RCFT-Pc-m} = E_{cr} / E_{total}$) damage indices. It was found that as the depth of the girder framing into RCFT beam-column increased, the specimens showed a stiffer and stronger response. This causes the damage index values at concrete cracking to decrease. Consequently, both d_{cr} / d_o and E_{cr} / E_{total} were correlated to girder depth (d_g) over D ratio, and Equations 3.95 and 3.96 were derived with R^2 values 0.84 and 0.97, respectively.

$$D_{cr}^{RCFT-Pc-m} = \frac{d_{cr}}{d_o} = 1.0048 \left(\frac{d_g}{D} \right)^{-3.70} \quad (3.95)$$

$$E_{cr}^{RCFT-Pc-m} = \frac{E_{cr}}{E_{total}} = 0.22 \left(\frac{d_g}{D} \right)^{-6.09} \quad (3.96)$$

The comparison of the Equations 3.95 and 3.96 with the experimental results is shown in Figures 3.73 and 3.74, respectively. Both of the equations achieved good correlation to the experiments.

Yielding of Compression Flange of Steel Tube

Compression yielding of the steel tube was detected from the cross-section analysis program for the specimens tested with loading schemes PCIb and PCIIa. Both deformation-based ($D_{cy}^{RCFT-Pc-m} = d_{cy} / d_o$) and energy-based ($E_{cy}^{RCFT-Pc-m} = E_{cy} / E_{total}$) damage indices were used to quantify the damage. The ratios of d_{cy} / d_o and E_{cy} / E_{total} were correlated to the eccentricity (e) over D ratio and axial load (P) over shear load (V) ratio as given in Equations 3.97 and 3.98, respectively. The trend in the data showed that both of the damage indices get larger for high e/D and P/V ratios. This is because high values of e/D and P/V ratios cause d_o and E_{total} to decrease.

$$D_{cy}^{RCFT-Pc-m} = \frac{d_{cy}}{d_o} = 0.097 \frac{e}{D} + 0.042 \frac{P}{V} + 0.021 \quad (3.97)$$

$$E_{cy}^{RCFT-Pc-m} = \frac{E_{cy}}{E_{total}} = 0.053 \frac{e}{D} + 0.055 \frac{P}{V} - 0.077 \quad (3.98)$$

The R^2 of Equations 3.97 and 3.98 was found as 0.77 and 0.79. Equations 3.97 and 3.98 exhibit good correlation to the experimental results, as can be seen in Figures 3.75 and 3.76, respectively.

The majority of the specimens tested with loading scheme PCIIb did not attain the moment level to initiate steel yielding. However, for only one specimen, steel yielding in compression occurred in the post-peak region. The values of d_{cy} / d_o and

E_{cy} / E_{total} were found as 0.64 and 0.57, respectively.

3.6.2 Steel Girders

No local buckling and plastic hinging was reported in the tests. In addition, the yield moment levels calculated for the girders showed that the applied moment levels are not sufficient to initiate yielding. This shows that steel girders remained elastic during the tests.

3.6.3 Connection Components

The connection components used for the pinned connections included tee-stubs and end-plates. It was reported that these specimens underwent deformation and yielding during the tests. However, the occurrences of the local damages on the connection components were not reported. Therefore, the damage evaluation of the connection components could not be made.

The summaries of the equations for the deformation-based and energy-based damage functions of the monotonically loaded pinned connection tests are given in Tables 3.8 and 3.9, including appropriate statistical information and bounds on the independent variables for all the equations based upon the range of values available from the experimental research.

3.7 Monotonically Loaded Steel Girder-to-RCFT Column Moment Connections

Monotonically loaded moment connections were considered to consist of four parts including RCFT columns, panel zone, steel girders, and connection elements. The damage levels observed at each of these components during monotonic tests were investigated in this section. The occurrence of the damage levels on the load-deflection curves was tracked either by using the data provided in the experimental reports or by analytical means through the use of cross-section analysis of the CFT columns and steel girders. Only energy-based damage indices were used to quantify the damage. Two specimens were available for this study. All the specimens had a hardening type load-deflection curve, and the peak displacements were thus not clear. Therefore, deformation-based damage indices were not used for the monotonic moment connection

tests in the database. The end of the tests was signified by failure of the bolts, as reported by the researchers.

3.7.1 Beam-Columns

The columns of the connection tests are subjected to axial load and bending moments. Therefore, it is probable that the local damage observed in isolated beam-columns tests may occur in the beam-columns of moment connection tests. The specimens in the monotonic moment connection database were blind-bolted connections. The authors did not provide any data regarding the damage that occurred in the beam-columns, except that it was reported that steel yielding was observed in the beam-columns.

The cross-section analysis program developed for the beam-columns was used to obtain the damage levels of concrete cracking, steel yielding, and concrete crushing in the columns. The steel and concrete constitutive models used in the cross-section analysis program were taken from Gourley and Hajjar (1994) and Hajjar and Gourley (1996).

The experimental results were given as in the form of moment vs. girder rotation graphs. Therefore, after the moment values of concrete cracking, steel yielding, and concrete crushing were obtained using the cross-section analysis, the rotations corresponding to these local damages were scaled from the experimental moment vs. rotation curves.

The energy-based damage index at concrete cracking ($E_{cr}^{RCFT-Mc-m} = E_{cr} / E_{total}$) was found to be on the order of 0.0001 for the two available specimens. This indicates that concrete cracking has negligible effect on the behavior of the connection assembly. The value of the damage index at steel yielding in compression ($E_{yc}^{RCFT-Mc-m} = E_{yc} / E_{total}$) was found to be 0.0056 for the connection specimen with 275 MPa steel tube. When the yield strength of the steel tube increased to 355 MPa, the value of damage index at compression steel yielding decreased to 0.0046 because the specimen with 355 MPa steel tube had a stiffer response. The damage index at tension yielding in the steel tube ($E_{yt}^{RCFT-Mc-m} = E_{yt} / E_{total}$) was 0.015 for the 275 MPa steel tube and it was equal to 0.16

when 355 MPa steel was used. These results demonstrate that after steel yielding in the columns, the connections still have considerable reserve capacity. In addition, the compressive steel yielding and tension steel yielding occur with comparable values of damage indices. When concrete crushing was studied, the energy-based damage index ($E_c^{RCFT-Mc-m} = E_c / E_{total}$) was found to be 0.17 and 0.27 for the 275 MPa and 355 MPa specimens, respectively.

3.7.2 Panel Zone

High shear forces transferred from the girder flanges to the panel zone of the specimens cause damage in the panel zone region. The types of damage expected in this region include concrete cracking, steel yielding, concrete crushing, and local buckling. No concrete crushing or local buckling was reported for the specimens. However, both concrete cracking and steel yielding were evident by the end of the tests. The given moment vs. rotation curves in the experimental reports were converted into shear force vs. rotation curves. For this purpose, the moment arm of girder flange forces was assumed to be equal to the depth of the girder (d_g), and the moment values were thus divided by d_g . The resulting force was assumed to be equal to the shear force transferred to the panel zone.

Concrete Cracking

Concrete cracking at the panel zone of the specimens occurred at the early stages of the tests. The concrete cracking points were extracted from the experimental data by superimposing the assumed load-deflection behavior of the concrete core and steel tube in Figures 3.45 and 3.46, respectively as described in Section 3.5.

The energy-based damage index ($E_{cr}^{RCFT-Mc-m} = E_{cr} / E_{total}$) was calculated as the ratio of energy absorption until shear cracking in concrete (E_{cr}) to the total energy absorption (E_{total}). The average value of the damage index ($E_{cr}^{RCFT-Mc-m}$) was 0.00029 with a standard deviation of 0.00003, indicating that concrete cracking in the panel zone has an insignificant effect on the response in these moment connections.

Steel Yielding

Similar to concrete cracking, the steel yielding points in the experimental tests were found by superimposing the load-deflection behavior of the steel tube and concrete core given in Figures 3.65 and 3.66, respectively as described in Section 3.5.

For all the specimens in the database, it was found that the shear forces acting on the panel zones are not large enough to initiate steel yielding. This shows that yielding reported during the tests for the steel tubes was not a consequence of shear force acting at the panel zone.

Concrete Crushing

While tracking the concrete crushing points on the experimental load-deflection curves, it was assumed that concrete crushing occurs when the level of shear force carried by the concrete core reaches V_{cc} . Concrete crushing points were identified in the same way as in Section 3.5.

It was found that for none of the specimens in the database, the shear forces were large enough to initiate concrete crushing. This theoretical observation is also justified by the experimental observations.

3.7.3 Steel Girder

The potential damage levels for the steel girders include steel yielding and local buckling at the flanges. In the moment connection tests, no local buckling at the flanges took place. Therefore, only steel yielding was investigated in this section.

The moment level at steel yielding was taken from the BS5950 (1993) design specifications. However, it was found that for all of the specimens the theoretical yield moment of the steel girder was 1% to 21% larger than the applied moment although, severe steel yielding at the flanges of the steel girders was noted in the experimental reports. This inconsistency between theoretical and experimental results might be

attributed to any possible variation in the measured and nominal yield strength of the steel girders, as well as localized strain concentrations in the stress transfer region.

3.7.4 Connection Components

The connection elements used for the specimens in the monotonic connection database were endplates. At the end of the tests, no damage was reported to the endplates, although bolt pull-out was observed at the end of the tests, which corresponds to a damage index value of 1.

The summaries of the energy-based damage functions of the monotonically loaded moment connection tests are given in Table 3.10, including appropriate statistical information based upon the range of values available from the experimental research.

3.8 Cyclically Loaded Steel Girder-to-RCFT Column Moment Connections

The majority of the moment connection tests in the database were tested under cyclic loading. All the specimens were cruciform frames where two steel girders framed into the RCFT beam-columns at mid-height. The specimens were tested under either zero or constant axial loads. In all of the tests existing in the database, cyclic lateral loading was applied in such a way that the RCFT beam-columns undergo double curvature bending. This was achieved by applying shear forces in opposite directions at the tips of the girders or by generating a shear force at the top of the RCFT beam-columns.

The damage levels observed in the RCFT beam-column, panel zone, steel girders, and connection components were investigated. The energy based-damage function given in Equation 3.62 was used to quantify the damage. The occurrences of damage levels on the experimental curves were either provided in the experimental reports or they were calculated by analytical methods. In order to utilize Equation 3.62, it is required to calculate the E_m (the area under the complete cyclic back-bone curve) for each test setup. The complete back-bone curve of each specimen in the database was obtained by analyzing the specimens using CFT-Macro, as developed by Gourley and Hajjar (1997a,

1997b). As CFT-Macro does not have a connection element, only the specimens designed for weak-column or weak-girder response were examined. If the complete back-bone curve from CFT-Macro and experimental cyclic back-bone curve of the specimens show good correlation, then the damage evaluation of these specimens was performed. Otherwise, they were not considered further at this stage of the research. Figures 3.77 to 3.79 show the computational and experimental results of some of the representative specimens that were found as appropriate for damage evaluation using Equation 3.62.

The experimental results were reported in three different forms as given below:

- lateral load (H) vs. lateral displacement (Δ)
- girder shear (V_g) vs. lateral drift (R)
- panel zone shear (V_p) vs. lateral drift (R)

Depending on which part of the connection was being investigated, the three types of experimental results were converted to one another by simple calculations. The schematic representations of force (H , V_g) and displacement (Δ , R) quantities may be seen in Figure 3.80 for the test setups in the cyclic moment connection database.

The damage levels investigated for the RCFT beam-columns included concrete cracking, yielding of the compression flange, yielding of the tension flange, and local buckling of the compression flange. These damage levels often occurred either before or very near the occurrence of the peak, which indicates that the damage function in Equation 3.62 is applicable. Concrete crushing and local buckling of the steel tube web could not be studied, as these damage levels are susceptible to the cyclic load history, which is not taken into account by Equation 3.62. The occurrence of the damage levels of the RCFT beam-columns was captured with the use of the cross-section analysis program discussed in Appendix A. First, all the experimental results were converted into M vs. R graphs. After that, the cross-section analysis program was run and the moment levels corresponding to the damage levels were calculated. Finally, the calculated moment levels were entered into the experimental curves, transformed into M vs. R format. Equation 3.99 was utilized while converting H vs. Δ to M vs. R graphs.

$$M = P \times \frac{\Delta}{2} + H \times \frac{L}{2} \quad (3.99)$$

In Equation 3.99, it was assumed that the ratio of the lateral mid-height deflection of the RCFT beam-column is equal to the half of the total lateral deflection. This assumption is also verified in CFT-Macro by analyzing a representative specimen. The computational result in Figure 3.81 shows that the ratio of deflection at the top the RCFT beam-column (Δ) to the deflection at its mid-height (Δ_m) do not deviate from 2.0 significantly. While converting V_g vs. Δ graphs to M vs. R graphs, Equation 3.100 was used.

$$M = V_g \times \frac{L}{2} \quad (3.100)$$

In Equation 3.100, it was assumed that the moment at the girders and beam-column at the connection region is equal to each other. This assumption is also verified for a representative specimen by analyzing it using CFT-Macro. The results from CFT-Macro in Figure 3.82 show that the ratio of girder moment (M_g) and the beam-column moment (M) and do not deviate from 1.0, significantly. The V_p vs. R graphs were transformed into the M vs. R graphs through Equation 3.101, which is adopted from Gupta and Krawinkler (1999) by assuming the moments and shears of the RCFT beam-columns above and below the connection region are equal to each other:

$$M = \frac{(V_p + H) \times d_g}{2} \quad (3.101)$$

The equality of the shear forces of the RCFT beam-columns above and below the connection is trivial due to equilibrium because the support conditions at the girder ends are either roller or free. In Figure 3.82, as the equality of M_g and M is already verified, the symmetry and equilibrium of the specimens require that the beam-column moments at the top and bottom of the connections should be equal to each other.

The damage levels of the steel girders were either taken from the experimental results or they were determined based on the moment levels that the steel girders were subjected to. Initiation of steel yielding, plastic hinging, and local flange buckling constitute the damage levels investigated for the steel girders. As it was already verified that the girder moments and beam-column moments were equal to each other, all of the experimental data reported were transformed into the form of M vs. R . After that, the computational values of the yield moment and plastic moment of the girders were entered

to the M vs. R curves. The occurrence of local buckling of the steel girder flanges was already provided in the experimental results and required no analytical calculation.

For the panel zone regions of the cyclic moment connections, the damage levels including concrete cracking and steel yielding were investigated. Concrete crushing could not be examined because for all of the specimens the computational value of crushing shear was reached in the post-peak response and the damage function in Equation 3.62 was not suitable for the damage levels occurring in the post-peak response. Similarly, panel zone buckling also occurred in the post-peak region for the majority of the specimens and it could not be examined. The shear load levels at concrete cracking and steel yielding were all calculated analytically based on the constitutive relations of the steel tube and concrete panel given in Figures 3.65 and 3.66 as described in Section 3.5. All the available experimental data were converted into the form of V_p vs. R . H vs. Δ plots were first transformed into M vs. R form using Equation 3.99 as described before. After that, Equation 3.102 was used to get the V_p vs. R data (Equation 3.102 is a different form of Equation 3.101):

$$V_p = \frac{2 \times M}{d_g} - H \quad (3.102)$$

To get V_p vs. R data from the V_g vs. R plots, Equation 3.103 was utilized:

$$V_p = 2 \times \left(V_g \times \frac{L}{2} \right) / d_g \quad (3.103)$$

where the moment level at one girder was obtained by $V_g \times (L/2)$ and this moment value was divided by the girder depth to get the shear force transferred from the girder flange to the panel zone. As there are two girders at both sides of the connection, the resulting shear force is multiplied by two. For the specimens where the conversion from V_g vs. R to V_p vs. R was performed, the RCFT beam-columns were not subjected to any lateral load. Therefore, Equation 3.103 is free of column shears.

3.8.1 Beam-Columns

In this section the damage levels including concrete cracking, compression flange yielding, steel flange yielding, and local flange buckling will be investigated for the

beam-columns of the cyclically loaded cruciform connection specimens available in the database. The cross-sectional analysis program was utilized to detect the occurrence of the first three damage levels. In the cross-sectional analysis program, steel and concrete constitutive models developed by Gourley and Hajjar (1994), Hajjar and Gourley (1996) were adopted. For the occurrence of compression flange buckling, no computation was performed, as it was already reported by the researchers.

Concrete Cracking

The data obtained from the tests showed that the energy-based damage function at concrete cracking ($E_{cr}^{RCFT-Mc-c} = E_{cr} / E_m$) correlates to the parameter P/P_o . The trend in the data indicates that concrete cracking is delayed when P/P_o gets larger. The data exhibited a decreasing trend with respect to the parameter P_s/P_o . This might be due to lower stiffness of the specimens with high P_s/P_o ratios, which makes the specimen more susceptible to cracking. In Figure 3.83, the results from Equation 3.104 are compared with the experiments and for the majority of the tests good correlation was obtained. The R^2 for Equation 3.104 was found to be 0.97. It should also be noted that Equation 3.104 might give negative values for the specimens with zero axial load level.

$$E_{cr}^{RCFT-Mc-c} = \frac{E_{cr}}{E_m} = 0.040 \frac{P}{P_o} - 0.056 \frac{P_s}{P_o} + 0.026 \quad (3.104)$$

Yielding of Compression Flange of Steel Tube

The energy-based damage function ($E_{cy}^{RCFT-Mc-c} = E_{cy} / E_m$) at yielding in the compression flange of the steel tube exhibited a decreasing trend for high P/P_o ratios. This is an expected result as under high axial loads, it is easier for the steel tube to yield. When the data investigated for the variation of the parameter P_s/P_o , it was observed that the values of E_{cy} / E_m are getting smaller as P_s/P_o ratios increase. The reason for this trend is that the rate of increase in E_m for high P_s/P_o is greater than the rate of increase of E_{cy} values. Using the parameters P/P_o and P_s/P_o , a multi-linear regression was performed to estimate E_{cy} / E_m and Equation 3.105 was developed with an R^2 value of 0.65. A

single data point that has an unexpectedly high value of E_{cy} / E_m was treated as an outlier.

$$E_{cy}^{RCFT-Mc-c} = \frac{E_{cy}}{E_m} = -0.093 \frac{P}{P_o} - 0.042 \frac{P_s}{P_o} + 0.13 \quad (3.105)$$

The comparison of Equation 3.105 with the experiments was performed in Figure 3.84 and good correlation was achieved.

Yielding of Tension Flange of Steel Tube

For the specimens with high axial load levels, the results from the cross-section analysis program indicated that yielding in the tension flange of the steel tube took place in the post-peak region. For these specimens, due to the limitations of the damage function in Equation 3.62, tension steel yielding points could not be studied. Using the remaining data, Equation 3.106 was derived to estimate the energy-based damage function at tension flange yielding ($E_{yt}^{RCFT-Mc-c} = E_{yt} / E_m$). The R^2 for Equation 3.106 was found to be 0.57.

$$E_{yt}^{RCFT-Mc-c} = \frac{E_{yt}}{E_m} = 0.20 \frac{P}{P_o} - 0.21 \frac{P_s}{P_o} + 0.19 \quad (3.106)$$

Equation 3.106 showed a fairly good correlation with the experiments as can be seen in Figure 3.85.

Local Buckling of Steel Tube Flange

In the cyclic moment connection database, the majority of the specimens were reported to undergo local buckling in the steel tube compression flange. However, the occurrences of the local buckling damage level were provided only for a limited number of tests. Despite the fact there are few data points to be studied for local buckling of the steel tube flange, the available data shows a strong correlation with respect to the parameter P_c/P_o . Therefore, Equation 3.107 was developed to estimate the energy-based

damage function at local buckling of the steel tube flange ($E_{lbf}^{RCFT-Mc-c} = E_{lbf} / E_m$). The R^2 for Equation 3.107 was found as 0.98.

$$E_{lbf}^{RCFT-Mc-c} = -2.09 \frac{P_c}{P_o} + 1.12 \quad (3.107)$$

According to Equation 3.107, as the values of P_c/P_o increases the steel tube becomes more susceptible to local buckling and the value of E_{lbf} / E_m decreases. The experimental and computational results from Equation 3.107 are compared in Figure 3.86 and good correlation was obtained.

3.8.2 Panel Zone

The damage levels for the panel zones of the cyclically loaded moment connections, including shear cracking of the concrete and steel tube yielding in shear are studied in this section.

Concrete Cracking

The energy-based damage index at shear cracking of concrete in the panel zone ($E_{cr}^{RCFT-Mc-c} = E_{cr} / E_m$) was estimated by Equation 3.108, which was derived by correlating E_{cr} / E_m to the variables d_g/D and P_c/P_o . Equation 3.108 shows that there is an increase in E_{cr} / E_m as the aspect ratio of the panel zone ($d_g/D = L_p/D$) increases. This is because the panel zone becomes susceptible to flexure rather than shear if its aspect ratio increases. Therefore, shear cracking is delayed. According to Equation 3.108, E_{cr} / E_m increases as P_c/P_o gets larger because large P_c/P_o ratios improve the resistance of concrete core to cracking.

$$E_{cr}^{RCFT-Mc-c} = \frac{E_{cr}}{E_m} = 0.042 \frac{d_g}{D} + 0.00027 \frac{P_c}{P_o} - 0.053 \quad (3.108)$$

The R^2 for Equation 3.108 was found as 0.75. The experimental and computational values of E_{cr} / E_m exhibits good correlation as can be seen in Figure 3.87.

Yielding of Steel Tube

The data from the experiments for the energy-based damage function at steel tube yielding in the panel zone ($E_y^{RCFT-Mc-c} = E_y / E_m$) was correlated to the parameters d_g/D and P_s/P_o . This correlation gave Equation 3.109 to estimate E_y / E_m . The R^2 for Equation 3.109 was calculated as 0.80.

$$E_y^{RCFT-Mc-c} = \frac{E_y}{E_m} = 1.24 \frac{d_g}{D} + 0.72 \frac{P_s}{P_o} - 2.05 \quad (3.109)$$

The trend of the data as reflected in Equation 3.109 exhibits an increase in E_y / E_m when the parameters d_g/D and P_s/P_o get larger. Large values of d_g/D make the panel zone less susceptible to shear and also the specimens with large values of P_s/P_o values become more resistive against yielding. Therefore, both of these effects delay steel yielding in the panel zone regions and cause E_y / E_m to increase. The comparison of experimental and computational values of E_y / E_m is shown in Figure 3.88, where good agreement was achieved.

3.8.3 Steel Girders

The major damage levels reported for the steel girders during the cyclic moment connection tests were yielding at the girder flanges, plastic hinging, and local buckling of the girder flanges. These three damage levels are investigated in this section.

Yielding of Girder Flange

The moment level at yielding of the girder flanges was determined by multiplying the elastic section modulus of the steel girders (S) with their measured yield strengths (f_y). After that, this moment level was entered to the experimental curves and the energy-

based damage function at girder flange yielding ($E_{gy}^{RCFT-Mc-c} = E_{gy} / E_m$) was calculated, where E_{gy} represents the energy absorption at the initiation of yielding at the girders.

The collected data showed that E_{gy} / E_m decreases when the ratio of nominal axial strength of steel girder (P_g) over nominal axial strength of RCFT beam-column (P_o) increases. In the cyclically loaded moment connection database, the specimens with a larger girder section had often a larger value of E_m . Therefore, a reduction in E_{gy} / E_m was observed for large P_g/P_o ratios. Equation 3.110 was developed to estimate E_{gy} / E_m . The R^2 for the developed equation was found as 0.67.

$$E_{gy}^{RCFT-Mc-c} = \frac{E_{gy}}{E_m} = -0.65 \frac{P_g}{P_o} + 0.35 \quad (3.110)$$

Equation 3.110 is compared with the experimental results in Figure 3.89 and the correlation was fairly accurate.

Plastic Hinging

Plastic hinging of the girders was detected by entering the plastic moment level of the steel girders to the experimental curves. The plastic moments were calculated by multiplying the plastic section modulus of the girders (Z) with their measured yield strengths (f_y).

From the experimental data, it was found that the energy-based damage function at the initiation of plastic hinging ($E_{gp}^{RCFT-Mc-c} = E_{gp} / E_m$) exhibits a decreasing trend for high values of P_g/P_o ratio. Equation 3.111 was developed to estimate E_{gp} / E_m and the R^2 was determined as 0.44. The comparison of Equation 3.111 is presented in Figure 3.90 and a good correlation was attained for the majority of the specimens.

$$E_{gp}^{RCFT-Mc-c} = \frac{E_{gp}}{E_m} = -0.65 \frac{P_g}{P_o} + 0.43 \quad (3.111)$$

Local Buckling of the Steel Girder Flange

Among the available specimens in the database, local buckling of the steel girder flange was often observed during the tests. However, the occurrence time was reported only for one specimen, where the value of the energy based-damage function when local buckling of the girder flange takes place ($E_{lbg}^{RCFT-Mc-c} = E_{lbg} / E_m$) was found to be 0.23.

3.8.4 Connection Components

The connection elements used for the specimens in the cyclically loaded moment connection database included tee-stubs and stiffeners. At the end of the tests, yielding and local buckling of connection components were reported. As the specimens were selected in a manner that the failure occurred either at the girders or at the RCFT beam-columns, the connection components are subjected to any damage at the very post-peak response. Therefore, the damage evaluation of the connection components could not be investigated.

The summaries of the equations for the energy-based damage functions of the cyclic moment connection tests are given in Tables 3.11a, 3.11b and 3.11c, including appropriate statistical information and bounds on the independent variables for all the equations based upon the range of values available from the experimental research.

3.9 Monotonically Loaded RCFT Frames

The intent of the monotonically loaded RCFT frame tests is typically to investigate the load and deformation capacity of RCFT beam-columns and connections. Depending on the design of the test specimens, the behavior of the frame is governed by the weakest of these components. In the monotonically loaded RCFT frame database, only the specimens with strong connections and weak beam-columns were stored. Therefore, the purpose of this section is to investigate the effect of the damage levels of the RCFT beam-columns to portal frames. Note that the monotonically and cyclically loaded RCFT frame tests could possibly be used to verify the damage indices for members and connections derived earlier. However, the loading, material, and geometric

parameters of the frame tests tended to place them outside the applicable range of parameters for several of the damage indices derived earlier, and so new damage indices for these members and connections are derived for the frame tests. Therefore, the damage levels of the beam-column members were investigated as story-based limit states.

All of the monotonically loaded RCFT frame tests existing in the database were tested by Matsui (1986). The damage levels reported in these tests included local buckling of RCFT beam-column flange and local buckling of beam-column web. The remaining damage parameters including concrete cracking, yielding of compression flange, and yielding of steel flange were calculated with the use of cross-section analysis program. The failure point was taken as 6% percent drift for all the specimens. The steel and concrete material models proposed by Gourley and Hajjar (1994) and Hajjar and Gourley (1996) were employed for the analyses, since the ranges of material and geometric properties in the monotonically loaded frames fall within the limits of the material models proposed by Gourley and Hajjar (1994) and Hajjar and Gourley (1996). In order to utilize the cross-section analysis program, the experimental results given as horizontal load (H) vs. lateral deflection (Δ) plots were converted to moment (M) vs. lateral deflection (Δ) plots. For this purpose, the moment was calculated as given in Equation 3.112 by assuming the inflection point of the columns to be at the middle and the shear load is equally shared among the two columns of the portal frames. The verification of the validity of Equation 3.112 will be given in Section 3.10.

$$M = \frac{H}{2} \times \frac{L}{2} + P \times \Delta \quad (3.112)$$

The specimens all had the same material and geometric properties. However, their connection details were different. Two types of fully-restrained connections were used. The first type of connection detail included external stiffeners, while the second type connection detail was through-diaphragm.

Concrete Cracking

The moment at concrete cracking was determined using the cross-sectional analysis program developed for RCFT cross sections. Cracking in the concrete was

assumed to occur when the strain at the outermost steel fiber reaches the cracking strain of concrete. Once the cracking moment was computed, the point corresponding to that moment on the monotonic experimental curve for a given specimen was identified from the available experimental data.

The damage level when tension cracking of the concrete occurred was quantified using the displacement-based damage index ($D_{cr}^{RCFT-Fr-m} = d_{cr} / d_o$). For the monotonic frame specimens the value of d_{cr} / d_o remained almost constant and did not show any variation. The average value of d_{cr} / d_o was found to be 0.069 with a standard deviation of 0.0089.

If the damage level at concrete cracking is quantified using the energy-based damage index ($E_{cr}^{RCFT-Fr-m} = E_{cr} / E_{total}$), similar to the deformation-based damage index, the value of E_{cr} / E_{total} remained almost constant with an average value of 0.0031 and a standard deviation of 0.00044.

Yielding of Compression Flange of Steel Tube

The cross-section analysis program was used to capture the compression steel yielding points. For the deformation-based damage index ($D_{cy}^{RCFT-Fr-m} = d_{cy} / d_o$), the main parameter for the monotonic beam-column tests, the P_c/P_o ratio, was used to correlate d_{cy} / d_o by linear regression. Equation 3.113 was developed to estimate $D_{cy}^{RCFT-Fr-m}$. The R^2 for Equation 3.113 was found as 0.75.

$$D_{cy}^{RCFT-Fr-m} = \frac{d_{cy}}{d_o} = 0.48 \frac{P_c}{P_o} - 0.10 \quad (3.113)$$

Figure 3.91 shows the comparisons of Equation 3.113 with the experimental results. Equation 3.113 achieves a good accuracy to predict d_{cy}/d_o . According to the trend in Equation 3.113, d_{cy}/d_o increases when P_c/P_o gets larger values. This attributed to the fact that as concrete contribution to the response improves, steel yielding is delayed.

The energy-based damage index ($E_{cy}^{RCFT-Fr-m} = E_{cy} / E_{total}$) at compression flange yielding was also investigated. It was found that the value of E_{cy} / E_{total} remains constant

for the majority of the specimens. The average value of E_{cy} / E_{total} was found to be 0.025 with a standard deviation of 0.0026.

Yielding of Tension Flange of Steel Tube

In the monotonically loaded frame tests, similar to concrete cracking and compression steel yielding, the moment level at tension flange yielding was determined from the cross-sectional analysis program. After that, the tension yielding points were scaled from the experimental graphs.

The displacement-based damage function ($D_{yt}^{RCFT-Fr-m} = d_{yt} / d_o$) was utilized to quantify the damage. The ratio d_{yt} / d_o was correlated to P_c / P_o and Equation 3.114 was derived to calculate d_{yt} / d_o . The trend in Equation 3.114 also shows a decrease in d_{yt} / d_o as P_c / P_o takes larger values. This is because as concrete contribution to the response gets larger, less load is transferred to the steel tube.

$$D_{yt}^{RCFT-Fr-m} = \frac{d_{yt}}{d_o} = 1.25 \frac{P_c}{P_o} - 0.38 \quad (3.114)$$

Equation 3.114 was compared with the experimental results in Figure 3.92 and Equation 3.114 achieved a good correlation with an R^2 of 0.94.

The energy-based damage index ($E_{yt}^{RCFT-Fr-m} = E_{yt} / E_{total}$) attained almost a constant value for the specimens. The average value of E_{yt} / E_{total} was found to be 0.087 with a coefficient of variation of 0.016.

Local Buckling of Steel Tube Flange

Local buckling took place at both ends of the beam-columns of the frames. However, local buckling at the bottom of the beam-column occurred earlier. This is likely due to fact that the connections were not as rigid as the girder, and thus the maximum moment occurred at the bottom of the beam-columns. While evaluating the damage level at local buckling, the first occurrence of local buckling was investigated.

The damage at local buckling was quantified using both the deformation-based damage index ($D_{lbf}^{RCFT-Fr-m} = d_{lbf} / d_o$) and the energy-based damage index ($E_{lbf}^{RCFT-Fr-m} = E_{lbf} / E_{total}$). The available data indicated that d_{lbf} / d_o and E_{lbf} / E_{total} values decrease for large values of P_c/P_o . RCFT members with thin-walled steel tube are susceptible to local buckling and for the tests in the monotonic frame database, the specimens with large values of P_c/P_o also have thin-walled steel tubes. Equations 3.115 and 3.116 were developed to estimate the damage functions in terms of the parameter P_c/P_o . The R^2 for the aforementioned equations were found to be 0.95 and 0.74, respectively.

$$D_{lbf}^{RCFT-Fr-m} = \frac{d_{lbf}}{d_o} = -0.33 \frac{P_c}{P_o} + 0.56 \quad (3.115)$$

$$E_{lbf}^{RCFT-Fr-m} = \frac{E_{lbf}}{E_{total}} = -0.13 \frac{P_c}{P_o} + 0.17 \quad (3.116)$$

Equations 3.115 and 3.116 were compared with the experimental results in Figures 3.93 and 3.94. For both of the equations good correlation was achieved.

Local Buckling of Steel Tube Web

Local buckling of the steel tube web was reported in the monotonically loaded RCFT frame tests as the second damage level following local buckling of the steel tube flange. For all the specimens, local buckling of the steel tube web occurred in the post-peak region. In the frame tests, no sudden change in the load-deflection response was observed after the steel tube web buckled. This might be due to fact that the frames were already in the softening region that was initiated by the other major damage levels, including concrete crushing and local buckling of the steel tube.

The damage level of the steel tube web buckling was quantified using the deformation-based ($D_{lbw}^{RCFT-Fr-m} = d_{lbw} / d_o$) and energy-based damage indices ($E_{lbw}^{RCFT-Fr-m} = E_{lbw} / E_{total}$). The strain level at local buckling of the web was high for all the specimens, as can be seen from the average value of d_{lbw} / d_o calculated as 1.60 with a standard deviation of 0.15. The average value of E_{lbw} / E_{total} was found to be 0.57 with

a standard deviation of 0.10, indicating that significant reduction in energy absorption capacity was caused prior to buckling of web. No equation was proposed to estimate the damage functions due to low correlation.

The summaries of the equations for the displacement-based and energy-based damage functions of the monotonic RCFT frame tests are given in Table 3.12 and Table 3.13, respectively, including appropriate statistical information and bounds on the independent variables for all the equations based upon the range of values available from the experimental research.

3.10 Cyclically Loaded RCFT Frames

Similar to the approach taken for assessing damage in the cyclically loaded RCFT beam-column tests, a semi-empirical method was developed to extract local damage levels from the experimental load-deflection curves given in the reports. This method is similar to the one used for the cyclically loaded RCFT beam-column tests. The cross-section analysis program and the experimental load-deflection curves were used, together to examine the damage evolution of the cyclically loaded RCFT frames. As in the case of monotonic frame tests, the local damage of the beam-column members was used to investigate story-based limits states of RCFT frames.

In the literature, the experimental load-deflection curves were given in terms of lateral load (H) and chord rotation (R) of the frames. The approach taken to assess damage was to calculate the moments acting on the individual RCFT members from the H vs. R graphs. This requires, first, to determine the amount of horizontal force carried by each beam-column of the portal frame. As the portal frames were symmetric structures, the horizontal load was assumed to be equally-shared by the windward and leeward columns. The next-step was to determine the location of the inflection point of the columns. For this purpose, the analysis program CFT-Macro (Gourley and Hajjar, 1997a, 1997b) was used. As referenced in Kawaguchi (2000), Kato et al. (1969) showed that the monotonic load-deflection curves of RCFT members envelope their cyclic response. Therefore, monotonic analysis in CFT-Macro was used to estimate the backbone curve of the specimens.

The portal frames tested by Kawaguchi et al. (1997) and Kawaguchi (2000) were compared with the results from CFT-Macro. The analysis model input to CFT-Macro can be seen in Figure 3.95. Only one-half of the frames was modeled, taking advantage of the symmetry of the frames, and the analysis was run under monotonic loading. The results from the CFT-Macro and the experimental back-bone curves can be seen in Figure 3.96 through Figure 3.98. These figures show that the both the computational and experimental results match with a reasonable accuracy up to the peak response (CFT-Macro does not capture softening response). This proves that CFT-Macro reproduces the experimental results for the RCFT frame structures and it is reliable to determine the location of the inflection points of the frame members. Figure 3.99 to Figure 3.101 exhibit the final moment distribution at the end of the analysis along the height of the windward column of the RCFT frames analyzed by CFT-Macro. In all of the cases, the moment was found to vanish at approximately the mid-height, indicating that the location of the inflection point remains constant.

The RCFT beam-columns in a portal frame undergo double curvature bending if the frame is subjected to a horizontal load. With this fact in mind, the free-body diagram of the upper portion of the windward column is shown in Figure 3.102 as an illustration of the calculation of the bending moment transferred to the columns. Taking the moments of the forces in Figure 3.102 with respect to the inflection point and then equating the sum of the moments to zero, the moment (M) at the top of the column can be calculated using Equation 3.117. The lateral displacement (Δ) can be determined by multiplying the whole length of the column (L) with the amount of chord rotation (R).

$$M = \frac{H}{2} \times \frac{L}{2} + P \times \frac{\Delta}{2} \quad (3.117)$$

When conducting the calculations for assessment of the damage levels in RCFT frames, it was required to use accurate constitutive models for the steel and concrete. In the reports of the frame tests by Kawaguchi et al. (1997) and Kawaguchi (2000), the information given on the constitutive models for steel and concrete was not comprehensive. However, the selected ranges of the material strengths for both steel and concrete were found to be within the limits of the constitutive models provided by Gourley and Hajjar (1994) and Hajjar and Gourley (1996). Therefore, while using the

cross-section analysis program to determine the moment levels corresponding to the local damages, the constitutive models recommended by Gourley and Hajjar (1994) and Hajjar and Gourley (1996) were used.

The damage levels observed for the cyclically loaded RCFT frames are similar to the cyclically loaded RCFT beam-columns, except for the cyclic frames, concrete crushing and local buckling of the steel tube web were not studied as there is no data available for these damage levels. The damage function given in Equation 3.62 was also utilized for the cyclically loaded frame specimens. The monotonic energy absorption capacity required in the damage index was calculated by analyzing the specimens using CFT-Macro. The end of the analysis was taken as 6% drift as in the case of beam-column specimens. However, CFT-Macro gave only pre-peak response of the specimens. In the post-peak range, as recommended by Kawaguchi (2000), rigid plastic behavior was assumed.

Concrete Cracking

A semi-empirical method was used to estimate the occurrence of the tensile cracking of the concrete. The moment level when the concrete cracking strain is reached was calculated using the cross-section analysis program described earlier. The corresponding chord rotation (R) was then determined from the RCFT beam-column experimental M vs. R graphs, which were converted from the experimental H vs. R graphs of the frames.

The data extracted from the experimental curves indicated that the energy-based damage index at concrete cracking ($E_{cr}^{RCFT-Fr-c} = E_{cr} / E_m$) shows strong correlation with respect to P/P_o . The trend in the data indicates that for high axial load ratios, concrete cracking is delayed and the value of E_{cr} / E_m increases. Under high axial load ratios, the effect of the D/t ratio on concrete cracking is suppressed. For the specimens with high P/P_o ratios, the value of E_m exhibits an increasing trend. This also affected E_{cr} / E_m and it was found that E_{cr} / E_m is decreasing when P/P_o values get larger. A multi-linear

regression was performed and Equation 118 was developed to estimate E_{cr} / E_m . The R^2 for Equation 3.118 was found as 0.77.

$$E_{cr}^{RCFT-Fr-c} = \frac{E_{cr}}{E_m} = 0.024 \frac{P}{P_o} - 0.0033 \frac{P_c}{P_o} - 0.0031 \quad (3.118)$$

Equation 3.118 is compared with the experimental results in Figure 3.103. It should be noted that for low axial load values Equation 3.103 gives negative values. Therefore, it is recommended that for axial load values smaller than 0.15, Equation 3.103 should be avoided to be used.

Yielding of Compression Flange of Steel Tube

Points corresponding to yielding of the compression flange of the steel tube for cyclically loaded RCFT frames were also determined using the semi-empirical approach. Similar to concrete cracking, the moment level for yielding of the compression flange of the steel tube was determined from the cross-sectional analysis program. After that, the corresponding chord rotation value, R , was scaled or interpolated from the experimental data.

When the available data for compression steel yielding was examined, it was found that the energy based-damage function ($E_{cy}^{RCFT-Fr-c} = E_{cy} / E_m$) is mainly affected by P_s/P_o ratios. A clear trend in Figure 3.104 shows that E_{cy} / E_m increases for high P_s/P_o values. For low values of P_s/P_o , the effect of P/P_o on steel yielding is suppressed. However, when P_s/P_o increases, the steel tube takes more axial load and yielding occurs earlier. Equation 3.119 and 3.120 were proposed to estimate E_{cy} / E_m . The R^2 for Equation 3.119 and 3.120 were found as 0.82 and 0.65, respectively.

$$E_{cy}^{RCFT-Fr-c} = \frac{E_{cy}}{E_m} = 0.070 \frac{P_s}{P_o} - 0.035 \text{ for } P/P_o = 0.15 \quad (3.119)$$

$$E_{cy}^{RCFT-Fr-c} = \frac{E_{cy}}{E_m} = 0.028 \frac{P_s}{P_o} - 0.0063 \text{ for } P/P_o \geq 0.30 \quad (3.120)$$

Figure 3.105 exhibits the comparison of Equations 3.119 and 3.120 with the experimental results. For both of the equations a good correlation was obtained.

Yielding of Tension Flange of Steel Tube

Yielding of the tension flange of the steel tube in the RCFT frames was investigated in the same way as yielding of the compression flange of the steel tube. Using the semi-empirical approach, the tension flange yielding points were extracted from the experimental load-deflection curves. Then, the energy-based damage index at yielding of the tension flange of the steel tube ($E_{yt}^{RCFT-Fr-c} = E_{yt} / E_m$) was investigated to determine a correlation between the structural parameters of the RCFT beam-columns.

When the available data for tension steel yielding was examined, it was found that E_{yt} / E_m is mainly affected by P/P_o ratios. A clear trend in Figure 3.106 shows that E_{yt} / E_m increases for high P/P_o values. However, no definite trend for P_s/P_o to affect E_{yt} / E_m can be observed from Figure 3.106. Due to low correlation, no equation was developed to estimate E_{yt} / E_m . The average value of E_{yt} / E_m was found as 0.068 with a standard deviation of 0.048.

Local Buckling of Steel Tube Flange

Among the specimens in the database, local buckling was first initiated at the bottom and then at the top of the columns. Local buckling points were available for both directions of loading. Therefore, each specimen was considered as two specimens. The energy-based damage index at local buckling of the steel tube flange ($E_{lbf}^{RCFT-Fr-c} = E_{lbf} / E_m$) was found to correlate to the P/P_o ratio. The other parameters including P_s/P_o were constant for the specimens where local buckling was reported. The trend in the data showed that for large axial load levels, E_{lbf} / E_m increases. This is because any increase in axial load ratio causes a reduction E_m . Equation 3.121 was developed to estimate E_{lbf} / E_m . The R^2 for Equation 3.121 was found as 0.96.

$$E_{lbf}^{RCFT-Fr-c} = \frac{E_{lbf}}{E_m} = 0.10 \frac{P}{P_o} + 0.25 \quad (3.121)$$

Equation 3.121 was compared with the experiments in Figure 3.107 and good correlation was obtained.

The summaries of the Equations for the energy-based damage functions of the cyclic RCFT frame tests are given in Table 3.14, including appropriate statistical information and bounds on the independent variables for all the equations based upon the range of values available from the experimental research.

3.11 Ductility of RCFT Members

Ductility is defined as the ability of RCFT members to undergo inelastic deformation without a sudden decrease in strength. Ductility (μ) can be quantified with the use of a ductility factor defined as in Equation 3.91.

$$\mu = \frac{d_u}{d_y} \quad (3.122)$$

where:

d_y – yield displacement

d_u – displacement at failure

The ductility of RCFT members were investigated in this section. For each type of specimen in the database, the available ductility was calculated and correlated to the material and geometric properties.

3.11.1 Monotonically Loaded Columns

Two main types of load deflection curves were identified for the monotonic column specimens as shown in Figure 3.7. Different procedures were used to determine d_y and d_u to calculate ductility depending on the type of load-deflection curve.

For all the column specimens, d_y was defined as the deflection where the axial load level reached 90% of its maximum value. The 90% load level was based on the experimental results by Schneider (1998), where an average value of 0.91 with a standard deviation of 0.10 was obtained.

Three different methods were employed in detecting the failure point of the specimens. For RCFT columns having a softening type of post-peak behavior, d_u was assumed to be reached when the reduction in the axial load level was 15%. The 15% limit was also used for reinforced concrete columns that exhibit a sudden decrease in the strength following the peak load (Rao et al., 1998). If RCFT columns underwent hardening, the failure point was assumed to take place at the end of the hardening region (Elchalakani et al., 2001). On the other hand, if the post-peak response of the specimens was close to perfectly plastic, a limiting strain value of 0.015 was selected for the concrete core, and the instant when a 0.015 axial strain was reached was assumed to be the failure point. A 0.015 strain value was taken from the constitutive model for the concrete core of RCFTs by Tomii and Sakino (1979b), as shown in Figure 3.85. A similar type of failure definition was also employed by Mehanny and Deierlein (2000) for reinforced-concrete members. For the slender specimens that have high L/D ratios, if the post-peak response is close to perfectly plastic, the failure point was decided based on an interstory drift limit of 6%. The 6% drift limit was also used for the beam-column tests as will be presented later.

Using the available data in the data in the monotonic column database, Equations 3.123/3.124 and 3.125 were derived to estimate the ductility of the specimens with R^2 values 0.51 and 0.90. In deriving Equation 3.123/3.124, outlier data was eliminated if the residual over predicted value was greater than 1.0. Among the stocky specimens ($L/D < 12$), the ductility was found to remain approximately constant at an average value of 1.84 with a standard deviation of 0.57 if f'_c/f_y ratio was above 0.20.

for $L/D < 12$

$$\mu = -22.23 \frac{f'_c}{f_y} - 0.17 \frac{D}{t} + 3.59 \frac{L}{D} + 2.60 - \text{if } f'_c / f_y < 0.20 \quad (3.123)$$

$$\mu = 1.84 - \text{if } f'_c / f_y \geq 0.20 \quad (3.124)$$

for $L/D \geq 12$

$$\mu = 0.13 \frac{L}{D} + 1.38 \frac{P_c}{P_o} + 1.20 \quad (3.125)$$

For stocky specimens with low L/D ratios, it was found that the ductility of the specimens decreases when the concrete contribution to the response increases. This trend can be seen in Equation 3.123, where a decrease in ductility can be noticed as D/t and f'_c get larger. However, for the slender specimens, the experimental results exhibited an opposite trend and ductility increased when P_c/P_o values got larger. For all the specimens whether they are stocky or slender, ductility was found to improve if the L/D ratio gets larger (i.e., even specimens that buckled due to large L/D were often found to be able to retain their strength through further deformation thereafter).

The comparison of Equation 3.123 through 3.125 with the experimental results can be seen in Figure 3.109. A fairly good correlation between the experimental and computational values can be seen.

3.11.2 Monotonically Loaded Beam-Columns

The ductility of the monotonic beam-columns was investigated in three groups based on the type of loading. The ductility for each group of specimens was calculated and the correlation of ductility to the material and geometric properties was studied.

For each specimen in the monotonic beam-column database, the yield displacement was defined in the same way. The calculation of yield displacement was adopted from Varma (2000) and it is presented in Equation 3.126 and in Figure 3.110.

$$d_y = \frac{L_o}{K_{sec}} \quad (3.126)$$

where:

L_o – peak load

K_{sec} – secant stiffness at $0.60L_o$

However, different methods were employed to define the ultimate points. For all the beam-column specimens having a softening type of post-peak behavior, the failure was assumed to occur when the load capacity of the specimens decreased to 90% of its peak value (Varma, 2000). If the specimens exhibited a hardening type post-peak behavior, the failure point was assumed to be the end of the hardening region. There also exist beam-column specimens in the database with approximately perfectly plastic post-peak response. For this type of specimen, two different methods were adopted to detect

failure. In the first method, if the deflection of the specimens was given in terms of curvature, the failure was assumed to take place when the compressive strain at the outermost concrete fiber reached a strain value of 0.015. This failure criteria required moment-curvature analysis of the specimens using the cross-section analysis program (see Appendix A) and it was mainly applied to the specimens with the MIII type loading scheme, which were mostly short specimens. When using the cross-sectional analysis, the steel and concrete constitutive models developed by Gourley and Hajjar (1994) and Hajjar and Gourley (1996) were utilized. On the other hand, the second failure criterion for the perfectly plastic post-peak response involved taking a lateral drift of 6% as the deflection at the ultimate point. This method of failure detection was applied to specimens with MII type loading, and the 6% drift limit was based on the test results by Tomii and Sakino (1979b) and Sakino and Ishibashi (1985), where the tests were stopped at an average lateral drift value of 6%.

The specimens with MI type loading scheme in the database exhibited either a hardening or softening type of post-peak behavior. The ductility of the specimens in the database was evaluated and Equation 3.127 was derived to estimate ductility. The R^2 for Equation 3.127 was 0.50. While deriving Equation 3.127, outlier points were eliminated if the residual over predicted ratio was greater than 1.0.

$$\mu = -7.26 \frac{P_c}{P_o} + 4.72 \frac{e}{D} - 0.28 \frac{L}{D} + 12.68 \quad (3.127)$$

The trend in Equation 3.127 shows that there is a reduction in ductility when P_c/P_o or L/D ratio increases. On the other hand, ductility was found to improve for large values of eccentricity. Equation 3.127 is compared with the experimental results in Figure 3.111 and relatively good correlation was obtained.

The experimental results of beam-column specimens tested with loading scheme MII exhibited all types of post-peak behavior including softening, hardening, and perfectly plastic. Equation 3.128 was developed to estimate the ductility for the MII type beam-column specimens. The R^2 for Equation 3.128 was calculated as 0.53.

$$\mu = -0.32 \frac{L}{D} - 3.78 \frac{P_c}{P_o} - 0.28 \frac{P}{P_o} + 23.24 \quad (3.128)$$

Equation shows that the ductility of the beam-columns reduces when the parameters L/D , P_c/P_o and P/P_o get larger. The computational results from Equation 3.128 were compared with the experiments and good correlation was obtained as can be seen in Figure 3.112.

MIII type specimens also underwent all types of post-peak response including softening, hardening, and perfectly plastic. Equation 3.129 was derived to estimate the ductility of the specimens. The R^2 for Equation 3.129 was found as 0.53. In deriving Equation 3.129, the outlier points were eliminated if the residual over predicted ratio is greater than 1.0.

$$\mu = -4.73 \frac{P_c}{P_o} - 9.64 \frac{P}{P_o} + 9.93 \quad (3.129)$$

The trend in Equation 3.129 indicates that ductility reduces if P/P_o and P_c/P_o values of the specimens get larger. Equation 3.129 was compared with the experimental results in Figure 3.114 and good correlation was achieved.

3.11.3 Cyclically Loaded Beam-Columns

The backbone curves of the load-deformation response for the cyclic beam-column specimens in the database showed a softening type of post-peak behavior. The same definition of yield point with the monotonic beam-columns was utilized to determine yield displacement. The specimens were assumed to fail when the load capacity of the specimens decrease to 90% of its peak value.

To estimate the ductility of the specimens Equation 3.130 was derived with an R^2 value of 0.68. While deriving Equation 3.130, only the data from the specimens having a saw-teeth type loading rule was used.

$$\mu = -7.12 \frac{P}{P_o} - 0.33 \frac{P_c}{P_o} + 5.48 \quad (3.130)$$

Equation 3.130 shows that when the axial load level increases a reduction in ductility takes place. In addition, any increase in P_c/P_o also causes a decrease in ductility.

Equation 3.130 is compared with the experimental results in Figure 3.114 and good correlation was attained.

3.11.4 Monotonically Loaded Panel-Zones

In the monotonic panel-zone tests, the specimens underwent either softening or perfectly plastic type post-peak response. The yield points of the monotonic panel zone specimens were determined in the same way as monotonic beam-columns. For the specimens having a softening post-peak response, the failure point was taken as the instant when the capacity of the member drops to 90% of its peak value. However, if the specimens exhibited a perfectly plastic type of post-peak response, a limiting shear deformation of 0.02 radians was assumed. The 0.02 radian deformation level was taken from the panel zone tests by Kamba et al. (1991), where the specimens were able to attain 0.02 radian shear deformation without any significant strength degradation.

Using the available data in the database, Equation 3.131 was derived to estimate ductility. The R^2 for Equation 3.131 was determined as 0.88.

$$\mu = -28.44 \frac{P}{P_o} - 1.81 \frac{L_p}{D} + 23.96 \frac{P_c}{P_o} + 9.27 \quad (3.131)$$

According to the trend in Equation 3.131, high axial load ratios and high aspect ratios are both detrimental to ductility. However, an improvement in ductility is evident for large P/P_o ratios. As can be seen from Figure 3.115, Equation 3.131 is successful in simulating the experimental results.

3.11.5 Monotonically Loaded Pinned Connections

Among monotonically loaded pinned connection tests, PCIIa, PCIIb and PCIIa type specimens did not have available data for their post-peak response. Therefore, the ductility assessment of monotonically loaded pinned connections could only be made for PCIIb type specimens.

For the pinned connection specimens, while calculating ductility, the yield point was determined similarly to the beam-column tests. Type PCIIb specimens all had a

hardening response and they were able to attain a deformation level of 0.05 radians without any deterioration in strength. The 0.05 radian deformation limit was taken as the failure point as it represents an upper bound of deformation for all the available specimens.

Equation 3.132 was developed to estimate ductility of the pinned connection specimens. The R^2 for Equation 3.132 was determined as 0.57.

$$\mu = 959.13 \frac{d_g / D}{(D/t)^2} + 0.90 \quad (3.132)$$

Equation 3.132 indicates that high D/t ratios are detrimental to ductility. On the other hand, it can also be seen from Equation 3.132 that an increase in ductility takes place when the size of the girders with respect to the RCFT member depth increases. Figure 3.116 shows that the correlation of experimental and computational ductility values is relatively satisfactory.

3.11.6 Monotonically Loaded Moment Connections

Monotonically loaded moment connection specimens available in the database also exhibited a hardening type of post-peak response. The yield point was detected using the same technique as in the case of monotonically loaded beam-column specimens. The failure point was estimated at a deformation limit of 0.05 radian which was also assumed to be the limiting deformation for the PCIIb type specimens.

However, the number of specimens was not sufficient to derive an equation for ductility. Therefore, the ductility of the available specimens was calculated and the average value was found to be 5.8 with a standard deviation of 0.56.

3.11.7 Cyclically Loaded Moment Connections

For the specimens in the cyclic moment connection database, the ductility of only the specimens having either weak column or weak girder was investigated. In addition, the specimens having premature fracture were excluded. The yield point of the specimens was detected using the same method as in the case of monotonically loaded

beam-column specimens. The backbone curve was used for the ductility assessment, and all of the cyclically loaded moment connections available in the database had a backbone curve with a softening post-peak response. Therefore, the failure point was determined when the capacity of the members reduces to 90% of its peak value.

Equation 3.133 was derived to calculate the ductility of the specimens. The R^2 for Equation 3.133 was calculated to be 0.73.

$$\mu = 1.06 \frac{P}{P_o} + 4.52 \frac{P_g}{P_o} - 1.12 \frac{P_c}{P_o} + 1.59 \quad (3.133)$$

According to the trend in Equation 3.133, axial load acting on the specimens improves ductility. Although this is an unexpected trend, in the database, the specimens with high axial loads underwent more deformation in their post peak-response. When the P_g/P_o ratios attain larger values, an increase in ductility is also evident from Equation 3.133. On the other hand, large values of P_c/P_o ratios cause a reduction in ductility. Equation 3.133 is compared with the experimental results in Figure 3.117 and a good agreement was obtained.

3.11.8 Monotonically Loaded Frame Tests

Monotonically loaded frame tests showed either softening or perfectly plastic post-peak response. Both the yield point and failure point were decided using the same methods employed for the monotonically loaded beam-columns. Two types of failure criteria's were adopted from the beam-columns. If the frame specimens have a softening post-peak response, 90% of the peak capacity was taken as the failure point. On the other hand, for the frame specimens with perfectly plastic post-peak response, a 6% drift limit was adopted as a failure criteria, similarly to that of RCFT beam-columns.

The correlation of the material and geometric properties of the RCFT members to the ductility was investigated and Equation 3.134 was derived with an R^2 value of 0.46. The D/t ratio and f'_c was the main parameter in the monotonic frame tests available in the database. Therefore, the ductility was only correlated to the ratio of P_c/P_o .

$$\mu = -13.0 \frac{P_c}{P_o} + 14.1 \quad (3.134)$$

Equation 3.134 shows that P_c/P_o has a detrimental effect on ductility. Equation 3.134 is compared with the experimental results in Figure 3.118 and the correlation between the results was fairly good.

3.11.9 Cyclically Loaded Frame Tests

The backbone curve for cyclically loaded frame tests exhibited only softening type of post-peak behavior. Both the detection of yield point and failure point were adopted from the monotonically loaded frame tests. The ductility of the specimens having premature fracture was not investigated.

Equation 3.135 was developed to estimate the ductility of the cyclically loaded frame specimens. The R^2 for Equation 3.135 was found to be 0.92.

$$\mu = 0.067 \frac{D}{t} - 8.76 \frac{P}{P_o} + 4.08 \quad (3.135)$$

The trend in Equation 3.135 shows that for the frame specimens, larger ductility ratios can be obtained when large D/t ratios were utilized. Equation 3.135 also shows that high axial loads cause a reduction in ductility. The comparison of the computational results from Equation 3.135 with the experimental results showed good agreement can be seen in Figure 3.119.

The summaries of the equations for ductility of the RCFT members are given in Table 3.15, including appropriate statistical information and bounds on the independent variables for all the equations based upon the range of values available from the experimental research.

3.12 Comparison of Damage Levels for RCFT Members

In the previous sections, the damage of RCFT members was quantified through deformation-based or energy-based damage indices. Equations were proposed to estimate the values of the damage indices in terms of fundamental parameters of RCFTs.

In this section, a parametric study is reported for the equations derived in Sections 3.2 to 3.10. Multiple specimens were generated and the damage indices were calculated for each specimen at different damage levels. Ductilities were also calculated for the specimens in the parametric study to help assess which members had ductile response in conjunction with the progression of damage. The characteristics and associated damage indices and ductility values are listed for all generated specimens in Appendix B.

The objective of the parametric study was to compare the effect of specific damage levels (e.g., concrete cracking vs. local buckling, etc.) relative to each other. This is performed using the equations or average values for the damage indices given in Tables 3.1 to 3.15. Each equation or average value found from the experimental results has bounds in terms of material properties (e.g., f_y , f'_c) or geometric properties (e.g., L/D , D/t). In generating multiple specimens, it was ensured to use common limits of material and geometric properties for the equation or average value of the damage index at each damage level. Therefore, the number of specimens generated for each graph shown within this parametric study depends on the common limits of the material or geometric properties, with more specimens being generated for situations in which the common limits encompassed a broader range of parameters. Note that each graph thus represents one subset of the parametric study, and has its own set of specimens associated with it, corresponding to its common limits. The specimen numbering is thus restarted for each graph, numbering from one to the number of specimens generated for that specific branch of the parametric study.

Recall that a deformation-based index value of 1.0 represents the damage type occurring at the peak load achieved in the corresponding experimental tests upon which the damage index was based. An energy-based index value of 1.0 represents the damage type occurring at the final failure of the specimen, as defined for each type of structural component (i.e., typically the end of the experiment).

3.12.1 Monotonically Loaded Columns

For monotonically loaded columns, the parametric study was completed for both deformation-based ($D^{RCFT_Col_m}$) and energy-based ($E^{RCFT_Col_m}$) damage indices. The main parameters used for the generating multiple specimens were L/D , D/t , f'_c , and f_y .

The parametric study performed for the deformation-based damage index is presented in Figure 3.120. It was found that the damage levels including steel yielding and concrete crushing often take place sequentially. Both of the damage levels were found to have an average damage index value of approximately 0.50. Local buckling is the latest damage level for most of the cases. However, for the specimens having thin-walled and high strength steel tubes (specimens 15 and 16), local buckling was also observed to occur at approximately the same time with steel yielding. The specimens having large D/t ratio and/or high strength concrete were found to have low ductility values (e.g., less than 2.0; see Table B1 in Appendix B). These specimens usually fail abruptly soon after concrete crushing or local buckling.

The results from the parametric study of the energy-based damage index are shown in Figure 3.121. If the damage index values at steel yielding, concrete crushing, and local buckling are compared, it can be seen that the specimens with small D/t ratios (e.g., specimens 1 through 4 and 9 through 12) undergo a significant amount of damage prior to the initiation of local buckling. This is due to the fact that local buckling is delayed if the specimens have low D/t ratios. The value of the damage index at local buckling varies from 0.15 for specimens with large D/t ratios to 0.74 for specimens with small D/t ratios. The damage index at initiation of concrete crushing has values ranging from 0.006 up to 0.31. The range of the damage index values at steel yielding was similar to concrete crushing showing that the specimens often have significant reserve strength following concrete crushing and steel yielding. This is consistent with the conclusions drawn in Figure 3.120. The majority of the specimens exhibited ductility levels above 3.0. Therefore, the specimens retained significant strength following the damage levels of steel yielding, concrete crushing and even local buckling. It can be seen from Table B2 of Appendix B that for low values of D/t ratios and low material strengths, the specimens can attain very high ductility levels up to 8.0.

3.12.2 Monotonically Loaded Beam-Columns

The monotonically loaded beam-column tests were divided into three groups according to their loading setup. Therefore, the parametric study was completed for deformation-based ($D^{RCFT_Bc_m}$) and energy-based ($E^{RCFT_Bc_m}$) damage indices of each group of specimens.

Figure 3.122 shows the comparison of deformation-based damage index for the specimens with MI type loading. In Figure 3.122, concrete cracking is shown to be the first damage level to occur, with a maximum d_{cr}/d_o value of 0.45. Following concrete cracking, compression flange yielding and tension flange yielding occur sequentially for the majority of the specimens, and tension flange yielding typically either occurs close to when or after the peak load of the specimen is reached. The parametric study for local buckling of the compression flange can only be compared with tension flange yielding because the bounds of the equation to estimate d_{lb}/d_o given in Table 3.3 match only with the bounds of the tension flange yielding data available. According to Figure 3.123, the deformation-based damage index for local buckling of the compression flange attains values ranging from 1.68 to 2.25. For all of the specimens, the damage index values at local buckling are greater than the average value of the damage index at tension flange yielding. The sequence of the damage levels did not cause a significant impact on the reserve strength of the specimens. As can be seen in Figure 3.122 and in Table B3 of Appendix B, slender specimens with low eccentricity were found to attain the lowest ductility values. In Figure 3.122, it was also found that for the specimens with high values of ductility, compression flange yielding usually takes place prior to the peak load being attained. This trend confirms that flexural action improves the deformation capacity of the specimens. If the MI type specimens have L/D values less than 14, the ductility was found to improve as the L/D of the specimens gets smaller. This trend is evident in Table B4 of Appendix B. Compared to their slender counterparts presented in Figure 3.122, the specimens having L/D ratios less than 14 attained larger ductility values, which can be seen in Figure 3.123.

The results of the parametric study of the energy-based damage indices for MI type specimens are presented in Figures 3.124 and 3.125. In Figure 3.124, it can be seen that the damage index values of tension flange yielding are often larger than compression flange yielding. The specimens were also found to have significant damage by the time tension flange yielding occurred. The amount of damage at compression steel yielding was larger than concrete cracking for majority of the specimens. However, it was also found that for the specimens with low L/D and e/D ratios, the amount of damage at initiation of concrete cracking might exceed the initiation of yielding of the compression flange. In Figure 3.125, the energy-based damage index values at damage levels of local buckling of the compression flange and tension flange yielding are compared. A similar result as in Figure 3.123 was obtained, and it also may be concluded that local buckling of the compression flange occurs at a larger damage level than tension flange yielding for the range of parameters studied. The specimens having similar damage index values at steel yielding and at local buckling were found to have more reserve strength compared to the others. Figure 3.124 and Table B5 of Appendix B indicate that slender specimens having low eccentricity usually have lower ductility. A similar trend can also be seen in Figure 3.125 and Table B6 for short specimens. Figure 3.124 also shows that if steel yielding in tension and compression are delayed, these specimens usually have lower ductility. The effect of local buckling on the ductility of the specimens can be seen in Figure 3.125. It was found that the specimens can undergo significant deformation even after local buckling takes place.

The deformation-based damage indices for the MII type specimens are compared in Figure 3.126 and Table B7. According to Figure 3.126, when local buckling of the steel tube web takes place, the beam-column specimens attain their most damaged state with an average damage index value of 2.47. If the axial load level acting on the specimens is low, compression steel yielding or tension steel yielding are the damage levels occurring first. For the specimens having high axial compressive loads, local buckling might precede both compression flange yielding and tension flange yielding. The value of the damage index at tension flange yielding can reach up to 1.59 under high axial compressive load levels, clearly showing the effects of the axial compression on delaying tensile yielding after the peak load level in many cases. In contrast, the

maximum value of the damage index at compression flange yielding is 0.92. The value of the damage index at local buckling of the compression flange attains an average value of 0.72. All the specimens generated for the parametric study are expected to show ductile behavior with d_u/d_y ratios that can reach up to 16, which indicates that the specimens still have considerable reserve strength after the occurrence of the local damage. However, as seen in Figure 3.126 and Table B7, the specimens that had occurrence of early local buckling clearly exhibit lower ductility as compared to those specimens that have local buckling delayed.

Figure 3.127 exhibits the parametric study prepared for the energy-based damage index values of the MII type beam-column specimens at specific damage levels. According to Figure 3.127 and Table B8, for the majority of the specimens, local buckling of the steel tube web occurs last. If the specimens have low axial load ratios, yielding of the compression flange occurs first. It can also be seen from Figure 3.127 that it is common for local buckling of the compression flange to take place at a lower damage index value than the other damage levels if the axial load ratio is high. All of the damage indices being relatively low as compared to 1.0 indicates that these specimens have significant reserve energy absorption capacity after these damage levels take place. It can also be seen from Figure 3.127 and Table B8 that the MII type beam-column specimens have considerable ductility. All of the specimens presented in Figure 3.127 have ductility values above 6.0.

The parametric study of the deformation-based damage index for the MIII type beam-column specimens is shown in Figure 3.128 and Table B9. Figure 3.128 indicates that local buckling of the steel tube web is the latest damage level to be observed for the specimens. The damage index at local buckling of the steel tube web can reach up to 2.0. The first damage level to be expected was determined as concrete cracking. The parametric study also showed that for all the specimens, yielding in the compression flange precedes yielding in the tension flange. The ductility levels of the specimens in Figure 3.128 and Table B9 tend to decrease if the specimens experiences concrete crushing before local buckling of the compression flange. The specimens in the database exhibited an almost constant damage index value of 0.88 for concrete crushing.

The energy-based damage index of the MIII type specimens was investigated through the parametric study presented in Figure 3.129 and Table B10. Figure 3.129 shows that the occurrence of local damage varies considerably with the specimen parameters. The damage index at initiation of concrete cracking and yielding of compression flange have average values of 0.031 and 0.052,, respectively, indicating that the specimens had significant reserve strength after concrete cracking or yielding of compression flange initiated. The average damage index at concrete crushing was found to be smaller than tension flange yielding. This might be attributed to the fact that the axial load acting on the specimens delays tension flange yielding. Either local buckling of the steel tube web or flange occurred last. The specimens in Figure 3.129 achieved high ductility unless the axial load level is high or the D/t ratio is large, as seen in Table B10. Therefore, the local damage levels were deteriorating the capacity of the specimens with high axial loads or thin-walled tubes more significantly. In Figure 3.129, it can be seen that if local buckling of the specimens takes place before yielding of the tension flange, the ductility decreases significantly.

3.12.3 Cyclically Loaded Beam-Columns

The parametric study of the cyclically loaded beam-columns was completed for only the energy-based damage index ($E^{RCFT_Bc_c}$). The specimens for the parametric study were generated using the parameters including P/P_o , L/D , D/t , f_y and f'_c .

As seen in Figure 3.130 and Table B11, concrete cracking is the earliest damage level to be observed in cyclically loaded beam-columns, with the value of the damage index reaching only as high as 0.010 for the specimens in within the range of the study shown in Figure 3.130. This indicates significant reserve strength in the RCFT beam-columns after concrete cracking. Concrete cracking is followed by compression flange yielding, tension flange yielding, local buckling of the steel tube flange and local buckling of the steel tube web. Local buckling of the steel tube web takes place the last, with the damage index attaining an average value of 0.48. The ductility levels calculated for the specimens in Figure 3.130 and Table B11 show that as long as the specimens do

not have high axial load and large D/t ratios, even after local buckling of web, the specimens still have significant reserve strength.

3.12.4 Monotonically Loaded Panel Zones

For the panel zone specimens, deformation-based ($D^{RCFT_Pz_m}$) and energy-based ($E^{RCFT_Pz_m}$) damage indices were both investigated. The main variables in the parametric study were selected as L_p/D , D/t , f_y and f'_c .

The result of the parametric study for the deformation-based damage index at specific damage levels is given in Figure 3.131. Among the damage levels reported for panel zones, concrete cracking represents a low level of damage, with an average damage index value of 0.14 occurs very early in the loading history but also that it has little impact on the panel zone response. The average values of the damage indices at yielding and local buckling of the steel tube were 0.70 and 0.25, respectively. Figure 3.131 shows that concrete crushing is the latest damage type to occur, with the average value of the damage index equaling 0.82, indicating that all damage levels occur pre-peak. The specimens having high axial load ratio and thin-walled steel tubes were found to have little reserve strength following concrete crushing. The ductility values presented in Figure 3.131 and Table B12 illustrate that once steel tube yielding and concrete crushing damage levels are delayed, a decreasing trend in ductility is evident. Due to high level of axial load applied to the specimens, the ductility values were less than 4.0 for the majority of the specimens.

The energy-based damage index for the panel-zone was also investigated for multiple specimens. Figure 3.132 and Table B13 show the comparison of the damage index values at specific damage levels. According to the results given in Figure 3.132, the initiation of damage occurs at relatively low energy levels for all damage indices. The latest damage level to be observed is concrete crushing with a maximum damage index value of 0.12. Since the specimens in Figure 3.132 were generated with respect to a constant high level of axial load, the ductility of the specimens in Figure 3.132 was found to be relatively less. However, it was found that even under high axial load levels, the specimens still have the ability to undergo inelastic deformation and keep their

available strength as long as the steel tube has a low L_p / D and a large P_c / P_o ratio. The ductility of the specimens exhibited a similar trend as in Figure 3.131. It was found that the ductility values did not reach to the levels of beam-column tests. This can be attributed to the high level of axial load acting on the specimens. In addition, the ductility of the specimens in Figure 3.132 and Table B13 also showed a decreasing trend if the occurrences of the damage levels concrete crushing and steel yielding are delayed.

3.12.5 Monotonically Loaded Pinned Connections

There were four types of pinned connections, designated as PCIIa, PCIIb, PCIIa and PCIIb in the pinned-connection database, as described in Chapter 2. However, due to the limitations in the available data from the tests, the damage assessment of only PCIIb, PCIIa, and PCIIb type connections was performed in Section 3.6. Therefore, the parametric study in this section can only be made for these types of connections. Also in Section 3.6, the damage assessment of PCIIb and PCIIa type connections were performed together and in this section the parametric study of PCIIb and PCIIa type connections was also made together and the main variables were selected as e/D and P/V . For the PCIIa type connections, the only variable for the parametric study was d_g/D . The parametric studies were performed for both deformation-based ($D^{RCFT-Pc-m}$) and energy-based ($E^{RCFT-Pc-m}$) damage indices and the limits for the material and geometric properties given in Tables 3.8 and 3.9 were taken into consideration.

The d_{cr}/d_o and E_{cr}/E_{total} values for PCIIb type connections were calculated for only two specimens using the extreme values of the main variable d_g/D . The variation of d_{cr}/d_o and E_{cr}/E_{total} can be seen in Figures 3.133 and 3.134, respectively, and Table B14. According to these figures, d_{cr}/d_o varies from 0.046 to 0.38 and E_{cr}/E_{total} varies from 0.13 to 0.18. The decreasing trend in Figures 3.133 and 3.134 is attributed to the decrease in the damage level for the specimens having high d_g/D ratios. It should also be noted that the ductility of the PCIIb type specimens generated for the parametric could not be calculated since PCIIb type specimens were generated with respect to the parameter d_g/D which is not alone sufficient to calculate ductility. However, the PCIIb type specimens in the database all had hardening type of post-peak response with considerable ductility.

The parametric study for the PC1b and PC11a specimens was also conducted for both energy-based and deformation-based damage indices. Figures 3.135 and 3.136 and Table B15 show the variation of the d_{cy}/d_o and E_{cy}/E_{total} over the specimens generated for the parametric study. The values of d_{cy}/d_o range from 0.21 to 0.60, while E_{cy}/E_{total} takes values between 0.08 and 0.50. The values of d_{cy}/d_o and E_{cy}/E_{total} exhibit an increasing trend in Figures 3.135 and 3.136, respectively. This is due to the fact that the damage level at compression flange yielding gets larger when the main variables e/D and P/V increase. The ductility of the specimens in Figures 3.135 and 3.136 could not be evaluated since there were not any post-peak data available for the PC1b and PC11a specimens in the database to derive any formulation to compute ductility approximately.

3.12.6 Monotonically Loaded Moment Connections

For the monotonically-loaded moment connections only the variation of energy-based ($E^{RCFT_Mc_m}$) damage indices was investigated. Figure 3.137 shows the histogram of the energy-based damage index at specific damage levels. From Figure 3.137, it can be concluded that the majority of the damage levels, including concrete cracking, compression flange yielding, and tension flange yielding, occur very early in the load history, because the maximum value of the damage index in the aforementioned damage levels does not exceed 0.1. The monotonically-loaded moment connections have concrete crushing taking place in the beam-column of the connection assembly at a later stage of loading, with the average value of the damage index at concrete crushing being 0.21. However, the ductility of the specimens was usually satisfactory and significant reserve strength exists in these specimens relative to all of the damage levels.

3.12.7 Cyclically Loaded Moment Connections

The parametric study of cyclically loaded moment-connections was conducted for the energy-based damage index ($E^{RCFT_Mc_c}$), with the primary variables being P/P_o , d_g/d , P_g/P_o , D/t , f_y , and f'_c . Multiple specimens were generated based on the ranges of the parameters given in Table 3.11.

Figure 3.138 and Table B16 exhibits the variation of the energy-based damage index for the specimens used in the parametric study. The damage levels of concrete cracking, tension flange yielding, compression flange yielding, and concrete cracking at the panel zone all has damage index values below 0.1 or equal to 0.1. The most delayed damage state of the specimens was local buckling of the compression flange, or the steel tube yielding in shear at the panel zone. The maximum damage levels reached at the time of local buckling of compression flange and panel zone yielding were 0.37 and 0.48, respectively, thus exhibiting only moderate reserve strength thereafter. The ductility of specimens did not exhibit a significant variation. For the majority of the specimens, the ductility was ranging from 2.5 to 3.0.

3.12.8 Monotonically Loaded Frame Tests

The parametric study of the monotonically loaded frames was performed for both deformation-based ($E^{RCFT_Fr_m}$) and energy-based ($E^{RCFT_Fr_m}$) damage indices. The main parameters in the parametric study were chosen as D/t , f_y and f'_c . Figures 3.139 and Figure 3.140 show the variation of deformation-based and energy-based damage indices, respectively.

Figure 3.139 and Table B17 indicate that that the majority of the damage levels, including concrete cracking, compression flange yielding, tension flange yielding and local buckling of the compression flange, take place sequentially in the pre-peak response. Concrete cracking was the first damage level to be observed, with an average value of d_{cr}/d_o of 0.069. After concrete cracking, yielding at the compression flange initiates, with the damage index having an average value of 0.20. Yielding of the compression flange is followed by either tension flange yielding or compression flange local buckling. For the specimens with high D/t ratios, local buckling of the compression flange precedes yielding of the tension flange; otherwise, tension flange yielding takes place earlier. The maximum values of the damage indices attained by tension flange yielding and local buckling of the compression flange were 0.46 and 0.37, respectively. Local buckling of the steel tube web is the latest damage level to be observed with an average d_{bw}/d_o value of 1.61.

The result of the parametric study of the energy-based damage index is shown in Figure 3.140 and Table B18. From Figure 3.140, it can be concluded that RCFT frame specimens exhibit a very ductile response, since the value of the damage index attained for most of the damage types occurring during pre-peak response do not exceed 0.1. Local buckling of the steel tube web was found to be the latest observed during the experiments. The average value of the E_{lbw}/E_{total} was 0.57.

The ductility of the specimens in Figures 3.139 and 3.140 were all found to be satisfactory. Therefore, the damage levels defined for the monotonic beam-column tests do not deteriorate the reserved strength of the specimens.

3.12.9 Cyclically Loaded Frame Tests

In the parametric study of the cyclic frame tests, the main variables were chosen as P/P_o , D/t , f'_c and f_y . According to the limits given in Table 3.14, multiple specimens were generated and the energy-based damage index was evaluated at specific damage levels for each specimen. The results from the parametric study are presented in Figure 3.141.

From Figure 3.141 and Table B19, it can be seen that local buckling of the compression flange occurs latest, with the value of the damage index reaching up to 0.30. The other damage levels including concrete cracking, compression flange yielding, tension flange yielding, have damage index values less than 0.10. The frame specimens having high axial load levels do not retain significant reserve strength following the occurrence of the damage levels defined for them. As can be seen in Figure 3.141 and Table B19, the specimens subjected to high axial load levels attain poor ductility values of around 1.1.

Table 3.1: Deformation-Based Damage Functions for Monotonically Loaded Columns

| Type of Member | Damage Level | <u>Equation for Deformation -Based Damage Index</u> | <u>Range of Parameters</u> [L/D ; D/t ; f'_c ; f_y ; P_c/P_o] | <u>Statistics</u> [N ; R^2 ; μ ; σ] | <u>Researchers</u> |
|------------------------------|--------------------------|---|---|--|--|
| Monotonically Loaded Columns | Steel Yielding | <i>for $L/D \leq 4$</i> $D_y^{RCFT_Col_m} = 0.61 \frac{P_s}{P_o} + 0.044$ | <i>for $L/D \leq 4$</i> [2.0-4.2; 15.0-74.0; 19.8-119.0; 194.2-835.0; 0.16-0.86] | <i>for $L/D \leq 4$</i> [55; 0.51; 0.38; 0.15] | <i>for $L/D \leq 4$</i> Tomii and Sakino, 1979a; Grauers, 1993; Bergmann, 1994; Inai and Sakino, 1996; Schneider, 1998; Nakahara and Sakino, 1998. |
| | | <i>for $L/D \geq 15$</i> $D_y^{RCFT_Col_m} = 1.76 \frac{P_s}{P_o} - 0.26$ | <i>for $L/D \geq 15$</i> [15.0-23.0; 20.3-36.6; 31.10-92.40; 290.0-413.0; 0.25-0.65] | <i>for $L/D \geq 15$</i> [5; 0.97; 0.76; 0.33] | <i>for $L/D \geq 15$</i> Bridge, 1976; Shakir-Khalil and Zeghiche, 1989; Shakir-Khalil and Mouli, 1990; Bergmann, 1994. |
| | Concrete Crushing | <i>for $L/D \leq 5$</i> $D_{cc}^{RCFT_Col_m} = 1.03 \frac{P_c}{P_o} + 0.20$ | <i>for $L/D \leq 5$</i> [2.0-5.6; 15.0-74.0; 20.6-119.0; 194.2-835.0; 0.16-0.86] | <i>for $L/D \leq 5$</i> [68; 0.51; 0.67; 0.27] | <i>for $L/D \leq 5$</i> Tomii and Sakino, 1979, Grauers, 1993; Bergmann, 1994; Inai and Sakino, 1996; Schneider, 1998; Nakahara and Sakino, 1998. |
| | | <i>for $L/D \geq 15$</i> $D_{cc}^{RCFT_Col_m} = 1.0$ | <i>for $L/D \geq 15$</i> [15.4, 22.2; 28.6, 36.6; 92.4; 412.6, 413.0; 0.60, 0.65] | <i>for $L/D \geq 15$</i> [2; 1.0; 1.0; 0] | <i>for $L/D \geq 15$</i> Bergmann, 1994. |
| | Local Buckling | $D_{lb}^{RCFT_Col_m} = 2.68 \times \left(\frac{D}{t} \sqrt{\frac{f_y}{E_s}} \right)^{-1.02}$ | [3.0-12.0; 17.0-74.0; 19.8-119.0; 194.2-835; 0.14-0.81] $\frac{D}{t} \sqrt{\frac{f_y}{E_s}} : 0.70-3.83$ | [39, 0.55, 1.83, 0.76] | Liu and Goel, 1987; Lu and Kennedy, 1992; Tomii and Sakino, 1979; Inai and Sakino, 1996; Nakahara and Sakino, 1998; Varma, 2000; Chung et al., 2001. |

Table 3.2: Energy-Based Damage Functions for Monotonically Loaded Columns

| Type of Member | Damage Level | Equation for Energy -Based Damage Index | Range of Parameters [L/D; D/t; f _c ; f _y ; P _c /P _o] | Statistics [N; R ² ; μ; σ] | Researchers |
|------------------------------|--------------------------|--|---|--|--|
| Monotonically Loaded Columns | Steel Yielding | $E_{cy}^{RCFT-Col-m} = 0.20 \frac{P_s}{P_o} + 0.021 \frac{L}{D} - 0.17$ | [3.0-23.0; 15.0-73.7; 19.8-103.0; 194.2-835.0; 0.16-0.65] | [52; 0.55; 0.050; 0.14] | Bridge, 1976; Tomii and Sakino, 1979; Grauers, 1993; Bergmann, 1994; Inai and Sakino, 1996; Schneider, 1998; Nakahara and Sakino, 1998; Varma, 2000. |
| | Concrete Crushing | $E_c^{RCFT-Col-m} = 0.28 \frac{P_c}{P_o} + 0.022 \frac{L}{D} - 0.14$ | [2.0-22.2; 15.0-74.0; 20.6-119.0; 194.2-835.0; 0.19-0.86] | [56; 0.73; 0.092; 0.098] | Tomii and Sakino, 1979; Grauers, 1993; Bergmann, 1994; Inai and Sakino, 1996; Schneider, 1998; Nakahara and Sakino, 1998. |
| | Local Buckling | $E_{lb}^{RCFT-Col-m} = 0.50 \left(\frac{D}{t} \sqrt{\frac{f_y}{E_s}} \right)^{-1.04}$ | [3.0-12.0; 17.0-74.0; 19.8-119.0; 194.2-835.0; 0.14-0.81] $\frac{D}{t} \sqrt{\frac{f_y}{E_s}} : 0.70-3.83$ | [38, 0.41, 0.36, 0.22] | Lu and Kennedy, 1992; Tomii and Sakino, 1979; Inai and Sakino, 1996; Nakahara and Sakino, 1998; Varma, 2000; Chung et al., 2001. |

Table 3.3: Deformation-Based Damage Functions for Monotonically Loaded Beam-Columns

| Type of Member | Damage Level | Equation for Deformation-Based Damage Index | Range of Parameters [P/P_o ; L/D ; D/t ; f'_c ; f_y ; P_c/P_o] | Statistics [N ; R^2 ; μ ; σ] | Researchers |
|-----------------------------------|--------------------------------|--|--|---|---|
| Monotonically Loaded Beam-Columns | Concrete Cracking | <u>MI Type Loading:</u> $D_{cr}^{RCFT-Bc-m} = -1.02 \frac{e}{D} - 3.74 \frac{P_c}{P_o} + 1.76$ | <u>MI Type Loading:</u> [NA; 23.0-35.0; 16.0-30.0; 38.8-43.0; 343.3-386.3; 0.30-0.37] $e/D : 0.20-0.50$ | <u>MI Type Loading:</u> [4; 0.90; 0.16; 0.21] | <u>MI Type Loading:</u> Shakir-Khalil and Zeghiche, 1989; Shakir-Khalil, 1994. |
| | | <u>MIII Type Loading:</u> $D_{cr}^{RCFT-Bc-m} = 0.42 \frac{P_c}{P_o} + 1.13 \frac{P}{P_o} - 0.38$ | <u>MIII Type Loading:</u> [0.19-0.43; 5.0; 34.2-50.0; 110.0; 259.0-560.0; 0.61-0.78] | <u>MIII Type Loading:</u> [8; 0.95; 0.22; 0.12] | <u>MIII Type Loading:</u> Varma, 2000. |
| | Yielding of Compression Flange | <u>MI Type Loading:</u> for $e/D < 0.2$ $D_{cy}^{RCFT-Bc-m} = 0.035 \frac{L}{D} + 0.021 \frac{D}{t} - 0.31$ | <u>MI Type Loading:</u> [NA; 10.5-26.6; 15.0-31.3; 30.0-103.0; 291.0-439.0; 0.20-0.63] $e/D : 0.08-0.19$ | <u>MI Type Loading:</u> [15; 0.41; 0.88; 0.36] | <u>MI Type Loading:</u> Bridge, 1976; Grauers, 1993. |
| | | <u>MI Type Loading:</u> for $e/D \geq 0.2$ $D_{cy}^{RCFT-Bc-m} = 0.026 \frac{L}{D} + 0.045 \frac{D}{t} - 1.03$ | <u>MI Type Loading:</u> [NA; 20.0-46.1; 16.0-30.0; 31.1-43.0; 254.0-386.0; 0.30-0.39] $e/D : 0.20-0.50$ | <u>MI Type Loading:</u> [7; 0.84; 0.71; 0.23] | <u>MI Type Loading:</u> Bridge, 1976; Shakir-Khalil and Zeghiche, 1989; Shakir-Khalil, 1994. |
| | | <u>MII Type Loading:</u> $D_{cy}^{RCFT-Bc-m} = -1.60 \frac{P}{P_o} - 2.47 \frac{P_s}{P_o} + 2.64$ | <u>MII Type Loading:</u> [0.20-0.50; 3.0; 23.5-45.5; 20.5-22.1; 290.4-315.9; 0.26-0.43] | <u>MII Type Loading:</u> [9; 0.86; 0.51; 0.29] | <u>MII Type Loading:</u> Sakino and Ishibashi, 1985. |
| | | <u>MIII Type Loading:</u> $D_{cy}^{RCFT-Bc-m} = -1.16 \frac{P}{P_o} - 0.97 \frac{P_s}{P_o} - 0.19 \frac{L}{D} + 1.95$ | <u>MIII Type Loading:</u> [0.00-0.62; 3.0-6.0; 23.5-52.6; 19.8-110.0; 194.2-660.0; 0.26-0.77] | <u>MIII Type Loading:</u> [28; 0.60; 0.41; 0.33] | <u>MIII Type Loading:</u> Tomii and Sakino, 1979a; Lu and Kennedy, 1992; Varma, 2000. |

Table 3.3: Deformation-Based Damage Functions for Monotonically Loaded Beam-Columns (cont'd)

| Type of Member | Damage Level | Equation for Deformation -Based Damage Index | Range of Parameters [P/P_o ; L/D ; D/t ; f'_c ; f_y ; P_s/P_o] | Statistics [N ; R^2 ; μ ; σ] | Researchers |
|-----------------------------------|----------------------------|--|--|---|---|
| Monotonically Loaded Beam-Columns | Yielding of Tension Flange | <u>MI Type Loading:</u> for $L/D \leq 15$ $D_{yt}^{RCFT-Bc-m} = 8.63 \frac{P_s}{P_o} - 1.88 \frac{e}{D} - 0.90$ | <u>MI Type Loading:</u> [NA; 2.8-14.1; 15.0-74.0; 25.4-92.0; 379.0-618.0; 0.20-0.78] $e/D : 0.08-0.93$ | <u>MI Type Loading:</u> [14; 0.68; 2.04; 1.78] | <u>MI Type Loading:</u> Grauers, 1993; Fujimoto et al., 1995. |
| | | <u>MI Type Loading:</u> for $L/D > 15$ $D_{ty}^{RCFT-Bc-m} = 3.04 \frac{P_s}{P_o} - 4.76 \frac{e}{D} + 0.99$ | <u>MI Type Loading:</u> [NA; 23.0-46.1; 15.0-30.0; 38.0-103.0; 323.0-439.0; 0.24-0.61] $e/D : 0.17-0.50$ | <u>MI Type Loading:</u> [15; 0.57; 1.78; 0.57] | <u>MI Type Loading:</u> Shakir-Khalil and Zeghiche, 1989; Shakir-Khalil, 1994. |
| | | <u>MII Type Loading:</u> $D_{ty}^{RCFT-Bc-m} = 1.47 \frac{P}{P_o} - 5.28 \frac{P_s}{P_o} + 3.85$ | <u>MII Type Loading:</u> [0.20-0.61; 3.0; 23.5-45.5; 20.5-22.1; 290.4-315.9; 0.26-0.37] | <u>MII Type Loading:</u> [11; 0.70; 0.94; 0.46] | <u>MII Type Loading:</u> Sakino and Ishibashi, 1985. |
| | | <u>MIII Type Loading:</u> $D_{ty}^{RCFT-Bc-m} = 1.52 \frac{P}{P_o} - 0.21 \frac{P_s}{P_o} - 0.034 \frac{L}{D} + 0.59$ | <u>MIII Type Loading:</u> [0.00-0.43; 3.0-9.0; 17.0-52.6; 19.8-110.0; 194.2-660.0; 0.28-0.77] | <u>MIII Type Loading:</u> [31; 0.60; 0.75; 0.54] | <u>MIII Type Loading:</u> Tomii and Sakino, 1979a; Lu and Kennedy, 1992; Varma et al., 2002. |
| | Concrete Crushing | <u>MIII Type Loading:</u> $D_{cc}^{RCFT-Bc-m} = 0.88$ | <u>MIII Type Loading:</u> [0.00-0.40; 3.0-8.6; 17.0-64.7; 40.5-119.0; 259.0-781.0; 0.28-0.85] | <u>MIII Type Loading:</u> [26; NA; 0.88; 0.18] | <u>MIII Type Loading:</u> Lu and Kennedy, 1992; Nakahara and Sakino, 1998; Varma et al., 2002. |

Table 3.3: Deformation-Based Damage Functions for Monotonically Loaded Beam-Columns (cont'd)

| Type of Member | Damage Level | Equation for Deformation -Based Damage Index | Range of Parameters [P/P_o ; L/D ; D/t ; f'_c ; f_y ; P_c/P_o] | Statistics [N ; R^2 ; μ ; σ] | Researchers |
|-----------------------------------|-------------------------------------|--|---|---|--|
| Monotonically Loaded Beam-Columns | Local Buckling of Steel Tube Flange | <u>MI Type Loading:</u> $D_{lb_f}^{RCFT-Bc-m} = -0.42 \frac{e}{D} - 0.047 \frac{L}{D} + 2.51$ | <u>MI Type Loading:</u> [NA; 4.0-18.0; 39.1; 94.0; 443.0; 0.66] $e/D : 0.16-0.49$ | <u>MI Type Loading:</u> [7; 0.53; 1.81; 0.37] | <u>MI Type Loading:</u> Chung et al., 2001. |
| | | <u>MII Type Loading:</u> $D_{lb_f}^{RCFT-Bc-m} = -3.68 \frac{P}{P_o} - 3.11 \frac{P_s}{P_o} + 3.97$ | <u>MII Type Loading:</u> [0.00-0.52; 1.0-3.0; 23.5-45.4; 20.5-45.3; 194.2-315.8; 0.30-0.74] | <u>MII Type Loading:</u> [32; 0.42; 1.00; 0.92] | <u>MII Type Loading:</u> Tomii and Sakino, 1979b; Sakino and Ishibashi, 1985. |
| | | <u>MIII Type Loading:</u> $D_{lb_f}^{RCFT-Bc-m} = -15.64 \frac{P}{P_o} - 5.57 \frac{P_s}{P_o} - 3.47 \frac{L}{D} + 23.01$ | <u>MIII Type Loading:</u> [0.00-0.62; 3.0-5.0; 23.5-52.6; 19.8-110.0; 194.2-660.0; 0.26-0.67] | <u>MIII Type Loading:</u> [17; 0.69; 3.23; 4.09] | <u>MIII Type Loading:</u> Tomii and Sakino, 1979a; Varma, 2000. |
| | Local Buckling of Steel Tube Web | <u>MII Type Loading:</u> $D_{lb_w}^{RCFT-Bc-m} = -4.81 \frac{P}{P_o} - 10.49 \frac{P_s}{P_o} + 10.81$ | <u>MII Type Loading:</u> [0.20-0.50; 3.0; 23.5-45.4; 20.5-22.1; 290.4-315.9; 0.26-0.43] | <u>MII Type Loading:</u> [9; 0.62; 2.43; 1.24] | <u>MII Type Loading:</u> Sakino and Ishibashi, 1985. |
| | | <u>MIII Type Loading:</u> for $P/P_o < 0.40$ $D_{lb_w}^{RCFT-Bc-m} = 0.63 \frac{D}{t} \sqrt{\frac{f_y}{E_s}} + 0.33$ | <u>MIII Type Loading:</u> [0.19-0.39; 5.0; 34.3-52.6; 110.0; 471.0-660.0; 0.61-0.74] $\frac{D}{t} \sqrt{\frac{f_y}{E_s}} : 1.83-2.92$ | <u>MIII Type Loading:</u> [5; 0.46; 5; 1.94; 0.41] | <u>MIII Type Loading:</u> Tomii and Sakino, 1979a; Varma, 2002. |
| | | <u>MIII Type Loading:</u> for $P/P_o \geq 0.40$ $D_{lb_w}^{RCFT-Bc-m} = 1.88$ | <u>MIII Type Loading:</u> [0.41-0.59; 3.0-5.0; 33.4-52.6; 20.6-110.0; 288.4-660.0; 0.35-0.74] | <u>MIII Type Loading:</u> [5; NA; 1.88; 0.20] | <u>MIII Type Loading:</u> Tomii and Sakino, 1979a; Varma, 2002. |

Table 3.4: Energy-Based Damage Functions for Monotonically Loaded Beam-Columns

| Type of Member | Damage Level | Equation for Deformation - Based Damage Index | Range of Parameters [P/P_o ; L/D ; D/t ; f'_c ; f_y ; P/P_o] | Statistics [N ; R^2 ; μ ; σ] | Researchers |
|-----------------------------------|--------------------------------|--|--|---|--|
| Monotonically Loaded Beam-Columns | Concrete Cracking | <u>MI Type Loading:</u> $E_{cr}^{RCFT-Bc-m} = -1.40 \frac{P}{P_o} - 0.33 \frac{e}{D} + 0.64$ | <u>MI Type Loading:</u> [NA; 23.0-35.0; 16.0-30.0; 38.8-43.0; 343.3-386.3; 0.30-0.37] $e/D : 0.2-0.50$ | <u>MI Type Loading:</u> [4; 0.82; 0.059; 0.076] | <u>MI Type Loading:</u> Shakir-Khalil and Zeghiche, 1989; Shakir-Khalil, 1994. |
| | | <u>MIII Type Loading:</u> $E_{cr}^{RCFT-Bc-m} = -0.16 \frac{P}{P_o} + 0.11 \frac{P}{P_o} + 0.11$ | <u>MIII Type Loading:</u> [0.19-0.61; 5.0; 34.2-50.0; 110; 259.0-560.0; 0.61-0.78] | <u>MIII Type Loading:</u> [8, 0.44; 0.032; 0.027] | <u>MIII Type Loading:</u> Varma, 2000. |
| | Yielding of Compression Flange | <u>MI Type Loading:</u> $E_{cy}^{RCFT-Bc-m} = 0.49 \frac{e}{D} + 0.0092 \frac{D}{t} + 0.016 \frac{L}{D} - 0.49$ | <u>MI Type Loading:</u> [NA; 10.4-46.1; 15.0-31.3; 31.0-103.0; 254.0-439.0; 0.20-0.63] $e/D : 0.080-0.50$ | <u>MI Type Loading:</u> [23; 0.81; 0.19; 0.17] | <u>MI Type Loading:</u> Bridge, 1976; Shakir-Khalil and Zeghiche, 1989; Grauers, 1993; Shakir-Khalil, 1994. |
| | | <u>MII Type Loading:</u> $E_{cy}^{RCFT-Bc-m} = 0.068 \frac{D}{t} \sqrt{\frac{f_y}{E_s}} - 0.073 \frac{P}{P_o} - 0.014$ | <u>MII Type Loading:</u> [0.20-0.50; 3.0; 23.5-45.4; 20.5-22.1; 290.4-315.9; 0.26-0.43] $\frac{D}{t} \sqrt{\frac{F_y}{E_s}} : 0.94-1.73$ | <u>MII Type Loading:</u> [9; 0.60; 0.15; 0.11] | <u>MII Type Loading:</u> Sakino and Ishibashi, 1985. |
| | | <u>MIII Type Loading:</u> $E_{cy}^{RCFT-Bc-m} = 0.0038 \frac{L}{D} - 0.056 \frac{P}{P_o} - 0.046 \frac{P}{P_o} + 0.064$ | <u>MIII Type Loading:</u> [0.00-0.71; 3.0-6.0; 23.5-52.6; 19.8-110.0; 194.2-660.0; 0.26-0.78] | <u>MIII Type Loading:</u> [27; 0.38; 0.038; 0.027] | <u>MIII Type Loading:</u> Tomii and Sakino, 1979a; Lu and Kennedy, 1992; Varma, 2000. |

Table 3.4: Energy-Based Damage Functions for Monotonically Loaded Beam-Columns (cont'd)

| Type of Member | Damage Level | <u>Equation for Deformation - Based Damage Index</u> | <u>Range of Parameters</u> [P/P_o ; L/D ; D/t ; f'_c ; f_y ; P_c/P_o] | <u>Statistics</u> [N ; R^2 ; μ ; σ] | <u>Researchers</u> |
|--|-----------------------------------|---|---|---|---|
| Monotonically Loaded Beam-Columns | Yielding of Tension Flange | <u>MI Type Loading:</u> $E_{yt}^{RCFT_Bc_m} = 0.16 \frac{e}{D} + 0.47 \frac{P_s}{P_o} + 0.011 \frac{L}{D} - 0.18$ | <u>MI Type Loading:</u> [NA; 3.0-34.5; 15.0-74.9; 25.4-103.0; 261.9-618.0; 0.20-0.78] e/D : 0.17-0.93 | <u>MI Type Loading:</u> [27; 0.70; 0.31; 0.23] | <u>MI Type Loading:</u> Shakir-Khalil and Zeghiche, 1989; Grauers, 1993; Shakir-Khalil, 1994; Fujimoto et al., 1995. |
| | | <u>MII Type Loading:</u> $E_{yt}^{RCFT_Bc_m} = 0.62 \frac{P}{P_o} - 0.16 \frac{P_s}{P_o} + 0.039$ | <u>MII Type Loading:</u> [0.20-0.61; 3.0; 23.5-45.4; 20.5-22.1; 290.4-315.9; 0.26-0.43] | <u>MII Type Loading:</u> [11; 0.60; 0.15; 0.11] | <u>MII Type Loading:</u> Sakino and Ishibashi, 1985. |
| | | <u>MIII Type Loading:</u> $E_{yt}^{RCFT_Bc_m} = 0.024 \frac{P_s}{P_o} + 1.07 \frac{P}{P_o} + 0.045 \frac{L}{D} - 0.26$ | <u>MIII Type Loading:</u> [0.00-0.71; 3.0-6.0; 23.5-52.6; 19.8-110.0; 194.2-660.0; 0.26-0.78] | <u>MIII Type Loading:</u> [28; 0.57; 0.25; 0.32] | <u>MIII Type Loading:</u> Tomii and Sakino, 1979a; Lu and Kennedy, 1992; Varma, 2000. |
| | Concrete Crushing | <u>MIII Type Loading:</u> $E_{cc}^{RCFT_Bc_m} = -0.25 \frac{P}{P_o} - 1.11 \frac{P_c}{P_o} - 0.034 \frac{L}{D} + 1.22$ | <u>MIII Type Loading:</u> [0.00-0.43; 3.0-9.0; 17.0-64.7; 40.5-119.0; 259.0-781.0; 0.15-0.72] | <u>MIII Type Loading:</u> [26; 0.76; 0.33; 0.26] | <u>MIII Type Loading:</u> Lu and Kennedy, 1992; Nakahara and Sakino, 1998; Varma, 2000. |

Table 3.4: Energy-Based Damage Functions for Monotonically Loaded Beam-Columns (cont'd)

| Type of Member | Damage Level | Equation for Deformation -Based Damage Index | Range of Parameters [P/P_o ; L/D ; D/t ; f'_c ; f_y ; P_c/P_o] | Statistics [N ; R^2 ; μ ; σ] | Researchers |
|-----------------------------------|--|---|--|---|--|
| Monotonically Loaded Beam-Columns | Local Buckling of Steel Tube Flange | <u>MI Type Loading:</u> for $e/D = 0.16$ $E_{lbf}^{RCFT-Bc-m} = 0.031 \frac{L}{D} - 0.027$ | <u>MI Type Loading:</u> [NA; 8.0-18.0; 39.1; 94.0; 443; 0.66] $e/D : 0.16$ | <u>MI Type Loading:</u> [3; 0.99; 0.37; 0.16] | <u>MI Type Loading:</u> Chung et al., 2001. |
| | | <u>MI Type Loading:</u> for $e/D = 0.49$ $E_{lbf}^{RCFT-Bc-m} = 0.039 \frac{L}{D} + 0.041$ | <u>MI Type Loading:</u> [NA; 4.0-18.0; 39.1; 94.0; 443; 0.66] $e/D : 0.49$ | <u>MI Type Loading:</u> [4; 0.76; 0.45; 0.26] | <u>MI Type Loading:</u> Chung et al., 2001. |
| | | <u>MII Type Loading:</u> $E_{lbf}^{RCFT-Bc-m} = -0.41 \frac{P}{P_o} - 0.32 \frac{P_s}{P_o} + 0.46$ | <u>MII Type Loading:</u> [0.00-0.52; 2.0-6.0; 23.5-45.4; 20.5-45.3; 194.2-315.8; 0.30-0.74] | <u>MII Type Loading:</u> [32; 0.41; 0.12; 0.097] | <u>MII Type Loading:</u> Tomii and Sakino, 1979b; Sakino and Ishibashi, 1985. |
| | | <u>MIII Type Loading:</u> $E_{lbf}^{RCFTBc-m} = 0.015 \frac{L}{D} - 0.25 \frac{D}{t} \sqrt{\frac{f_y}{E_s}} - 0.75 \frac{P}{P_o} + 0.97$ | <u>MIII Type Loading:</u> [0.00-0.62; 3.0-5.0; 23.5-52.6; 19.8-110.0; 194.2-560.0; 0.26-0.78] $\frac{D}{t} \sqrt{\frac{f_y}{E_s}} : 0.84-2.92$ | <u>MIII Type Loading:</u> [20; 0.55; 0.39; 0.24] | <u>MIII Type Loading:</u> Tomii and Sakino, 1979a; Varma, 2000. |

Table 3.4: Energy-Based Damage Functions for Monotonically Loaded Beam-Columns (cont'd)

| Type of Member | Damage Level | Equation for Deformation -Based Damage Index | Range of Parameters [P/P_o ; L/D ; D/t ; f_c ; f_y ; P_c/P_o] | Statistics [N ; R^2 ; μ ; σ] | Researchers |
|-----------------------------------|----------------------------------|--|---|---|--|
| Monotonically Loaded Beam-Columns | Local Buckling of Steel Tube Web | <p><u>MII Type Loading:</u> for $P / P_o < 0.40$</p> $E_{lbw}^{RCFT-Bc-m} = -0.75 \frac{P_s}{P_o} + 0.84$ | <p><u>MII Type Loading:</u> [0.20-0.30; 3.0; 23.5-45.4; 20.5-22.1; 290.4-315.9; 0.26-0.43]</p> | <p><u>MII Type Loading:</u> [5; 0.59; 0.35; 0.080]</p> | <p><u>MII Type Loading:</u> Sakino and Ishibashi, 1985.</p> |
| | | <p><u>MII Type Loading:</u> for $P / P_o \geq 0.40$</p> $E_{lbw}^{RCFT-Bc-m} = 1.03 \frac{P_s}{P_o} - 0.34$ | <p><u>MII Type Loading:</u> [0.50; 3.0; 23.5-45.4; 20.5-22.1; 290.4-315.9; 0.26-0.43]</p> | <p><u>MII Type Loading:</u> [3; 0.90; 0.32; 0.090]</p> | <p><u>MII Type Loading:</u> Sakino and Ishibashi, 1985.</p> |
| | | <p><u>MIII Type Loading:</u></p> $E_{lbw}^{RCFT-Bc-m} = 0.25 \frac{D}{t} \sqrt{\frac{f_y}{E_s}} + 1.42 \frac{P}{P_o} - 0.38$ | <p><u>MIII Type Loading:</u> [0.19-0.59; 3.0-5.0; 33.4-52.6; 20.6-110.0; 288.4-660.0; 0.35-0.74]</p> $\frac{D}{t} \sqrt{\frac{f_y}{E_s}} : 1.25-2.92$ | <p><u>MIII Type Loading:</u> [10; 0.38; 0.64; 0.24]</p> | <p><u>MIII Type Loading:</u> Tomii and Sakino, 1979a; Varma, 2000.</p> |

Table 3.5: Energy-Based Damage Functions for Cyclically Loaded Beam-Columns

| Type of Member | Damage Level | Equation for Energy-Based Damage Index | Range of Parameters [P/P_o ; L/D ; D/t ; f'_c ; f_y ; P_c/P_o] | Statistics [N ; R^2 ; μ ; σ] | Researchers |
|--------------------------------|--------------------------------|--|---|--|-------------------------------------|
| Cyclically Loaded Beam-Columns | Concrete Cracking | $E_{cr}^{RCFT_Bc_c} (\%) = 3.21 \frac{P}{P_o} + 0.30 \frac{P_c}{P_o} - 0.52$ | [0.10-0.41; 5.0-7.0; 18.9-52.6; 39.0-110.0; 269.0-825.0; 0.17-0.78] | [40; 0.53; 0.59; 0.53] | Fujimoto et al., 1996; Varma, 2000. |
| | Yielding of Compression Flange | $E_{cy}^{RCFT_Bc_c} = -0.15 \frac{P}{P_o} + 0.11 \frac{P_s}{P_o} + 0.038$ | [0.10-0.41; 5.0-7.0; 18.9-52.6; 39.0-110.0; 269.0-825.0; 0.22-0.83] | [40; 0.56; 0.041; 0.023] | Fujimoto et al., 1996; Varma, 2000. |
| | Yielding of Tension Flange | for $P/P_o \leq 0.20$ $E_{yt}^{RCFT_Bc_c} = 0.56 \frac{P_s}{P_o} - 0.059$ | [0.10-0.21; 5.0; 34.3-52.6; 110.0; 269.0-660.0; 0.60-0.77] | [16; 0.66; 0.11; 0.050] | Varma, 2000. |
| | | for $P/P_o > 0.20$ $E_{yt}^{RCFT_Bc_c} = 0.24 \frac{P_s}{P_o} - 0.024$ | [0.37-0.41; 6.0-7.1; 18.9-46.7; 39.2-94.5; 276.0-825.0; 0.17-0.78] | [24; 0.56; 0.11; 0.060] | Fujimoto et al., 1996. |
| | Concrete Crushing | $E_{cc}^{RCFT_Bc_c}$ | NA | NA | NA |

Table 3.5: Energy-Based Damage Functions for Cyclically Loaded Beam-Columns (cont'd)

| Type of Member | Damage Level | Equation for Energy-Based Damage Index | Range of Parameters [P/P_o ; L/D ; D/t ; f'_c ; f_y ; P_c/P_o] | Statistics [N ; R^2 ; μ ; σ] | Researchers |
|--------------------------------|--|--|--|--|------------------------|
| Cyclically Loaded Beam-Columns | Local Buckling of Steel Tube Flange | for $P/P_o \leq 0.20$ $E_{lb_f}^{RCFT - Bc - c} = -0.067 \frac{D}{t} \sqrt{\frac{f_y}{E_s}} + 0.32$ | [0.10-0.21; 5.0; 34.3-52.6; 110.0; 269.0-660.0; 0.60-0.77] $\frac{D}{t} \sqrt{\frac{F_y}{E_s}} : 1.31-2.92$ | [16; 0.38; 0.20; 0.081] | Varma, 2000. |
| | | for $P/P_o > 0.20$ $E_{lb_f}^{RCFT - Bc - c} = -0.20 \frac{D}{t} \sqrt{\frac{f_y}{E_s}} + 0.49$ | [0.37-0.41; 6.0-7.1; 18.9-46.7; 39.2-94.5; 276.0-825.0; 0.17-0.78] $\frac{D}{t} \sqrt{\frac{F_y}{E_s}} : 1.21-1.80$ | [22; 0.54; 0.19; 0.066] | Fujimoto et al., 1996. |
| | Local Buckling of Steel Tube Web $E_{lb_w}^{RCFT - Bc - c} = -0.24 \frac{D}{t} \sqrt{\frac{f_y}{E_s}} + 1.01$ | [0.10-0.21; 5.0; 34.3-52.6; 110.0; 269.0-660.0; 0.60-0.77] $\frac{D}{t} \sqrt{\frac{F_y}{E_s}} : 1.31-2.92$ | [15; 0.41; 0.51; 0.23] | Varma, 2000. | |

Table 3.6: Deformation-Based Damage Functions for Monotonically Loaded Panel Zones

| Type of Member | Damage Level | <u>Equation for Deformation-Based Damage Index</u> | <u>Range of Parameters</u> [P/P_o ; L_p/D ; D/t ; f'_c ; f_y ; P_c/P_o] | <u>Statistics</u> [N ; R^2 ; μ ; σ] | <u>Researchers</u> |
|----------------------------------|-------------------------------------|--|---|---|---|
| Monotonically Loaded Panel Zones | Concrete Cracking | $D_{cr}^{RCFT-Pz-m} = 0.050 \frac{P_c}{P_o} + 0.062 \frac{L_p}{D} - 0.031$ | [0.0-0.50; 1.0-3.0; 20.8-48.1; 24.5-57.1; 333.5-558.0; 0.28-0.57] | [14; 0.74; 0.088; 0.038] | Kamba et al., 1991; Ricles et al., 1995; Takemura et al., 1999. |
| | Steel Tube Yielding | $D_y^{RCFT-Pz-m} = 0.18 \frac{P_s}{P_o} + 0.37 \frac{L_p}{D} - 0.27$ | [0.0-0.50; 1.0-3.0; 20.8-48.1; 24.5-57.1; 333.5-558.0; 0.28-0.57] | [14; 0.67; 0.39; 0.22] | Kamba et al., 1991; Ricles et al., 1995; Takemura et al., 1999. |
| | Concrete Crushing | $D_c^{RCFT-Pz-m} = -0.48 \frac{P_c}{P_o} + 0.28 \frac{L_p}{D} + 0.38$ | [0.0-0.50; 1.0-3.0; 20.8-48.1; 24.5-57.1; 333.5-558.0; 0.28-0.57] | [12; 0.41; 0.70; 0.43] | Kamba et al., 1991; Ricles et al., 1995; Takemura et al., 1999. |
| | Local Buckling of Steel Tube | $D_{lb}^{RCFT-Pz-m} = 0.25$ | [0.5; 2.0, 3.0; 32.2-46.1; 39.0; 377.0, 412.0; 0.41-0.53] | [3; NA; 0.25; 0.001] | Ricles et al., 1995. |

Table 3.7: Energy-Based Damage Functions for Monotonically Loaded Panel Zones

| Type of Member | Damage Level | Equation for Energy-Based Damage Index | Range of Parameters [P/P_o ; L_p/D ; D/t ; f'_c ; f_y ; P_c/P_o] | Statistics [N ; R^2 ; μ ; σ] | Researchers |
|----------------------------------|-------------------------------------|---|---|--|---|
| Monotonically Loaded Panel Zones | Concrete Cracking | $E_{cr}^{RCFT-Pz-m} = 0.0025 \frac{L_p}{D} + 0.0034 \frac{P_c}{P_o} - 0.0037$ | [0.0-0.50; 1.0-3.0; 20.8-48.1; 24.5-57.1; 333.5-558.0; 0.28-0.57] | [14; 0.87; 0.0017; 0.0014] | Kamba et al., 1991; Ricles et al., 1995; Takemura et al., 1999. |
| | Steel Tube Yielding | $E_y^{RCFT-Pz-m} = 0.020 \frac{P_s}{P_o} + 0.053 \frac{L_p}{D} - 0.058$ | [0.0-0.50; 1.0-3.0; 20.8-48.1; 24.5-57.1; 333.5-558.0; 0.28-0.57] | [14; 0.77; 0.037; 0.030] | Kamba et al., 1991; Ricles et al., 1995; Takemura et al., 1999. |
| | Concrete Crushing | $E_c^{RCFT-Pz-m} = -0.14 \frac{P_c}{P_o} + 0.060 \frac{L_p}{D} + 0.041$ | [0.0-0.50; 1.0-3.0; 20.8-48.1; 24.5-57.1; 333.5-416.0; 0.28-0.57] | [11; 0.53; 0.070; 0.045] | Kamba et al., 1991; Ricles et al., 1995; Takemura et al., 1999. |
| | Local Buckling of Steel Tube | $E_{lb}^{RCFT-Pz-m} = 0.011$ | [0.5; 2.0, 3.0; 32.2-46.1; 39.0; 377.0, 412.0; 0.41-0.53] | [3; NA; 0.011; 0.0010] | Ricles et al., 1995. |

Table 3.8: Deformation-Based Damage Functions for Monotonically Loaded Pinned-Connection Tests

| Type of Member | Damage Level | Equation for Deformation-Based Damage Index | Range of Parameters [P/P_o ; d_g/D ; L/D ; D/t ; f'_c ; f_y ; P_c/P_o] | Statistics [N ; R^2 ; μ ; σ] | Researchers |
|---|--------------------------------|--|--|--|---|
| Monotonically Loaded Pinned Connections | Concrete Cracking | <p>PCI Ib:</p> $D_{cr}^{RCFT-Pc-m} = 1.0048 \left(\frac{d_g}{D}\right)^{-3.70}$ | <p>PCI Ib:</p> <p>[0.16, 0.18; 1.3-2.3; 7.5; 25.0, 31.7; 34.7; 318.0, 336.0; 0.38, 0.43]</p> | <p>PCI Ib:</p> <p>[4; 0.84; 0.20; 0.23]</p> | <p>PCI Ib:</p> <p>France et al., 1998.</p> |
| | Yielding of Compression Flange | <p>PCI b, PCI Ia:</p> $D_{cy}^{RCFT-Pc-m} = 0.097 \frac{e}{D} + 0.042 \frac{P}{V} + 0.021$ | <p>PCI b, PCI Ia:</p> <p>[NA; 2.7; 18.7; 30.0; 29.6-34.3; 330.0-343.0; 0.37-0.41]</p> <p>e/D : 1.33-2.53 P/V : 1.5-8.0</p> | <p>PCI b, PCI Ia:</p> <p>[6; 0.77; 0.38; 0.16]</p> | <p>PCI b, PCI Ia:</p> <p>Shakir-Khalil and Al-Rawdan, 1995.</p> |

Table 3.9: Energy-Based Damage Functions for Monotonically Loaded Pinned-Connection Tests

| Type of Member | Damage Level | Equation for Energy-Based Damage Index | Range of Parameters [P/P_o ; d_g/D ; L/D ; D/t ; f'_c ; f_y ; P_c/P_o] | Statistics [N ; R^2 ; μ ; σ] | Researchers |
|---|--------------------------------|--|--|--|---|
| Monotonically Loaded Pinned Connections | Concrete Cracking | <p>PCI Ib:</p> $E_{cr}^{RCFT-Pc-m} = 0.22 \left(\frac{d_g}{D}\right)^{-6.09}$ | <p>PCI Ib:</p> <p>[0.16, 0.18; 1.3-2.3; 7.5; 25.0, 31.7; 34.7; 318.0, 336.0; 0.38, 0.43]</p> | <p>PCI Ib:</p> <p>[4; 0.97; 0.016; 0.020]</p> | <p>PCI Ib:</p> <p>France et al., 1998.</p> |
| | Yielding of Compression Flange | <p>PCI b, PCI Ia:</p> $E_{cy}^{RCFT-Pc-m} = 0.053 \frac{e}{D} + 0.055 \frac{P}{V} - 0.077$ | <p>PCI b, PCI Ia:</p> <p>[NA; 2.7; 18.7; 30.0; 29.6-34.3; 330.0-343.0; 0.37-0.41]</p> <p>e/D : 1.33-2.53 P/V : 1.5-8.0</p> | <p>PCI b, PCI Ia:</p> <p>[6; 0.79; 0.24; 0.17]</p> | <p>PCI b, PCI Ia:</p> <p>Shakir-Khalil and Al-Rawdan, 1995.</p> |

Table 3.10: Energy-Based Damage Functions for Monotonically Loaded Moment Connection Tests

| Type of Member | | Damage Level | Equation for Energy-Based Damage Index | Range of Parameters [P/P_o ; L/D ; D/t ; f'_c ; f_y ; P_c/P_o] | Statistics [N ; R^2 ; μ ; σ] | Researchers |
|---|-------------------|--------------------------------|--|---|--|----------------------|
| Monotonically Loaded Moment Connections | RCFT Beam- Column | Concrete Cracking | $E_{cr}^{RCFT_Mc_m} = 0.000073$ | [0.12, 0.14; 7.5; 20; 40.4; 329.0, 427.0; 0.26, 0.31] | [2; NA; 0.000073; 0.000005] | France et al., 1998. |
| | | Yielding of Compression Flange | $E_{cy}^{RCFT_Mc_m} = 0.0051$ | [0.12, 0.14; 7.5; 20; 40.4; 329.0, 427.0; 0.26, 0.31] | [2; NA; 0.0051; 0.00071] | France et al., 1998. |
| | | Yielding of Tension Flange | $E_{yt}^{RCFT_Mc_m} = 0.016$ | [0.12, 0.14; 7.5; 20; 40.4; 329.0, 427.0; 0.26, 0.31] | [2; NA; 0.016; 0.00097] | France et al., 1998. |
| | | Concrete Crushing | $E_c^{RCFT_Mc_m} = 0.21$ | [0.12, 0.14; 7.5; 20; 40.4; 329.0, 427.0; 0.26, 0.31] | [2; NA; 0.21; 0.023] | France et al., 1998. |
| | Panel Zone | Concrete Cracking | $E_{cr}^{RCFT_Mc_m} = 0.00029$ | [0.12, 0.14; 7.5; 20; 40.4; 329.0, 427.0; 0.26, 0.31] | [2; NA; 0.00029; 0.000032] | France et al., 1998. |

Table 3.11a: Energy-Based Damage Functions for Cyclically Loaded Moment Connection Tests

| Type of Member | | Damage Level | Equation for Energy-Based Damage Index | Range of Parameters [P/P_o ; L/D ; D/t ; f'_c ; f_y ; P_c/P_o] | Statistics [N ; R^2 ; μ ; σ] | Researchers |
|--------------------------------------|------------------|--|--|---|--|---|
| Cyclically Loaded Moment Connections | RCFT Beam-Column | Concrete Cracking | $E_{cr}^{RCFT-Mc-c} = 0.040 \frac{P}{P_o} - 0.056 \frac{P_c}{P_o} + 0.026$ | [0.00-0.30; 9.0-12.0; 26.7-41.7; 30.1-49.6; 317.1-420.8; 0.36-0.52] | [9; 0.97; 0.0066; 0.0079] | Kanatani et al., 1987; Vermaas, 1995; Koester, 2000; Kawano and Matsui, 2000. |
| | | Yielding of Compression Flange | $E_{cy}^{RCFT-Mc-c} = -0.093 \frac{P}{P_o} - 0.042 \frac{P_s}{P_o} + 0.13$ | [0.00-0.30; 9.0-12.0; 26.7-41.7; 30.1-49.6; 317.1-420.8; 0.36-0.52] | [8; 0.65; 0.089; 0.018] | Kanatani et al., 1987; Vermaas, 1995; Koester, 2000; Kawano and Matsui, 2000. |
| | | Yielding of Tension Flange | $E_{yt}^{RCFT-Mc-c} = 0.20 \frac{P}{P_o} - 0.21 \frac{P_s}{P_o} + 0.19$ | [0.00-0.16; 9.0-12.0; 26.7-41.7; 31.1-49.6; 317.1-419.8; 0.42-0.52] | [6; 0.57; 0.091; 0.033] | Kanatani et al., 1987; Vermaas, 1995; Koester, 2000. |
| | | Local Buckling of Compression Flange of Steel Tube | $E_{lbf}^{RCFT-Mc-c} = -2.09 \frac{P_c}{P_o} + 1.12$ | [0.00-0.30; 9.0-10.0; 34.5, 41.7; 30.1-33.8; 419.9-420.9; 0.36-0.42] | [3; 0.98; 0.31; 0.061] | Kanatani et al., 1987; Kawano and Matsui, 2000. |

Table 3.11b: Energy-Based Damage Functions for Cyclically Loaded Moment Connection Tests

| Type of Member | | Damage Level | <u>Equation for Energy-Based Damage Index</u> | <u>Range of Parameters</u> [P/P_o ; L_p/D ; D/t ; f'_c ; f_y ; P_c/P_o] | <u>Statistics</u> [N ; R^2 ; μ ; σ] | <u>Researchers</u> |
|--------------------------------------|------------|---------------------|--|--|---|---|
| Cyclically Loaded Moment Connections | Panel Zone | Concrete Cracking | $E_{cr}^{RCFT-Mc-c} = 0.042 \frac{d_g}{D} + 0.00027 \frac{P_c}{P_o} - 0.053$ | [0.00-0.30; 1.40-1.67; 26.7-41.7; 30.1-49.6; 317.1-420.8; 0.36-0.52] | [9; 0.75; 0.0066; 0.0032] | Kanatani et al., 1987; Vermaas, 1995; Koester, 2000; Kawano and Matsui, 2000. |
| | | Steel Tube Yielding | $E_y^{RCFT-Mc-c} = 1.24 \frac{d_g}{D} + 0.72 \frac{P_s}{P_o} - 2.05$ | [0.00-0.30; 1.40-1.67; 26.7-41.7; 30.1-49.6; 317.1-420.8; 0.36-0.52] | [9; 0.80; 0.27; 0.18] | Kanatani et al., 1987; Vermaas, 1995; Koester, 2000; Kawano and Matsui, 2000. |

Table 3.11c: Energy-Based Damage Functions for Cyclically Loaded Moment Connection Tests

| Type of Member | | Damage Level | <u>Equation for Energy-Based Damage Index</u> | <u>Range of Parameters</u> [P/P_o ; d_g ; b_f ; t_w ; t_f ; f_{yw} ; f_{yf} ; P_g/P_o] | <u>Statistics</u> [N ; R^2 ; μ ; σ] | <u>Researchers</u> |
|--------------------------------------|--------------|------------------------|---|---|---|-------------------------------|
| Cyclically Loaded Moment Connections | Steel Girder | Girder Flange Yielding | $E_{gy}^{RCFT-Mc-c} = -0.65 \frac{P_g}{P_o} + 0.35$ | [0.00-0.16; 459.7-607.1; 154.9- 180.3; 9.14-10.9; 14.7-15.5; 341.9-379.2; 293.0-379.2; 0.31, 0.37] | [5; 0.67; 0.12; 0.022] | Vermaas, 1995; Koester, 2000. |
| | | Plastic Hinging | $E_{gp}^{RCFT-Mc-c} = -0.65 \frac{P_g}{P_o} + 0.43$ | [0.00-0.16; 459.7-607.1; 154.9- 180.3; 9.14-10.9; 14.7-15.5; 341.9-379.2; 293.0-379.2; 0.31, 0.37] | [5; 0.44; 0.19; 0.023] | Vermaas, 1995; Koester, 2000. |

Table 3.12: Deformation-Based Damage Functions for Monotonically Loaded Frames

| Type of Member | Damage Level | Equation for Deformation-Based Damage Index | Range of Parameters [P/P_o ; L/D ; D/t ; f'_c ; f_y ; P_c/P_o] | Statistics [N ; R^2 ; μ ; σ] | Researchers |
|-----------------------------|-------------------------------------|--|---|--|---------------|
| Monotonically Loaded Frames | Concrete Cracking | $D_{cr}^{RCFT_Fr_m} = 0.069$ | [0.30; 6.7; 46.9-65.2; 35.3-37.8; 287.4-288.4; 0.57-0.67] | [4; NA; 0.069; 0.0089] | Matsui, 1986. |
| | Yielding of Compression Flange | $D_{yc}^{RCFT_Fr_m} = 0.48 \frac{P_c}{P_o} - 0.10$ | [0.30; 6.7; 46.9-65.2; 35.3-37.8; 287.4-288.4; 0.57-0.67] | [4; 0.75; 0.20; 0.027] | Matsui, 1986. |
| | Yielding of Tension Flange | $D_{yt}^{RCFT_Fr_m} = 1.25 \frac{P_c}{P_o} - 0.38$ | [0.30; 6.7; 46.9-65.2; 35.3-37.8; 287.4-288.4; 0.57-0.67] | [4; 0.94; 0.39; 0.064] | Matsui, 1986. |
| | Concrete Crushing | $D_{cc}^{RCFT_Fr_m}$ | NA | NA | NA |
| | Local Buckling of Steel Tube Flange | $D_{lbf}^{RCFT_Fr_m} = -0.33 \frac{P_c}{P_o} + 0.56$ | [0.30; 6.7; 46.9-65.2; 35.3-37.8; 287.4-288.4; 0.57-0.67] | [4; 0.95; 0.34; 0.13] | Matsui, 1986. |
| | Local Buckling of Steel Tube Web | $D_{lbw}^{RCFT_Fr_m} = 1.60$ | [0.30; 6.7; 46.9-65.2; 35.3-37.8; 287.4-288.4; 0.57-0.67] | [3; NA; 1.60; 0.15] | Matsui, 1986. |

Table 3.13: Energy-Based Damage Functions for Monotonically Loaded Frames

| Type of Member | Damage Level | <u>Equation for Energy-Based Damage Index</u> | <u>Range of Parameters</u> [P/P_o ; L/D ; D/t ; f_c ; f_y ; P_o/P_o] | <u>Statistics</u> [N ; R^2 ; μ ; σ] | Researchers |
|-----------------------------|-------------------------------------|--|---|---|---------------|
| Monotonically Loaded Frames | Concrete Cracking | $E_{cr}^{RCFT_Fr_m} = 0.0031$ | [0.30; 6.7; 46.9-65.2; 35.3-37.8; 287.4-288.4; 0.57-0.67] | [4; NA; 0.0031; 0.00044] | Matsui, 1986. |
| | Yielding of Compression Flange | $E_{yc}^{RCFT_Fr_m} = 0.025$ | [0.30; 6.7; 46.9-65.2; 35.3-37.8; 287.4-288.4; 0.57-0.67] | [4; 0.56; 0.025; 0.0026] | Matsui, 1986. |
| | Yielding of Tension Flange | $E_{yt}^{RCFT_Fr_m} = 0.087$ | [0.30; 6.7; 46.9-65.2; 35.3-37.8; 287.4-288.4; 0.57-0.67] | [4; NA; 0.087; 0.016] | Matsui, 1986. |
| | Concrete Crushing | $E_{cc}^{RCFT_Fr_m}$ | NA | NA | NA |
| | Local Buckling of Steel Tube Flange | $E_{lbf}^{RCFT_Fr_m} = -0.13 \frac{P_c}{P_o} + 0.17$ | [0.30; 6.7; 46.9-65.2; 35.3-37.8; 287.4-288.4; 0.57-0.67] | [4; 0.74; 0.077; 0.057] | Matsui, 1986. |
| | Local Buckling of Steel Tube Web | $E_{lbw}^{RCFT_Fr_m} = 0.57$ | [0.30; 6.7; 46.9-65.2; 35.3-37.8; 287.4-288.4; 0.57-0.67] | [3; NA; 0.57; 0.23] | Matsui, 1986. |

Table 3.14: Energy-Based Damage Functions for Cyclically Loaded Frames

| Type of Member | Damage Level | Equation for Energy-Based Damage Index | Range of Parameters [P/P_o ; L/D ; D/t ; f'_c ; f_y ; P_c/P_o] | Statistics [N ; R^2 ; μ ; σ] | Researchers |
|--------------------------------------|--------------------------------|--|--|--|------------------|
| Cyclically Loaded Moment Connections | Concrete Cracking | $E_{cr}^{RCFT-Fr-c} = 0.024 \frac{P}{P_o} - 0.0033 \frac{P_c}{P_o} - 0.0031$ | [0.15-50; 8.0; 21.6-55.2; 13.7-24.4; 155.2-493.3; 0.17-0.45] | [7; 0.77; 0.0021; 0.0034] | Kawaguchi, 2000. |
| | Yielding of Compression Flange | $P/P_o = 0.15$ $E_{cy}^{RCFT-Fr-c} = 0.070 \frac{P_s}{P_o} - 0.035$ | [0.15; 8.0; 21.6-55.2; 13.7- 18.6; 255.2-403.3; 0.18- 0.39] | [3; 0.82; 0.013; 0.0086] | Kawaguchi, 2000. |
| | | $P/P_o \geq 0.30$ $E_{cy}^{RCFT-Fr-c} = 0.028 \frac{P_s}{P_o} - 0.0063$ | [0.30-0.50; 8.0; 21.6-54.9; 13.7-24.4; 155.2-493.3; 0.17-0.45] | [4; 0.65; 0.012; 0.0043] | Kawaguchi, 2000. |
| | Yielding of Tension Flange | $E_{yt}^{RCFT-Fr-c} = 0.068$ | [0.15-0.50; 8.0; 21.6-55.2; 13.7-24.4; 155.2-493.3; 0.17-0.45] | [7; NA; 0.068; 0.048] | Kawaguchi, 2000. |
| | Local Buckling of Flange | $E_{lbf}^{RCFT-Fr-c} = 0.10 \frac{P}{P_o} + 0.25$ | [0.15-0.30; 8.0; 21.6; 17.8, 18.6; 403.3; 0.17-0.18] | [4; 0.96; 0.27; 0.0088] | Kawaguchi, 2000. |

Table 3.15: Summary of Equations to Calculate Ductility of RCFT Members

| Type of Member | <u>Equation for Ductility</u> | <u>Range of Parameters</u> [P/P_o ; L/D ; D/t ; f'_c ; f_y ; P_c/P_o] | <u>Statistics</u> [N ; R^2 ; μ ; σ] | <u>Researchers</u> |
|--|--|---|--|---|
| Monotonically Loaded Columns | <p>for $L/D < 12$</p> $\mu = -22.23 \frac{f'_c}{f_y} - 0.17 \frac{D}{t} + 3.59 \frac{L}{D} + 2.60 - \text{if } f'_c/f_y < 0.20$ $\mu = 1.84 - \text{if } f'_c/f_y \geq 0.20$ | <p>for $L/D < 12$ & $f'_c/f_y < 0.20$ [NA; 2.0-5.1; 15.0-50.8; 19.8-119.0; 194.2-835.0; 0.17-0.66]</p> <p>f'_c/f_y: 0.030-0.170</p> <p>for $L/D < 12$ & $f'_c/f_y \geq 0.20$ [NA; 2.0-5.6; 15.0-74.0; 80.0-119.0; 259.0-560.0; 0.20-0.86]</p> <p>f'_c/f_y: 0.196-0.425</p> | <p>for $L/D < 12$ & $f'_c/f_y < 0.20$ [48; 0.51; 7.70; 5.56]</p> <p>for $L/D < 12$ & $f'_c/f_y \geq 0.20$ [18; NA.; 1.84; 0.57]</p> | <p>for $L/D < 12$ & $f'_c/f_y < 0.20$ Tomii and Sakino, 1979a; Grauers, 1993; Inai and Sakino, 1996; Schneider, 1998; Nakahara and Sakino, 1998; Varma, 2000.</p> <p>for $L/D < 12$ & $f'_c/f_y \geq 0.20$ Grauers, 1993; Bergmann, 1994; Inai and Sakino, 1996; Nakahara and Sakino, 1998; Varma, 2000.</p> |
| | <p>for $L/D \geq 12$</p> $\mu = 0.13 \frac{L}{D} + 1.38 \frac{P_c}{P_o} + 1.20$ | <p>for $L/D \geq 12$ [NA; 12.0-30.0; 24.0, 39.1; 28.6-94.0; 357.5-443.0; 0.27-0.66]</p> | <p>for $L/D \geq 12$ [5; 0.90; 4.77; 0.93]</p> | <p>for $L/D \geq 12$ Shakir-Khalil and Mouli, 1990; Chung et al., 2001.</p> |
| Monotonically Loaded Beam-Columns | <p><u>MI Type Loading:</u></p> $\mu = -7.26 \frac{P_c}{P_o} + 4.72 \frac{e}{D} - 0.28 \frac{L}{D} + 12.68$ | <p>[NA; 2.8-37.0; 15.0-74.0; 25.4-103.0; 254.0-618.0; 0.20-0.78]</p> <p>e/D: 0.040-1.39</p> | <p>[56; 0.50; 6.31; 3.55]</p> | <p>Bridge, 1976; Shakir-Khalil and Zeghiche, 1989; Grauers, 1993; Shakir-Khalil, 1994; Fujimoto et al., 1995; Chung et al., 2001.</p> |
| | <p><u>MII Type Loading:</u></p> $\mu = -0.32 \frac{L}{D} - 3.78 \frac{P_c}{P_o} - 0.28 \frac{P}{P_o} + 23.24$ | <p>[0.00-0.50; 2.0-6.0; 23.5-45.5; 20.5-45.3; 194.2-315.9; 0.26-0.70]</p> | <p>[38; 0.53; 11.9; 3.70]</p> | <p>Tomii and Sakino, 1979b; Sakino and Ishibashi, 1985.</p> |
| | <p><u>MIII Type Loading:</u></p> $\mu = -4.73 \frac{P_c}{P_o} - 9.64 \frac{P}{P_o} + 9.93$ | <p>[0.00-0.58; 3.0-20.0; 17.0-64.7; 19.8-119.0; 194.2-781.0; 0.26-0.85]</p> | <p>[50; 0.53; 5.39; 2.24]</p> | <p>Tomii and Sakino, 1979a; Lu and Kennedy, 1992; Nakahara and Sakino, 1998; Varma, 2000.</p> |

Table 3.15: Summary of Equations to Calculate Ductility of RCFT Members (cont'd)

| Type of Member | <u>Equation for Deformation -Based Damage Index</u> | <u>Range of Parameters</u> [P/P_o ; L/D ; D/t ; f'_c ; f_y ; P_c/P_o] | <u>Statistics</u> [N ; R^2 ; μ ; σ] | <u>Researchers</u> |
|-------------------------------------|--|--|---|---|
| Cyclic Beam-Columns | $\mu = -7.12 \frac{P}{P_o} - 0.33 \frac{P_c}{P_o} + 5.48$ | [0.10-0.43; 4.9-7.1; 18.9-52.6; 39.2-110.1; 269.0-825.0; 0.17-0.78] | [20; 0.68; 3.18; 0.88] | Fujimoto et al., 1996; Varma, 2000. |
| Monotonic Panel Zones | $\mu = -28.44 \frac{P}{P_o} - 1.81 \frac{L_p}{D} + 23.96 \frac{P_c}{P_o} + 9.27$ | [0.00-0.50; 1.0-3.0; 20.8-48.1; 23.2-57.1; 333.5-416.0; 0.28-0.57] | [14; 0.88; 13.75; 6.78] | Kamba et al., 1991; Ricles et al., 1995; Takemura et al., 1999. |
| Monotonic Pinned Connections | $\mu = 959.13 \frac{d_g / D}{(D / t)^2} + 0.90$ | [0.16, 0.18; 7.5; 25.0, 31.7; 34.7; 318, 336; 0.38-0.43] $d_g/D : 1.26-2.25$ | [4; 0.57; 3.34; 1.06] | France et al., 1998. |
| Monotonic Moment Connections | $\mu = 5.80$ | [0.12, 0.14; 7.5; 20.0; 40.4; 329.0, 427.0; 0.26, 0.31] | [2; NA; 5.80; 0.56] | France et al., 1998. |

Table 3.15: Summary of Equations to Calculate Ductility of RCFT Members (cont'd)

| Type of Member | Equation for Ductility | Range of Parameters [P/P_o ; L/D ; D/t ; f'_c ; f_y ; P_c/P_o] | Statistics [N ; R^2 ; μ ; σ] | Researchers |
|---|---|--|---|---|
| Cyclically Loaded Moment Connections | $\mu = 1.06 \frac{P}{P_o} + 4.52 \frac{P_{go}}{P_o} - 1.118 \frac{P_c}{P_o} + 1.59$ | [0.00-0.30; 4.5-12.0; 26.7-41.7; 30.1-61.1; 317.1-420.8; 0.36-0.57] | [16; 0.73; 2.86; 0.83] | Kanatani et al., 1987; Vermaas, 1995; Koester, 2000; Kawano and Matsui, 2000; Peng, 2001. |
| Monotonically Loaded Frames | $\mu = -13.0 \frac{P_c}{P_o} + 14.1$ | [0..30; 6.7; 46.9-65.2; 35.3-37.8; 287.4-288.4; 0.57-0.67] | [4; 0.46; 6.1; 0.94] | Matsui, 1986. |
| Cyclically Loaded Frames | $\mu = 0.067 \frac{D}{t} - 8.76 \frac{P}{P_o} + 4.08$ | [0.15-0.50; 8.0; 21.6-55.2; 13.7-24.4; 155.2-493.3; 0.17-0.45] | [6; 0.92; 4.47; 1.60] | Kawaguchi, 2000. |

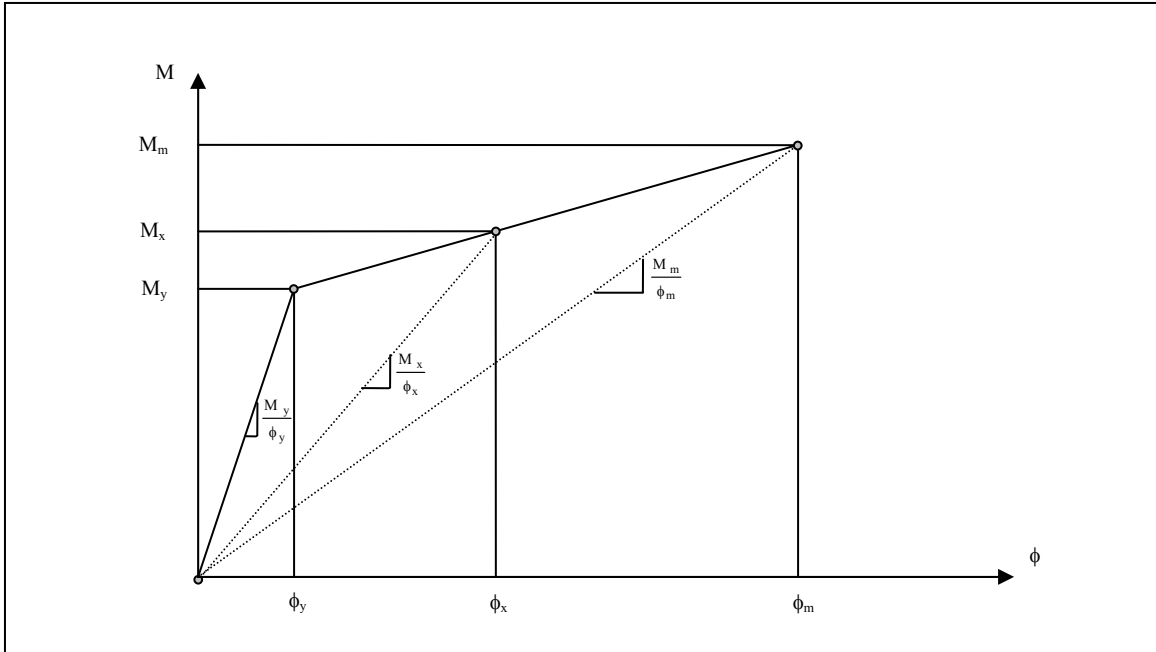


Figure 3.1: Definition of Flexural Damage Ratio by Roufaiel and Meyer (1987)

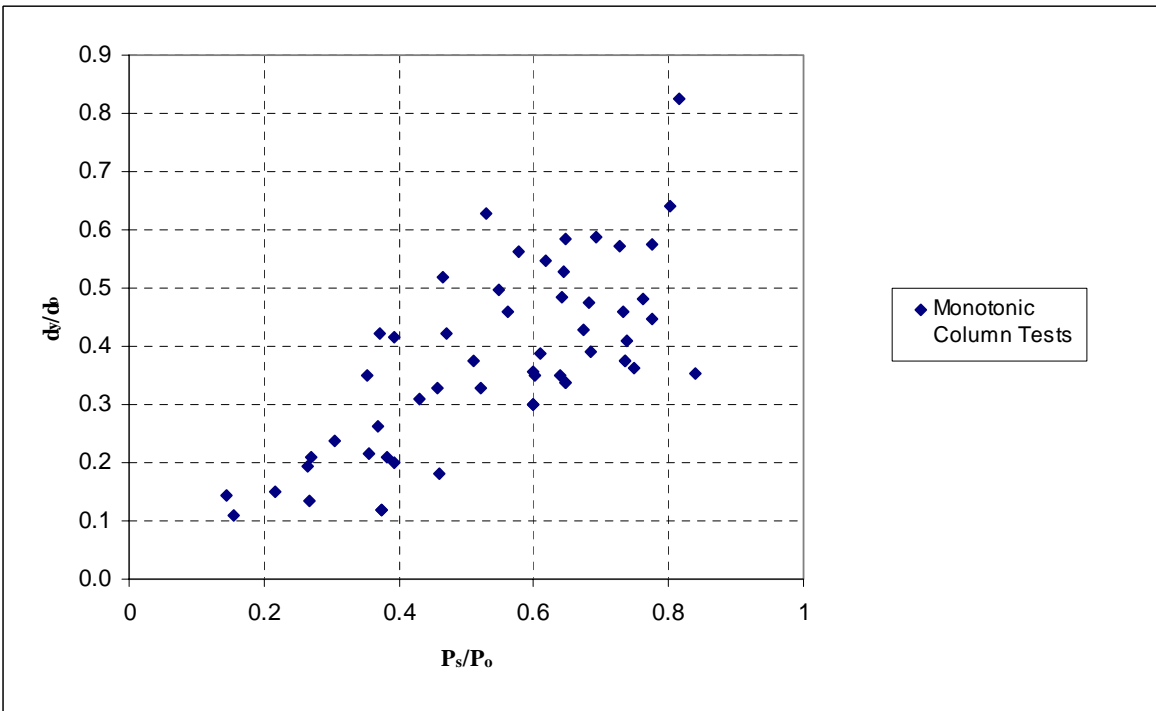


Figure 3.2: Comparison of d_y/d_o versus P_s/P_o : Monotonically-Loaded RCFT Column Tests for $L/D \leq 4$

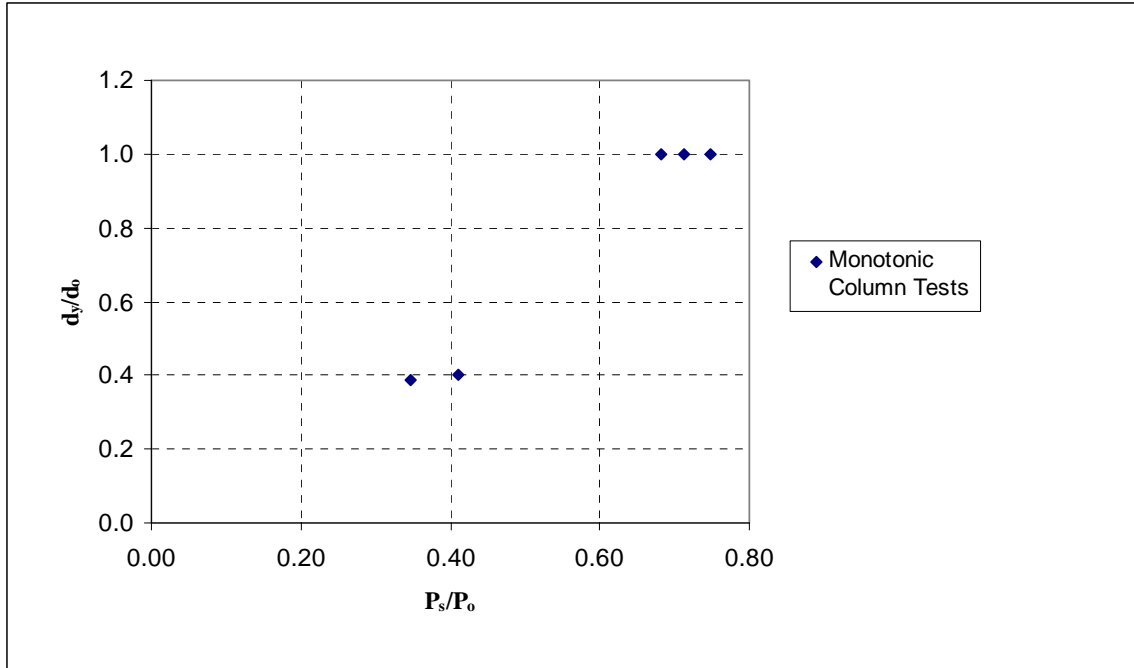


Figure 3.3: Comparison of d_y/d_o versus P_s/P_o : Monotonically-Loaded RCFT Column Tests for $L/D \geq 15$

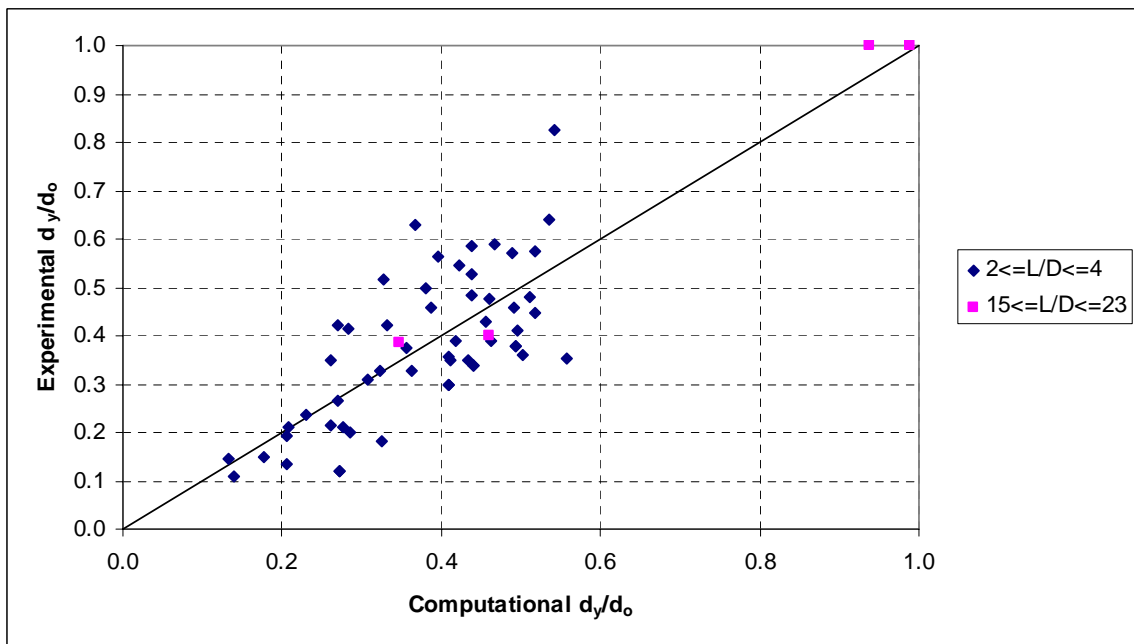


Figure 3.4: Comparison of Computational and Experimental Values of d_y/d_o : Monotonically-Loaded RCFT Column Tests

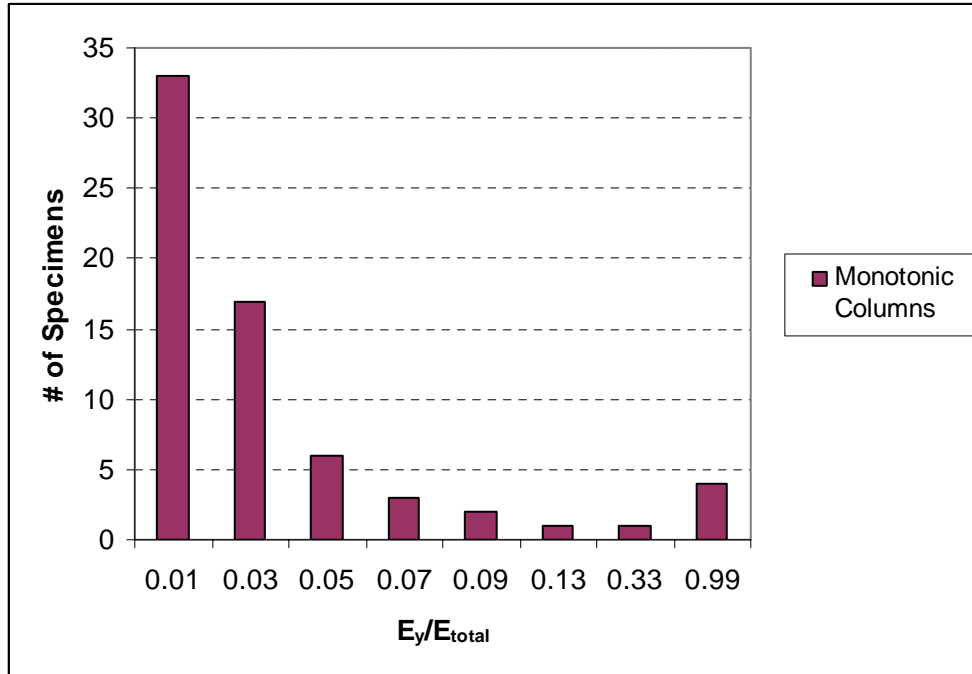


Figure 3.5: Histogram of E_y/E_{total} : Monotonically-Loaded RCFT Column Tests

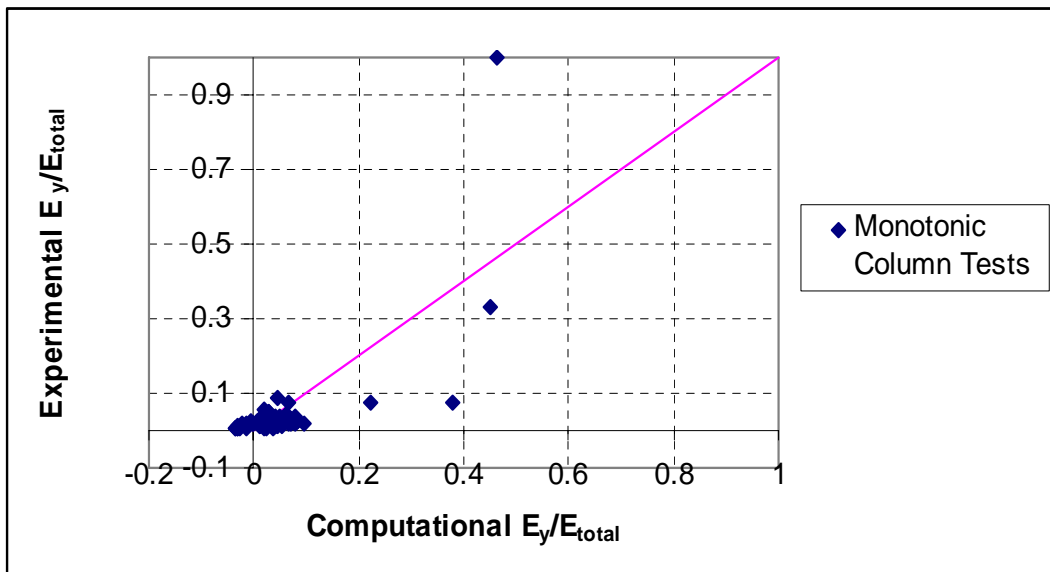


Figure 3.6: Comparison of Computational and Experimental E_y/E_{total} Values: Monotonically-Loaded RCFT Column Tests

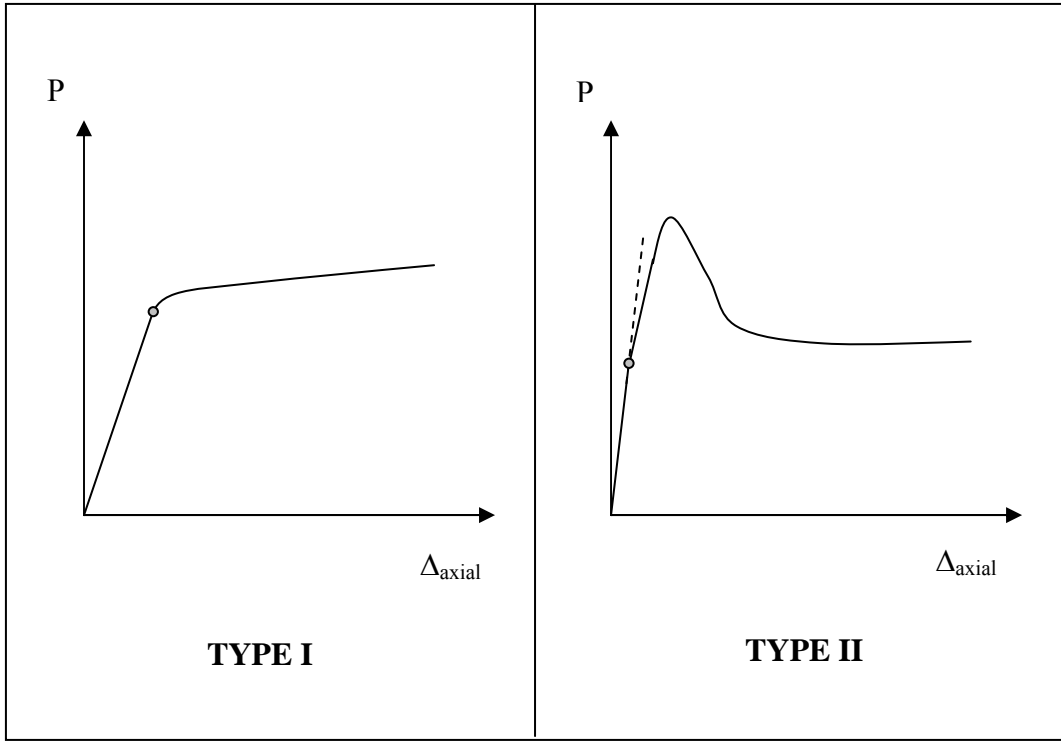


Figure 3.7: Load-Deflection Schemes: Monotonically-Loaded RCFT Column Tests

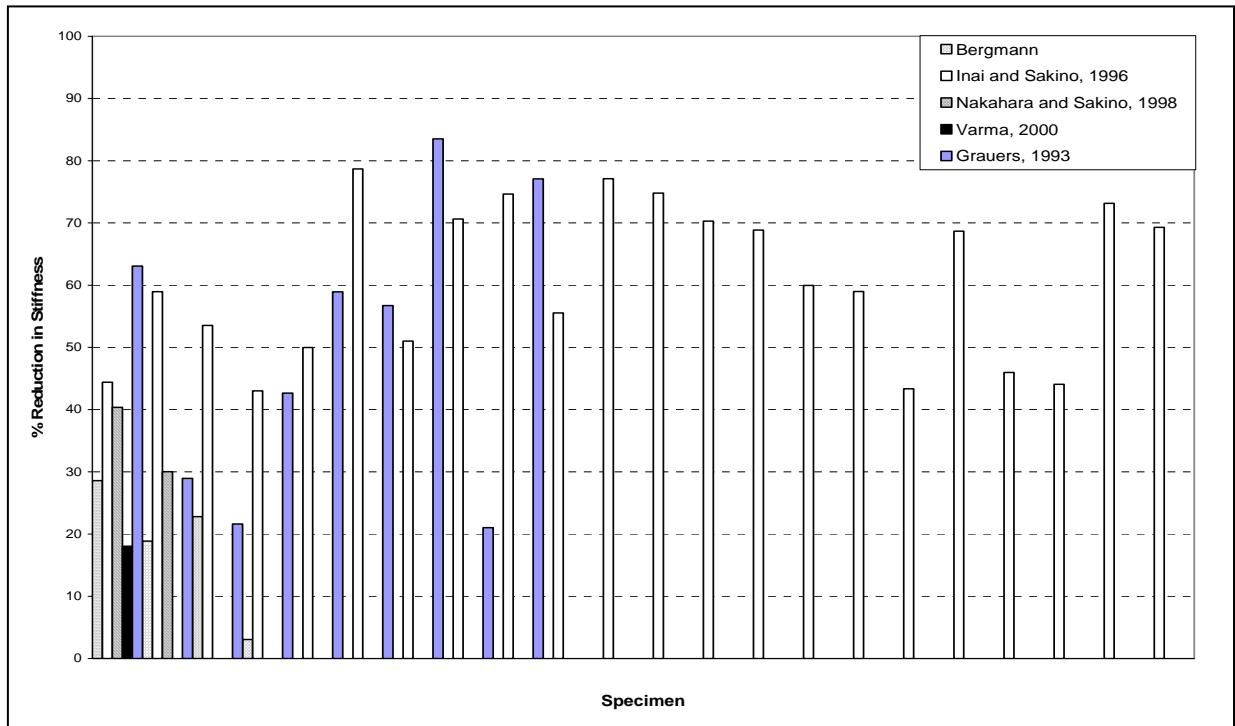


Figure 3.8: Reduction in Axial Stiffness (%): Monotonically-Loaded RCFT Column Specimens with Type II Load-Deflection Curve

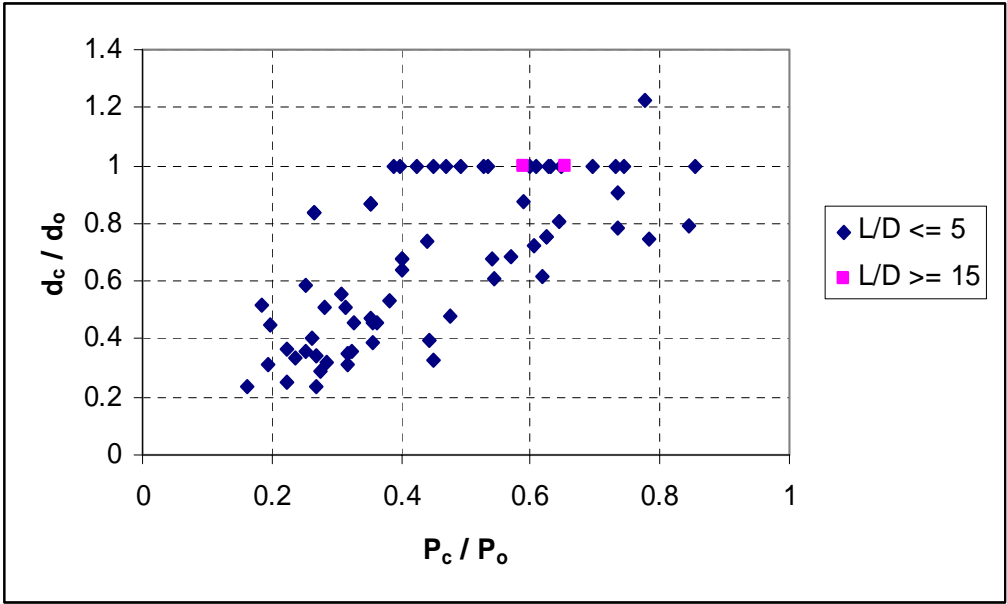


Figure 3.9: Comparison of d_c/d_o versus P_c/P_o : Monotonically-Loaded RCFT Column Tests

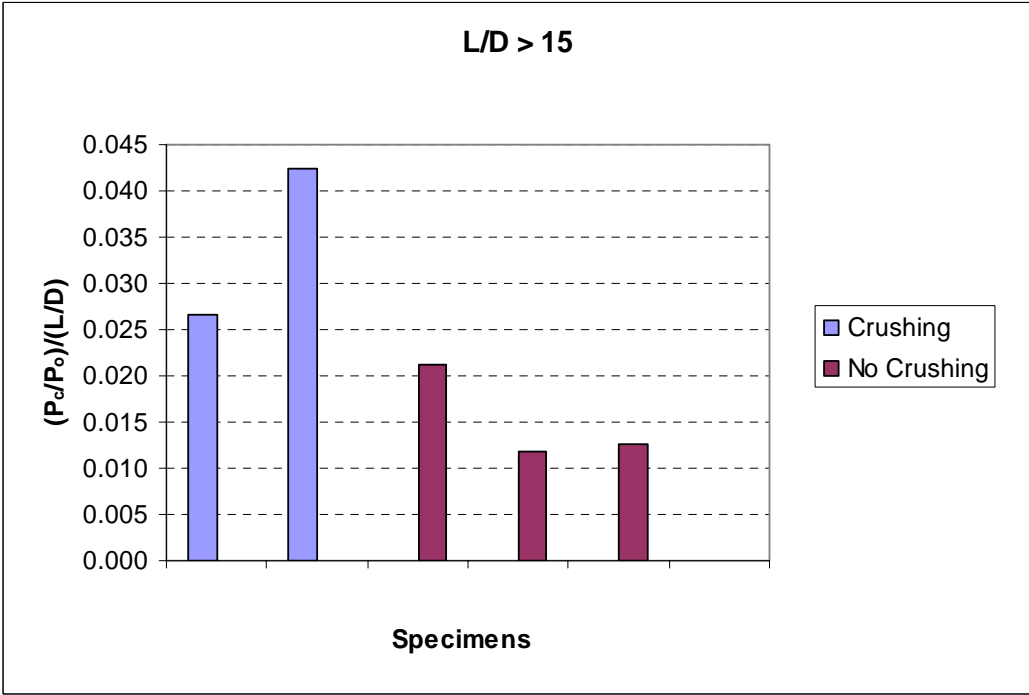


Figure 3.10: Histogram of $(P_c/P_o)/(L/D)$: Monotonically-Loaded RCFT Column Tests

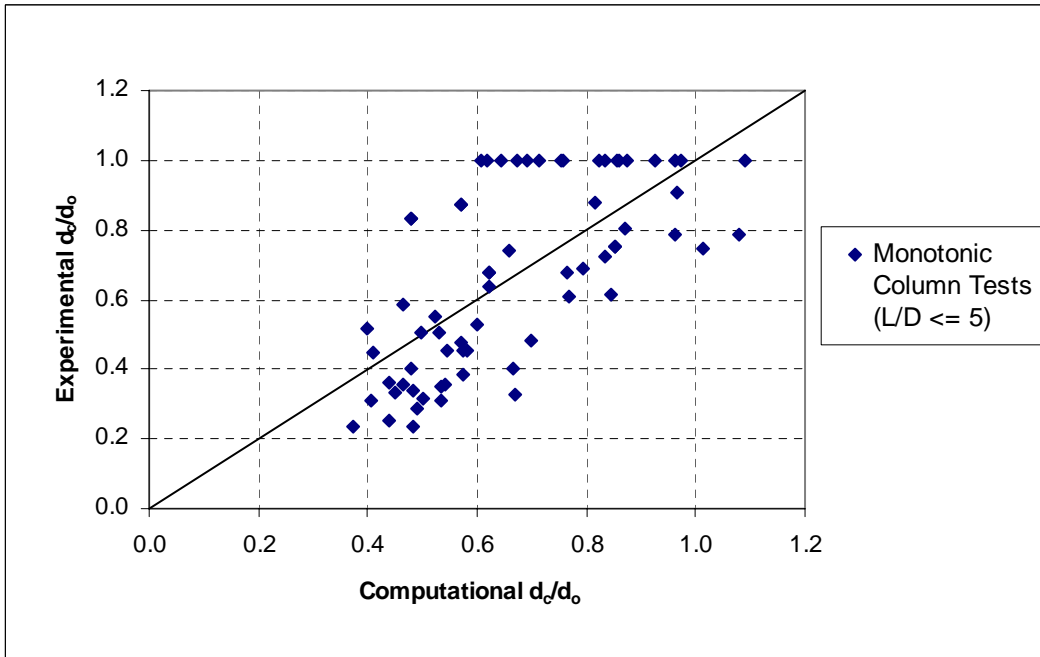


Figure 3.11: Comparison of Computational and Experimental d_c/d_o Values: Monotonically-Loaded RCFT Column Tests

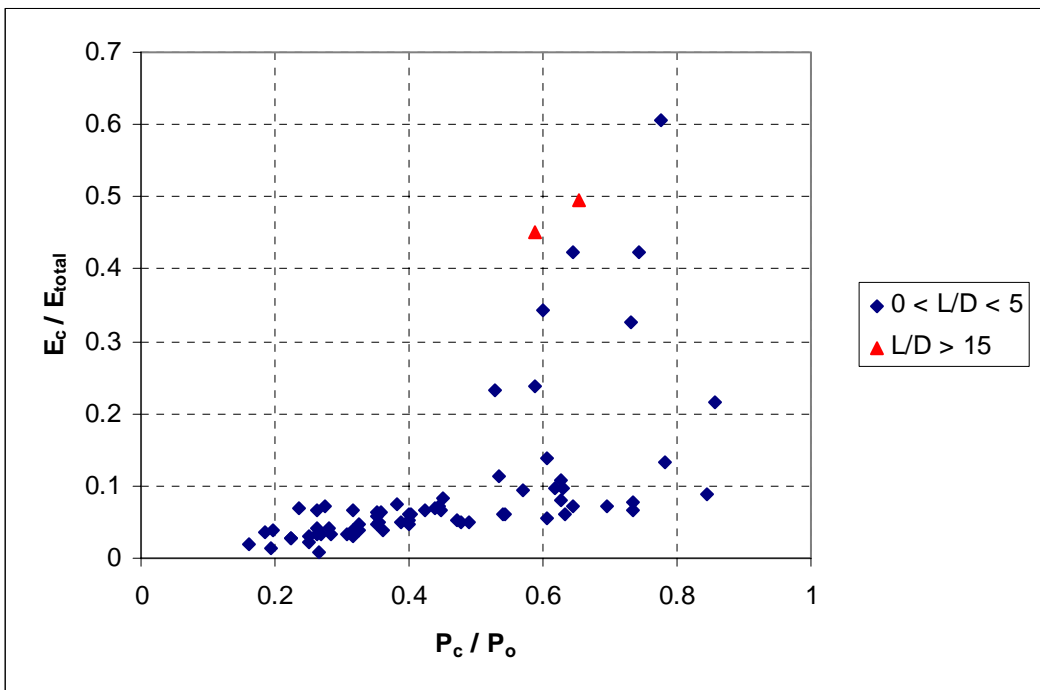


Figure 3.12: Comparison of E_c/E_{total} versus P_c/P_o : Monotonically-Loaded RCFT Column Tests

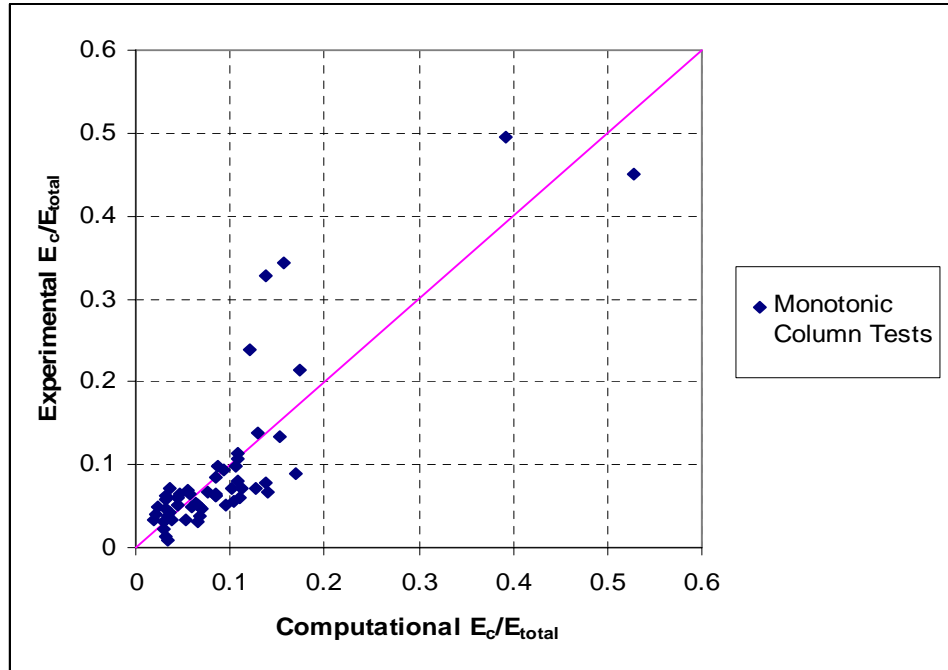


Figure 3.13: Comparison of Computational and Experimental E_c/E_{total} Values: Monotonically-Loaded RCFT Column Tests

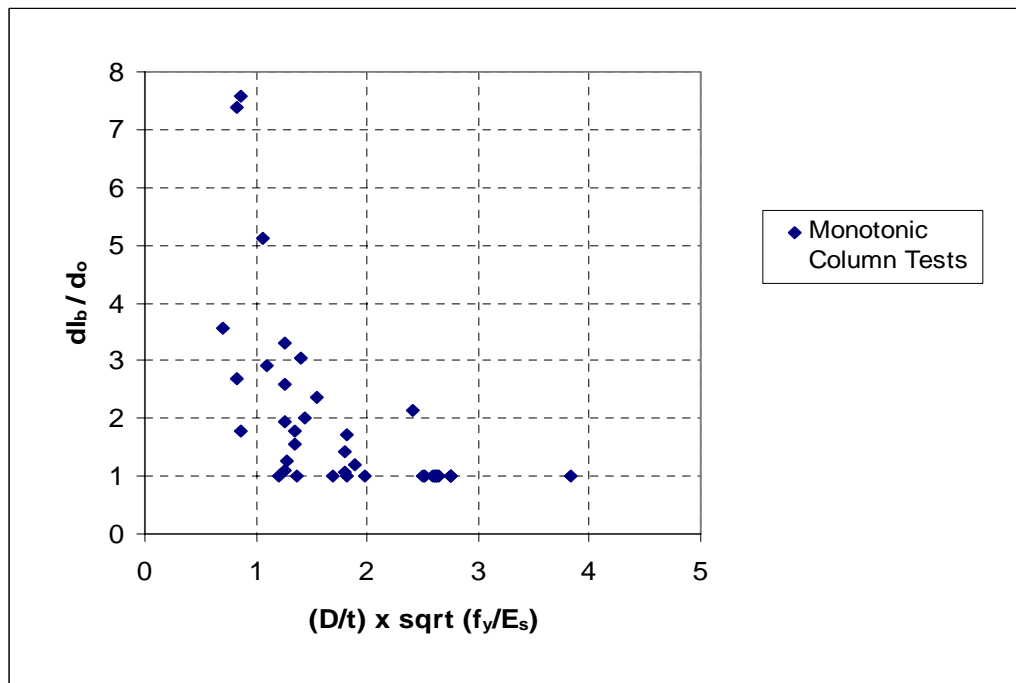


Figure 3.14: Comparison of d_{lb}/d_o versus $\frac{D}{t} \sqrt{\frac{f_y}{E_s}}$: Monotonically-Loaded RCFT Column Tests

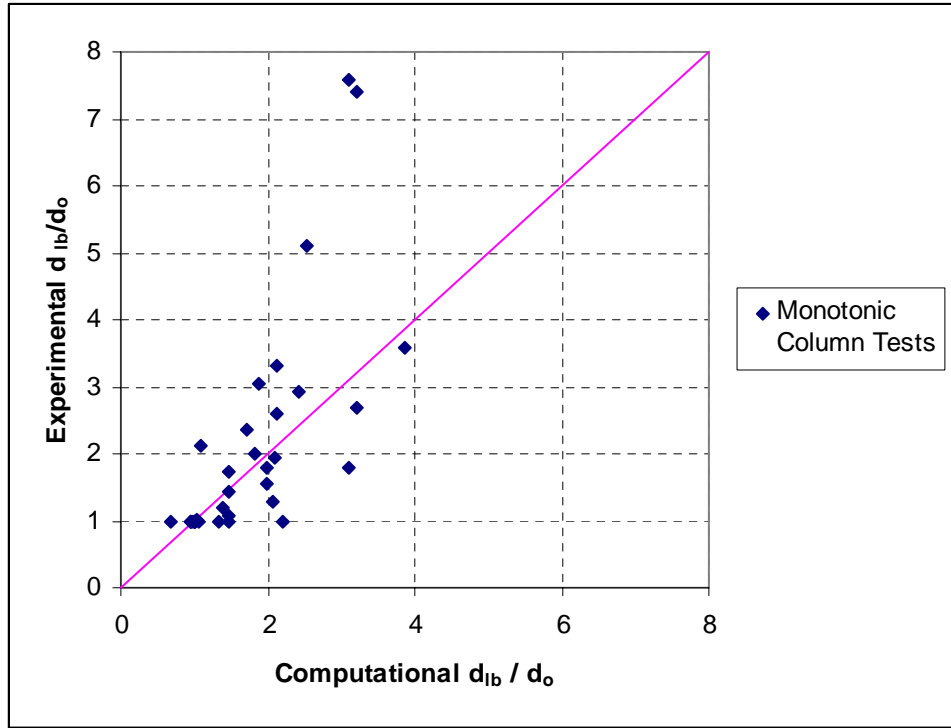


Figure 3.15: Comparison of Computational and Experimental d_{lb}/d_o Values: Monotonically-Loaded RCFT Column Tests

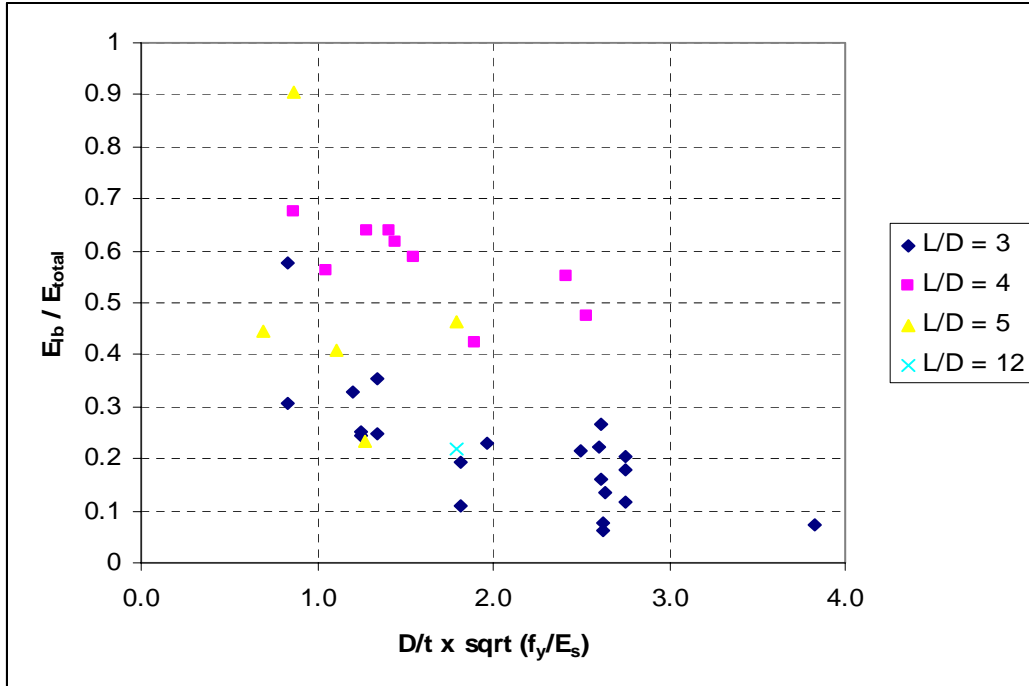


Figure 3.16: Comparison of E_{lb}/E_{total} versus $\frac{D}{t} \sqrt{\frac{f_y}{E_s}}$: Monotonically-Loaded RCFT Column Tests

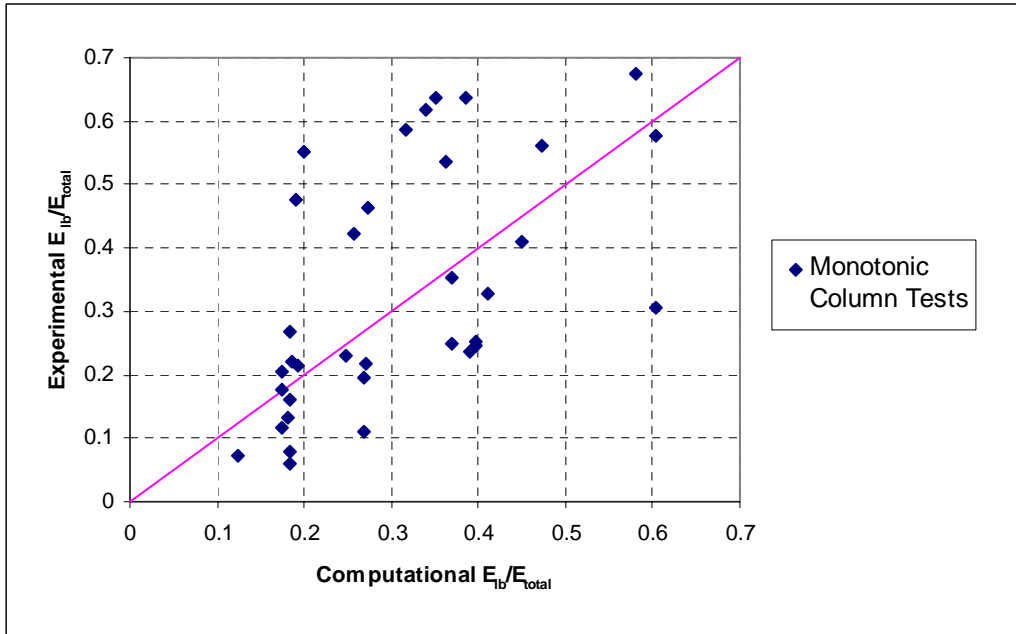


Figure 3.17: Comparison of Computational and Experimental E_{lb}/E_{total} Values: Monotonically-Loaded RCFT Column Tests

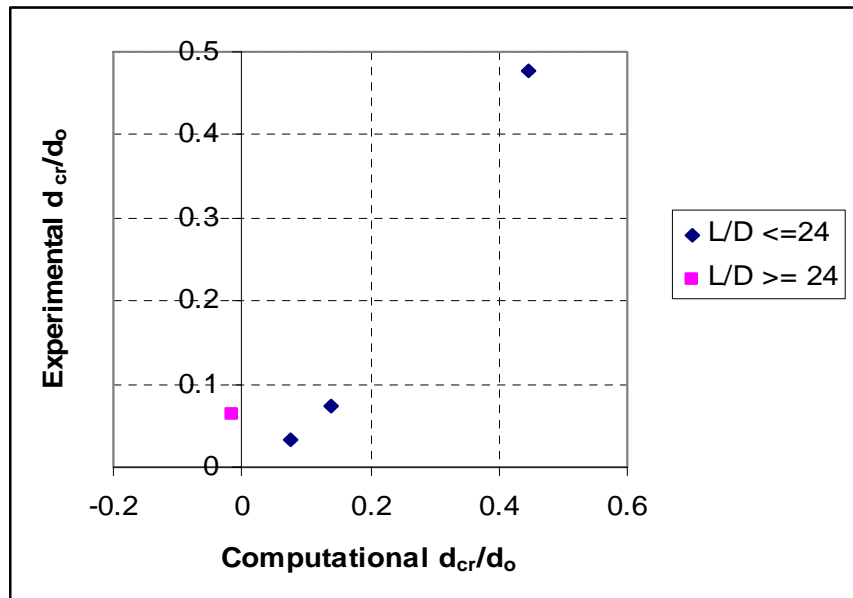


Figure 3.18: Comparison of Computational and Experimental d_{cr}/d_o Values: Monotonically-Loaded RCFT Beam-Column Tests with Loading Scheme MI

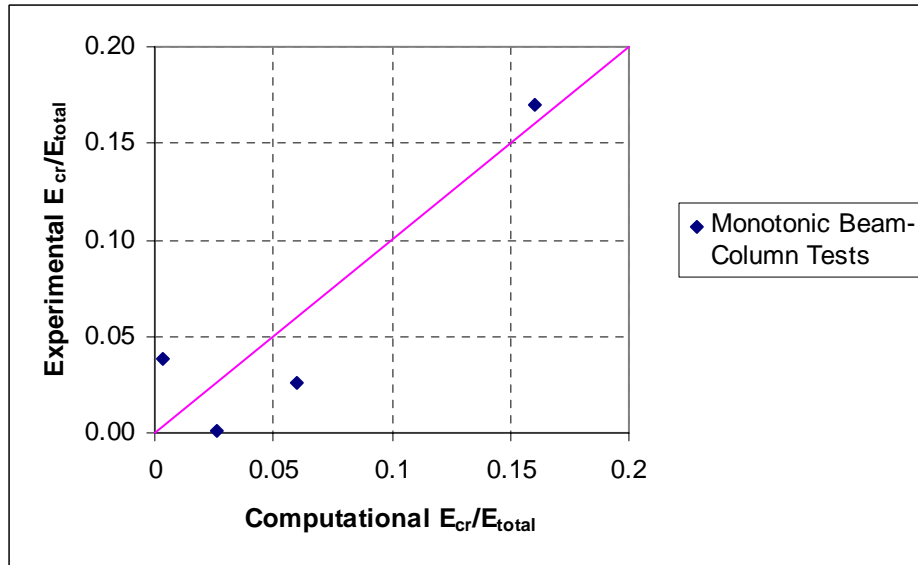


Figure 3.19: Comparison of Computational and Experimental E_{cr}/E_{total} Values: Monotonically-Loaded RCFT Beam-Column Tests with Loading Scheme MI

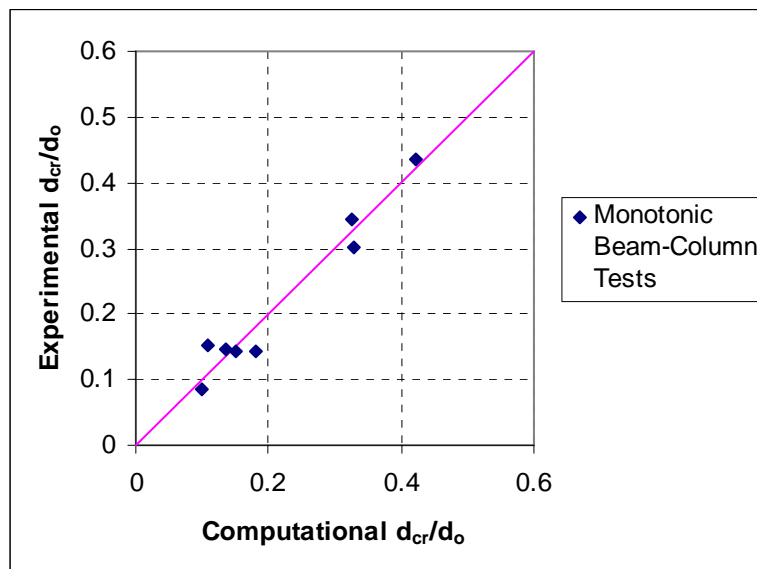


Figure 3.20: Comparison of Computational and Experimental d_{cr}/d_o Values: Monotonically-Loaded RCFT Beam-Column Tests with Loading Scheme MIII

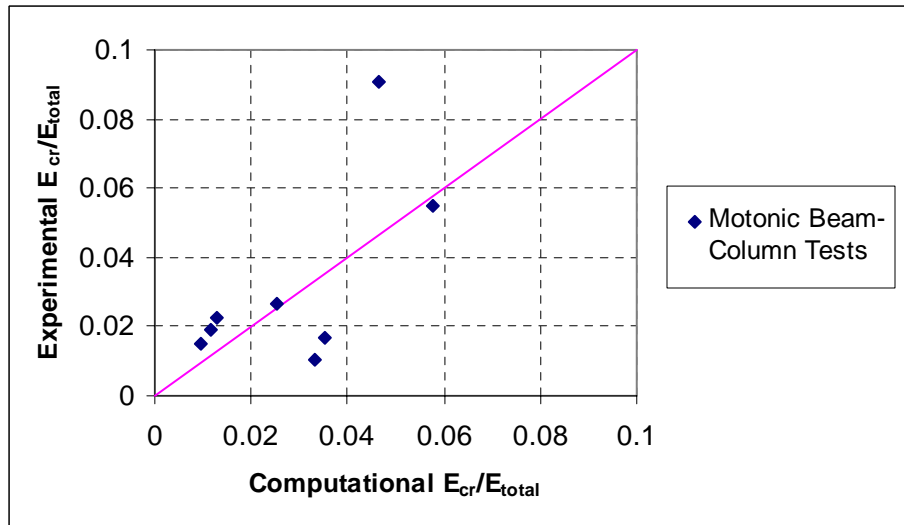


Figure 3.21: Comparison of Computational and Experimental E_{cr}/E_{total} Values: Monotonically-Loaded RCFT Beam-Column Tests with Loading Scheme MIII

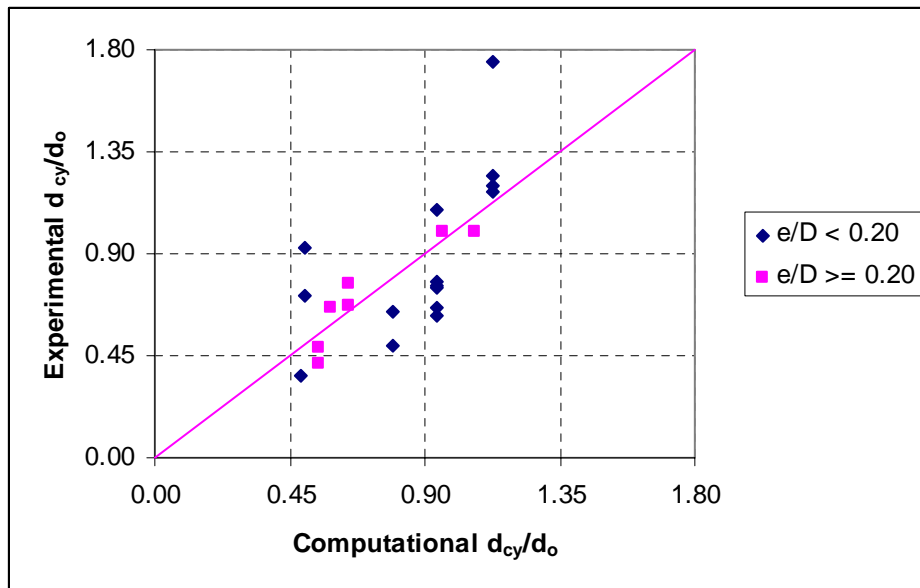


Figure 3.22: Comparison of Computational and Experimental d_{cy}/d_o Values: Monotonically-Loaded RCFT Beam-Column Tests with Loading Scheme MI

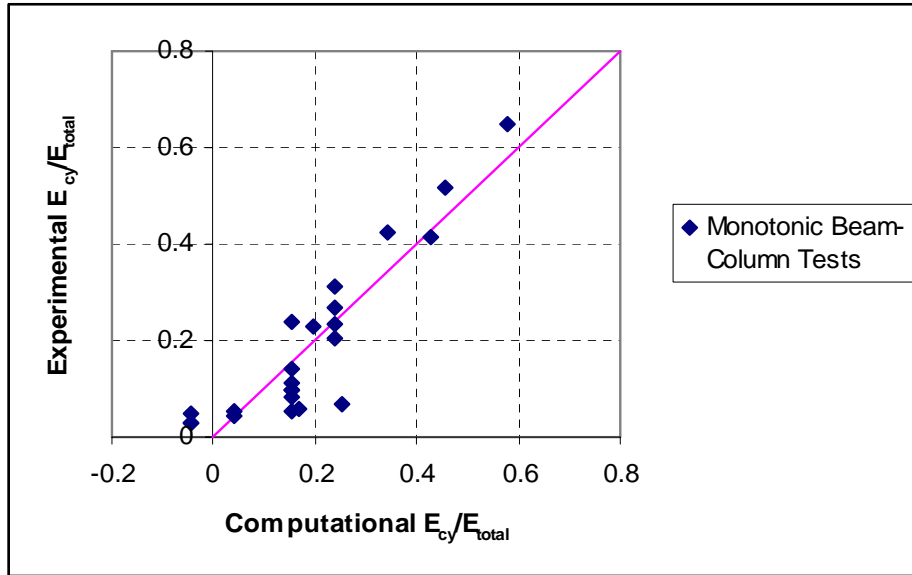


Figure 3.23: Comparison of Computational and Experimental E_{cy}/E_{total} Values: Monotonically-Loaded RCFT Beam-Column Tests with Loading Scheme MI

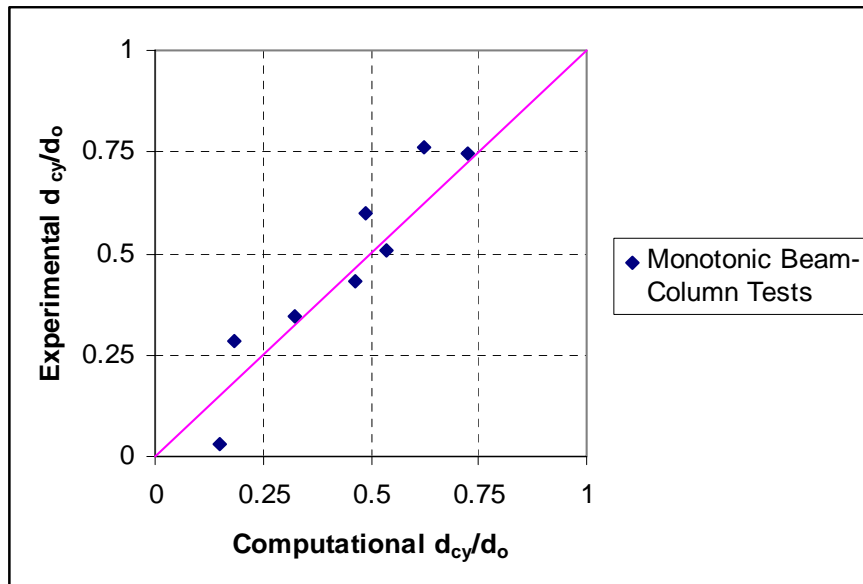


Figure 3.24: Comparison of Computational and Experimental d_{cy}/d_o Values: Monotonically-Loaded RCFT Beam-Column Tests with Loading Scheme MII

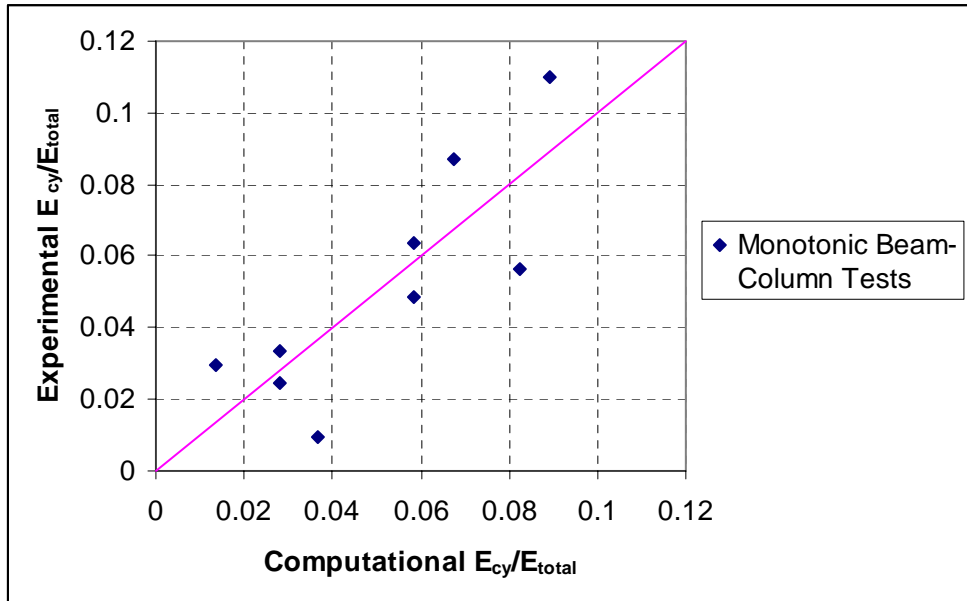


Figure 3.25: Comparison of Computational and Experimental E_{cy}/E_{total} Values: Monotonically-Loaded RCFT Beam-Column Tests with Loading Scheme MII

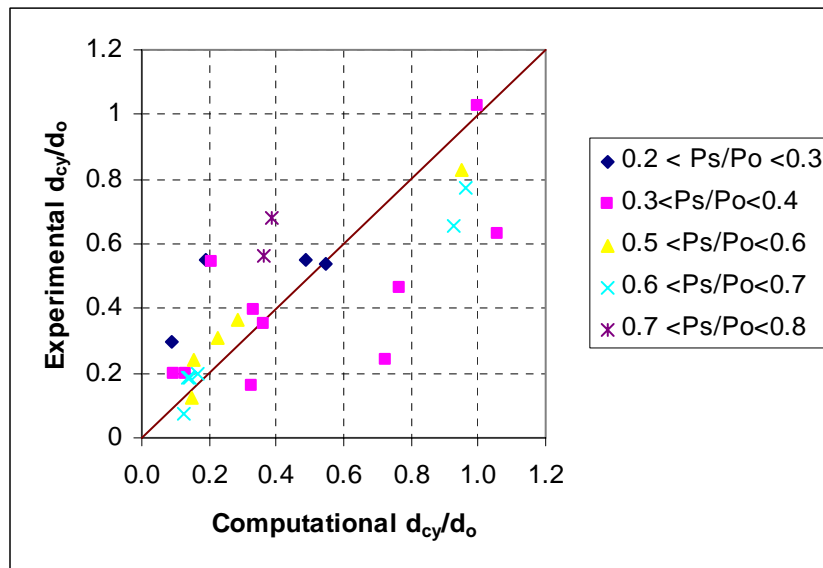


Figure 3.26: Comparison of Computational and Experimental d_{cy}/d_o Values: Monotonically-Loaded RCFT Beam-Column Tests with Loading Scheme MIII

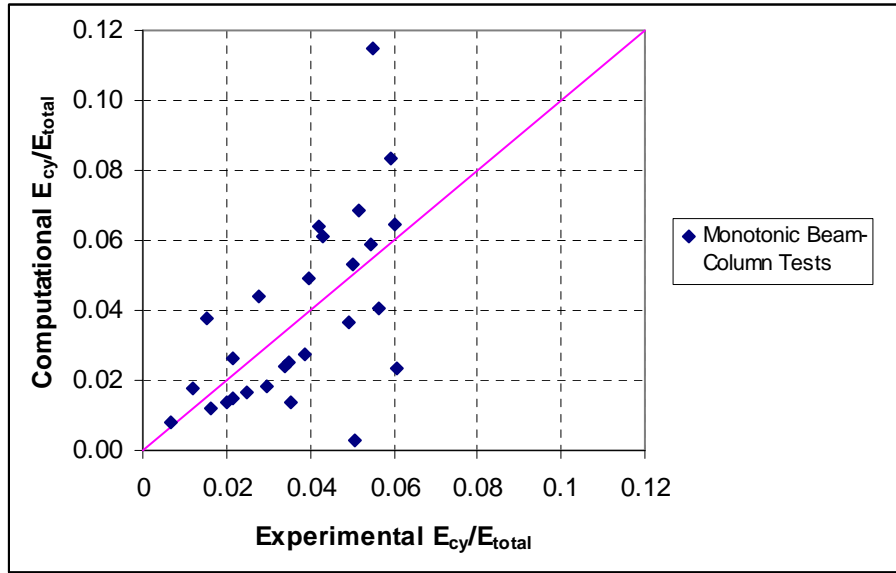


Figure 3.27: Comparison of Computational and Experimental E_{cy} / E_{total} Values: Monotonically-Loaded RCFT Beam-Column Tests with Loading Scheme MIII

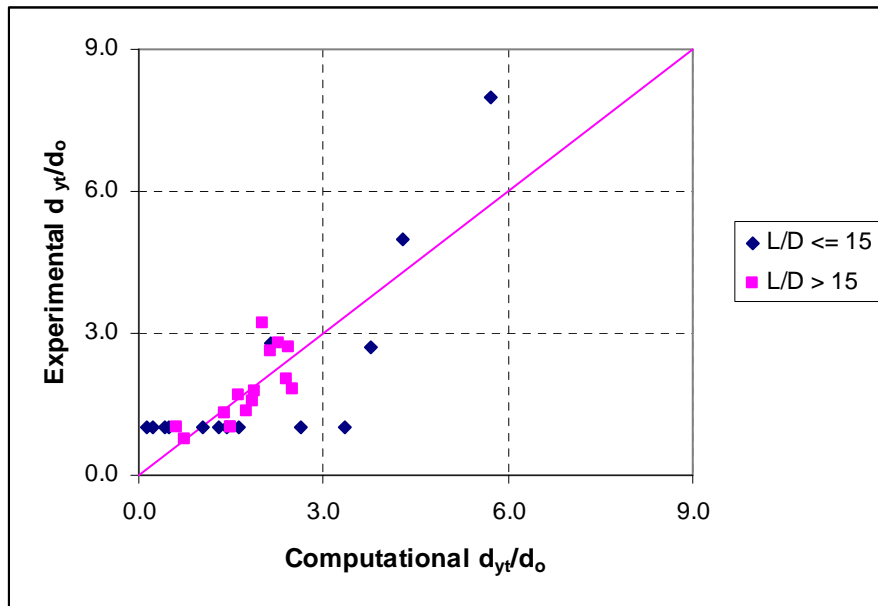


Figure 3.28: Comparison of Computational and Experimental d_{yt}/d_o Values: Monotonically-Loaded RCFT Beam-Column Tests with Loading Scheme MI

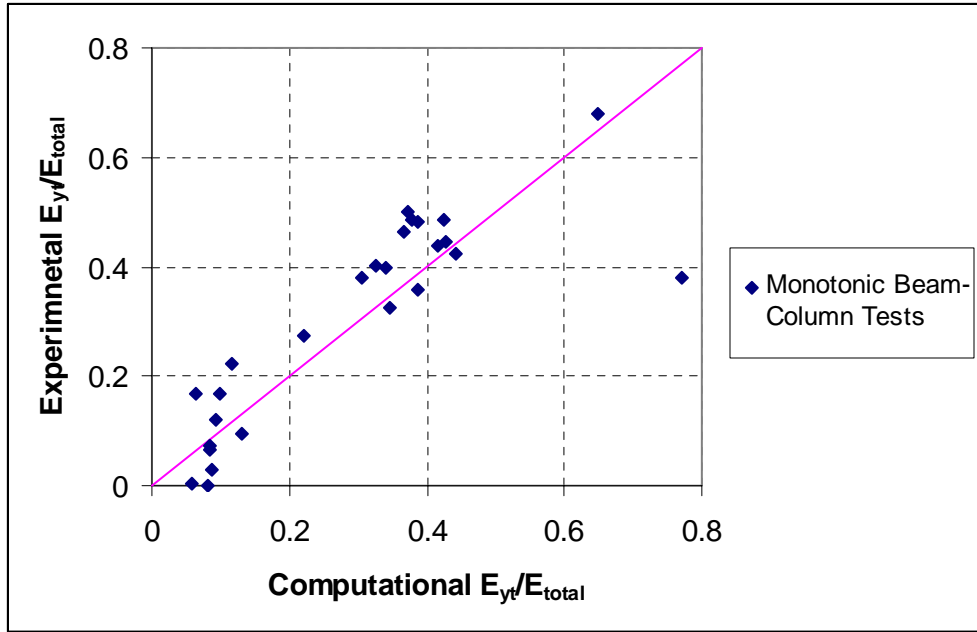


Figure 3.29: Comparison of Computational and Experimental E_{yt}/E_{total} Values: Monotonically-Loaded RCFT Beam-Column Tests with Loading Scheme MI

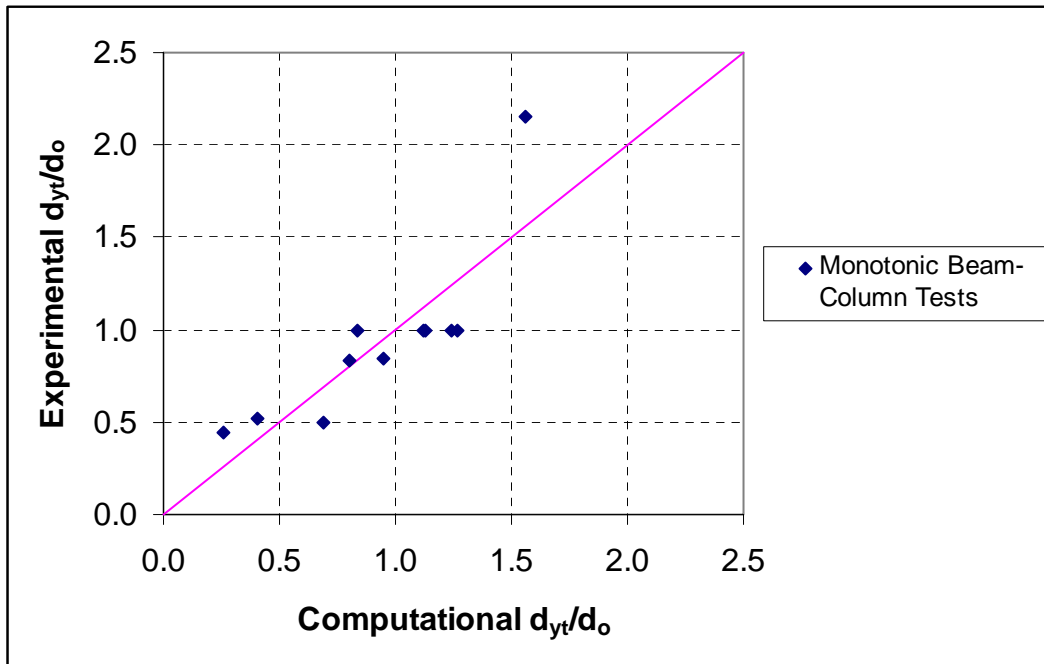


Figure 3.30: Comparison of Computational and Experimental d_{yt}/d_{total} Values: Monotonically-Loaded RCFT Beam-Column Tests with Loading Scheme MII

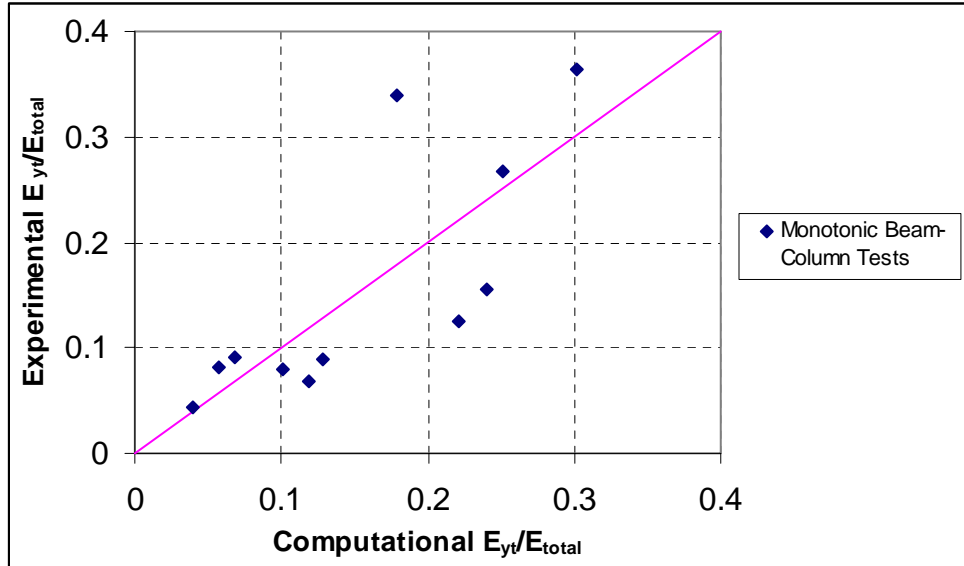


Figure 3.31: Comparison of Computational and Experimental E_{yt}/E_{total} Values: Monotonically-Loaded RCFT Beam-Column Tests with Loading Scheme MII

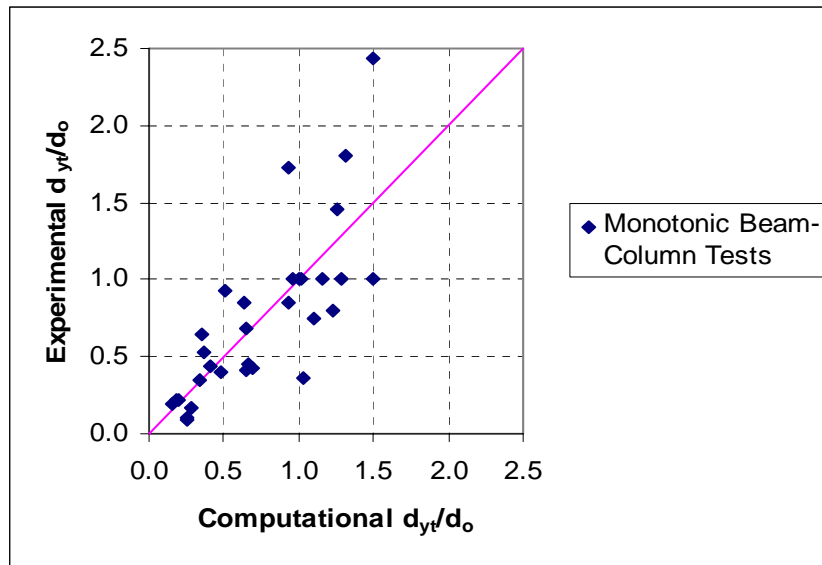


Figure 3.32: Comparison of Computational and Experimental d_{yt}/d_{total} Values: Monotonically-Loaded RCFT Beam-Column Tests with Loading Scheme MIII

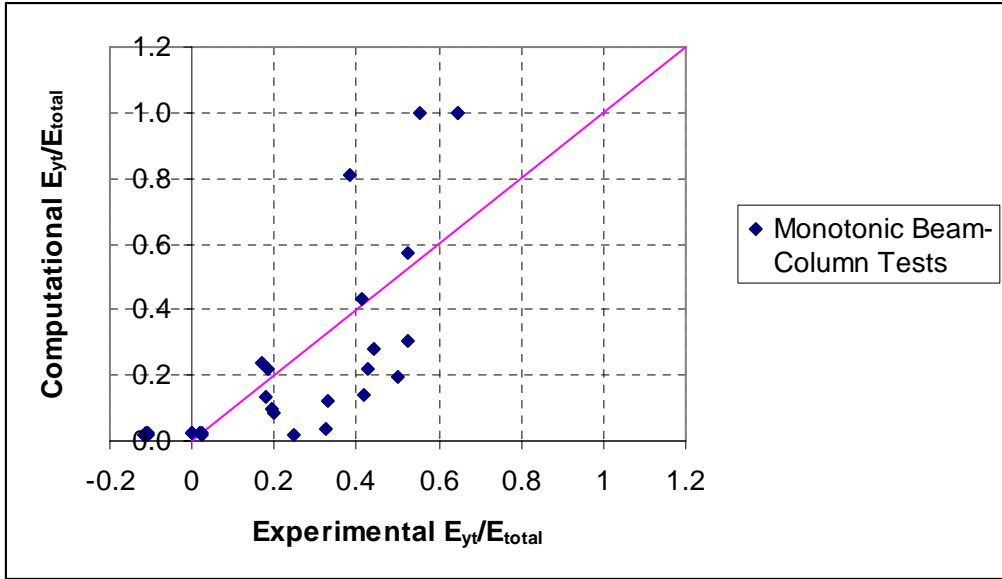


Figure 3.33: Comparison of Computational and Experimental E_{yt}/E_{total} Values: Monotonically-Loaded RCFT Beam-Column Tests with Loading Scheme MIII

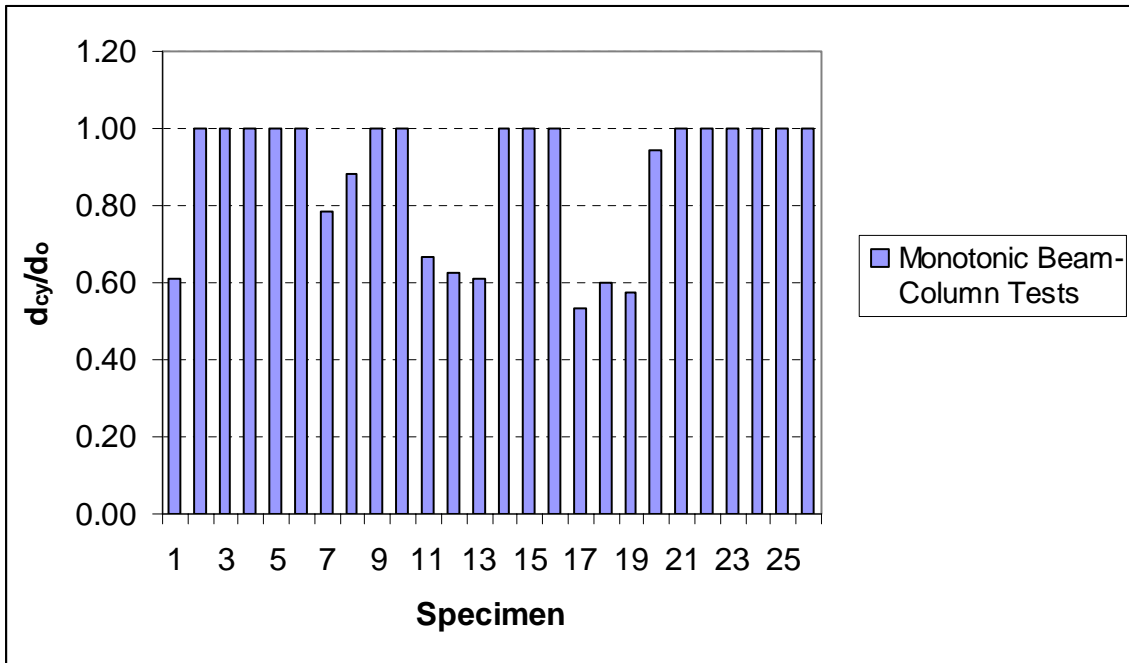


Figure 3.34: Histogram of d_{cy}/d_o for Monotonically-Loaded RCFT Beam-Column Tests with Loading Scheme MIII

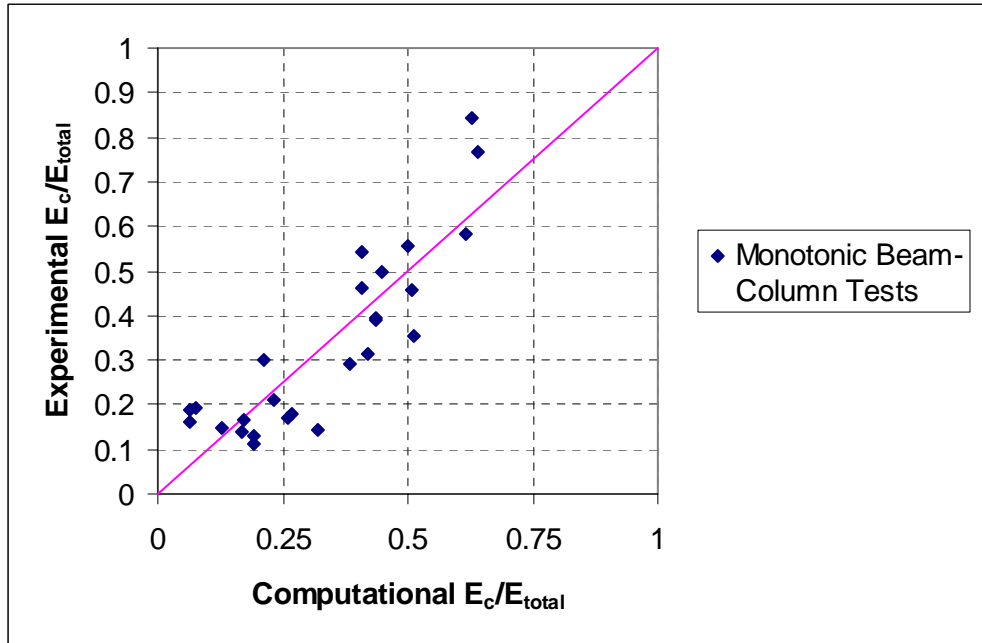


Figure 3.35: Comparison of Computational and Experimental E_c/E_{total} Values: Monotonically-Loaded RCFT Beam-Column Tests with Loading Scheme MIII

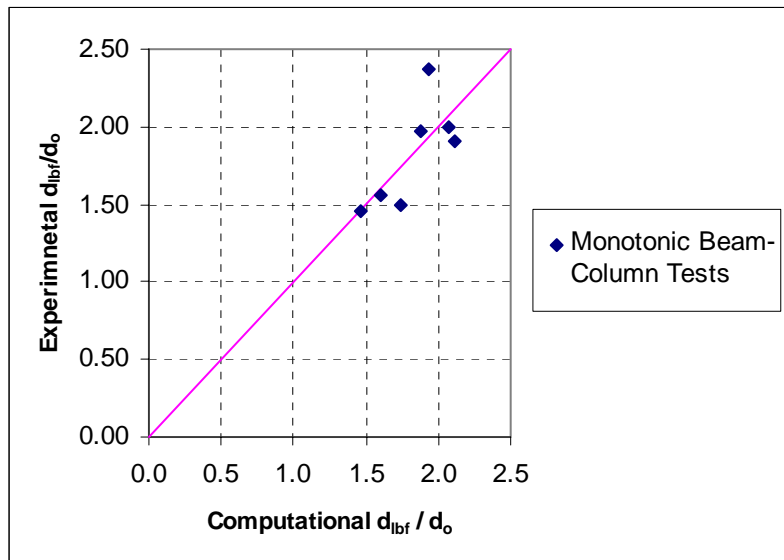


Figure 3.36: Comparison of Computational and Experimental d_{lbf}/d_o Values: Monotonically-Loaded RCFT Beam-Column Tests with Loading Scheme MI

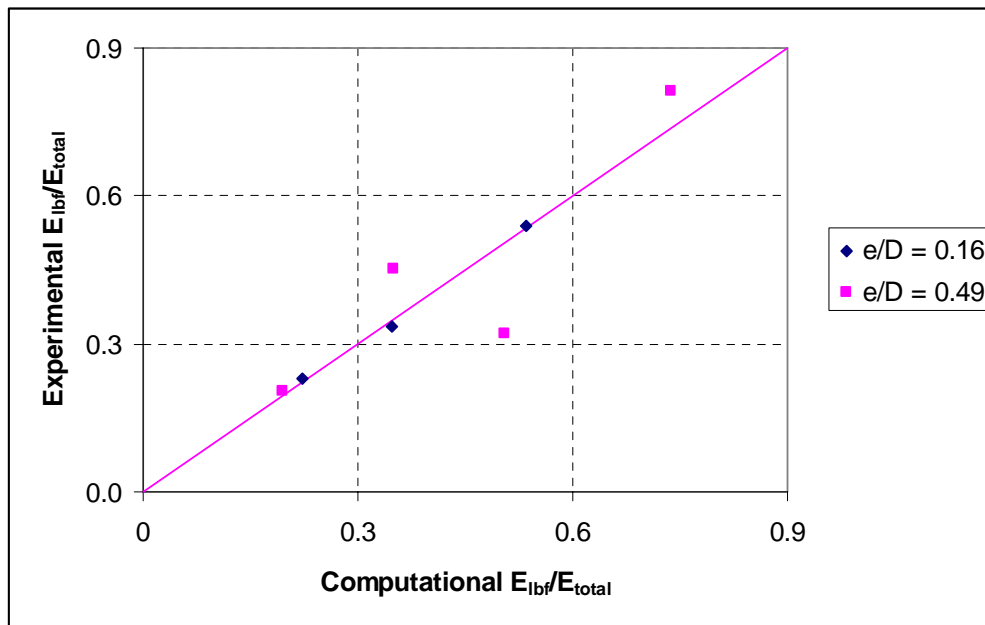


Figure 3.37: Comparison of Computational and Experimental E_{lbf}/E_{total} Values: Monotonically-Loaded RCFT Beam-Column Tests with Loading Scheme MI

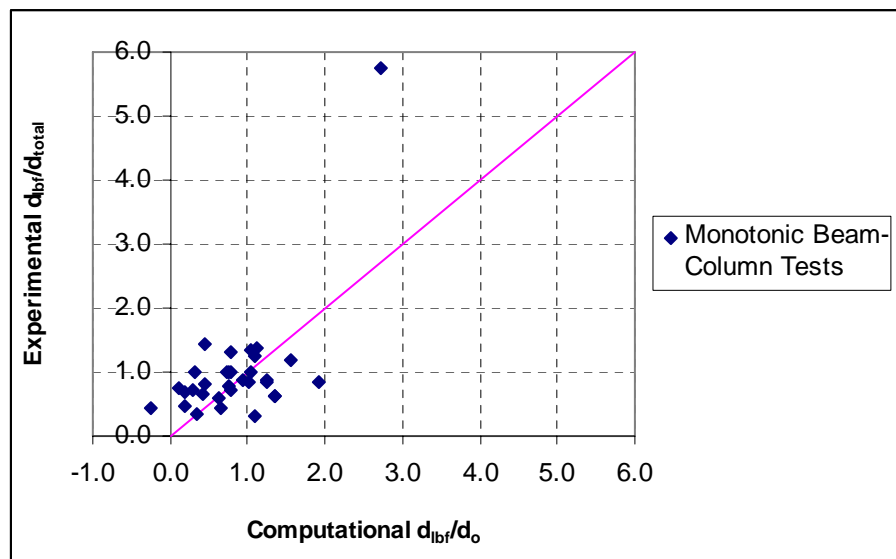


Figure 3.38: Comparison of Computational and Experimental d_{lbf}/d_o Values: Monotonically-Loaded RCFT Beam-Column Tests with Loading Scheme MII

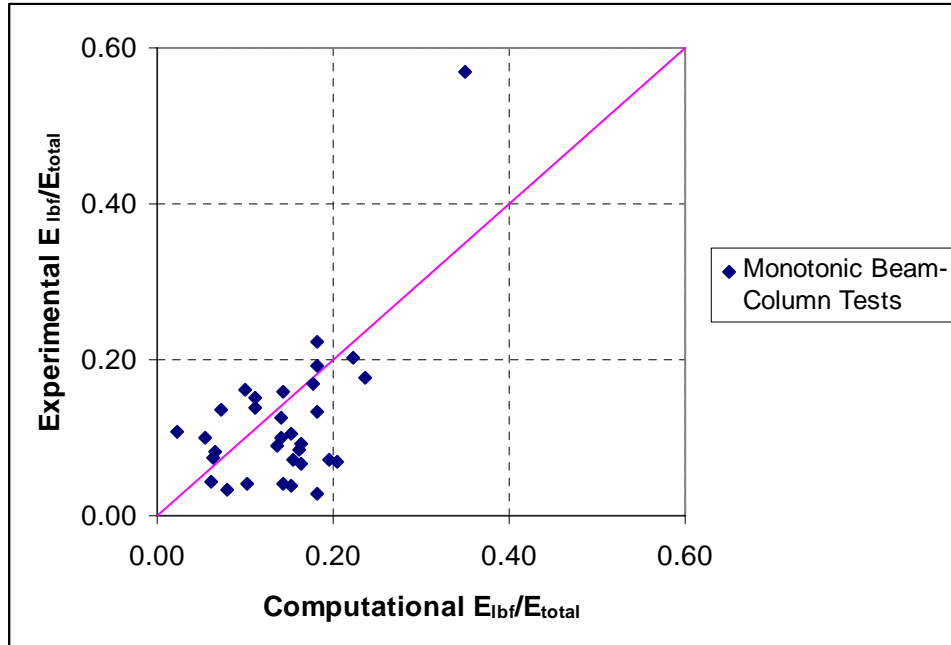


Figure 3.39: Comparison of Computational and Experimental E_{lbf}/E_{total} Values: Monotonically-Loaded RCFT Beam-Column Tests with Loading Scheme MII

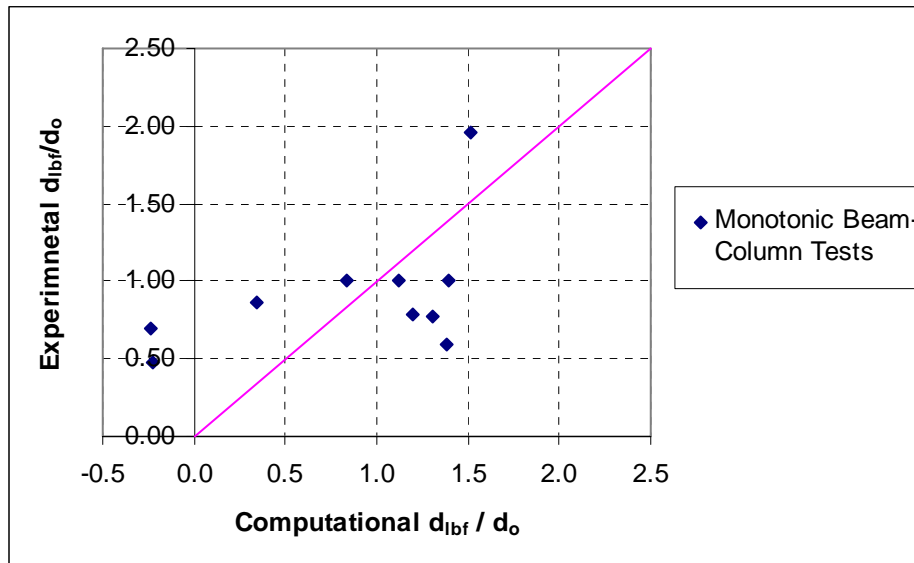


Figure 3.40: Comparison of Computational and Experimental d_{lbf}/d_o Values: Monotonically-Loaded RCFT Beam-Column Tests with Loading Scheme MIII

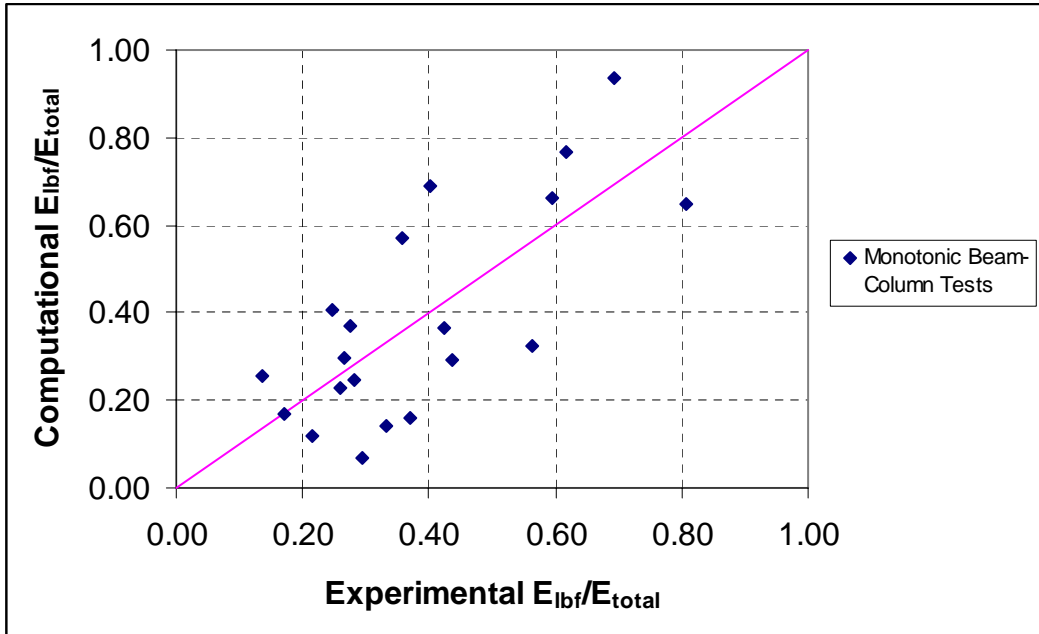


Figure 3.41: Comparison of Computational and Experimental E_{lbf}/E_{total} Values: Monotonically-Loaded RCFT Beam-Column Tests with Loading Scheme MIII

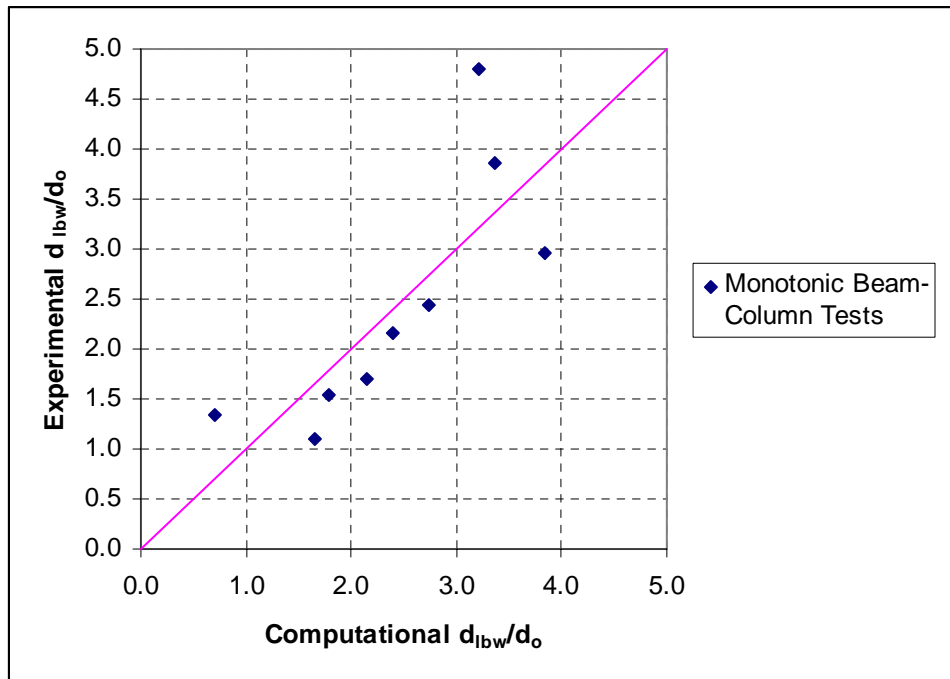


Figure 3.42: Comparison of Computational and Experimental d_{lbw}/d_o Values: Monotonically-Loaded RCFT Beam-Column Tests with Loading Scheme MII

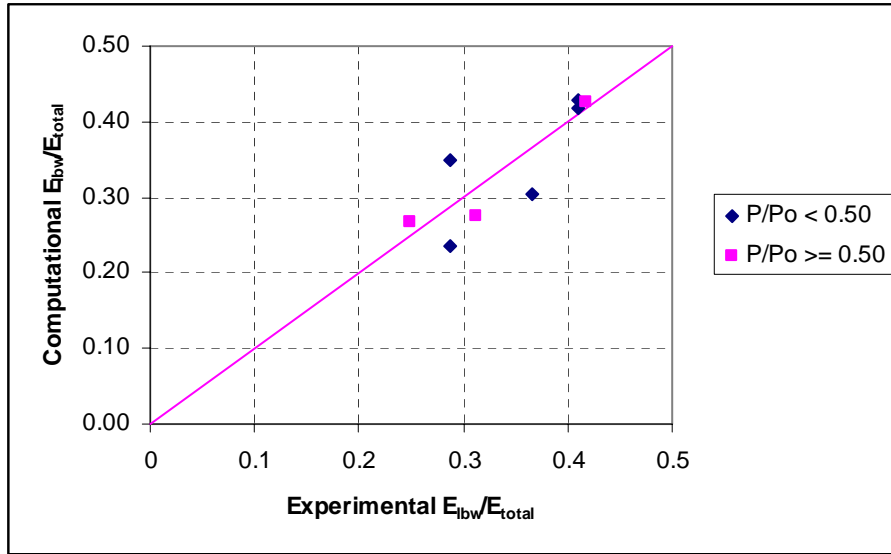


Figure 3.43: Comparison of Computational and Experimental E_{lbW}/E_{total} Values: Monotonically-Loaded RCFT Beam-Column Tests with Loading Scheme MII

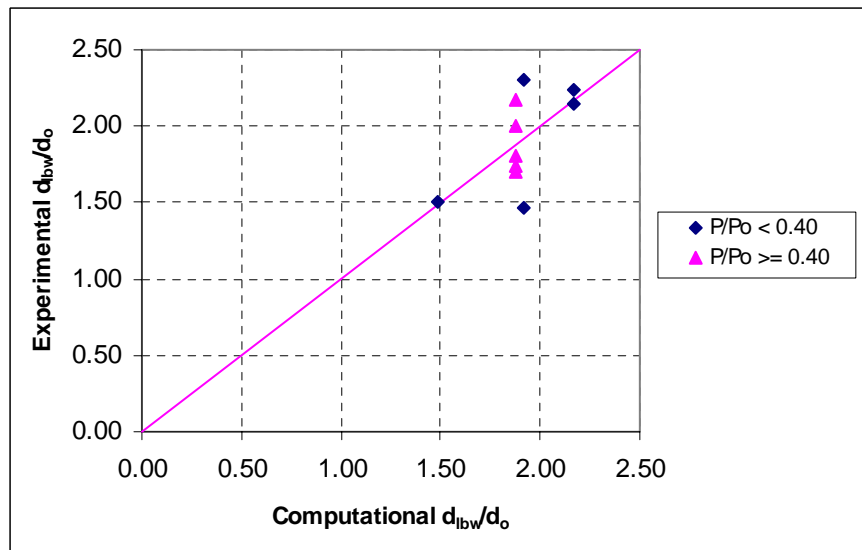


Figure 3.44: Comparison of Computational and Experimental d_{lbW}/d_o Values: Monotonically-Loaded RCFT Beam-Column Tests with Loading Scheme MIII

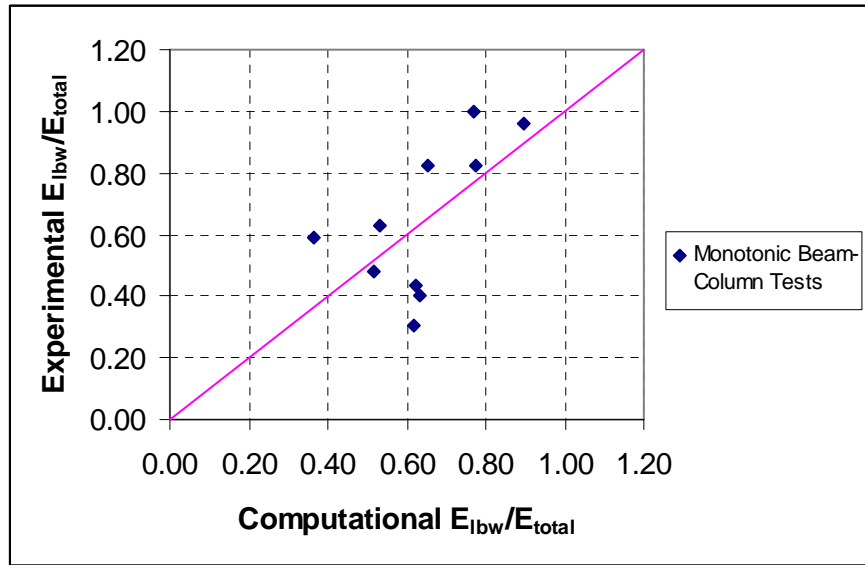


Figure 3.45: Comparison of Computational and Experimental E_{lbw}/E_{total} Values: Monotonically-Loaded RCFT Beam-Column Tests with Loading Scheme MIII

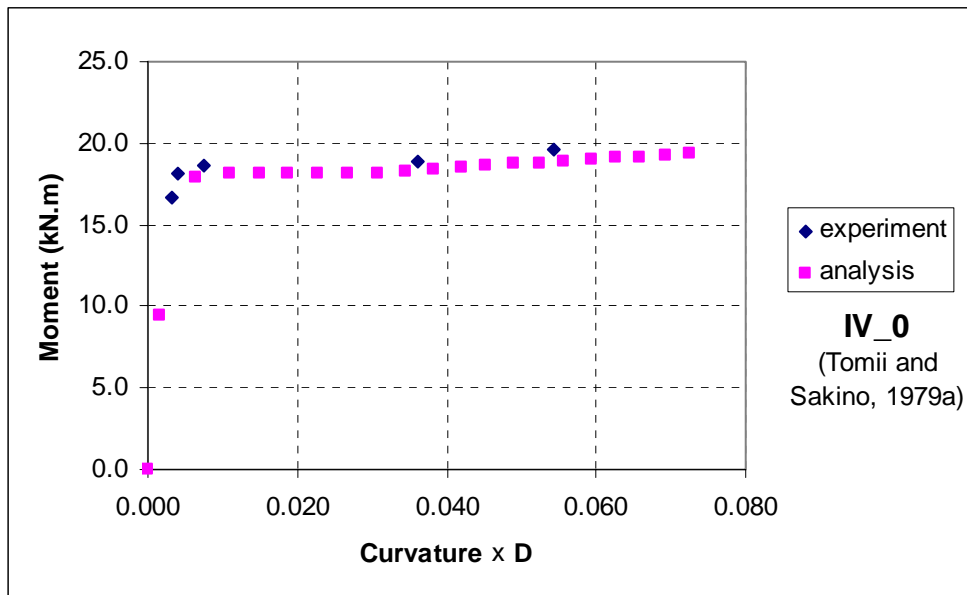


Figure 3.46: Comparison of Computational and Experimental Moment-Curvature Diagram for a Square CFT: $D/t = 24$, $f'_c = 19.8$ MPa, $f_y = 284.5$ MPa, $P/P_o = 0.0$

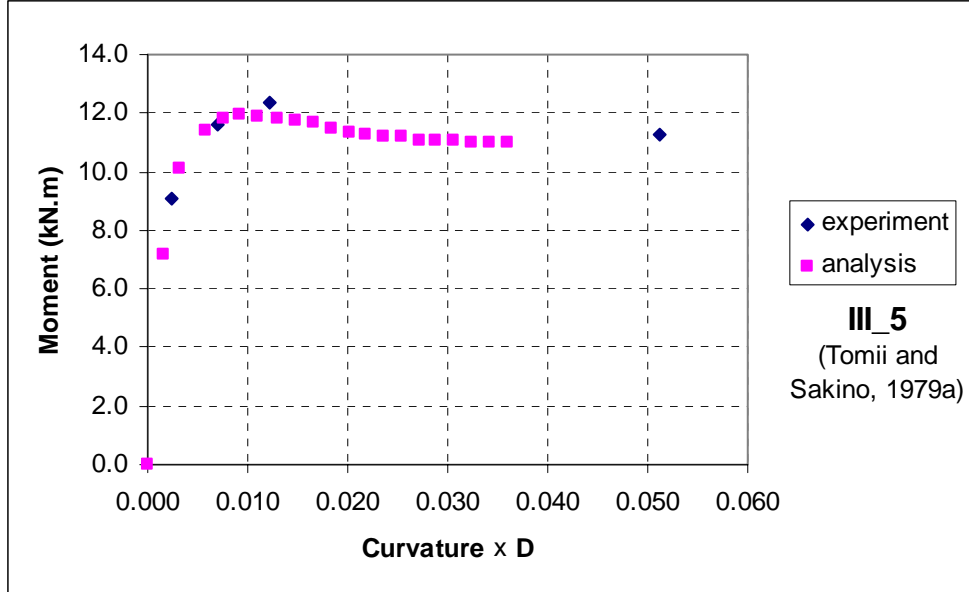


Figure 3.47: Comparison of Computational and Experimental Moment-Curvature Diagram for a Square CFT: $D/t = 33, f'_c = 20.6 \text{ MPa}, f_y = 288.4 \text{ MPa}, P/P_o = 0.47$

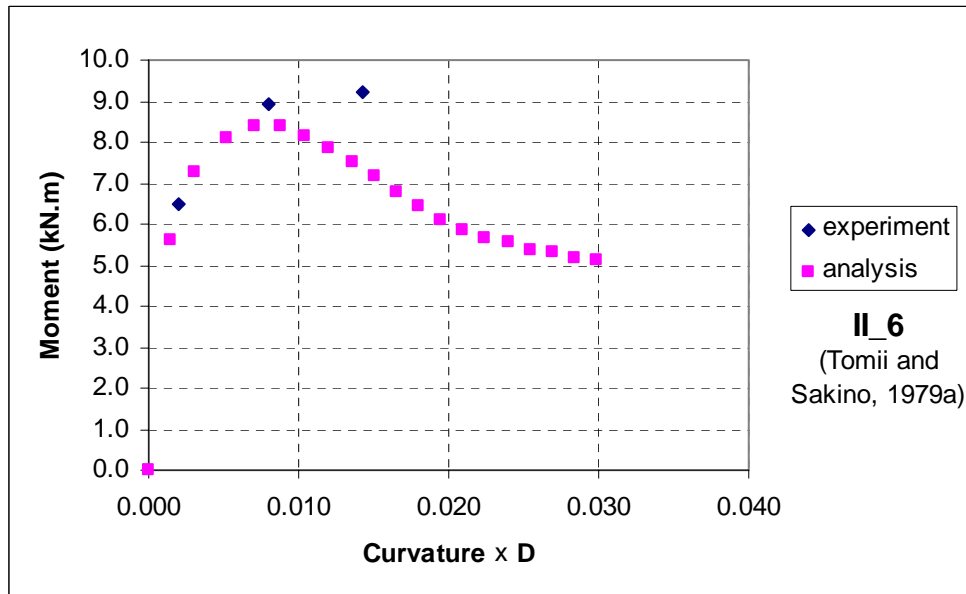


Figure 3.48: Comparison of Computational and Experimental Moment-Curvature Diagram for a Square CFT: $D/t = 44, f'_c = 21.4 \text{ MPa}, f_y = 289.4 \text{ MPa}, P/P_o = 0.57$

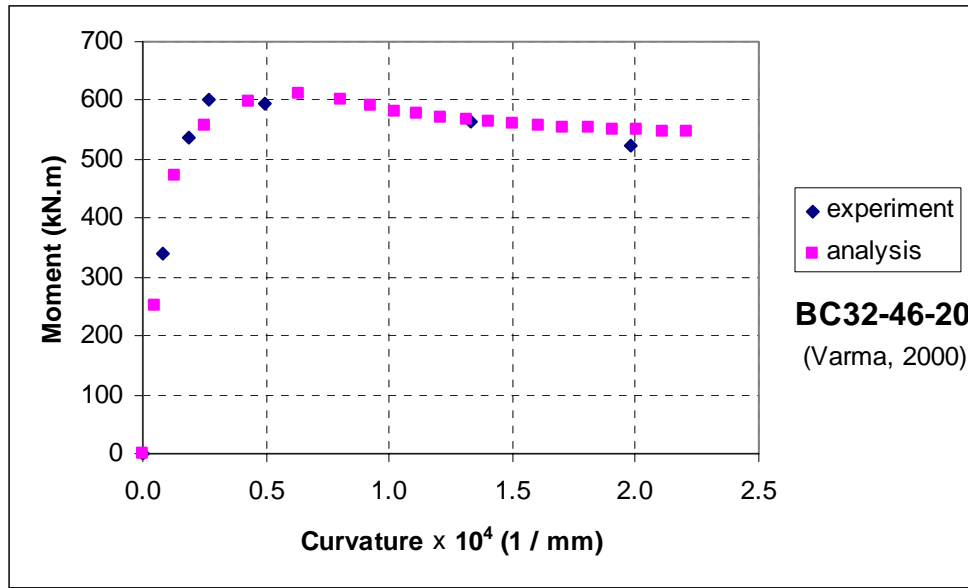


Figure 3.49: Comparison of Computational and Experimental Moment-Curvature Diagram for a Square CFT: $D/t = 32, f'_c = 110$ MPa, $f_y = 317$ MPa, $P/P_o = 0.2$

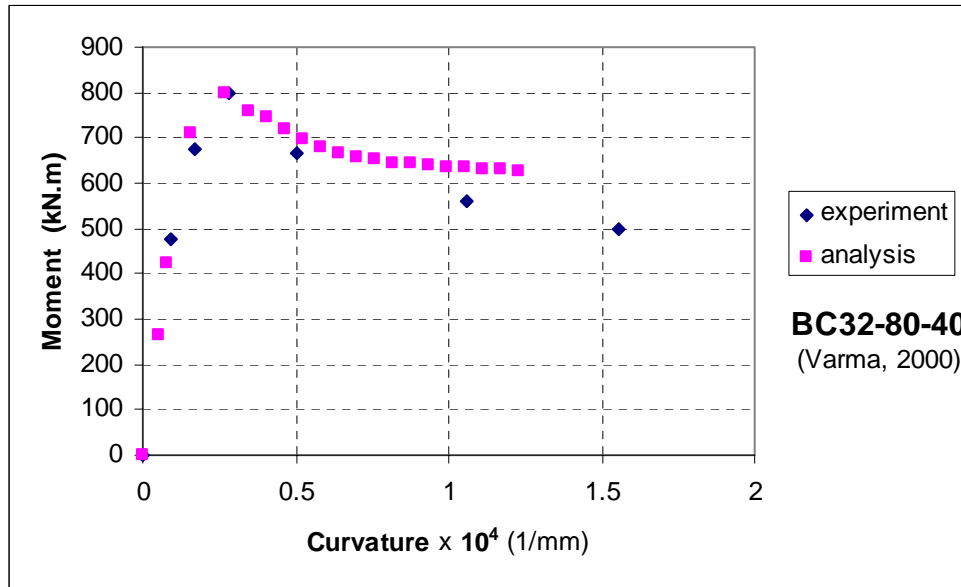


Figure 3.50: Comparison of Computational and Experimental Moment-Curvature Diagram for a Square CFT: $D/t = 32, f'_c = 110$ MPa, $f_y = 552$ MPa, $P/P_o = 0.40$

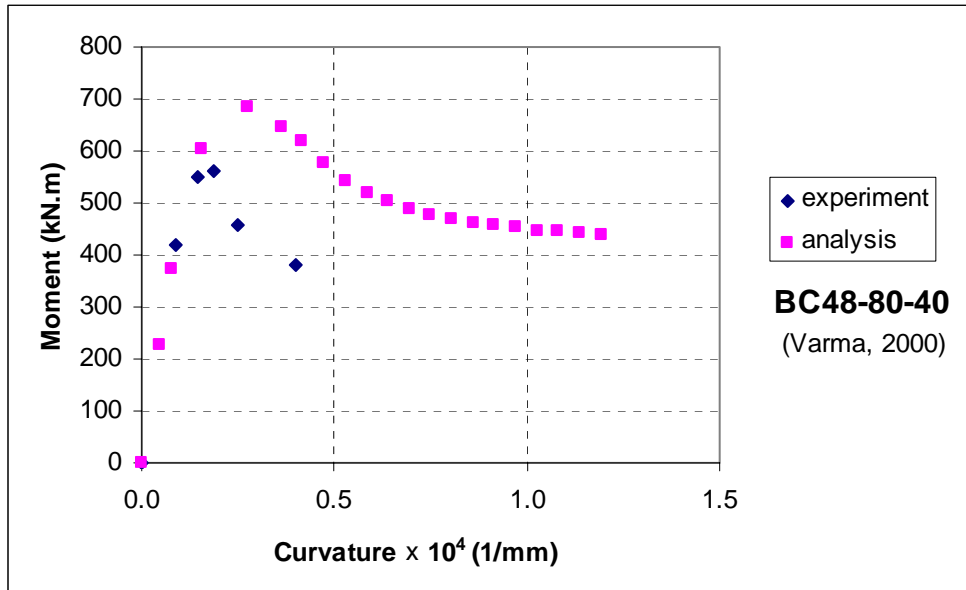


Figure 3.51: Comparison of Computational and Experimental Moment-Curvature Diagram for a Square CFT: $D/t = 48$, $f'_c = 110$ MPa, $f_y = 552$ MPa, $P/P_o = 0.40$

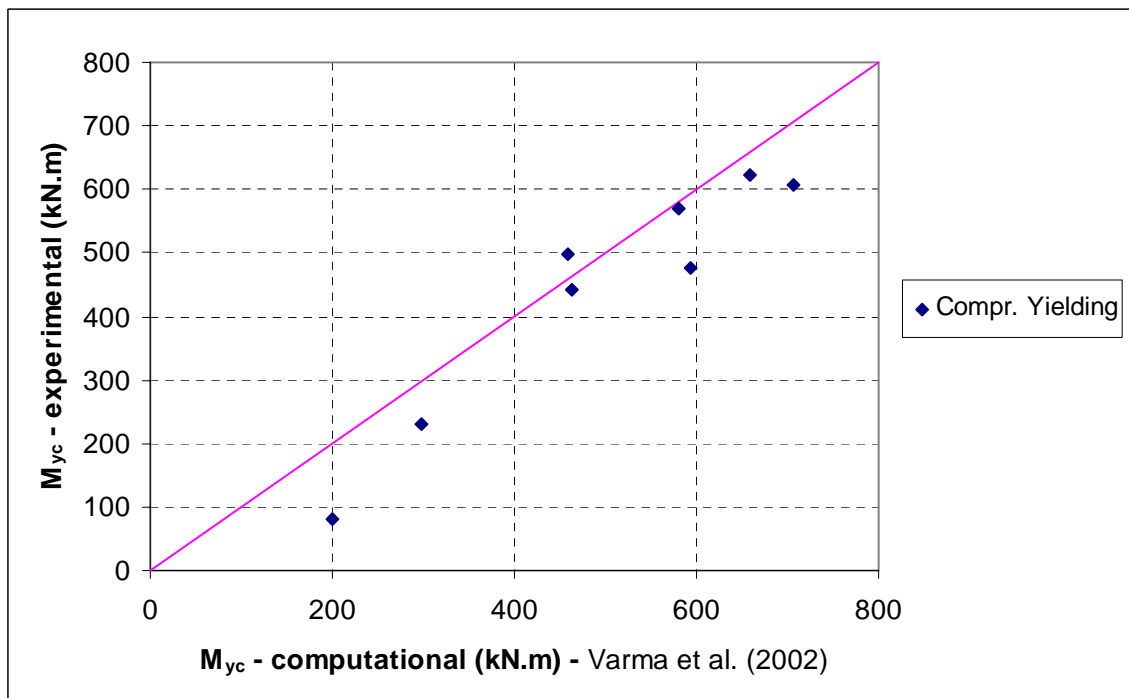


Figure 3.52: Comparison of Computational and Experimental Moment Values at Compression Yielding: Monotonically-Loaded RCFT Beam-Column Tests

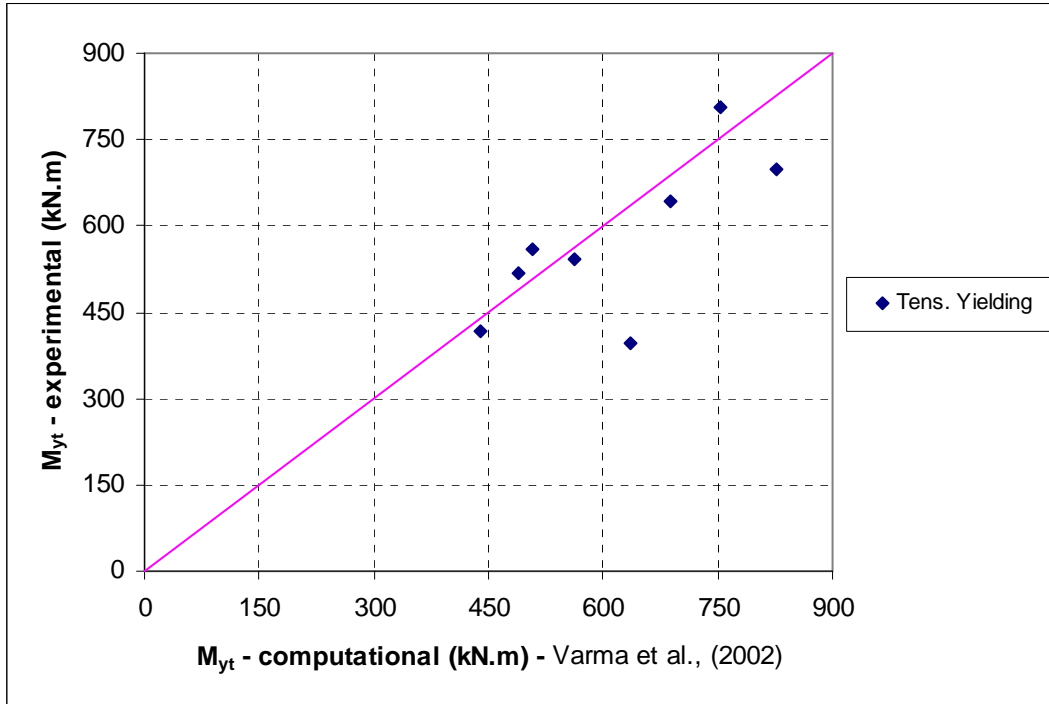


Figure 3.53: Comparison of Computational and Experimental Moment Values at Tension Yielding: Monotonically-Loaded RCFT Beam-Column Tests

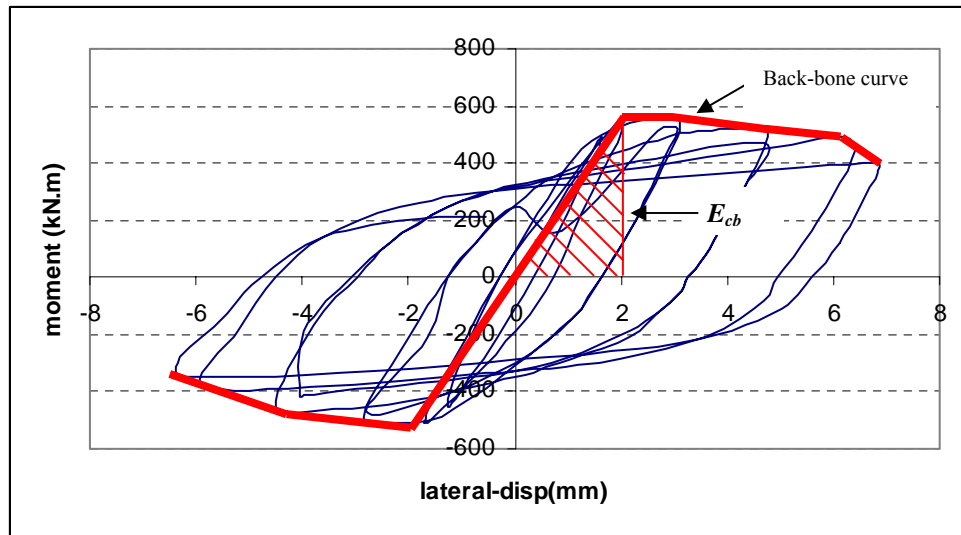


Figure 3.54: Representation of E_{cb} for Specimen CBC-32-80-10 of Varma et al. (2002) [after Varma et al. (2002)]

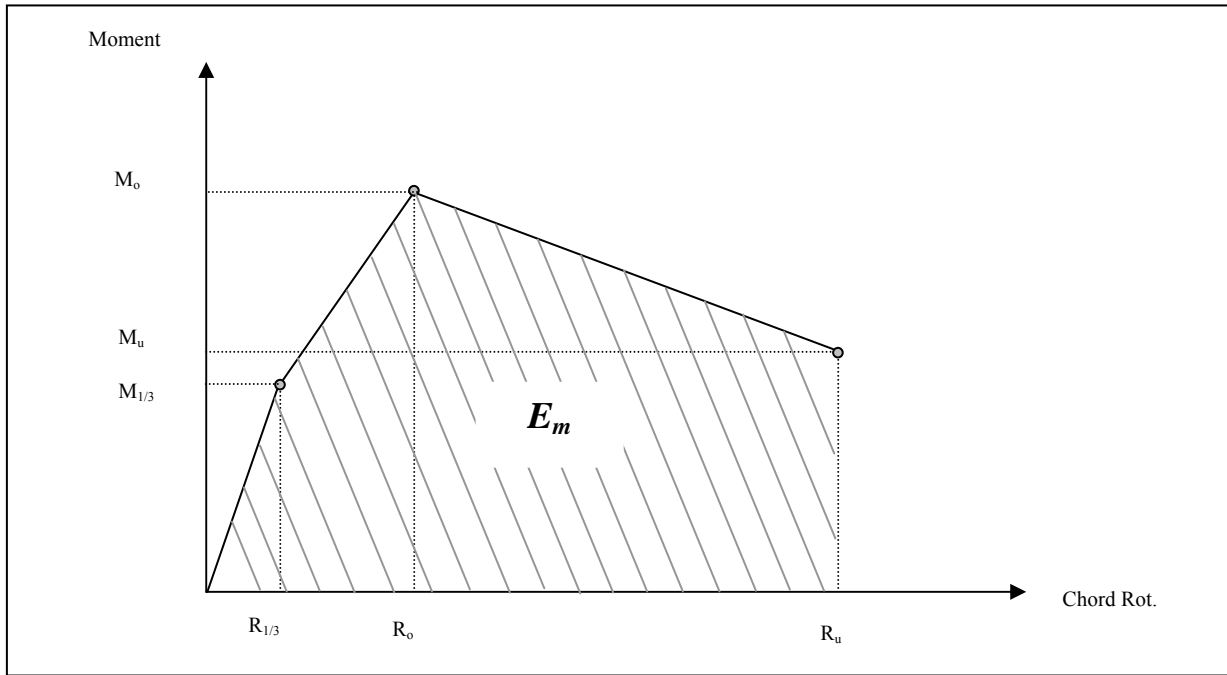


Figure 3.55: Representation of the Area under Monotonic Moment-Rotation Curve (E_m)

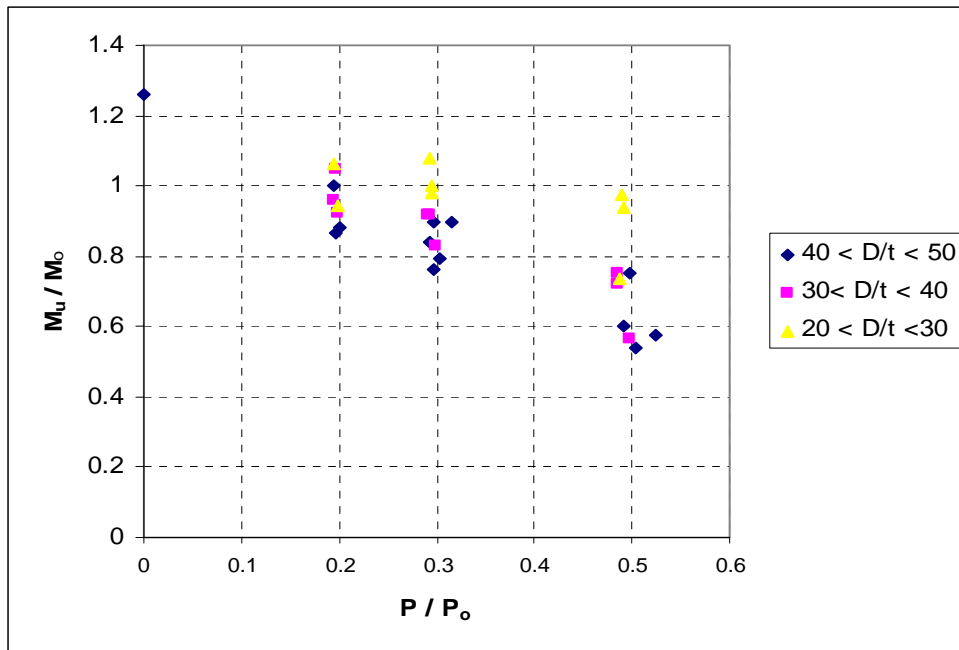


Figure 3.56: Comparison of M_u/M_o versus P/P_o and D/t : Cyclically-Loaded RCFT Beam-Column Tests

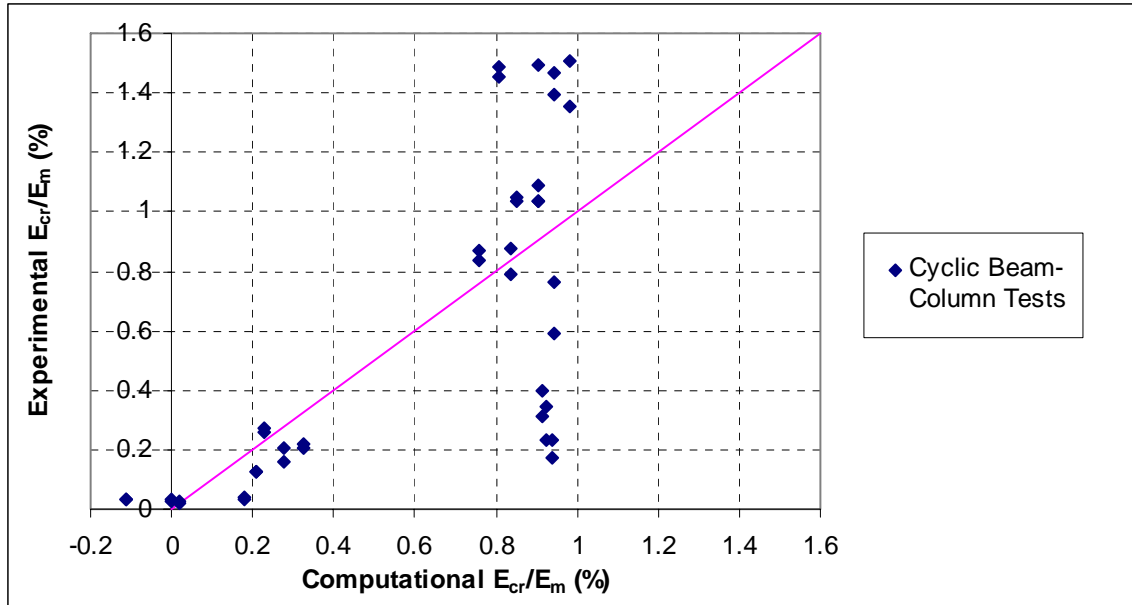


Figure 3.57: Comparison of Computational and Experimental E_{cr}/E_m Values: Cyclically-Loaded RCFT Beam-Column Tests

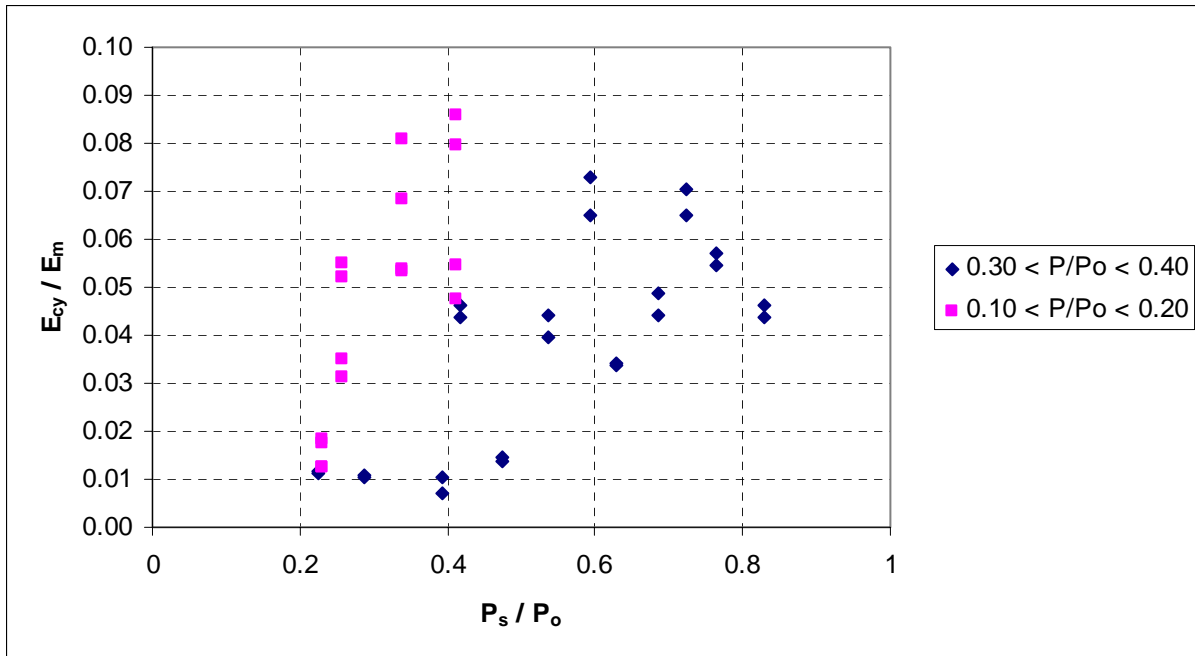


Figure 3.58: Comparison of E_{cy}/E_m versus P_s/P_o : Cyclically-Loaded RCFT Beam-Columns

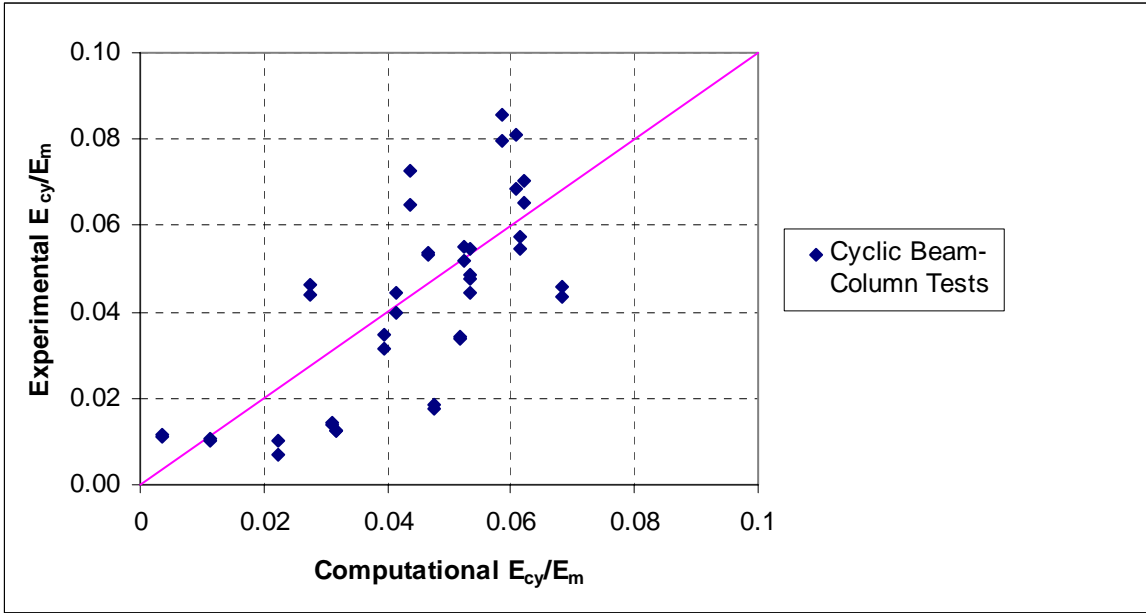


Figure 3.59: Comparison of Computational and Experimental E_{cy}/E_m Values: Cyclically-Loaded RCFT Beam-Column Tests

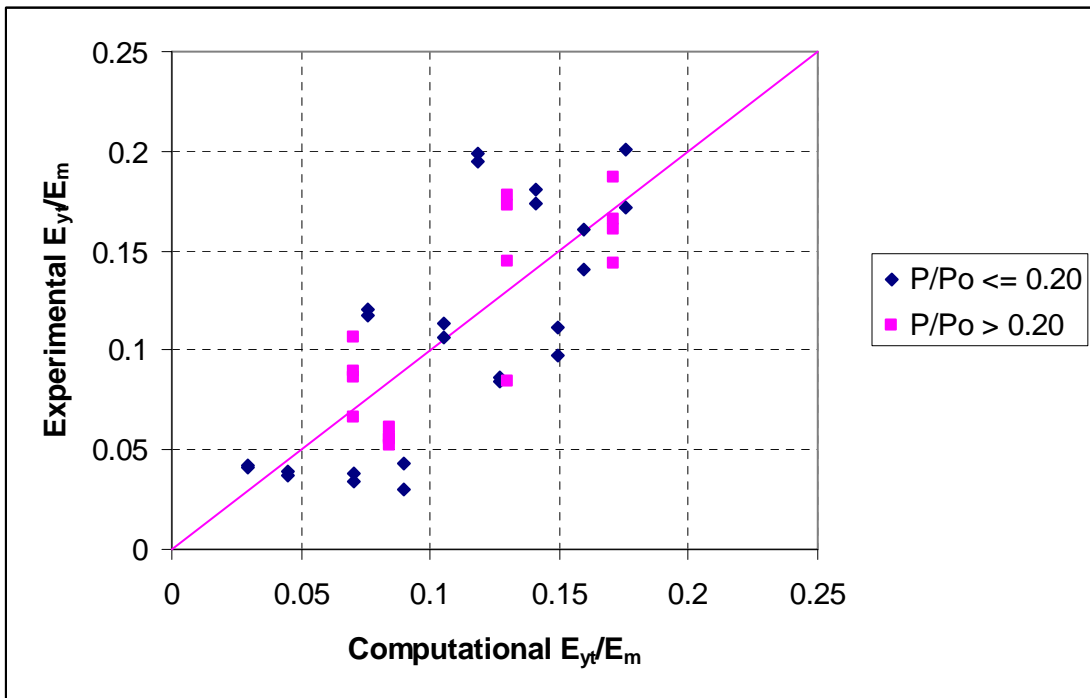


Figure 3.60: Comparison of Computational and Experimental E_{y}/E_m Values: Cyclically-Loaded RCFT Beam-Column Tests

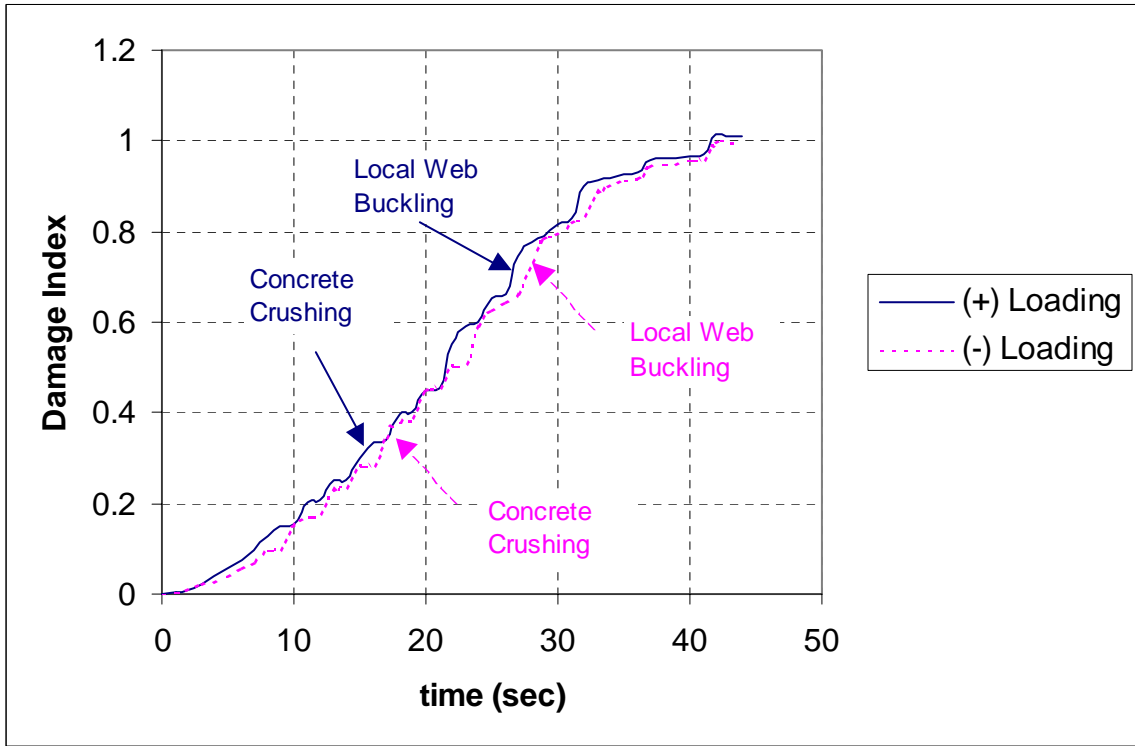


Figure 3.61: Damage Index by Kradzig et al. (1989) Applied to CBC-32-46-20 by Varma et al. (2002)

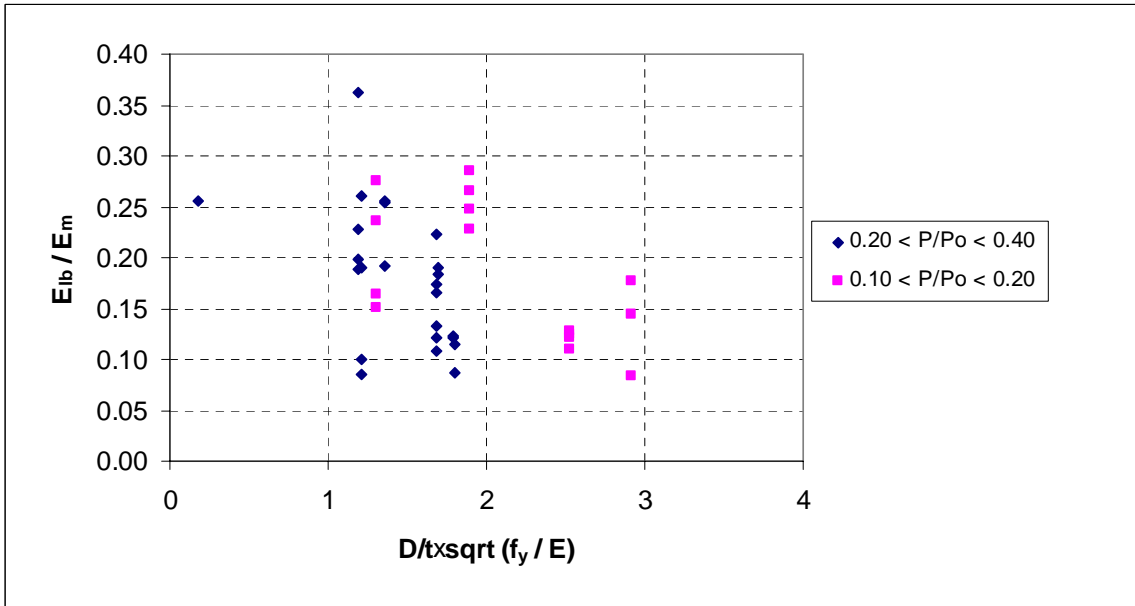


Figure 3.62: Comparison of E_{lb}/E_m versus $D/t\sqrt{f_y/E_s}$: Cyclically-Loaded RCFT Beam-Columns

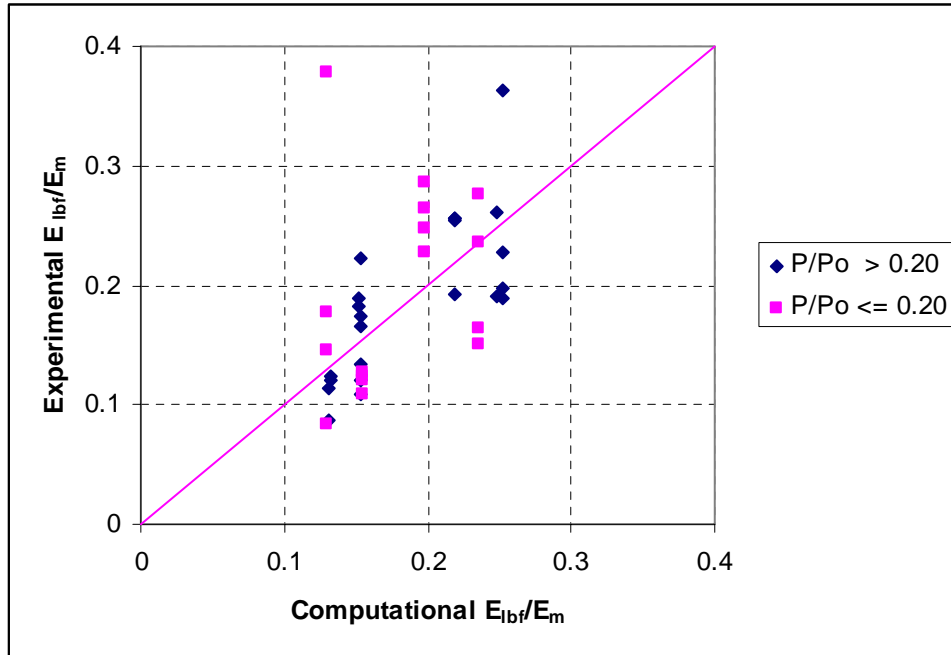


Figure 3.63: Comparison of Computational and Experimental E_{lbf}/E_m Values: Cyclically-Loaded RCFT Beam-Column Tests

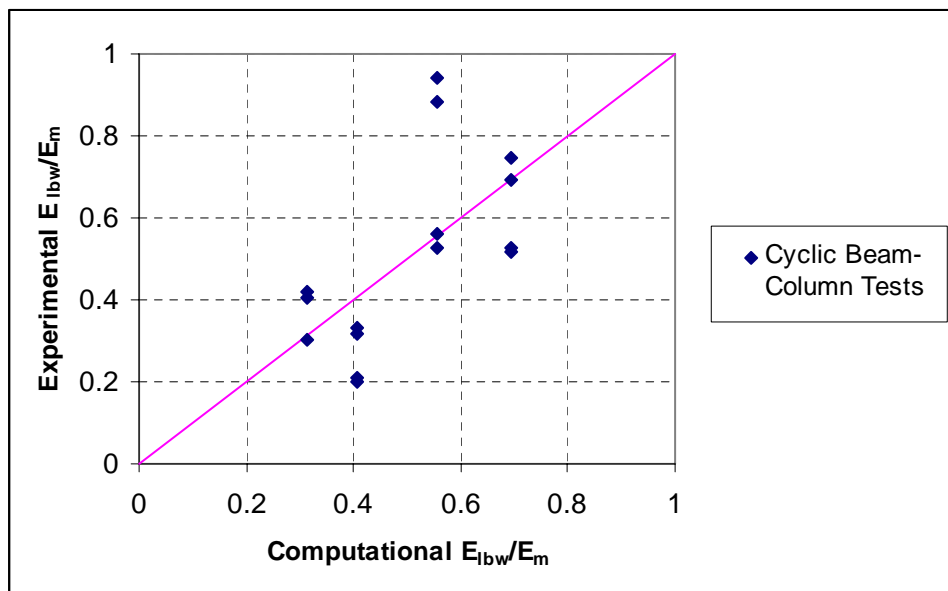


Figure 3.64: Comparison of Computational and Experimental E_{lbw}/E_m Values: Cyclically-Loaded RCFT Beam-Column Tests

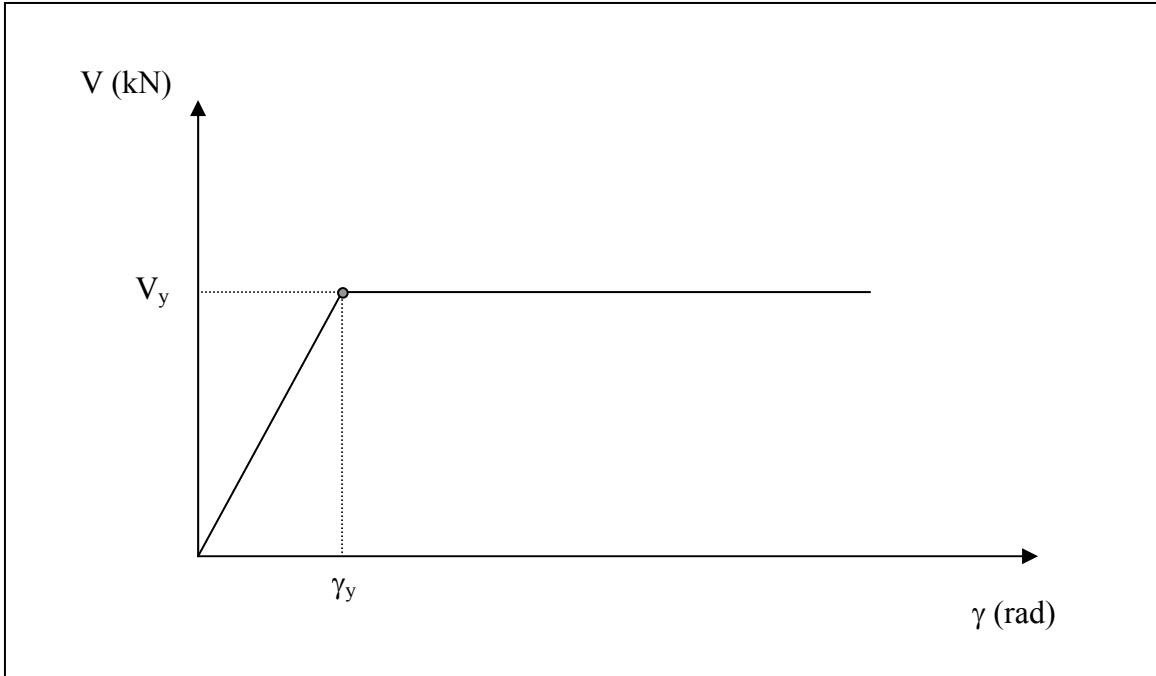


Figure 3.65: Shear Force-Deformation Relation of Steel Panel

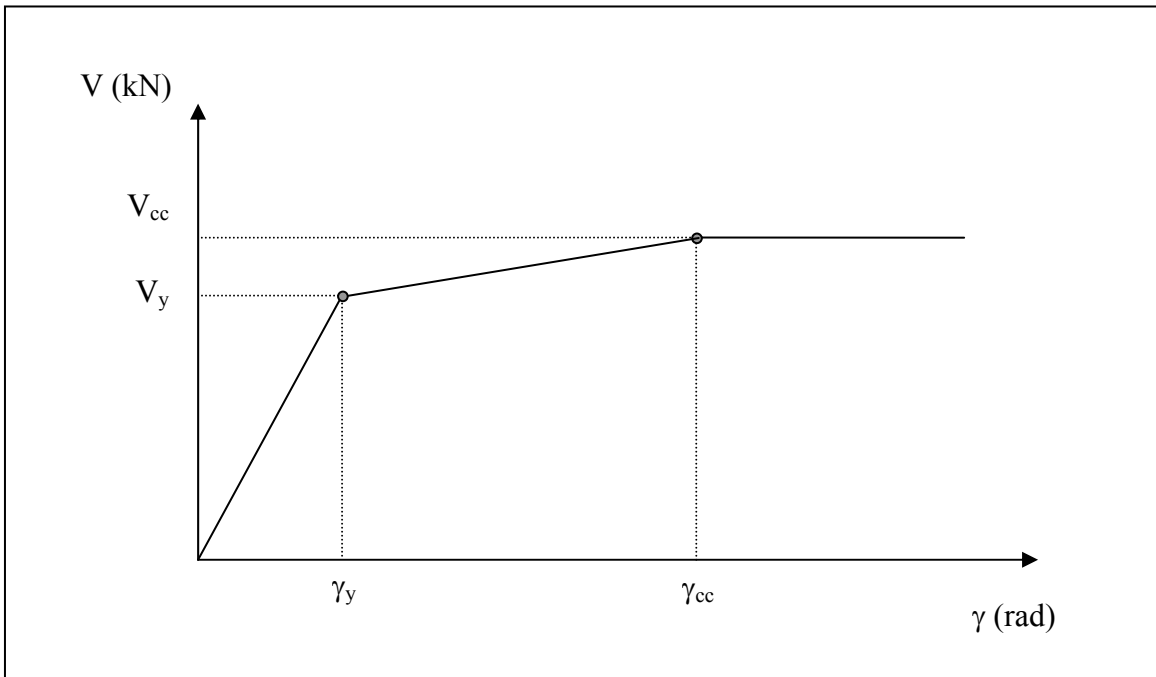


Figure 3.66: Shear Force-Deformation Relation of Concrete Panel

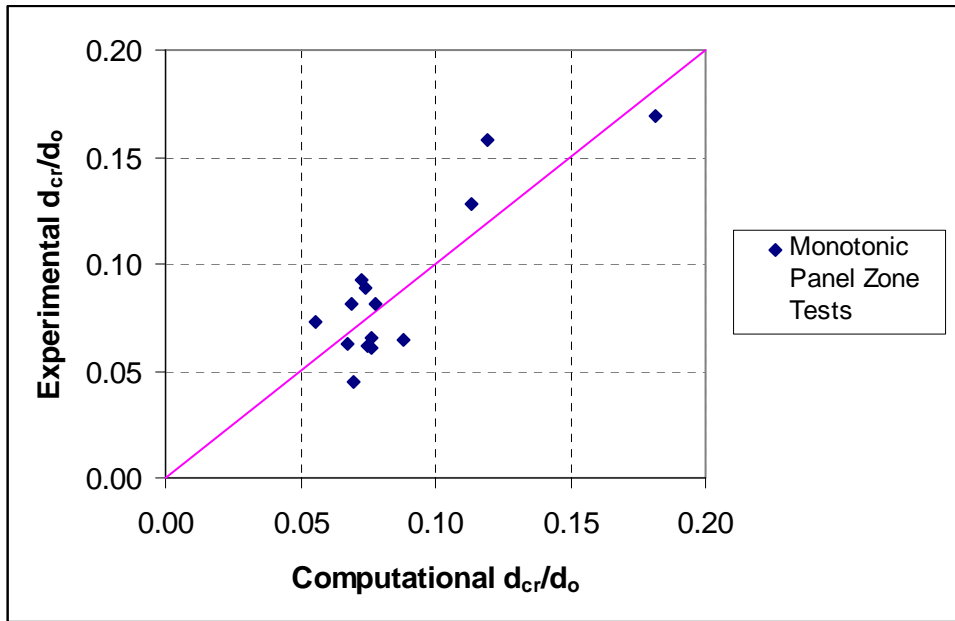


Figure 3.67: Comparison of Computational and Experimental d_{cr}/d_o Values: Monotonically-Loaded RCFT Panel-Zone Tests

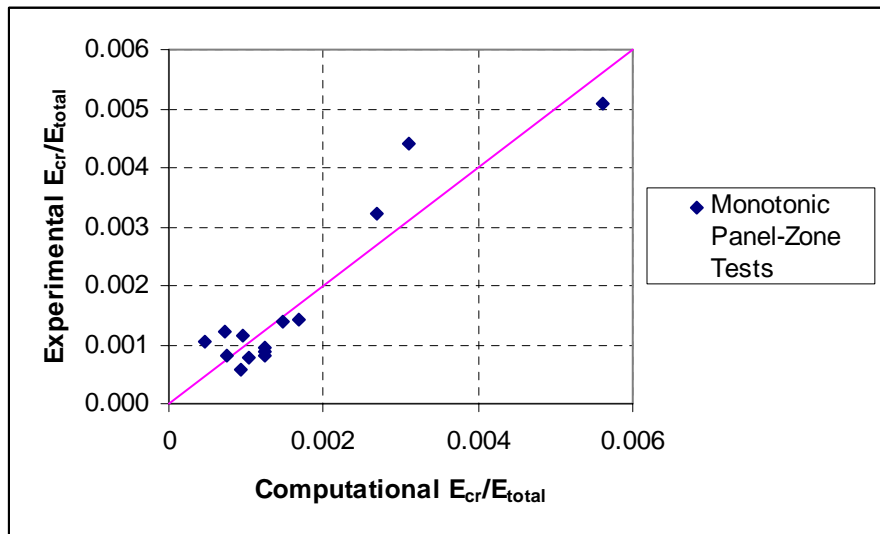


Figure 3.68: Comparison of Computational and Experimental E_{cr}/E_{total} Values: Monotonically-Loaded RCFT Panel-Zone Tests

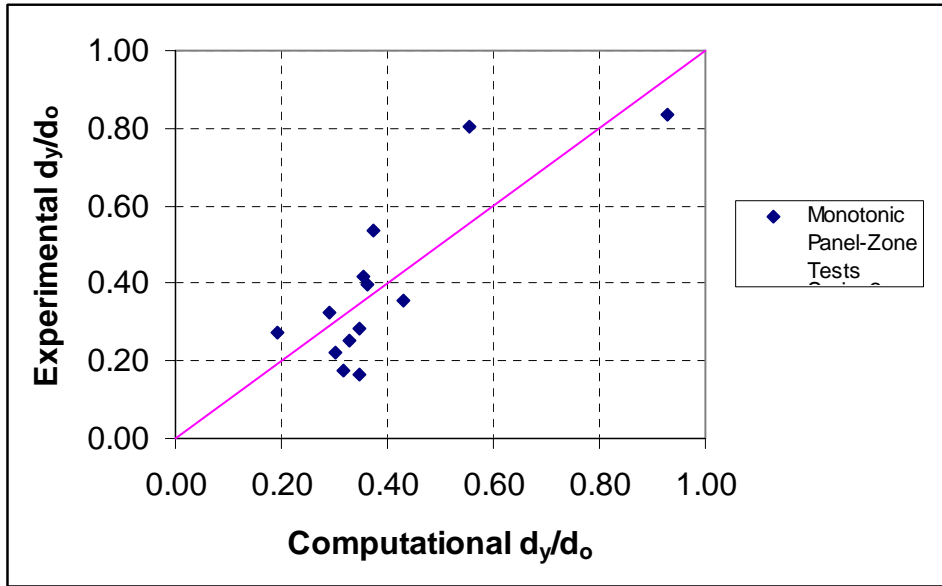


Figure 3.69: Comparison of Computational and Experimental d_y/d_o Values: Monotonically-Loaded RCFT Panel-Zone Tests

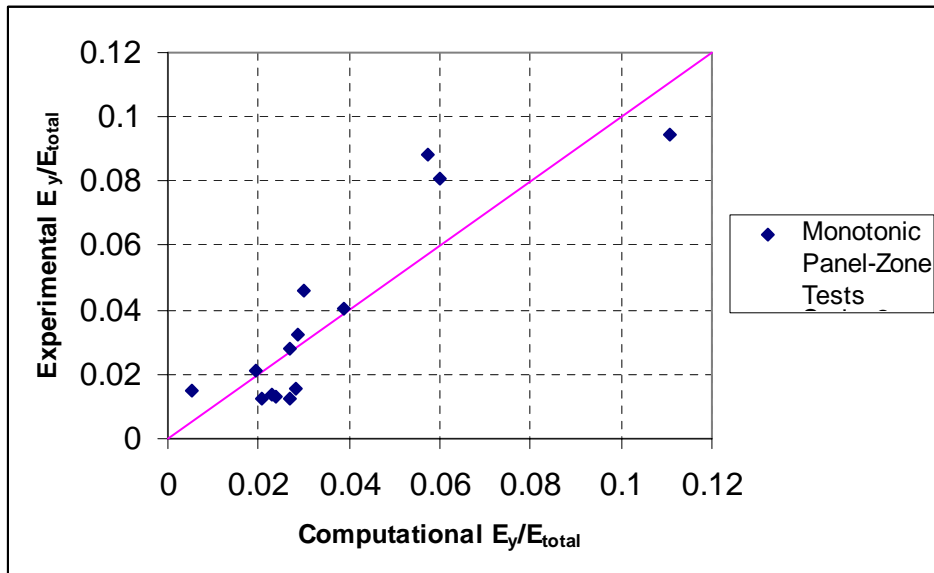


Figure 3.70: Comparison of Computational and Experimental E_y/E_{total} Values: Monotonically-Loaded RCFT Panel-Zone Tests

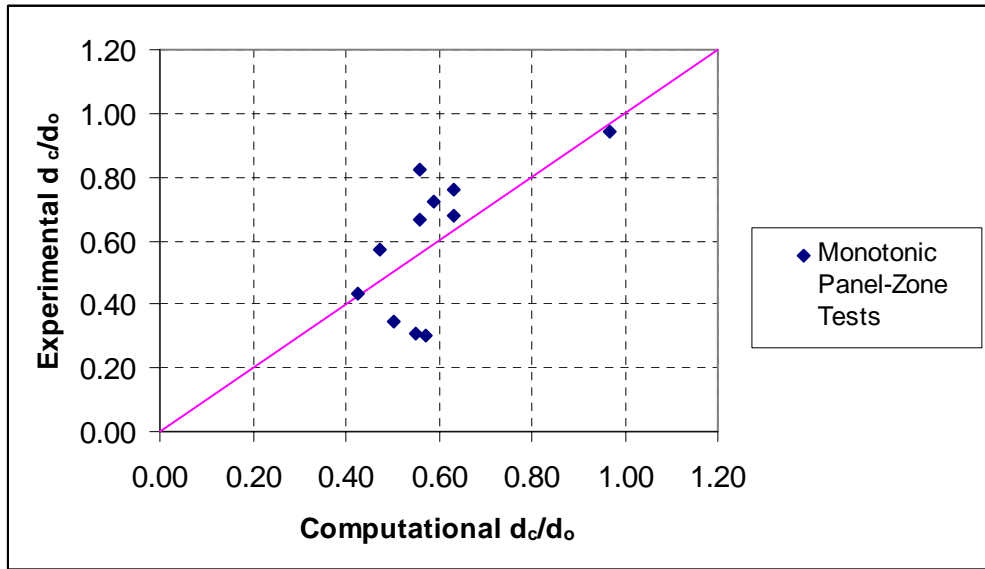


Figure 3.71: Comparison of Computational and Experimental d_c/d_o Values: Monotonically-Loaded RCFT Panel-Zone Tests

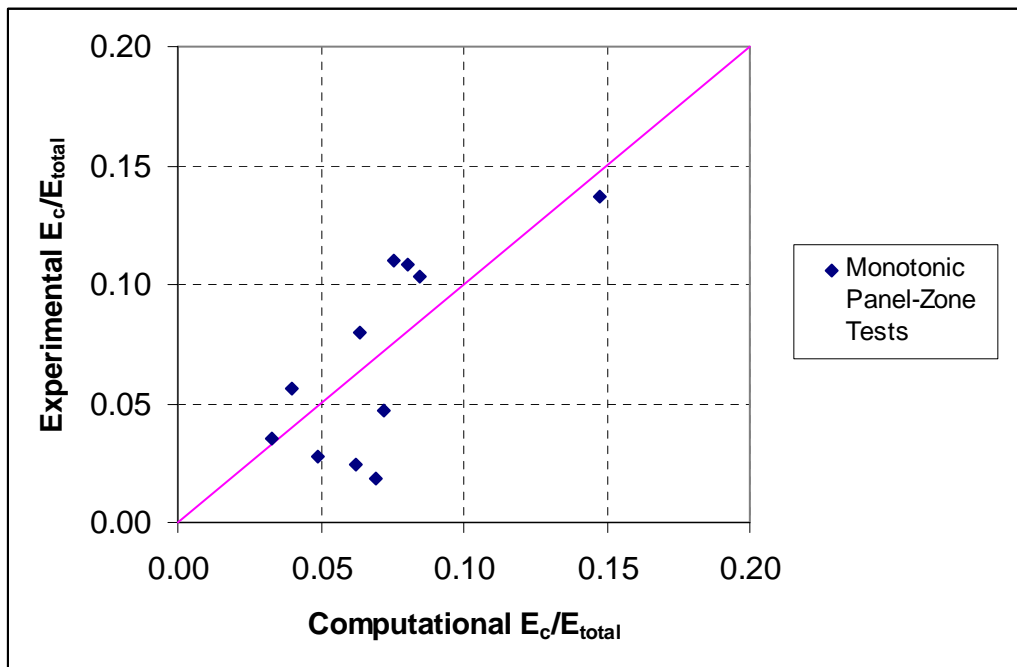


Figure 3.72: Comparison of Computational and Experimental E_c/E_{total} Values: Monotonically-Loaded RCFT Panel-Zone Tests

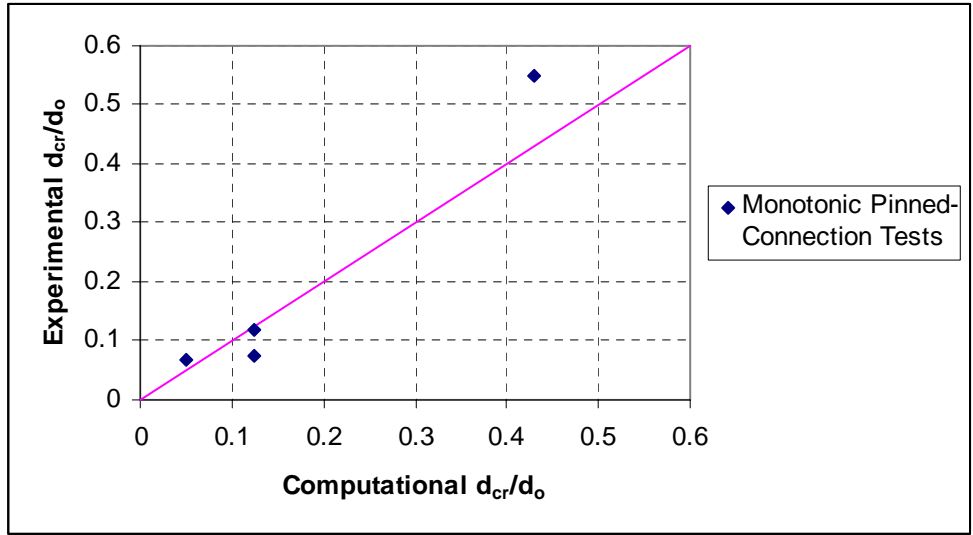


Figure 3.73: Comparison of Computational and Experimental d_{cr}/d_o Values: Monotonically-Loaded RCFT Pinned-Connection Tests

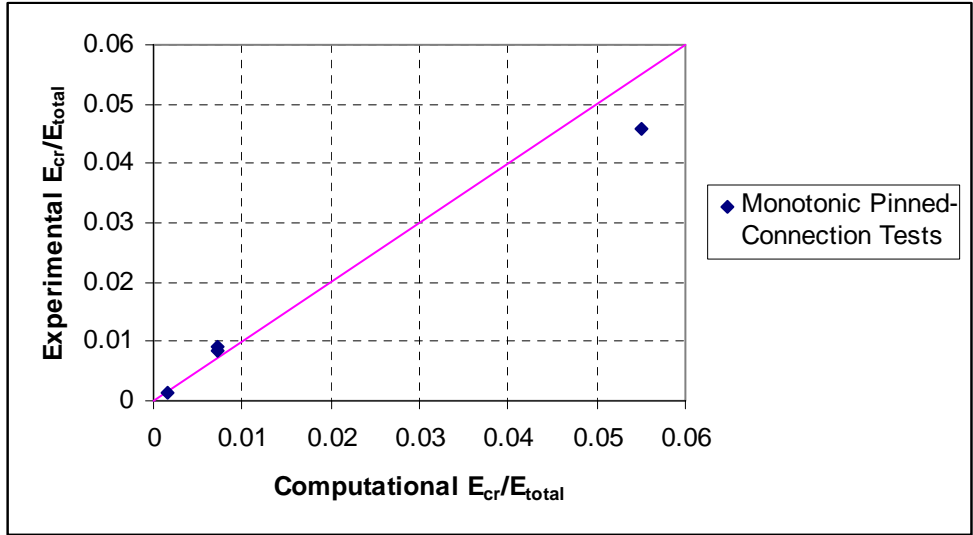


Figure 3.74: Comparison of Computational and Experimental E_{cr}/E_{total} Values: Monotonically-Loaded RCFT Pinned-Connection Tests

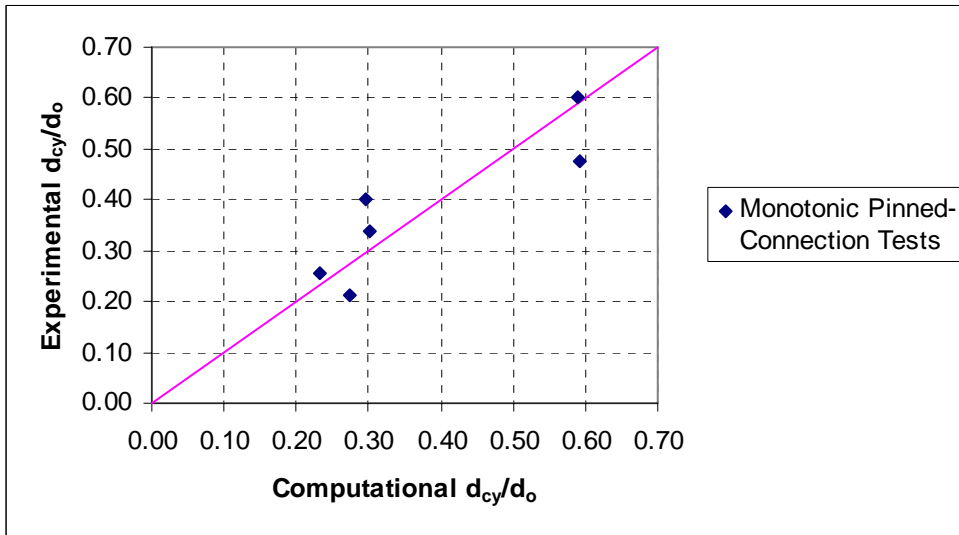


Figure 3.75: Comparison of Computational and Experimental d_{cy}/d_o Values: Monotonically-Loaded RCFT Pinned-Connection Tests

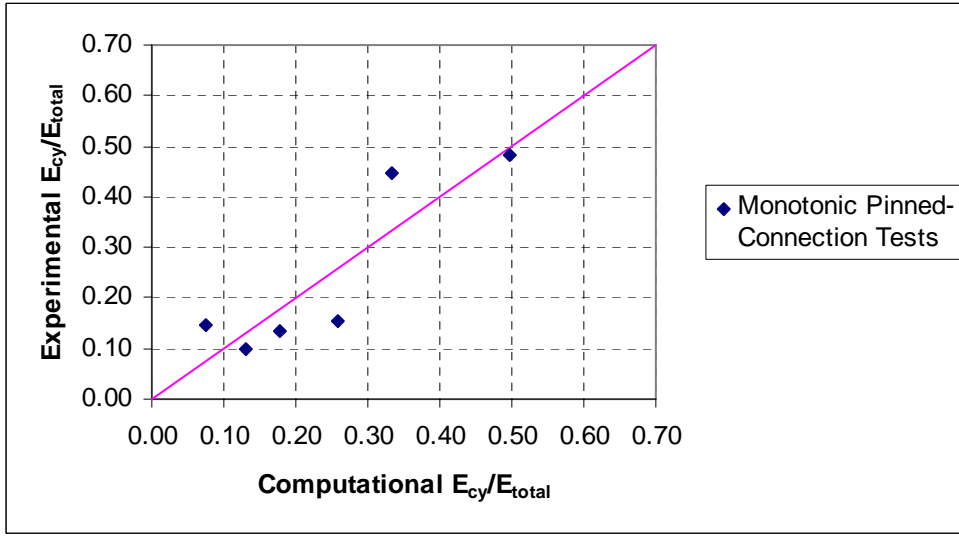


Figure 3.76: Comparison of Computational and Experimental E_{cy}/E_{total} Values: Monotonically-Loaded RCFT Pinned-Connection Tests

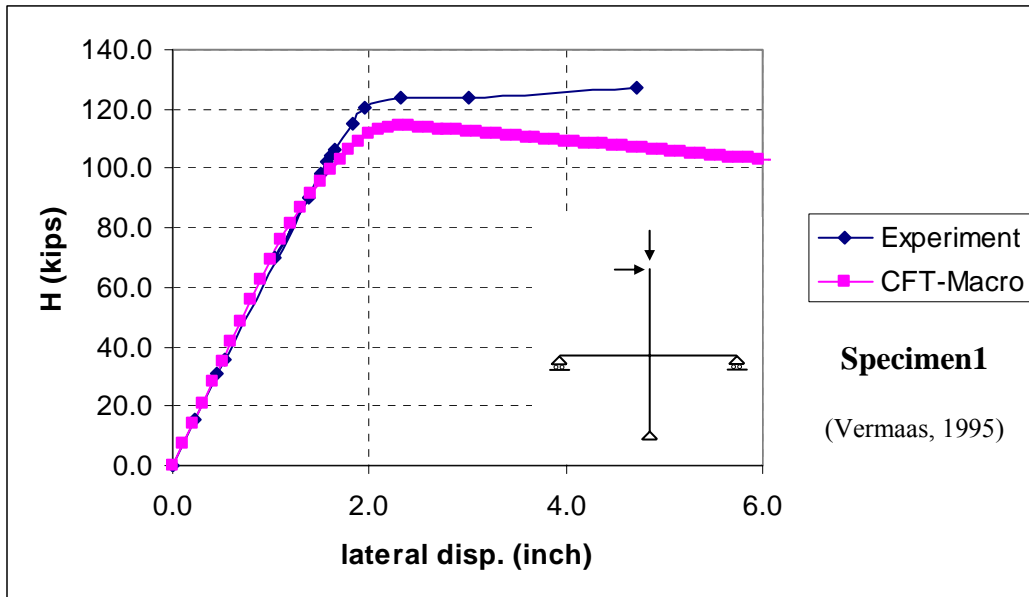


Figure 3.77: Comparison of Computational and Experimental H versus Δ Curve for a Cruciform Frame with Square CFT: $D/t = 35, f'_c = 43.4$ MPa, $f_y = 317.1$ MPa, $P/P_o = 0.16$

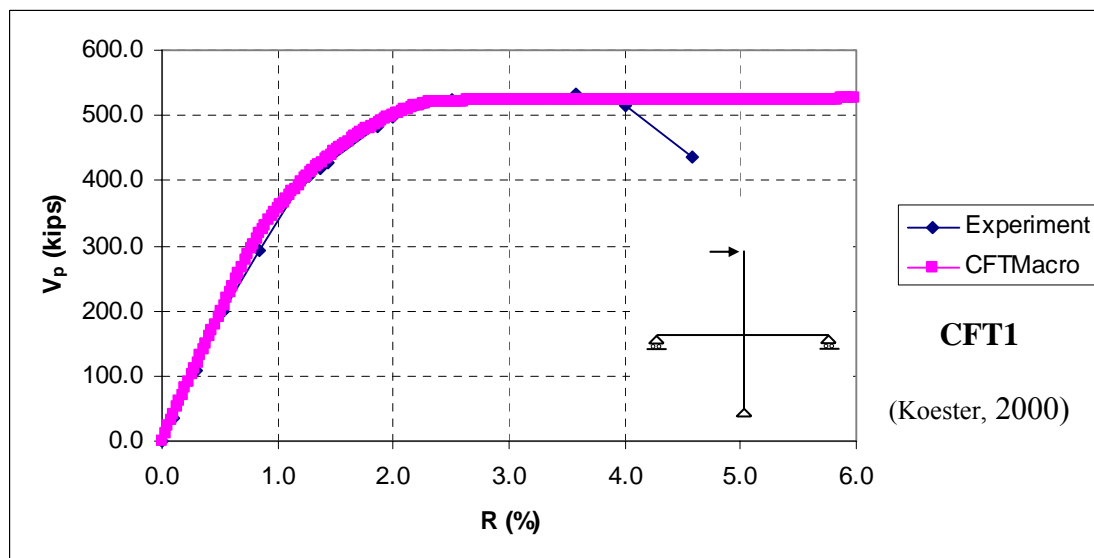


Figure 3.78: Comparison of Computational and Experimental V_p versus R Curve for a Cruciform Frame with Square CFT: $D/t = 27, f'_c = 49.6$ MPa, $f_y = 366.1$ MPa, $P/P_o = 0$

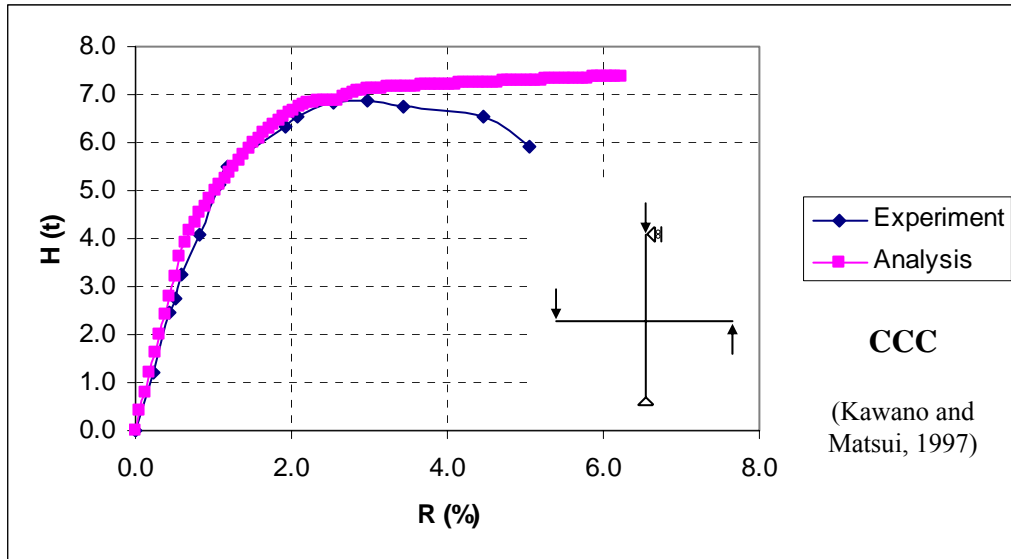


Figure 3.79: Comparison of Computational and Experimental H versus R Curve for a Cruciform Frame with Square CFT: $D/t = 34.5, f'_c = 33.3$ MPa, $f_y = 420.8$ MPa, $P/P_o = 0.30$

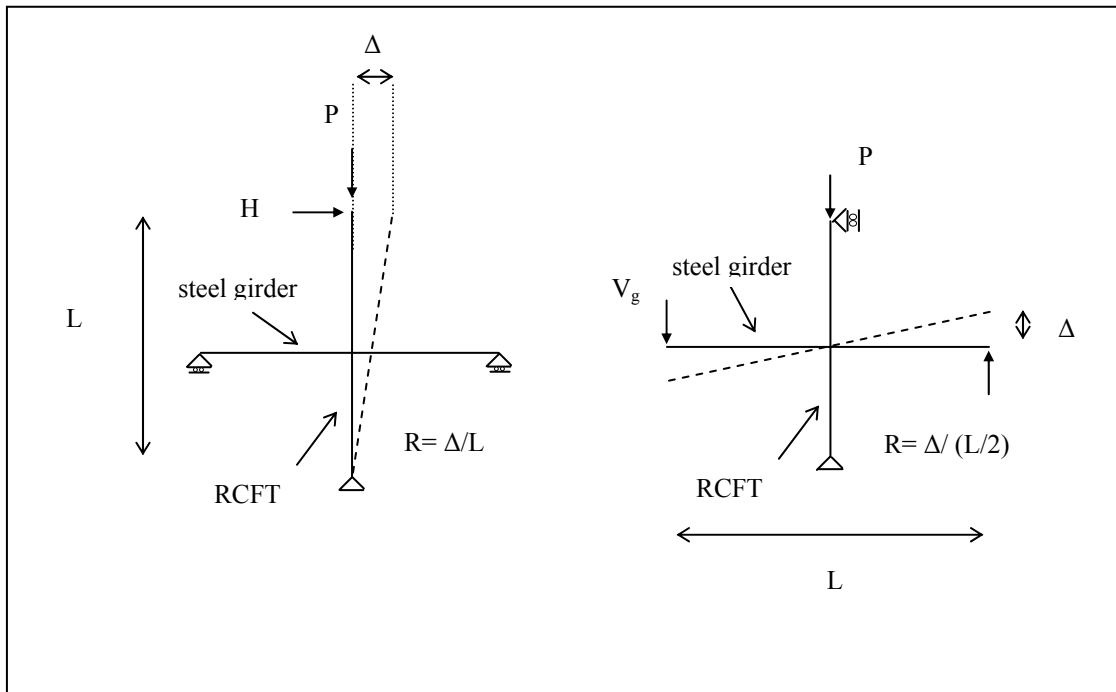


Figure 3.80: Representation of Force and Displacement Quantities in Cyclically Loaded Moment Connection Tests

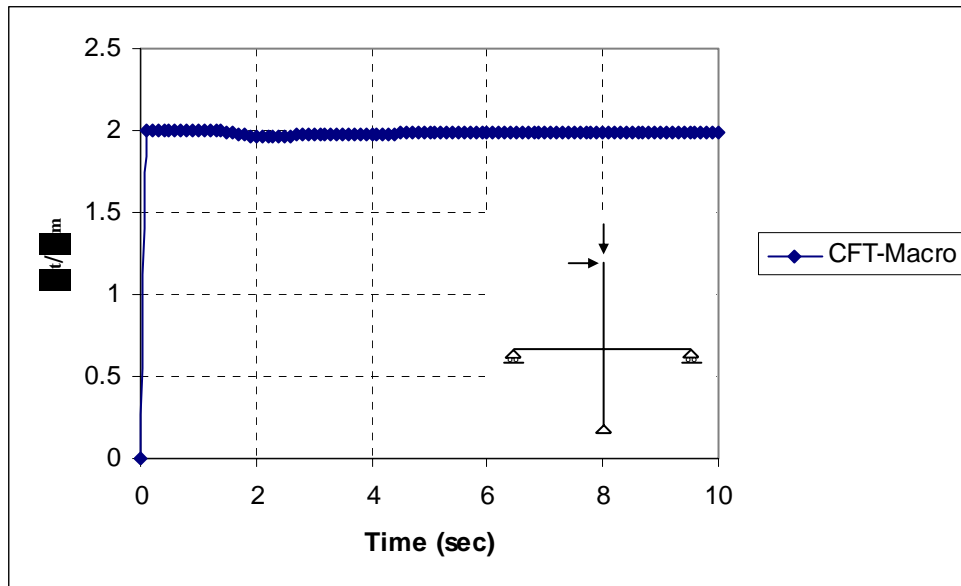


Figure 3.81: Comparison of the Lateral Deflection at the Top and Mid-height of a RCFT Beam-Column in a Cruciform Frame

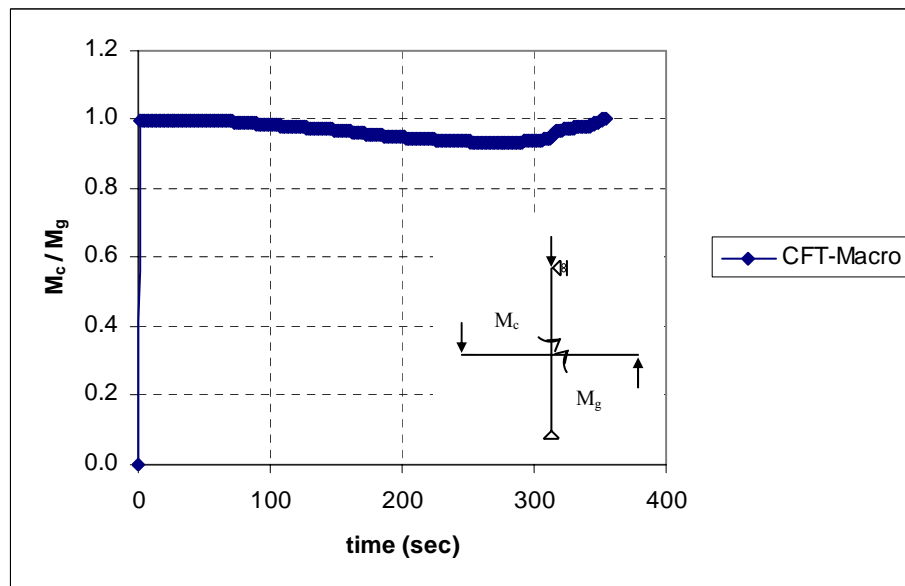


Figure 3.82: Comparison of the Beam-Column Moment (M_c) to the Girder Moment (M_g) at the Connection Region in a Cruciform Frame

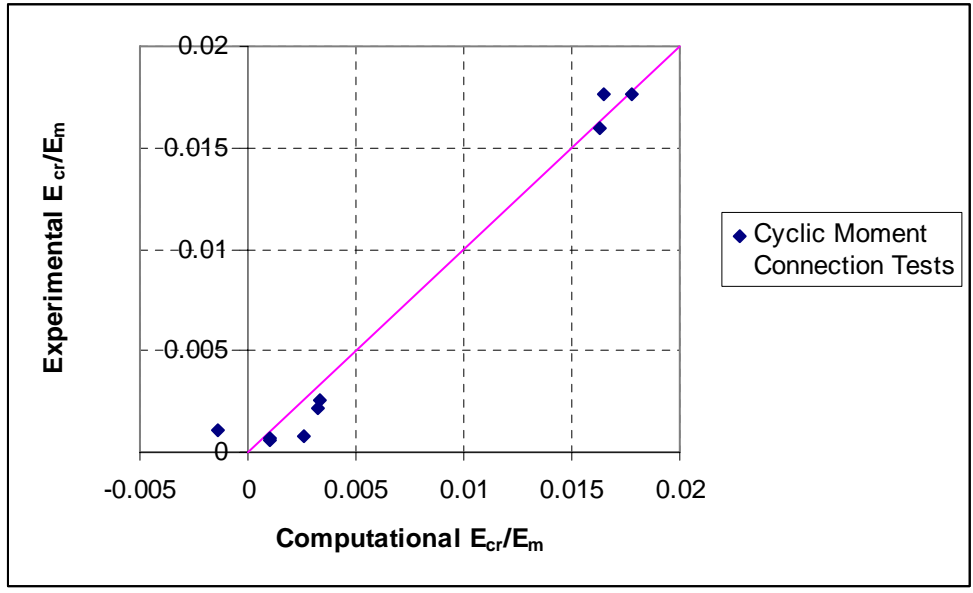


Figure 3.83: Comparison of Computational and Experimental E_{cr}/E_m Values: Cyclically-Loaded RCFT Moment Connection Tests

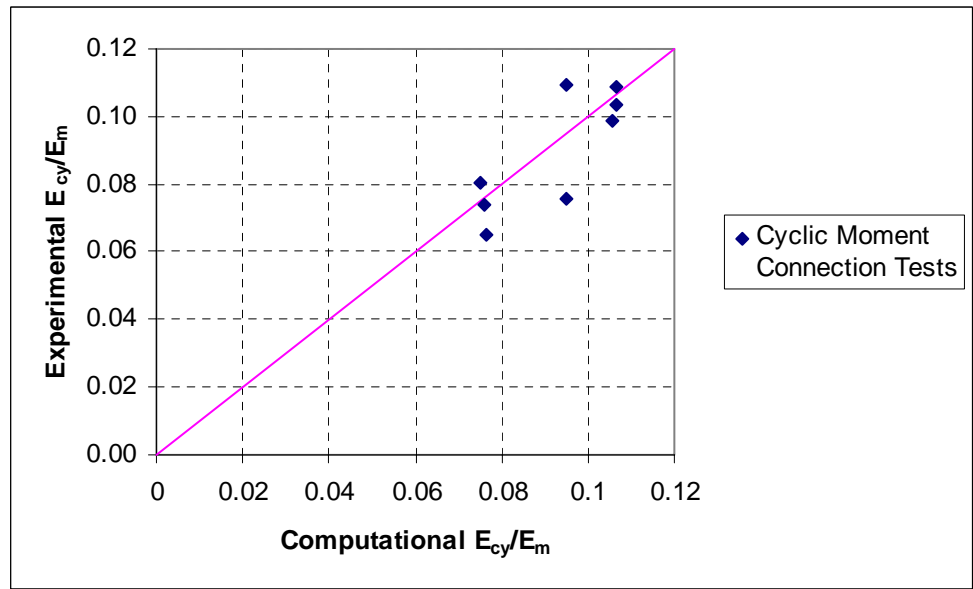


Figure 3.84: Comparison of Computational and Experimental E_{cy}/E_m Values: Cyclically-Loaded RCFT Moment Connection Tests

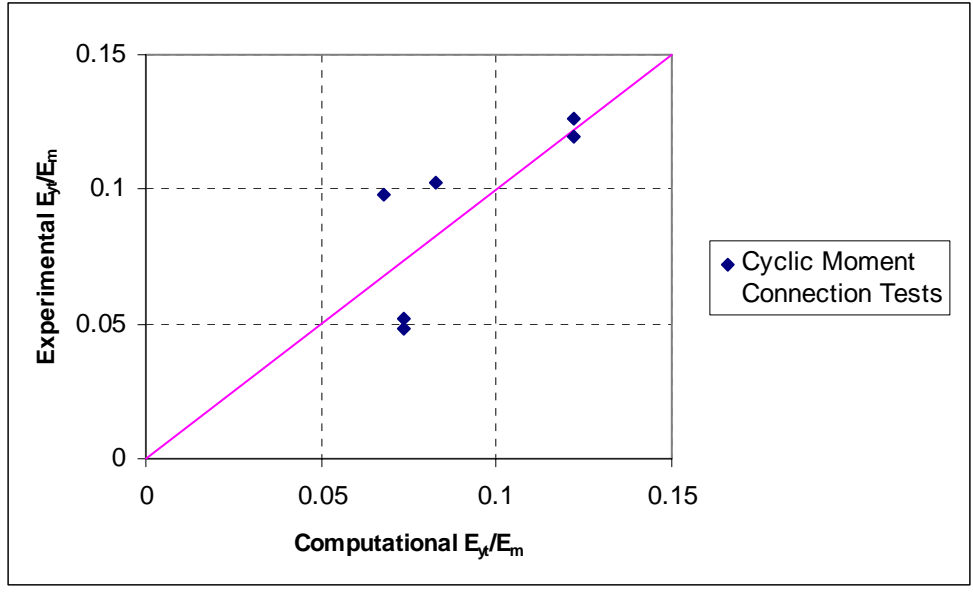


Figure 3.85: Comparison of Computational and Experimental E_y/E_m Values: Cyclically-Loaded RCFT Moment Connection Tests

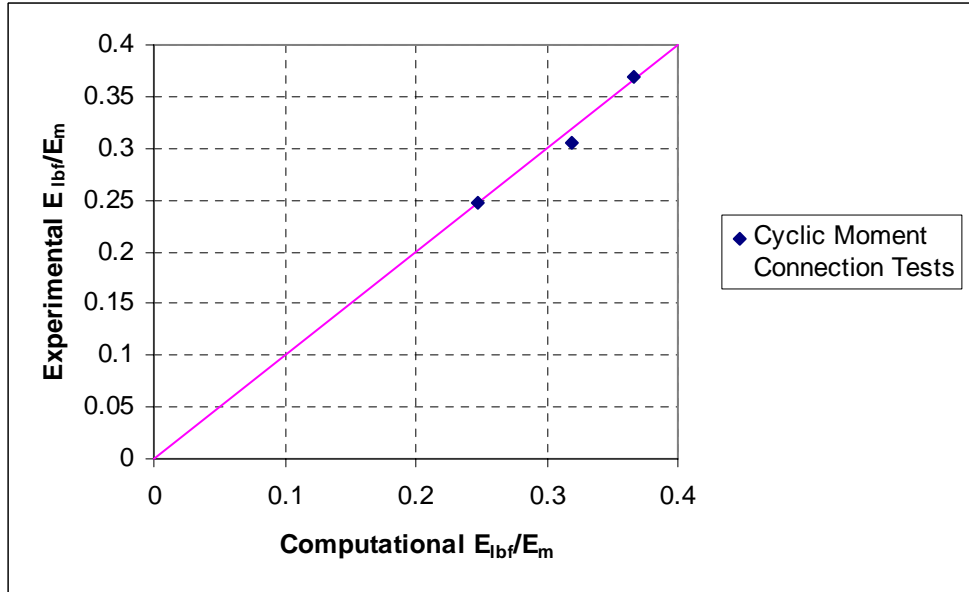


Figure 3.86: Comparison of Computational and Experimental E_{lb}/E_m Values: Cyclically-Loaded RCFT Moment Connection Tests

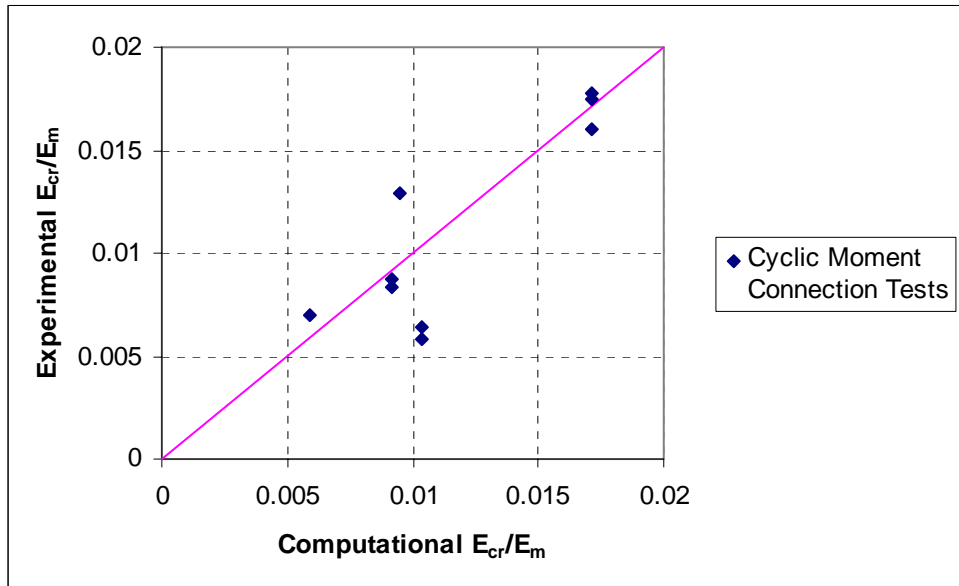


Figure 3.87: Comparison of Computational and Experimental E_{cr}/E_m Values: Cyclically-Loaded RCFT Moment Connection Tests

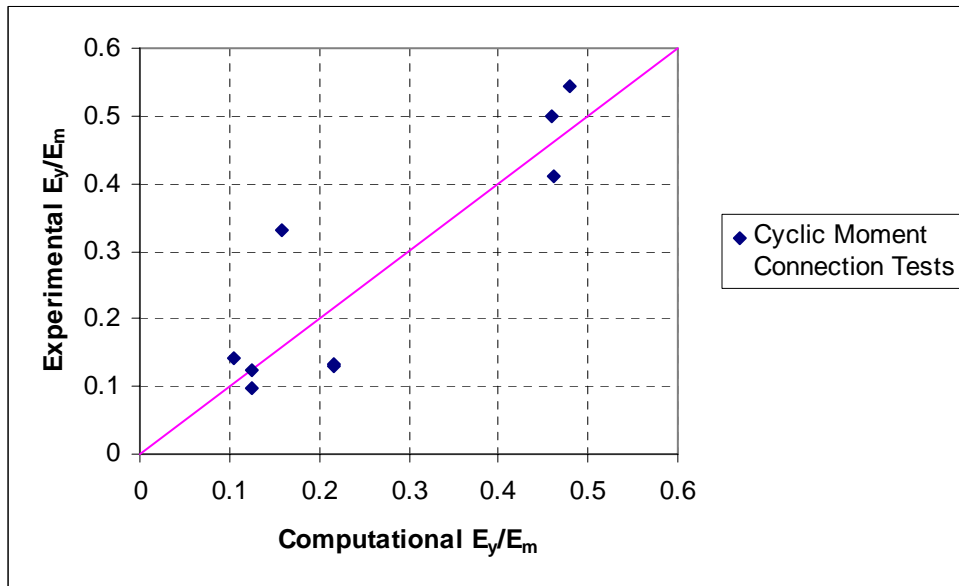


Figure 3.88: Comparison of Computational and Experimental E_y/E_m Values: Cyclically-Loaded RCFT Moment Connection Tests

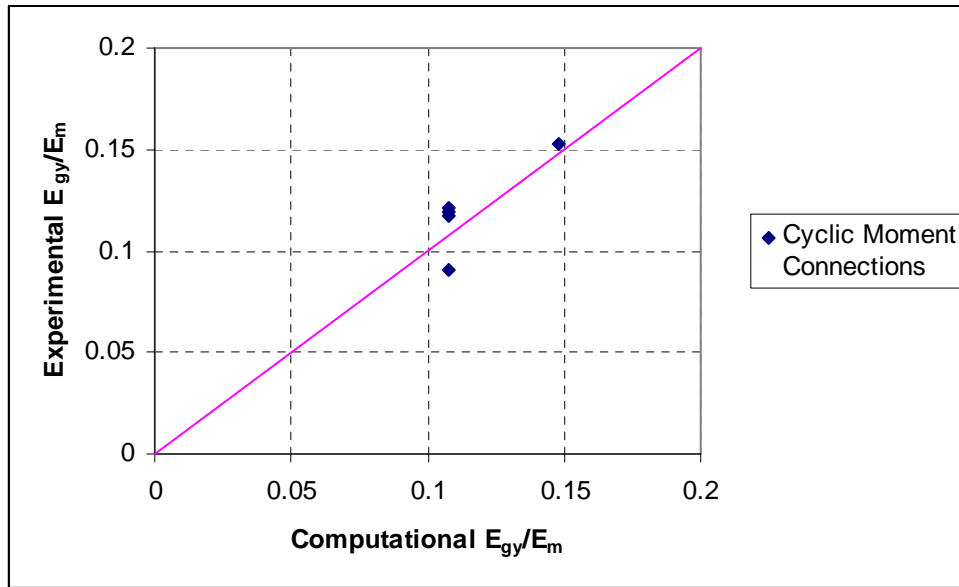


Figure 3.89: Comparison of Computational and Experimental E_{gy}/E_m Values: Cyclically-Loaded RCFT Moment Connection Tests

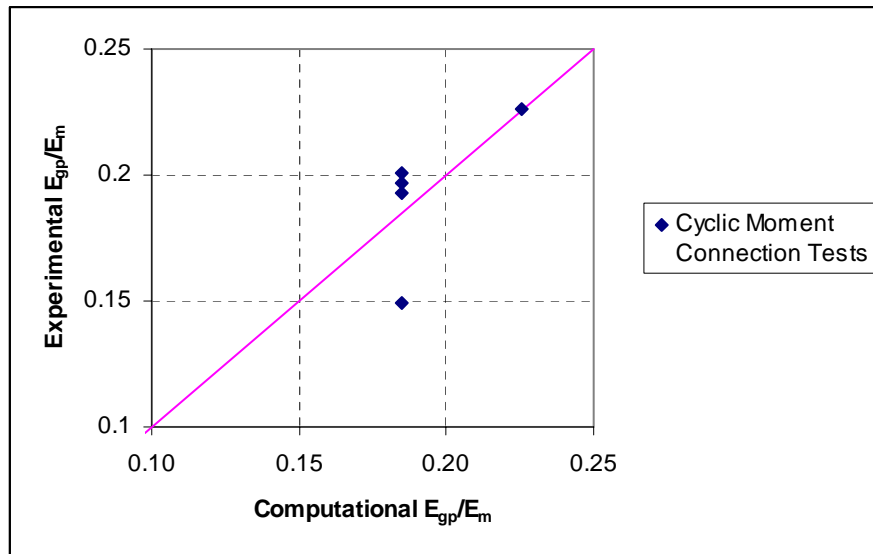


Figure 3.90: Comparison of Computational and Experimental E_{gp}/E_m Values: Cyclically-Loaded RCFT Moment Connection Tests

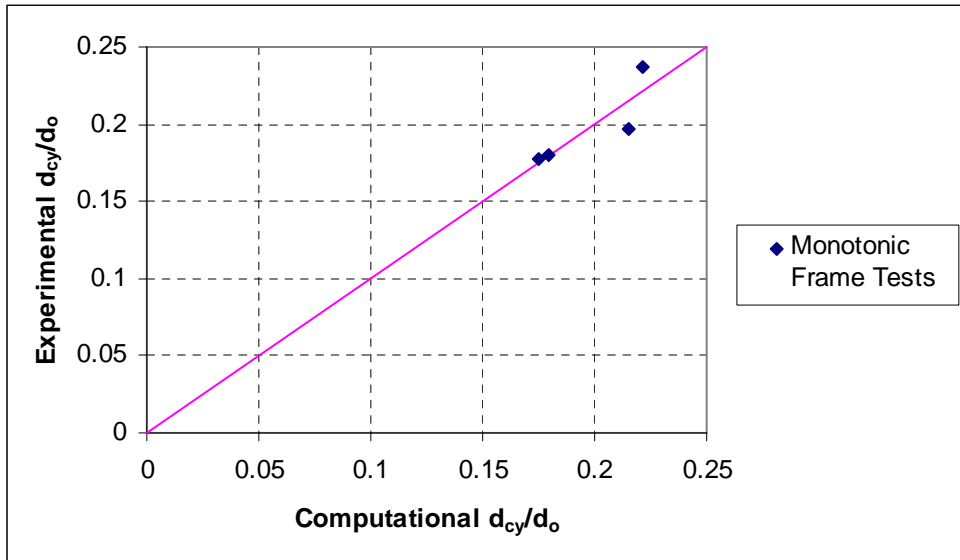


Figure 3.91: Comparison of Computational and Experimental d_{cy}/d_o Values: Monotonically-Loaded RCFT Frame Tests

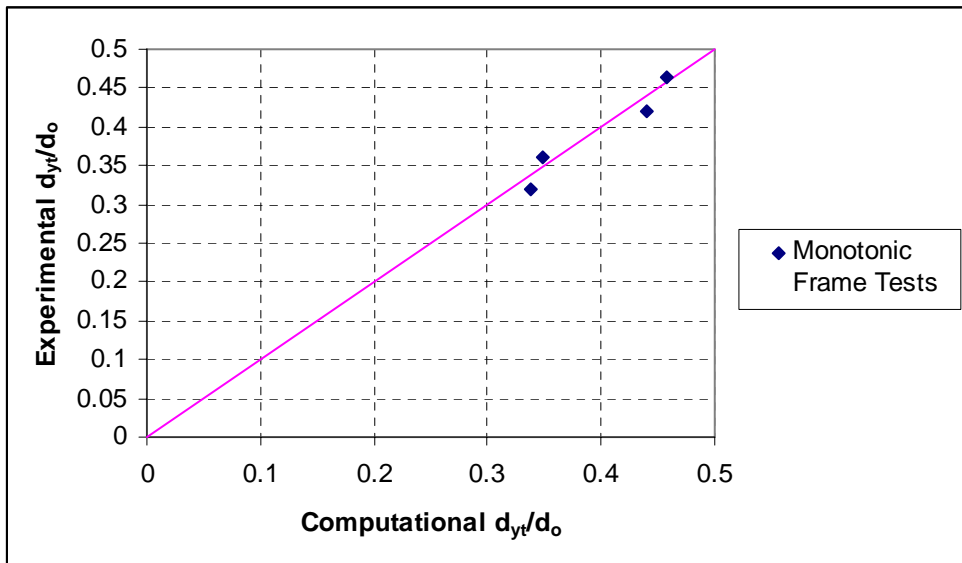


Figure 3.92: Comparison of Computational and Experimental d_{yt}/d_o Values: Monotonically-Loaded RCFT Frame Tests

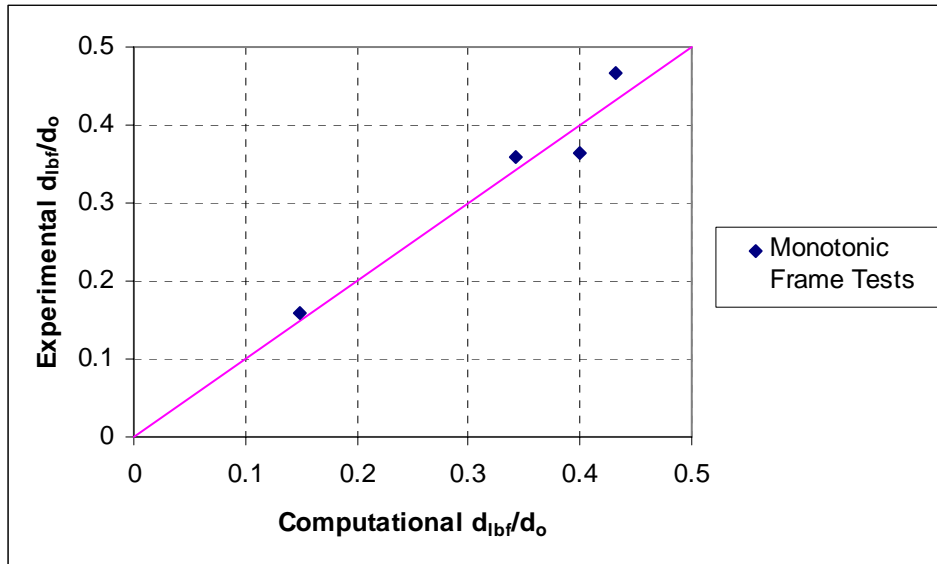


Figure 3.93: Comparison of Computational and Experimental d_{lbf}/d_o Values: Monotonically-Loaded RCFT Frame Tests

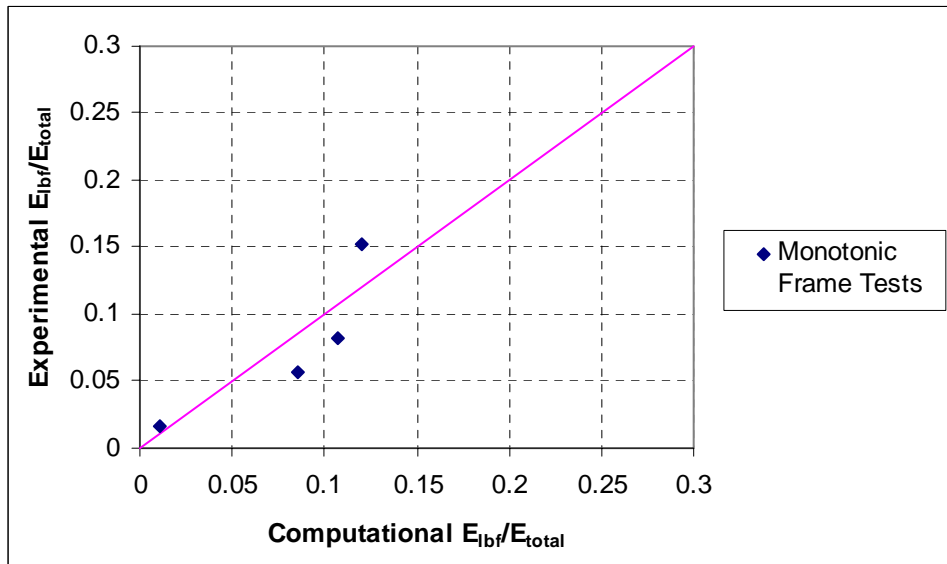


Figure 3.94: Comparison of Computational and Experimental d_{lbf}/d_o Values: Monotonically-Loaded RCFT Frame Tests

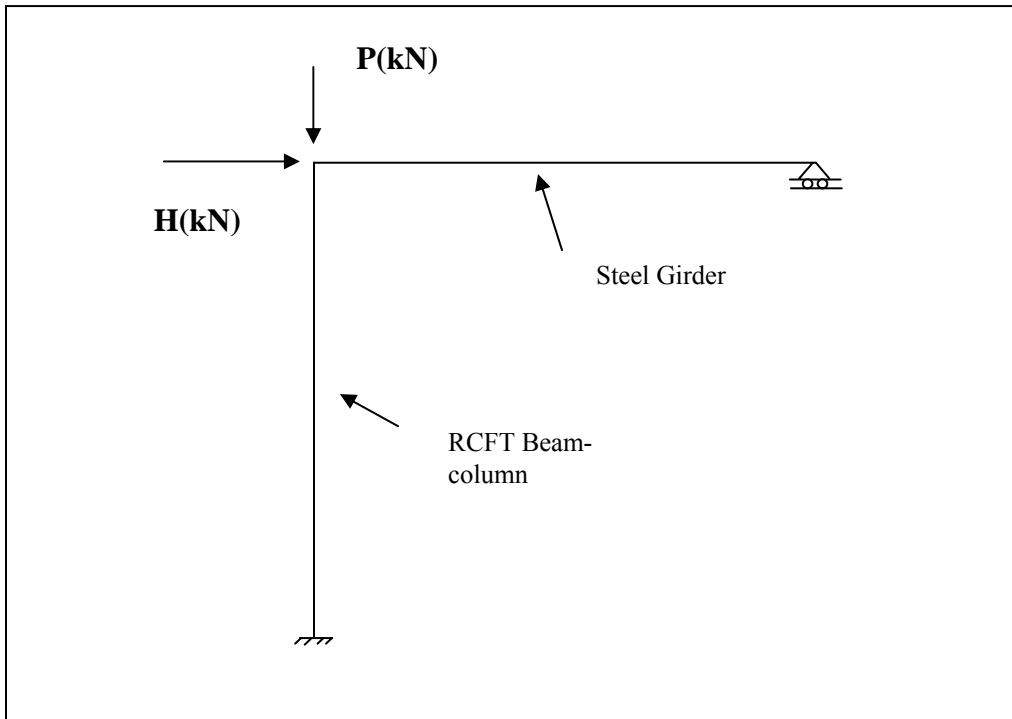


Figure 3.95: Analysis Model of Portal Frames Used in CFT-Macro

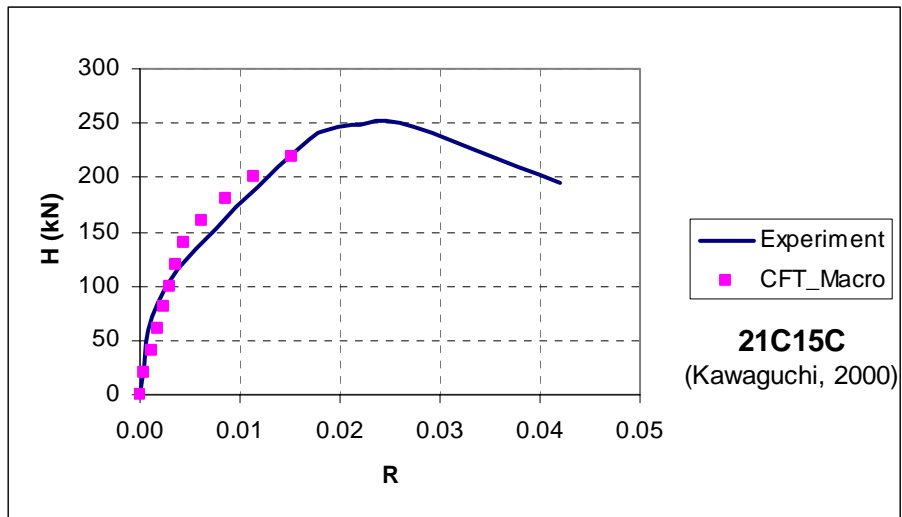


Figure 3.96: Comparison of Computational and Experimental H versus R Curve for a Square CFT: $D/t = 21, f'_c = 18 \text{ MPa}, f_y = 403 \text{ MPa}, P/P_o = 0.15$

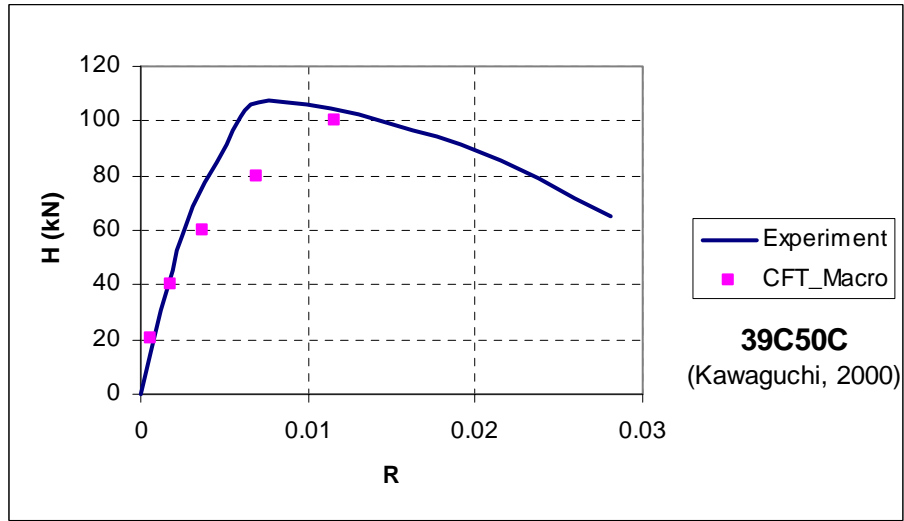


Figure 3.97: Comparison of Computational and Experimental H versus R Curve for a Square CFT: $D/t = 39, f'_c = 18 \text{ MPa}, f_y = 403 \text{ MPa}, P/P_o = 0.50$

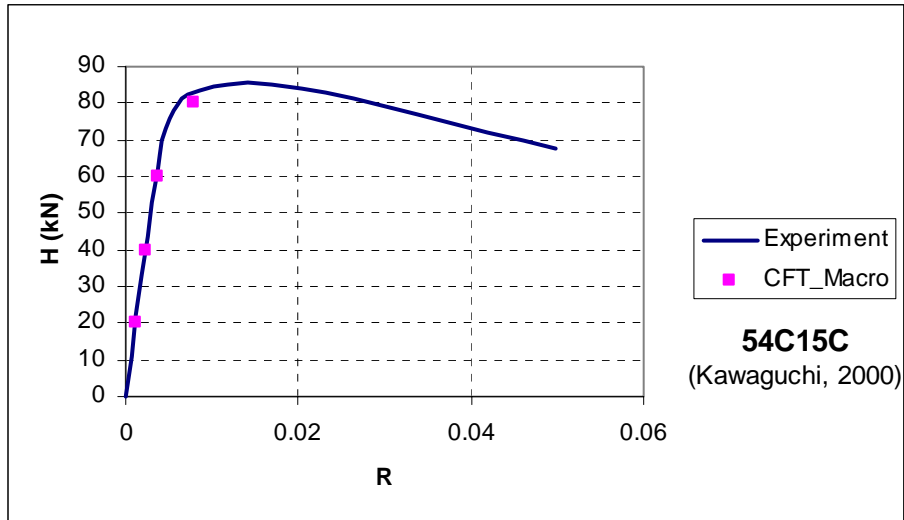


Figure 3.98: Comparison of Computational and Experimental H versus R Curve for a Square CFT: $D/t = 54, f'_c = 16 \text{ MPa}, f_y = 328 \text{ MPa}, P/P_o = 0.15$

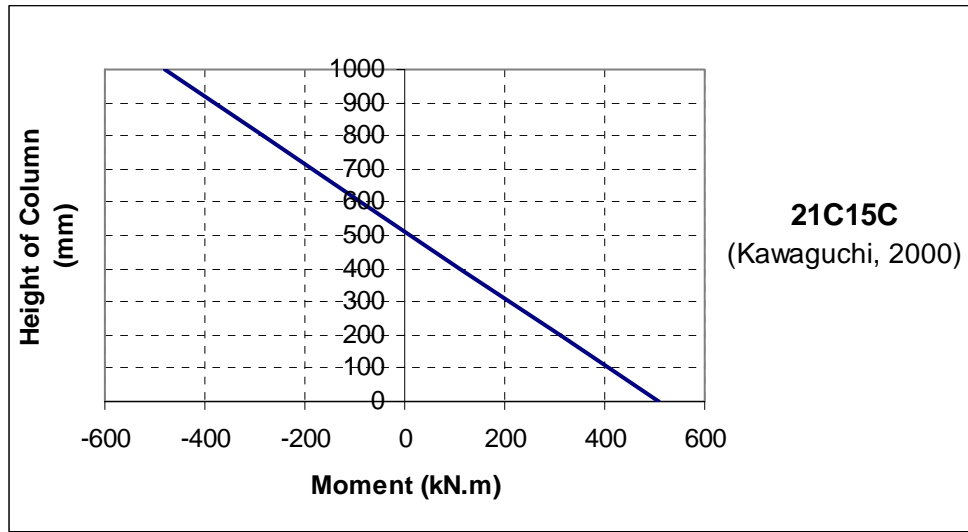


Figure 3.99: Moment Distribution Along the Column Height for a Square CFT: $D/t = 21, f'_c = 18 \text{ MPa}, f_y = 403 \text{ MPa}, P/P_o = 0.15$

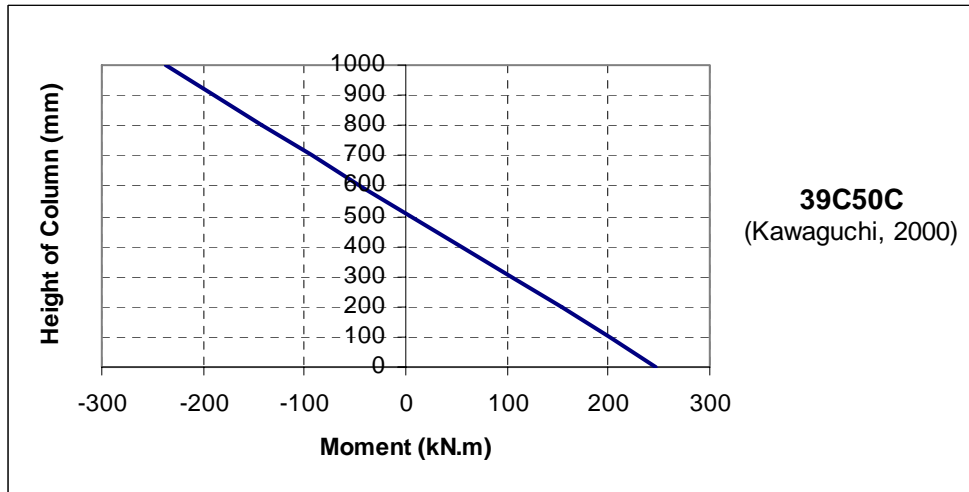


Figure 3.100: Moment Distribution Along the Column Height for a Square CFT: $D/t = 39, f'_c = 18 \text{ MPa}, f_y = 403 \text{ MPa}, P/P_o = 0.50$

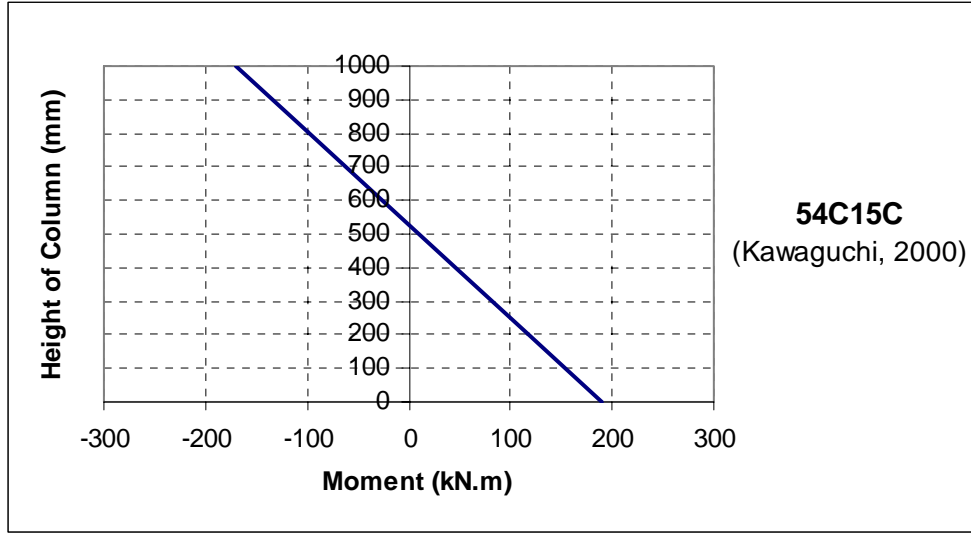


Figure 3.101: Moment Distribution Along the Column Height for a Square CFT: $D/t = 54, f'_c = 16 \text{ MPa}, f_y = 328 \text{ MPa}, P/P_o = 0.15$

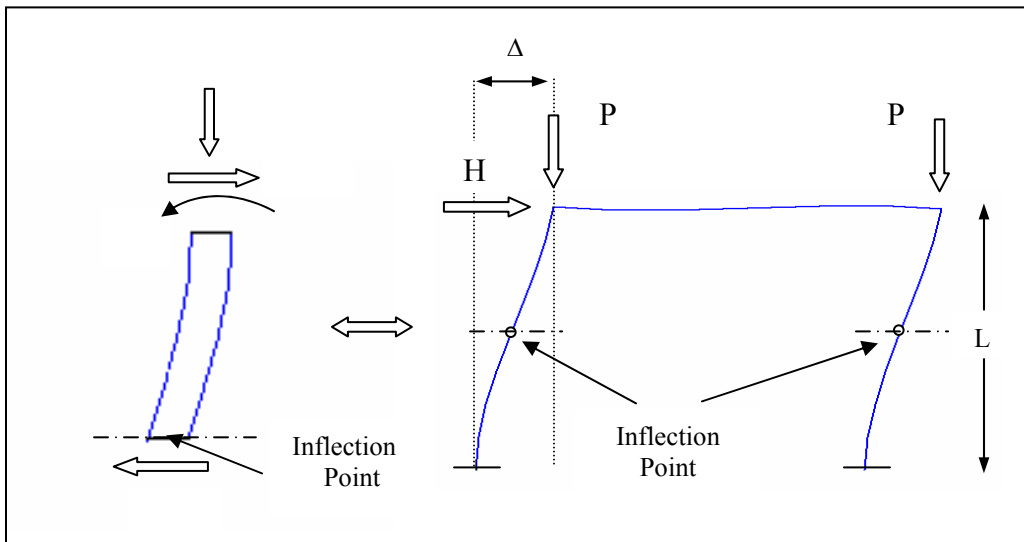


Figure 3.102: Calculation of Moment Due to Lateral Load Transferred to the Columns

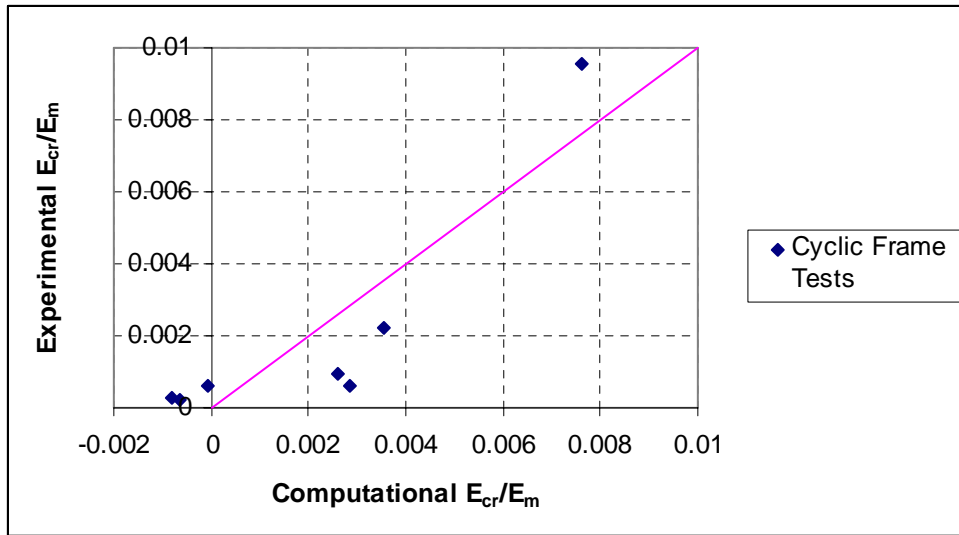


Figure 3.103: Comparison of Computational and Experimental E_{cr}/E_m Values: Cyclically-Loaded RCFT Frame Tests

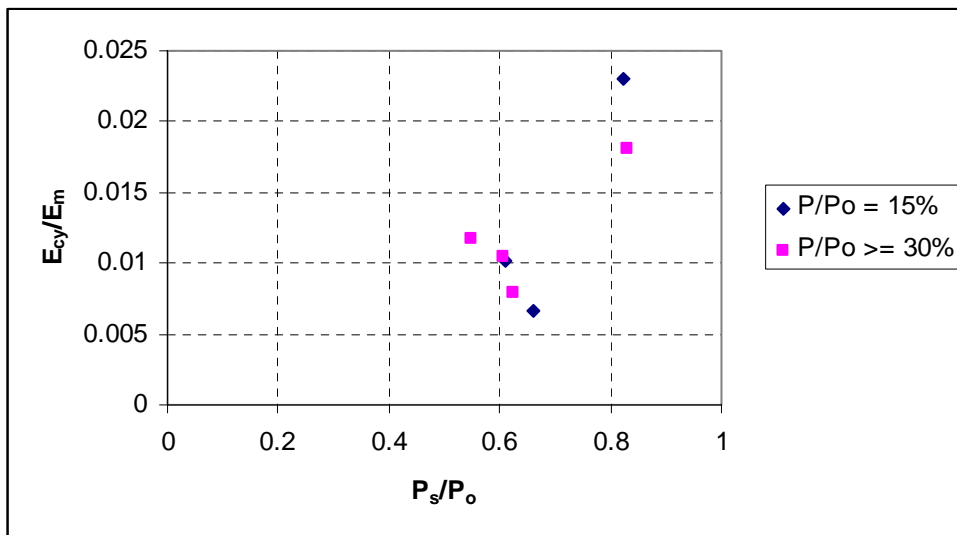


Figure 3.104: Comparison of E_{cy}/E_m versus P_s/P_o : Cyclically-Loaded RCFT Frame Tests

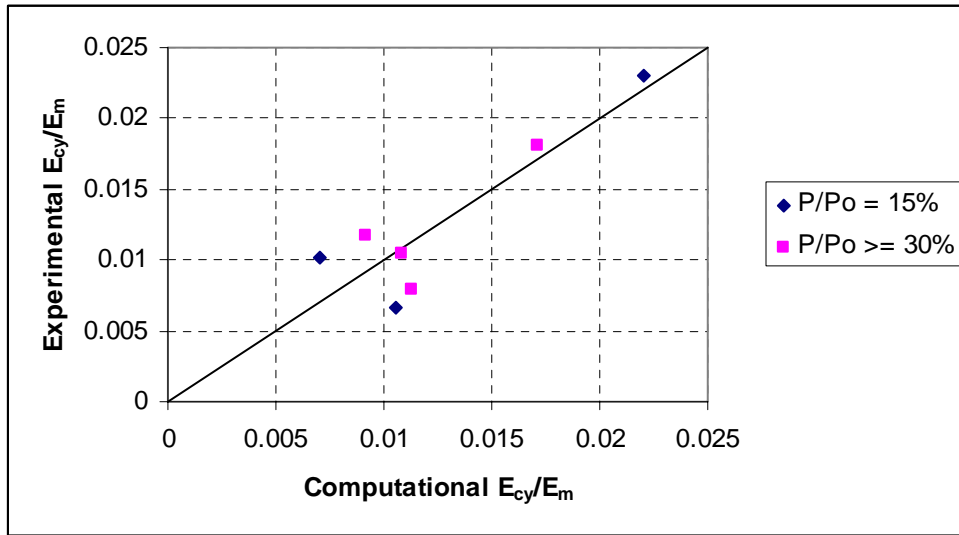


Figure 3.105: Comparison of Computational and Experimental E_{cy}/E_m Values: Cyclically-Loaded RCFT Frame Tests

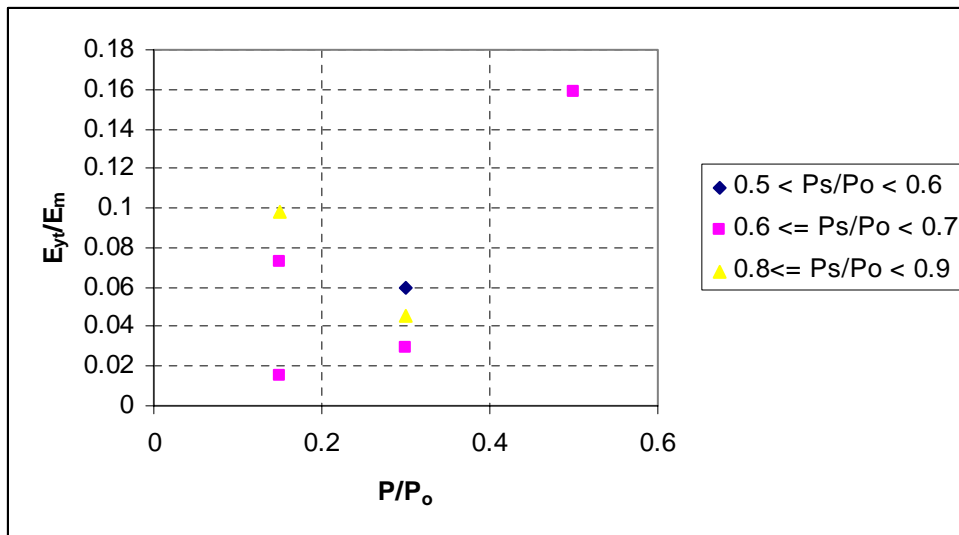


Figure 3.106: Comparison of E_{yt}/E_m versus P/P_o : Cyclically-Loaded RCFT Frame Tests

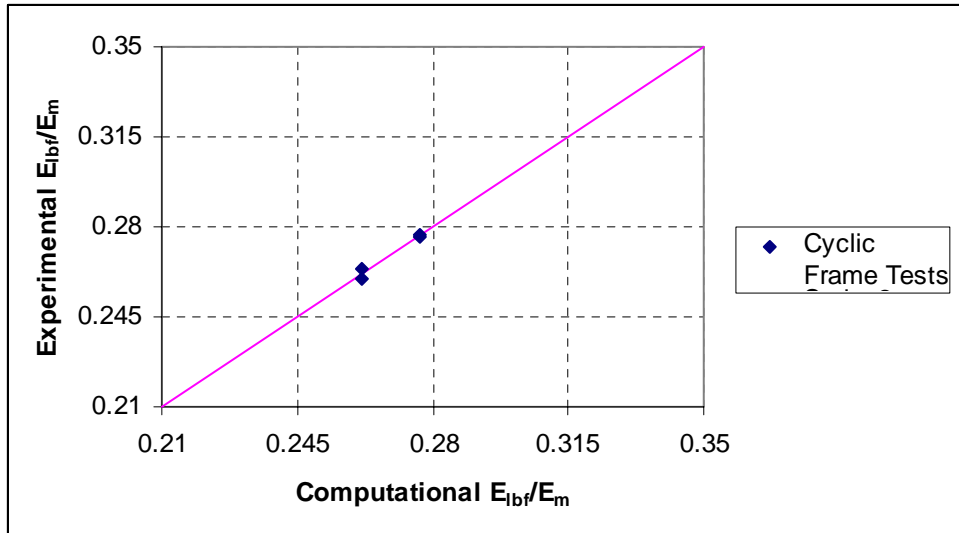


Figure 3.107: Comparison of Computational and Experimental E_{lbf}/E_m Values: Cyclically-Loaded RCFT Frame Tests

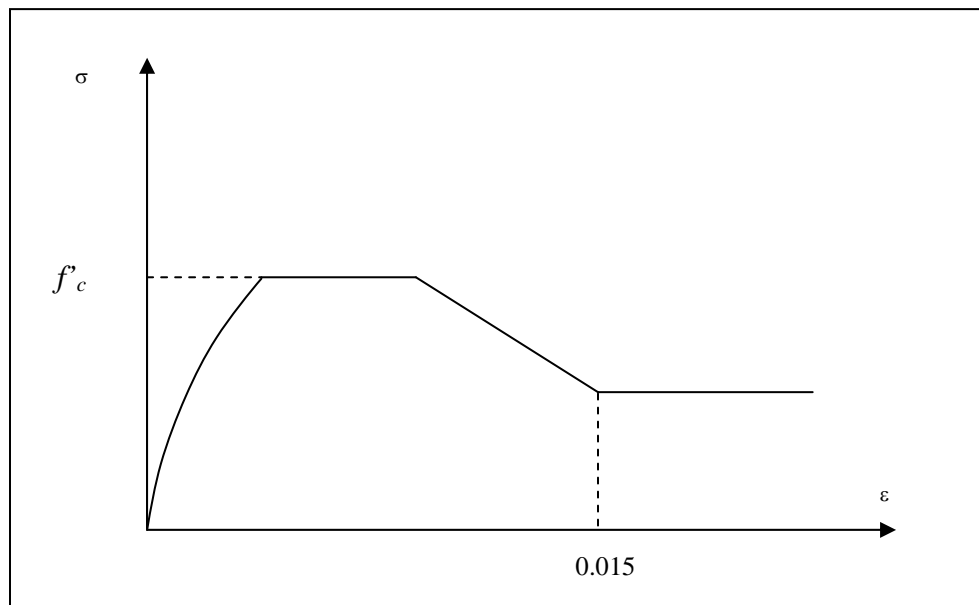


Figure 3.108: Representation of concrete stress-strain model of Tomii and Sakino (1979b)

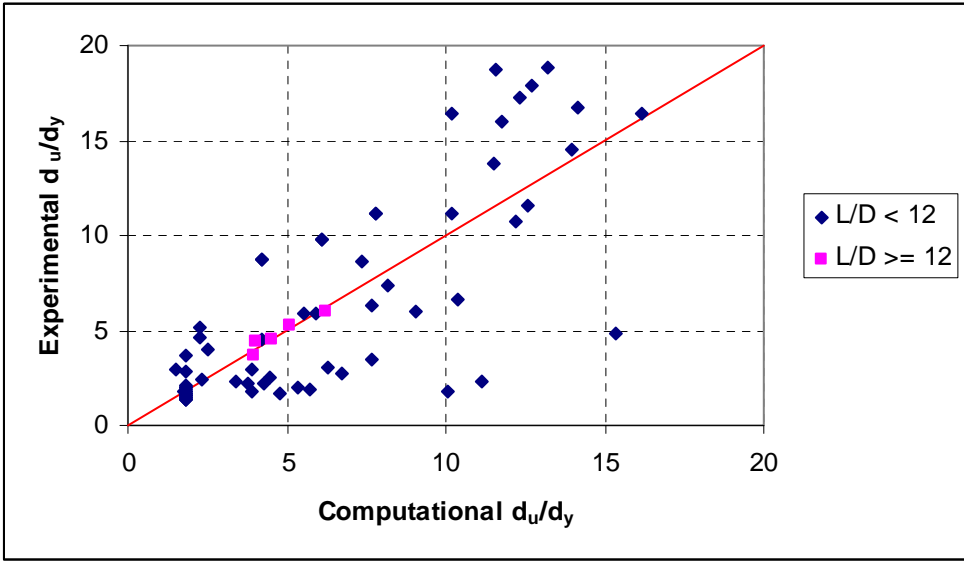


Figure 3.109: Comparison of Computational and Experimental d_u/d_y Values: Monotonically Loaded Column Tests

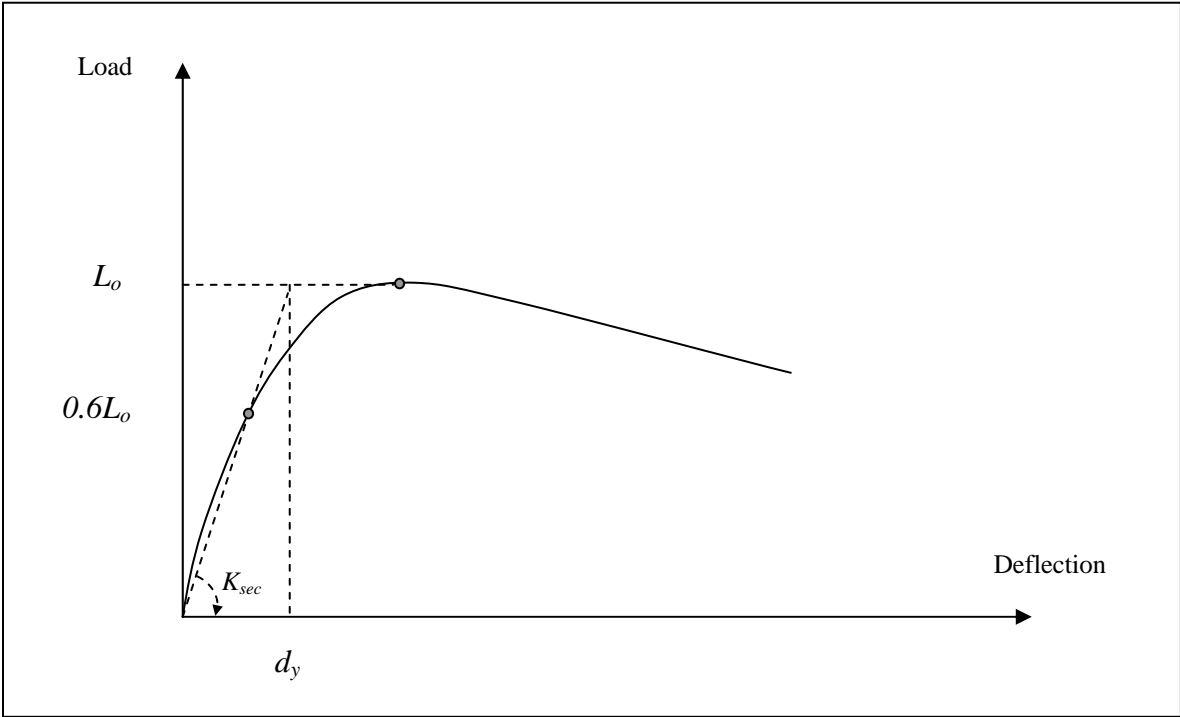


Figure 3.110: Definition d_y for the monotonic beam-column specimens

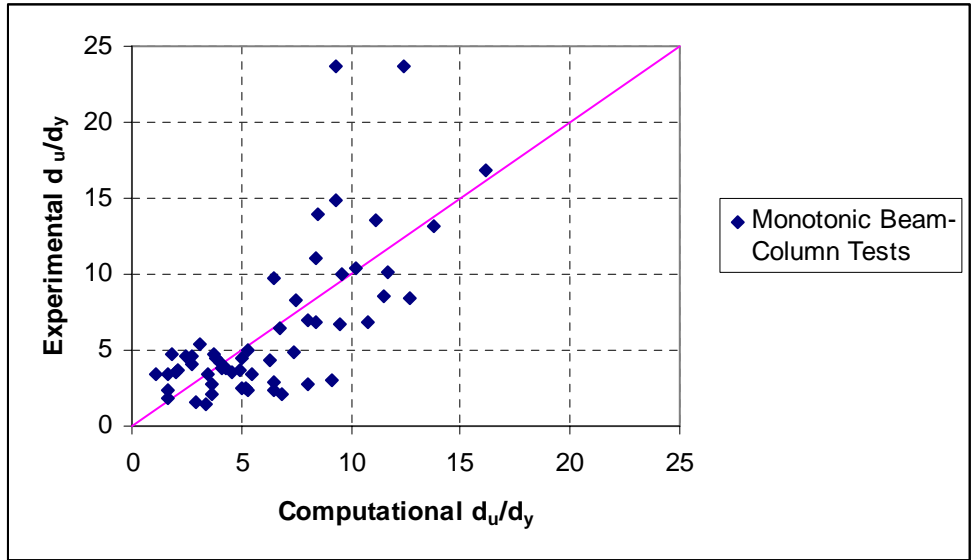


Figure 3.111: Comparison of Computational and Experimental d_u/d_y Values: Monotonically Loaded MI Type Beam-Column Tests

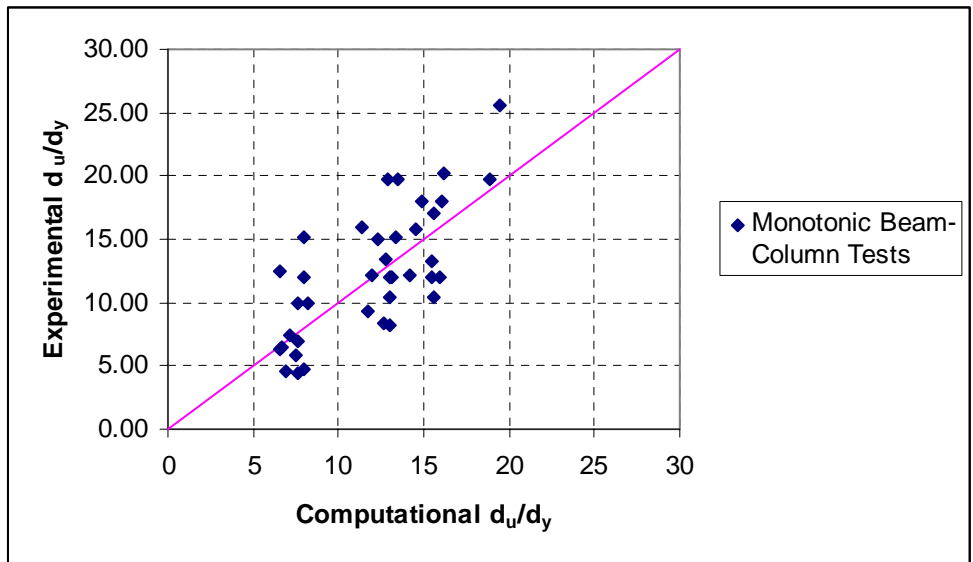


Figure 3.112: Comparison of Computational and Experimental d_u/d_y Values: Monotonically Loaded MII Type Beam-Column Tests

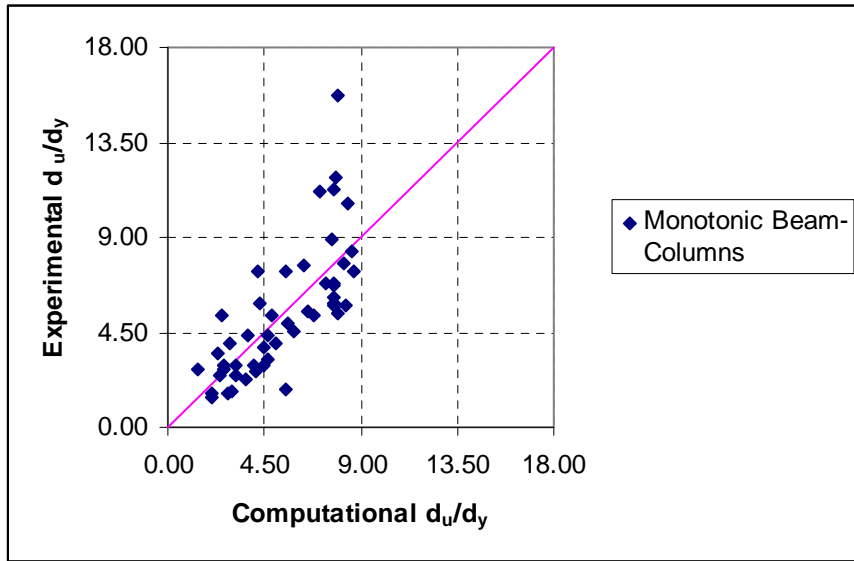


Figure 3.113: Comparison of Computational and Experimental d_u/d_y Values: Monotonically Loaded MIII Type Beam-Column Tests

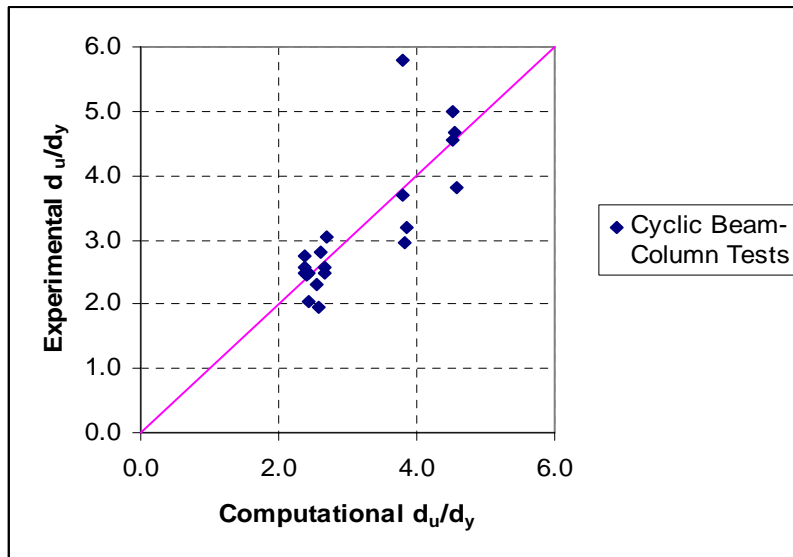


Figure 3.114: Comparison of Computational and Experimental d_u/d_y Values: Cyclically Loaded Beam-Column Tests

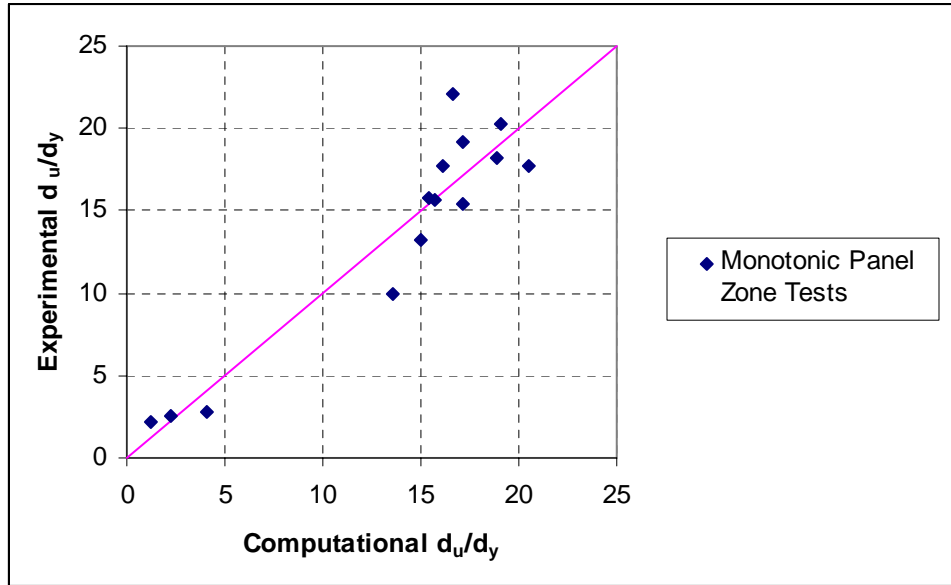


Figure 3.115: Comparison of Computational and Experimental d_u/d_y Values: Monotonically Loaded Panel-Zone Tests

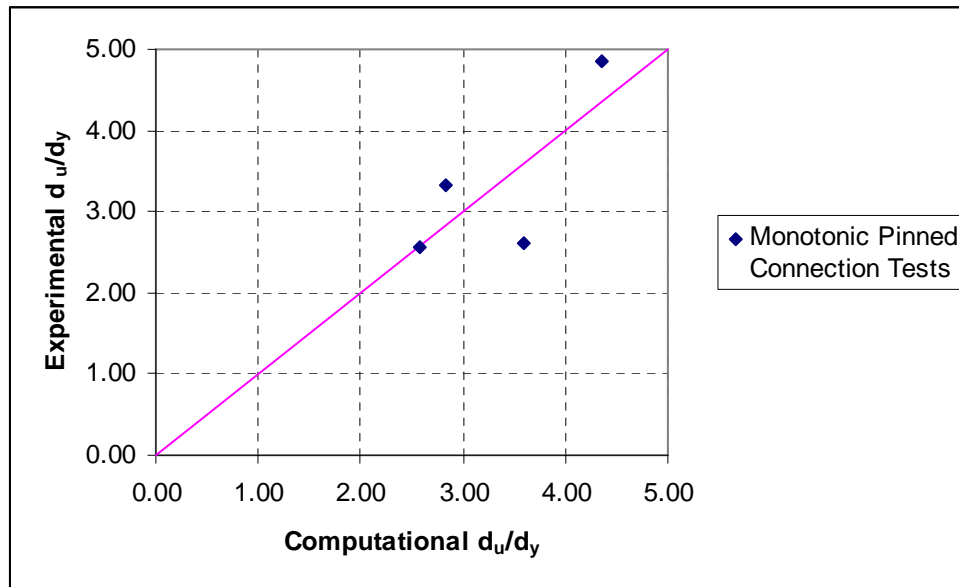


Figure 3.116: Comparison of Computational and Experimental d_u/d_y Values: Monotonically Loaded Pinned Connection Tests

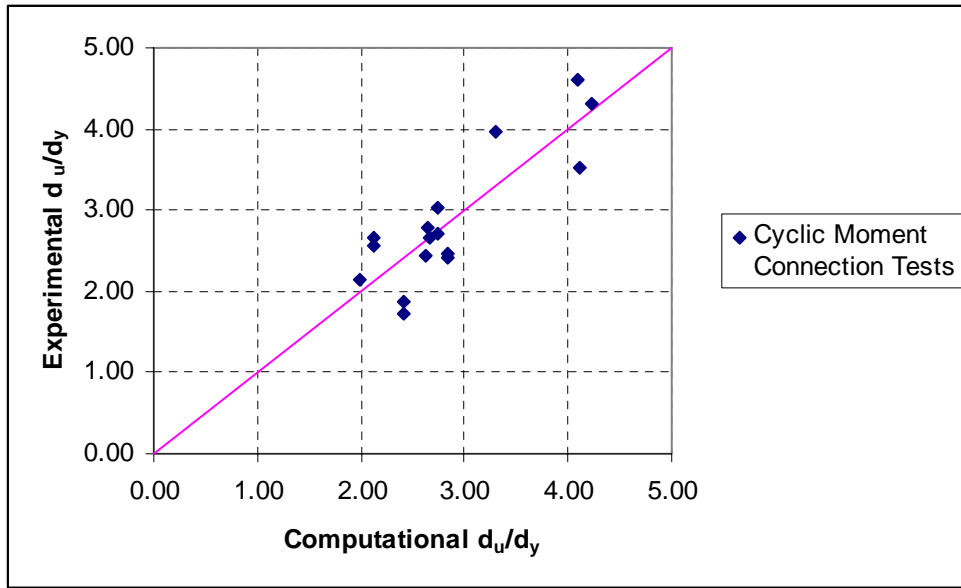


Figure 3.117: Comparison of Computational and Experimental d_u/d_y Values: Cyclically Loaded Moment Connection Tests

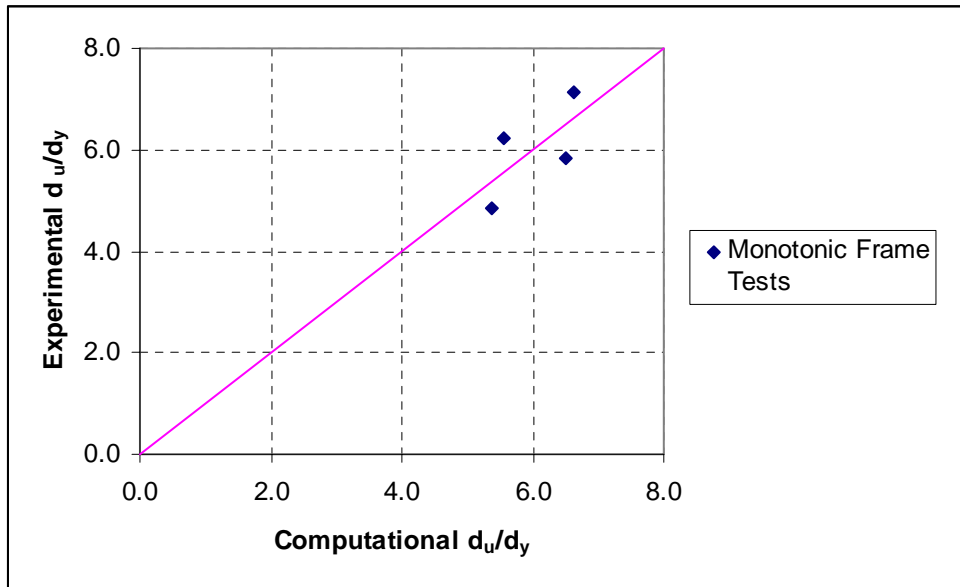


Figure 3.118: Comparison of Computational and Experimental d_u/d_y Values: Monotonically Loaded Frame Tests

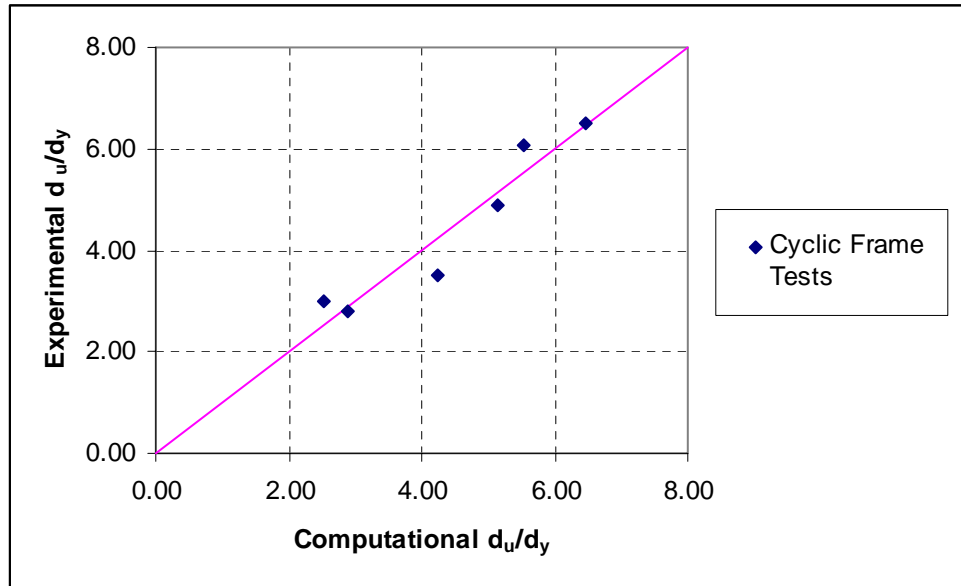


Figure 3.119: Comparison of Computational and Experimental d_u/d_y Values: Cyclically Loaded Frame Tests

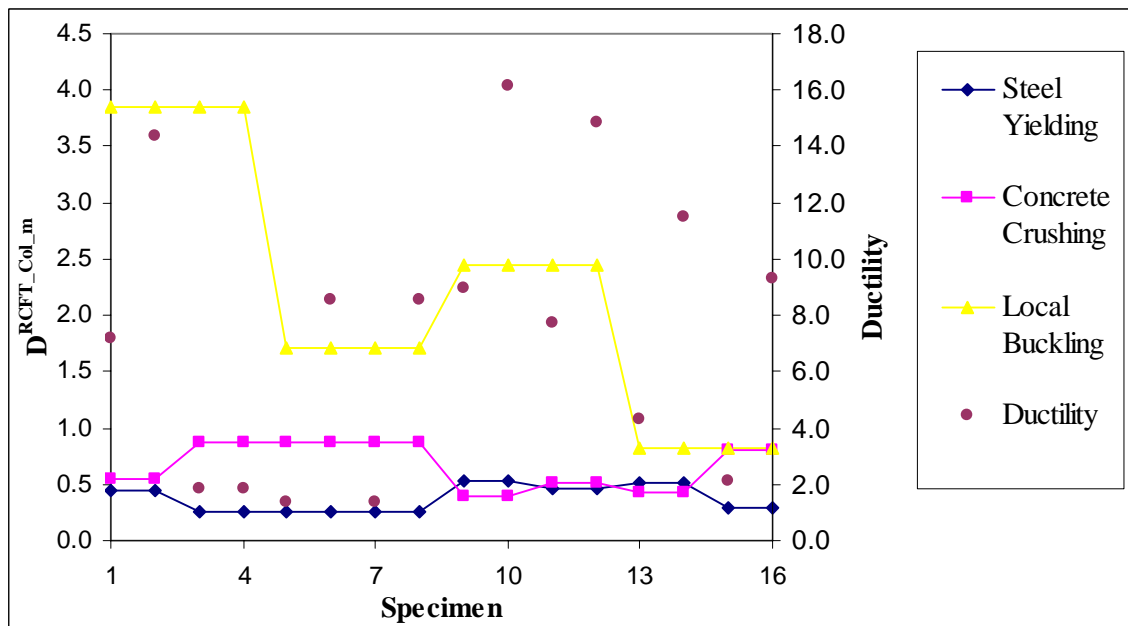


Figure 3.120: Comparison of Deformation-Based Damage Indices for Monotonically-Loaded Column Tests ($L/D = 3.0-12.0$; $D/t = 17.0-50.0$; $f_y = 194.2-835.0$ MPa; $f'_c = 20.6-103.0$ MPa; $P/P_o = 0.19-0.65$)

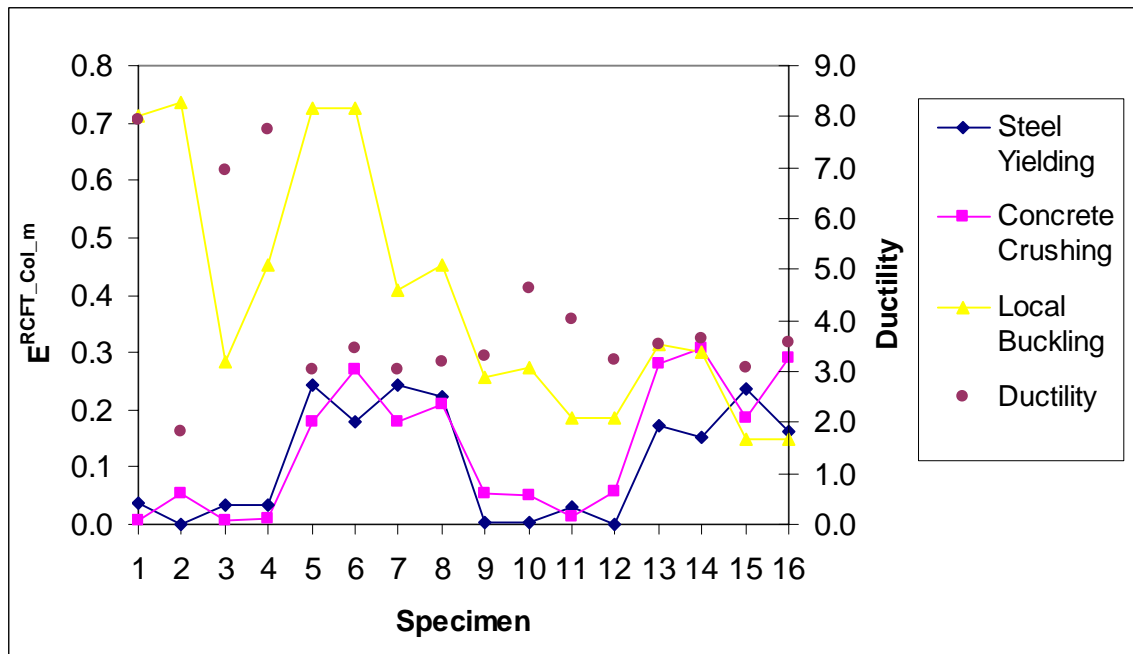


Figure 3.121: Comparison of Energy-Based Damage Indices for Monotonically-Loaded Column Tests ($L/D = 3.0-12.0$; $D/t = 17.0-50.0$; $f_y = 194.2-835.0$ MPa; $f'_c = 20.6-103.0$ MPa; $P_c/P_o = 0.19-0.65$)

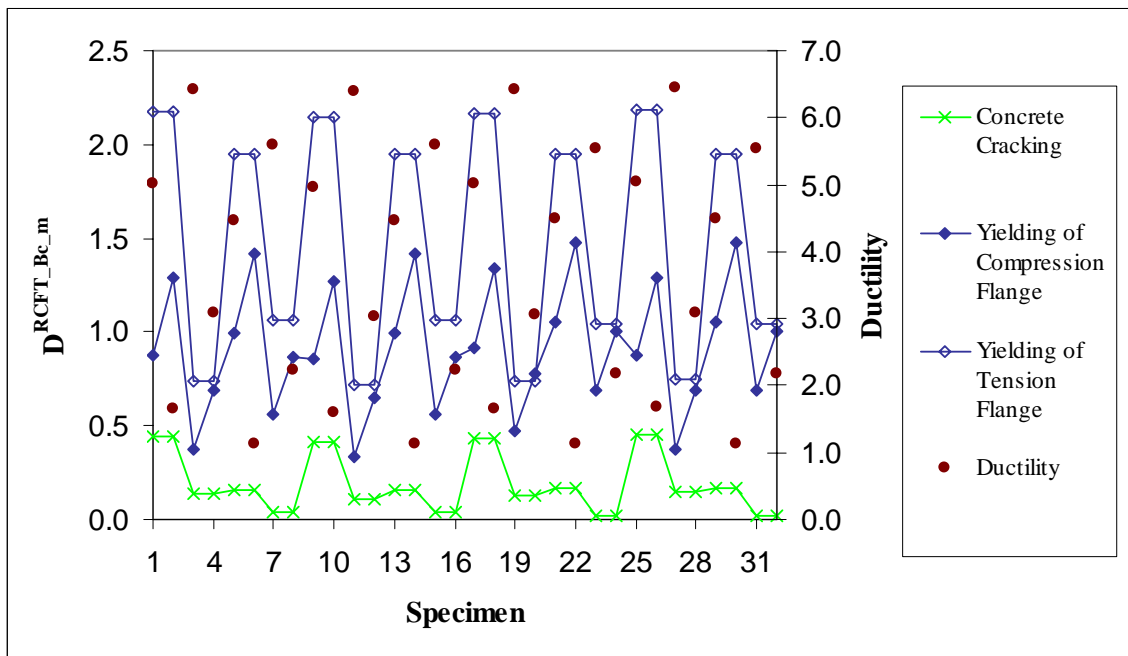


Figure 3.122: Comparison of Deformation-Based Damage Indices for Monotonically-Loaded MI Type Beam-Column Tests ($e/D = 0.2-0.5$; $L/D = 23.0-34.5$; $D/t = 17.0-26.5$; $f_y = 343.3-386.3$ MPa; $f'_c = 38.8-43.0$ MPa; $P_c/P_o = 0.30-0.37$)

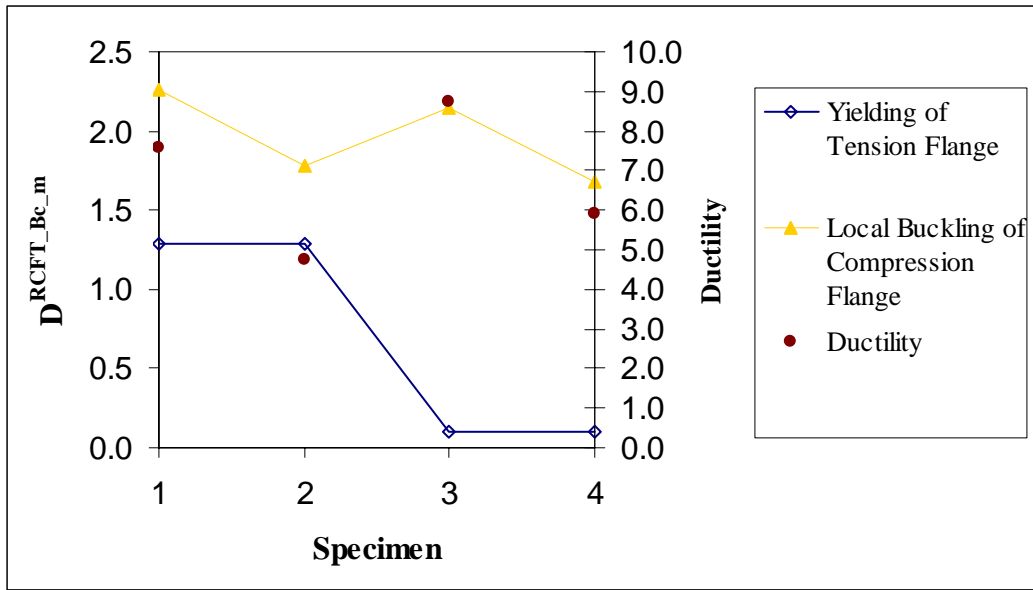


Figure 3.123: Comparison of Deformation-Based Damage Indices for Monotonically-Loaded MI Type Beam-Column Tests ($e/D = 0.16-0.41$; $L/D = 4.0-14.1$; $D/t = 39.1$; $f_y = 443.0$ MPa; $f'_c = 92.0$ MPa; $P_o/P_o = 0.66$)

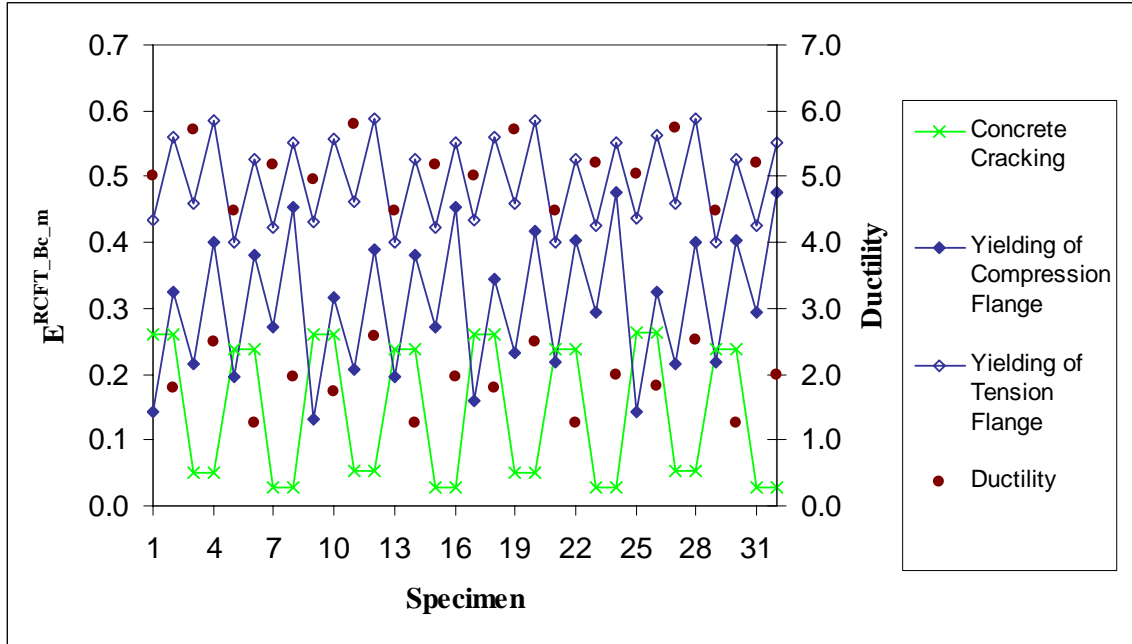


Figure 3.124: Comparison of Energy-Based Damage Indices for Monotonically-Loaded MI Type Beam-Column Tests ($e/D = 0.2-0.35$; $L/D = 23.0-34.5$; $D/t = 17.0-26.5$; $f_y = 343.3-386.3$ MPa; $f'_c = 38.8-43.0$ MPa; $P_o/P_o = 0.30-0.37$)

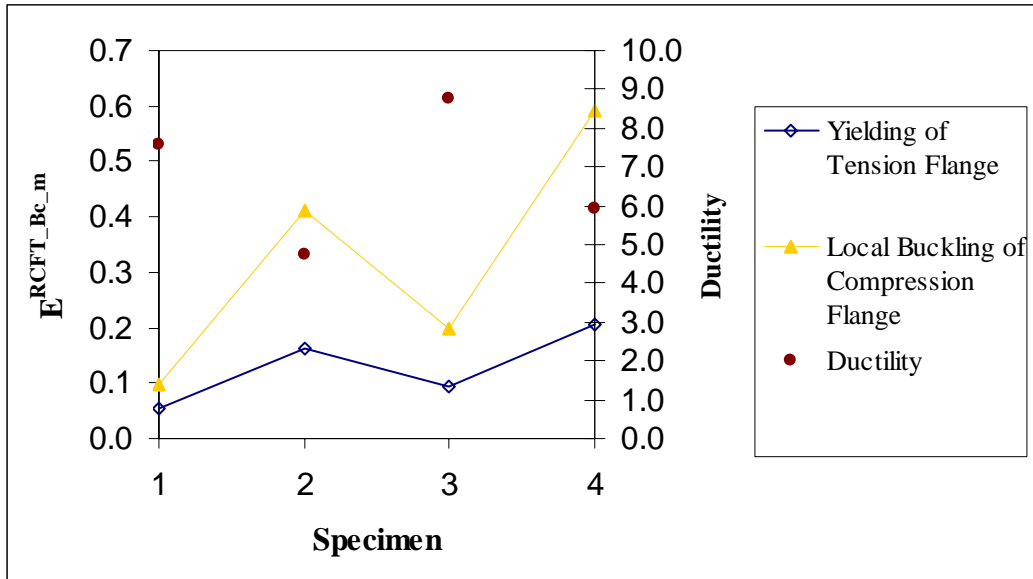


Figure 3.125: Comparison of Energy-Based Damage Indices for Monotonically-Loaded MI Type Beam-Column Tests ($e/D = 0.16-0.41$; $L/D = 4.0-14.1$; $D/t = 39.1$; $f_y = 443.0$ MPa; $f'_c = 92.0$ MPa; $P_o/P_o = 0.66$)

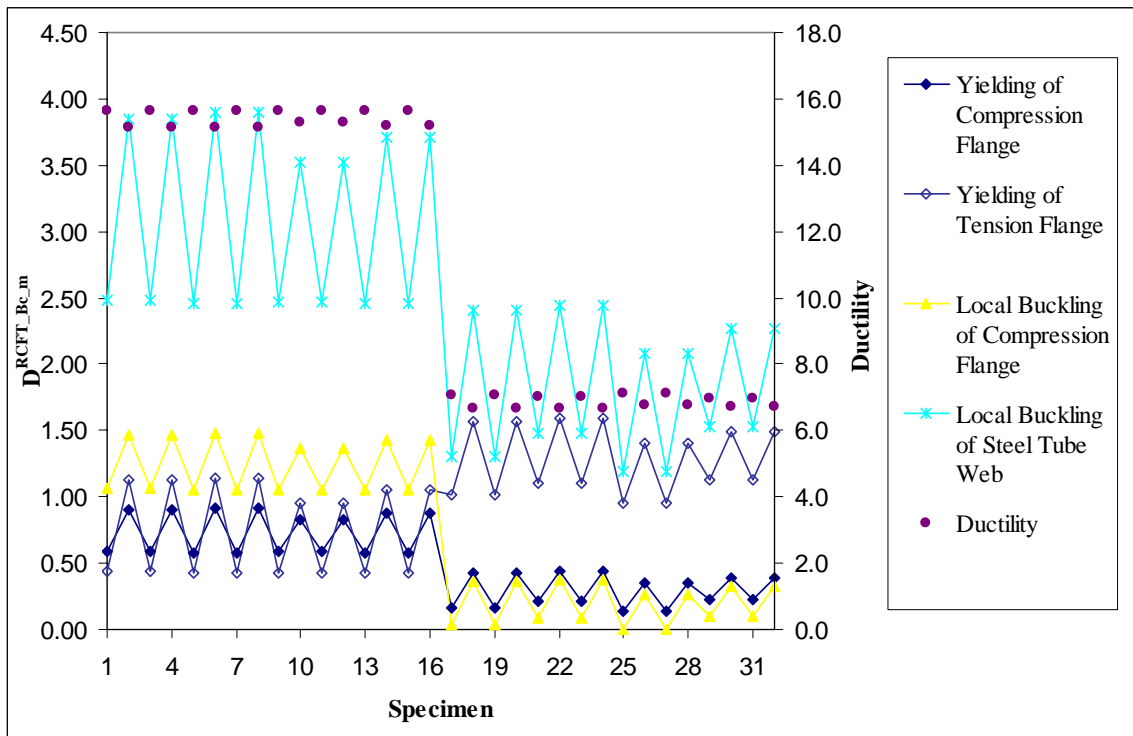


Figure 3.126: Comparison of Deformation-Based Damage Indices for Monotonically-Loaded MII Type Beam-Column Tests ($P/P_o = 0.2-0.5$; $L/D = 3.0$; $D/t = 25.0-45.4$; $f_y = 290.4-315.9$ MPa; $f'_c = 20.5-22.1$ MPa; $P_o/P_o = 0.30-0.43$)

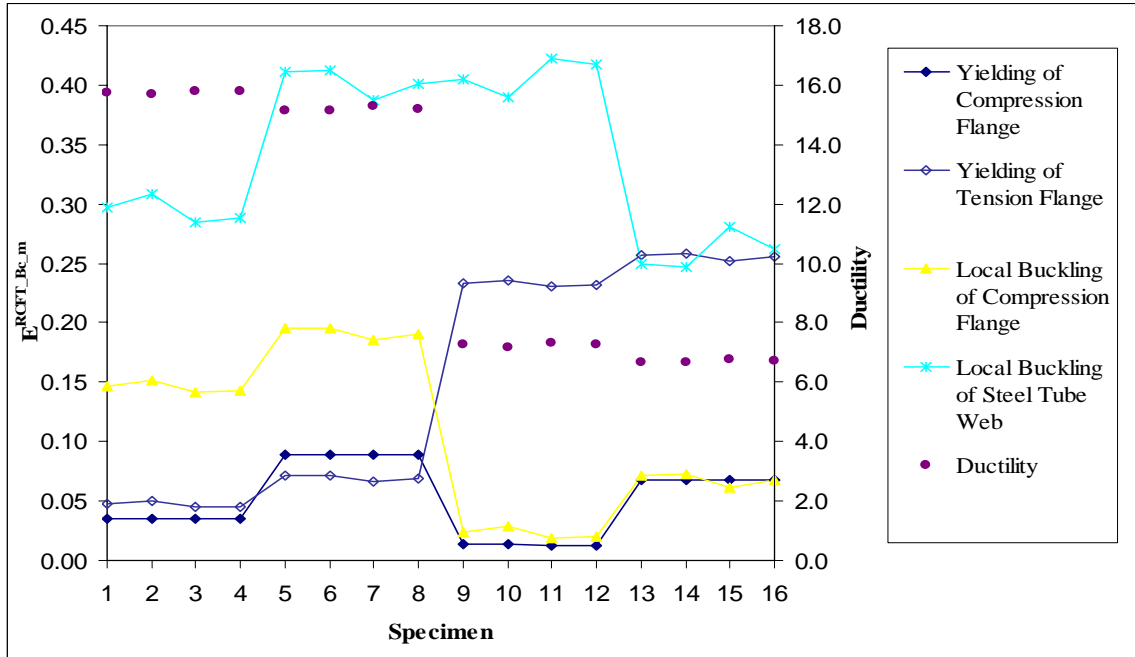


Figure 3.127: Comparison of Energy-Based Damage Indices for Monotonically-Loaded MII Type Beam-Column Tests ($P/P_o = 0.2-0.5$; $L/D = 3.0$; $D/t = 23.5-45.4$; $f_y = 290.4-315.9$ MPa; $f'_c = 20.5-22.1$ MPa; $P_c/P_o = 0.30-0.43$)

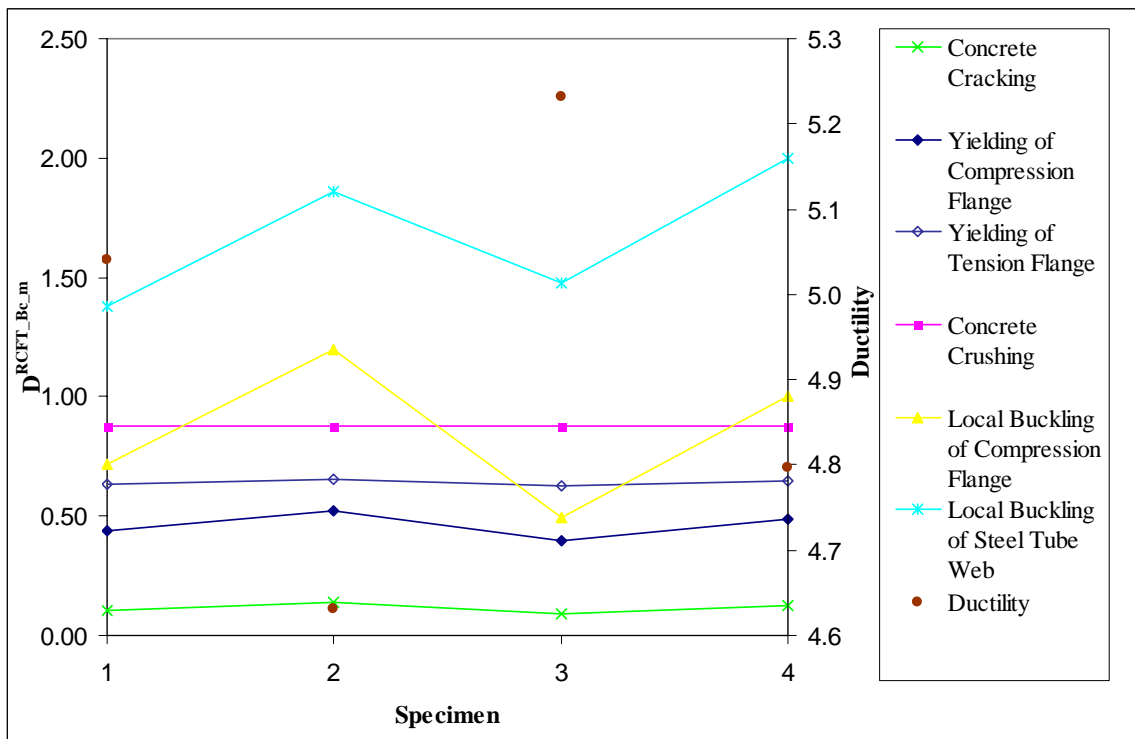


Figure 3.128: Comparison of Deformation-Based Damage Indices for Monotonically-Loaded MIII Type Beam-Column Tests ($P/P_o = 0.19$; $L/D = 5.0$; $D/t = 34.3-50.0$; $f_y = 471.0-560.0$ MPa; $f'_c = 110.0$ MPa; $P_c/P_o = 0.61-0.74$)

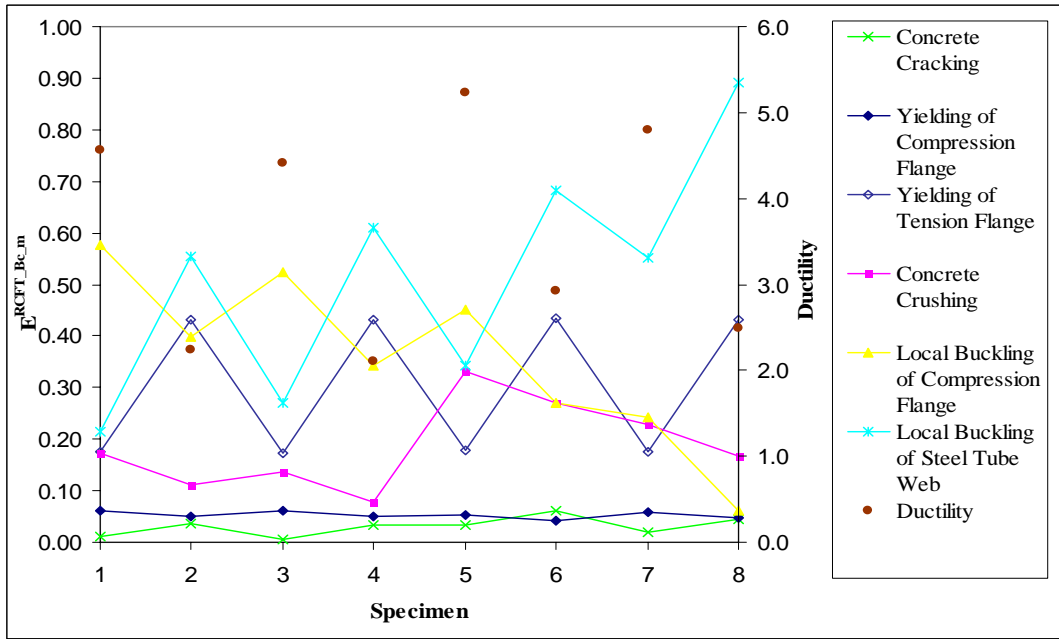


Figure 3.129: Comparison of Energy-Based Damage Indices for Monotonically-Loaded MIII Type Beam-Column Tests ($P/P_o = 0.19-0.43$; $L/D = 5.0$; $D/t = 34.2-50.0$; $f_y = 288.4-560.0$ MPa; $f'_c = 110.0$ MPa; $P_c/P_o = 0.61-0.78$)

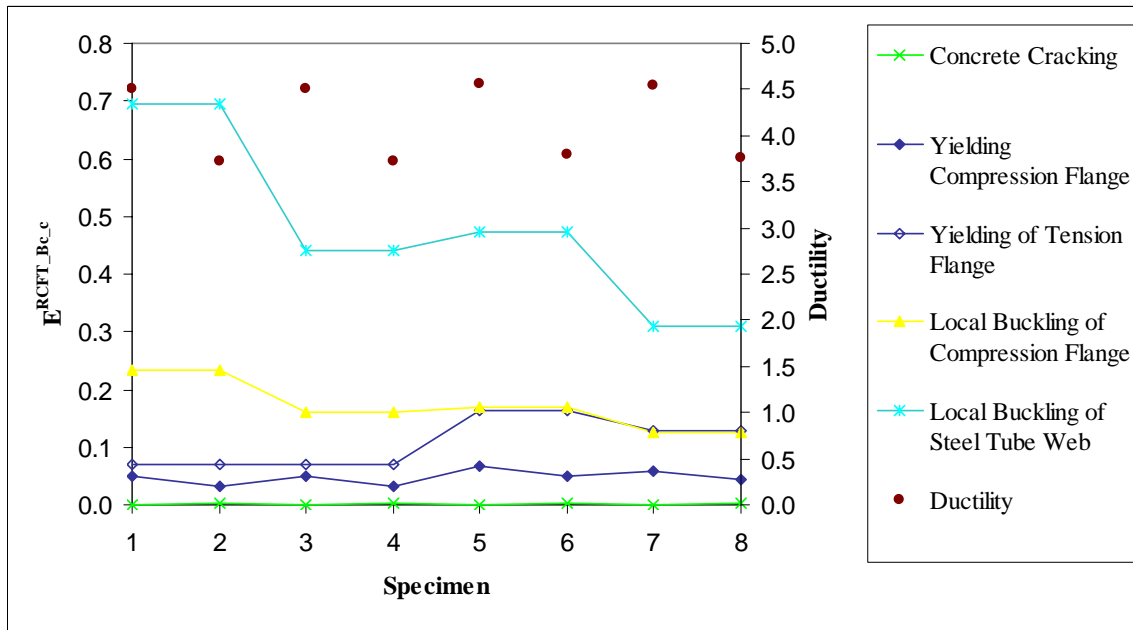


Figure 3.130: Comparison of Energy-Based Damage Indices for Cyclically-Loaded Beam-Column Tests ($P/P_o = 0.10-0.21$; $L/D = 5.0$; $D/t = 35.7-52.6$; $f_y = 269.0-660.0$ MPa; $f'_c = 110.0$ MPa; $P_c/P_o = 0.60-0.77$)

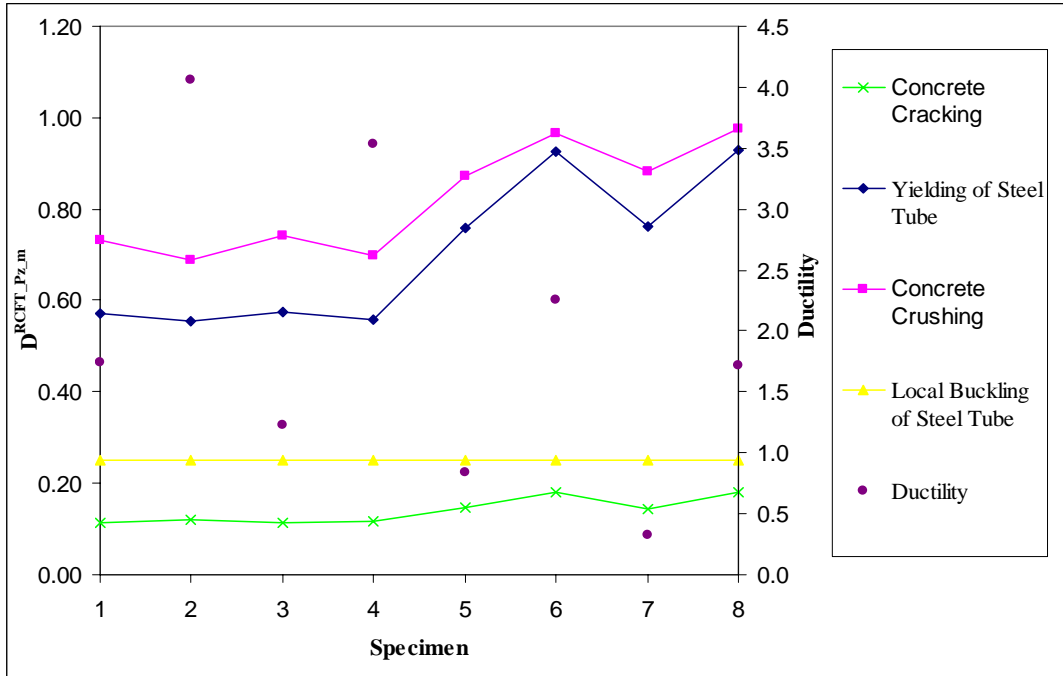


Figure 3.131: Comparison of Deformation-Based Damage Indices for Monotonically-Loaded Panel Zone Tests ($P/P_o = 0.5$; $L_p/D = 2.0-3.0$; $D/t = 32.2-46.1$; $f_y = 377.0-412.0$ MPa; $f'_c = 39.0-57.1$ MPa; $P_o/P_o = 0.41-0.53$)

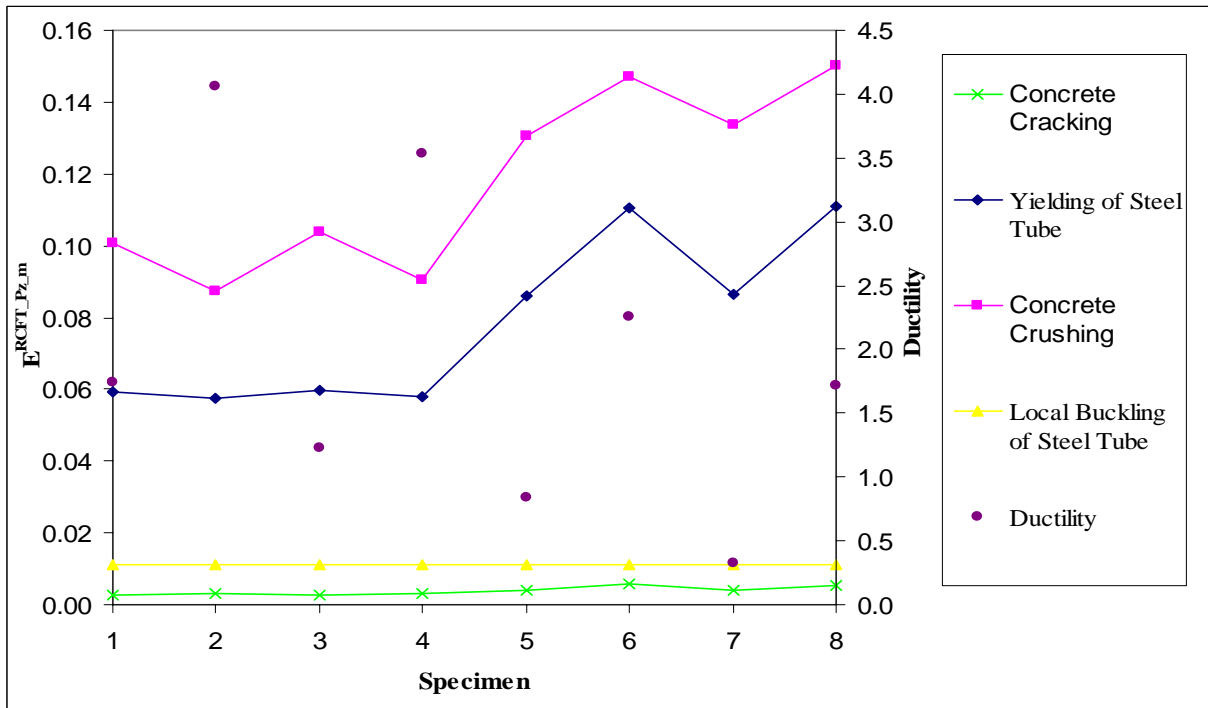


Figure 3.132: Comparison of Energy-Based Damage Indices for Monotonically-Loaded Panel Zone Tests ($P/P_o=0-0.5$; $L_p/D = 2.0-3.0$; $D/t = 39.0-57.1$; $f_y = 377.0-416.0$ MPa; $f'_c = 39.0-57.1$ MPa; $P_o/P_o = 0.41-0.53$)

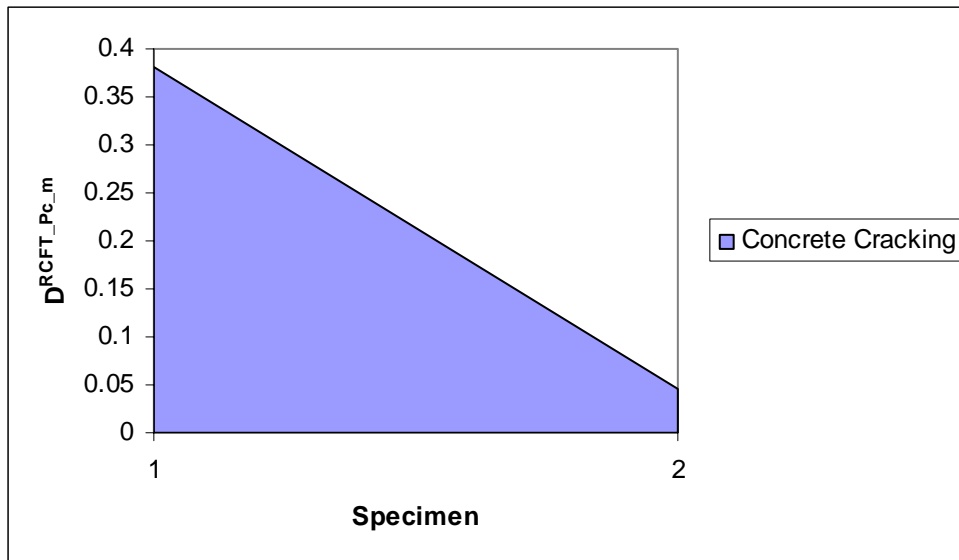


Figure 3.133: Comparison of Deformation-Based Damage Indices for Monotonically-Loaded Pinned-Connection Tests ($P/P_o = 0.16-0.18$; $d_g/D = 1.3-2.3$; $L/D=7.5$; $D/t = 25.0, 31.7$; $f_y = 318.0, 336.0$ MPa; $f'_c = 34.7$ MPa; $P_o/P_o = 0.38-0.43$)

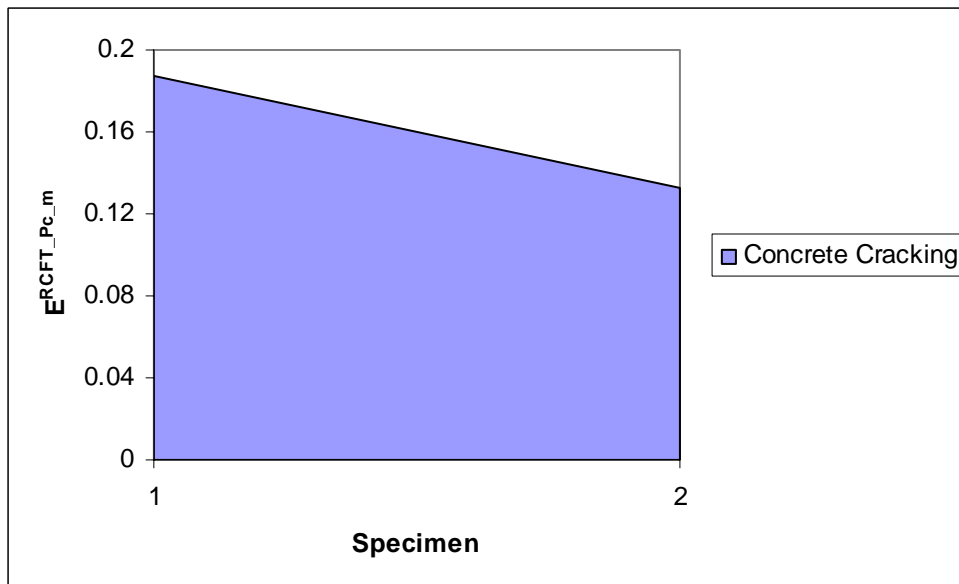


Figure 3.134: Comparison of Energy-Based Damage Indices for Monotonically Loaded Pinned-Connection Tests ($P/P_o = 0.16-0.18$; $d_g/D = 1.3-2.3$; $L/D=7.5$; $D/t = 25.0, 31.7$; $f_y = 318.0, 336.0$ MPa; $f'_c = 34.7$ MPa; $P_o/P_o = 0.38-0.43$)

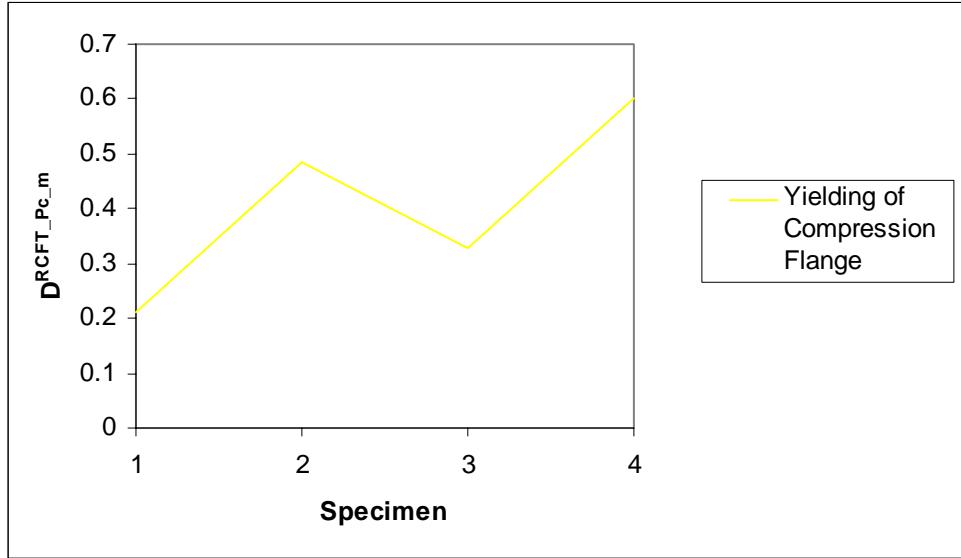


Figure 3.135: Comparison of Deformation-Based Damage Indices for Monotonically Loaded Pinned-Connection Tests ($e/D = 1.3-2.5$; $P/V = 1.5-8.0$; $L/D=18.7$; $D/t = 30.0$; $f_y = 330.0-343.0$ MPa; $f'_c = 29.6-34.3$ MPa; $P_e/P_o = 0.37-0.41$)

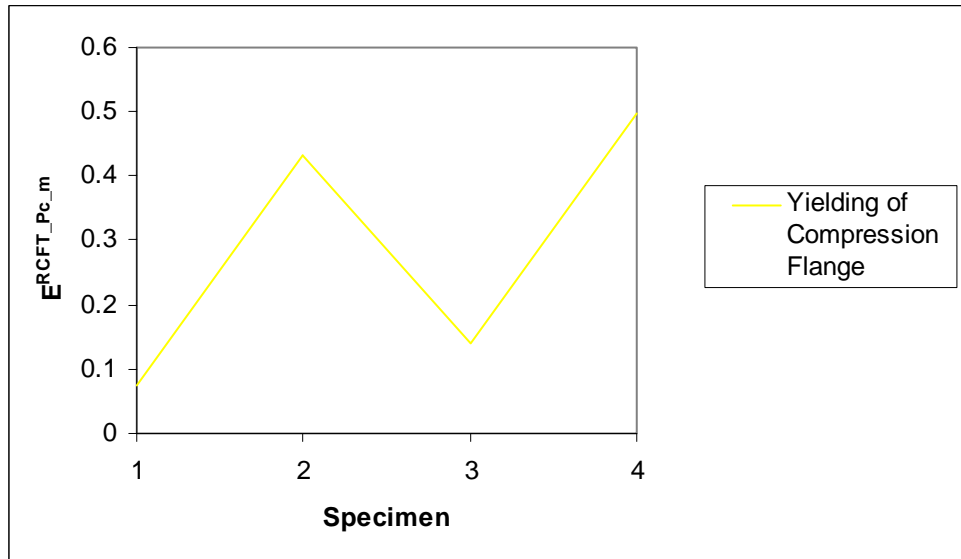


Figure 3.136: Comparison of Energy-Based Damage Indices for Monotonically Loaded Pinned-Connection Tests ($e/D = 1.3-2.5$; $P/V = 1.5-8.0$; $L/D=18.7$; $D/t = 30.0$; $f_y = 330.0-343.0$ MPa; $f'_c = 29.6-34.3$ MPa; $P_e/P_o = 0.37-0.41$)

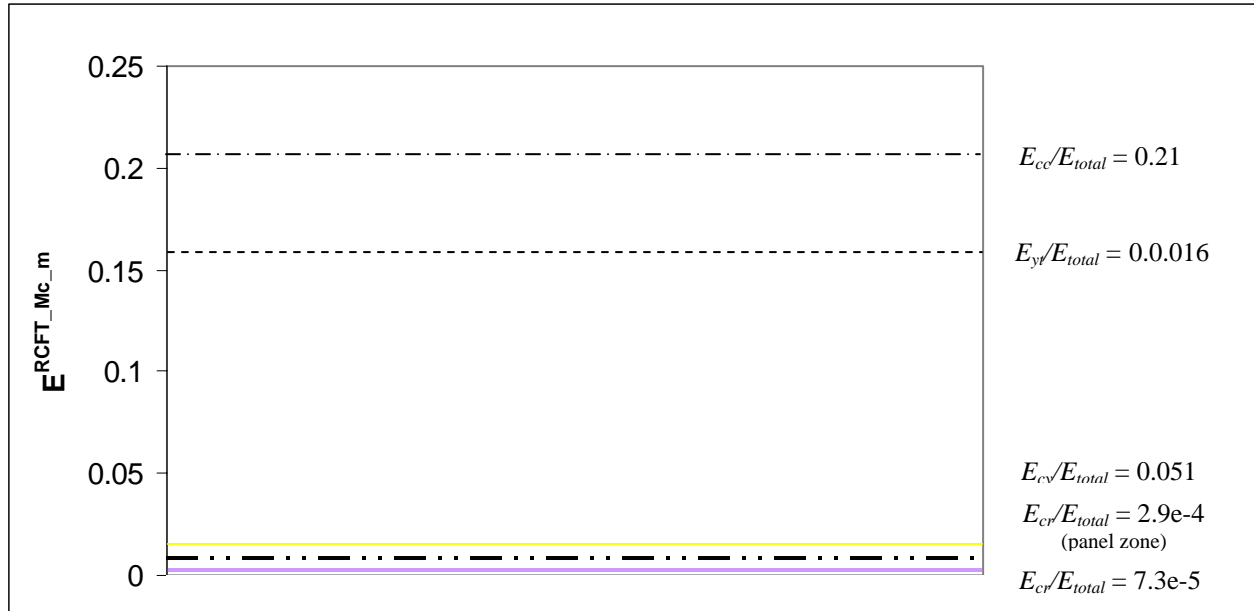


Figure 3.137: Comparison of Energy-Based Damage Indices for Monotonically Loaded Moment-Connection Tests ($P/P_o = 0.12, 0.14$; $d_g/D = 2.0-3.0$; $D/t = 20.0$; $f_y = 329.0, 427.0$ MPa; $f'_c = 40.4$ MPa; $P_o/P_o = 0.26, 0.31$)

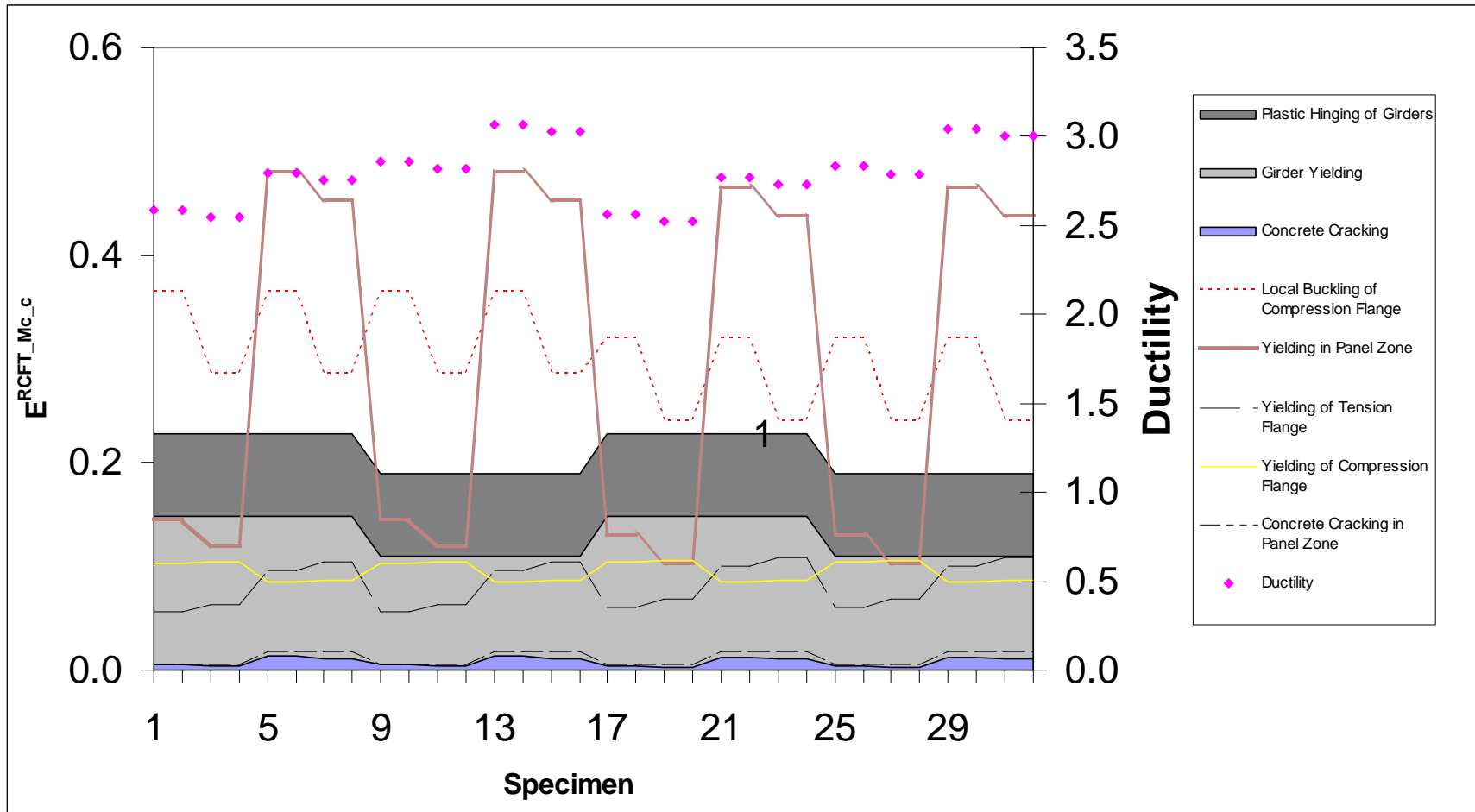


Figure 3.138: Comparison of Energy-Based Damage Indices for Cyclically Loaded Moment-Connection Tests ($d_g/D = 1.4-1.7$; $P_g/P_o=0.31-0.37$; $P/P_o=0.00-0.20$; $D/t = 34.5-40.0$; $f_y = 420.0$ MPa; $f'_c = 30.1-33.0$ MPa; $P_c/P_o = 0.36-0.42$)

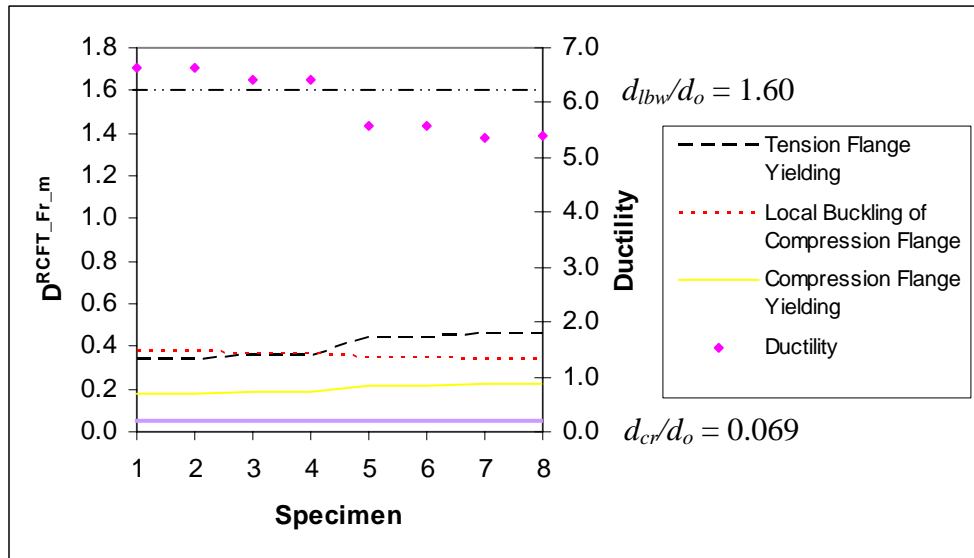


Figure 3.139: Comparison of Deformation-Based Damage Indices for Monotonically Loaded Frame Tests ($L/D = 6.7$; $D/t = 46.9-65.2$; $f_y = 287.4-288.4$ MPa; $f'_c = 35.3-37.8$ MPa; $P_c/P_o = 0.57-0.67$)

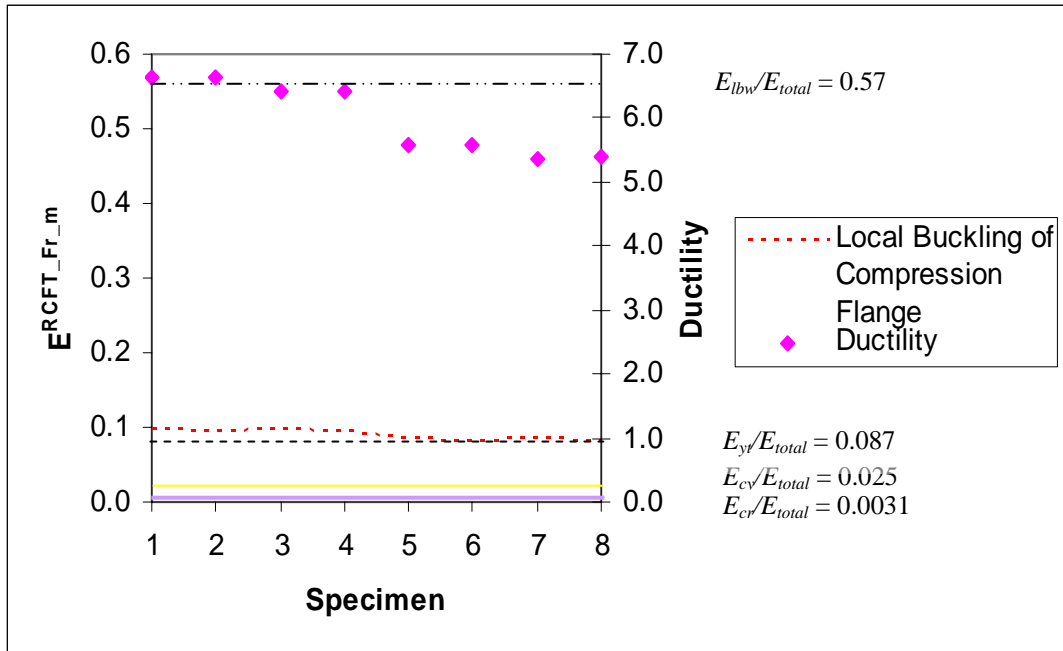


Figure 3.140: Comparison of Energy-Based Damage Indices for Monotonically Loaded Frame Tests ($L/D = 6.7$; $D/t = 46.9-65.2$; $f_y = 287.4-288.4$ MPa; $f_c = 35.3-37.8$ MPa; $P/P_o = 0.57-0.67$)

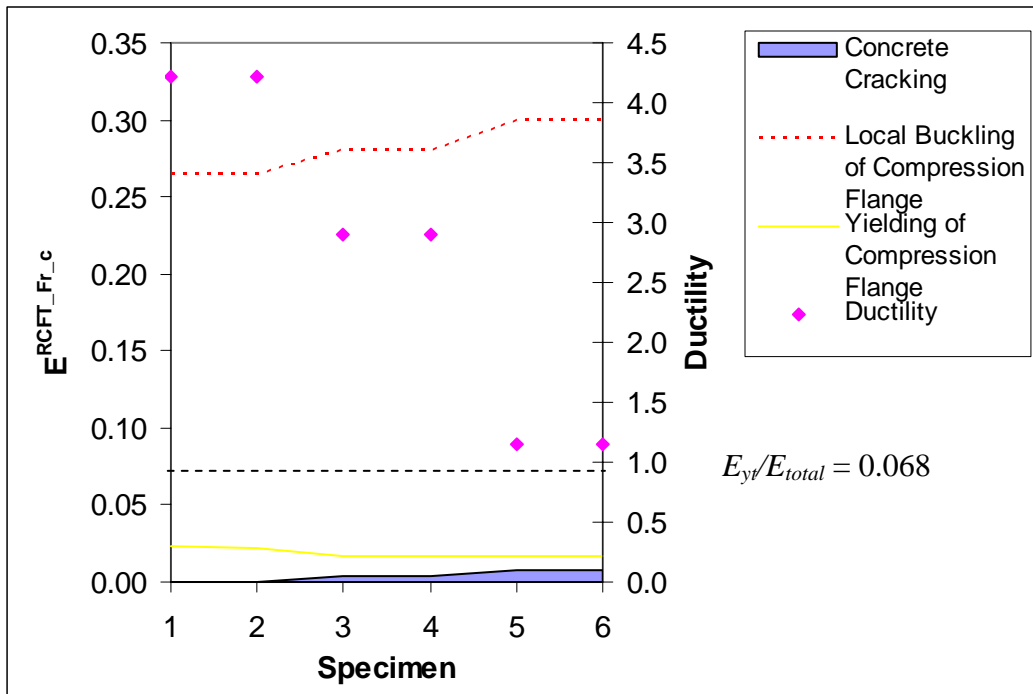


Figure 3.141: Comparison of Energy-Based Damage Indices for Cyclically Loaded Frame Tests ($P/P_o = 0.15-0.50$; $D/t = 21.6$; $f_y = 403.3$ MPa; $f'_c = 17.8-18.6$ MPa; $P_o/P_o = 0.17-0.18$)

Chapter 4

Conclusions

The summary and major findings of this research program will be presented in this chapter. In addition, recommendations for future research will be given.

The first task of the research study included the construction of a database of RCFT members. The database consisted of six main parts, covering columns, beam-columns, panel zones, pinned connections, moment connections, and frames. These main parts were further divided into separate groups depending on whether the tests were conducted under monotonic or cyclic loading.

In each database, the material and geometric properties of the specimens were recorded including their nominal and measured values. In Tables 4.1 and 4.2, the variation between the nominal and measured values of the material and geometric properties of the RCFT members can be seen. The data presented in Tables 4.1 and 4.2 are intended to be used, in part, for determining the resistance factors (ϕ) in developing performance-based design methodologies of RCFT systems. The collected data from the experiments showed that the ratio of f_y/f_{yo} increases when high strength steel tubes are used. This trend can be clearly seen in Figure 4.1. On the other hand, as shown in Figure 4.2, the ratio of the measured and nominal values of the compressive strength of the concrete decreases to approximately 1.0 when high strength concrete is utilized. No specific trend has been observed for the variation of nominal and measured values of the elastic modulus of the steel tube. The average and standard deviation of E_s/E_{so} indicates that elastic modulus of the steel tubes do not show significant variation among their nominal and measured values.

The majority of the geometric properties of the RCFT members showed less variation with respect to their measured and nominal values compared to the material

properties. Examining the available data, it was observed that the variation of D and D_o takes its largest values when specimens with large dimensions have been utilized. It is possible to see this trend in Figure 4.3. The nominal and measured values of steel tube thickness and D/t ratio of the specimens revealed a larger and more random dispersion compared to the depth of the steel tubes.

Developing performance-based design methodologies requires extensive parametric studies involving analysis of individual members or frames. Each analysis requires some key material properties (e.g., f_u , E_{sh} , E_c) for the constitutive models of the steel tube or concrete core to be used. Therefore, it is important to estimate these parameters when they are not available. As shown in Figures 4.4 and 4.5, it was found that the ratio of measured values of f_u/f_y and E_{sh}/E_s decrease when the yield strength of the steel tubes increases. The statistical properties f_u/f_y and E_{sh}/E_s can be seen in Table 4.3

The experimental studies collected from the literature indicated that the behavior of RCFT members under monotonic loads was investigated more commonly. Therefore, more cyclic tests for each type of RCFT members are needed. The experimentalists investigated the behavior of RCFT column and beam-column members with a wide range of material and geometric properties. However, for connections and frames, the range of material and geometric properties investigated to date remains quite limited, primarily with stocky members with low or moderate strength materials being investigated. There remains a need for experimental data of RCFT members and, particularly, connections with slender dimensions and high strength materials should be studied more often.

In the second part of the database, based on the observations during the tests, several damage levels were defined for each type of RCFT member. The force and deformation values at each damage level were recorded in the database. The occurrence of the damage levels on the load-deflection curves were either reported by the researchers or they were extracted from the load-deflection curves of the specimens with the help of analytical techniques (e.g., cross-section analysis). To quantify the damage experienced by the RCFT members, two types of damage functions were defined. The first type of damage function was deformation-based (D^{RCFT}) as given in Equation 4.1.

$$D^{RCFT} = \frac{d}{d_o} \quad (4.1)$$

where:

d = deformation at the local damage level

This type of damage function is more appropriate for RCFT specimens having a ductile response with hardening exhibited in the load-deflection curves. However, even for specimens having a softening response in the post-peak region, a deformation-based damage index still provides valuable information for the derivation of accurate models to analyze RCFT members. The deformation-based damage function was only used for monotonic specimens, as it does not account for the effect of a cyclic loading history.

The energy-based damage function defined in Equation 4.2 is appropriate to use for all types of specimens, including those exhibiting softening or hardening response, as well as RCFTs subjected to cyclic loading.

$$E^{RCFT} = \frac{E}{E_{total}} \quad (4.2)$$

where:

E = energy absorption until the occurrence of the load damage level

When the energy-based damage index is used for the cyclic specimens, it approximately accounts for the effect of the cyclic loading history, and E and E_{total} in Equation 4.2 are replaced by E_{cb} and E_m , which are defined as the area under the cyclic back-bone curve until the specified damage level, and the area under the complete cyclic back-bone curve, respectively. In Equation 4.2, for simplicity, the effect of secondary cycles was not taken into account and it was assumed that the monotonic load-deflection curve of RCFT members envelopes their cyclic response.

Once the values of both deformation-based and energy-based damage functions at specific damage levels were obtained for the available specimens existing in the database, equations were derived to estimate the damage index values at the occurrences of the local damage levels. All the related equations and their limitations are given in Tables 3.1 to Table 3.14. Although the damage functions are useful in assessing the performance of the structural members at different instants during the loading history, they do not give any indication about the available ductility of the members. Therefore, for every specimen available specimens in the database, the ductility was calculated using consistent definitions of yield point and ultimate point, where the specimens were

considered to fail. The ductility of the members was then correlated to the material and geometric properties of the specimens.

Using the derived equations for both the damage indices and ductility, a parametric study was run to examine the effect of the local damages on the behavior of RCFT members. Based on the results from the parametric study, each damage level is correlated below to a performance level. The intent of this association is to determine which damage levels are appropriate for consideration for the different performance levels. The performance levels used were based on the deformation-based and energy-based damage levels defined in Table 4.4; the energy-based damage levels were in turn were adopted from Mehanny and Deierlein (2000). These damage indices may then be combined with more traditional strength-based assessments of RCFT response (e.g., predictions of peak load or moment) to form a comprehensive performance-based design assessment for RCFTs. It should be stated that scope of the conclusions about the damage assessment of the RCFT members presented below is limited to the ranges of material and geometric properties of the available experimental data, as documented in Chapter 3.

Monotonic Columns

Three types of damage levels, including concrete crushing, steel yielding and local buckling were identified for monotonically loaded columns. Local buckling occurs the latest in the loading history. However, it is not possible to correlate local buckling to a single performance level. Local buckling occurs early in the loading history for short and thin-walled columns, exhibiting a ductility level of about 3.0 thereafter, and thus is appropriate for consideration in the Immediate Occupancy performance level for these cases. For the thick-walled short specimens, the damage accumulated until local buckling is larger than their thin-walled counterparts and local buckling can be associated with a Near Collapse performance level. In the case of short members, the amount damage at concrete crushing generally falls within the limits of either Immediate Occupancy or Life Safety performance level. The average values of the deformation-based damage index and energy-based damage index at steel yielding were less than 0.8

and 0.3, respectively. It can be concluded that significant reserve strength occurs after steel yielding, and it could be considered most appropriate only for the Immediate Occupancy performance level.

Monotonic Beam-Columns

The damage assessment of the beam-column members is dependent on the type of loading acting on the members. Three types of loading schemes were identified which were defined as MI, MII and MIII. The damage levels investigated for the beam-columns were concrete cracking, compression flange yielding, tension flange yielding, concrete crushing, local buckling of the compression flange and local buckling of the steel tube web.

For the thick-walled MI type specimens, tension flange yielding and compression flange yielding are the damage levels observed the latest. It is possible to correlate tension flange yielding and compression flange yielding to any performance level ranging from Immediate Occupancy to Near Collapse performance levels, depending on the material and geometric properties of the members. The average values of the deformation-based and energy-based damage indices at concrete cracking both fall into the range of the Immediate Occupancy performance level, indicating that concrete cracking can be considered only in the Immediate Occupancy performance level. In the case of thin-walled MI type specimens, local buckling of the compression flange takes place at an average energy-based damage index value of 0.30, which is within the limits of the Life Safety performance level. On the other hand, the deformation-based damage index values at local buckling of the compression flange shows that it can also be considered in the Near Collapse performance level.

Local buckling of the steel tube web is the latest damage level to be observed for the MII type monotonic beam-columns and the level of damage corresponds to the Life Safety or Near Collapse performance levels. All the remaining damage levels investigated for the MII type specimens, including yielding of compression flange, yielding of tension flange, and local buckling of the compression flange should be considered either in the Immediate Occupancy or Life Safety performance levels. This

insignificant amount of damage is attributed to the fact that MII type specimens exhibit a considerable amount of ductility.

MIII type specimens often have local buckling of steel tube web or local buckling of the compression flange to occur the latest during the loading history. According to the amount of accumulated damage, local buckling of steel tube web can be correlated to any performance level from Immediate Occupancy to Near Collapse. Concrete cracking and yielding of the compression flange both have damage index values within the range of the Immediate Occupancy performance level. The average values of the damage indices for tension flange yielding and local buckling of the compression flange fall into Immediate Occupancy or Life Safety performance levels. Similarly, concrete crushing can also be correlated to either Immediate Occupancy or Life Safety performance levels.

Cyclic Beam-Columns

The damage levels investigated for the cyclic beam-column specimens were the same as in the case of monotonic beam-columns. The damage level to occur the latest during the loading history was identified to be local buckling of the steel tube web. According to the ranges of damage index values, local buckling of the steel tube web can be correlated to either Life Safety or Near Collapse performance levels. The remaining damage levels, including concrete cracking, yielding of tension flange, yielding of compression flange, and local buckling of compression flange all correspond to the Immediate Occupancy performance level with average energy-based damage index values less than 0.3.

Monotonic Panel Zones

The monotonic panel zone tests showed that RCFT members have a very stable and ductile response in the panel zone regions. Among the damage levels studied for the panel zones including concrete cracking and local buckling have deformation-based and energy-based damage index values less than 0.8 and 0.3, respectively. Therefore, they were all correlated to Immediate Occupancy performance level. On the other hand, the

damage levels of concrete crushing and steel yielding can be considered in both Immediate Occupancy and Life Safety performance levels.

Monotonic Pinned-Connections

Limited amount of damage levels were investigated for pinned connections. For the PCIb type specimens, concrete cracking corresponds to Immediate Occupancy performance level. On the other hand, PCIb and PCIIa type connections had yielding of compression flange as the only damage that could be quantified and it is possible to correlate yielding of compression flange to the Immediate Occupancy or Life Safety performance levels. For the pinned-connection specimens, the damage levels that could be quantified are not enough for a complete performance evaluation. Therefore, it is also required to define new damage levels for the lower performance levels.

Monotonic Moment Connections

In the monotonic moment-connection tests, the damages of the members making up the connection were investigated individually. It was found that the amount of damage accumulated at the point of concrete crushing is larger than the other damage levels examined for the connections. Nevertheless, the value of the damage index at concrete crushing falls into the range of Immediate Occupancy. Due to stable and ductile post peak response of the tested monotonic moment connections, all the other damage levels had lower damage index values than concrete crushing and they mapped into the Immediate Occupancy performance level. Monotonic moment connections also require new damage levels to be defined for other performance levels.

Cyclic Moment Connections

The damage assessment of cyclic moment connections was conducted by investigating the damage levels observed in the beam-column, panel zone and steel girders of these connection tests. It was found that local buckling of the compression

flange and yielding of the steel tube in the panel zone are the two damage levels to occur the latest during the loading history. The damage level of local buckling of the compression flange can be correlated to either Life Safety performance level or Immediate Occupancy performance level. Similarly, it is possible to map yielding at the panel zone to either the Immediate Occupancy or Life Safety performance levels. The former performance level is appropriate for the specimens with small d_g/D ratios. Otherwise, the latter performance level is more appropriate. Concrete cracking at the beam-column and concrete cracking at the panel zone are the earliest damage levels to take place and they can only be mapped to the Immediate Occupancy damage level. Among the remaining damage levels investigated for the cyclic moment connections including yielding and hinging of the steel girder, yielding of the compression flange and yielding of the tension flange all have energy-based damage index values less than 0.2 and they can also be considered in the Immediate Occupancy performance level. For the cyclic moment connections, the damage levels investigated in this research are mostly appropriate for high level of performance levels and it is required to define more damage levels to describe Near Collapse or Collapse Prevention performance levels.

Monotonic Frame Tests

The monotonic frame tests also experienced the same type of damage levels as monotonic beam-columns. Among the damage levels investigated for monotonic frames tests, at the time of local buckling of the steel tube web, the accumulated damage was found to be the largest, and local buckling of the steel tube web was mapped to the Life Safety or Near Collapse performance levels. As expected, the monotonic frames have the slightest damage when concrete cracking takes place, and it is most appropriate to map concrete cracking to the Immediate Occupancy performance level. When the damage levels of local buckling of the compression flange, yielding of the compression flange and yielding of the tension flange take place, the damage index values are within the limits of Immediate Occupancy performance level.

Cyclic Frame Tests

In the cyclic beam-column tests, the same type of damage levels as in the case of their monotonic counterparts were investigated. The data collected from the cyclic frame tests showed that local buckling of the compression flange is the latest damage level to be observed. However, the energy-based damage index value when local buckling of the compression flange takes place does not exceed 0.3. This indicates that local buckling of the compression flange is most appropriate for the Immediate Occupancy or Life Safety performance level. The remaining damage levels covered tension flange yielding, compression flange yielding and concrete cracking. At the occurrence of all of these damage levels, the accumulated damage is less than local buckling of the compression flange. Therefore, they should also be correlated to the Immediate Occupancy performance level.

The damage assessment performed for RCFT members in this research study is mainly based on empirical and semi-empirical data, and it is hoped that this study will help researchers to better understand the evolution of damage in RCFTs during experiments. However, it is required for this research study to be supplemented further research on the following topics:

1. *Development of new damage functions accounting for the effect of cyclic loading history in an accurate manner:* The effect of cyclic loading history was only approximately accounted for in this work. This prevented thorough investigation of damage levels occurring in the post-peak range of the RCFT members, where cyclic loading effects are significant. Therefore, it is required to develop and use more advanced damage functions to define the limits of additional performance levels related to cyclic loading.
2. *Defining additional damage levels for the more severe performance levels:* It was found that the majority of the damage levels defined for the RCFT members, especially in the cyclic tests, were appropriate only for consideration of the Immediate Occupancy performance level. This indicates that there is a need for defining new damage levels having more significant effect on the behavior than

the damage function defined in this study. Conducting tests that report the amount of different types of damage, and not just the initiation of different types of damage, may be fundamental to furthering this research.

3. *Development of advanced analytical models for RCFT members:* Both the use of damage functions accounting for cyclic loading history and the definition of new damage levels requires an accurate simulation technique for all types of RCFT members. The database constructed in this study will help in the development accurate analytical models for RCFT members.
4. *Database enhancement:* The database should be updated frequently as more tests are conducted worldwide.

Table 4.1: Comparison of Measured and Nominal Values of Major Material Properties

| Statistical Parameters | f_y/f_{yo} | f_c/f_{co} | E_s/E_{so} |
|-------------------------------|--------------|--------------|--------------|
| N | 289 | 182 | 76 |
| μ | 1.21 | 1.080 | 1.01 |
| σ | 0.21 | 0.19 | 0.017 |

Table 4.2: Comparison of Measured and Nominal Values of Major Geometric Properties

| Statistical Parameters | D/D_o | t/t_o | $(D/t)/(D/t)_o$ |
|-------------------------------|---------|---------|-----------------|
| N | 88 | 192 | 147 |
| μ | 1.0029 | 0.99 | 1.037 |
| σ | 0.0052 | 0.059 | 0.066 |

Table 4.3: Comparison of Measured and Nominal Values of Major Geometric Properties

| Statistical Parameters | f_u/f_y | E_{sh}/E_s |
|-------------------------------|-----------|--------------|
| N | 288 | 73 |
| μ | 1.31 | 0.0086 |
| σ | 0.18 | 0.0022 |

Table 4.4: Correlation of Damage Index and Performance Level (after Mehanny and Deierlein, 2000)

| Performance Level | Deformation-Based Damage Index | Energy-Based Damage Index |
|----------------------------|---------------------------------------|----------------------------------|
| Immediate Occupancy | < 0.8 | < 0.30 |
| Life Safety | 0.8-1.5 | 0.30-0.60 |
| Near Collapse | 1.5-5.0 | 0.60-0.95 |
| Collapse Prevention | > 5.0 | > 0.95 |

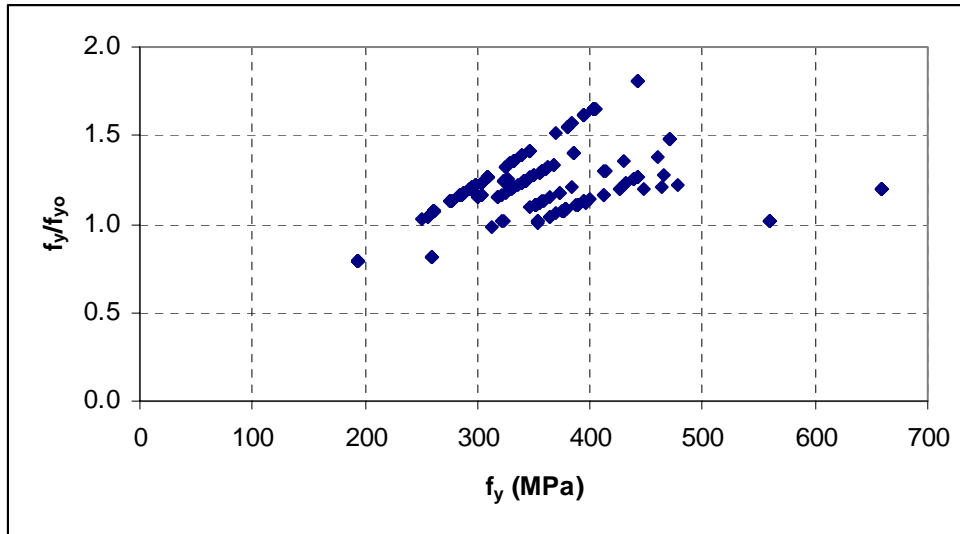


Figure 4.1: Comparison of f_y vs. f_y/f_{y0} for the Whole Database

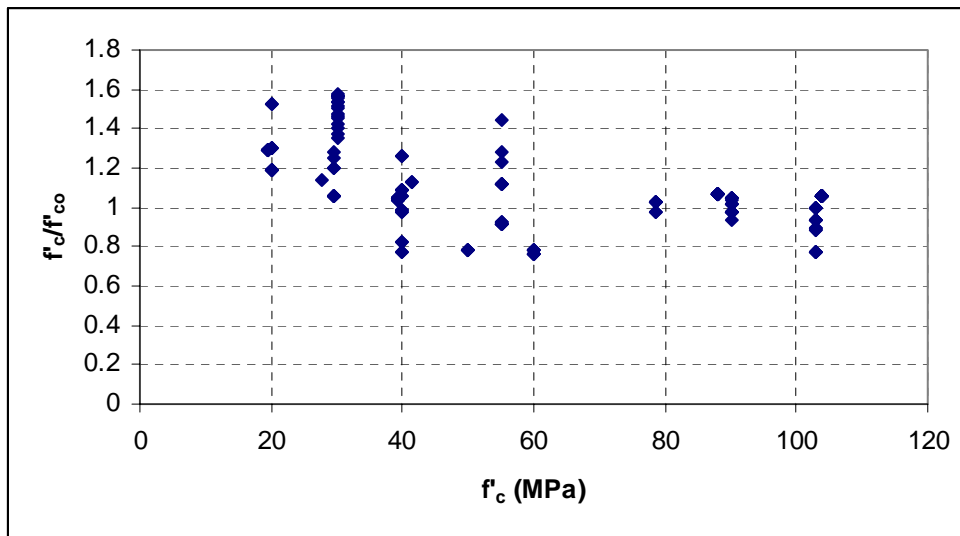


Figure 4.2: Comparison of f_c vs. f_c/f_{c0} for the Whole Database

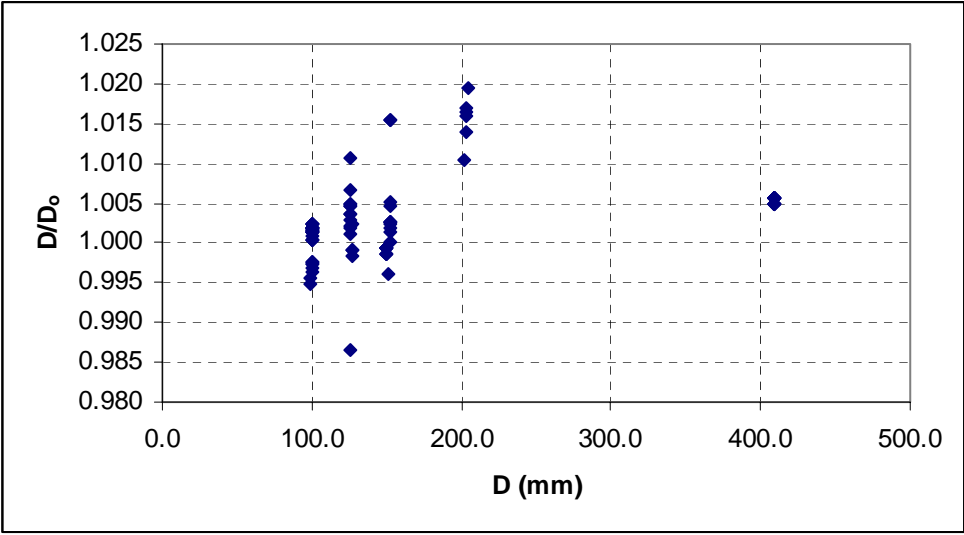


Figure 4.3: Comparison of D vs. D/D_0 for the Whole Database

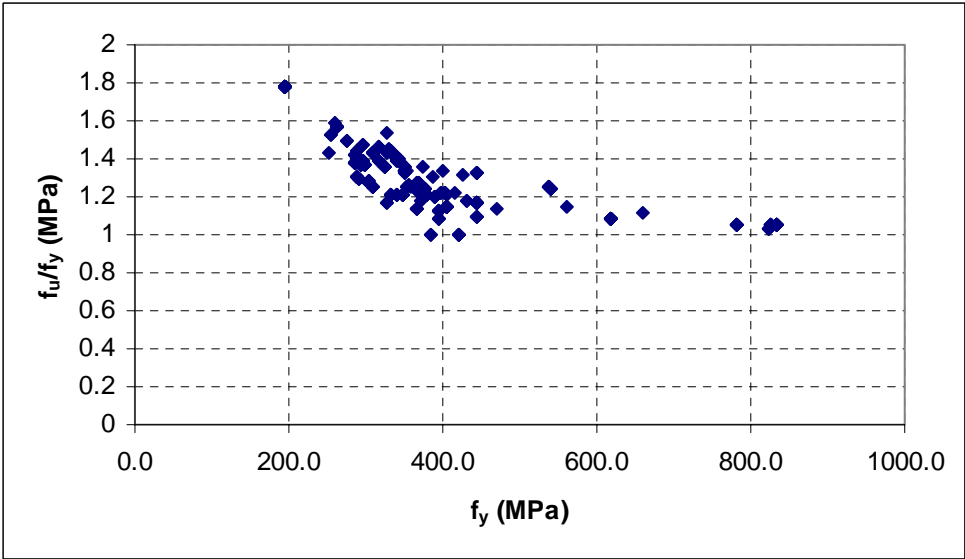


Figure 4.4: Comparison of f_y vs. f_u/f_y for the Whole Database

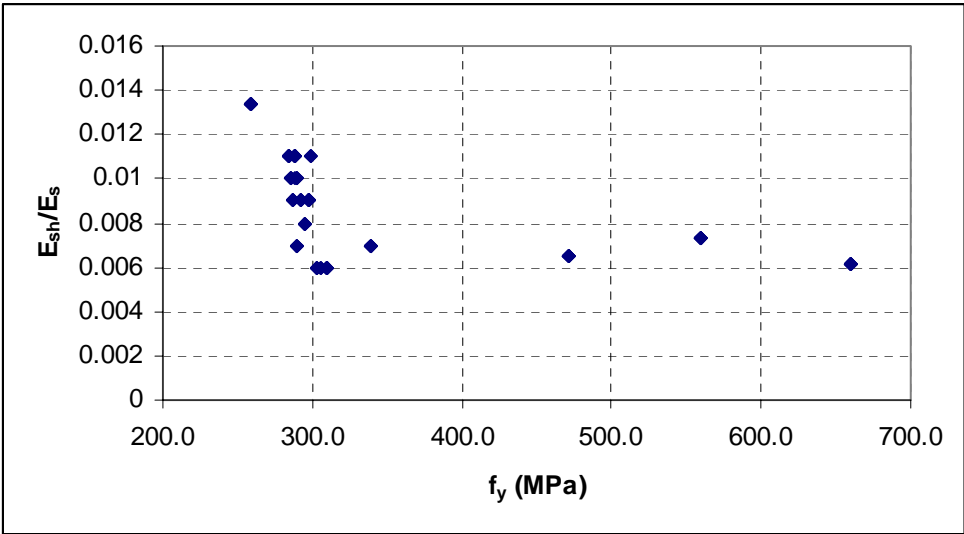


Figure 4.5: Comparison of f_y vs. E_{sh}/E_s for the Whole Database

Appendix A

Cross Section Analysis Program

A cross-section analysis program was developed to investigate the moment-curvature characteristics of RCFT sections. In this program, RCFT sections are divided into individual steel and concrete fibers along the depth of the sections. The strain and stress state of each fiber is monitored during the analysis. The resultant forces and axial forces are computed by numerical integration over the cross-section.

Each cross-section is divided into two distinct regions including flanges and web. The discretization of the cross-section is performed by specifying the number of fibers along the flanges and number of fiber along the web. The schematic view of the cross-section can be seen in Figure A1.

Each analysis starts by incrementing the compressive strain starting up to 0.03, which is taken as the limiting strain. The number of steps to reach the limiting strain level is given as an input parameter for the program. At each strain level, the neutral axis level is searched both inside and outside the cross-section. The correct position of the neutral axis is found by bisection algorithm. Neutral axis is forced to coincide with the boundaries of the fibers. Therefore, the accuracy of the program is limited with the force resultant of a horizontal fiber slice over the cross-section. The constitutive models used for the steel and concrete fibers were taken from Gourley and Hajjar, 1994.

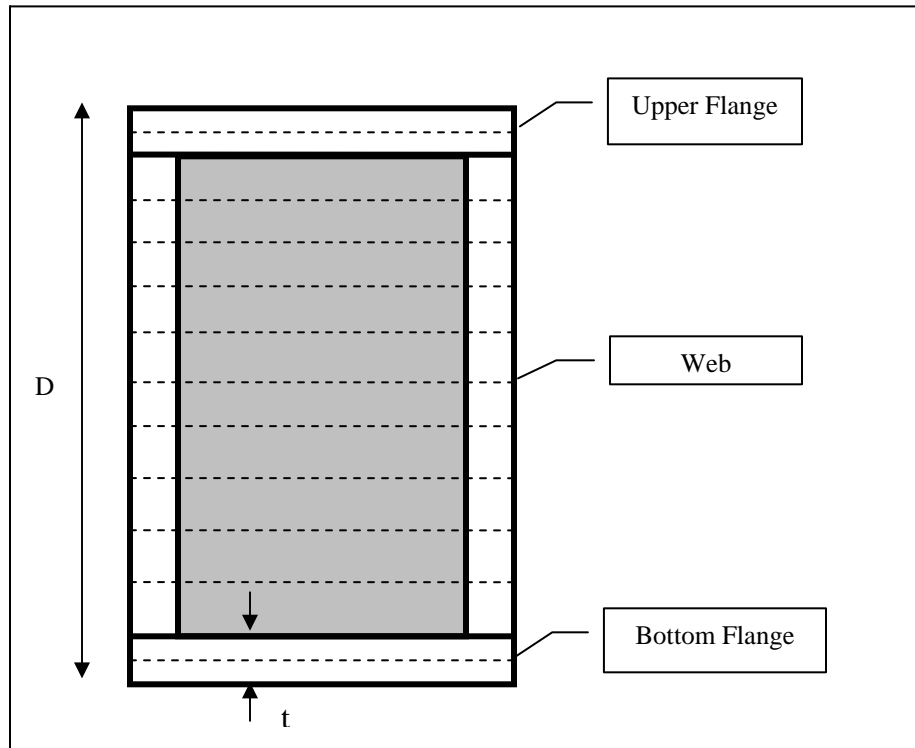


Figure A1: Discretization Scheme of an RCFT Cross-Section

Appendix B

Concrete-Filled Steel Tubes Used in Parametric Study

In Appendix B, the specimens generated to perform the parametric study in Section 3.11 are presented. The dimensions and geometric properties of the specimens are provided. In addition, the values of the damage indices and ductility levels calculated for the specimens are also given. The specimens were generated based on the extreme values of the parameters given in Tables 3.1 to 3.15. Any quantity that is not relevant or available was designated as “na”. The “pz” designation was used to identify the panel zone.

Table B1: Geometric and Material Properties of the Specimens Generated for the Parametric Study of Deformation-Based Damage Index of Monotonically Loaded Column Tests

| <i>Specimen</i> | <i>L/D</i> | <i>f_c</i> (MPa) | <i>D/t</i> | <i>f_y</i> (MPa) | <i>P_o/P_o</i> | <i>d_{cy}/d_o</i> | <i>d_{yt}/d_o</i> | <i>d_{bt}/d_o</i> | <i>μ</i> |
|-----------------|------------|----------------------------|------------|----------------------------|------------------------------------|-------------------------------------|-------------------------------------|-------------------------------------|----------|
| 1 | 3.0 | 20.6 | 22.5 | 194.2 | 0.34 | 0.45 | 0.55 | 3.86 | 7.19 |
| 2 | 5.0 | 20.6 | 22.5 | 194.2 | 0.34 | 0.45 | 0.55 | 3.86 | 14.37 |
| 3 | 3.0 | 74.0 | 22.5 | 194.2 | 0.65 | 0.26 | 0.87 | 3.86 | 1.84 |
| 4 | 5.0 | 74.0 | 22.5 | 194.2 | 0.65 | 0.26 | 0.87 | 3.86 | 1.84 |
| 5 | 3.0 | 30.7 | 50.0 | 194.2 | 0.65 | 0.26 | 0.87 | 1.70 | 1.36 |
| 6 | 5.0 | 30.7 | 50.0 | 194.2 | 0.65 | 0.26 | 0.87 | 1.70 | 8.54 |
| 7 | 3.0 | 30.7 | 50.0 | 194.2 | 0.65 | 0.26 | 0.87 | 1.70 | 1.36 |
| 8 | 5.0 | 30.7 | 50.0 | 194.2 | 0.65 | 0.26 | 0.87 | 1.70 | 8.54 |
| 9 | 3.0 | 55.0 | 17.0 | 825.0 | 0.19 | 0.54 | 0.40 | 2.45 | 9.00 |
| 10 | 5.0 | 55.0 | 17.0 | 825.0 | 0.19 | 0.54 | 0.40 | 2.45 | 16.18 |
| 11 | 3.0 | 103.0 | 17.0 | 825.0 | 0.31 | 0.47 | 0.51 | 2.45 | 7.70 |
| 12 | 5.0 | 103.0 | 17.0 | 825.0 | 0.31 | 0.47 | 0.51 | 2.45 | 14.88 |
| 13 | 3.0 | 20.6 | 50.0 | 825.0 | 0.23 | 0.52 | 0.43 | 0.82 | 4.31 |
| 14 | 5.0 | 20.6 | 50.0 | 825.0 | 0.23 | 0.52 | 0.43 | 0.82 | 11.49 |
| 15 | 3.0 | 103.0 | 50.0 | 825.0 | 0.59 | 0.29 | 0.81 | 0.82 | 2.09 |
| 16 | 5.0 | 103.0 | 50.0 | 825.0 | 0.59 | 0.29 | 0.81 | 0.82 | 9.27 |

Table B2: Geometric and Material Properties of the Specimens Generated for the Parametric Study of Energy-Based Damage Index of Monotonically Loaded Column Tests

| <i>Specimen</i> | <i>L/D</i> | f'_c (MPa) | <i>D/t</i> | f_y (MPa) | P_c/P_o | E_{cy}/E_{total} | E_c/E_{total} | E_{lb}/E_{total} | μ |
|-----------------|------------|--------------|------------|-------------|-----------|--------------------|-----------------|--------------------|-------|
| 1 | 3.0 | 40.0 | 17.0 | 350.0 | 0.954 | 0.036 | 0.006 | 0.713 | 7.94 |
| 2 | 3.0 | 80.0 | 17.0 | 330.0 | 0.951 | 0.001 | 0.055 | 0.735 | 1.84 |
| 3 | 3.0 | 40.0 | 30.0 | 668.0 | 0.957 | 0.035 | 0.007 | 0.282 | 6.94 |
| 4 | 3.0 | 103.0 | 17.0 | 835.0 | 0.980 | 0.033 | 0.011 | 0.453 | 7.74 |
| 5 | 12.0 | 23.0 | 17.0 | 339.1 | 0.952 | 0.243 | 0.178 | 0.725 | 3.03 |
| 6 | 12.0 | 103.0 | 17.0 | 339.1 | 0.952 | 0.179 | 0.269 | 0.725 | 3.47 |
| 7 | 12.0 | 30.0 | 22.1 | 600.0 | 0.964 | 0.243 | 0.178 | 0.410 | 3.03 |
| 8 | 12.0 | 103.0 | 17.0 | 835.0 | 0.980 | 0.222 | 0.209 | 0.453 | 3.18 |
| 9 | 3.0 | 20.6 | 50.0 | 290.0 | 0.853 | 0.002 | 0.053 | 0.256 | 3.29 |
| 10 | 3.0 | 35.0 | 40.0 | 400.0 | 0.909 | 0.004 | 0.051 | 0.273 | 4.62 |
| 11 | 3.0 | 20.6 | 50.0 | 535.8 | 0.915 | 0.031 | 0.013 | 0.186 | 4.02 |
| 12 | 3.0 | 40.0 | 50.0 | 535.8 | 0.915 | 0.000 | 0.057 | 0.186 | 3.21 |
| 13 | 12.0 | 20.6 | 50.0 | 194.2 | 0.795 | 0.171 | 0.279 | 0.315 | 3.53 |
| 14 | 12.0 | 57.7 | 42.2 | 301.0 | 0.877 | 0.151 | 0.307 | 0.299 | 3.66 |
| 15 | 12.0 | 20.6 | 50.0 | 835.0 | 0.944 | 0.237 | 0.187 | 0.148 | 3.07 |
| 16 | 12.0 | 103.0 | 50.0 | 835.0 | 0.944 | 0.164 | 0.290 | 0.148 | 3.58 |

Table B3: Geometric and Material Properties of the Specimens Generated for the Parametric Study of Deformation-Based Damage Index of Monotonically Loaded MI Type Beam-Column Tests ($L/D = 23.0-35.0$)

| <i>Specimen</i> | e/D | L/D | D/t | f'_c (MPa) | f_y (MPa) | P_c/P_o | d_{cr}/d_o | d_{cy}/d_o | d_y/d_o | μ |
|-----------------|-------|-------|-------|--------------|-------------|-----------|--------------|--------------|-----------|-------|
| 1 | 0.20 | 23.0 | 18.0 | 38.8 | 343.3 | 0.898 | 0.44 | 0.87 | 2.17 | 5.02 |
| 2 | 0.20 | 35.0 | 18.0 | 38.8 | 343.3 | 0.898 | 0.44 | 1.29 | 2.17 | 1.66 |
| 3 | 0.50 | 23.0 | 18.0 | 38.8 | 343.3 | 0.898 | 0.13 | 0.38 | 0.74 | 6.43 |
| 4 | 0.50 | 35.0 | 18.0 | 38.8 | 343.3 | 0.898 | 0.13 | 0.69 | 0.74 | 3.07 |
| 5 | 0.20 | 23.0 | 24.0 | 38.8 | 343.3 | 0.898 | 0.16 | 1.00 | 1.94 | 4.48 |
| 6 | 0.20 | 35.0 | 24.0 | 38.8 | 343.3 | 0.898 | 0.16 | 1.42 | 1.94 | 1.12 |
| 7 | 0.40 | 23.0 | 22.0 | 38.8 | 343.3 | 0.898 | 0.04 | 0.56 | 1.06 | 5.59 |
| 8 | 0.40 | 35.0 | 22.0 | 38.8 | 343.3 | 0.898 | 0.04 | 0.87 | 1.06 | 2.23 |
| 9 | 0.20 | 23.0 | 17.0 | 43.0 | 343.3 | 0.889 | 0.41 | 0.85 | 2.15 | 4.96 |
| 10 | 0.20 | 35.0 | 17.0 | 43.0 | 343.3 | 0.889 | 0.41 | 1.27 | 2.15 | 1.60 |
| 11 | 0.50 | 23.0 | 17.0 | 43.0 | 343.3 | 0.889 | 0.11 | 0.33 | 0.72 | 6.38 |
| 12 | 0.50 | 35.0 | 17.0 | 43.0 | 343.3 | 0.889 | 0.11 | 0.65 | 0.72 | 3.02 |
| 13 | 0.20 | 23.0 | 24.0 | 38.8 | 343.3 | 0.898 | 0.16 | 1.00 | 1.94 | 4.48 |
| 14 | 0.20 | 35.0 | 24.0 | 38.8 | 343.3 | 0.898 | 0.16 | 1.42 | 1.94 | 1.12 |
| 15 | 0.40 | 23.0 | 22.0 | 38.8 | 343.3 | 0.898 | 0.04 | 0.56 | 1.06 | 5.59 |
| 16 | 0.40 | 35.0 | 22.0 | 38.8 | 343.3 | 0.898 | 0.04 | 0.87 | 1.06 | 2.23 |
| 17 | 0.20 | 23.0 | 20.0 | 38.8 | 386.3 | 0.909 | 0.43 | 0.92 | 2.17 | 5.01 |
| 18 | 0.20 | 35.0 | 20.0 | 38.8 | 386.3 | 0.909 | 0.43 | 1.34 | 2.17 | 1.65 |
| 19 | 0.50 | 23.0 | 20.0 | 38.8 | 386.3 | 0.909 | 0.13 | 0.47 | 0.74 | 6.42 |
| 20 | 0.50 | 35.0 | 20.0 | 38.8 | 386.3 | 0.909 | 0.13 | 0.78 | 0.74 | 3.06 |
| 21 | 0.20 | 23.0 | 26.5 | 38.8 | 386.3 | 0.909 | 0.17 | 1.05 | 1.95 | 4.49 |
| 22 | 0.20 | 35.0 | 26.5 | 38.8 | 386.3 | 0.909 | 0.17 | 1.47 | 1.95 | 1.13 |
| 23 | 0.40 | 23.0 | 25.0 | 38.8 | 386.3 | 0.909 | 0.02 | 0.69 | 1.04 | 5.54 |
| 24 | 0.40 | 35.0 | 25.0 | 38.8 | 386.3 | 0.909 | 0.02 | 1.01 | 1.04 | 2.18 |
| 25 | 0.20 | 23.0 | 18.0 | 43.0 | 386.3 | 0.900 | 0.45 | 0.87 | 2.18 | 5.04 |
| 26 | 0.20 | 35.0 | 18.0 | 43.0 | 386.3 | 0.900 | 0.45 | 1.29 | 2.18 | 1.68 |
| 27 | 0.50 | 23.0 | 18.0 | 43.0 | 386.3 | 0.900 | 0.15 | 0.38 | 0.75 | 6.46 |
| 28 | 0.50 | 35.0 | 18.0 | 43.0 | 386.3 | 0.900 | 0.15 | 0.69 | 0.75 | 3.10 |
| 29 | 0.20 | 23.0 | 26.5 | 38.8 | 386.3 | 0.909 | 0.17 | 1.05 | 1.95 | 4.49 |
| 30 | 0.20 | 35.0 | 26.5 | 38.8 | 386.3 | 0.909 | 0.17 | 1.47 | 1.95 | 1.13 |
| 31 | 0.40 | 23.0 | 25.0 | 38.8 | 386.3 | 0.909 | 0.02 | 0.69 | 1.04 | 5.54 |
| 32 | 0.40 | 35.0 | 25.0 | 38.8 | 386.3 | 0.909 | 0.02 | 1.01 | 1.04 | 2.18 |

Table B4: Geometric and Material Properties of the Specimens Generated for the Parametric Study of Deformation-Based Damage Index of Monotonically Loaded MI Type Beam-Column Tests ($L/D = 4.0-14.1$)

| <i>Specimen</i> | e/D | L/D | D/t | f'_c (MPa) | f_y (MPa) | P/P_o | d_{ty}/d_o | d_{lb}/d_o | μ |
|-----------------|-------|-------|-------|--------------|-------------|---------|--------------|--------------|-------|
| 1 | 0.16 | 4.0 | 39.1 | 92.0 | 443.0 | 0.652 | 1.29 | 2.25 | 7.58 |
| 2 | 0.16 | 14.1 | 39.1 | 92.0 | 443.0 | 0.652 | 1.29 | 1.78 | 4.75 |
| 3 | 0.41 | 4.0 | 39.1 | 92.0 | 443.0 | 0.652 | 0.10 | 2.15 | 8.76 |
| 4 | 0.41 | 14.1 | 39.1 | 92.0 | 443.0 | 0.652 | 0.10 | 1.68 | 5.93 |

Table B5: Geometric and Material Properties of the Specimens Generated for the Parametric Study of Energy-Based Damage Index of Monotonically Loaded MI Type Beam-Column Tests ($D/t = 17.0-26.5$)

| <i>Specimen</i> | e/D | L/D | D/t | f'_c (MPa) | f_y (MPa) | P_c/P_o | E_{cr}/E_o | E_{cy}/d_o | E_{vy}/d_o | μ |
|-----------------|-------|-------|-------|--------------|-------------|-----------|--------------|--------------|--------------|-------|
| 1 | 0.20 | 23.0 | 18.0 | 38.8 | 343.3 | 0.30 | 0.261 | 0.142 | 0.435 | 5.02 |
| 2 | 0.20 | 34.5 | 18.0 | 38.8 | 343.3 | 0.30 | 0.261 | 0.326 | 0.561 | 1.80 |
| 3 | 0.35 | 23.0 | 18.0 | 38.8 | 343.3 | 0.30 | 0.051 | 0.215 | 0.459 | 5.72 |
| 4 | 0.35 | 34.5 | 18.0 | 38.8 | 343.3 | 0.30 | 0.051 | 0.399 | 0.585 | 2.50 |
| 5 | 0.20 | 23.0 | 24.0 | 38.8 | 343.3 | 0.37 | 0.237 | 0.197 | 0.400 | 4.48 |
| 6 | 0.20 | 34.5 | 24.0 | 38.8 | 343.3 | 0.37 | 0.237 | 0.381 | 0.526 | 1.26 |
| 7 | 0.35 | 23.0 | 24.0 | 38.8 | 343.3 | 0.37 | 0.027 | 0.270 | 0.424 | 5.18 |
| 8 | 0.35 | 34.5 | 24.0 | 38.8 | 343.3 | 0.37 | 0.027 | 0.454 | 0.550 | 1.96 |
| 9 | 0.20 | 23.0 | 17.0 | 43.0 | 343.3 | 0.31 | 0.259 | 0.132 | 0.431 | 4.96 |
| 10 | 0.20 | 34.5 | 17.0 | 43.0 | 343.3 | 0.31 | 0.259 | 0.316 | 0.558 | 1.74 |
| 11 | 0.35 | 23.0 | 17.0 | 40.0 | 343.3 | 0.29 | 0.054 | 0.206 | 0.462 | 5.78 |
| 12 | 0.35 | 34.5 | 17.0 | 40.0 | 343.3 | 0.29 | 0.054 | 0.390 | 0.589 | 2.56 |
| 13 | 0.20 | 23.0 | 24.0 | 38.8 | 343.3 | 0.37 | 0.237 | 0.197 | 0.400 | 4.48 |
| 14 | 0.20 | 34.5 | 24.0 | 38.8 | 343.3 | 0.37 | 0.237 | 0.381 | 0.526 | 1.26 |
| 15 | 0.35 | 23.0 | 24.0 | 38.8 | 343.3 | 0.37 | 0.027 | 0.270 | 0.424 | 5.18 |
| 16 | 0.35 | 34.5 | 24.0 | 38.8 | 343.3 | 0.37 | 0.027 | 0.454 | 0.550 | 1.96 |
| 17 | 0.20 | 23.0 | 20.0 | 38.8 | 386.3 | 0.30 | 0.261 | 0.160 | 0.434 | 5.01 |
| 18 | 0.20 | 34.5 | 20.0 | 38.8 | 386.3 | 0.30 | 0.261 | 0.344 | 0.561 | 1.79 |
| 19 | 0.35 | 23.0 | 20.0 | 38.8 | 386.3 | 0.30 | 0.051 | 0.234 | 0.458 | 5.72 |
| 20 | 0.35 | 34.5 | 20.0 | 38.8 | 386.3 | 0.30 | 0.051 | 0.418 | 0.585 | 2.50 |
| 21 | 0.20 | 23.0 | 26.5 | 38.8 | 386.3 | 0.37 | 0.237 | 0.220 | 0.400 | 4.49 |
| 22 | 0.20 | 34.5 | 26.5 | 38.8 | 386.3 | 0.37 | 0.237 | 0.404 | 0.527 | 1.27 |
| 23 | 0.35 | 23.0 | 26.5 | 38.8 | 386.3 | 0.37 | 0.027 | 0.293 | 0.424 | 5.19 |
| 24 | 0.35 | 34.5 | 26.5 | 38.8 | 386.3 | 0.37 | 0.027 | 0.477 | 0.551 | 1.97 |
| 25 | 0.20 | 23.0 | 18.0 | 43.0 | 386.3 | 0.30 | 0.263 | 0.142 | 0.436 | 5.04 |
| 26 | 0.20 | 34.5 | 18.0 | 43.0 | 386.3 | 0.30 | 0.263 | 0.326 | 0.563 | 1.82 |
| 27 | 0.35 | 23.0 | 18.0 | 43.0 | 386.3 | 0.30 | 0.053 | 0.215 | 0.460 | 5.75 |
| 28 | 0.35 | 34.5 | 18.0 | 43.0 | 386.3 | 0.30 | 0.053 | 0.399 | 0.587 | 2.53 |
| 29 | 0.20 | 23.0 | 26.5 | 38.8 | 386.3 | 0.37 | 0.237 | 0.220 | 0.400 | 4.49 |
| 30 | 0.20 | 34.5 | 26.5 | 38.8 | 386.3 | 0.37 | 0.237 | 0.404 | 0.527 | 1.27 |
| 31 | 0.35 | 23.0 | 26.5 | 38.8 | 386.3 | 0.37 | 0.027 | 0.293 | 0.424 | 5.19 |
| 32 | 0.35 | 34.5 | 26.5 | 38.8 | 386.3 | 0.37 | 0.027 | 0.477 | 0.551 | 1.97 |

Table B6: Geometric and Material Properties of the Specimens Generated for the Parametric Study of Energy-Based Damage Index of Monotonically Loaded MI Type Beam-Column Tests ($D/t = 39.1$)

| <i>Specimen</i> | e/D | L/D | D/t | f'_c (MPa) | f_y (MPa) | P_c/P_o | E_{vt}/d_o | E_{lb}/E_o | μ |
|-----------------|-------|-------|-------|--------------|-------------|-----------|--------------|--------------|-------|
| 1 | 0.16 | 4.0 | 39.1 | 92.0 | 443.0 | 0.652 | 0.053 | 0.097 | 7.58 |
| 2 | 0.16 | 14.1 | 39.1 | 92.0 | 443.0 | 0.652 | 0.164 | 0.410 | 4.75 |
| 3 | 0.41 | 4.0 | 39.1 | 92.0 | 443.0 | 0.652 | 0.093 | 0.197 | 8.76 |
| 4 | 0.41 | 14.1 | 39.1 | 92.0 | 443.0 | 0.652 | 0.204 | 0.591 | 5.93 |

Table B7: Geometric and Material Properties of the Specimens Generated for the Parametric Study of Deformation-Based Damage Index of Monotonically Loaded MII Type Beam-Column Tests

| <i>Specimen</i> | P/P_o | L/D | D/t | f_y (MPa) | f'_c (MPa) | P_c/P_o | d_{cy}/d_o | d_{ty}/d_o | d_{lb}/d_o | d_{lbw}/d_o | μ |
|-----------------|---------|-------|-------|-------------|--------------|-----------|--------------|--------------|--------------|---------------|-------|
| 1 | 0.20 | 3.0 | 27.0 | 290.4 | 20.5 | 0.298 | 0.586 | 0.437 | 1.060 | 2.483 | 15.65 |
| 2 | 0.20 | 3.0 | 45.4 | 290.4 | 20.5 | 0.428 | 0.908 | 1.125 | 1.466 | 3.849 | 15.16 |
| 3 | 0.20 | 3.0 | 27.0 | 290.4 | 20.5 | 0.298 | 0.586 | 0.437 | 1.060 | 2.483 | 15.65 |
| 4 | 0.20 | 3.0 | 45.4 | 290.4 | 20.5 | 0.428 | 0.908 | 1.125 | 1.466 | 3.849 | 15.16 |
| 5 | 0.20 | 3.0 | 25.0 | 290.4 | 22.1 | 0.295 | 0.580 | 0.424 | 1.053 | 2.457 | 15.66 |
| 6 | 0.20 | 3.0 | 43.0 | 290.4 | 22.1 | 0.432 | 0.918 | 1.147 | 1.478 | 3.893 | 15.15 |
| 7 | 0.20 | 3.0 | 25.0 | 290.4 | 22.1 | 0.295 | 0.580 | 0.424 | 1.053 | 2.457 | 15.66 |
| 8 | 0.20 | 3.0 | 43.0 | 290.4 | 22.1 | 0.432 | 0.918 | 1.147 | 1.478 | 3.893 | 15.15 |
| 9 | 0.20 | 3.0 | 29.0 | 315.9 | 20.5 | 0.297 | 0.583 | 0.432 | 1.058 | 2.473 | 15.66 |
| 10 | 0.20 | 3.0 | 43.5 | 315.9 | 20.5 | 0.397 | 0.830 | 0.958 | 1.368 | 3.519 | 15.28 |
| 11 | 0.20 | 3.0 | 29.0 | 315.9 | 20.5 | 0.297 | 0.583 | 0.432 | 1.058 | 2.473 | 15.66 |
| 12 | 0.20 | 3.0 | 43.5 | 315.9 | 20.5 | 0.397 | 0.830 | 0.958 | 1.368 | 3.519 | 15.28 |
| 13 | 0.20 | 3.0 | 27.0 | 315.9 | 22.1 | 0.296 | 0.581 | 0.427 | 1.055 | 2.463 | 15.66 |
| 14 | 0.20 | 3.0 | 43.5 | 315.9 | 22.1 | 0.415 | 0.874 | 1.054 | 1.424 | 3.709 | 15.21 |
| 15 | 0.20 | 3.0 | 27.0 | 315.9 | 22.1 | 0.296 | 0.581 | 0.427 | 1.055 | 2.463 | 15.66 |
| 16 | 0.20 | 3.0 | 43.5 | 315.9 | 22.1 | 0.415 | 0.874 | 1.054 | 1.424 | 3.709 | 15.21 |
| 17 | 0.50 | 3.0 | 30.0 | 290.4 | 20.5 | 0.323 | 0.168 | 1.010 | 0.035 | 1.303 | 7.07 |
| 18 | 0.50 | 3.0 | 45.4 | 290.4 | 20.5 | 0.428 | 0.428 | 1.566 | 0.362 | 2.406 | 6.67 |
| 19 | 0.50 | 3.0 | 30.0 | 290.4 | 20.5 | 0.323 | 0.168 | 1.010 | 0.035 | 1.303 | 7.07 |
| 20 | 0.50 | 3.0 | 45.4 | 290.4 | 20.5 | 0.428 | 0.428 | 1.566 | 0.362 | 2.406 | 6.67 |
| 21 | 0.50 | 3.0 | 30.0 | 290.4 | 22.1 | 0.340 | 0.209 | 1.098 | 0.086 | 1.478 | 7.01 |
| 22 | 0.50 | 3.0 | 43.0 | 290.4 | 22.1 | 0.432 | 0.438 | 1.588 | 0.374 | 2.450 | 6.66 |
| 23 | 0.50 | 3.0 | 30.0 | 290.4 | 22.1 | 0.340 | 0.209 | 1.098 | 0.086 | 1.478 | 7.01 |
| 24 | 0.50 | 3.0 | 43.0 | 290.4 | 22.1 | 0.432 | 0.438 | 1.588 | 0.374 | 2.450 | 6.66 |
| 25 | 0.50 | 3.0 | 31.0 | 315.9 | 20.5 | 0.313 | 0.142 | 0.956 | 0.002 | 1.194 | 7.11 |
| 26 | 0.50 | 3.0 | 43.5 | 315.9 | 20.5 | 0.397 | 0.350 | 1.399 | 0.264 | 2.076 | 6.79 |
| 27 | 0.50 | 3.0 | 31.0 | 315.9 | 20.5 | 0.313 | 0.142 | 0.956 | 0.002 | 1.194 | 7.11 |
| 28 | 0.50 | 3.0 | 43.5 | 315.9 | 20.5 | 0.397 | 0.350 | 1.399 | 0.264 | 2.076 | 6.79 |
| 29 | 0.50 | 3.0 | 33.0 | 315.9 | 22.1 | 0.344 | 0.221 | 1.123 | 0.101 | 1.527 | 6.99 |
| 30 | 0.50 | 3.0 | 43.5 | 315.9 | 22.1 | 0.415 | 0.394 | 1.495 | 0.320 | 2.266 | 6.72 |
| 31 | 0.50 | 3.0 | 33.0 | 315.9 | 22.1 | 0.344 | 0.221 | 1.123 | 0.101 | 1.527 | 6.99 |
| 32 | 0.50 | 3.0 | 43.5 | 315.9 | 22.1 | 0.415 | 0.394 | 1.495 | 0.320 | 2.266 | 6.72 |

Table B8: Geometric and Material Properties of the Specimens Generated for the Parametric Study of Energy-Based Damage Index of Monotonically Loaded MII Type Beam-Column Tests

| <i>Specimen</i> | P/P_o | L/D | D/t | f_y (MPa) | f'_c (MPa) | P_o/P_o | E_{cv}/E_{total} | E_{iv}/E_{total} | E_{ibf}/E_{total} | E_{lbw}/E_{total} | μ |
|-----------------|---------|-------|-------|-------------|--------------|-----------|--------------------|--------------------|---------------------|---------------------|-------|
| 1 | 0.20 | 3.0 | 24.6 | 290.4 | 20.5 | 0.28 | 0.0351 | 0.0472 | 0.146 | 0.297 | 15.74 |
| 2 | 0.20 | 3.0 | 24.6 | 290.4 | 22.1 | 0.29 | 0.0351 | 0.0497 | 0.151 | 0.309 | 15.68 |
| 3 | 0.20 | 3.0 | 23.5 | 315.8 | 21.6 | 0.26 | 0.0349 | 0.0446 | 0.141 | 0.285 | 15.80 |
| 4 | 0.20 | 3.0 | 23.5 | 315.8 | 22.1 | 0.26 | 0.0349 | 0.0453 | 0.143 | 0.288 | 15.78 |
| 5 | 0.20 | 3.0 | 45.4 | 290.4 | 20.5 | 0.43 | 0.0890 | 0.0715 | 0.195 | 0.411 | 15.16 |
| 6 | 0.20 | 3.0 | 45.4 | 290.4 | 20.7 | 0.43 | 0.0890 | 0.0718 | 0.196 | 0.413 | 15.15 |
| 7 | 0.20 | 3.0 | 43.54 | 315.8 | 20.5 | 0.40 | 0.0890 | 0.0665 | 0.185 | 0.388 | 15.28 |
| 8 | 0.20 | 3.0 | 43.54 | 315.8 | 22.1 | 0.42 | 0.0890 | 0.0694 | 0.191 | 0.401 | 15.21 |
| 9 | 0.50 | 3.0 | 24.6 | 290.4 | 20.5 | 0.28 | 0.0132 | 0.2332 | 0.023 | 0.405 | 7.25 |
| 10 | 0.50 | 3.0 | 24.6 | 290.4 | 22.1 | 0.29 | 0.0132 | 0.2357 | 0.028 | 0.390 | 7.19 |
| 11 | 0.50 | 3.0 | 23.5 | 315.8 | 21.6 | 0.26 | 0.0130 | 0.2306 | 0.018 | 0.422 | 7.31 |
| 12 | 0.50 | 3.0 | 23.5 | 315.8 | 22.1 | 0.26 | 0.0130 | 0.2313 | 0.020 | 0.418 | 7.29 |
| 13 | 0.50 | 3.0 | 45.4 | 290.4 | 20.5 | 0.43 | 0.0671 | 0.2575 | 0.072 | 0.249 | 6.67 |
| 14 | 0.50 | 3.0 | 45.4 | 290.4 | 20.7 | 0.43 | 0.0671 | 0.2578 | 0.073 | 0.247 | 6.66 |
| 15 | 0.50 | 3.0 | 43.54 | 315.8 | 20.5 | 0.40 | 0.0671 | 0.2525 | 0.062 | 0.281 | 6.79 |
| 16 | 0.50 | 3.0 | 43.54 | 315.8 | 22.1 | 0.42 | 0.0671 | 0.2554 | 0.068 | 0.262 | 6.72 |

Table B9: Geometric and Material Properties of the Specimens Generated for the Parametric Study of Deformation-Based Damage Index of Monotonically Loaded MIII Type Beam-Column Tests

| <i>Specimen</i> | P/P_o | L/D | D/t | f_y (MPa) | f'_c (MPa) | P_o/P_o |
|-----------------|---------|-------|-------|-------------|--------------|-----------|
| 1 | 0.19 | 5.0 | 34.3 | 471.0 | 110.0 | 0.65 |
| 2 | 0.19 | 5.0 | 50.0 | 471.0 | 110.0 | 0.73 |
| 3 | 0.19 | 5.0 | 34.3 | 560.0 | 110.0 | 0.61 |
| 4 | 0.19 | 5.0 | 50.0 | 560.0 | 110.0 | 0.70 |

Table B9: Geometric and Material Properties of the Specimens Generated for the Parametric Study of Deformation-Based Damage Index of Monotonically Loaded MIII Type Beam-Column Tests (cont'd)

| <i>Specimen</i> | d_{cr}/d_o | d_{cv}/d_o | d_{iv}/d_o | d_c/d_o | d_{bf}/d_o | d_{bw}/d_o | μ |
|-----------------|--------------|--------------|--------------|-----------|--------------|--------------|-------|
| 1 | 0.11 | 0.44 | 0.63 | 0.88 | 0.72 | 1.38 | 5.04 |
| 2 | 0.14 | 0.52 | 0.65 | 0.88 | 1.20 | 1.86 | 4.63 |
| 3 | 0.09 | 0.40 | 0.63 | 0.88 | 0.49 | 1.47 | 5.23 |
| 4 | 0.13 | 0.49 | 0.65 | 0.88 | 1.01 | 2.00 | 4.80 |

Table B10: Geometric and Material Properties of the Specimens Generated for the Parametric Study of Energy-Based Damage Index of Monotonically Loaded MIII Type Beam-Column Tests

| <i>Specimen</i> | P/P_o | L/D | D/t | f_y (MPa) | f'_c (MPa) | P_c/P_o |
|-----------------|---------|-------|-------|-------------|--------------|-----------|
| 1 | 0.19 | 5.0 | 34.2 | 288.4 | 110.0 | 0.75 |
| 2 | 0.43 | 5.0 | 34.2 | 288.4 | 110.0 | 0.75 |
| 3 | 0.19 | 5.0 | 40.0 | 288.4 | 110.0 | 0.78 |
| 4 | 0.43 | 5.0 | 40.0 | 288.4 | 110.0 | 0.78 |
| 5 | 0.19 | 5.0 | 34.2 | 560.0 | 110.0 | 0.61 |
| 6 | 0.43 | 5.0 | 34.2 | 560.0 | 110.0 | 0.61 |
| 7 | 0.19 | 5.0 | 50.0 | 560.0 | 110.0 | 0.70 |
| 8 | 0.43 | 5.0 | 50.0 | 560.0 | 110.0 | 0.70 |

Table B10: Geometric and Material Properties of the Specimens Generated for the Parametric Study of Energy-Based Damage Index of Monotonically Loaded MIII Type Beam-Column Tests (cont'd)

| <i>Specimen</i> | E_{cr}/E_{total} | E_{cy}/E_{total} | E_{ty}/E_{total} | E_c/E_{total} | E_{lb}/E_{total} | E_{lbw}/E_{total} | μ |
|-----------------|--------------------|--------------------|--------------------|-----------------|--------------------|---------------------|-------|
| 1 | 0.0111 | 0.0602 | 0.1743 | 0.1715 | 0.5778 | 0.2145 | 4.56 |
| 2 | 0.0375 | 0.0491 | 0.4311 | 0.1115 | 0.3978 | 0.5553 | 2.24 |
| 3 | 0.0062 | 0.0619 | 0.1736 | 0.1375 | 0.5228 | 0.2695 | 4.41 |
| 4 | 0.0326 | 0.0509 | 0.4304 | 0.0775 | 0.3428 | 0.6103 | 2.10 |
| 5 | 0.0341 | 0.0522 | 0.1778 | 0.3306 | 0.4501 | 0.3422 | 5.24 |
| 6 | 0.0605 | 0.0411 | 0.4346 | 0.2706 | 0.2701 | 0.6830 | 2.92 |
| 7 | 0.0193 | 0.0573 | 0.1756 | 0.2279 | 0.2411 | 0.5512 | 4.80 |
| 8 | 0.0457 | 0.0463 | 0.4324 | 0.1679 | 0.0611 | 0.8920 | 2.48 |

Table B11: Geometric and Material Properties of the Specimens Generated for the Parametric Study of Energy-Based Damage Index of Cyclically Loaded Beam-Column Tests

| <i>Specimen</i> | P/P_o | L/D | D/t | f_y (MPa) | f'_c (MPa) | P/P_o |
|-----------------|---------|-------|-------|-------------|--------------|---------|
| 1 | 0.10 | 5.0 | 35.7 | 269.0 | 110.0 | 0.77 |
| 2 | 0.21 | 5.0 | 35.7 | 269.0 | 110.0 | 0.77 |
| 3 | 0.10 | 5.0 | 52.6 | 407.6 | 110.0 | 0.77 |
| 4 | 0.21 | 5.0 | 52.6 | 407.6 | 110.0 | 0.77 |
| 5 | 0.10 | 5.0 | 39.0 | 660.0 | 110.0 | 0.60 |
| 6 | 0.21 | 5.0 | 39.0 | 660.0 | 110.0 | 0.60 |
| 7 | 0.10 | 5.0 | 50.8 | 660.0 | 110.0 | 0.67 |
| 8 | 0.21 | 5.0 | 50.8 | 660.0 | 110.0 | 0.67 |

Table B11: Geometric and Material Properties of the Specimens Generated for the Parametric Study of Energy-Based Damage Index of Cyclically Loaded Beam-Column Tests (cont.)

| <i>Specimen</i> | E_{cp}/E_{total} | E_{cy}/E_{total} | E_{ty}/E_{total} | E_{tb}/E_{total} | E_{tbw}/E_{total} | μ |
|-----------------|--------------------|--------------------|--------------------|--------------------|---------------------|-------|
| 1 | 0.0003 | 0.0483 | 0.0698 | 0.2322 | 0.6956 | 4.51 |
| 2 | 0.0039 | 0.0318 | 0.0698 | 0.2322 | 0.6956 | 3.73 |
| 3 | 0.0003 | 0.0483 | 0.0698 | 0.1609 | 0.4401 | 4.51 |
| 4 | 0.0039 | 0.0318 | 0.0698 | 0.1609 | 0.4401 | 3.73 |
| 5 | -0.0002 | 0.0670 | 0.1649 | 0.1699 | 0.4723 | 4.57 |
| 6 | 0.0033 | 0.0505 | 0.1649 | 0.1699 | 0.4723 | 3.79 |
| 7 | 0.0000 | 0.0597 | 0.1281 | 0.1244 | 0.3092 | 4.55 |
| 8 | 0.0035 | 0.0432 | 0.1281 | 0.1244 | 0.3092 | 3.77 |

Table B12: Geometric and Material Properties of the Specimens Generated for the Parametric Study of Deformation-Based Damage Index of Monotonically Loaded Panel Zone Tests

| <i>Specimen</i> | L_p/D | D/t | f_y (MPa) | f'_c (MPa) | P_o/P_o | d_{cr}/d_o | d_v/d_o | d_c/d_o | d_{ib}/d_o | μ |
|-----------------|---------|-------|-------------|--------------|-----------|--------------|-----------|-----------|--------------|-------|
| 1 | 2.0 | 32.2 | 377.0 | 39.0 | 0.43 | 0.115 | 0.573 | 0.733 | 0.25 | 1.75 |
| 2 | 2.0 | 46.1 | 377.0 | 39.0 | 0.53 | 0.119 | 0.555 | 0.687 | 0.25 | 4.06 |
| 3 | 2.0 | 32.2 | 412.0 | 39.0 | 0.41 | 0.113 | 0.576 | 0.744 | 0.25 | 1.23 |
| 4 | 2.0 | 46.1 | 412.0 | 39.0 | 0.51 | 0.118 | 0.559 | 0.698 | 0.25 | 3.53 |
| 5 | 2.5 | 32.2 | 377.0 | 39.0 | 0.43 | 0.146 | 0.758 | 0.873 | 0.25 | 0.84 |
| 6 | 3.0 | 46.1 | 377.0 | 39.0 | 0.53 | 0.181 | 0.925 | 0.967 | 0.25 | 2.25 |
| 7 | 2.5 | 32.2 | 412.0 | 39.0 | 0.41 | 0.144 | 0.761 | 0.884 | 0.25 | 0.32 |
| 8 | 3.0 | 46.1 | 412.0 | 39.0 | 0.51 | 0.180 | 0.929 | 0.978 | 0.25 | 1.72 |

Table B13: Geometric and Material Properties of the Specimens Generated for the Parametric Study of Energy-Based Damage Index of Monotonically Loaded Panel Zone Tests

| <i>Specimen</i> | L_p/D | D/t | f_y (MPa) | f'_c (MPa) | P_c/P_o | E_{cr}/E_{total} | E_v/E_{total} | E_c/E_{total} | E_{lb}/E_{total} | μ |
|-----------------|---------|-------|-------------|--------------|-----------|--------------------|-----------------|-----------------|--------------------|-------|
| 1 | 2.0 | 32.2 | 377.0 | 39.0 | 0.43 | 0.0028 | 0.0594 | 0.1007 | 0.0110 | 1.75 |
| 2 | 2.0 | 46.1 | 377.0 | 39.0 | 0.53 | 0.0031 | 0.0575 | 0.0872 | 0.0110 | 4.06 |
| 3 | 2.0 | 32.2 | 412.0 | 39.0 | 0.41 | 0.0027 | 0.0598 | 0.1038 | 0.0110 | 1.23 |
| 4 | 2.0 | 46.1 | 412.0 | 39.0 | 0.51 | 0.0030 | 0.0579 | 0.0903 | 0.0110 | 3.53 |
| 5 | 2.5 | 32.2 | 377.0 | 39.0 | 0.43 | 0.0040 | 0.0859 | 0.1307 | 0.0110 | 0.84 |
| 6 | 3.0 | 46.1 | 377.0 | 39.0 | 0.53 | 0.0056 | 0.1105 | 0.1472 | 0.0110 | 2.25 |
| 7 | 2.5 | 32.2 | 412.0 | 39.0 | 0.41 | 0.0039 | 0.0863 | 0.1338 | 0.0110 | 0.32 |
| 8 | 3.0 | 46.1 | 412.0 | 39.0 | 0.51 | 0.0055 | 0.1109 | 0.1503 | 0.0110 | 1.72 |

Table B14: Geometric and Material Properties of the Specimens Generated for the Parametric Study of Deformation-Based and Energy Based Damage Indices of Monotonically Loaded Pinned-Connection Tests for Concrete Cracking

| <i>Specimen</i> | <i>e/D</i> | <i>d_{cr}/d_o</i> | <i>E_{cr}/E_{total}</i> | <i>μ</i> |
|-----------------|------------|-------------------------------------|---|----------|
| 1 | 1.30 | 0.38 | 0.19 | na |
| 2 | 2.30 | 0.05 | 0.13 | na |

Table
Geometric

B15:
and

Material Properties of the Specimens Generated for the Parametric Study of Deformation-Based and Energy Based Damage Indices of Monotonically Loaded Pinned-Connection Tests for Yielding of Compression Flange

| <i>Specimen</i> | <i>e/D</i> | <i>P/V</i> | <i>d_{cy}/E_{total}</i> | <i>E_{cy}/E_{total}</i> | <i>μ</i> |
|-----------------|------------|------------|---|---|----------|
| 1 | 1.33 | 1.5 | 0.21 | 0.08 | na |
| 2 | 1.33 | 8.0 | 0.49 | 0.43 | na |
| 3 | 2.53 | 1.5 | 0.33 | 0.14 | na |
| 4 | 2.53 | 8.0 | 0.60 | 0.50 | na |

Table B16: Geometric and Material Properties of the Specimens Generated for the Parametric Study of Energy-Based Damage Index of Cyclically-Loaded Moment Connection Tests

| <i>Specimen</i> | P_g/P_o | d_g/D | P/P_o | D/t | f_y | f'_c | E_{cr}/E_{total} | E_{cy}/E_{total} | E_{vy}/E_{total} | E_{lb}/E_{total} | $E_{cr}/E_{total}(p_z)$ | $E_{vy}/E_{total}(p_z)$ | E_{gy}/E_{total} | E_{gp}/E_{total} | μ |
|-----------------|-----------|---------|---------|-------|-------|--------|--------------------|--------------------|--------------------|--------------------|-------------------------|-------------------------|--------------------|--------------------|-------|
| 1 | 0.31 | 1.40 | 0.00 | 34.5 | 420.0 | 30.1 | 0.009 | 0.10 | 0.043 | 0.50 | 0.006 | 0.19 | 0.15 | 0.23 | 2.59 |
| 2 | 0.31 | 1.40 | 0.00 | 34.5 | 420.0 | 30.1 | 0.008 | 0.10 | 0.048 | 0.44 | 0.006 | 0.17 | 0.15 | 0.23 | 2.59 |
| 3 | 0.31 | 1.40 | 0.00 | 40.0 | 420.0 | 30.1 | 0.009 | 0.10 | 0.043 | 0.50 | 0.006 | 0.19 | 0.15 | 0.23 | 2.54 |
| 4 | 0.31 | 1.40 | 0.00 | 40.0 | 420.0 | 30.1 | 0.008 | 0.10 | 0.048 | 0.44 | 0.006 | 0.17 | 0.15 | 0.23 | 2.54 |
| 5 | 0.31 | 1.67 | 0.20 | 34.5 | 420.0 | 30.1 | 0.021 | 0.07 | 0.103 | 0.50 | 0.006 | 0.19 | 0.15 | 0.23 | 2.80 |
| 6 | 0.31 | 1.67 | 0.20 | 34.5 | 420.0 | 30.1 | 0.020 | 0.07 | 0.108 | 0.44 | 0.006 | 0.17 | 0.15 | 0.23 | 2.80 |
| 7 | 0.31 | 1.67 | 0.20 | 40.0 | 420.0 | 30.1 | 0.021 | 0.07 | 0.103 | 0.50 | 0.006 | 0.19 | 0.15 | 0.23 | 2.76 |
| 8 | 0.31 | 1.67 | 0.20 | 40.0 | 420.0 | 30.1 | 0.020 | 0.07 | 0.108 | 0.44 | 0.006 | 0.17 | 0.15 | 0.23 | 2.76 |
| 9 | 0.37 | 1.40 | 0.00 | 34.5 | 420.0 | 30.1 | 0.009 | 0.10 | 0.043 | 0.50 | 0.006 | 0.19 | 0.03 | 0.19 | 2.86 |
| 10 | 0.37 | 1.40 | 0.00 | 34.5 | 420.0 | 30.1 | 0.008 | 0.10 | 0.048 | 0.44 | 0.006 | 0.17 | 0.03 | 0.19 | 2.86 |
| 11 | 0.37 | 1.40 | 0.00 | 40.0 | 420.0 | 30.1 | 0.009 | 0.10 | 0.043 | 0.50 | 0.006 | 0.19 | 0.03 | 0.19 | 2.82 |
| 12 | 0.37 | 1.40 | 0.00 | 40.0 | 420.0 | 30.1 | 0.008 | 0.10 | 0.048 | 0.44 | 0.006 | 0.17 | 0.03 | 0.19 | 2.82 |
| 13 | 0.37 | 1.67 | 0.20 | 34.5 | 420.0 | 30.1 | 0.021 | 0.07 | 0.103 | 0.50 | 0.006 | 0.19 | 0.03 | 0.19 | 3.07 |
| 14 | 0.37 | 1.67 | 0.20 | 34.5 | 420.0 | 30.1 | 0.020 | 0.07 | 0.108 | 0.44 | 0.006 | 0.17 | 0.03 | 0.19 | 3.07 |
| 15 | 0.37 | 1.67 | 0.20 | 40.0 | 420.0 | 30.1 | 0.021 | 0.07 | 0.103 | 0.50 | 0.006 | 0.19 | 0.03 | 0.19 | 3.03 |
| 16 | 0.37 | 1.67 | 0.20 | 40.0 | 420.0 | 30.1 | 0.020 | 0.07 | 0.108 | 0.44 | 0.006 | 0.17 | 0.03 | 0.19 | 3.03 |
| 17 | 0.31 | 1.40 | 0.00 | 34.5 | 420.0 | 33.0 | 0.009 | 0.10 | 0.043 | 0.50 | 0.017 | 0.53 | 0.15 | 0.23 | 2.56 |
| 18 | 0.31 | 1.40 | 0.00 | 34.5 | 420.0 | 33.0 | 0.008 | 0.10 | 0.048 | 0.44 | 0.017 | 0.51 | 0.15 | 0.23 | 2.56 |
| 19 | 0.31 | 1.40 | 0.00 | 40.0 | 420.0 | 33.0 | 0.009 | 0.10 | 0.043 | 0.50 | 0.017 | 0.53 | 0.15 | 0.23 | 2.52 |
| 20 | 0.31 | 1.40 | 0.00 | 40.0 | 420.0 | 33.0 | 0.008 | 0.10 | 0.048 | 0.44 | 0.017 | 0.51 | 0.15 | 0.23 | 2.52 |
| 21 | 0.31 | 1.67 | 0.20 | 34.5 | 420.0 | 33.0 | 0.021 | 0.07 | 0.103 | 0.50 | 0.017 | 0.53 | 0.15 | 0.23 | 2.77 |
| 22 | 0.31 | 1.67 | 0.20 | 34.5 | 420.0 | 33.0 | 0.020 | 0.07 | 0.108 | 0.44 | 0.017 | 0.51 | 0.15 | 0.23 | 2.77 |
| 23 | 0.31 | 1.67 | 0.20 | 40.0 | 420.0 | 33.0 | 0.021 | 0.07 | 0.103 | 0.50 | 0.017 | 0.53 | 0.15 | 0.23 | 2.73 |
| 24 | 0.31 | 1.67 | 0.20 | 40.0 | 420.0 | 33.0 | 0.020 | 0.07 | 0.108 | 0.44 | 0.017 | 0.51 | 0.15 | 0.23 | 2.73 |
| 25 | 0.37 | 1.40 | 0.00 | 34.5 | 420.0 | 33.0 | 0.009 | 0.10 | 0.043 | 0.50 | 0.017 | 0.53 | 0.03 | 0.19 | 2.83 |
| 26 | 0.37 | 1.40 | 0.00 | 34.5 | 420.0 | 33.0 | 0.008 | 0.10 | 0.048 | 0.44 | 0.017 | 0.51 | 0.03 | 0.19 | 2.83 |
| 27 | 0.37 | 1.40 | 0.00 | 40.0 | 420.0 | 33.0 | 0.009 | 0.10 | 0.043 | 0.50 | 0.017 | 0.53 | 0.03 | 0.19 | 2.79 |
| 28 | 0.37 | 1.40 | 0.00 | 40.0 | 420.0 | 33.0 | 0.008 | 0.10 | 0.048 | 0.44 | 0.017 | 0.51 | 0.03 | 0.19 | 2.79 |
| 29 | 0.37 | 1.67 | 0.20 | 34.5 | 420.0 | 33.0 | 0.021 | 0.07 | 0.103 | 0.50 | 0.017 | 0.53 | 0.03 | 0.19 | 3.05 |
| 30 | 0.37 | 1.67 | 0.20 | 34.5 | 420.0 | 33.0 | 0.020 | 0.07 | 0.108 | 0.44 | 0.017 | 0.51 | 0.03 | 0.19 | 3.05 |
| 31 | 0.37 | 1.67 | 0.20 | 40.0 | 420.0 | 33.0 | 0.021 | 0.07 | 0.103 | 0.50 | 0.017 | 0.53 | 0.03 | 0.19 | 3.00 |
| 32 | 0.37 | 1.67 | 0.20 | 40.0 | 420.0 | 33.0 | 0.020 | 0.07 | 0.108 | 0.44 | 0.017 | 0.51 | 0.03 | 0.19 | 3.00 |

Table B17: Geometric and Material Properties of the Specimens Generated for the Parametric Study of Deformation-Based Damage Indices of Monotonically Loaded Frame Tests

| <i>Specimen</i> | <i>D/t</i> | f_y (MPa) | f'_c (MPa) | P_c/P_o | d_{cy}/d_o | d_{yt}/d_o | d_{lbf}/d_o | μ |
|-----------------|------------|-------------|--------------|-----------|--------------|--------------|---------------|-------|
| 1 | 46.9 | 287.4 | 35.3 | 0.57 | 0.18 | 0.34 | 0.37 | 6.64 |
| 2 | 46.9 | 288.4 | 35.3 | 0.57 | 0.18 | 0.34 | 0.37 | 6.65 |
| 3 | 46.9 | 287.4 | 37.8 | 0.59 | 0.18 | 0.36 | 0.37 | 6.42 |
| 4 | 46.9 | 288.4 | 37.8 | 0.59 | 0.18 | 0.36 | 0.37 | 6.43 |
| 5 | 65.2 | 287.4 | 35.3 | 0.66 | 0.22 | 0.44 | 0.34 | 5.57 |
| 6 | 65.2 | 288.4 | 35.3 | 0.66 | 0.21 | 0.44 | 0.34 | 5.58 |
| 7 | 65.2 | 287.4 | 37.8 | 0.67 | 0.22 | 0.46 | 0.34 | 5.37 |
| 8 | 65.2 | 288.4 | 37.8 | 0.67 | 0.22 | 0.46 | 0.34 | 5.38 |

Table B18: Geometric and Material Properties of the Specimens Generated for the Parametric Study of Deformation-Based Damage Indices of Monotonically Loaded Frame Tests

| <i>Specimen</i> | <i>D/t</i> | f_y (MPa) | f'_c (MPa) | P_c/P_o | E_{lbf}/E_{total} | μ |
|-----------------|------------|-------------|--------------|-----------|---------------------|-------|
| 1 | 46.9 | 287.4 | 35.3 | 0.57 | 0.10 | 8.56 |
| 2 | 46.9 | 287.4 | 37.8 | 0.59 | 0.09 | 8.78 |
| 3 | 46.9 | 288.4 | 35.3 | 0.57 | 0.10 | 8.55 |
| 4 | 46.9 | 288.4 | 37.8 | 0.59 | 0.09 | 8.77 |
| 5 | 65.2 | 287.4 | 35.3 | 0.66 | 0.08 | 9.63 |
| 6 | 65.2 | 287.4 | 37.8 | 0.67 | 0.08 | 9.83 |
| 7 | 65.2 | 288.4 | 35.3 | 0.66 | 0.08 | 9.62 |
| 8 | 65.2 | 288.4 | 37.8 | 0.67 | 0.08 | 9.82 |

Table B19: Geometric and Material Properties of the Specimens Generated for the Parametric Study of Deformation-Based and Deformation-Based Damage Indices of Cyclically Loaded Frame Tests

| <i>Specimen</i> | P/P_o | D/t | f_y (MPa) | f'_c (MPa) | E_{cr}/E_{total} | P_c/P_o | E_{cy}/E_{total} | E_{lb}/E_{total} | μ |
|-----------------|---------|-------|-------------|--------------|--------------------|-----------|--------------------|--------------------|-------|
| 1 | 0.15 | 21.6 | 403.3 | 17.8 | 0.00001 | 0.17 | 0.023 | 0.27 | 4.21 |
| 2 | 0.15 | 21.6 | 403.3 | 18.6 | 0.00001 | 0.18 | 0.023 | 0.27 | 4.21 |
| 3 | 0.30 | 21.6 | 403.3 | 17.8 | 0.00354 | 0.17 | 0.017 | 0.28 | 2.90 |
| 4 | 0.30 | 21.6 | 403.3 | 18.6 | 0.00352 | 0.18 | 0.017 | 0.28 | 2.90 |
| 5 | 0.50 | 21.6 | 403.3 | 17.8 | 0.00834 | 0.17 | 0.017 | 0.30 | 1.15 |
| 6 | 0.50 | 21.6 | 403.3 | 18.6 | 0.00832 | 0.18 | 0.017 | 0.30 | 1.15 |

Appendix C

References

American Concrete Institute (ACI) (2002). *Building Code Requirements for Reinforced Concrete*, ACI 318-02, American Concrete Institute, Detroit, Michigan.

Aho, M. and Leon, R. T. (1997). "A Database for Encased and Concrete-Filled Columns," Report No. 97-01, School of Civil and Environmental Engineering, Georgia Institute of Technology, Atlanta, Georgia.

American Institute of Steel Construction (AISC) (1999). *Load and Resistance Factor Design Specification for Structural Steel Buildings*, AISC, Chicago, Illinois.

American Institute of Steel Construction (AISC) (2002). *Seismic Provision for Structural Steel Buildings*, AISC, Chicago, Illinois.

Applied Technology Council (ATC) (1996). "Seismic Evaluation and Retrofit of Concrete Buildings," *Report No. SSC 96-01*, Applied Technology Council, Redwood City, California.

Banon H., Biggs, J. M., and Irvine H. M. (1981). "Seismic Damage in Reinforced Concrete Frames," *Journal of the Structural Division*, ASCE, Vol. 107, No. ST9, pp. 1713-1729.

Bergmann, R. (1994). "Load Introduction in Composite Columns Filled with High Strength Concrete," *Tubular Structures VI*, Proceedings of the Sixth International Symposium on Tubular Structures, Grundy, P., Holgate, A., and Wong, W. (eds.), Melbourne, Australia, December 14-16, 1994, A. A. Balkema, Rotterdam, the Netherlands, pp. 373-380.

Bertero, V. V., (1997). "Performance-Based Seismic Engineering: A Critical Review of Proposed Guidelines," *Seismic Design Methodologies for the Next Generation of Codes*, Fajfar, P. and Krawinkler, H. (eds.), A. A. Balkema, Rotterdam, the Netherlands, pp. 1-31.

Bridge, R. Q. (1976). "Concrete Filled Steel Tubular Columns," Report No. R283, School of Civil Engineering, University of Sydney, Sydney, Australia.

British Standards Institution (BS) (1993). "Structural Use of Steel in Building," *Code of Practice for Design in Simple and Continuous Construction: Hot Rolled Sections*, BS 5950, British Standards Institution, London, United Kingdom.

Building Seismic Safety Council (BSSC) (2001). *NEHRP Recommended Provisions for Seismic Regulations for New Buildings and Other Structures*, FEMA 368, Federal Emergency Management Agency, Washington, D.C.

Cederwall, K., Engstrom, B., and Grauers, M. (1990). "High-Strength Concrete Used in Composite Columns," Proceedings of the Second International Symposium on Utilization of High-Strength Concrete, Hester, W. T. (ed.), Berkeley, California, pp. 195-214.

Chung, J., Matsui, C., and Tsuda, K. (2001). "Simplified Design Formula of Slender Concrete-Filled Steel Tubular Beam-Columns," *Structural Engineering and Mechanics*, Vol. 12, No. 1, pp. 71-84.

Clarke, M. J. and Hancock, G. J. (1991). "Finite-Element Nonlinear Analysis of Stressed-Arch Frames," *Journal of Structural Engineering*, ASCE, Vol. 117, No. 10, pp. 2819-2837.

Elchalakani, M., Zhao, X. L., Grzebieta, R.H. (2001). "Concrete-Filled Circular Steel Tubes Subjected to Pure Bending," *Journal of Constructional Steel Research*, Volume 57, No. 11, pp. 1141-1168.

Ersoy, U. (1997). *Reinforced Concrete*, Middle East Technical University, Ankara, Turkey.

Fajfar P. (1992). "Equivalent Ductility Factors, Taking into Account Low Cycle Fatigue," *Earthquake Engineering and Structural Dynamics*, Vol. 21, pp. 837-848.

Federal Emergency Management Agency (FEMA) (1997). *NEHRP Guidelines for the Seismic Rehabilitation of Buildings*, FEMA 273, Federal Emergency Management Agency, Washington, D.C.

FEMA (2000a). *Recommended Seismic Design Criteria for New Steel Moment-Frame Buildings*, FEMA 350, Federal Emergency Management Agency, Washington, D.C.

FEMA (2000b). *Prestandard and Commentary for the Seismic Rehabilitation of Buildings*, FEMA 356, Federal Emergency Management Agency, Washington, D.C.

Fujimoto, T., Nishiyama, I., Mukai, A., and Baba, T. (1995). "Test Results of Eccentrically Loaded Short Columns – Square CFT Columns," Proceedings of the Second Joint Technical Coordinating Committee (JTCC) on Composite and Hybrid Structures, Hawaii, June 26-28, 1995, National Science Foundation, Arlington, Virginia.

Fujinaga, T., Tsuda, K., and Matsui, C. (2000). "Hysteresis Model for Concrete-Filled Steel Square Tubular Beam-Columns," Proceedings of the Twelfth World Conference on Earthquake Engineering, Auckland, New Zealand, January 30-February 4, 2000, New Zealand Society of Earthquake Engineering, Wellington, New Zealand.

Furlong, R. W. (1967). "Strength of Steel-Encased Concrete Beam Columns," *Journal of the Structural Division*, ASCE, Vol. 93, No. ST5, pp. 113-124.

Furlong, R. W. (1968). "Design of Steel-Encased Concrete Beam Columns," *Journal of the Structural Division*, ASCE, Vol. 94, No. ST1, pp. 267-281.

Gourley, B. C. and Hajjar, J. F. (1994). "A Synopsis of Studies of the Monotonic and Cyclic Behavior of Concrete-Filled Steel Tube Beam-Columns," Structural Engineering Report No. ST-94-1, Department of Civil Engineering, University of Minnesota, Minneapolis, Minnesota, February.

Gourley, B. C., Tort, C., Hajjar, J. F., and Schiller, P. H. (2001). "A Synopsis of Studies of the Monotonic and Cyclic Behavior of Concrete-Filled Steel Tube Beam-Columns," Structural Engineering Report No. ST-01-4, Department of Civil Engineering, University of Minnesota, Minneapolis, Minnesota, Version 3.0, December.

Grauers, M. (1993). "Composite Columns of Hollow Steel Sections Filled With High Strength Concrete," Ph.D. dissertation, Chalmers University, Goteborg, Sweden, June.

Gupta, A. and Krawinkler, H. (1999). "Seismic Demands for Performance Evaluation of Steel Moment Frame Structures," Report No. 132, John A. Blume Earthquake Engineering Center, Stanford University, June.

Gunderson, C. A. (2002). "Braced Frame Connections with Concrete-Filled Tube (CFT) Columns," M. S. thesis, Department of Civil Engineering, University of Washington, Seattle, Washington.

Hajjar, J. F. and Gourley, B. C. (1996). "Representation of Concrete-Filled Tube Cross-Section Strength," *Journal of Structural Engineering*, ASCE, Vol. 122, No. 11, November, pp. 1327-1336.

Hajjar, J. F. and Gourley, B. C. (1997a). "A Cyclic Nonlinear Model for Concrete-Filled Tubes. I. Formulation," *Journal of Structural Engineering*, ASCE, Vol. 123, No. 6, June, pp. 736-744.

Hajjar, J. F., Gourley, B. C., and Olson, M. C. (1997b). "A Cyclic Nonlinear Model for Concrete-Filled Tubes. II. Verification," *Journal of Structural Engineering*, ASCE, Vol. 123, No. 6, June, pp. 745-754.

Hajjar, J. F., Molodan, A., and Schiller, P. H. (1998). "A Distributed Plasticity Model for Cyclic Analysis of Concrete-Filled Steel Tube Beam-Columns and Composite Frames," *Engineering Structures*, Vol. 20, Nos. 4-6, April-June, pp. 398-412.

Hajjar, J. F. (2002). "Composite Steel and Concrete Structural Systems for Seismic Engineering," *Journal of Constructional Steel Research*, Vol. 58, Nos. 5-8, May-August 2002, pp. 703-723.

- Hamburger, R. O., (1998). "Performance Based Analysis and Design Procedure for Moment Resisting Steel Frames," Internal SAC Document, SAC Joint Venture, Sacramento, California.
- Inai, E. and Sakino, K. (1996). "Simulation of Flexural Behavior of Square Concrete Filled Steel Tubular Columns," Proceedings of the Third Joint Technical Coordinating Committee Meeting, U.S.-Japan Cooperative Research Program, Phase 5: Composite and Hybrid Structures, Hong Kong, December 12-14, 1996, National Science Foundation, Arlington, Virginia.
- Kamba, T., Kanatani, H., and Tabuchi, M. (1991). "Strength and Rigidity of Joint Panel of Concrete Filled CHS Column-to-Beam Connections," Proceedings of the Third International Conference on Steel-Concrete Composite Structures, Wakabayashi, M. (ed.), Fukuoka, Japan, September 26-29, 1991, Association for International Cooperation and Research in Steel-Concrete Composite Structures, pp. 189-194.
- Kanatani, H., Tabuchi, M., Kamba, T., Ji, H.-L., and Ishikawa, Mikio (1988). "A Study on Concrete Filled RHS Column to H Beam Connections," *Composite Construction in Steel and Concrete*, Proceedings of the Engineering Foundation Conference, June 7-12, 1987, Henniker, New Hampshire, American Society of Civil Engineers, New York, New York, pp. 614-635.
- Kanno, R. (1993). "Strength, Deformation, and Seismic Resistance of Joints Between Steel Beams and Reinforced Concrete Columns," Ph.D. dissertation, Vol. I, Department of Civil Engineering, Cornell University, Ithaca, New York, August.
- Kappos, A. J. (1997). "Seismic Damage Indices for RC Buildings: Evaluation of Concepts and Procedures" *Progress in Structural Engineering and Materials*, Vol. 1, No. 1, pp. 78-87.
- Kato, B. and Akiyama, H. (1969). "Inelastic Bar Subjected to Thrust and Cyclic Bending", *Journal of the Structural Division*, ASCE, ST1, pp. 33-56.
- Kawaguchi, J., Morino, S., Shirai, J. and Tatsuta, E. (1998). "Database and Structural Characteristics of CFT Beam-Columns," Proceedings of the Fifth Pacific Structural Steel Conference, Seoul, Korea, October 13-16, 1998.
- Kawaguchi, J. (2000). "Experimental Study on The Elastic-Plastic Behavior of Concrete-Filled Steel Tube Structures," Internal Report, Mie University, Tsu-shi, Japan, December.
- Kawaguchi, J. and Morino, S. (2001). "Experimental Study on Post-Local Buckling Behavior of CFT Beam-Columns under Cyclic Loading," *Journal of Structural Construction Engineering*, AIJ, No. 540, February, pp. 141-147.
- Kawano, A. and Matsui, C. (1988). "Experimental Study on Hysteretic Behavior of Concrete Filled Tubular Members under Repeated Axial Loading," Proceedings of the

Ninth World Conference on Earthquake Engineering, Tokyo-Kyoto, Japan, August 2-9, 1988, Japan Association for Earthquake Disaster Prevention, Tokyo, Japan, Vol. IV, pp. IV-133 - IV-138.

Kawano, A. and Matsui, C. (1997). "Buckling Behavior and Aseismic Properties of Concrete-Filled Tubular Members under Cyclic Axial Loading," *Composite Construction in Steel and Concrete III*, Buckner, C. D. and Shahrooz, B. M. (eds.), Proceedings of the Engineering Foundation Conference, Irsee, Germany, June 9-14, 1996, American Society of Civil Engineers, New York, New York, pp. 602-615.

Kawaguchi, J., Morino, S., and Sugimoto, T. (1997). "Elasto-Plastic Behavior of Concrete-Filled Steel Tubular Frames," *Composite Construction in Steel and Concrete III*, Proceedings of the Engineering Foundation Conference, Buckner, C. D. and Shahrooz, B. M. (eds.), Irsee, Germany, June 9-14, 1996, American Society of Civil Engineers, New York, New York, pp. 272-281.

Kawano, A. and Matsui, C. (2000). "New Connections Using Vertical Stiffeners Between H-Shaped Beams and Hollow or Concrete-filled Square Tubular Columns," *Composite Construction in Steel and Concrete III*, Proceedings of the Engineering Foundation Conference, Buckner, C. D. and Shahrooz, B. M. (eds.), Irsee, Germany, June 9-14, 1996, American Society of Civil Engineers, New York, New York, pp. 172-185.

Koester, D. B., Yura, J. A., and Jirsa, J. O. (2000). "Behavior of Moment Connections Between Concrete-filled Steel Tube Columns and Wide Flange Steel Beams Subjected to Seismic Loads," Proceedings of the Twelfth World Conference on Earthquake Engineering, Auckland, New Zealand, January 30-February 4, 2000, New Zealand Society of Earthquake Engineering, Wellington, New Zealand.

Koester, D. B. (2000). "Panel Zone Behavior of Moment Connections Between Rectangular Concrete Filled Steel Tubes and Wide Flange Beams," Ph.D. dissertation, University of Texas, Austin, Texas.

Kradzig, W. B., Meyer, I. F., and Meskouris, K. (1989), "Damage Evolution in Reinforced Concrete Members Under Cyclic Loading," Proceedings Fifth International Conference on Structural Safety and Reliability (ICOSSAR 89), San Francisco, California, August 7-11, 1989, Vol. II, pp. 795-802.

Krawinkler, H., (1998). "Issues and Challenges in Performance Based Seismic Design," Proceedings of the First Structural Engineers World Congress, San Francisco, California, July 18-23, 1998, Elsevier Science Ltd., Oxford, United Kingdom.

Liu, Z. and Goel, S. C. (1987). "Cyclic Load Behavior of Concrete-Filled Tubular Braces," Research Report No. UMCE 87-3, Department of Civil Engineering, The University of Michigan, Ann Arbor, Michigan, April.

- Lu, Y. and Kennedy, D. (1992). "The Flexural Behavior of Concrete-Filled Hollow Structural Sections," Structural Engineering Report 178, Department of Civil Engineering, University of Alberta, Edmonton, Alberta, Canada, April.
- Lu, Y. and Kennedy, D. (1994). "The Flexural Behavior of Concrete-Filled Hollow Structural Sections," *Canadian Journal of Civil Engineering*, Vol. 21, No. 1, February, pp. 11-130.
- Lundberg, J. E. and Galambos, T. V. (1996). "Load and Resistance Factor Design of Composite Columns," *Structural Safety*, Vol. 18, No. 2-3, pp. 169-177.
- Lybas, J. M. and Sozen, M. A. "Effect of Beam Strength and Stiffness on Dynamic Behavior of Reinforced Concrete Coupled Walls," Internal Report, Department of Civil Engineering, University of Illinois, Urbana, Illinois, July.
- Matsui, C. (1986). "Strength and Deformation Capacity of Frames Composed of Wide Flange Beams and Concrete Filled Square Steel Tubular Columns," Proceedings of the Pacific Structural Steel Conference, Auckland, New Zealand, August 5-8, 1986, New Zealand Society for Earthquake Engineering, Wellington, New Zealand, Vol. 2, pp. 169-181.
- Matsui, C. and Kawano, A. (1988). "Strength and Behavior of Concrete-Filled Tubular Trusses," Proceedings of the International Specialty Conference on Concrete Filled Steel Tubular Structures, Zhong, S.-T. (ed.), Harbin, China, August 1988, pp. 113-119.
- McCabe S. L. and Hall W. J. (1989). "Assessment of Seismic Structural Damage," *Journal of Structural Engineering*, ASCE, Vol. 115, No. 9, September, pp. 2166-2183.
- Mehanny, S. S. F. and Deierlein, G. G. (2000). "Modeling of Assessment of Seismic Performance of Composite Frames with Reinforced Concrete Columns and Steel Beams," Report No. 135, John A. Blume Earthquake Engineering Center, Stanford University, August.
- Mehanny S. S. F. and Deierlein G. G., (2001). "Seismic Damage and Collapse Assessment of Composite Moment Frames," *Journal of Structural Engineering*, ASCE, Vol. 127, No. 9, September, pp. 1045-1053.
- Morino, S., Kawaguchi, J., Yasuzaki, C., and Kanazawa, S. (1993). "Behavior of Concrete-Filled Steel Tubular Three-Dimensional Subassemblages," Composite Construction in Steel and Concrete II, Easterling, W. S. and Roddis, W. M. (eds.), Engineering Foundation, ASCE, New York, NY, pp. 726-741.
- Morino, S. (2000). "Recent Developments on CFT Column Systems - U.S.-Japan Cooperative Earthquake Research Program," *Composite and Hybrid Structures*, Proceedings of the Sixth ASCCS International Conference on Steel-Concrete Composite Structures, Xiao, Y. and Mahin, S. A. (eds.), Los Angeles, California, March 22-24,

2000, Association for International Cooperation and Research in Steel-Concrete Composite Structures, Los Angeles, California, pp. 531-538

Nakahara, H., Sakino, K. and Inai, E. (1998). "Investigation of Concrete-Filled Steel Tubes Under Cyclic Bending and Buckling," *Transactions of the Japan Concrete Institute*, Vol. 20, pp. 171-178.

Nakahara, H. and Sakino, K. (1998). "Axial Compressive and Uniform Bending Tests of High Strength Concrete Filled Square Steel Tubular Columns," Proceedings of the Fifth Pacific Structural Steel Conference, Seoul, Korea, October 13-16, 1998, pp. 943-948.

Nishiyama, Morino, S., Sakino, K., Nakahara, H., Fujimoto, T., Mukai, A., Inai, E., Kai, M., Tokinoya, H., Fukumoto, T., Mori, K., Yoshioka, K., Mori, O., Yonezawa, K., Uchikoshi, M., and Hayashi, Y. (2002). "Summary of Research on Concrete-filled Structural Steel Tube Column System Carried Out Under The US-JAPAN Cooperative Research Program on Composite and Hybrid Structures," BRI Research Paper No. 147, Building Research Institute, Tsukuba, Japan, January.

O'Shea, M. D. and Bridge, R. Q. (1997). "Behaviour of Thin-Walled Box Sections with Lateral Restraint," *Research Report No. R739*, School of Civil Engineering, University of Sydney, Sydney, Australia, March.

Park Y. and Ang A. H. S. (1985). "Mechanistic Seismic Damage Model for Reinforced Concrete," *Journal of Structural Engineering*, ASCE, Vol. 111, No. 4, April, pp. 722-739.

Peng, S., Ricles, J. M., and Lu, L. (2000). "Full-scale Testing of Seismically Resistant Moment Connections For Concrete-filled Tube Column-to-WF Beam Hybrid Systems," *Composite and Hybrid Structures*, Proceedings of the Sixth ASCCS International Conference on Steel-Concrete Composite Structures, Xiao, Y. and Mahin, S. A. (eds.), Los Angeles, California, March 22-24, 2000, Association for International Cooperation and Research in Steel-Concrete Composite Structures, Los Angeles, California, pp. 591-598.

Peng, S. (2001). "Seismic Resistant Connections for Concrete-Filled Tube Column-to-WF Beam Moment Resisting Frames," Ph.D. dissertation, Department of Civil Engineering, Lehigh University, Bethlehem, Pennsylvania, March.

Rao, P. S., Sarma, B. S., Lakshmanan, N., and Stangenberg, F. (1998). "Damage Model for Reinforced Concrete Elements under Cyclic Loading," *ACI Materials Journal*, ACI, Vol. 95, No. 6, November-December, pp. 682-690.

Roufaiel M. S. L. and Meyer, C. (1987). "Analytical Modelling of Hysteretic Behavior of R/C Frames," *Journal of Structural Engineering*, ASCE, Vol. 113, No. 3, March, pp. 429-444.

- Ricles, J. M., Lu, L.-W., Sooi, T.-K., Vermaas, G. W., and Graham, W. W., Jr. (1995). "Seismic Performance of Concrete Filled Tube Column-to-WF Beam Moment Connections," Proceedings of the ACI Fall Conference 1995, American Concrete Institute, Detroit, Michigan.
- Ricles, J. M., Lu, L.-W., Graham, W. W., Jr., and Vermaas, G. W. (1997). "Seismic Performance of CFT Column-WF Beam Rigid Connections," *Composite Construction in Steel and Concrete III*, Buckner, C. D. and Shahrooz, B. M. (eds.), Proceedings of the Engineering Foundation Conference, Irsee, Germany, June 9-14, 1996, American Society of Civil Engineers, New York, New York, pp. 282-297.
- Sakino, K. and Ishibashi, H. (1985). "Experimental Studies on Concrete Filled Square Steel Tubular Short Columns Subjected to Cyclic Shearing Force and Constant Axial Force," *Transactions of the Architectural Institute of Japan*, No. 353, pp. 81-89.
- Schneider, S. P. (1998). "Axially Loaded Concrete-Filled Steel Tubes," *Journal of Structural Engineering*, ASCE, Vol. 124, No. 10, October, pp. 1125-1138.
- Shakir-Khalil, H. and Zeghiche, Z. (1989). "Experimental Behavior of Concrete-Filled Rolled Rectangular Hollow-Section Columns," *The Structural Engineer*, Vol. 67, No. 19, pp. 345-353.
- Shakir-Khalil, H. and Mouli, M. (1990). "Further Tests on Concrete-Filled Rectangular Hollow-Section Columns," *The Structural Engineer*, Vol. 68, No. 20, pp. 405-413.
- Shakir-Khalil, H. (1993). "Connection of Steel Beams to Concrete-Filled Tubes," Proceedings of the Fifth International Symposium on Tubular Structures, Nottingham, England, U.K., August, pp. 195-203.
- Shakir-Khalil, H. (1994). "Experimental Study of Concrete-Filled Rectangular Hollow Section Columns," *Structural Engineering Review*, Vol. 6, No. 2, pp. 85-96.
- Shakir-Khalil, H. and Al-Rawdan, A. (1995). "Behaviour of Concrete-Filled Tubular Edge Columns," Proceedings, Istanbul, Turkey, June.
- Shakir-Khalil, H. and Mahmoud, M. A. (1995). "Steel Beam Connections to Concrete-Filled Tubular Columns," Nordic Steel Construction Conference '95, Sweden, June.
- Sully, R. M. and Hancock, G. J. (1996). "Behavior of Cold-Formed SHS Beam-Columns," *Journal of Structural Engineering*, ASCE, Vol. 122, No. 3, pp. 326-336.
- Tomii, M. and Sakino, K. (1979a). "Experimental Studies on the Ultimate Moment of Concrete Filled Square Steel Tubular Beam-Columns," *Transactions of the Architectural Institute of Japan*, No. 275, January, pp. 55-63.

Tomii, M. and Sakino, K. (1979b). "Experimental Studies on Concrete Filled Square Steel Tubular Beam-Columns Subjected to Monotonic Shearing Force and Constant Axial Force," *Transactions of the Architectural Institute of Japan*, No. 281, July, pp. 81-90.

Varma, A. H. (2000). "Seismic Behavior, Analysis, and Design of High Strength Square Concrete Filled Steel Tube (CFT) Columns," Ph.D. dissertation, Department of Civil Engineering, Lehigh University, Bethlehem, Pennsylvania, November.

Varma, A. H., Ricles, J. M., Sause, R., Hull, B. K., and Lu, L.-W. (2001). "An Experimental Evaluation of High Strength Square CFT Columns," *Special Publication on Composite Steel-Reinforced Concrete Structures -- In Honor of the Late Dr. Walter P. Moore, Jr.*, ACI SP-196, Aboutaha, R. S. and Bracci, J. M. (eds.), American Concrete Institute, Detroit, Michigan, pp. 51-86.

Varma, A. H., Ricles, J. M., Sause, R., Lu L. (2002a). "Experimental Behavior of High Strength Square Concrete-Filled Steel Tube Beam-Columns," *Journal of Structural Engineering*, ASCE, Vol. 128, No. 3, March, pp. 309-318.

Varma, A. H., Ricles, J. M., Sause, R., Lu L. (2002b). "Seismic Behavior and Modeling of High-Strength Composite Concrete-Filled Steel Tube (CFT) Beam-Columns," *Journal of Constructional Steel Research*, Volume 58, Nos. 5-8, pp. 725-758.

Vermaas, G. W. (1995). "Seismic Performance of Concrete Filled Steel Tube to Wide Flange Beam Moment Connections With Diaphragms," M.S. thesis, Department of Civil Engineering, Lehigh University, Bethlehem, Pennsylvania, December.

VISION 2000 (1995). *A Framework for Performance-Based Earthquake Engineering*, Structural Engineers Association of California, Sacramento, California.

Wang Y. C. (1999). "Tests on Slender Composite Columns," *Journal of Constructional Steel Research*, Volume 49, No. 1, January, pp. 25-41.

Wen, Y. K., (1995). "Building Reliability and Code Calibration," *Earthquake Spectra*, EERI, Vol. 11, No. 2, pp. 269-296.

Wen, Y. K., (2001). "Reliability and Performance-Based Design," *Structural Safety*, Volume 23, Issue 4, October, pp. 407-428.

Williams, M. S. and Sexsmith, R. G. (1995). "Seismic Damage Indices for Concrete Structures: A State-of-the-Art Review," *Earthquake Spectra*, EERI, Vol. 11, No. 2, pp. 319-349.

Wright, H. D. (1993). "Buckling of Plates in Contact with a Rigid Medium," *The Structural Engineer*, Vol. 71, No. 12, June 15, 1993, pp. 209-215.